Study of $B^0 \to \rho\rho$ Decays with the Belle Experiment

Pit Vanhoefer

Ludwig-Maximilians-Universität
Department für Physik

München 2015

Study of $B^0 \to \rho\rho$ Decays with the Belle Experiment

Dissertation an der
Ludwig-Maximilians-Universität
Department für Physik

vorgelegt von Pit Vanhoefer
aus Lauf a.d. Pegnitz

München 12.3.2015

Erstgutachter: Prof. Dr. Christian Kiesling
Zweitgutachter: Prof. Dr. Thomas Kuhr
Tag der mündlichen Prüfung: 18.5.2015

Weitere Mitglieder des Prüfungskomitees:
Vorsitzender: Prof. Dr. Steffan Hoffmann
Schriftführer: Prof. Dr. Otmar Biebel
Ersatz: Prof. Dr. Gerhhard Buchalla
Weiterer Ersatz: Prof. Dr. Ulrich Schollwck

Abstract

We present a measurement of the branching fraction of $B^0 \to \rho^+\rho^-$ decays, the fraction of longitudinally polarized $\rho^\pm$ mesons and the CP violating parameters in the decay. The results are obtained from Belle's final data set of 772×10^6 $B\bar{B}$ pairs, collected at the $\Upsilon(4S)$ resonance at the asymmetric e^+e^- collider KEKB. We obtain

$$\begin{aligned}
\mathcal{B}(B^0 \to \rho^+\rho^-) &= (28.3 \pm 1.5\ (\text{stat}) \pm 1.5\ (\text{syst})) \times 10^{-6}, \\
f_L &= 0.988 \pm 0.012\ (\text{stat}) \pm 0.023\ (\text{syst}), \\
\mathcal{S}_{CP} &= -0.13 \pm 0.15\ (\text{stat}) \pm 0.06\ (\text{syst}), \\
\mathcal{A}_{CP} &= 0.00 \pm 0.10\ (\text{stat}) \pm 0.08\ (\text{syst}).
\end{aligned}$$

This is currently the most precise measurement of the branching fraction and the longitudinal polarization fraction as well as the tightest constraint on CP violation in this decay. We use the result together with our measurement of the branching fraction of $B^0 \to \rho^0\rho^0$ and the fraction of longitudinally polarized ρ^0 mesons in the decay

$$\begin{aligned}
\mathcal{B}(B^0 \to \rho^0\rho^0) &= (1.02 \pm 0.30\ (\text{stat}) \pm 0.15\ (\text{syst})) \times 10^{-6}, \\
f_L^{00} &= 0.21^{+0.18}_{-0.22}\ (\text{stat}) \pm 0.15\ (\text{syst}),
\end{aligned}$$

and an early Belle measurement of $B^\pm \to \rho^\pm\rho^0$ decays to obtain a constraint on the internal angle ϕ_2 of CKM unitarity triangle. We obtain two solutions with

$$\phi_2 = (93.6 \pm 10.7)^\circ, \tag{1}$$

being best compatible with other SM-based fits to the data.

Zusammenfassung

Diese Arbeit stellt eine Messung der Zerfallsrate von $B^0 \to \rho^+\rho^-$ Zerfällen, des Anteils an longitudinal polarisierten $\rho^\pm$ Mesonen und der CP verletzenden Parametern in diesem Zerfall vor. Dafür wurde Belles kompletter Datensatz von 772×10^6 $B\bar{B}$ Paaren analysiert. Diese wurden an der $\Upsilon(4S)$ Resonanz am asymmetrischen e^+e^- Speicherring KEKB erzeugt. Wir erhalten folgende Ergebnisse

$$\begin{aligned}
\mathcal{B}(B^0 \to \rho^+\rho^-) &= (28.3 \pm 1.5\ (\text{stat}) \pm 1.5\ (\text{syst})) \times 10^{-6}, \\
f_L &= 0.988 \pm 0.012\ (\text{stat}) \pm 0.023\ (\text{syst}), \\
\mathcal{S}_{CP} &= -0.13 \pm 0.15\ (\text{stat}) \pm 0.06\ (\text{syst}), \\
\mathcal{A}_{CP} &= 0.00 \pm 0.10\ (\text{stat}) \pm 0.08\ (\text{syst}).
\end{aligned}$$

Dies ist die zurzeit genaueste Messung der Zerfallsrate und Polarisation sowie die genaueste Einschränkung von CP Verletzung in diesem Zerfall. Zusammen mit den Ergebnissen unserer Messung der Zerfallsrate von $B^0 \to \rho^0\rho^0$ Zerfällen und dem Anteil an longitudinal polarisierten ρ^0 Mesonen in dem Zerfall

$$\begin{aligned}
\mathcal{B}(B^0 \to \rho^0\rho^0) &= (1.02 \pm 0.30\ (\text{stat}) \pm 0.15\ (\text{syst})) \times 10^{-6}, \\
f_L^{00} &= 0.21^{+0.18}_{-0.22}\ (\text{stat}) \pm 0.15\ (\text{syst}),
\end{aligned}$$

und einer frühen Belle Messung von $B^\pm \to \rho^\pm\rho^0$ Zerfällen bestimmen wir den Winkel ϕ_2 des CKM Unitaritätsdreiecks. Wir erhalten zwei Lösungen, wobei

$$\phi_2 = (93.6 \pm 10.7)^\circ \tag{2}$$

am besten mit anderen Standardmodell Fits übereinstimmt.

Contents

Introduction

Reverting the observed expansion of the nowadays 2.7 K cold universe suggests that it originated from a very dense and hot phase almost 14 billion years ago, see Fig. 1. In the early times huge amounts of elementary particle-antiparticle pairs, such as quarks and leptons, were created from quantum fluctuations. As the universe cooled down through expansion, the particles began to form compounds. First the constituents of nuclei, which then formed the atoms and light elements, coalescing to stellar objects some million years later.

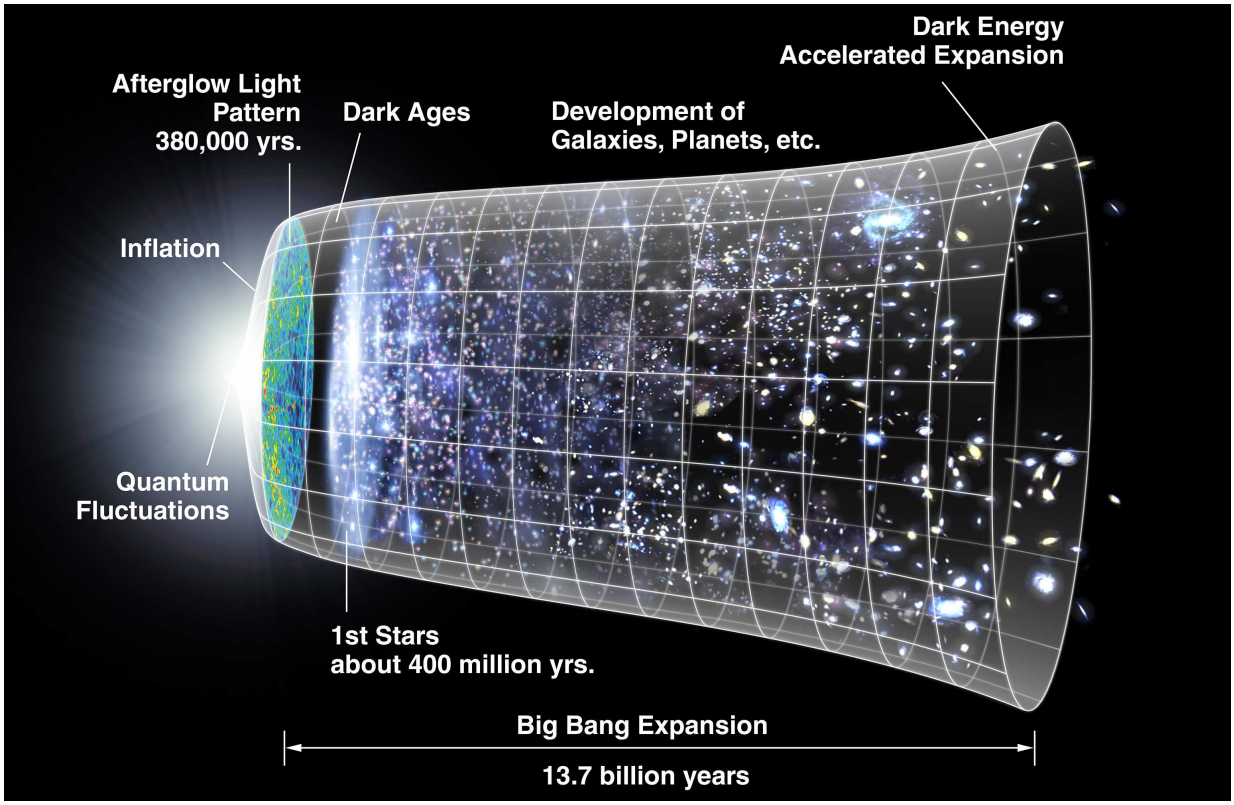

Figure 1: The evolution of the universe [1].

When particles meet their antiparticles, they annihilate and transform into energy, e.g. photons. Since particle-antiparticle pairs were created originally and all stable objects in the universe are made out of particles only, the question arises why did not all matter annihilate? Where did all the antiparticles go?
The present observed photon to matter ratio is about 10^9, and no evidence for a corresponding universal antimatter exists. Since the early dense phase excludes the possibility of

macroscopic separation, this asymmetry should be based on violations of matter-antimatter symmetries (C, CP) as well as of violations of the thermodynamic equilibrium in the early stage, as Sakharov postulated in 1976 [2].
The first CP-violating process was discovered in the neutral kaon sector by Cronin and Fitch in 1964 [3], a CP-violating mechanism has been successfully included into the Standard Model by Cabbibo, Kabayashi and Maskawa [4] and confirmed in many experiments later on. Although, this mechanism is able to describe all CP violating phenomena studied in laboratories within the experimentally achievable precision, it fails to explain the matter dominated universe. The generated amount of CP violation is by far not sufficient.
We expect to improve our understanding of nature through the discovery of new phenomena, which might require additional particles and introduce new CP violating sources. Since no such particles have been found in high-energy collisions, yet, challenging the theory with precision measurements is a promising way of finding the "New Physics".

B mesons are the heaviest flavored mesons we know and offer a rich field of phenomena to study. Also, due to relatively large CP violation in B decays, four experiments are/were dominantly dedicated to study this system. BaBar, located at SLAC (PEP-II), as well as Belle and Belle II, located at KEK, obtain the B mesons from electron positron collisions, while LHCb studies B mesons from proton-proton collisions at the LHC. BaBar was operating from the year 1999 until the end of 2008 and Belle's period of data taking ended in June 2010 after a run time of more than 10 years. The first runs of data taking for Belle's successor, Belle II, are expected in 2018. These B-factories are capable of producing huge amounts of $B\bar{B}$ pairs needed for the study of CP violation. By comparing B mesons decaying into a certain final state with the CP conjugated process, CP asymmetries can be measured.

This work presents the study of $B^0 \to \rho\rho$ decays observed with the Belle experiment and contributes to constrain fundamental parameters of the Standard Model related to the violation of the CP symmetry. We first present a brief theoretical overview in Chapter 1, followed by the description of the experimental setup in Chapter 2. The procedure of the measurement of the branching fraction, the longitudinal polarization fraction and the CP violating parameters of $B^0 \to \rho^+\rho^-$ decays is described in Chapters 3 and 4 and the results are presented and discussed in Chapters 5 to 7.
We have also performed the measurement of the branching fraction and longitudinal polarization fraction of $B^0 \to \rho^0\rho^0$ decays with the Belle data. As the measurement procedure has many similarities and the results are published [5], we restrict ourselves to $B^0 \to \rho^+\rho^-$ decays in the discussion of the measurement procedure.

Chapter 1

Theoretical Motivation

1.1 A Brief Introduction To The Standard Model

In the following, we will introduce the elementary particles and highlight a few properties of their interactions. Then we give a more general introduction to the structure of the Standard Model (SM), where more attention is paid to the electroweak interaction, as it is relevant for CP violating processes.
The SM is based on a few symmetry principles and a number of constants and successfully describes three of the four fundamental interactions of matter, see Table 1.1. Within the SM non-gravitational interactions of fermionic (spin-$\frac{1}{2}$) matter particles are described in relativistic and renormalizable quantum field theories (QFT) through the exchange of bosonic (spin-1) mediators, which couple to the corresponding "charge" of the interaction. For example, Quantum Electro Dynamics (QED) describes all electromagnetic phenomena through the exchange of a massless photon that couples to the electric charge [1]. Quantum Chromo Dynamics (QCD) describes the strong interaction, which holds together nuclei despite their coulomb repulsion, and Quantum Flavor Dynamics (QFD) describes the weak interaction, for example beta decays.

The 12 known particles that form matter are grouped in three families. Each family consists of two quarks (one up-type with charge $+\frac{2}{3}$ and one down-type with charge $-\frac{1}{3}$) and two leptons (one charged and one neutral). The three families represent a mass hierarchy, with the first one (u, d, e^-, ν_e) being the lightest. Fig. 1.1 shows these families together with the four known force-mediating bosons and the Higgs boson. For each fermionic particle a corresponding antiparticle exists which has the same mass but opposite charge.

Quarks come in six different flavors: u, d, c, s, t, b and are the only fermions that carry the quantum number color (green, red, blue), the "charge" of the strong interaction. Quarks cannot exist alone, but only in composite systems, where the sum of all colors is neutral (either all three colors or color-anticolor). This phenomenon is known as confinement and originates in the running coupling of the strong interaction, which is almost negligible (asymptotic freedom) when the distance between two quarks goes to zero and becomes stronger with larger

[1] Because the photon is massless, the electromagnetic potential is proportional to $1/r$ and the range of the interaction is infinite. If the exchange particle has a mass m, the potential is multiplied by $e^{-r/\lambda}$, whith the compton wave length $\lambda = \hbar/mc$.

Interaction	Strong	Weak	EM	Gravitation
Mediator	gluon g	$W^{\pm}, Z^0$	γ	graviton(?)
Range(m)	10^{-15}	10^{-18}	∞	∞
Potential distance dependency	$\alpha r^{-1} + \beta r$	$e^{-r/\lambda}/r$	$1/r$	$1/r$
Relative strength	1	10^{-5}	1/137	10^{-38}

Table 1.1: The fundamental interactions.

distances. When separating two quarks, at some point enough binding energy becomes available to create a new quark-antiquark pair that neutralizes the color charge of each separated quark. Therefore, the range of the strong interaction is limited to distances of the order of the size of a nuclei (∼fm), and the nature of quarks can only be studied in systems which are composed of quarks, called hadrons.
Two kinds of hadrons exist: quark-antiquark pairs called mesons, e.g. the pion, and those who consists out of three quarks [2], called baryons, e.g. the proton. Hadronic systems are held together through the exchange of colored gluons (color-anticolor), the mediators of the strong interaction. Up and down type quarks carry $+\frac{2}{3}$ and $-\frac{1}{3}$ electric charge, respectively, consequently the hadron's charge is an integer.

The leptons can be separated in two groups, where the electron e^- and its heavier brothers, the muon μ^- and the tau τ^-, have an electric charge of -1, while the neutrinos are chargeless and therefore only interact weakly. The mediators of the weak interaction are the heavy bosons $W^{\pm}$ and Z^0.

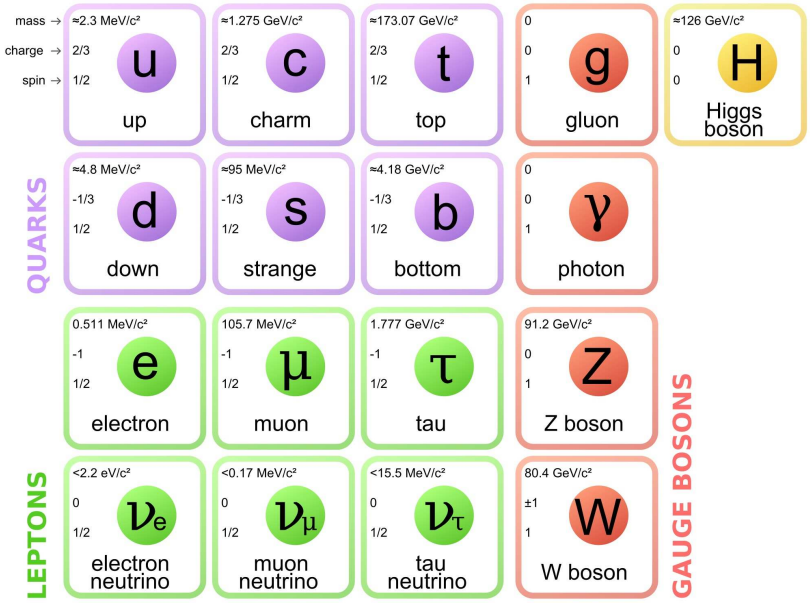

Figure 1.1: The elementary particles of the SM [6].

Symmetry plays a very important role in physics. In 1918, Emmy Noether proved her famous theorem [7], which states that any action which is invariant under a local symmetry transformation leads to a corresponding conservation law and vice versa. For example, the homogeneity of space and time leads to momentum and energy conservation, respectively,

[2] Recently systems composed out of more quarks have caught more attention again, for example the meson f_0 can also be described as a tetraquark.

and the isotropy of space leads to angular momentum conversation.
Symmetries also plays a crucial role in the SM. The SM is a local gauge theory [8], made up from the internal symmetry groups $SU(3)_{\text{color}}$ for the strong, $SU(2)_{\text{L}}$ for the weak and $U(1)_{\text{Q}}$ for the electromagnetic interaction. The numbers represent the respective degrees of freedom of the group and the last two groups can be further unified to $SU(2)_{\text{L}} \otimes U(1)_{\text{Y}}$, the internal symmetry of the electroweak theory. Thus, the SM describes two kind of phenomena, strong and electroweak, and its Lagrangian can be written as

$$\mathcal{L}_{\text{SM}} = \mathcal{L}_{\text{QCD}} + \mathcal{L}_{\text{EW}}. \tag{1.1}$$

The action $\int d^4x\mathcal{L}$ is required to be invariant under local gauge transformations which is realized by adding the gauge fields of the force carriers to the free fermion fields and results in a conserved charge, e.g. the electric charge for $U(1)$ [3]. Demanding that one can freely rotate among the n degrees of freedom defines rotation operations of dimension $n\times n$.

A fundamental representation of $SU(3)$ are quark triplets $(Q^i_{\text{red}}, Q^i_{\text{green}}Q^i_{\text{blue}})^T$, where the three eigenstates correspond to the three color charges and i labels the quark flavor. The rotations can be realized by $n^2 - 1 = 8$ generators, the Gell-Mann matrices, where each matrix gives rise to a gluon with a certain color-anticolor combination: the eight gluons are eigenstates of the adjoint representation of $SU(3)$. Because the range of the strong interaction is found to be limited, the symmetry group $U(3)$ is excluded as it would also allow for one color neutral gluon which has not been observed.

A remarkable feature of the weak interaction is the maximal violation of parity. The weak interaction involves only left-handed particles and right-handed antiparticles. To fit the experimental data, the theory of the weak interaction has been constructed with a (V-A) structure and has been successfully unified with the electromagnetic interaction by Glashow, Salem and Weinberg [10, 11] later on.

The γ_5 matrix [12] allows to project onto a certain helicity component of the fermion spinor ψ,

$$\psi_L = \frac{1}{2}(1-\gamma_5)\psi, \qquad \psi_R = \frac{1}{2}(1+\gamma_5)\psi, \tag{1.2}$$

and the fermion fields are grouped in left-handed doublets with a weak isospin of $T = \pm\frac{1}{2}$, and right-handed singlets ($T = 0$). For the first family these multiplets take the form

$$Q_L = \begin{pmatrix} u_L \\ d_L \end{pmatrix}, u_R, d_R, \tag{1.3}$$

$$L_L = \begin{pmatrix} e_L \\ \nu_L \end{pmatrix}, e_R, \tag{1.4}$$

the other two families are equally arranged and right-handed neutrinos have not been observed, so far. The $W^{\pm}$ couples only to charged leptons and neutrinos of the same family but allows for flavor changing processes of quarks, as we will see later on.

The three generators of the weak isopsin group $SU(2)$ are $T^i = \frac{1}{2}\sigma^i$ $(i = 1, 2, 3)$, where σ^i are the Pauli matrices. Similar to the eight gluons, one postulates an isotriplet of massless vector

[3] Local gauge invariance of a free fermionic field is only possible if a (4-vector) interaction field is added to the Lagrangian and a gauge covariant derivative is introduced. The interaction then depends on the gauge symmetry [9]

fields W_μ^i which couple to the fermions with a strength g. $U(1)_Y$ has only one generator, the weak hypercharge Y, which is related to the electrical charge Q by

$$Y = 2(Q - T_z), \tag{1.5}$$

where T_z is the conserved z-component of the weak isopsin T. Associated to Y is one additional massless vector field B^μ with a coupling g'. In analogy to the interaction part of the Lagrangian of QED, $\mathcal{L}_{\text{QED}}^{\text{inter}} = -ie j_\mu^{\text{em}} A^\mu$, where $j_\mu^{\text{em}} = \bar{\psi} e \gamma^\mu \psi$ is the electromagnetic current, e the electric charge and A^μ the photon field, one can now write down a Lagrangian of the interaction leading to the electroweak force

$$\mathcal{L}_{\text{EW}}^{\text{inter}} = -ig j_\mu^i W^{i\mu} - i\frac{1}{2} g' j_\mu^Y B^\mu, \tag{1.6}$$

where j_μ^i and j_μ^Y are $SU(2)$ invariant currents. This allows to construct two charged bosons

$$W^{\pm\mu} = \frac{1}{2}(W^{1\mu} \mp W^{2\mu}), \tag{1.7}$$

and two neutral ones

$$Z^\mu = (-B^\mu \sin\theta_W + W^{3\mu} \cos\theta_W), \tag{1.8}$$

$$A^\mu = (B^\mu \cos\theta_W + W^{3\mu} \sin\theta_W), \tag{1.9}$$

which are the four known vector bosons $W^\pm$, Z^0 and γ. θ_W is the weak mixing (Weinberg) angle. Expressing the neutral current (NC) part in Eq. (1.6) in terms of the neutral bosons yields

$$\mathcal{L}_{\text{EW}}^{\text{NC}} = -ig j_\mu^3 W^{3\mu} - i\frac{1}{2} g' j_\mu^Y B^\mu \tag{1.10}$$

$$= -i\big(g \sin\theta_W j_\mu^3 + g' \cos\theta_W \frac{j_\mu^Y}{2}\big) A^\mu \tag{1.11}$$

$$-i\big(g \cos\theta_W j_\mu^3 - g' \sin\theta_W \frac{j_\mu^Y}{2}\big) Z^\mu. \tag{1.12}$$

Identifying $j_\mu^{\text{em}} = j_\mu^3 + \frac{1}{2} j_\mu^Y$ links together the three couplings

$$g \sin\theta_W = g' \cos\theta_W = e. \tag{1.13}$$

This relation establishes the electroweak unification. The Lagrangian for the electroweak theory of massless particles reads

$$\mathcal{L}_{\text{EW}}^{\text{kin}} = [\sum_{\text{fermions}} (D^\mu \psi)^\dagger (D_\mu \psi)] - \frac{1}{4} W_{\mu\nu}^i W^{i\mu\nu} - \frac{1}{4} B_{\mu\nu} B^{\mu\nu} \tag{1.14}$$

with

$$W_{\mu\nu}^i = \delta_\nu W_\mu^i - \delta_\mu W_\nu^i + g\epsilon^{ijk} W_\mu^j W_\nu^k, \tag{1.15}$$

$$B_{\mu\nu} = \delta_\nu B_\mu - \delta_\mu B_\nu, \tag{1.16}$$

and the covariant derivative

$$D_\mu = \delta_\mu + igTW_\mu + i\frac{g'}{2} B_\mu Y. \tag{1.17}$$

So far, all interaction fields are massless. This does not describe the observed heavy particles $W^{\pm}$ and Z^0, whose heavy masses weakens the strength of their interaction at low energies. Unfortunately, simply adding a mass term, e.g. $mZ_\mu Z^\mu$, to the Lagrangian violates the required gauge symmetry. In order to generate masses, the $SU(2) \times U(1)$ symmetry has to be spontaneously broken. This is known as the Brout-Englert-Higgs mechanism [13–15] which adds a new complex scalar doublet of $SU(2)$ with a hypercharge Y=1

$$\phi = \begin{pmatrix} \phi_1 + i\phi_2 \\ \phi_3 + i\phi_4 \end{pmatrix} = \begin{pmatrix} \phi^+ \\ \phi^0 \end{pmatrix} \tag{1.18}$$

and a Lagrangian of the form

$$\mathcal{L}_{\text{Higgs}} = (D^\mu \phi)^\dagger (D_\mu \phi) - \mu^2 \phi^\dagger \phi - \lambda (\phi^\dagger \phi)^2 \tag{1.19}$$

to the model. D^μ is the covariant derivative from Eq. (1.17). One can choose the ground state of the field to be $\phi_3 = v$ and $\phi_1 = \phi_2 = \phi_4 = 0$. Then its vacuum expectation value $v =< \phi >= \sqrt{\frac{-\mu^2}{2\lambda}}$ is nonzero for $\lambda > 0$ and therefore breaks the $SU(2)_{\text{L}} \otimes U(1)_{\text{Y}}$ symmetry. The electromagnetic gauge $U(1)_Q$ remains invariant, as one can see when applying the charge operator Q from Eq. (1.5) to $< \phi >$: $Q < \phi >= 0$. Inserting the ground state in the kinetic part of Eq. (1.19) results in mass terms for the three massive gauge bosons;

$$M_{W^\pm} = \frac{1}{2} v g \qquad\qquad M_Z = \frac{1}{2} v \sqrt{g^2 + g'^2}. \tag{1.20}$$

Gauge invariant fermion masses arise from a coupling to the Higgs doublet; e.g. for down type quarks

$$\mathcal{L}_{\text{m}}^{T_z = -\frac{1}{2}} = -Y^d (\bar{Q}_L^T \phi d_R) + h.c., \tag{1.21}$$

where Y^d is the Yukawa coupling of the corresponding quark. Inserting the Higgs ground state results in $m_d = \frac{1}{2} v Y^d$. The masses of the charged leptons are generated analogously, and without right-handed neutrinos, no neutrino mass term can be constructed.
Considering more than one generation, quark flavor mixing can occur. Let's denote the multiplets of the three generations of quarks with

$$Q_L^i = \begin{pmatrix} u_L^i \\ d_L^i \end{pmatrix} = \left(\begin{pmatrix} u_L \\ d_L \end{pmatrix}, \begin{pmatrix} c_L \\ s_L \end{pmatrix}, \begin{pmatrix} t_L \\ b_L \end{pmatrix} \right), \tag{1.22}$$

$$u_R^i = (u_R, c_R, t_R) \quad \text{and} \quad d_R^i = (d_R, s_R, b_R). \tag{1.23}$$

Then the Yukawa couplings for flavor currents with two flavors i, j read

$$\mathcal{L}_{\text{Yukawa}} = -(Y_u^{ij} \bar{Q}_L^{iT} \phi u_R^j + Y_d^{ij} \bar{Q}_L^{iT} \phi d_R^j) + h.c., \tag{1.24}$$

where $Y_{f=u,d}$ are complex 3×3 matrices of Yukawa couplings. The transformation matrix can be diagonalized, in order to rotate into a basis of the fermion fields, where the masses are the eigenvalues of

$$Y_M = U_L^\dagger Y_f U_R, \tag{1.25}$$

with unitary transformations U_L, U_R. When applying this to the Lagrangian, all unitary transformations cancel except for the ones in the couplings to the $W^\pm$

$$j^\pm = g \bar{u}_L^i \gamma_\mu (U_L^{u\dagger} U_R^d)^{ij} d_L^j, \tag{1.26}$$

where $(U_L^{u\dagger} U_R^d) = V_{\mathrm{CKM}}$ is known as the CKM matrix and allows for quark flavor mixing. A complex V_{CKM} matrix can lead to a violation of the combined charge and parity symmetry, which will be discussed in the next section in more detail.

The SM was constructed to explain some experimentally observed phenomena. Many predictions follow from its structure and so far all examined ones are in excellent agreement with numerous experimental results [16–18]. A prominent example is the discovery of a Higgs boson in 2012 [19, 20]. It is fair to say that the SM is one of the best tested theories ever formulated.

Nevertheless, the SM has to be an approximation of a more fundamental theory. First of all, we have experimentally observed phenomena that are not explained by the SM, e.g. the observed matter dominated universe cannot be explained by SM mechanisms, as already stated in the Introduction.
Furthermore, neutrinos are massless in the SM. But they must have small masses to allow for neutrino flavor mixing, a process being formulated in the PMNS mechanism in 1967 [21, 22], one year before the first experimental indication was observed [23]. The electron neutrino flux from the sun showed a deficit of two third compared to SM predictions, because this fraction mixed into muon and tau neutrinos before arriving on earth. Neutrino mixing can be observed in terestial experiments, too, for example neutrinos from nuclear reactors or from interactions of cosmic rays with the atmosphere [24, 25]. These sources allow to examine also different neutrino flavor transitions. There are many ideas about the true nature of neutrinos, which can be added to the SM once experimentally verified.

We observe roughly five times more dark matter (DM) than ordinary matter in the universe. First of all, simulations of the evolution of the universe require DM to create the large scale structures we observe today [26]. Furthermore, the gravitational dynamics of large structure objects cannot be explained with ordinary matter alone [27, 28] and the existence of space-time bending mass can directly be observed through gravitational lensing of radiation from background objects [29]. DM certainly interacts gravitationally, maybe also weakly but neither electromagnetically nor strongly. The SM neutrinos alone cannot explain DM. They have very small masses and therefore are relativistic. Such a hot gas would have trouble forming smaller structures like galaxies. A significant amount of non-relativistic (cold) dark matter is required.
While high energy experiments examine the possibility to produce DM particles in collision, the direct search, as for example done by the experiments CRESST [30] and XENON [31], is a complementary approach to find new physics that is capable of explaining the above mentioned phenomena, as Einstein's general relativity is as persevering as the SM.

The existence of a vacuum energy density (dark energy) is postulated, to explain the observed accelerating expansion of the universe. Although it makes up roughly 70% of the energy budget of the universe, dark energy is the least understood phenomena. It could be related to the cosmological constant Λ in Einstein's field equation, but this would still not explain its origin.

There are also open questions in the SM on the theoretical side. Why is the weak scale, which is related to the mass of the weakly interacting bosons (Higgs mechanism), so much smaller than the planck scale, where gravity can no longer be neglected. Because the Higgs is a scalar particle (the only one in the SM), its mass is sensitive to new physics (e.g. quantum gravity) as their contributions to the mass cannot be compensated by renormalization in a

natural way. A precise fine tuning of the theory is needed, to match the measured value of the Higgs mass of 125 GeV, which does not seem to be natural. This so called the hierarchy problem [32, 33] can be avoided in extended theories such as supersymmetry (SUSY) [34]. In SUSY theories, each elementary particle has a corresponding super partner, whose spin differs by $\frac{1}{2}$. With this additional particle spectrum the fermionic loop contributions to the Higgs mass are canceled by corresponding bosonic contribution and vice versa, avoiding the necessity of fine-tuning.

It is also not understood why the strong interaction conserves the CP symmetry. The Lagrangian of QCD has terms that allow for a violation of CP due to a complex phase $\Theta_{CP}^{\text{strong}}$. However, measurements, of e.g. the electric dipole moments of a neutron [35], indicate that this phase is zero. A spontaneous broken global Peccei-Quinn symmetry can explain this behavior and would result in a new particle, the axion [36].

Not only because simplicity is regarded as beautiful, it is attractive to unify the various theories to one. While, for example, supersymmetric models allow for a unification of the strong and the electroweak theory, gravity resists. Combining the concepts of Einstein's general relativity and relativistic quantum mechanics (QM) is problematic, so far. While in general relativity the vacuum is regarded as "empty" space-time, in a QFT the vacuum exhibits zero point fluctuations of the fields everywhere in space. Trying to derive the cosmological constant from the QM vacuum energy density gives a huge discrepancy of the order of 10^{120} [37]. String theory, in particular M-theory [38], provides a mathematically consistent description, but no firm testable predictions exist.

Although, the SM is a complete theory, it is obvious that it is an approximation of a more fundamental theory. The question is, what is the scale at which new phenomena will appear. Many experiments are currently operating or in the planning/construction phase in order to challenge the SM (the particle and the cosmological one). Experimental particle physics has two complementary approaches: Either we find new particles at the energy frontier or deviations from the predictions of the SM at the precision frontier. In the latter case it is important to reduce the uncertainties on for example decay rates or asymmetries observables through more data and improved methods.
This work presents a study of decays of B mesons into final states that consist of two ρ mesons and are invariant under a CP transformation. The results from this study contribute to further constrain parameters of the SM related to the different properties of matter and antimatter.

1.2 CP Violation

The weak interaction does not only violate parity but also charge conjugation and time reversal. This implies that the laws of physics change under such a symmetry transformation, which will be explored in the following.

1.2.1 The C, P and T Symmetries

Charge conjugation C, transforms a particle A into its antiparticle $\bar{A}$ and therefore acts on its charge and other additive quantum numbers but is retaining its spin,

$$C|A\rangle = |\bar{A}\rangle. \tag{1.27}$$

In terms of quantum field theory, the C operator can be expressed through Dirac gamma matrices [12],$C = i\gamma^2\gamma^0$, for example, applied on a spinor field: $\psi \rightarrow \psi_C \equiv C\bar{\psi}$. C is violated maximally in the weak interaction. For example, left-handed antineutrinos (the charge conjugated partner of the left-handed neutrino) have not been observed so far.

Parity inversion P, is basically a reflection on the origin and flips the sign of a vector $\vec{x} = (x, y, z)^T$,

$$P(\vec{x}) = -\vec{x}, \tag{1.28}$$

where P can be identified with $P = \gamma^0$. Acting on a spinor gives: $\psi \rightarrow \psi_P \equiv \gamma^0\psi$. In general one can distinguish between the four following cases,

1. P(V) = -V, where V is a polar vector, e.g. the momentum $\vec{p}$,
2. P(A) = A, where A is a axial vector, e.g. the angular momentum $\vec{l}$,
3. P(S) = S, where S is a scalar, e.g. $\vec{p}_1 \cdot \vec{p}_2$,
4. P(P) = -P, where P is a pseudo-scalar, e.g. $\vec{p} \cdot \vec{l}$,

where $\vec{l} \equiv \vec{r} \times \vec{p}$ and $\vec{r}$ points from the center of the rotation to the reference point with momentum $\vec{p}$. As already mentioned, parity is maximally violated in the weak interaction. This first came to light in the $\theta - \tau$-puzzle which was solved by questioning the fundamental P-symmetry (T. Lee and C. Yang, Nobel price 1957) and was explicitly verified in the Wu experiment [39] in 1956. The left-handed nature of the neutrino was finally confirmed one year later by Goldhaber *et al.* [40].

Before these discoveries, the consensus was that these global symmetries were universal and therefore conserved as is the case in strong and electromagnetic interactions. Then, in 1964, the violation of the combined symmerty CP, which again was considered to be fundamental, was observed in K_L^0 decays into CP-even states ($\pi\pi$). This result, obtained by J. Cronin and V. Fitch, was awarded with the Nobel prize in 1980. The effect is rather small compared to the maximal violations in each symmetry alone.

Time reversal T, reverses the direction of time t:

$$T(t) = -t. \tag{1.29}$$

In an macroscopic sense, transformations under the T symmetry seem not to be invariant in general. The second law of thermodynamics gives a preferred direction of time, towards increasing entropy. An evident example is friction. An object sliding down some slope and dissipating kinetic energy through friction until it stops is very unlike to slide up while accelerating when the direction of time is reverted. In a microscopic sense, however, the

dynamics of a system are in general invariant under such a transformation.
The SM is described by a Lagrange density which is Lorentz invariant, local, hermitian and normal ordered. Because it is also quantized so that bosonic fields commute and fermionic fields anticommute, the symmetry CPT is a conserved symmetry [41]. Consequently, if CP is violated, T has to be violated, too, in order to conserve CPT [4].

The C and P eigenvalues are multiplicative quantum numbers.

1.2.2 Neutral Kaon System

Since CP violation was discovered in kaon decays, a short introduction to the phenomenology of the neutral kaon mixing is given [43,44]. The neutral kaon K^0 is composed of $(d\bar{s})$ and has strangeness quantum number $S = +1$. Kaons are produced via the strong interaction and decay weakly, dominantly into pions. Since flavor is not conserved in the weak interaction, $K^0 - \bar{K^0}$ transitions ($\Delta S = 2$) are possible. The two CP eigenstates are superpositions of the flavor states and are given by

$$|K_1\rangle = \frac{1}{\sqrt{2}}(|K^0\rangle + |\bar{K^0}\rangle) \quad \text{with} \quad CP|K_1\rangle = +1|K_1\rangle, \tag{1.30}$$

$$|K_2\rangle = \frac{1}{\sqrt{2}}(|K^0\rangle - |\bar{K^0}\rangle) \quad \text{with} \quad CP|K_2\rangle = -1|K_2\rangle. \tag{1.31}$$

If CP is conserved then only the decays $K_1 \to \pi\pi$ ($CP = +1$) and $K_2 \to \pi\pi\pi$ ($CP = -1$) are allowed, because the pion is a pseudo-scalar. The K^0 has mass of 498 MeV and the lighter pion's mass is almost 140 MeV [45]. Therefore the decay $K_2 \to \pi\pi\pi$ is suppressed by the available phase space and its lifetime is two orders of magnitude larger than for the K_1. J. Cronin and V. Fitch [3] studied kaon decays into two pions in a beam of kaons that lived long enough to theoretically consist entirely of CP-odd kaons. They observed a rate of

$$\frac{\Gamma(K_2 \to \pi\pi)}{\Gamma(K_2 \to \text{ all})} = (2.0 \pm 0.4) \times 10^{-3}. \tag{1.32}$$

The first CP violating process was discovered, the short and long living states called K_S^0 and K_L^0, respectively, were identified as mixtures of the CP eigenstates:

$$|K_S^0\rangle = \frac{1}{\sqrt{1+\epsilon^2}}(|K_1\rangle + \epsilon|K_2\rangle) \qquad |K_L^0\rangle = \frac{1}{\sqrt{1+\epsilon^2}}(|K_2\rangle + \epsilon|K_1\rangle), \tag{1.33}$$

with the small admixture parameter $|\epsilon| \sim 2 \times 10^{-3}$.

1.2.3 CKM Mechanism

As first postulated by Nicola Cabibbo (the C in CKM) in 1963 to explain flavor transitions in the charged weak interaction, the weak eigenstates of the quarks are linear combinations

[4] Indeed there are observables that allow the measurement of a T asymmetry in for example B decays [42] or electric dipole moments [35].

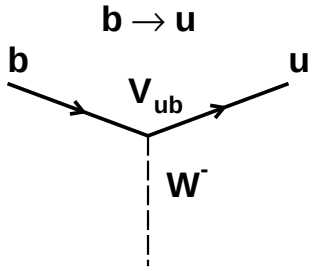

Figure 1.2: A b-quark becomes a u-quark through the emittance of a W^-. The weak charged current coupling is suppressed by the constant $|V_{ub}| \sim 0.004$.

of the mass eigenstates, that can be expressed by a rotation by the Cabibbo angle $\theta_C = 13.04°$ [46],

$$\begin{pmatrix} d' \\ s' \end{pmatrix}_{\text{weak}} = \begin{pmatrix} \cos\theta_C & \sin\theta_C \\ -\sin\theta_C & \cos\theta_C \end{pmatrix} \begin{pmatrix} d \\ s \end{pmatrix}_{\text{mass}} . \tag{1.34}$$

Back then, only the lightest quarks u, d, s were known. In order to incorporate CP violation, as observed in the kaon system, into the SM, Cabibbo's idea was extended to three generations of quark doublets by Kobayashi and Maskawa [4] in 1972. Two years later the charm quark was discovered as postulated by the GIM mechanism [47], the discovery of the bottom quark in 1977 and the top quark in 1995, both at the Fermilab, followed. For their successful model which, in addition to explaining the observed CP violation, also predicted a third generation quark doublet unknown at the time, Kobayashi and Maskawa were honored with the Nobel prize in 2008. The CKM mechanism takes the form

$$\begin{pmatrix} d' \\ s' \\ b' \end{pmatrix}_{\text{weak}} = V_{\text{CKM}} \begin{pmatrix} d \\ s \\ b \end{pmatrix}_{\text{mass}} \equiv \begin{pmatrix} V_{ud} & V_{us} & V_{ub} \\ V_{cd} & V_{cs} & V_{cb} \\ V_{td} & V_{ts} & V_{tb} \end{pmatrix} \begin{pmatrix} d \\ s \\ b \end{pmatrix}_{\text{mass}} , \tag{1.35}$$

where the matrix elements V_{ij} represent the probability of the transition of a quarks with flavor j to one with flavor i (Fig. 1.2), and have to be obtained experimentally.

So why are three generations needed to make CP violation possible? The number of independent physical parameters of a complex $n \times n$ mixing matrix V can be determined as follows [48]. The original $2n^2$ real parameters (V is complex) can be further reduced by requiring unitarity, which implies

$$V_{ik} V_{jk}^* = V_{ki} V_{kj}^* = \delta_{ij}, \tag{1.36}$$

to preserve probability. This removes half of the parameters. Also the quark fields have an arbitrary phase that can be rotated freely and absorbed in a phase convention: $V_{ij} \to e^{i(\phi(j)-\phi(i))} V_{ij}$. This removes an additional $2n-1$ parameters. Thus we have $n^2 - 2n + 1 = (n-1)^2$ independent parameters which can be translated to $n(n-1)/2$ rotation angles and $(n-1)(n-2)/2$ complex phases. At least one complex phase is required for a violation of the CP symmetry. $n = 3$ gives three angles θ_i, and one phase δ and is therefore the first representation of a quark mixing matrices that allows for CP violation. In addition, it

is required that quarks with equal charge can be distinguished by their masses or else the complex phase could be absorbed by a block-diagonal matrix which mixes the degenerated quarks. The parametrization chosen by Kobayashi and Maskawa is given by

$$V_{\mathrm{CKM}} = \begin{pmatrix} c_1 & -s_1c_3 & -s_1s_3 \\ s_1c_2 & c_1c_2c_3 - s_2s_3e^{i\delta} & c_1c_2s_3 + s_2c_3e^{i\delta} \\ s_1s_2 & c_1s_2c_3 + c_2s_3e^{i\delta} & c_1s_2s_3 - c_2c_3e^{i\delta} \end{pmatrix}, \tag{1.37}$$

where $s_i(c_i)$ is $\sin\theta_i(\cos\theta_i)$ for $i = 1, 2, 3$ and $\theta_1 = \theta_C$. The CKM matrix has an interesting hierarchy, the diagonal elements are approximately one and the remaining elements are smaller, whereas those which represent a transition over two generations are the smallest and close to zero. This characteristic is used in the Wolfenstein parametrization [49] in which the CKM matrix is expanded in terms of the parameter $\lambda \equiv \sin\theta_C = 0.221 \pm 0.002$,

$$V_{\mathrm{CKM}} = \begin{pmatrix} 1 - \lambda^2/2 & \lambda & A\lambda^3(\rho - i\eta) \\ -\lambda & 1 - \lambda^2/2 & A\lambda^2 \\ A\lambda^3(1 - \rho - i\eta) & -A\lambda^2 & 1 \end{pmatrix} + \mathcal{O}(\lambda^4). \tag{1.38}$$

The remaining real parameters are A, ρ and η, with $0 < A, \rho, \eta < 1$ and the deviation from its original form is negligible compared to the present experimental resolution.
The unitarity of the CKM matrix (see Eq. (1.36)) can be used to derive some very useful relations, for example,

$$\begin{array}{ccccccc} V_{ud}V_{ub}^* & + & V_{cd}V_{cb}^* & + & V_{td}V_{tb}^* & = & 0, \\ \mathcal{O}(\lambda^3) & & \mathcal{O}(\lambda^3) & & \mathcal{O}(\lambda^3) & & \end{array} . \tag{1.39}$$

being relevant for B decays. These relations can be expressed geometrically as triangles in the complex plane, so called unitarity triangles. CP violation is reflected by the area of the unitarity triangles, which is the same for all of them, since the internal angles correspond to the complex phase. If the complex phase is zero, the representation in the complex plane is reduced to the real axis and the area is zero [5]. It can be shown [48] that the area is given by

$$\mathrm{Area}_{\mathrm{CKM}} = \frac{1}{2}J, \tag{1.40}$$

with the measure of CP violation,

$$J = |\Im(V_{km}^* V_{lm} V_{kn} V_{ln}^*)| = |\Im(V_{mk}^* V_{ml} V_{nk} V_{nl}^*)| \approx A^2\lambda^6\eta. \tag{1.41}$$

For B decays, it is more practical to use a phase convention [6] where one side of the triangles is rotated onto the real axis and is rescaled to length one. Equation 1.39 for example, is divided by $V_{cd}V_{cb}^*$. This leads to the CKM unitary triangle sketched in Fig. 1.3, where the apex takes the form

$$\overline{\rho} \equiv \left(1 - \frac{\lambda^2}{2}\right)\rho, \quad \overline{\eta} \equiv \left(1 - \frac{\lambda^2}{2}\right)\eta. \tag{1.42}$$

The internal angles are given by

$$\phi_1 \equiv \pi - \arg\left(\frac{-V_{td}V_{tb}^*}{-V_{cd}V_{cb}^*}\right), \quad \phi_2 \equiv \arg\left(\frac{V_{td}V_{tb}^*}{-V_{ud}V_{ub}^*}\right), \quad \phi_3 \equiv \arg\left(\frac{V_{ud}V_{ub}^*}{-V_{cd}V_{cb}^*}\right). \tag{1.43}$$

The length of these triangles are products of V_{CKM} elements and can be obtained from measuring proper decay rates. The angles are obtained from CP asymmetries.

[5] This would also be the case when the phase is $n\pi$

[6] The physical observables (length od the sides and angles) are of course phase convention independent.

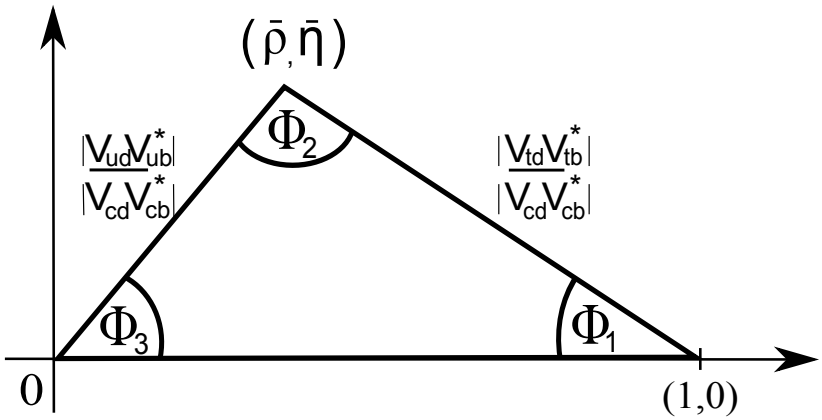

Figure 1.3: The unitary triangle corresponding to Eq. 1.39.

In this case, the sides have similar lengths ($\mathcal{O}(\lambda^3)$) [7], thus the angles are large and CP violation was expected to be large in the B sector, which nowadays is confirmed. As one side is already fixed to (1,0), the triangle is fully determined by two quantities (sides or internal angles). Measuring the three angles and two sides offers an excellent and over-constrained test of the SM. If unitarity of V_{CKM} is fulfilled, then the triangle closes. Observing a deviation from unitarity would be an clear hint for physics beyond the SM.
Other observables, for example the mass differences of the mass-eigenstates of neutral B mesons, provide additional constraints. The present status of the CKM theory is shown in Fig. 1.4. Within the errors, the data show good agreement with the CKM theory. But there is still room for new physics. Therefore, it is necessary to tighten the constraints through improved measurements. The studies presented in this work address the internal angle ϕ_2, sometimes also referred to as α.

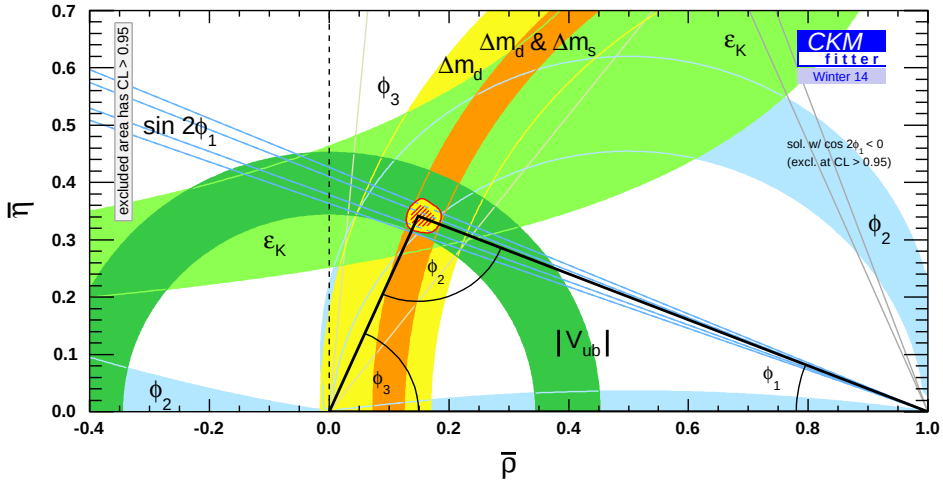

Figure 1.4: The current constraints on the CKM triangle [50].

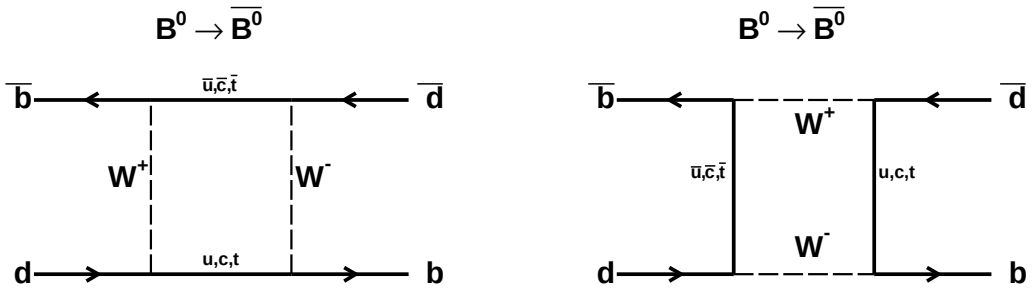

Figure 1.5: Example of the leading order contribution to neutral meson mixing. The $B^0(\bar{b}d)$ can be interchanged with e.g. $K^0(\bar{s}d)$, $D^0(c\bar{u})$ or $B_s^0(\bar{b}s)$.

1.2.4 Time Evolution of Neutral Mesons

Due to non-conservation of flavor quantum numbers in the weak interaction, neutral mesons, called P^0 in this section, can couple to their antiparticle and form mixed states (see Section 1.2.2). Particle and antiparticle are distinguished by the sign of their flavor quantum number, $\Delta S = 2$. The leading order contributions are shown in Fig. 1.5. In the Weisskopf-Wigner approximation [51] [48], the time evolution of such a state is given by

$$|\tilde{\psi}(t)\rangle = |P^0(t)\rangle + |\bar{P}^0(t)\rangle = a(t)|P^0\rangle + b(t)|\bar{P}^0\rangle. \tag{1.44}$$

Since we are only interested in the coefficients $a(t)$ and $b(t)$, we can write the time-dependent Schrödinger equation,

$$i\hbar\frac{\partial}{\partial t}\psi(t) = \mathcal{H}\psi(t), \tag{1.45}$$

where

$$\psi(t) = \begin{pmatrix} a(t) \\ b(t) \end{pmatrix}, \tag{1.46}$$

and $\mathcal{H}$ is the decomposed effective Hamiltonian

$$\mathcal{H} = H_{ij} = \mathbf{M} - \frac{i}{2}\mathbf{\Gamma} = M_{ij} - \frac{i}{2}\Gamma_{ij}. \tag{1.47}$$

$\mathbf{M}$ is a 2×2 dispersive hermitian mass matrix and $\mathbf{\Gamma}$ an 2×2 absorptive decay hermitian matrix [8]. Therefore they satisfy

$$M_{ij} = M_{ji}^* \quad \text{and} \quad \Gamma_{ij} = \Gamma_{ji}^*. \tag{1.48}$$

The elements of $\mathcal{H}$ are calculated in terms of box diagrams, where the off-diagonal terms are flavor changing transitions, e.g. $\langle\bar{P}^0|\mathcal{H}|P^0\rangle$, while the diagonal elements are flavor conserving, e.g. $\langle P^0|\mathcal{H}|P^0\rangle$. CPT invariance requires the equality of mass and width of the particle and antiparticle [52], hence

$$M_{11} = M_{22} \equiv M \quad \text{and} \quad \Gamma_{11} = \Gamma_{22} \equiv \Gamma. \tag{1.49}$$

It follows that

$$\mathbf{M} - \frac{i}{2}\mathbf{\Gamma} = \begin{pmatrix} M - \frac{i}{2}\Gamma & M_{12} - \frac{i}{2}\Gamma_{12} \\ M_{12}^* - \frac{i}{2}\Gamma_{12}^* & M - \frac{i}{2}\Gamma \end{pmatrix}. \tag{1.50}$$

[7] in e.g. the kaon system the length of the sides are of order λ and λ^5

[8] Note that $\mathcal{H}$ is not hermitian.

By diagonalizing this operator, its eigenvalues $\alpha_\pm$, are obtained

$$\alpha_\pm = M - \frac{i}{2}\Gamma \pm \sqrt{(M_{12} - \frac{i}{2}\Gamma_{12})(M_{12}^* - \frac{i}{2}\Gamma_{12}^*)}, \tag{1.51}$$

and the masses and lifetimes are given by

$$m_+ = \Re(\alpha_+), \quad \Gamma_+ = -2\Im(\alpha_+), \tag{1.52}$$
$$m_- = \Re(\alpha_-), \quad \Gamma_- = -2\Im(\alpha_-). \tag{1.53}$$

We will use the notation

$$\Delta m \equiv m_+ - m_- = 2\Re(\sqrt{(M_{12} - \frac{i}{2}\Gamma_{12})(M_{12}^* - \frac{i}{2}\Gamma_{12}^*)}), \tag{1.54}$$

$$\Delta\Gamma \equiv \Gamma_- - \Gamma_+ = 4\Im(\sqrt{(M_{12} - \frac{i}{2}\Gamma_{12})(M_{12}^* - \frac{i}{2}\Gamma_{12}^*)}). \tag{1.55}$$

The associated eigenvectors $v_\pm = (1, \pm q/p)^T$, lead to the (unnormalized) eigenstates,

$$\begin{aligned} |P_+(t)\rangle &\equiv p|P^0(t)\rangle + q|\bar{P}^0(t)\rangle, \\ |P_-(t)\rangle &\equiv p|P^0(t)\rangle - q|\bar{P}^0(t)\rangle, \end{aligned} \tag{1.56}$$

with

$$\frac{q}{p} = \sqrt{\frac{M_{12}^* - \frac{i}{2}\Gamma_{12}^*}{M_{12} - \frac{i}{2}\Gamma_{12}}} \equiv \frac{1-\epsilon}{1+\epsilon} \qquad \text{and} \qquad \sqrt{p^2+q^2} = 1. \tag{1.57}$$

If CP invariance is fulfilled, the asymmetry parameter $\epsilon = 0 \Leftrightarrow p = q$ and only then are the states pure (even and odd) CP eigenstates. Otherwise, they are not orthogonal to each other and the overlap is

$$\langle P_+|P_-\rangle = \frac{2\Re(\epsilon)}{1+|\epsilon|^2}. \tag{1.58}$$

The time evolution of $P_{+,-}$ is given by

$$|P_+(t)\rangle = e^{-i\alpha_+ t}(p|P^0\rangle + q|\bar{P}^0\rangle), \tag{1.59}$$
$$|P_-(t)\rangle = e^{-i\alpha_- t}(p|P^0\rangle - q|\bar{P}^0\rangle), \tag{1.60}$$

so that $P_{+,-}$ decays as $e^{-\Gamma_\pm t}$ modulated with a complex phase $-im_\pm$. It is common to call $|P_{+,-}\rangle$ "$|P_{H,L}\rangle$" where H and L stand for the heavier and lighter state, respectively [9].
The time evolution of the pure flavor states is more important for understanding CP violation. Solving Eq. 1.56 for the flavor states yields

$$|P^0(t)\rangle = \frac{1}{2p}(|P_+(t)\rangle + |P_-(t)\rangle), \tag{1.61}$$

$$|\bar{P}^0(t)\rangle = \frac{1}{2q}(|P_+(t)\rangle - |P_-(t)\rangle). \tag{1.62}$$

[9] In the Kaon system light and heavy are interchanged with long and short (see Section 1.2.2).

Inserting Eq. 1.60 gives the desired evolution,

$$\begin{aligned}
|P^0(t)\rangle &= \frac{1}{2}((e^{-i\alpha_+ t} + e^{-i\alpha_- t})|P^0\rangle + \frac{q}{p}(e^{-i\alpha_+ t} - e^{-i\alpha_- t})|\bar{P}^0\rangle) \\
&= \frac{1}{2}e^{-i\alpha_+ t}[(1 + e^{-i(\Delta m - \frac{i}{2}\Delta\Gamma)t})|P^0\rangle + \frac{q}{p}(1 - e^{-i(\Delta m - \frac{i}{2}\Delta\Gamma)t})|\bar{P}^0\rangle], \qquad (1.63) \\
|\bar{P}^0(t)\rangle &= \frac{1}{2}(\frac{p}{q}(e^{-i\alpha_+ t} - e^{-i\alpha_- t})|P^0\rangle + (e^{-i\alpha_+ t} + e^{-i\alpha_- t})|\bar{P}^0\rangle) \\
&= \frac{1}{2}e^{-i\alpha_+ t}[\frac{q}{p}(1 - e^{-i(\Delta m - \frac{i}{2}\Delta\Gamma)t})|P^0\rangle + (1 + e^{-i(\Delta m - \frac{i}{2}\Delta\Gamma)t})|\bar{P}^0\rangle]. \qquad (1.64)
\end{aligned}$$

This indicates that with time, an initial pure flavor state will develop an opposite flavored component as long as Δm and $\Delta\Gamma$ are non zero. Starting with a particular flavor, e.g. $|P^0\rangle$, the probability of observing for example $|\bar{P}^0\rangle$ after the time t, is the given by

$$\begin{aligned}
|\langle\bar{P}^0|P^0(t)\rangle|^2 &= \frac{1}{4}e^{-2i\alpha_+ t}|\frac{q}{p}|^2(1 - e^{-i(\Delta m - \frac{i}{2}\Delta\Gamma)t})^2 \\
&= \frac{1}{2}e^{-i2\alpha_+ t}|\frac{q}{p}|^2(1 - cos((\Delta m - \frac{i}{2}\Delta\Gamma)t)), \qquad (1.65)
\end{aligned}$$

where the orthogonality of P^0 to $\bar{P}^0$ was used.

1.2.5 The Different Types of CP Violation

Consider the amplitudes of a neutral meson $P(\bar{P})$ decaying into a hadronic CP eigenstate: $f = \bar{f} \equiv f_{CP}$,

$$A_f = \langle f|H|P\rangle, \qquad (1.66)$$
$$\bar{A}_f = \langle f|H|\bar{P}\rangle, \qquad (1.67)$$

where H is the Hamiltonian. The complex quantity,

$$\lambda_{CP} \equiv \frac{q\bar{A}_f}{pA_f} = e^{-i\phi_M}\left|\frac{q}{p}\right|\left|\frac{\bar{A}_f}{A_f}\right|e^{-i\phi_D} \qquad (1.68)$$

with the weak phase difference in mixing denoted as ϕ_M and a strong phase ϕ_D in the decay amplitude, allows to distinguish three different categories of CP violation:

1. CP violation in the decay, also called "direct CP violation": $|A_f| \neq |\bar{A}_{\bar{f}}|$. This kind of CP violation can be measured by comparing the decay rates of a particle and antiparticle and is not restricted only to neutral mesons but can also occur in charged meson, baryon and lepton decays.

2. CP violation in the mixing: $|q/p| \neq 1 (\Leftrightarrow \epsilon \neq 0)$. From its definition, it follows that this type occurs if the flavor eigenstates are different from the CP eigenstates (Eq. 1.57). Thus it represents an asymmetry in the neutral meson flavor oscillation, where an example was given in Section 1.2.2.

3. Mixing induced CP violation: $\Im(\lambda_{CP}) \neq 0$. CP violation still can occur even if $|A_{f_{CP}}/\bar{A}_{f_{CP}}| = |q/p| = 1$, but the phase difference is non-zero. This is an interference of the processes 1.) and 2.) and can be measured by observing an asymmetry in the time evolution of particles and antiparticles decaying into the same final state f_{CP}. An example is the so-called "golden channel" $B \to J/\psi K_S^0$ [10], where this type of CP violation was first observed by the BaBar [53] and the Belle [54] collaborations.

1.3 B Phenomenology

The B meson is produced via the strong interaction, consists of a heavy $\bar{b}$ quark and a light(u, d) quark and decays weakly. Another beneficial property, besides the large CP violation, is the B meson's long lifetime

$$\tau_{B^0} = (1.525 \pm 0.009) \times 10^{-12} \text{ s}. \tag{1.69}$$

Because it is relatively heavy, $m_B \sim 5.28$ GeV [45], the B meson offers a rich field of physics for theory and experiment alike. One of the most difficult challenges of particle physics theory is the strong interaction. The running coupling constant α_s becomes large at low energy scales and perturbation expansion is not applicable any more [11].
However, perturbation theory is partly accessible in the B system as the b quark mass (~ 5 GeV) corresponds to a strong coupling $\alpha_s(m_b) \sim 0.22$ [55]. But approximations have to be made, for example by setting the mass of the b quark to infinity as it is done in the Heavy Quark Expansion (HQE) [56, 57], or assuming the light quarks (u, d, s) to be massless. Another approximation, QCD factorization, allows to disentangle perturbative from non-perturbative effects [58–60]. It is often employed in hadronic decays of heavy hadrons and will be discussed in 1.4.2.

1.3.1 Time Evolution of Neutral B Mesons

For neutral B mesons, Eq. 1.62 can be simplified as follows. Unlike the K_S^0 and K_L^0, the two states B_H and B_L have almost equal lifetimes $\Gamma_+ \sim \Gamma_- \equiv \Gamma$, and $\Delta\Gamma$ can be ignored ($\Delta\Gamma/\Gamma \sim \mathcal{O}(10^{-3})$). Also, the box diagram of $B^0 - \bar{B}^0$ mixing (Fig. 1.5) is dominated by virtual t-quark exchange as the corresponding CKM element is $V_{tb} \sim 1$. The other light quark contributions can be neglected due to GIM cancellations [61, 62]. Furthermore, the states B_H and B_L can be considered as pure flavor states as $|q/p| \sim 1$ is a good approximation [12]

$$\begin{aligned} \left.\frac{q}{p}\right|_{B_d} &= \sqrt{\frac{M_{12}^*}{M_{12}}} + \mathcal{O}\left(\frac{\Gamma_{12}}{M_{12}}\right)\Bigg|_{B_d} \simeq \frac{V_{tb}^* V_{td}}{V_{tb} V_{td}^*} \\ &\Rightarrow \left|\frac{q}{p}\right|_{B_d} \sim 1 \end{aligned} \tag{1.70}$$

[10] Aside from being experimentally clean, the asymmetry in the golden channel is relatively free from hadronic uncertainties as the tree and dominant c, t penguin contributions share the same CKM phase.
[11] A rough threshold is the QCD scale, $\Lambda_{\text{QCD}} \sim 0.5$ GeV.
[12] This was predicted by Bander, Silverman and Soni [63] in 1979, long before being experimentally confirmed about 20 years later.

since $\Gamma_{12}/M_{12} \sim m_b^2/m_t^2 \approx 10^{-2}$ [52]. Note that $\lambda_{CP} = \bar{A}_f/A_f$ still can have a non-trivial complex phase. Consequently, the time evolution of neutral B mesons, starting as a pure flavor state, is given by

$$|B^0(t)\rangle = \tfrac{1}{2}e^{-\Gamma t/2}[(1+e^{-i\Delta mt})|B^0\rangle + \tfrac{q}{p}(1-e^{-i\Delta mt})|\bar{B}^0\rangle], \tag{1.71}$$

$$|\bar{B}^0(t)\rangle = \tfrac{1}{2}e^{-\Gamma t/2}[\tfrac{p}{q}(1-e^{-i\Delta mt})|B^0\rangle + (1+e^{-i\Delta mt})|\bar{B}^0\rangle], \tag{1.72}$$

where e^{-im_+} is removed by a phase convention. When the initial state is a pure B^0, then the probabilities of observing a B^0 or a $\bar{B}^0$ after some time t, is

$$|\langle B^0|B^0(t)\rangle|^2 = \tfrac{1}{2}e^{-\Gamma t}(1+\cos(\Delta mt)), \tag{1.73}$$

$$|\langle \bar{B}^0|B^0(t)\rangle|^2 = \tfrac{1}{2}e^{-\Gamma t}(1-\cos(\Delta mt)). \tag{1.74}$$

From $B^0 - \bar{B}^0$ mixing measurements the ratio $\Delta m/\Gamma = 0.775 \pm 0.006$ is known [64], therefore most B mesons decay before changing flavor.

1.3.2 Time-Dependent CP Violation

A B^0 or a $\bar{B}^0$ meson can decay into the same CP eigenstate f_{CP}. Squaring the corresponding decay amplitudes

$$\begin{aligned} A_{CP} = \langle f_{CP}|H|B^0(t)\rangle &= \frac{1}{2}e^{-\Gamma t/2}[(1+e^{-i\Delta mt})A_{CP} + \frac{q}{p}(1-e^{-i\Delta mt})\bar{A}_{CP}] \\ &= \frac{1}{2}e^{-\Gamma t/2}A_{CP}[(1+e^{-i\Delta mt}) + \lambda_{CP}(1-e^{-i\Delta mt})], \end{aligned} \tag{1.75}$$

$$\begin{aligned} \bar{A}_{CP} = \langle f_{CP}|H|\bar{B}^0(t)\rangle &= \frac{1}{2}e^{-\Gamma t/2}[\frac{p}{q}(1-e^{-i\Delta mt})A_{CP} + (1+e^{-i\Delta mt})\bar{A}_{CP}] \\ &= \frac{1}{2}e^{-\Gamma t/2}A_{CP}[(1-e^{-i\Delta mt}) + \lambda_{CP}(1+e^{-i\Delta mt})], \end{aligned} \tag{1.76}$$

gives the time-dependent decay rate,

$$\begin{aligned} \Gamma(B^0(t)\to f_{CP}) &= |\langle f_{CP}|H|B^0(t)\rangle|^2 \\ &= \frac{1}{2}e^{-\Gamma t}|A_{CP}|^2[1+\cos(\Delta mt) - 2\Im(\lambda_{CP})\sin(\Delta mt) + (1-cos(\Delta mt))|\lambda_{CP}|^2], \end{aligned} \tag{1.77}$$

$$\begin{aligned} \Gamma(\bar{B}^0(t)\to f_{CP}) &= |\langle f_{CP}|H|\bar{B}^0(t)\rangle|^2 = \\ &= \frac{1}{2}e^{-\Gamma t}|A_{CP}|^2[1-\cos(\Delta mt) + 2\Im(\lambda_{CP})\sin(\Delta mt) + (1+cos(\Delta mt))|\lambda_{CP}|^2]. \end{aligned} \tag{1.78}$$

The time-dependent CP rate asymmetry is defined as

$$\begin{aligned} a_{CP}(t) &\equiv \frac{\Gamma(\bar{B}^0(t)\to f_{CP}) - \Gamma(B^0(t)\to f_{CP})}{\Gamma(\bar{B}^0(t)\to f_{CP}) + \Gamma(B^0(t)\to f_{CP})} \\ &= \frac{(|\lambda_{CP}|^2-1)\cos(\Delta mt) + 2\Im(\lambda_{CP})\sin(\Delta mt)}{|\lambda_{CP}|^2+1} \\ &= \mathcal{A}_{CP}\cos(\Delta mt) + \mathcal{S}_{CP}\sin(\Delta mt). \end{aligned} \tag{1.79}$$

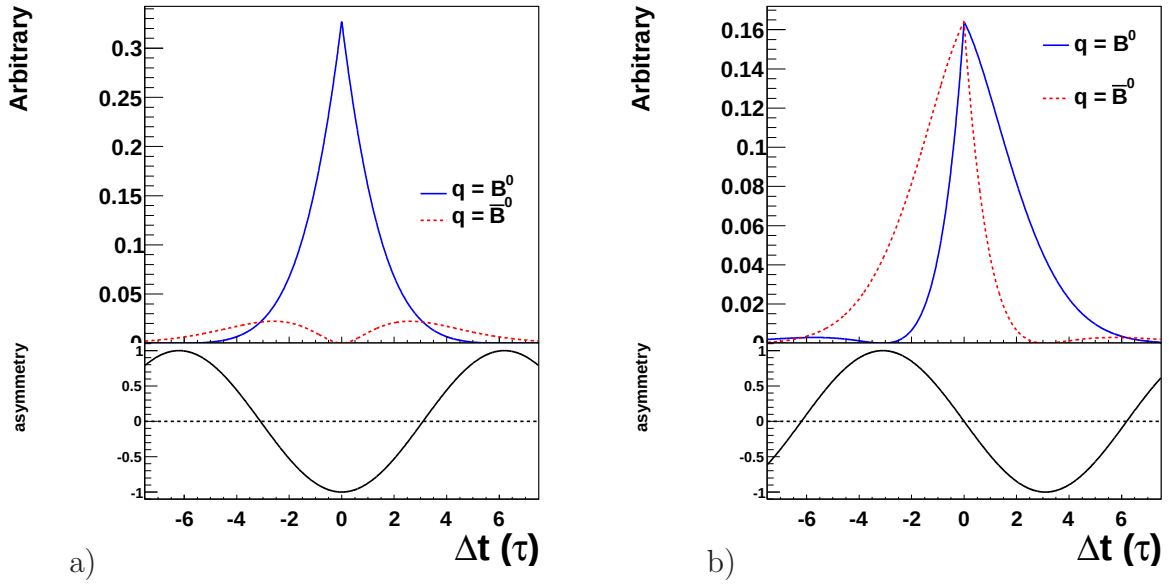

Figure 1.6: The B lifetime distributions show maximal a) direct ($\mathcal{S}_{CP}$=0, $\mathcal{A}_{CP}$=1) and b) mixing induced CP ($\mathcal{S}_{CP}$=1, $\mathcal{A}_{CP}$=0) violation with the corresponding asymmetry below. A negative lifetime appears due to our experimental environment, see Section 1.3.3.

The CP violating parameters are defined as

$$\mathcal{A}_{CP} \equiv \frac{|\lambda_{CP}|^2 - 1}{|\lambda_{CP}|^2 + 1}, \quad \mathcal{S}_{CP} \equiv \frac{2\Im(\lambda_{CP})}{|\lambda_{CP}|^2 + 1}. \tag{1.80}$$

where $\mathcal{A}_{CP} \neq 0$ is results in direct CP violation and $\mathcal{S}_{CP} \neq 0$ in mixing-induced CP violation (type 1 and 3, see Section 1.2.5). Examples of either maximal direct or mixing induced CP violation are shown in Fig. 1.6. Because $a_{CP}(t)$ is normalized, the parameters have to fulfill

$$\mathcal{A}_{CP}^2 + \mathcal{S}_{CP}^2 + (\frac{(\mathcal{R}\lambda_{CP})^2}{\lambda_{CP}^2 + 1})^2 = 1, \tag{1.81}$$

and thus $\mathcal{A}_{CP}^2 + \mathcal{S}_{CP}^2 \leq 1$ defines the unit circle as the physically allowed region.
CP violations can be measured by comparing the time-dependent rates of $B \to f_{CP}$ and $\bar{B}^0 \to f_{CP}$. This is quite a challenge for experimentalists, as we aim for high precision and mostly rare hadronic final states.

1.3.3 Time-Dependent CP Violation Measurement

B meson are produced in pairs in an asymmetric e^+e^- collider ("B factory"), operating at the $\Upsilon(4S)$ resonance (see Fig. 1.7). This has a couple of nice advantages. First of all, it is the first bottonium resonance where B mesons can be produced. To be more specific, with a mass of 10.579GeV/c^2, the $\Upsilon(4S)$ sits right above the B pair production threshold. Consequently, the B pair is almost at rest in the center-of-mass frame (CMS). The $\Upsilon(4S)$ resonance decays almost entirely ($\sim$ 96%) into $B\bar{B}$ pairs and with almost equal fractions into B^+B^- ($51.6 \pm 0.6\%$) and $B^0\bar{B}^0$ ($48.4 \pm 0.6\%$) pairs. The exact equality manifested in the equal Clebsh-Gorden coefficients is slightly disturbed through electromagnetic or higher-order strong effects and the lighter u quark in the charged B.

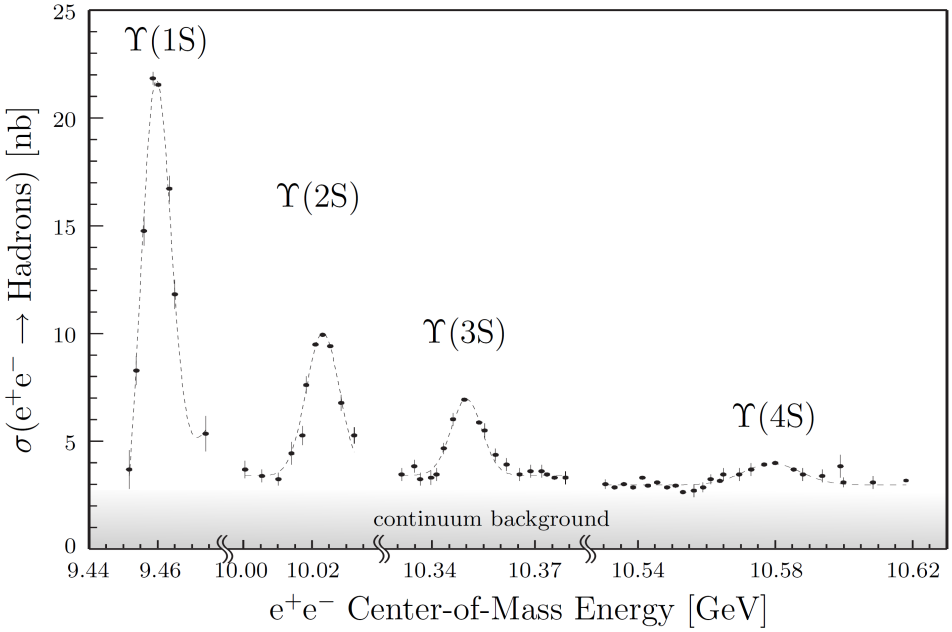

Figure 1.7: Hadronic cross section for e^+e^- in the bottonium range. The possibility of decaying strongly and hence very fast into a B meson pair becomes evident in the broad shape of $\Upsilon(4S)$.

The vector particle $\Upsilon(4S)$ ($J^{PC} = 1^{--}$) decays into two pseudo-scalar B mesons ($J^P = 0^-$). On the one hand, the two B mesons have to be in a p-wave configuration to conserve angular momentum. On the other hand, because the $\Upsilon(4S)$ has an asymmetric wave function, the state of the two B mesons has to be asymmetric, as well. Bose-Einstein statistics forbids the coexistence of two neutral B mesons with the same flavor at the same time. Consequently, the two B mesons form an entangled state.

If one of the B^0s, referred to as B_{Tag}, decays into a flavor specific mode at a time t_1, the other B must have opposite flavor at that time. From there on it is free to evolve until it decays at a time t_2. The time difference $\Delta t = t_2 - t_1$, together with the information of the flavor can be used to extract the CP asymmetry parameters. In other words, the clock starts at t_1 and the probability of observing f_{CP} for a determined flavor q, of B_{Tag} at time Δt, is given by

$$\mathcal{P}(\Delta t, q) = \frac{e^{-|\Delta t|/\tau_{B^0}}}{4\tau_{B^0}} \left[1 + q \Big(\mathcal{A}_{CP} \cos(\Delta m \Delta t) + \mathcal{S}_{CP} \sin(\Delta m \Delta t) \Big) \right], \tag{1.82}$$

where $q = +1(-1)$ for $B_{\text{Tag}} = B^0(\bar{B}^0)$ and τ_{B^0} is the B^0 lifetime.

Although the B lifetime is relatively large for its mass, it is practically impossible to directly measure it with the precision needed for the study of CP violation. An asymmetry in the beam energies is employed to translate the lifetime difference into a distance,

$$\Delta t = \frac{\Delta z}{\langle \beta\gamma \rangle c}, \tag{1.83}$$

being measurable by precisely determining the B vertices, see Fig. 1.8. Because the B mesons are almost at rest in the CMS, the kinematics simplify to a one-dimensional problem. Since

only a small fraction of all events will decay into a specific final state under study, events that belong to the desired mode have to be identified in first place.

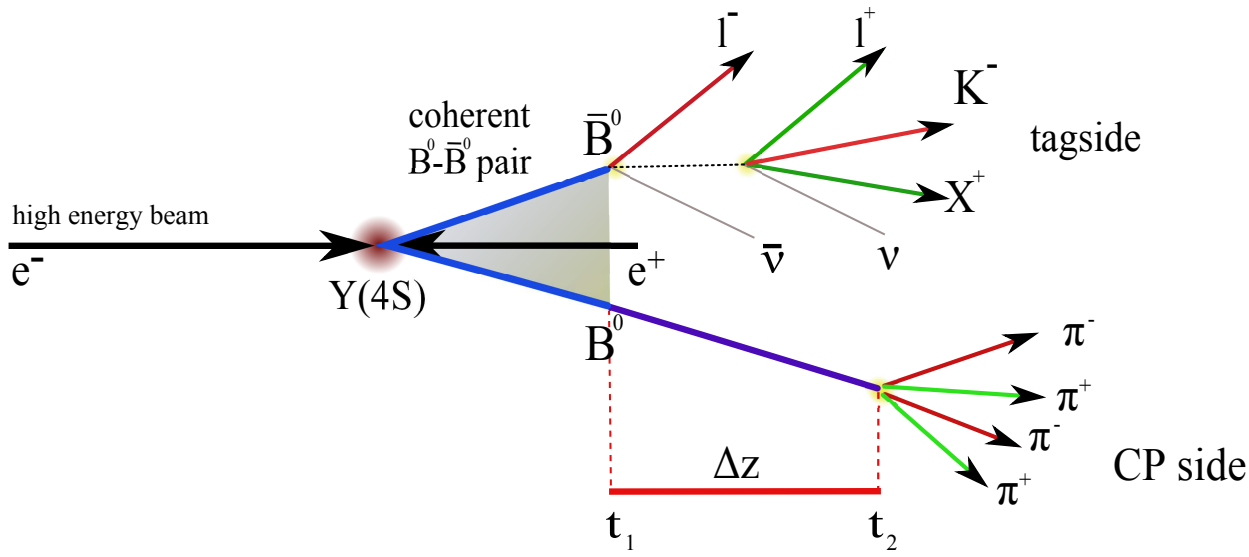

Figure 1.8: Schematic of the time-dependent rate asymmetry measurement. Here the $\bar{B}^0$'s decay products are used for determining the initial flavor of the other B which decays into a four pion CP final state.

1.4 Prospects of $B \to \rho\rho$

In this thesis we study neutral B mesons decaying into two ρ mesons. The $\rho(770)$ consists out of u and d quarks and is the lightest vector (spin-1) meson. It builds an isospin triplet (I=1), with
$\rho^+ \ (u\bar{d}) : I_3 = 1; \qquad \rho^0 \ (\frac{1}{\sqrt{2}}(u\bar{u} - d\bar{d})) : I_3 = 0; \qquad \rho^- \ (\bar{u}d) : I_3 = -1.$
As it decays strongly (almost exclusively) into two pions ($\pi^+\pi^-$ for ρ^0), its lifetime is very short and corresponds to a broad width of $\Gamma_\rho = 149.1 \pm 0.8\text{MeV/c}^2$ [45] which is approximately a fifth of its mass, $m_\rho = 775.49 \pm 0.34\text{MeV/c}^2$. $\rho^\pm$ has the quantum numbers $J^P = 1^-$ and ρ^0, being its own antiparticle, has $J^{PC} = 1^{--}$.

1.4.1 Helicity Dependency

The overall angular momentum of the two spin-1 daughters has to conserve the spin-0 of the pseudo-scalar B. This can be achieved through s, p and d-wave configurations. Following [65], a general amplitude for a B meson with momentum p_B and mass m_B decaying into two vector particles V_1V_2 can be decomposed as the sum of three Lorentz scalars,

$$\mathcal{A}_{B\to V_1V_2} = i\epsilon_1^{*\mu}\epsilon_2^{*\nu}\Big[S_1 g_{\mu\nu} - S_2\frac{p_B^\mu p_B^\nu}{m_B^2} + iS_3\epsilon_{\mu\nu\sigma\tau}\frac{p_1^\sigma p_2^\tau}{p_1 p_2}\Big], \tag{1.84}$$

where ϵ_i^μ and p_i^μ are the polarization vectors and four-momenta of V_i, respectively. The first two terms are CP-even and the last one is CP-odd and S_i are the amplitudes of each term.

One can construct three helicity amplitudes

$$A_0 \sim S_1 + \frac{1}{2}S_2 \tag{1.85}$$

$$A_\pm \sim i(S_1 \mp S_3), \tag{1.86}$$

where A_0 is a pure CP-even state and corresponds to longitudinal polarization (LP), while the remaining states are an admixture of CP-even and odd states and correspond to transversal polarization (TP). The fraction of longitudinal polarized states is thus given by

$$f_L = \frac{|A_0|^2}{|A_0|^2 + |A_+|^2 + |A_-|^2}. \tag{1.87}$$

Using the transversity basis with

$$A_\parallel = \frac{1}{\sqrt{2}}(A_+ + A_-) \sim S_1, \tag{1.88}$$

$$A_\perp = \frac{1}{\sqrt{2}}(A_+ - A_-) \sim S_3, \tag{1.89}$$

allows to further separate CP-even and odd parts for transverse polarization [66]. A separation of CP-even and odd states is necessary for the measurement of CP asymmetries.

The spin quantization axis can be chosen to be the flight direction of the ρ in the B frame, then LP (TP) corresponds to $s_z = 0$ (± 1) and angular momentum conservation leads to distinct signatures for each amplitude. The angular dependence for each vector particle decaying into two pseudo-scalars is proportional to

$$\begin{aligned}\frac{1}{\Gamma}\frac{d^2\Gamma}{d\cos\theta_{\mathrm{H},1}\, d\cos\theta_{\mathrm{H},2}} \propto\ & |A_0|^2 \cos^2\theta_{\mathrm{H},1}\cos^2\theta_{\mathrm{H},2} + \frac{1}{4}\big(|A_+|^2 + |A_-|^2\big)\sin^2\theta_{\mathrm{H},1}\sin^2\theta_{\mathrm{H},2}\Big) \\ & - \cos\theta_{\mathrm{H},1}\sin\theta_{\mathrm{H},1}\cos\theta_{\mathrm{H},2}\sin\theta_{\mathrm{H},2}[\mathcal{R}(e^{-i\phi}A_0A_+^*) + \mathcal{R}(e^{+i\phi}A_0A_-^*)] \\ & + \frac{1}{2}\sin^2\theta_{\mathrm{H},1}\sin^2\theta_{\mathrm{H},2}\mathcal{R}(e^{2i\phi}A_+A_-^*),\end{aligned} \tag{1.90}$$

where the helicity angles $\theta_{\mathrm{H,i=1,2}}$ are defined as the angle between the B flight direction and the direction of one of the daughters of the ρ in the ρ rest frame, see Fig. 1.9. The acoplanarity angle ϕ is the angle between the normal vectors of the planes defined by each ρ's daughter pairs.

1.4.2 $\mathcal{B}(B \to \rho\rho)$ and f_L

In leading order, $B \to \rho\rho$ decays are $b \to u\bar{u}d$ transitions and therefore suppressed by $V_{ub} \sim 0.004$. On top of that, the decay $B^0 \to \rho^0\rho^0$ is color-suppressed relative to the other two $B \to \rho\rho$ decays, which can be seen when comparing the tree-level Feynman diagrams in Fig. 1.10. Therefore, $B^0 \to \rho^0\rho^0$ has the smallest branching fraction out of the three $B \to \rho\rho$ decays [13] decays.
$B \to \rho\rho$ decays are considered to be tree-dominated, nevertheless, penguin amplitudes (see Fig. 1.10) can contribute as well. $B^0 \to \rho^0\rho^0$ decays are more sensitive to such contributions

[13] Simply speaking, the lack of color freedom leads to a suppression by 1/9 as there are three colors.

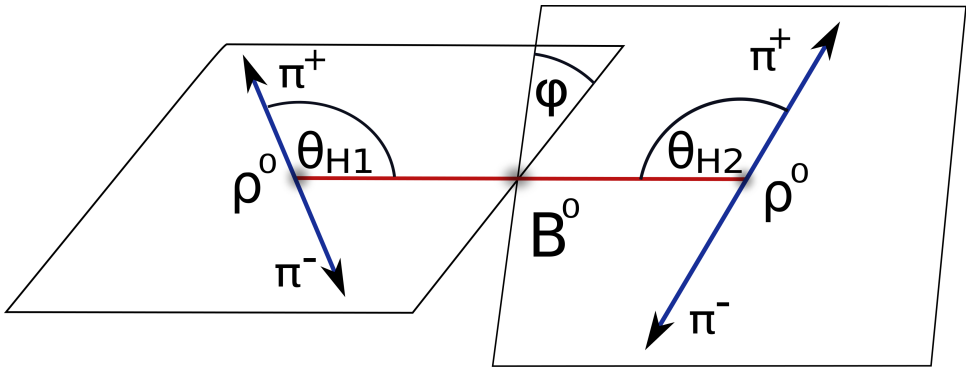

Figure 1.9: Definition of the helicity angles θ_H, each defined in the corresponding rest frame of the ρ^0. For $B^0 \to \rho^+\rho^-$ the π^+s have to be replaced with the charged pions and the π^- with a π^0.

as the tree amplitude is rather small. While color-allowed tree-dominated decays are the best predicted $B \to VV$ decays, color-suppressed decays suffer from difficulties in the calculation of their transverse amplitude [65] and other theoretical unknowns [67]. Because the amplitude for transverse polarization does not allow for factorization, the theoretical calculations focus on predictions for longitudinal polarization. Finding the longitudinally polarized mode to be dominant makes this less problematic. Luckily, the SM indicates that transversely polarized light hadronic final states are suppressed [14] by powers of λ_{QCD}/m_b, so that $1-f_L \sim \mathcal{O}(1/m_b^2)$ is a good approximation for color-allowed decays [68]. For $B^0 \to \rho^0\rho^0$ this statement is weaker because the amplitude could have sizable other contributions besides the relatively small tree [69]. There, a suppression of longitudinal polarization is possible due to non-factorisable transverse polarized contributions that are not helicity-flip suppressed [70]. It is important to compare measured polarization observables with the calculations.

In general, in the heavy quark limit $m_b >> \lambda_{\rm QCD}$, the decay amplitude of a B decaying into two light charmless vector mesons $\langle V_1V_2|\mathcal{H}_{\rm eff}|B\rangle$, is calculated with the effective weak Hamiltonian [57],

$$\mathcal{H}_{\rm eff} = \frac{G_F}{\sqrt{2}} \sum_{i=u,c} \lambda_i^j \left(\sum_{k=1,2} C_k(\mu) Q_k^i + \sum_{\rm penguins} C_p(\mu) Q_p \right) + h.c., \tag{1.91}$$

with CKM factors $\lambda_i^j = V_{ib}V_{ij}^*$ for $j = d, s$ and the Fermi constant G_F. $Q_{1,2}^p$ are the left-handed current-current operators from W exchange and the others contain QCD and electroweak penguins as well as dipole operators. $C_i(\mu)$ are Wilson coefficients that account for hadronic short distance effects. The decay amplitude is then given by

$$\mathcal{A}(B \to V_1V_2) = \frac{G_F}{\sqrt{2}} \sum_i \lambda_i C_i(\mu) \langle V_1V_2|Q_i|B\rangle. \tag{1.92}$$

The matrix elements $\langle V_1V_2|Q_i|B\rangle$, can be computed by approximating the four fermion operator with the product of two currents, which is called naive factorization. For example

$$\begin{aligned} \langle V_1V_2|Q_1|B\rangle \quad &= \langle V_1V_2|(u\bar{b})_{V-A}(d\bar{u})_{V-A}|B\rangle \\ &\to \langle V_1|(d\bar{u})_{V-A}|0\rangle\langle V_2|(u\bar{b})_{V-A}|B\rangle, \end{aligned} \tag{1.93}$$

[14] This suppression is associated with the V-A structure of the SM and the "helicity flip" of a collinear quark.

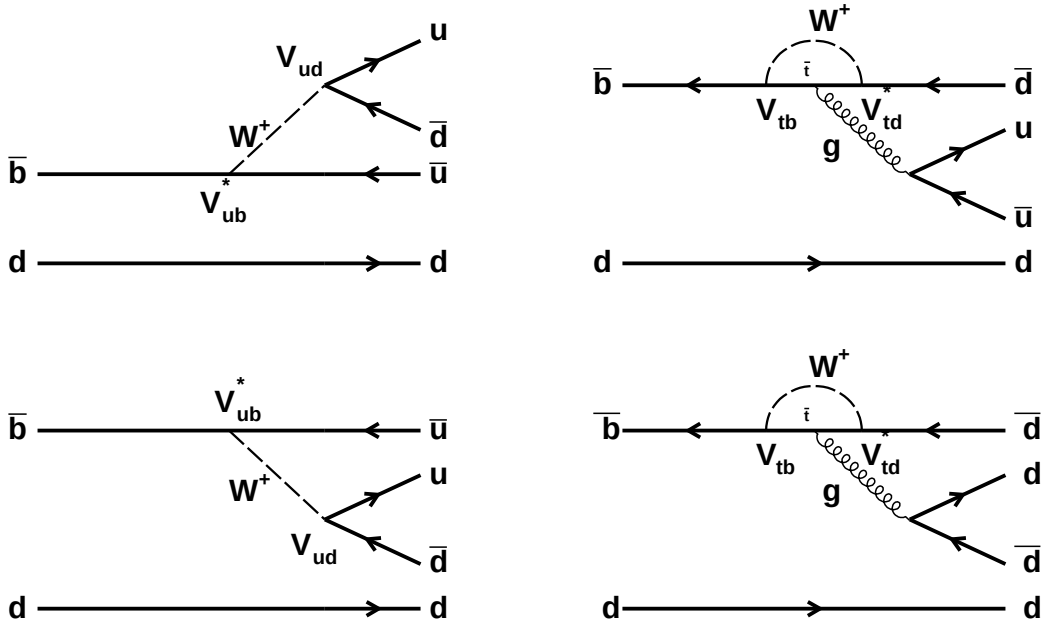

Figure 1.10: Tree level and penguin Feynman diagrams for $B^0 \to \rho^+\rho^-$ (top) and $B^0 \to \rho^0\rho^0$.

where the first part describes the hadronisation of the W and the second involves picking up the spectator quark [15]. Another method, the hard-scattering approach, assumes the decay to be dominated by hard gluon exchange and the amplitude is expanded in terms of $\lambda_{\rm QCD}/Q$ where Q is the scale for hard gluons. For a decay into two light mesons the matrix elements consist of form factors, perturbatively calculable hard scattering functions and light-cone distribution amplitudes that account for non-perturbative effects. Whereas in the original form the transition matrix elements are hardly calculable, factorization allows computing the "ingredients" separately and is at present the most promising ansatz for phenomenological predictions of hadronic B decays. The current theoretical predictions for longitudinal polarization are listed in Table 1.2.

	$\rho^+\rho^-_{\rm LP}$	$\rho^0\rho^0_{\rm LP}$
$\mathcal{B} \times 10^6$	$30.4^{+12.9}_{-11.2}$	$0.44^{+0.66}_{-0.37}$
f_L	$0.913^{+0.004+0.056}_{-0.003-0.064}$	$0.90^{+0.03+0.08}_{-0.04-0.56}$
$\mathcal{A}^{00}_{CP}$	$-0.02^{+0.04}_{-0.02}$	$-0.08^{+0.02+0.59}_{-0.01-0.28}$

Table 1.2: Theoretical predictions of the branching ratios [67] , longitudinal polarization fraction and direct CP violation [65] in $B^0 \to \rho\rho$ decays.

In order to decrease theoretical uncertainties, it is often helpful to compare ratios of certain amplitudes where the hadronic dependence cancels [16]. (See also References [59, 60, 65]).

[15] for a color-allowed decay

[16] e.g. by normalizing by the semileptonic counter-process $B \to \rho l \nu$.

1.4.3 CP Violation in $B \to \rho\rho$

Fig. 1.11 a) shows two different pathes of a decay of a B meson into a specific CP eigenstate via a $\bar{b} \to \bar{u}u\bar{d}$ transition. The B^0 meson can decay directly into the final state or first mix into its antiparticle ($\bar{B}^0$) before the decay. These two pathes can interfere. If the interference is not invariant under a CP transformation, mixing induced CP violation can be observed. This is illustrated in Fig. 1.11 b).
In the case of $\bar{b} \to \bar{u}u\bar{d}$ transitions (e.g. $B \to \pi\pi, \rho\pi, \rho\rho$), the tree level decay carries the weak phases $\arg(V_{ub}V_{ud}^*)$, while the dominant contribution to the mixing is the t-quark loop with $\arg(V_{td}V_{tb}^*)$. As only the sign of the CKM phase in the amplitude changes for the CP conjugated decay, the remaining terms cancel and λ_{CP} (see Eq. (1.68)) can be expressed in terms of CKM elements,

$$\begin{aligned} \lambda_{CP} &= \frac{V_{td}^* V_{tb}}{V_{td} V_{tb}^*} \frac{V_{ub}^* V_{ud}}{V_{ub} V_{ud}^*} \\ &= \eta_{CP}\, e^{i2\phi_2}, \end{aligned} \tag{1.94}$$

with the CP eigenvalue $\eta_{CP} = +1$ for LP. ϕ_2 is the angle from the unitarity triangle and is introduced in Section 1.2.3. Alternatively, λ_{CP} can also be expressed in terms of the other two internal angles $\phi_{i=1,3}$ (see Eq. (1.43) for the definitions of the three CKM angles): with $\arg(V_{td}V_{tb}^*) \to \phi_1 - \pi$ and $\arg(V_{ub}V_{ud}^*) \to \phi_3$ (the $V_{cd}V_{cb}^*$ terms cancel), Eq. 1.94 reads $\lambda_{CP} = e^{i2(\pi-\phi_1-\phi_3)}$. Assuming the SM, $\phi_2 = \pi - \phi_1 - \phi_3$.
At tree level direct CP violation does not occur, $\mathcal{A}_{CP}|_{\text{tree}} = 0$ and $\mathcal{S}_{CP}|_{\text{tree}} = \sin(2\phi_2)$. This results in the CP asymmetry

$$a_{CP}(t) = \mathcal{S}_{CP} \sin(\Delta m t) = \sin(2\phi_2) \sin(\Delta m t). \tag{1.95}$$

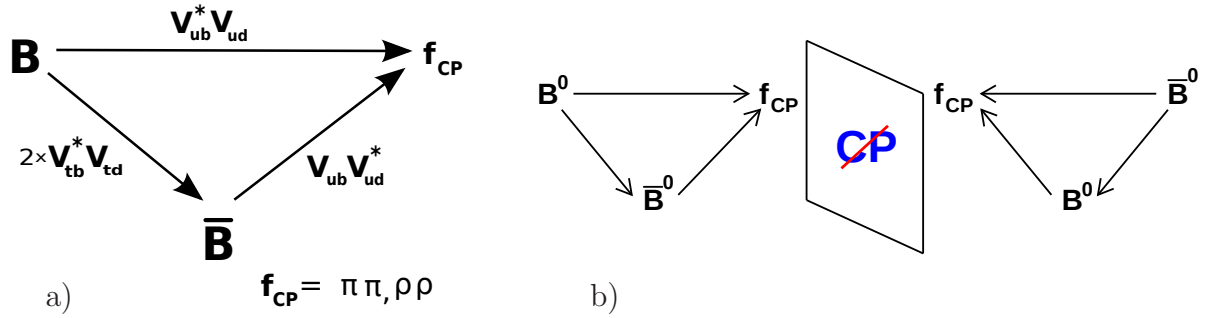

Figure 1.11: a) shows the two paths of a tree level $\bar{b}- \to \bar{u}u\bar{d}$ transition, where the CKM elements are indicated, b) shows an illustration of mixing induced CP violation.

The amplitude of the odd time-dependent oscillation ($\sin(\Delta m t)$) is equivalent to $\sin(2\phi_2)$. However, interference with different weak phases from penguin amplitudes, so-called penguin pollution, can alter the process and the CP asymmetry parameters have to be modified as follows [71],

$$\mathcal{A}_{CP} = -\frac{1}{R}\left(2\left|\frac{P}{T}\right| \sin(\phi_1 + \phi_2) \sin\delta\right), \tag{1.96}$$

$$\mathcal{S}_{CP} = \frac{1}{R}\left(\sin(2\phi_2) + 2\left|\frac{P}{T}\right| \sin(\phi_1 - \phi_2) \cos\delta - \left|\frac{P}{T}\right|^2 \sin(2\phi_1)\right), \tag{1.97}$$

where $|P/T|$ is the magnitude of the penguin to tree-amplitude ratio and δ is the strong phase difference between them. R is defined as

$$\begin{aligned} R \quad &\equiv \frac{\mathcal{B}(\tilde{B}^0 \to \rho\rho)}{\mathcal{B}(\tilde{B}^0 \to \rho\rho)|_{tree}} \\ &= 1 - 2\left|\frac{P}{T}\right| \cos\delta \cos(\phi_1 + \phi_2) + \left|\frac{P}{T}\right|^2, \end{aligned} \tag{1.98}$$

with the flavor averaged branching ratio $\mathcal{B}(\tilde{B}^0 \to \rho\rho\ ) \equiv 1/2[\mathcal{B}(B^0 \to \rho\rho\ ) + \mathcal{B}(\bar{B}^0 \to \rho\rho\ )]$. $\phi_1 = (21.65^{+0.92}_{-0.75})^\circ$ [50] is the best known angle from the unitary triangle, measured with the "golden" channel $B \to J/\psi K^0_S$. The measured (effective) phase

$$\phi_2 \to \phi_2^{\text{eff}} = \phi_2 + \Delta\phi_2, \tag{1.99}$$

is shifted by the unknown penguin contributions

$$\Delta\phi_2 = \pm \arctan \frac{|P/T| \sin\phi_3}{1 \pm |P/T| \cos\phi_3}; \qquad (+ \text{ for } \delta = 0; \ - \text{ for } \delta = \pi). \tag{1.100}$$

The observed mixing-induced CP asymmetry parameter becomes

$$\mathcal{S}_{CP} = \sqrt{1 - \mathcal{A}^2_{CP}} \sin(2(\phi_2 + \Delta\phi_2)). \tag{1.101}$$

The additional terms are in powers of $|P/T|$ and can be considered as small effects as the penguin contribution is expected to be small. Note that direct CP violation only exists if other contributions besides the dominant tree amplitude are not negligible. In order to restore the unpolluted value of ϕ_2, an isospin analysis can be performed. This is described in more detail in Chapter 7, and can result in a four-fold ambiguity for $\sin\phi_2$, if penguin pollution is present.

For B decays into two ρ mesons, $\Delta\phi_2$ is expected to be negligibly small, then the ambiguity from the isospin analysis vanishes. For this reason, $B \to \rho\rho$ decays are the most promising ones for determining $\sin\phi_2$ with the available data. Because of the larger branching fraction of $B^0 \to \rho^+\rho^-$ decays, $\sin\phi_2^{\text{eff}}$ is obtained from $\mathcal{S}_{CP}$ from $B^0 \to \rho^+\rho^-$ decays, where a limitation to the dominant longitudinally polarized component is convenient. But also branching ratios, f_L and CP asymmetries from its isospin partner decays are needed for the isospin analysis to determine an unpolluted value of ϕ_2.

All considerations made in this section are similar for $B \to \pi\pi$, which is experimentally cleaner but has larger penguin contributions [72–74]. This currently results in four solutions for $\sin\phi_2$. Measuring the mixing-induced CP violation parameter $\mathcal{S}_{CP}$ from $B \to \pi^0\pi^0$ decays and including it in the isospin constraint can resolve this ambiguity.

1.4.4 Previous Measurements

Previous measurements of $B^0 \to \rho\rho$ decays as performed by the two leading B experiments are briefly summarized in Table 1.3. The Belle measurements involving charged ρ mesons used only a fraction of the final data, consequently their errors are larger and an update is desired. Especially the charged $B^\pm$ decay has a lot of potential for improvement as it was only measured with 85×10^6 $B\bar{B}$ pairs. The branching ratio and f_L of $B^0 \to \rho^+\rho^-$ decays

were measured with 275×10^6 $B\bar{B}$ pairs and the CP parameters updated later-on with an increased data set of 535×10^6 $B\bar{B}$ pairs. This thesis presents an update of the measurement of $B^0 \to \rho^+\rho^-$ decays with Belle's final data set of 772×10^6 $B\bar{B}$ pairs, therefore we would like to point out the main difference to the predecessor measurements performed at Belle. There, the measurement was performed in three steps where first the branching ratio was extracted, followed by a determination of f_L and then both observables were used to measure the CP violation parameters in this mode. We combine the three steps into one and use all the information simultaneously. Because we are mostly interested in the CP parameters, we aim for a high signal yield, as these are still statistical limited. We also performed the study of $B^0 \to \rho^0\rho^0$ decays with the full data set, being published in [5]. Therefore the results are included in the summary table.
The current world average of ϕ_2 is $\phi_2 = (90.5^{+4.1}_{-3.6})^\circ$ [50].

f.s.	$\mathcal{B}[\times 10^{-6}]$	f_L	$\mathcal{S}_{CP}$	$\mathcal{A}_{CP}$
Belle				
$\rho^+\rho^-$	$22.8 \pm 3.8 \pm 2.6$	$0.94 \pm 0.04 \pm 0.03$	$0.19 \pm 0.30 \pm 0.07$	$0.16 \pm 0.21 \pm 0.07$
$\rho^0\rho^0$	$1.02 \pm 0.30 \pm 0.15$	$0.21 \pm 0.22 \pm 0.15$	-	-
$\rho^\pm\rho^0$	$31.7 \pm 7.1 \pm 6.7$	$0.95 \pm 0.11 \pm 0.02$	n.a.	$0.00 \pm 0.22 \pm 0.03$
BaBar				
$\rho^+\rho^-$	$25.5 \pm 2.1^{+3.6}_{-3.9}$	$0.992 \pm 0.024^{+0.026}_{-0.013}$	$-0.17 \pm 0.20^{+0.05}_{-0.06}$	$-0.01 \pm 0.15 \pm 0.06$
$\rho^0\rho^0$	$0.92 \pm 0.32 \pm 0.14$	$0.75^{+0.11}_{-0.14} \pm 0.04$	$0.3 \pm 0.7 \pm 0.2$	$-0.2 \pm 0.8 \pm 0.2$
$\rho^\pm\rho^0$	$23.7 \pm 1.4 \pm 1.4$	$0.950 \pm 0.015 \pm 0.006$	n.a.	$0.054 \pm 0.055 \pm 0.010$

Table 1.3: Previous measurements of $B \to \rho\rho$ decays. The first errors are statistical and the second are systematics. Belle's numbers are taken from [75] [76]($\rho^+\rho^-$), [5]($\rho^0\rho^0$) and [77]($\rho^\pm\rho^0$) and BaBars numbers are from [78]($\rho^+\rho^-$), [79]($\rho^0\rho^0$) and [80]($\rho^\pm\rho^0$).

Chapter 2

The Belle Experiment

The Belle experiment is located at the High Energy Accelerator Research Organization (KEK) in Tsukuba, Japan and basically consists of two entities, the KEKB asymmetric e^+e^- collider and the Belle detector. It is one of two first-generation experiments especially dedicated to CP violation in B meson decays. BaBar, the other experiment, resided at SLAC at the PEP II asymmetric e^+e^- collider.

2.1 The KEKB Collider

One of the main challenges for B factories was to achieve a luminosity that allows for precise measurements. The instantaneous luminosity $\mathcal{L}(t)$ times a cross-section σ of interest gives the event rate:

$$\frac{d\mathrm{N}}{dt} = \mathcal{L}(t)\sigma. \tag{2.1}$$

For two beams of bunches with n_1 and n_2 particles per bunch, colliding with a frequency f a basic expression for the luminosity is given by

$$\mathcal{L} = f\frac{n_1 n_2}{4\pi\sigma_x\sigma_y}, \tag{2.2}$$

where the transverse beams sizes σ_i are assumed to be equal for both beams and the particles are Gaussian distributed in the bunch. The KEKB collider was especially designed for a high luminosity and is at present the luminosity world record holder with $\mathcal{L} = 2.11 \times 10^{34}\mathrm{cm}^{-2}s^{-1}$ and reached an integrated luminosity of over 1 ab^{-1} [81], see Fig. 2.1. The collider consists of an 8 GeV electron storage ring (high energy ring, HER) and a 3.5 GeV positron storage ring (low energy ring, LER), both with a length of 3012 m, which cross at the interaction point (IP) (Fig. 2.2). The bunches from the two beams cross each other with a finite crossing angle of 22 mrad to avoid parasitic interactions with secondary bunches away from the IP. To compensate for luminosity losses due to the crossing angle, a crab cavity [82] is used to tilt the beams in such a way that their overlap at the crossing is optimized, see Fig. 2.3. Each beam is accelerated to its final energy with a linear accelerator (LINAC) and then injected into the storage rings which contain about 2500 bunches each. At the IP, the energy asymmetry corresponds to a Lorentz boost of $(\beta\gamma)_{\Upsilon(4S)} = 0.425$ of the center of mass which has a energy of $\sqrt{s} = 10.58$ GeV. Lumiosity losses due to the asymmetric beam energies are

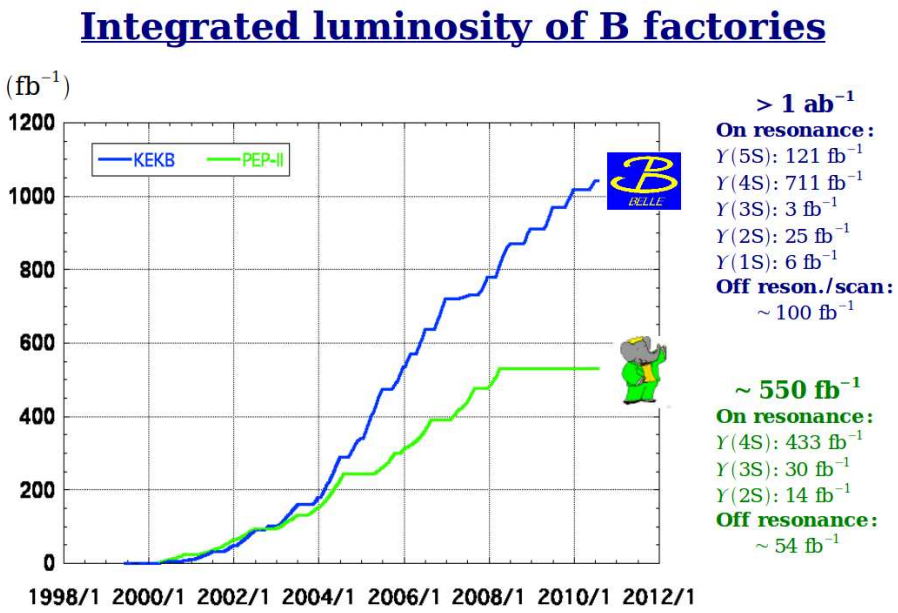

Figure 2.1: The luminosity recorded by Belle and Babar.

compensated by a higher beam current in the LER. e^+e^- collisions are regarded as clean as they can completely annihilate, while collisions of protons (like at the LHC) can also produce underlying events from spectator interactions.

2.2 The Belle Detector

The main purposes of the Belle detector are to measure the track, momentum, charge and energy deposition of the particles and to determine their species. It is a generic magnetic spectrometer asymmetrically surrounding the IP (see Fig. 2.4) and built for detecting and identifying the following final state particles:

Charged particles: $e^{\pm}, \mu^{\pm}, \pi^{\pm}, K^{\pm}, p$

Neutral particles: $\gamma, K^0_L, n,$

which covers most of the B meson final states. Because the entire center of mass energy goes into an event, neutrinos can be accessed when reconstructing all visible particles and using energy and momentum conservation. Special attention is paid to the spatial resolution at the vertex as this is required for the time-dependent CP violation measurement. Each sub-detector will be briefly described in the following, a detailed description can be found in [83].
The coordinate system used at Belle is illustrated in Fig. 2.5. The z-axis is defined anti-parallel to the positron beam line, the y-axis points vertically upwards and the x-axis is orthogonal to the z-y plane $\hat{x} = \hat{y} \times \hat{z}$. Thus the spherical coordinates are $r = \sqrt{x^2 + y^2}$, the azimuthal angle around the z-axis ϕ, and the polar angle θ, relative to the positive z-axis. The origin is the position of the nominal IP.

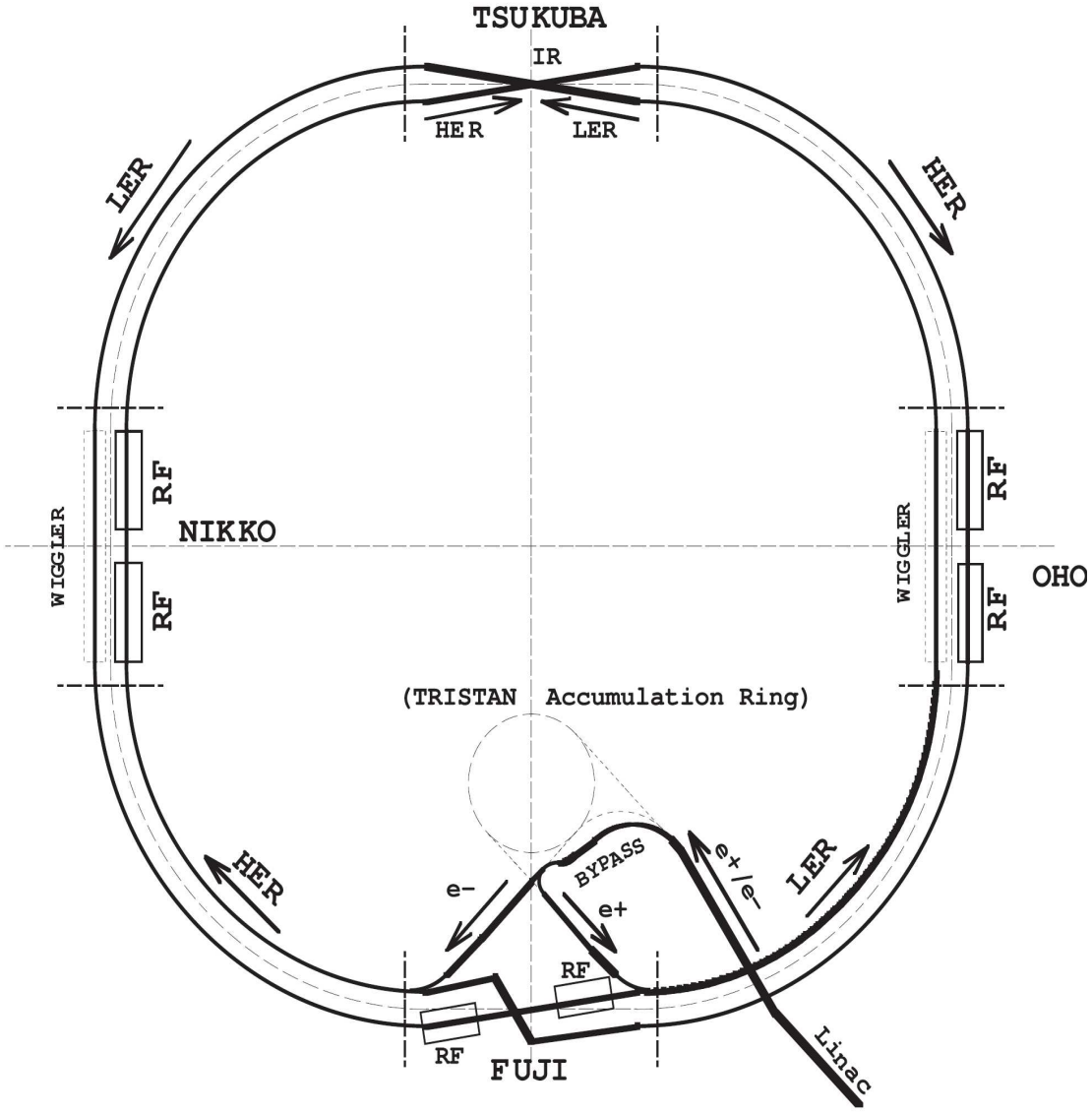

Figure 2.2: The KEKB e^+e^- electron-positron collider. The Belle detector is placed in the interaction region (IR) at the top [83].

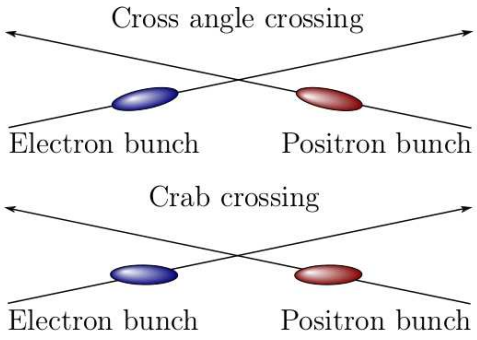

Figure 2.3: The finite crossing angle of 21 mrad with and without crab cavity [83].

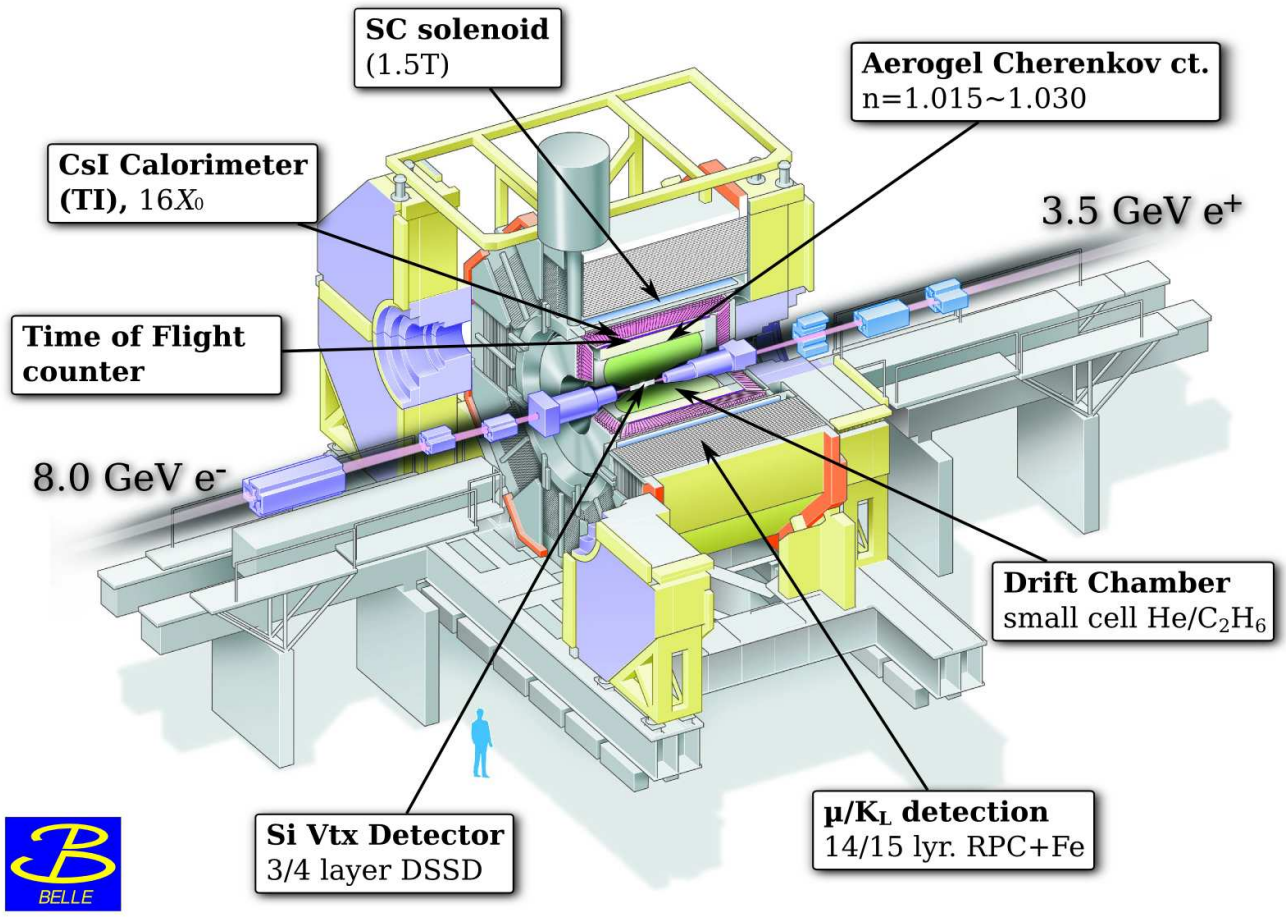

Figure 2.4: Cut-away view of the Belle detector [83].

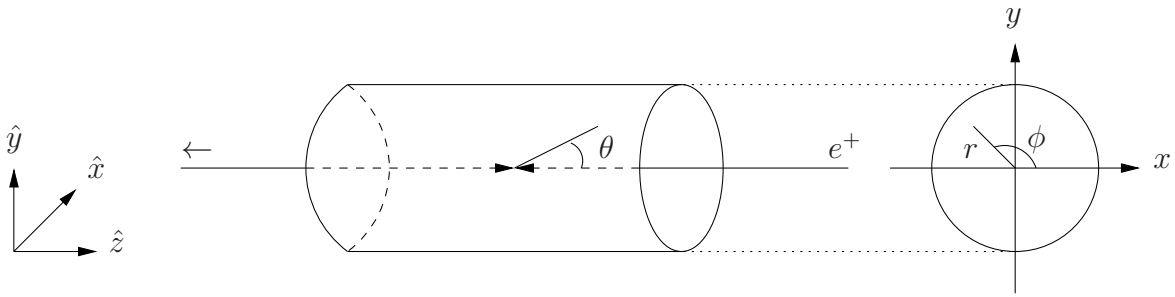

Figure 2.5: Coordinate systems of the Belle detector [83].

2.2.1 The Beampipe

The interaction region is inside a vacuum maintained by the beampipe. The beampipe is very thin and made of beryllium, which has a low atomic number, to minimize multiple scattering. The disturbance of a particle's trajectory when passing through material is deteriorating the track resolution, especially for low momentum tracks. It consists of two 0.5 mm thick cylindrical layers with 20 mm and 23 mm radius, respectively. In between, paraffin is used for cooling and the outer layer is covered with a 20 μm gold foil that blocks low energetic synchrotron radiation from damaging the innermost detector. The total thickness corresponds to less then 1% of a radiation length.
Because placing the detector closer to the IP improves the spatial resolution, also the radius of the beampipe and was reduced from 20 mm to 15 mm in the upgrade of the innermost detector in the year 2003.

2.2.2 The Silicon Vertex Detector (SVD)

The main purpose of the innermost detector is to determine the vertices of tracks as precisely as needed for time-dependent CP violation measurements. At least a spacial resolution of ~ 100 μm is needed for the z-component of the vertex position. Therefore, it has to be as close to the IP as possible. The SVD also contributes to the momentum determination of charged particles.
A low material budget minimizes multiple scattering, being the limiting factor for the vertex determination. The non-sensitive electronics are kept outside the tracking acceptance. Due to radiation damage, the SVD [84] was replaced in an upgrade in 2003 and redesigned to improve the z-vertex resolution. An additional layer was added, the detector placed closer to the IP and the acceptance increased. It is referred to as SVD1 before and SVD2 after the upgrade, the properties of both detector configurations are given in Table 2.1.

SVD1 [85] consist of three concentric cylindrical layers and covers the polar angle region, $23° < \theta < 139°$ which corresponds to 86% of the solid angle (Fig. 2.6). Each layer is made out of several ladders, consisting of two electrical-independent half-ladders which are held together by a support structure. Each ladder consist of one or two double-sided silicon strip detectors (DSSD) manufactured by Hamamatsu Photonics. Each DSSD consists of 1280 sense strips and 640 readout pads on each side. One side is p-doped, grounded and the strips are parallel to the beam to measure ϕ, whereas the other side is n-doped, biased with 75 V, with the strips perpendicular to the beam and measure z. In addition, p-stops are installed between the n-doped strips to provide better separation. As shown in Fig. 2.7, a charged particle traversing the DSSD will create electron-hole pairs, which are then collected for the read-out at the corresponding side. The momentum p, and polar-angle θ, dependent resolutions for SVD2 are represented by

$$\sigma_z = (28 \oplus \frac{32}{p\beta \sin^{5/2}\theta})\mu\text{m}, \qquad \sigma_\phi = (22 \oplus \frac{36}{p\beta \sin^{3/2}\theta})\mu\text{m}, \tag{2.3}$$

where $\oplus$ is the quadratic sum.Compared to SVD1, an improvement in the resolution can be seen in Fig. 2.8.

	SVD1	SVD2
Beam pipe radius (mm)	20	15
Layers	3	4
Radii of layers (mm)	30.0/45.5/60.5	20.0/43.5/70.0/88.8
Ladders per layer	8/10/14	6/12/18/18
Modules per ladder	2/3/4	2/3/5/6
Number of Modules	102	246
Module width (mm)	32.0	25.6 (33.28 for layer 4)
Module length (mm)	54.5	76.8 (74.75 for layer 4)
Module thickness (μm)	300	300
Pitch$r\phi$ (μm)	25	50 (65 for layer 4)
Pitch$z$ (μm)	84	75 (73 for layer 4)

Table 2.1: Comparison of the two SVD configurations.

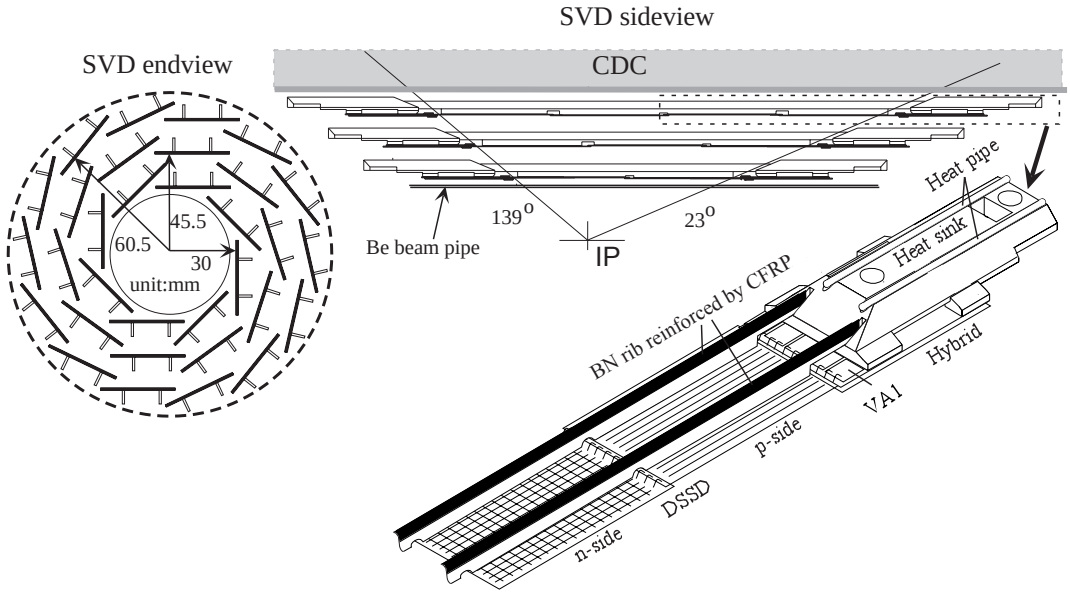

Figure 2.6: The SVD1 [83].

2.2.3 The Central Drift Chamber (CDC)

The CDC is a tracking device that allows to measure the momentum through the curvature of the track of a charged particle traversing a homogeneous magnetic field B_z. A track is parametrised with a helix [86], where besides the curvature($\sim p_T$) and the pitch, three impact parameters are used. In addition, an energy deposition (dE/dx) measurement is used for particle identification (PID).

The CDC, see Figs. 2.9 and 2.10, contains 50 layers of sense wires and has in total 8400 drift cells. Each drift cell has a positively biased sense wire being surrounded by eight negatively biased field wires to create a sufficiently strong electric field. It is a filled with a low-Z gas mixture of 50% helium and 50% ethane, chosen to minimize Coulomb scattering, which degrades momentum resolution. Its coverage of $17° < \theta < 150°$ is about 92% of the solid angle.

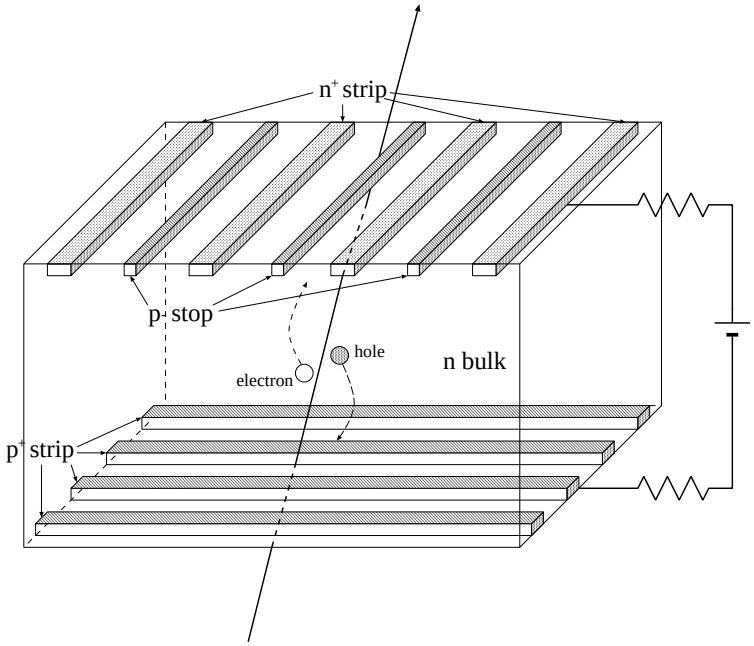

Figure 2.7: The principle of a double-sided silicon strip detector [83].

A charged particle traversing the CDC ionizes the gas and the released electrons are attracted by the fields of the sense wires. Accelerated by the strong electric field, the electrons create cascades through secondary ionization while drifting to the wires. This so-called gas amplification brings about $\sim 10^6$ signal enhancement. The time the electrons need to drift to the wires is used for tracking. Wires parallel to the beam are used for measuring p_T while others are rotated ± 50 mrad to the z-direction and give the polar angle θ. The p_T resolution is found to be

$$\sigma(p_T) = (0.2 p_T \oplus 0.29/\beta) \ \ \%, \tag{2.4}$$

as shown in Fig 2.11. dE/dx can be measured from the pulse height. Fig. 2.11 shows the deposited energy as a function of the momentum for electrons, pions, kaons and protons. Combining the momentum and the dE/dx measurements allow to identify the particle species for low momenta, $p_T \leq 1$ GeV/c. The truncated mean $\langle dE/dx \rangle$ of all pulses is used for this purpose. The reconstructed trajectory is improved by combining CDC tracks with SVD hits. The average track matching effiency between SVD and CDC is better then 98%.

2.2.4 The Aerogel Cherenkov Counter (ACC)

In order to distinguish light from heavy particles in the high momentum range (1.5 GeV/c - 3.5 GeV/c), an ACC is used. It is built out of 960 separate modules in the barrel region. Each module consists of an aluminum encased block of silica aerogel with one or two photomultipliers for the detection. The forward endcap has additional 228 modules. The layout is shown in Fig. 2.12.
Cherenkov radiation is emitted when a particle with mass m enters a medium with a velocity v, greater then the speed of light in that medium,

$$n > \frac{1}{\beta} = \sqrt{1 + \left(\frac{m}{p}\right)^2}. \tag{2.5}$$

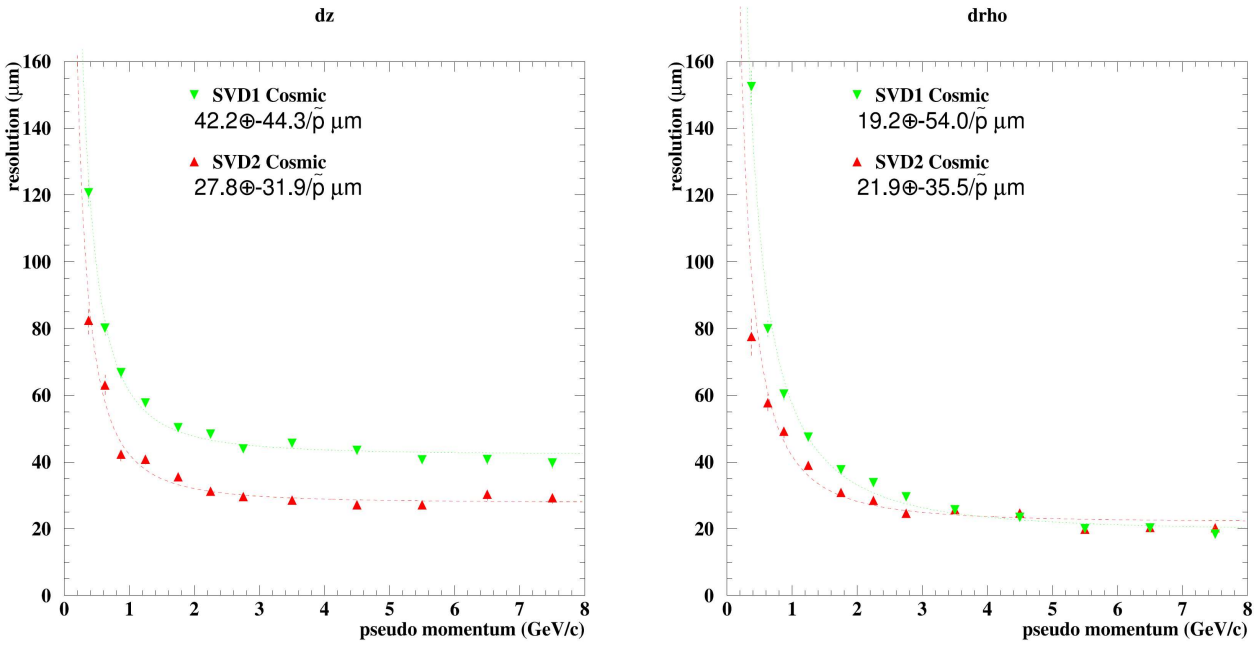

Figure 2.8: Momentum and angular-dependent impact parameter resolution [83]. The two configurations of the vertex detector are shown.

n is the refractive index and $\beta = v/c$. The silica aerogels's refractive indices for different polar angle regions are chosen such that light is emitted only for particles that are lighter than the kaon. Fig. 2.13 shows the performance of pion/kaon separation for different regions of the detector.

2.2.5 The Time Of Flight (TOF)

Approximately $\sim 90\%$ of the final states particles from B decays have a momentum smaller than 1.2 GeV/c. They can be identified with the TOF. The time a particle needs to travel from the IP to the TOF is

$$T = \frac{L}{c\beta} = \frac{L}{c}\sqrt{1 + \left(\frac{m}{p}\right)^2}, \tag{2.6}$$

where $L = 1.2$ m is the flight length. The mass m can be determined if the momentum p is known from the CDC. A time resolution of 100 ps is neccesary, which in turn provides fast timing signals for the trigger system. In total 64 TOF modules are installed in the barrel region and cover a polar angle of $34° < \theta < 120°$ (Fig. 2.12). Each module consists of scintillation counters attached to photo-multiplier tubes which have thin trigger scintillation counters (TSC) attached in the front to keep the fast trigger rate. The discrimination of pions, kaons and protons as well as the kaon-pion momentum-dependent separation performance are demonstrated in Fig. 2.14.

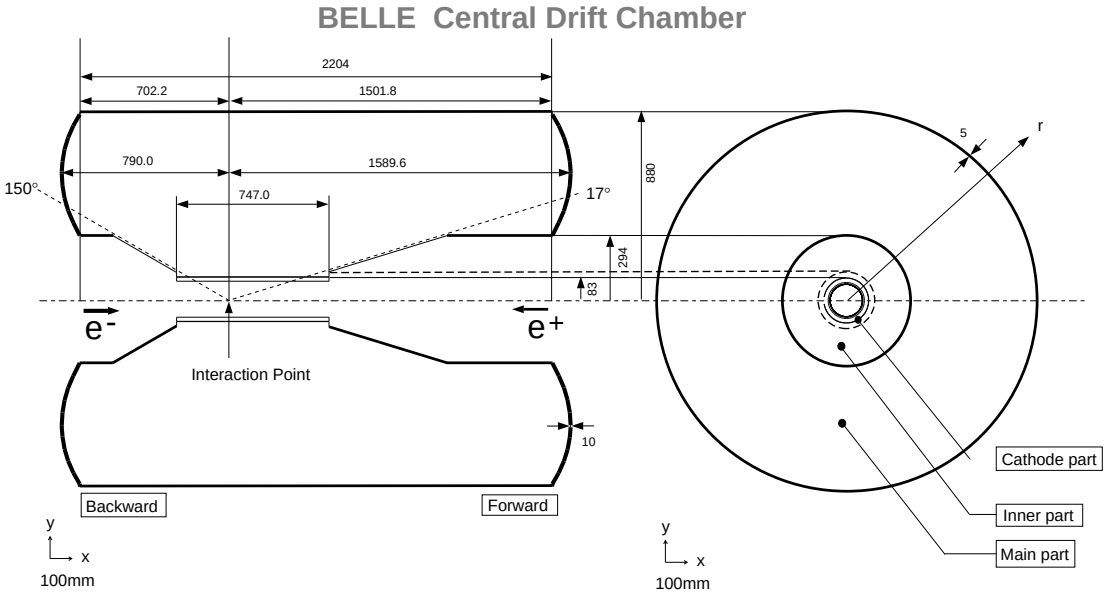

Figure 2.9: The CDC [83].

2.2.6 The Electromagnetic Calorimeter (ECL)

For photon detection and electron identification, a calorimeter with good energy and position resolution for energies below 500 MeV up to 4 GeV is used. These particles can be separated from hadrons from the signature shape of their electromagnetic showers. In contrast to hadrons which pass the ECL almost without dissipating energy, electrons and photons can deposit their entire energy through Compton scattering, bremsstrahlung and pair production. Photons can be distinguished from electrons since they are not detected by the SVD and CDC. Also the energy (ECL) momentum (CDC) ratio, E/p, should be consistent with one for electrons. The ECL has two parts. The the barrel section consists of 6624 (46 in θ and 144 in ϕ) tower-shaped CsI (Tl) crystals and the forward and backward end cap parts have 1152 (13 in θ and 48-144 in ϕ) and 960 (10 in θ and 64-144 in ϕ) crystals, respectively. As shown in Fig. 2.15, the crystals are pointing towards the IP, slightly tilted to avoid non-sensitive gaps. Their length of 30 cm corresponds to $16.2X_0$ (radiation lengths) and the readout is done with a pair of silicon photodiodes and charge-sensitive preamplifiers for each crystal. The energy and position resolutions are given by

$$\frac{\sigma_E}{E} = \left(1.34 \oplus \frac{0.066}{E} \oplus \frac{0.81}{\sqrt[4]{E}}\right), \tag{2.7}$$

$$\sigma_{pos} = \left(0.27 + \frac{3.4}{\sqrt{E}} + \frac{1.8}{\sqrt[4]{E}}\right), \tag{2.8}$$

and shown in Fig. 2.16. E is measured in GeV.

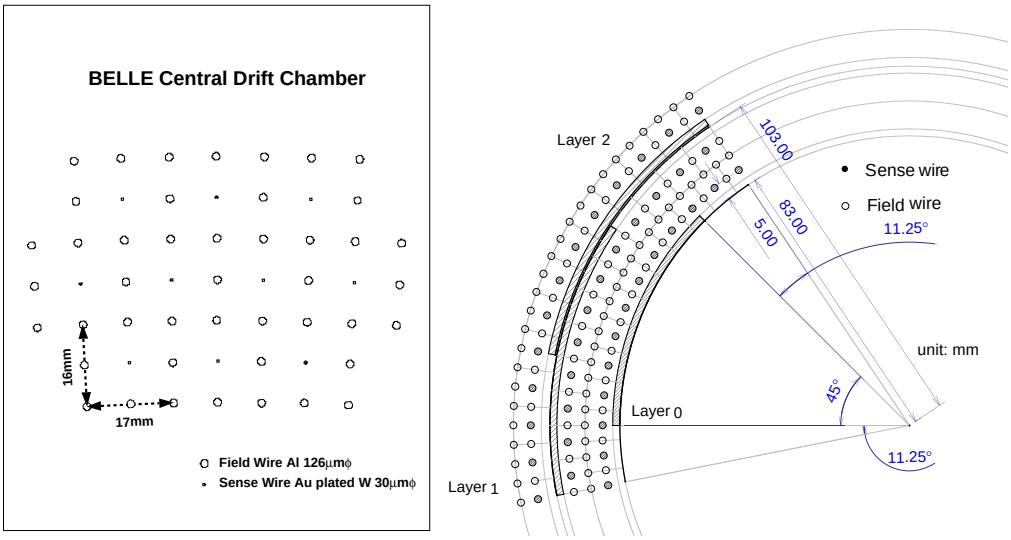

Figure 2.10: The CDC cell structure [83].

2.2.7 The Magnetic Field

A nearly homogeneous magnetic field of 1.5 T pointing in the z-direction is provided by a superconducting solenoid which consists of a single layer of niobium-titanium-copper alloy that is embedded in an aluminum stabilizer wound around an aluminum support cylinder. This cylinder has a radius of 1.7 m and is 4.4 m long. The magnet is cooled by liquid helium circulating through a tube on the inner side of the cylinder.

2.2.8 K_L^0 And Muon Detector (KLM)

As its name indicates, this subdetector is for detecting the neutral long living meson K_L^0, as well as muons in a broad momentum range above 600 MeV/c which is the minimal transverse momentum needed to reach the KLM. As these particles hardly interact with the subdetectors mentioned before, a rather dense and thick detector is necessary to absorb them efficiently. The KLM is placed outside of the solenoid and consists of 15 and 14 layers of Resistive Plate Counters (RPC) (Fig. 2.17) in the barrel region and the end-caps, respectively. 4.7 cm thick iron plates are placed in between as absorbers and also to return the magnetic flux. Since hadrons interact strongly, they get absorbed within a few layers, producing rather broad short hadronic showers that can be discriminated from long "tracks" associated with muons. In addition, muons leave tracks in the charge sensitive subdetectors.

2.2.9 Trigger And Data Acquisition

Primarily due to the high current, many processes lead to a signal in the detector but are not of interest. The main background sources are synchrotron radiation, beam-gas and beam-beam interactions. For this reason, a trigger system is used to make decisions which events are stored for further purposes. The trigger system consists of a level 1 hardware trigger, a real-time level 3 software trigger and an off-line level 4 trigger. Events of interest, besides

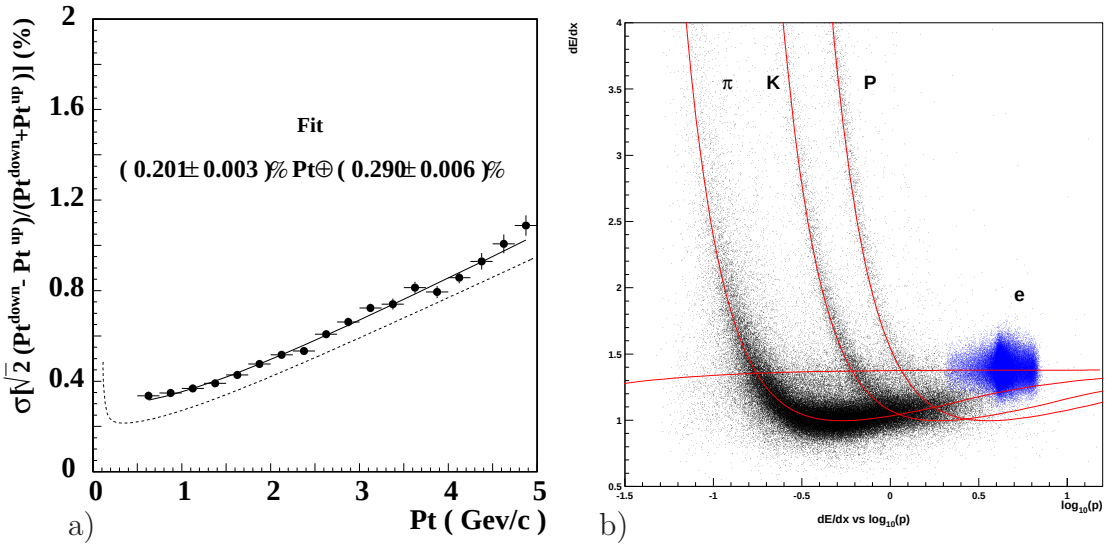

Figure 2.11: (a)t shows the data and fit of the p_T-dependent resolution for cosmic rays. The dotted curve is for the idealized case of $\beta = 1$. (b) shows the CDC dE/dx vs momentum of collision data [83].

hadronic events which might contain a $B\bar{B}$ pair, include for example two photon events, bhabha scattering and μ-pair production as they are also used for luminosity measurements and detector calibration.

Level 1 Trigger

For the so-called global decision logic (GDL), information of different subdetectors are combined and the decision to trigger depends on at least one of the following conditions,

- two tracks with an opening angle of at least 135°, where at least one track must have z-information and not less than 2 hits in the TOF.
- three tracks with, except for the opening angle, similar conditions as above.
- at least 4 isolated clusters in the ECL.
- at least 1 GeV of energy deposition in the ECL.

Having several triggers makes the trigger efficiency more independent of varying accelerator conditions. The trigger's effiency is greater then 99.5%. In order to keep up with the expected rates for physics events and background events, which are both approximately 100 Hz, the trigger operates typically at 200-250 Hz. But it is designed to handle a maximum trigger rate of 500 Hz to be robust against unexpected high beam background rates. The decision to pass an event to the data acquisition (DAQ) has to be made within 2.2 μs. A schematic view of the level 1 trigger is shown in Fig. 2.18.

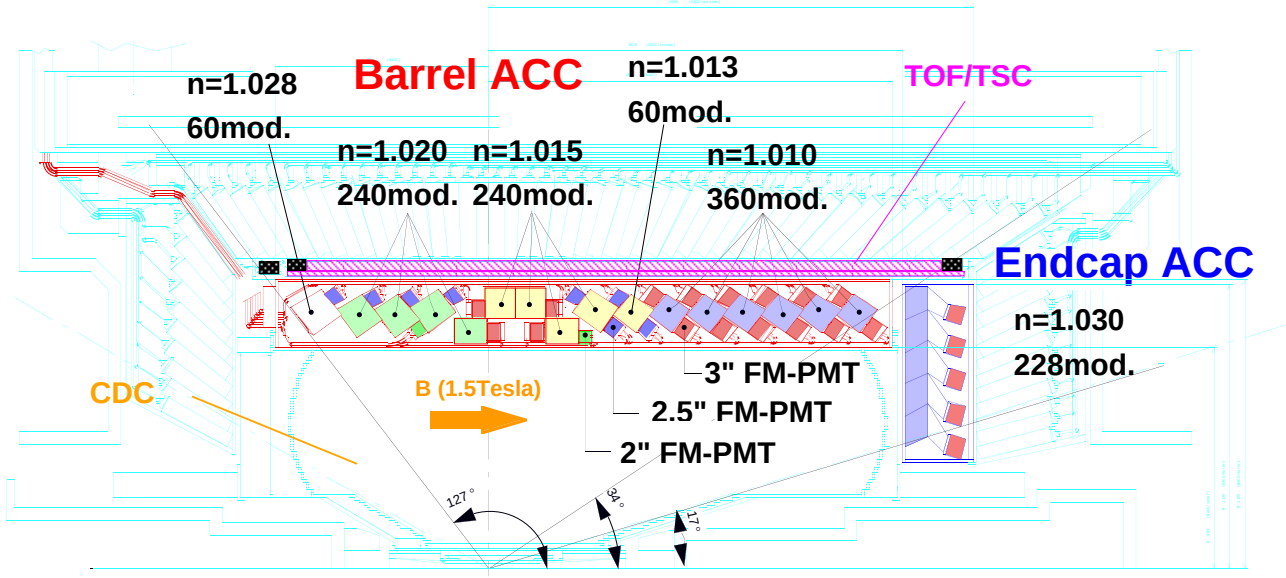

Figure 2.12: The ACC [83].

Level 3 and 4 Trigger

In order to reduce the number of events to be stored, an event rejection on tracks quickly reconstructed from GDL input, is performed on-line by the level 3 trigger. There, events with no tracks with $|dz| < 5$ cm are discarded. The level 4 trigger basically works the same way, but has tighter track requirements: $|dz| < 4$ cm, $|dr| < 1$ cm with $p_T > 300$ MeV/c. As this trigger operates off-line, a more careful and precise reconstruction can be performed. Here, tracks from the CDC are combined with SVD hits and also with hits from the outer detectors. Four-vectors and particle identification likelihoods are then assigned to the tracks. All events that reach the level 4 trigger are kept in raw format.

DAQ

Events which pass the level 4 trigger are stored on so-called Data Summery Tapes (DST) in the PANTHER [87] file format, accessible for all Belle collaborators. DAQ is designed to have a dead time fraction of less then 10% and is therefore parallelized.

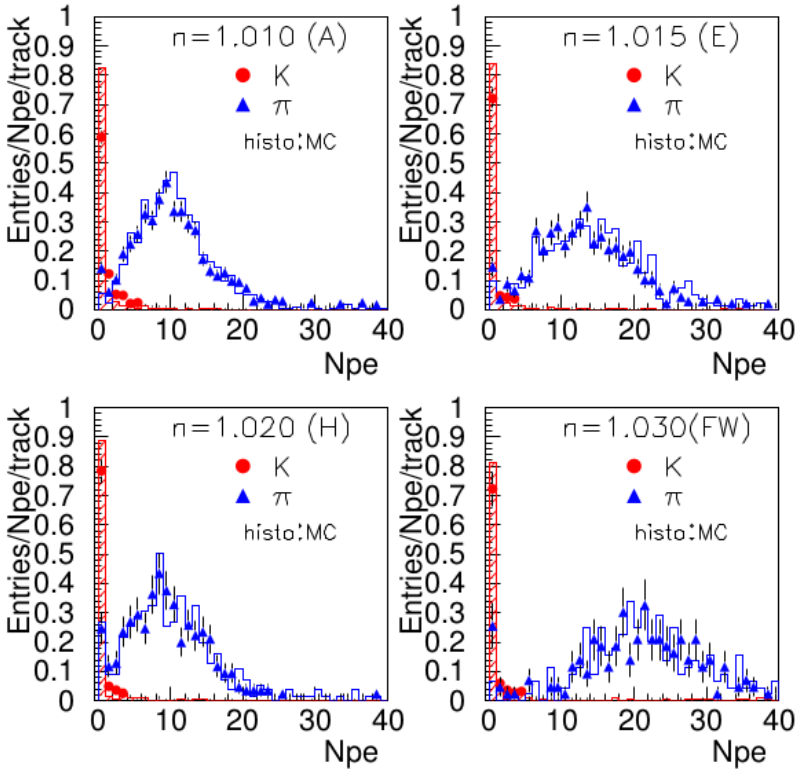

Figure 2.13: ACC kaon-pion discrimination for different refractive indices of the active material [83].

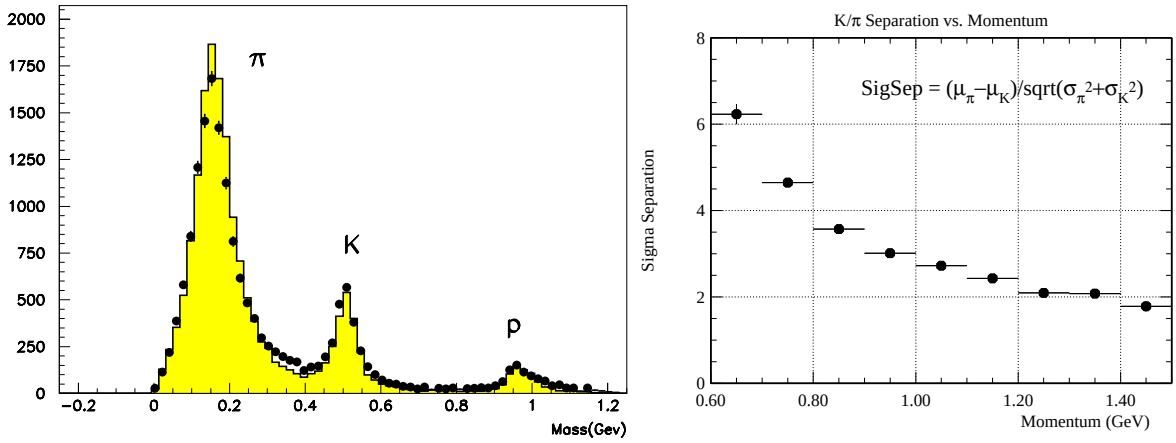

Figure 2.14: The left figure shows the TOF mass distribution obtained with TOF measurements for p below 1.2 GeV/c, where the area is MC and the points are data. The right plot shows the charged K/π separation as a function of the particle's momentum [83].

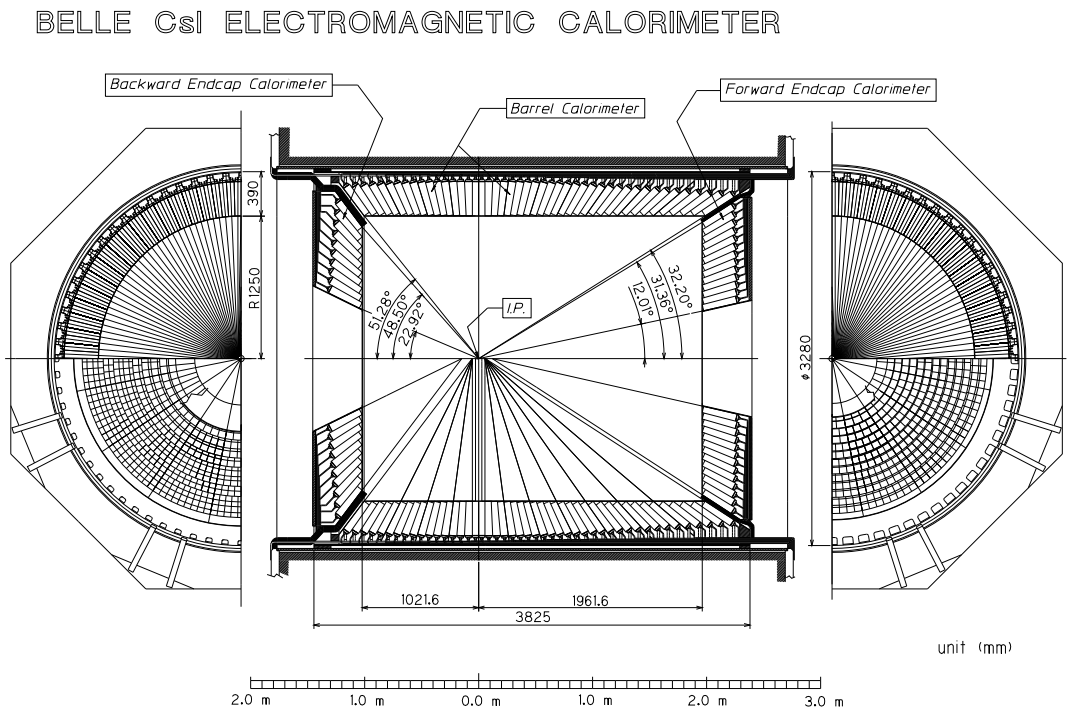

Figure 2.15: The ECL geometry [83].

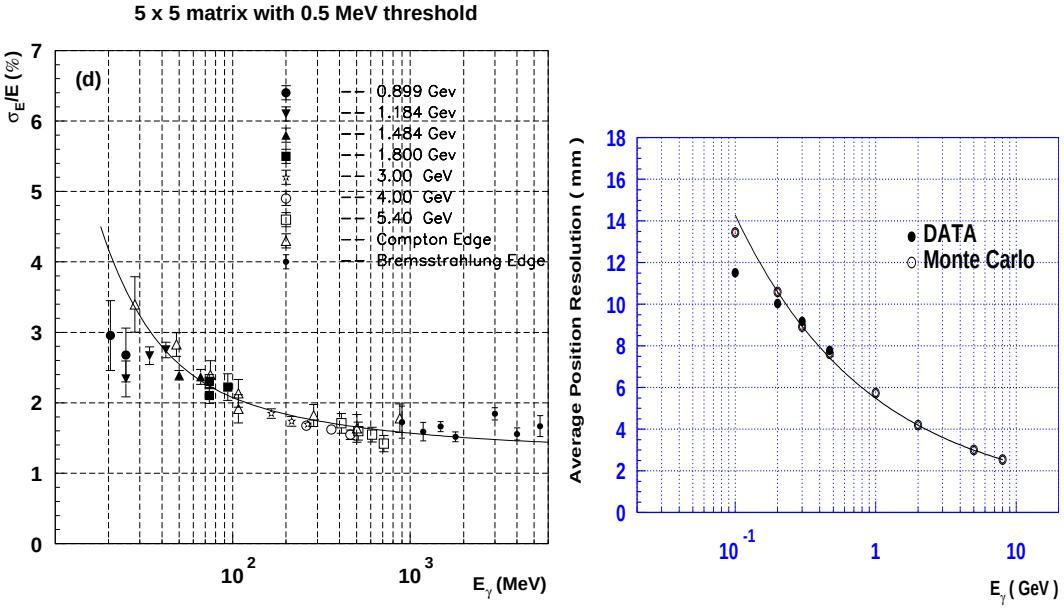

Figure 2.16: Energy (left) and position resolution (right) of the ECL [83].

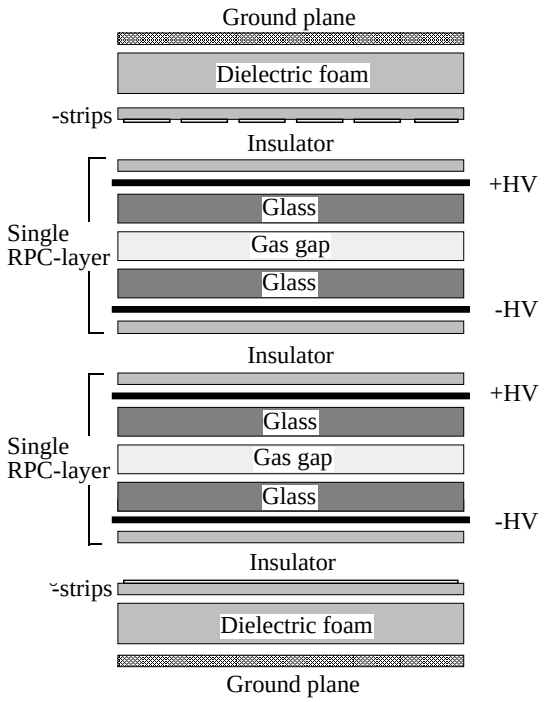

Figure 2.17: RPC superlayer [83].

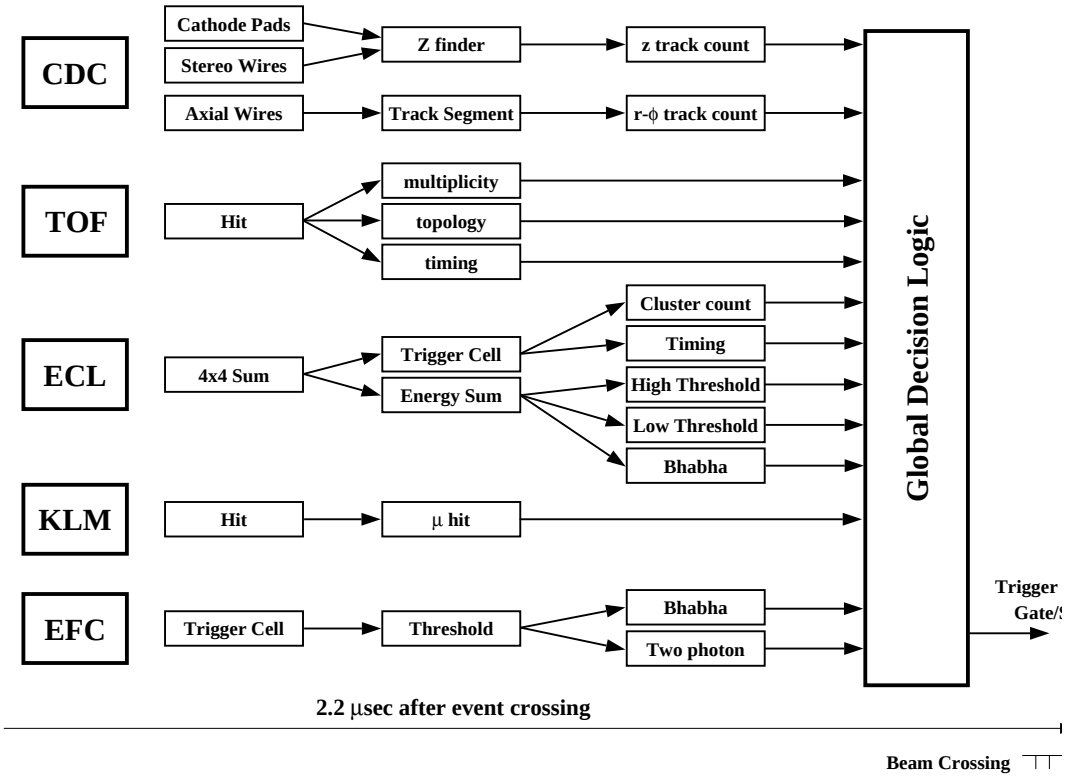

Figure 2.18: Schematic view of the level 1 trigger [83].

Chapter 3

Reconstruction and other Features of the Analysis

For this measurement, we need to identify $B^0 \to \rho^+\rho^-$ decays among all the events that are triggered and stored on tape. We perform two preselections on the data, the data composition is described in Section 3.1. First we remove non-hadronic processes, see Section 3.1.1. Then, B mesons are reconstructed from two ρ mesons which again are reconstructed from the final state particles seen by the detector, see Section 3.2. Combining the information from all sub detectors allows to obtain lists of the recorded particles in an event. Further selection criteria are imposed in the reconstruction and all required information, such as the vertices of the B mesons or a B flavor propablity, is obtained per event. The procedure is optimized by studying fully simulated $B^0 \to \rho^+\rho^-$ MC events. This also allows to estimate the selection efficiency (see Section 3.2.10) and we treat $B^0 \to \rho^+\rho^-$ decays with longitudinal (LP) and tranversal (TP) polarization separately.
The data sample after applying all selection criteria still consists almost entirely of background processes (other $B\bar{B}$ decays or the direct production of light hadrons from e^+e^- annihilation) passing our selection criteria. An overview of the considered contributions, the fit components, is given in Section 3.3.
Considering these multiple components, we perform a fit to several distributions (fit variables) to identify the signal component in the data and extract the observables of interest. The time-dependent CP violation parameters are obtained from the difference of the lifetime distributions from reconstructed B mesons identified as signal and tagged as B^0 or $\bar{B}^0$. Other variables, for example the reconstructed B and ρ masses, are useful to distinguish the different components and to measure their yields. In addition, the longitudinal polarization fraction can be obtained from fitting the distribution of the helicity angles. The fit variables are calculated for each event in the reconstruction.
Based on individual MC simulations for all considered components, see Section 3.3.1, we describe the distributions of the fit variables with multidimensional probability density functions (PDFs). We study each considered component separately, see Chapter 4 and Appendix C for a detailed description or Section 4.5 for a summary of all components, and combine them all in an extended maximum likelihood fit, as described in Sections 4.1 and 4.6. We validate the fitting procedure with fully simulated MC events composed according to our expectations, see Section 4.7 and fix the procedure before analyzing the data. This so called "blind analysis" approach prevents tuning the measurement procedure towards a more de-

sired result.
We study a high statistics control channel with a similar final state topology to extract correction factors for data/MC differences in Appendix A which are used in the fit to the data ($B \to \rho\rho$), presented in Chapter 5. The systematics uncertainties are estimated in Chapter 6.

The measurement of the branching fraction and longitudinal polarization fraction of $B^0 \to \rho^0\rho^0$ decays has many similarities and is published. Reference [5] describes the reconstruction and fitting procedures of $B^0 \to \rho^0\rho^0$, which are not discussed in this work.

3.1 Data Sample

During the total run-time of the Belle experiment, starting from January 2000 to July 2010, the Belle detector accumulated an integrated luminosity of 1.04 ab^{-1}, of which 772 million $B\bar{B}$ pairs were collected at the $\Upsilon(4S)$ resonance (Fig. 2.1). Due to an upgrade in the summer of 2003, two different configurations of the innermost detector, SVD1 and SVD2, exist. The data sample from the SVD1 era contains the first 152×10^6 $B\bar{B}$ pairs while the SVD2 configuration covers the remainder of the experiment, where 570×10^6 $B\bar{B}$ pairs were collected. KEKB holds the current world record on luminosity with 2.11×10^{34} cm^{-2}s^{-1} which greatly exceeds its initial design luminosity of 1.0×10^{34} cm^{-2}s^{-1}.

The data taken with SVD2 was reprocessed in 2010 with a new tracking algorithm which includes a better track pattern recognition (Hough finder), SVD only tracking and a more sophisticated treatment of the ECL information. This is improving the track finding by $\sim 2\%$ per track, so especially decays with high track multiplicity benefit. Since the features of the recorded events may differ depending on the SVD configuration, it is necessary to perform independent studies with both experimental setups, which can subsequently be merged in the study of real data.

3.1.1 Non Hadronic Event Suppression

Several processes in e^+e^- collisions at $\sqrt{s} = 10.58$ GeV can occur besides the production of a $B\bar{B}$ pair. The main contributions are shown in Table 3.1. We remove non-hadronic events, e.g. Bhabba scattering, lepton or photon pair production, by performing a preselection (hadronic skim) on the data [88].
The requirements are based on "good" reconstructed tracks defined as having transverse momentum, $p_t > 100$ MeV/c, and impact parameters from the interaction point $|\Delta r| < 2$ cm and $|\Delta z| < 4$ cm. They are also based on "good" neutral clusters defined as having energy $E_{\text{cluster}} > 100$ MeV deposited in the barrel region of the ECL, $-0.7 < \cos\theta < 0.9$. The criteria are as follows where all quantities are determined in the center of mass frame (CMS),

- Track Multiplicity

  $nTrk \geq 3$.

- Neutral Cluster Multiplicity

$$nCls \geq 2,$$

which removes QED and low-multiplicity beam gas events.

- Primary Event Vertex

  All good tracks are fitted to a primary vertex with the requirements $r_{\rm PV} < 1.5$ cm and $|z_{\rm PV}| < 3.5$ cm.

- Visible energy collected

  $$E_{\rm vis} \geq 0.18\sqrt{s},$$

  where $E_{\rm vis} = (\sum \vec{p}_{\rm Trk} + \sum E_{\rm Cls})$ per event.

- Calorimeter Energy Sum

  $$0.1 < \sum E_{\rm Cls}/\sqrt{s} < 0.8,$$

  which suppresses QED processes, as well as τ-pair production, beam gas and two γ events with low energy sum.

- Momentum Balance in z

  $$|\sum_{\rm Trk,\ Cls} p_z| < 0.5\sqrt{s}.$$

- Heavy Jet Mass, HJM

  $$HJM/E_{vis} > 0.25 \text{ or } HJM > 1.8\text{GeV}/c^2,$$

  to further remove double τ events. The heavy jet mass is defined as the invariant mass of the tracks in each hemisphere perpendicular to the boost.

With these criteria, 99% (79%) of all $B\bar{B}$ ($q\bar{q}$) events and only 5% of non-hadronic processes are kept.

Process	cross section before skim (nb)	cross section after skim (nb)
$b\bar{b}$	1.1	1.09
$q\bar{q}$	3.3	2.62
$\tau^+\tau^-$	0.93	0.05
QED	37.7	0.001
$\gamma\gamma \to q\bar{q}$	11.1	0.04

Table 3.1: Cross sections for e^+e^- at $\sqrt{s} = 10.58GeV$ in the Belle acceptance (data). QED includes the Bhabba, radiative Bhabba and muon production processes.

3.1.2 Number of B Pairs

The branching fraction $\mathcal{B}$ of a certain final state $f_{\rm sig}$ can be calculated by relating the observed signal yield $N_{\rm sig}$ to all available B mesons:

$$\mathcal{B}(B \to f_{\rm sig}) = \frac{N_{\rm sig}}{\epsilon_{\rm sig} N_{B\bar{B}}}, \tag{3.1}$$

where $\epsilon_{\rm sig}$ is the reconstruction efficiency, obtained from MC simulation (see Section 3.2.10). The total number of recorded $B\bar{B}$ pairs, $N_{B\bar{B}}$, is measured as explained in the following, a detailed description can be found in [89]. Two kinds of data sets exist:

- on-resonance: $\sqrt{s} \sim 10.58$ GeV $\rightarrow$ at the $\Upsilon(4S)$ rest energy and
- off-resonance: $\sqrt{s} \sim 10.50$ GeV $\rightarrow$ below the $\Upsilon(4S)$ threshold.

The total number of $B\bar{B}$ events in the hadronic skim then is given by,

$$N_{B\bar{B}} = N_{\rm on-resonance} - acN_{\rm off-resonance}, \tag{3.2}$$

where $N_{\rm on(off)-resonance}$ are the number of recorded events in each data set and a is a integrated luminosity scale factor,

$$a \equiv \frac{1}{2}[a(e^+e^-) + a(\mu^+\mu^-)], \tag{3.3}$$

which is calculated from number of recorded Bhabha (e^+e^-) and di-muon events before the skim; $a(\text{process}) \equiv N(\text{process})_{\rm on-res}/N(\text{process})_{\rm off-res}$. The uncertainty on a is given by $\delta a = \pm\frac{1}{2}[a(e^+e^-) - a(\mu^+\mu^-)]$. The parameter c is the ratio of the skim efficiency, ϵ, for $q\bar{q}$ in on- and off-resonance, which are calculated from MC. This number takes slightly different kinematics for both center of mass energies into account and is close to one,

$$c \equiv \frac{\epsilon_{q\bar{q}}^{\rm on-res}}{\epsilon_{q\bar{q}}^{\rm off-res}} \tag{3.4}$$

with an error δc accounting for the imperfections in the MC simulation. In addition, uncertainties in the beam background are taken into account. The subtraction in Eq. (3.2) cancels $\sim 5\%$ contamination from non-hadronic backgrounds after the skim.

Every other $B\bar{B}$ pair contains charged B mesons, the ratio of charged to neutral $B\bar{B}$ pair production is measured to be consistent with one, $f_{B^+B^-/B^0\bar{B}^0} = 1.06 \pm 0.03$ [64]. As there are two B per event, the total number of neutral B mesons corresponds to $N_{B\bar{B}}$ in the given precision.

3.2 Reconstruction

The decay chain of interest is given by

$$B^0 \to \rho^+\rho^-$$

$$\rho^{\pm} \rightarrow \pi^{\pm}\ \pi^{0}$$
$$\pi^{0} \rightarrow \gamma\gamma$$

where the $\rho^{\pm}$ decays instantaneously into two pions and the π^0 into two photons.

3.2.1 Particle Identification

All particle selection criteria used in this analysis are standard in Belle and have known systematic uncertainties from various independent studies. Fig. 3.2 shows the number of pions before and after the selection. We reconstruct the $\rho^{\pm}$ from a charged and a neutral pion.

Charged Pions

With information obtained from the CDC, ACC and TOF, particle identification (PID) is determined with the likelihood ratio, $\mathcal{L}_i/(\mathcal{L}_i + \mathcal{L}_{j\neq i})$, where $\mathcal{L}_i$ is the likelihood to be a particle of type i. A overview of the momentum range of the different sub detectors used for PID is shown in Fig. 3.1. We consider a track to be a charged pion candidate if:

- Kaon/π Likelihood: $\mathcal{L}(K:\pi) < 0.4$,
- Electron Likelihood: $\mathcal{L}(e:\text{Not } e) < 0.9$,
- Proton/π Likelihood: $\mathcal{L}(p:\pi) < 0.9$.

With these cuts 90% of all pions are retained while having a kaon contamination of 10%. We also include an IP constraint and require $dr < 0.5$ cm and $dz < 5$ cm. We do not apply a muon veto as that would introduce an additional systematic uncertainty associated with the ECL. This is justified because we do not find any peaking contribution in neither the invariant mass of any combination of two or three pions nor in the ΔE distribution (see Section 3.2.6) of the non-peaking backgrounds from other B decays.

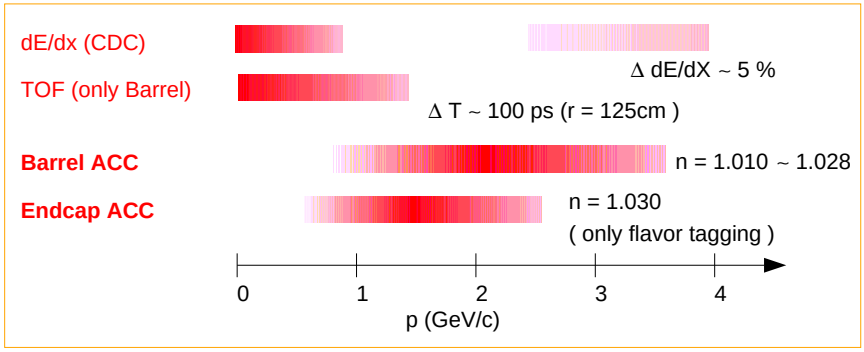

Figure 3.1: A schematic view of the momentum range for the detectors used for particle identification.

Neutral Pions

Isolated energy clusters in the calorimeter are identified as photons. π^0s are reconstruct from two photons. A loose vertex constraint mass fit of the two photons requiring

- $E_\gamma > 50$ MeV for $32° < \Theta_{\gamma,z} < 130°$ and
- $E_\gamma > 90$ MeV else,

is performed, with $\Theta_{\gamma,z}$ being the angle between the flight direction of the γ and the z-axis. The condition separates the barrel region from the end-caps. Furthermore, we require a chi-square of the fit below 50 and the invariant two-photon mass to be within 117.8 MeV $<$ $m_{\gamma\gamma} < 150.2$ MeV. We accept π^0s with a momentum in the CMS frame $|p^*_{\pi^0}| > 100$ MeV.

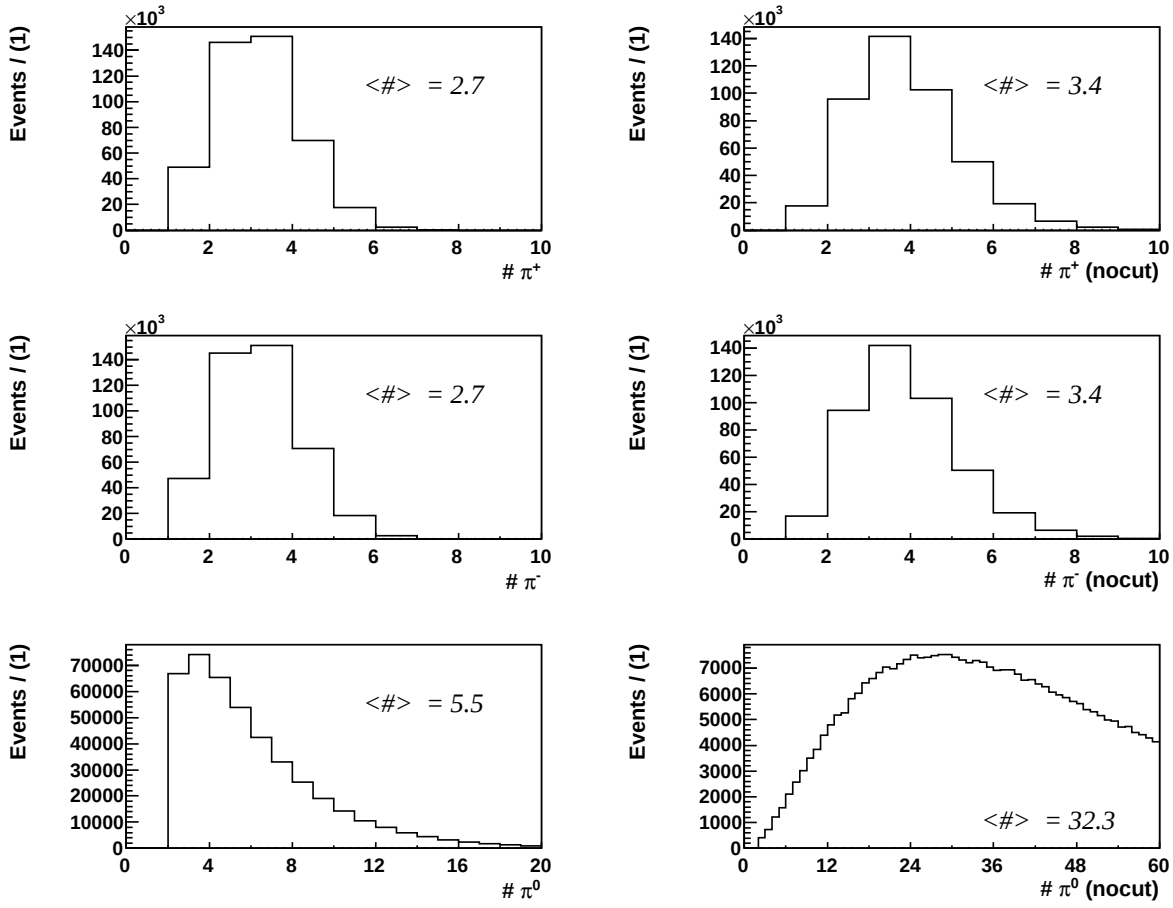

Figure 3.2: From top to bottom: number of π^+, π^- and π^0 candidates, respectively, after and before (no cut) the selection for signal MC simulation.

3.2.2 Reconstruction of the $B^0 \to \rho^+\rho^-$ Decay

The $\rho(770)$ is a broad resonance with a width of 149 MeV. The invariant mass of a $\rho^\pm$ candidate, reconstructed from a $\pi^\pm\pi^0$ pair, is required to fulfill: $m_{\pi^\pm\pi^0} \in [0.4\ \mathrm{GeV/c^2}, 1.15\ \mathrm{GeV/c^2}]$. According to the shape obtained from generated MC, this rejects 7.6% of all $\rho^+\rho^-$ pairs. Second, B^0 mesons are made from $\rho^+\rho^-$ pairs.

3.2.3 Vertex Fit

The accuracy of the vertex position is crucial for a time-dependent measurement, with the z-component of the vertex being of most importance as in coincides with the boost of the center of mass. We impose the same conditions under which the Δt resolution function is determined, a detailed procedure of kinematic (vertex) fitting can be found in Ref. [90]. A fit of the daughter tracks of each reconstructed $B^0 \to \rho^+\rho^-$ (B_{CP}) candidate to a common vertex is performed if the tracks have at least

- 2 hits in the z-layer and
- 1 hits in the $r\phi$-layer

of the SVD. We furthermore require an IP constraint: the vertex has to originate from a tube along the z-direction around the interaction point (IP). The tube's radius depends on the event-dependent IP profile, a typical IP profile is 100 μm in x, 5 μm in y and 4 mm in z. At least one track must enter the vertex fit, the IP constraint allows to obtain a vertex from only a single track. The best common vertex is calculated with the least square method using Lagrangian multipliers. The four-momenta of the tracks that are successfully fitted to a common vertex are recalculated and then used to update the momentum of B_{CP}.

Also the vertex position of the other B meson (B_{tag}) is needed for the calculation of Δt. Therefore, all tracks that do not belong to B_{CP} are fitted to a common vertex. The fit is repeated until $\chi^2/\text{ndf} < 20$ is fulfilled, where the tracks with the worst contribution are removed in each iteration. Since more than 90% of B_{tag} decays includes D-mesons, which have an unnegligible flight length, the residual of the tagside vertex is biased. An IP-tube constraint and rejecting displaced tracks ($|dr| > 0.5$ mm) or those with poor position measurement ($\sigma_z > 0.5$ mm) decreases the bias. The remaining bias is considered in the resolution function [91] for the Δt PDF (see Eq. (4.19)).

According to MC simulation, the resolution of the CP-side vertex is $\sigma_{CP} \sim 80\mu$m and the one of the tag-side vertex is $\sigma_{\text{tag}} \sim 120\mu$m. If one of these fit fails, the corresponding $B\bar{B}$ pair candidate is removed as Δt cannot be calculated.

Selection for Time-Dependent Measurement

Events with poor vertex information deteriorate the Δt measurement and are therefore excluded. We require that the vertex fit fulfills $\chi^2/\text{ndf} < 50$ and that the z-error of each vertex $\delta_z < 0.5$ mm for vertices from single tracks and $\delta_z < 0.2$ mm else. Those criteria furthermore help to exclude long-living particles, whose secondary vertices biases the determination of Δt. The δ_z and χ^2/ndf distributions for B_{CP} and B_{tag} are shown in Fig. 3.3.

3.2.4 Flavor Tagging

The flavor of the reconstructed B_{CP} has to be determined for a measurement of CP violation, a decay into a CP eigenstate, however, does not provided this information. But the flavor of

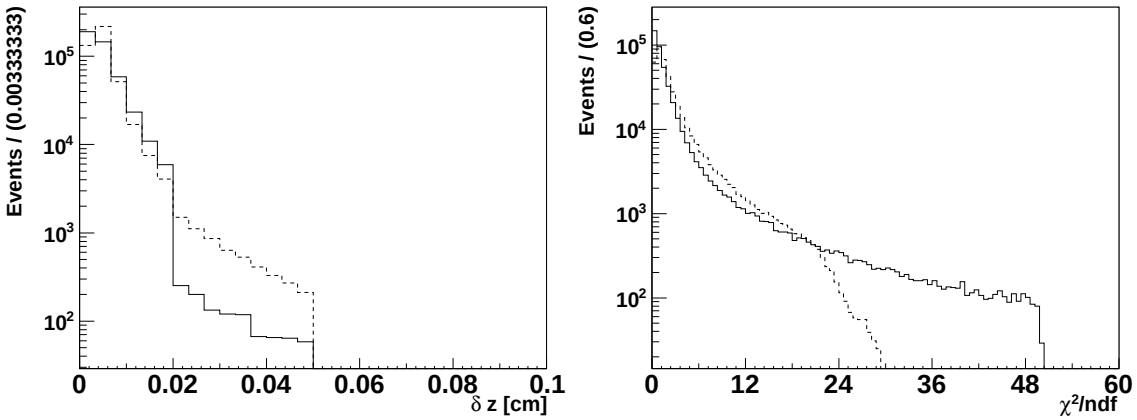

Figure 3.3: The distributions of the z error (left) and χ^2/ndf as obtained from the vertex fit for B_{CP} (solid line) and $B_{\rm tag}$ (dashed line).

the decay products that are produced together with B_{CP} can be used to identify its flavor. As mentioned in Section 1.3.3, a coherent $B^0\bar{B}^0$ pair is produced at the $\Upsilon(4S)$-resonance, so B_{CP} comes along with a second B with opposite flavor ($B_{\rm Tag}$). We use the flavor tagging algorithm developed at Belle, which determines the flavor of $B_{\rm Tag}$ by looking for the following tracks from flavor-specific decays of $B_{\rm Tag}$:

1. kaons coming from $B^0 \ \to K^+X$ via the $\bar{b} \to \bar{c} \to \bar{s}$ cascade transition,
2. $\bar{\Lambda}$ baryons from the same $\bar{b} \to \bar{c} \to \bar{s}$ transition,

Also, an origin near the IP ($dr < 2$ cm and $|dz| < 10$ cm) is required for

3. leptons: high-momentum from $B^0 \ \to Xl^+\nu$ and

   intermediate momentum from $\bar{b} \to \bar{c} \to \bar{s}l^-\bar{\nu}$,
4. high-momentum pions from $B^0 \ \to D^{(*)}\pi^+X$,
5. slow pions from $B^0 \ \to D^{*-}X \qquad D^{*-} \to \bar{D}^0\pi^-_{\rm slow}$.

Some of these processes are shown in Fig. 3.7. The algorithm works in two steps. In the first step, the track stage, each track delivers a flavor probability that is combined in the second step, the event stage, as Fig. 3.5 [92] illustrates. A detailed description can be found in Ref. [92]. Depending on the PID, the charge and sometimes also the momentum of the tracks, the flavor of $B_{\rm Tag}$ is accessible. Using a multi-dimensional binned look-up table obtained from large statistics MC studies, the signed tagging probability is given by

$$q \cdot r = \frac{N(B^0) - N(\bar{B}^0)}{N(B^0) + N(\bar{B}^0)} \tag{3.5}$$

where $q = \pm 1$ is the flavor of $B_{\rm Tag}$ ($B_{\rm Tag} \ = B^0$ for $q = +1$) and r is an MC based expected flavor dilution factor that ranges from 0 for no flavor assignment up to 1 for unambiguous flavor assignment. $N(B^0)$ ($N(\bar{B}^0)$) is the number of B^0 ($\bar{B}^0$) in each bin of the look-up table. In Fig. 3.4 the $q \cdot r$ distribution for signal MC is shown.

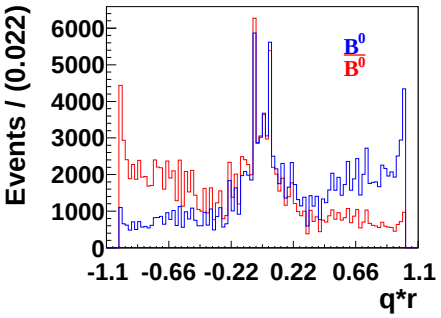

Figure 3.4: $q \cdot r$ of signal MC.

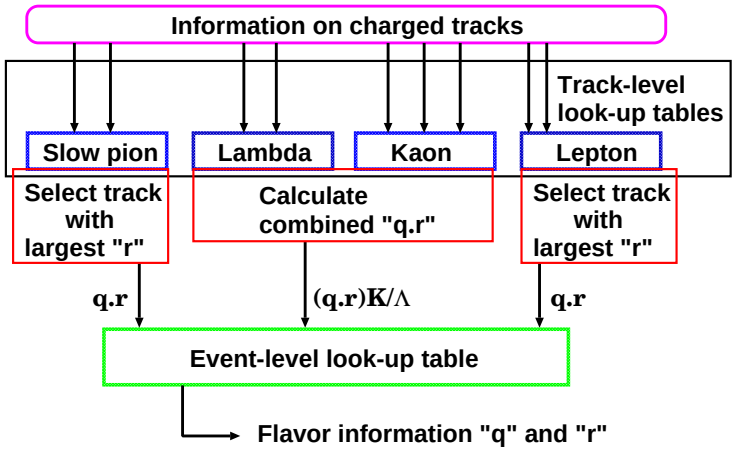

Figure 3.5: Flavor tagging algorithm.

In practice, the algorithm has an tagging efficiency $\epsilon_{\mathrm{MDLH}} < 1$. The main reasons are inefficiency in particle detection and identification as well as physical processes that provide little or no flavor information such as CP eigenstates. In addition, the variables that identify flavor are not unique and can be emulated by other decay processes. As a consequence, the flavor of a fraction of tagged B mesons will be identified incorrectly. This fraction is called the wrong tag fraction, w, and is related to r through $r = 1 - 2w$. An asymmetry between B^0 and $\bar{B}^0$ is accounted for with $\Delta w = \frac{1}{2}(w_{q=+1} - w_{q=-1})$ and $w = \frac{1}{2}(w_{q=+1} + w_{q=-1}) + q\Delta w$. The observed time dependence in Eq. (1.82) becomes

$$\mathcal{P}(\Delta t, q, w) = \frac{e^{-|\Delta t|/\tau_{B^0}}}{4\tau_{B^0}}\left[1 + (1-2w)q\Big(\mathcal{A}_{CP}\cos(\Delta m \Delta t) + \mathcal{S}_{CP}\sin(\Delta m \Delta t)\Big)\right], \tag{3.6}$$

the observed CP asymmetry from Section 1.3.2 is diluted by $(1 - 2w)$

$$a_{CP}(t, w) = (1-2w)a_{CP}(t) = (1-2w)\Big(\mathcal{A}_{CP}\cos(\Delta m \Delta t) + \mathcal{S}_{CP}\sin(\Delta m \Delta t)\Big). \tag{3.7}$$

The performance of the flavor tagging algorithm is evaluated with an effective tagging efficiency, $\epsilon_{\mathrm{eff}} \equiv \epsilon(1-2w)^2$, where ϵ is the number of tagged events divided by the number of all analyzed events. The statistical significance of the observed CP asymmetry is proportional to $\sqrt{\epsilon_{\mathrm{eff}}}$, so the tagging algorithm has been developed to maximize ϵ_{eff} while determining w experimentally from data.
All events are categorized into seven r-bins shown in Table 3.2, which have corresponding values of w. Each average value of r_l (MC) and w_l (data) satisfies $r_l \simeq (1 - 2w_l)$, $l = 0, 1, ..., 6$. Events with greater r values should receive more attention in a CP violation analysis. The total effective tagging efficiency is then given by the sum over all r-bins l, $\epsilon_{\mathrm{eff}} = \sum \epsilon_{\mathrm{eff},\,l}(1 - w_l)^2$ and adds up to $(29.20 \pm 1.37)\%$ for data.

The wrong tag fraction w is obtained from a fit of time-dependent $B^0 - \bar{B}^0$ mixing oscillations from self-tagging events like $B^0 \to D^{*-}l^+\nu^-$, $D^{*-}\pi^+$, $D^{*-}\rho^+$ and their charge conjugates. The time evolution of a $B^0\bar{B}^0$ pair with opposite flavor (OF) or same flavor (SF) is given by

$$\mathcal{P}_{\mathrm{OF(SF)}}(\Delta t) = \frac{e^{-|\Delta t|/-\tau_{B^0}}}{4\tau_{B^0}}[1 \pm (1-2w)\cos(\Delta m_d \Delta t)], \tag{3.8}$$

and the OF-SF asymmetry is given by

$$A_{\mathrm{mix}} \equiv \frac{\mathcal{P}_{\mathrm{OF}} - \mathcal{P}_{\mathrm{SF}}}{\mathcal{P}_{\mathrm{OF}} + \mathcal{P}_{\mathrm{SF}}} = (1-2w)\cos(\Delta m_d \Delta t). \tag{3.9}$$

bin, l	r	w	$\epsilon_{\text{eff},\,l}$
0	$0 < r \leq 0.1$	0.5	0
1	$0.1 < r \leq 0.25$	0.42 ± 0.01	0.398
2	$0.25 < r \leq 0.5$	0.32 ± 0.01	0.146
3	$0.5 < r \leq 0.625$	0.22 ± 0.01	0.104
4	$0.625 < r \leq 0.75$	0.16 ± 0.02	0.122
5	$0.75 < r \leq 0.875$	0.10 ± 0.00	0.094
6	$0.875 < r \leq 1$	0.03 ± 0.00	0.136

Table 3.2: r-bins l and the corresponding ranges of r and values of the wrong tag fraction w (including experimental uncertainties). The last column shows the effective tagging efficiencies ϵ_{eff} in each r-bin.

SF arises from assigning the wrong flavor from from $B^0 - \bar{B}^0$ mixing after B_{tag} decayed. The OF-SF asymmetries in different r-bins are shown in Fig. 3.6.

3.2.5 Best B Candidate Selection

The average number of reconstructed B candidates per event is 1.45 and 1.17 for signal MC events with longitudinal and transverse polarization, respectively. If more than one B candidate is reconstructed in an event, the one with the smallest sum of the two chi-squares of the π^0 mass fits is chosen. There are two possible combinations to make two $\rho^\pm$ mesons by interchanging the π^0 daughters: $\pi^+\pi^0_1, \pi^-\pi^0_2$ or $\pi^+\pi^0_2, \pi^-\pi^0_1$. If both are in the accepted mass range and thus are B candidates with the same "best B" criteria, the candidate with the largest momentum difference between the $\pi^\pm$ and π^0 is taken. Opposite to the helicity suppressed transversely polarized $\rho^\pm$s, longitudinal polarized ones tend to decay into a high and a low momentum pion in laboratory frame, as it can be seen in Fig. 3.8. Due to angular momentum conservation the momenta of these pions (LP) tend to be (anti-)parallel to the $\rho^\pm$ flight direction in the CMS [1]. For the detector configuration SVD1 and SVD2, this criteria selects 79.2% and 78.6% correctly reconstructed B mesons for events with multiple candidates, respectively.

3.2.6 ΔE and M_{bc}

Two kinematic variables are commonly used to identify the B meson. Since the process $e^+e^- \rightarrow B\bar{B}$ is a 2-body decay, the kinematics are well defined. In the center of mass frame, each B-meson carries half of the center of mass energy, $\sqrt{s}$, and the two B mesons have opposite momentum with equal magnitude. This allows to construct two almost orthogonal variables, ΔE and M_{bc}, as described in the following.
ΔE is basically the missing energy of the reconstructed B meson and defined as,

$$\Delta E = E^*_{\text{Rec}} - E_{\text{beam}}, \tag{3.10}$$

[1] Another, less strong, motivation is that because the ρ mass has a Breit-Wigner shape, this combination will reconstruct two ρ candidates with masses closer to the nominal mass in most cases. Therefore these combination have a higher probability.

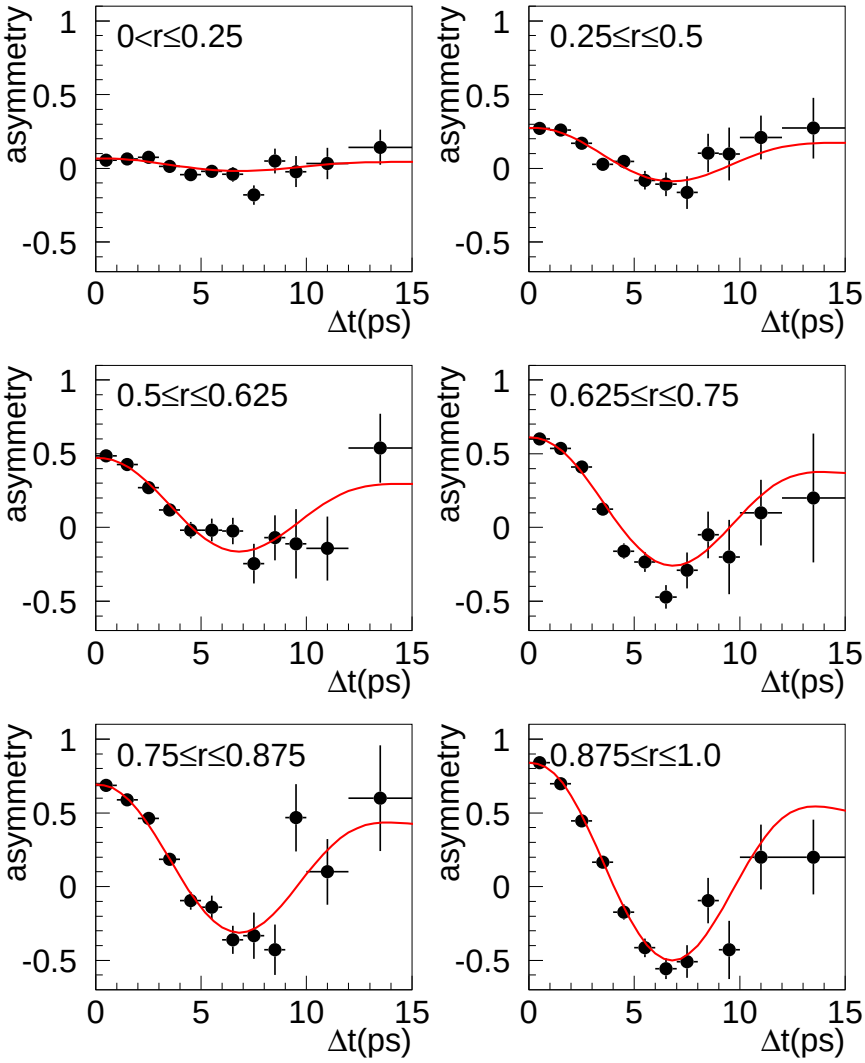

Figure 3.6: OF-SF asymmetries in 6 r-bins (the old flavor tagging used 6 r-bins, which has recently changed to 7 r-bins). The solid curve shows the fit result. The figure is taken from [92].

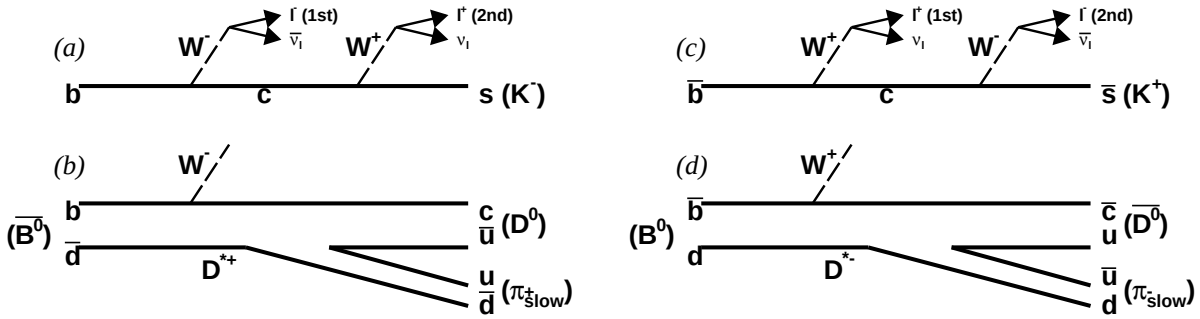

Figure 3.7: Feynman graphs for some processes used for flavor identification. Figures (a) and (c) show the lepton as well as the kaon category for B^0 and $\bar{B}^0$, respectively. Figures (b) and (d) show the pion category for B^0 and $\bar{B}^0$ respectively. In (a) and (c) the first lepton corresponds to the high momentum one, the second to the intermediate momentum one.

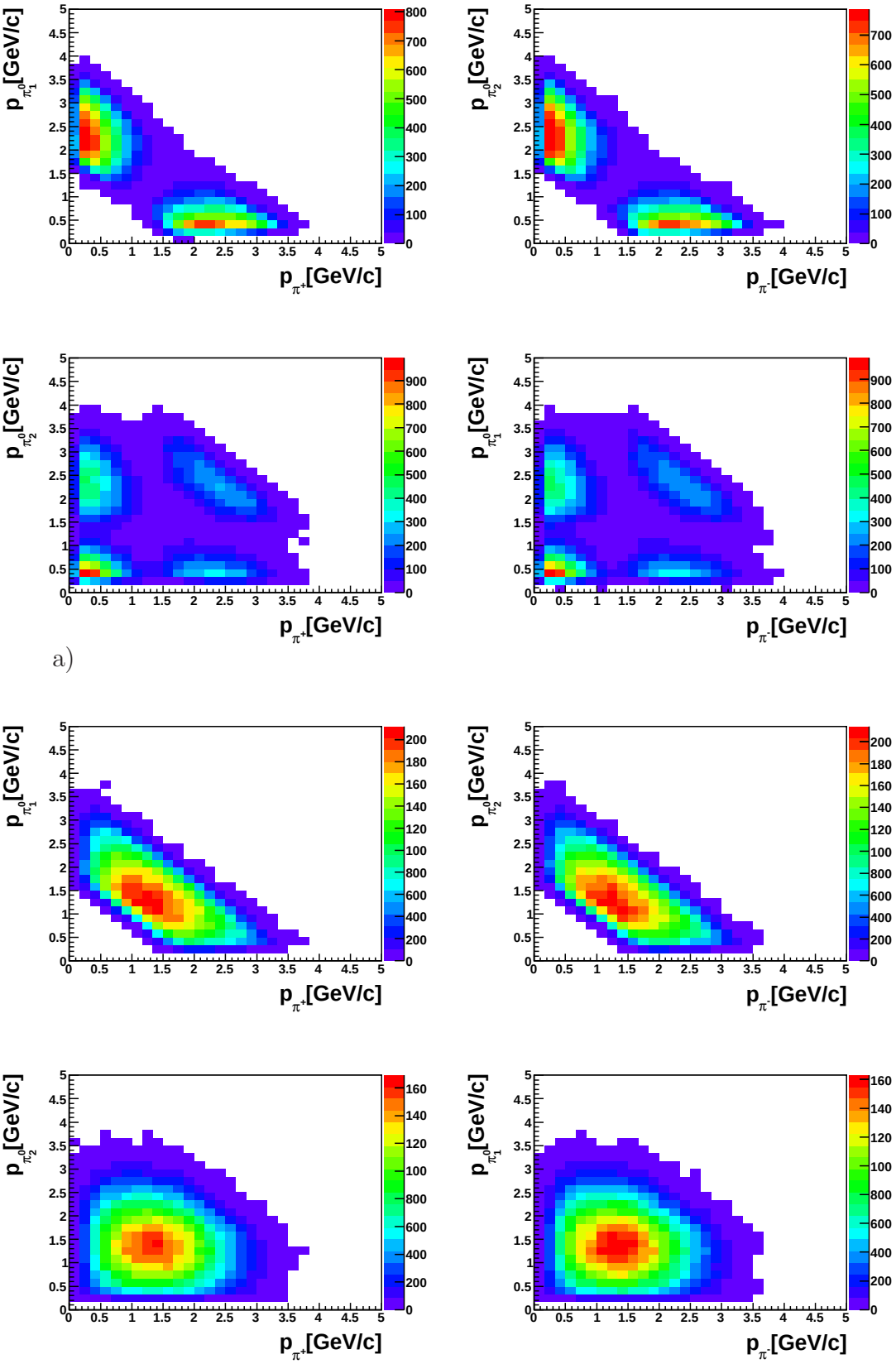

Figure 3.8: Scatter plots of the pion momenta from fully simulated signal MC (LP). The upper plots show the distribution for each reconstructed $\rho^{\pm}$ and the lower ones the combinations where the π^0s are interchanged.

where E^*_{Rec} is the energy of the reconstructed B meson in the CMS frame and $E_{\mathrm{beam}} = \sqrt{s}/2$. In a perfectly reconstructed event with a perfect detector, ΔE would be a delta-function peaking at zero. The uncertainty on ΔE is given by

$$\sigma^2(\Delta E) = \sigma^2(E^*_{\mathrm{Rec}}) + \sigma^2(E_{\mathrm{beam}}) \tag{3.11}$$

and is dominated by the uncertainty in the reconstructed energy, since $\sigma^2(E^*_{\mathrm{Rec}}) \gg \sigma^2(E_{\mathrm{beam}})$ [93].

The beam-constrained mass of the reconstructed B meson, M_{bc}, is defined as

$$M_{\mathrm{bc}} = \sqrt{(E_{\mathrm{beam}})^2 - (\vec{p}^{\,*}_B)^2}, \tag{3.12}$$

where $\vec{p}^{\,*}_B$ is the 3-momentum of B_{CP} in the CMS frame. In contrast to ΔE, M_{bc} is limited by the resolution of the beam energy, as

$$\sigma^2(M_{\mathrm{bc}}) = \sigma^2(E_{\mathrm{beam}}) + (|\vec{p}^{\,*}_B|/m_B)\sigma^2(\vec{p}^{\,*}_B) \tag{3.13}$$

with $(|\vec{p}^{\,*}_B|/m_B) = 0.34/5.28 \simeq 0.064$ and $\sigma(\vec{p}^{\,*}_B) \leq \sigma(E_{\mathrm{beam}})$ [93]. Substituting the reconstructed energy with E^{CMS}_{beam} (using M_{bc} instead of the invariant B mass) improves the mass resolution significantly, as Fig. 3.9 demonstrates.

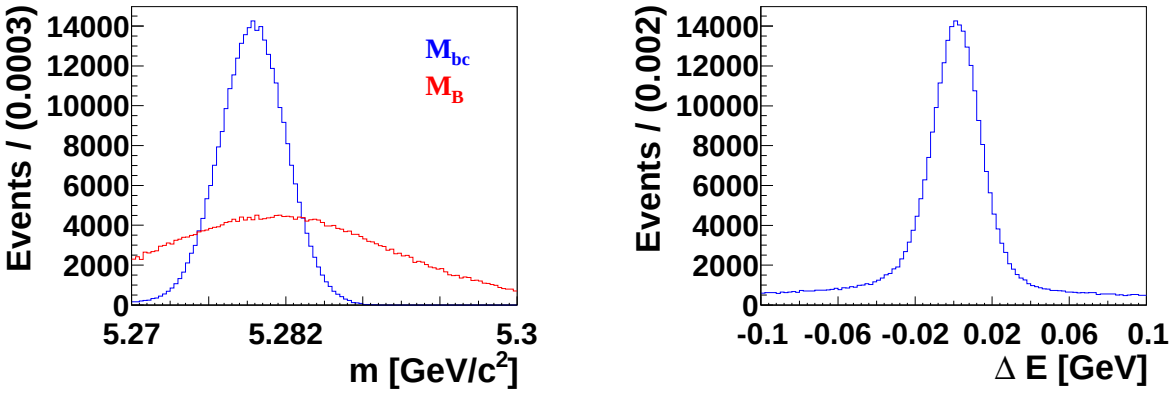

Figure 3.9: M_{bc}, the reconstructed B mass (left) and ΔE of $B^0 \to \rho^0\rho^0$ MC simulation, where especially the ΔE resolution is better compared to $B^0 \to \rho^+\rho^-$ decays, as the final state consists out of charged pions only.

3.2.7 Helicity

Because f_L is predicted and measured to be close to one, we use the helicity basis to obtain the longitudinal polarization fraction in order to isolate this CP-even component. The helicity angles $\cos\theta_{\mathrm{H}}$ are defined in Section 1.4.1. Integrating Eq. (1.90) over the acoplanarity angle ϕ removes the interference terms and yields in the helicity angle dependent differential decay amplitude in the helicity basis

$$\frac{1}{\Gamma}\frac{d^2\Gamma}{d\cos\theta^1_{\mathrm{Hel}}\, d\cos\theta^2_{\mathrm{Hel}}} = \frac{9}{4}\left(f_L \cos^2\theta^1_{\mathrm{Hel}} \cos^2\theta^2_{\mathrm{Hel}} + \frac{1}{4}(1-f_L)\sin^2\theta^1_{\mathrm{Hel}} \sin^2\theta^2_{\mathrm{Hel}} \right), \tag{3.14}$$

with the fraction of longitudinal polarized ρ mesons, f_L.

3.2.8 Continuum Identification

As Table 3.1 shows, 69% of all events come from $e^+e^- \to q\bar{q}$, $q = u, d, c, s$ (the continuum), which is by far the largest background in our measurement. Continuum events usually consist of a two-jet like final state (back-to-back). QCD also explains multi-jet final states, for example three jets through the emittance of a gluon from one of the quarks. This leads to light hadrons with high momentum that can populate the signal region. Because the $B\bar{B}$ pair is produced almost at rest in the center of mass frame and and each B decays isotropically, their decay topology is rather spherical-like. This is illustrated in Fig. 3.10. We exploit the difference in the event shape topology to discriminate jet-like continuum

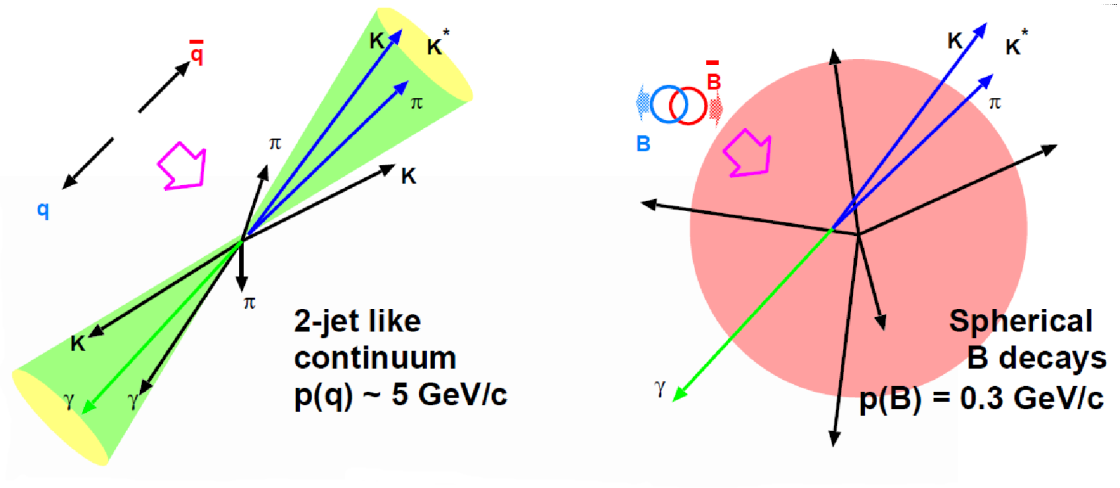

Figure 3.10: Event shape for jet-like continuum events and spherical $B\bar{B}$ events [94].

events from spherical $B\bar{B}$ events by combining the following event shape variables, shown in Fig. 3.13, with a Fisher discriminant [95]:

- L_0^n, L_2^n, L_2^c, $L_{0,n}$,
  where $L_i^{\mathrm{k}} = \sum_j |\vec{p_j}|(\cos\theta_j)^i$ for neutral clusters (k=n) and charged tracks (k=c) belonging to the tag side, where $i = 0, 2$, p_j is the momentum of the j-th particle and θ_j the angle between its direction and the thrust axis of the B candidate [78].

- $|cos(TB, TO)|$,
  which is the angle between the thrust axis of the B candidate(TB) and the thrust axis of the remaining tracks(TO).

- $|cos(TB, z)|$,
  which is the angle between the thrust axis of the B candidate(TB) and the z-axis.

- $|\cos(B, z)|$,
  the B flight direction, relative to the z-axis,

  and the following variables, closely related to the super fox wolfram moments [96]:

- $h_{so}^{02}, h_{so}^{04}, h_{so}^{10}, h_{so}^{12}, h_{so}^{14}, h_{oo}^{2}$
  with $h_{so}^{kl} = \sum_{i,j} |\vec{p}_i||\vec{p}_{j_k}| P_l(\cos\theta_{ij_k})$ where $\vec{p}_i$ is the CMS momentum of the i-th track from the signal side (s), $\vec{p}_{j_k}$ is the CMS momentum of the j_k-th particle from the other side

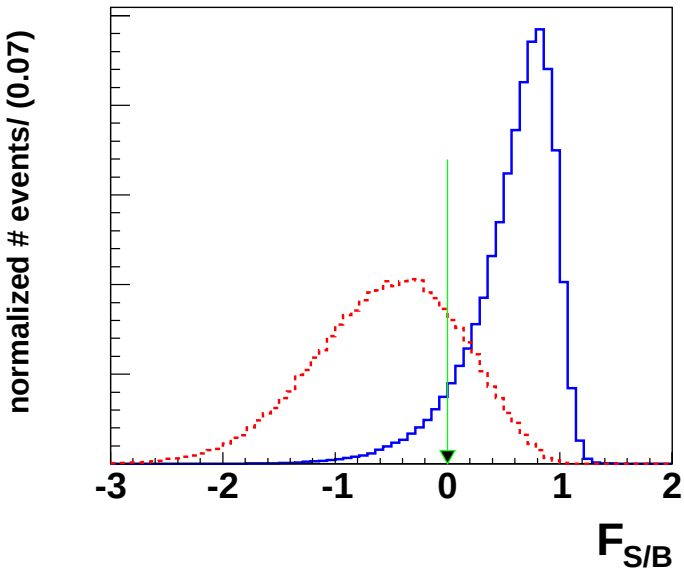

Figure 3.11: The output of the fisher discriminant for signal MC events (solid blue) and continuum data (dashed red), normalized to each other. The green arrow indicates the lower cut on this variable as described in the text.

(o), θ_{ij_k} is the angle between particle i and j_k and P_l is Legendre polynomial of order l. For the other side, we distinguish two cases using index $k = 0, 1$ for charged tracks and neutral particles, respectively. h^2_{oo} uses only tracks from the other side and does not depend on the charges.

We place a cut on the fisher output, $\mathcal{F}_{B\bar{B}/q\bar{q}} > 0$, which removes 80% off continuum events while the cut retains 90% of signal MC events as illustrated in Figs. 3.11 and 3.12. Including the B lifetime distribution in the fit further improves the continuum separation, because reconstructing two B mesons from this component yields in a significantly shorter "effective" lifetime (see for example Fig. 4.63).

3.2.9 Fit Region

We choose the fit region to be,

- -0.15 GeV $\leq \Delta E \leq 0.15$ GeV
- 5.27 GeV/$c^2 \leq M_{\rm bc}$
- 0.4 GeV/$c^2 \leq m_{\pi^+\pi^-} \leq 1.15$ GeV/c^2
- $-0.85 \leq \cos\theta_{\rm H} \leq 0.98$
- $\mathcal{F}_{B\bar{B}/q\bar{q}} > 0$
- $|\Delta t| < 70\ ps$

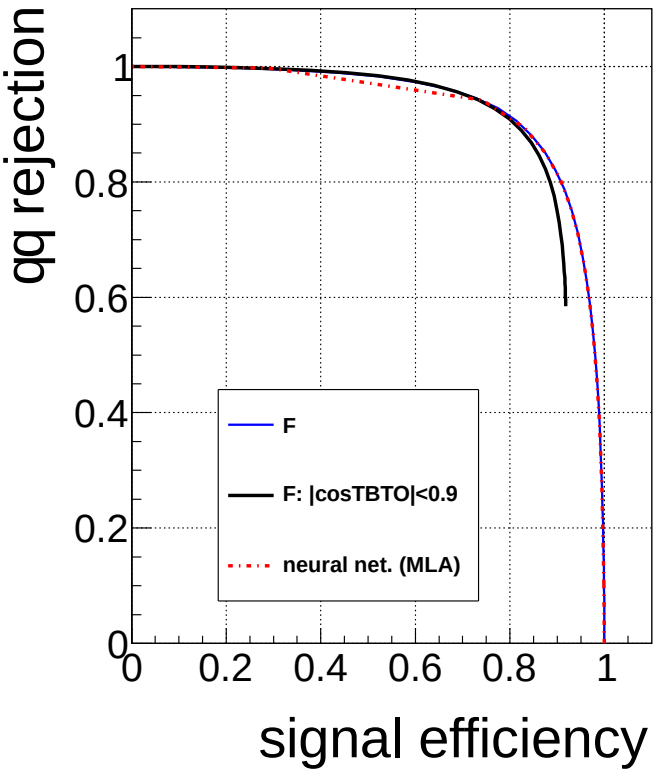

Figure 3.12: Continuum rejection as a function of the signal efficiency under a variation of the cut on $\mathcal{F}_{B\bar{B}/q\bar{q}}$. We compare the performance of the fisher discriminant weather a cut on $|\cos(\mathrm{TBTO})|$ has been applied before the training (dark line) or not (solid line). We find that the separation power would be reduced if a cut on cos(TBTO) would has been applied before the training (the dark line starts at (0.9, 0.6) because of the preselection). Moreover, we did not find any improvement from using a neural network (dashed line) instead of the fisher discriminate.

The region is chosen such that signal is retained in a reasonable way, while the lower restriction on the helicity angles and the upper limit on the mass range are powerfull in removing background. The Δt range suits the resolution function of the B lifetime.

3.2.10 Reconstruction Efficiencies

The reconstruction efficiencies are needed for the calculation of the branching fraction from the observed yield (see Section 3.1.2). Depending on the number of correctly assigned pions to the reconstructed $\rho^{\pm}$ mesons, the distributions of the fit-variables can change significantly (see Section 4.3). Therefore, we distinguish four categories of events. For $B^0 \to \rho^+\rho^-$ these are:

a) truth: all four pion correct,

b) noπ^0: both charged pions correct, one or more π^0 incorrect,

c) 1$\pi^{\pm}$: only one charged pion correct,

d) SC: self crossfed, else.

We give more importance to the charged pions, because their tracks are used for the vertex determination and their four-momenta are measured more precisely than the ones of neutral particles.

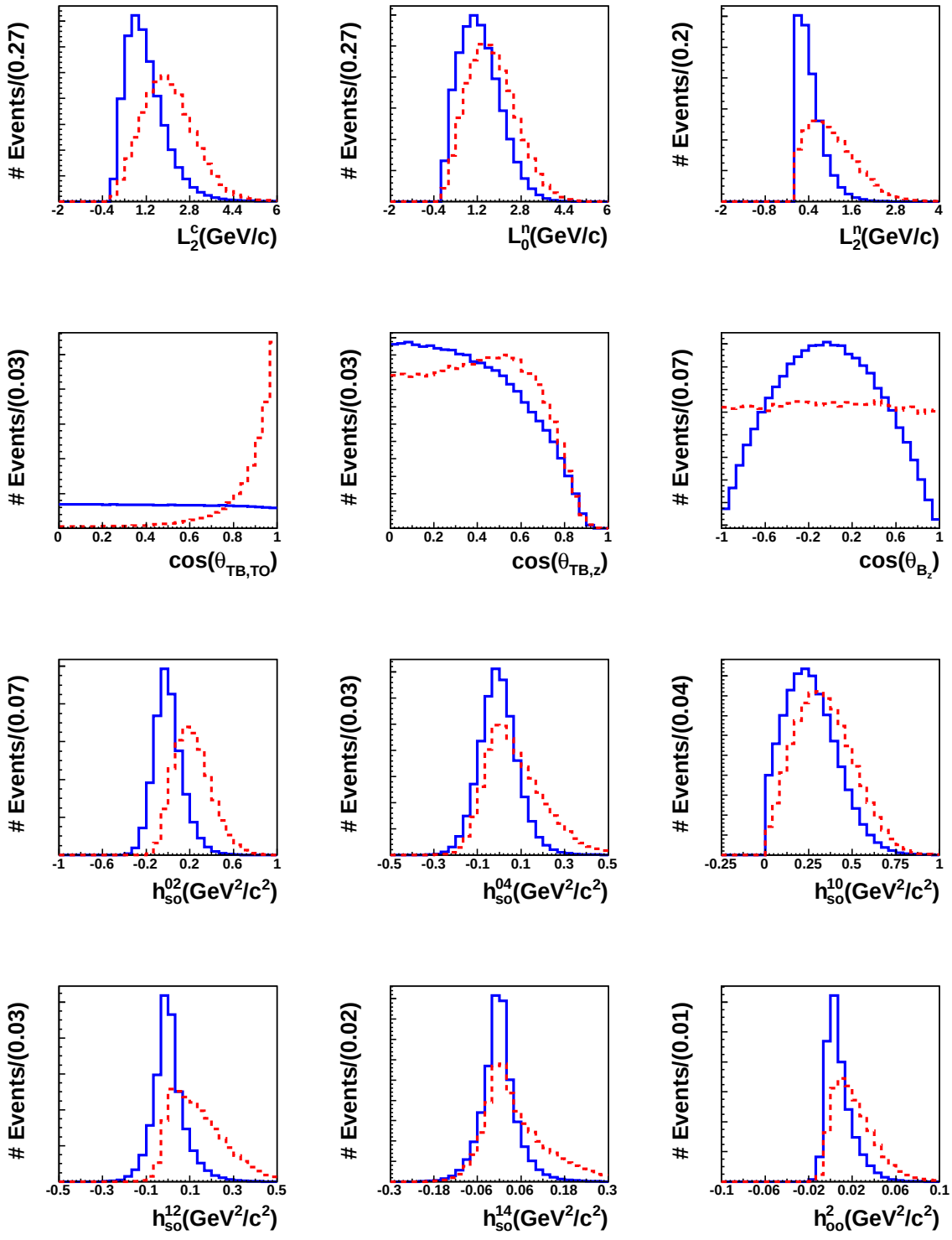

Figure 3.13: The twelve variables used for the fisher discriminant (see text). Signal MC events are shown in solid blue and off-resonance data are shown in dashed red. The distributions are normalized to the same area.

The number of reconstructed events from $N_{\text{rec, i}}$ from category i divided by the number of generated events N_{gen}

$$\epsilon_i \equiv \frac{N_{\text{rec, i}}}{N_{\text{gen}}}, \tag{3.15}$$

gives the corresponding reconstruction efficiency. Table 3.3 shows these quantities for both polarizations. A reconstruction purity p_i for each category i can be obtained via

mode	truth	noπ^0	1Cpi	SC	total
$\epsilon_{\text{Sig}}^{\text{SVD1 (LP)}}$	5.2	1.9	1.3	0.1	8.5
$\epsilon_{\text{Sig}}^{\text{SVD2 (LP)}}$	6.0	2.2	1.5	0.2	9.9
$\epsilon_{\text{Sig}}^{\text{SVD1 (TP)}}$	12.0	1.5	0.4	n.a.	13.9
$\epsilon_{\text{Sig}}^{\text{SVD2 (TP)}}$	13.4	1.7	0.4	n.a.	15.5

Table 3.3: Reconstruction efficiencies in percent for longitudinal (LP) and transverse (TP) polarizatioOAn obtained from fully simulated signal MC events.

$$p_i \equiv \frac{N_{\text{rec, i}}}{\sum_{i=1}^{4} N_{\text{rec, i}}} = \frac{\epsilon_i}{\sum_{i=1}^{4} \epsilon_i}. \tag{3.16}$$

3.3 The Fit Components

Most of the remaining events come from background processes. Even if all cross-sections would been known, the reconstruction efficiencies have to be considered, too, to estimate the relative contribution of these processes to the data after the reconstruction. Also, the distributions of the fit variables of the backgrounds need to be understood for a good description of the data with the fit model. Therefore, we study the possible background sources with individual MC simulation. In total, we consider 14 components in the data model, which are introduced here and discussed at length later (see Chapter 4 and Appendix C).

- $2\times$ $B^0 \to \rho^+\rho^-$: where we treat longitudinal (LP) and transverse (TP) polarization separately
- Continuum($q\bar{q}$): $e^+e^- \to q\bar{q}$, where $q = u, d, s, c$
- $4\times$ $B\bar{B}$ decays
  - B decays via $b \to c$ transitions

    $2\times$: neutral ($B^0\bar{B}^0$) and charged (B^+B^-)
  - B decays via $b \to u, d, s$ transitions (without modes with a $\pi^+\pi^0\pi^-\pi^0$ final state)

    $2\times$: neutral ($B^0\bar{B}^0$) and charged (B^+B^-)
- $7\times$ other four-pion final states (peaking background)

  $B^0 \to \pi^+\pi^0\pi^-\pi^0$

$(B^0 \to a_1^{\pm}(1260)\pi^{\mp}) \times (a_1^{\pm} \to \pi^{\pm}\pi^0\pi^0)$
$(B^0 \to a_1^0(1260)\pi^0) \times (a_1^0 \to \pi^+\pi^-\pi^0)$
$B^0 \to \rho^0(770)\pi^0\pi^0$
$B^0 \to \rho^{\pm}(770)\pi^{\mp}\pi^0$
$(B^0 \to f_0(980)\pi^0\pi^0) \times (f_0(980) \to \pi^+\pi^-)$
$B^0 \to \omega\pi^0 \times (\omega \to \pi^+\pi^-\pi^0)$

The ρ^0 meson decays into two charged pions.

3.3.1 Event Generation

For each component, MC events are generated with EvtGen [97], where we assume world averages [45] for the branching fractions of $B\bar{B}$ decays without four-pion final states. Then, a full detector simulation with GEANT3 [98] is performed. For each SVD configuration we generate and simulate

- four-pion final states: 10^6 events each

  to increase the statistics we generate $4 \cdot 10^6$ events for signal (LP) and $2 \cdot 10^6$ events for $B^0 \to a_1^{\pm}\pi^{\mp}$ decays.

- Continuum model: $\sim$ the amount off contiuum events in the data

- Charm model: $10\times$ the expected amount of events for both neutral and charged B decays

- Charmless model: $50\times$ the expected amount of events for both neutral and charged B decays

We use the standard hadronB skim (see Section 3.1.1) and apply the described reconstruction procedure.

Chapter 4

Likelihood Parametrization

To extract the branching fraction, the polarization fraction and the CP violating parameters of $B^0 \to \rho^+\rho^-$ decays from the data, we perform an nine-dimensional (ΔE, $M_{\rm bc}$, $m_{\pi^+\pi^0}$, $m_{\pi^-\pi^0}$, $\cos\theta_{\rm H}^+$, $\cos\theta_{\rm H}^-$, $\mathcal{F}_{B\bar{B}/q\bar{q}}$, Δt, q) extended maximum likelihood fit.

4.1 The Extended Maximum Likelihood Method

A probability density function (PDF) $f(x)$ of a continuous distributed variable x describes the probability $\mathcal{P}$ of observing x in a certain range $[a, b]$:

$$\mathcal{P}(a \leq x \leq b) = \int_a^b f(x')dx'. \tag{4.1}$$

Consider a set of N statistically independent measured quantities $X = x_1, ..., x_N$, which share the same PDF $f(X;\alpha)$, where $\alpha = \alpha_1, ..., \alpha_n$ is a set of n undetermined parameters. The likelihood function $\mathcal{L}$, is the product of the probabilities from each x_i obtained from the shared PDF as functions of the parameters α, evaluated with the data set X,

$$\mathcal{L}(\alpha) = \prod_{i=1}^{N} f(x_i;\alpha). \tag{4.2}$$

The aim of the maximum likelihood method [45] is to find the set of parameters, the estimators $\hat{\alpha}$, that maximizes the likelihood function $\mathcal{L}(\alpha)$. This is achieved by solving the partial derivatives of $L(\alpha)$ with respect to α_i.

$$\frac{\partial\mathcal{L}(\alpha)}{\partial\alpha_i} = 0, \qquad i = 1, ..., n. \tag{4.3}$$

The error matrix of the estimators, if assumed to be Gaussian distributed, is given by inverse of the matrix of second derivatives of $\mathcal{L}$,

$$E_{ij} = \left(\frac{\partial^2\mathcal{L}(\alpha)}{\partial\alpha_i\partial\alpha_j}\bigg|_{\alpha=\hat{\alpha}}\right)^{-1}. \tag{4.4}$$

If the number of events N is unknown, the extended maximum likelihood method can be used, where N is used as an additional estimator and assumed to be Poisson-distributed. For sets consisting of n different sub sets a N_j events, with $N = \sum N_j$, the corresponding function becomes

$$\mathcal{L}(N_1, .., N_n, \alpha) = \frac{e^{-\sum_j^n N_j}}{N!} \prod_{i=1}^{N} \sum_j N_j f(x_i; \alpha)_j. \tag{4.5}$$

It is more convenient to use $\log(\mathcal{L}(\alpha))$ which has the same maximum as $\mathcal{L}(\alpha)$,

$$\log(\prod_i x_i) = \sum_i \log(x_i). \tag{4.6}$$

4.1.1 MINUIT2

The derivatives do not need to be analytically solvable. We use the fitting package MINUIT2 [99] which calculates numerical solutions. An overview of numerical minimization techniques can be found in [100]. Instead of maximizing $\mathcal{L}(\alpha)$, the equivalent expression $-2\log(\mathcal{L}(\alpha))$ is minimized. The goodness of the fit is estimated by calculating a binned χ^2/ndf after the fit.
We use the algorithm MIGRAD, which can be used with three different minimization quality levels. We use the strategy with the highest quality, which means largest amount of function calls and therefore longer computing time. The errors are obtained from calculating the error matrix (see Eq. (4.4)) within the minimization and referred to as the HESSE error.
For parameters of physics interest, correlations between parameters and non-linearities are taking into account with the MINUIT2 processor MINOS. When a valid minimum has been found, an asymmetric error for a parameter α_i is calculated by varying this parameter and minimizing again with respect to all other parameters, in each variation step. When the difference of the original valid minimum to the new one is one standard deviation, the difference of α_i to its variation is taken as the error. This variation goes in two directions, therefore the error can be asymmetric and is referred to as the MINOS error.

4.2 Common Features

We consider the 14 components introduced in Section 3.3 and describe each with a particular model (nine-dimensional PDF). Each fit dimension contributes to single out signal events in the fit to data, their main purposes are:
$\mathcal{F}_{B\bar{B}/q\bar{q}}$ separates $B\bar{B}$ decays from the continuum (see Section 3.2.8). The ΔE and M_{bc} distributions (see Section 3.2.6) peak at zero and the B mass, respectively, if a B meson is correctly reconstructed from four pions, and discriminate against combinatorial background. The ρ mass and helicity angle distributions are important to further distinguish the individual components, in particular the various four-pion final states. In addition, the angular analysis allows to obtain the fraction of longitudinal polarized ρ mesons in $B^0 \to \rho^+\rho^-$ decays and their CP violating parameters are obtained from the Δt distributions for both B flavors $q = \pm 1$.
The model of the signal (LP and TP) and continuum components are described in this

Chapter. The remaining eleven backgrounds from $B\bar{B}$ decays are described in detail in Appendices C.1 and C.2. We provide a brief summary of the entire fit model in Section 4.5. In order to make the model description less repetitive, (partly) common features are described beforehand.

The most important functions used in this analysis are described in Appendix E, where also the abbreviations are given.

We correct for differences between the distributions of data and MC simulation in the fit to data. Calibration factors $\mu_{\rm CF}$ and $\sigma_{\rm CF}$ are included in the Gaussian parts of the PDFs of ΔE,$M_{\rm bc}$ for all four-pion final states and in the PDFs of $\mathcal{F}_{B\bar{B}/q\bar{q}}$ for all $B\bar{B}$ components. The factors are obtained from the control measurement presented in Appendix A. We add the correction of the mean, $\mu \to \mu + \mu_{\rm CF}$, and multiply the ones of the widths ,$\sigma_{l,r} \to \sigma_{l,r} \cdot \sigma_{l,r{\rm CF}}$. We set $\mu_{\rm CF} = 0$ and $\sigma_{l,r{\rm CF}} = 1$ for MC studies. In addition, a multiplicative correction is applied to the r-bin fractions $f_k \to f_k \cdot f_k^{\rm CF}$, again being fixed to one for MC studies. r is a measure of the flavor tagging quality, see Section 3.2.4.

The $\mathcal{F}_{B\bar{B}/q\bar{q}}$ distributions exhibit a correlation with r. This is accounted for by choosing a individual description of $\mathcal{F}_{B\bar{B}/q\bar{q}}$ in each r-bin.

All distributions are obtained from fully simulated MC events and we build separate models for each detector configuration: SVD1 and SVD2. The fit to data is performed simultaneously in SVD1 and SVD2 and the following projections onto the fit variables show both detector configurations together, weighted such that the expected fraction of SVD1 events is retained.

4.2.1 Correlations

When performing a fit in multi-dimensions, one has to be cautious of variable correlations. We provide correlation matrices for each component and account for correlations down to the percent level. In principle, an analytically description of a correlation can be obtained by projecting onto a fit variable in slices of another variable and obtain values of certain parameters of the model shape from a fit in each slice. Then, the distribution of each of these parameters can be fitted with a polynomial and the correlation can incorporated in the description of the PDF. An example is shown in Fig. 4.1. The values of the correlated parameter and of the parameters describing the correlation are finally obtained from a fit to the full projection. If such an analytical description is not applicable, we use binned PDFs.

A special kind of correlation occurs in most components due to the charges of the two $\rho^{\pm}$ mesons. Reconstruction is not perfect and other decays (even without $\rho^{\pm}$s in the final state) can be reconstructed as $B^0 \to \rho^+\rho^-$ candidates. It happens for example, that only one ρ^+ is correctly reconstructed in an event. Therefore we separate up to four distinct categories of reconstruction. Especially the $m_{\pi^+\pi^0}$-$m_{\pi^-\pi^0}$-$\cos\theta_{\rm H}^+$-$\cos\theta_{\rm H}^-$ distributions depend strongly on the charge and number of correctly reconstructed $\rho^{\pm}$ mesons. See Section 3.2.10 for the classification of signal events. The remaining components have a slightly different classification (nomenclature):

a) $2c\pi$: both charged pions correctly reconstructed

b) ±: only one charged pion is correctly reconstructed

c) mr: both charged pions misreconstructed.

In order to visualize these correlation we provide two-dimensional projections of the mass and helicity PDFs. They always come in sets of four plots where the upper left (right) plot shows the 2D data (PDF) distribution. The lower two plots show the projections of the data as black points with error bars and the PDF as colored lines.

4.3 Signal Model

$B^0 \to \rho^+\rho^-$ events are referred to as signal. We treat longitudinal (LP) and transverse (TP) polarization, separately, and consider four (LP) and three (TP) different cases of reconstruction quality (see Section 3.2.10). In total the $B^0 \to \rho^+\rho^-$ model is composed out of seven parts. Although being independent fit components, we often use similar functions for the PDFs of longitudinal and transverse polarization. Therefore both polarizations are described together in each of the four following subsections, labeled by the superscript LP and TP, respectively.

4.3.1 Truth Model

$B^0 \to \rho^+\rho^-$ MC events with all four pions correctly reconstructed are referred to as "truth". The fit projections are shown in Figs. 4.2, 4.5, 4.6, 4.9, 4.10 and 4.13, the correlations between the fit variables are given in Tables 4.1 and 4.2.
The truths model's ΔE distribution is described by the sum of two asymmetric width Gaussians (dbG) and a first order Chebychev polynomial

$$\mathcal{P}^{\mathrm{LP(TP)}}_{\mathrm{truth}}(\Delta E) \equiv (1 - f_{\Delta E})dbG(\Delta E) + f_{\Delta E}c_{\Delta E}C_1(\Delta E). \tag{4.7}$$

The M_{bc} distribution is taken to be a dbG,

$$\mathcal{P}^{\mathrm{TP}}_{\mathrm{truth}}(M_{\mathrm{bc}}) \equiv dbG(M_{\mathrm{bc}}). \tag{4.8}$$

For longitudinal polarization, the mean and widths of the core Gaussian of M_{bc} depend on ΔE, see Eq. (4.9)- Eq. (4.13) and Fig. 4.1.

$$\mathcal{P}^{\mathrm{LP}}_{\mathrm{truth}}(M_{\mathrm{bc}}|\Delta E) \equiv \ dbG(M_{\mathrm{bc}}|\Delta E), \tag{4.9}$$

where

$$dbG^{LP}(M_{\mathrm{bc}}|\Delta E) \equiv dbG(M_{\mathrm{bc}}, \mu_1(\Delta E), \sigma_l(\Delta E), \sigma_r(\Delta E), \mu_2, \sigma_{2l}, \sigma_{2r}, ..., f), \tag{4.10}$$

with

$$\mu_1(\Delta E) = \mu_1 + c_1\Delta E + c_2\Delta E^2, \tag{4.11}$$
$$\sigma_l(\Delta E) = \sigma_l + c_3\Delta E^2, \tag{4.12}$$
$$\sigma_r(\Delta E) = \sigma_r + c_4\Delta E + c_5\Delta E^2. \tag{4.13}$$

The $\mathcal{F}_{B\bar{B}/q\bar{q}}$ distribution is modeled with a triple-bifurcated Gaussian in each r-bin k,

$$\mathcal{P}^{k,\mathrm{LP}}_{\mathrm{truth}}(\mathcal{F}_{B\bar{B}/q\bar{q}}) \equiv tbG^k(\mathcal{F}_{B\bar{B}/q\bar{q}}), \tag{4.14}$$

For transverse polarization, only the core Gaussian is free in the determination of the shape, while the second and third Gaussians are taken from the PDF for longitudinal polarization (denoted by subscript sig). We find the small correlation with the dipion masses negligible.

$$\mathcal{P}^{k,\mathrm{TP}}_{\mathrm{truth}}(\mathcal{F}_{B\bar{B}/q\bar{q}}) \equiv tbG^k_{\mathrm{sig}}(\mathcal{F}_{B\bar{B}/q\bar{q}}). \tag{4.15}$$

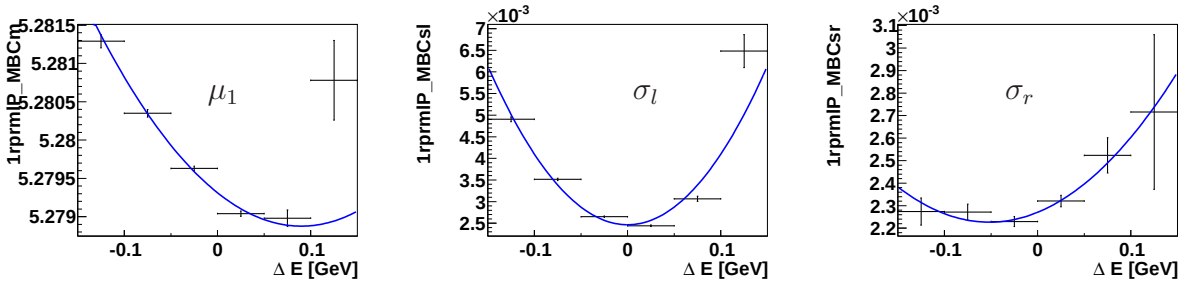

Figure 4.1: Dependence of the parameters of the core Gaussian of $M_{\rm bc}$ on ΔE. The imperfect description for $\Delta E \to 0.1$ can be ignored, because there are only few MC events, see Fig. 4.2.

0	ΔE	M_{bc}	$m^1_{\pi^+\pi^-}$	$m^2_{\pi^+\pi^-}$	$\mathcal{F}_{B\bar{B}/q\bar{q}}$	$\cos\theta^1_{\rm H}$	$\cos\theta^2_{\rm H}$	Δt
ΔE	1	-0.01	0.04	0.04	0.00	-0.09	-0.09	0.00
M_{bc}		1	-0.00	-0.00	0.00	-0.02	-0.02	0.00
$m^1_{\pi^+\pi^-}$			1	-0.00	-0.03	-0.02	-0.00	0.00
$m^2_{\pi^+\pi^-}$				1	-0.02	0.00	-0.02	-0.00
$\mathcal{F}_{B\bar{B}/q\bar{q}}$					1	0.00	0.01	-0.00
$\cos\theta^1_{\rm H}$						1	-0.04	-0.00
$\cos\theta^2_{\rm H}$							1	0.00
Δt								1

Table 4.1: Correlation matrix for the truth model (LP, SVD2).

The $\rho^\pm$ mass is modeled with a relativistic Breit-Wigner (see Appendix E.2), weighted with a mass-dependent reconstruction efficiency $\epsilon_{\rm M}^{\rm LP(TP)}(m_{\pi^\pm\pi^0})$,

$$\mathcal{P}_{\rm truth}^{\rm LP(TP)}(m_{\pi^\pm\pi^0}|\Delta E) \equiv \epsilon_{\rm M}^{\rm LP(TP)}(m_{\pi^\pm\pi^0}) \times BW(m_{\pi^\pm\pi^0}; m(\Delta E), \Gamma(\Delta E)). \tag{4.16}$$

$\epsilon_{\rm M}^{\rm LP(TP)}(m_{\pi^\pm\pi^0})$ are obtained from fully simulated MC events for each polarization and shown in Fig. 4.4. The dependence of the nominal mass $m(\Delta E) = m_0 + c_{1m_{\pi^\pm\pi^0}}\Delta E$ and the width $\Gamma(\Delta E) = \Gamma_0 + c_{2m_{\pi^\pm\pi^0}}\Delta E^2$ on ΔE are shown in Figs. 4.7 and 4.8. The parameters of the Breit-Wigner are made common between both polarizations and determined from fully simulated MC events.

We split Eq. 3.14 up into two parts, one for each polarization. Longitudinal polarized events

0	ΔE	M_{bc}	$m^1_{\pi^+\pi^-}$	$m^2_{\pi^+\pi^-}$	$\mathcal{F}_{B\bar{B}/q\bar{q}}$	$\cos\theta^1_{\rm H}$	$\cos\theta^2_{\rm H}$	Δt
ΔE	1	-0.01	0.04	0.04	0.01	-0.04	-0.03	0.00
M_{bc}		1	0.00	0.00	0.00	-0.01	-0.01	-0.00
$m^1_{\pi^+\pi^-}$			1	-0.01	-0.02	0.01	0.00	0.00
$m^2_{\pi^+\pi^-}$				1	-0.02	0.00	0.00	0.00
$\mathcal{F}_{B\bar{B}/q\bar{q}}$					1	0.00	0.01	-0.00
$\cos\theta^1_{\rm H}$						1	-0.01	0.00
$\cos\theta^2_{\rm H}$							1	-0.00
Δt								1

Table 4.2: Correlation matrix for the truth model (TP, SVD2).

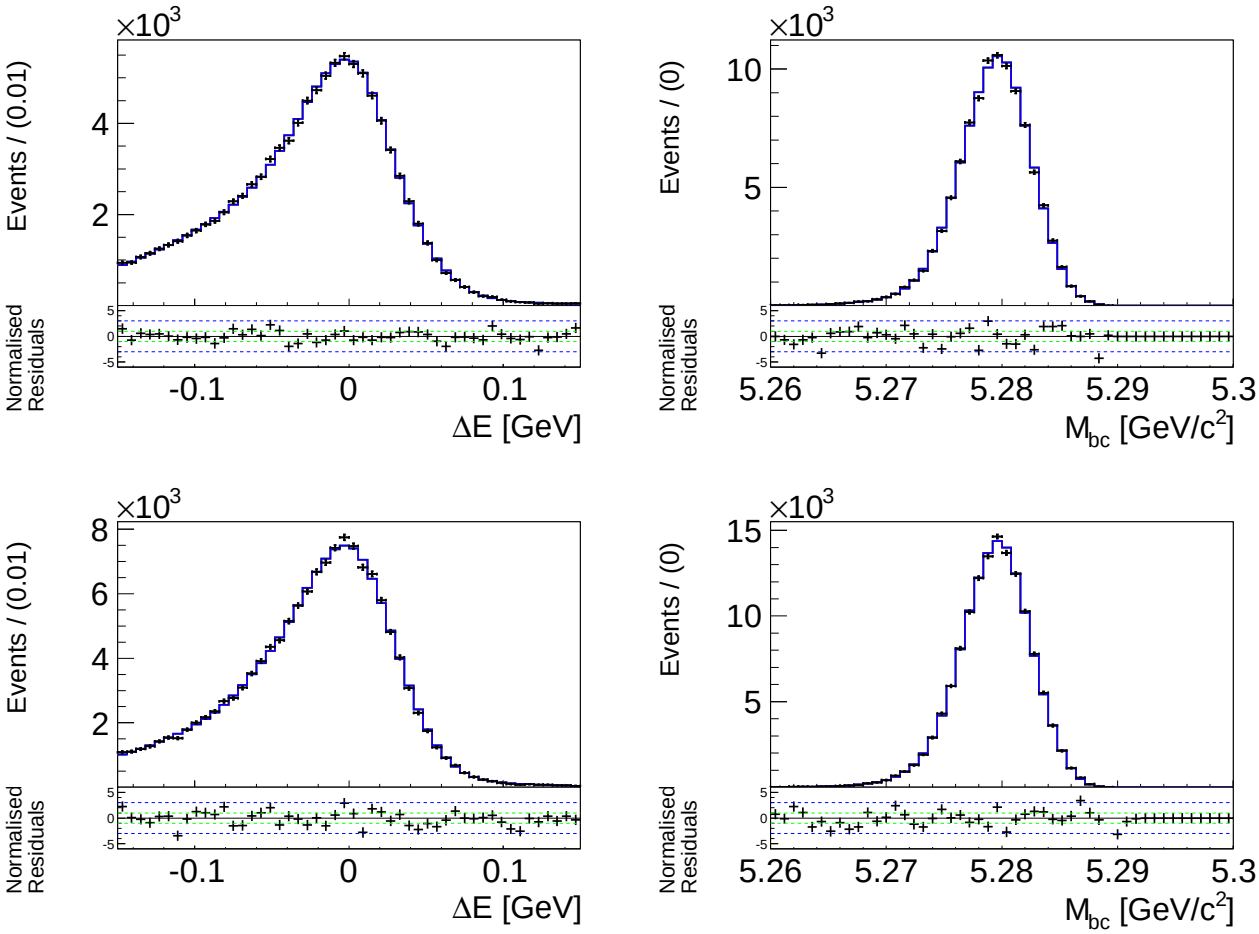

Figure 4.2: Full projections of correctly reconstructed signal MC events for ΔE and $M_{\rm bc}$. LP (top row) and TP. The black points show simulated MC events and the solid line shows the fit result. The residuals are given beneath each distribution.

are modeled with

$$\mathcal{P}^{\rm LP}_{\rm truth}(\cos\theta^+_{\rm H},\cos\theta^-_{\rm H}|\Delta E) = \frac{9}{4}\epsilon^{\rm LP}_{\rm H}(\cos\theta^+_{\rm H},\cos\theta^-_{\rm H}|\Delta E)\times(\cos\theta^+_{\rm H}\cos\theta^-_{\rm H})^2, \tag{4.17}$$

and transverse polarized ones with

$$\mathcal{P}^{\rm TP}_{\rm truth}(\cos\theta^+_{\rm H},\cos\theta^-_{\rm H}) = \frac{9}{16}\epsilon^{\rm TP}_{\rm H}(\cos\theta^+_{\rm H},\cos\theta^-_{\rm H})\times(1-(\cos\theta^+_{\rm H})^2)(1-(\cos\theta^-_{\rm H})^2). \tag{4.18}$$

$\epsilon^{\rm LP(TP)}_{\rm H}(\cos\theta^+_{\rm H},\cos\theta^-_{\rm H})$ are binned, two-dimensional, symmetrised ($\cos\theta^+_{\rm H}\leftrightarrow\cos\theta^-_{\rm H}$), helicity-angle dependent reconstruction efficiencies. For longitudinal polarization we account for the correlation of the helicity angles with ΔE by using reconstruction efficiency histograms in five bins of ΔE, as shown in Fig. 4.11. In order to choose the bins, we project into slices of ΔE of 0.01 GeV and combine neighborhoods with similar features. A finer slicing of ΔE is shown in Fig. C.99 in Appendix C and projections onto the helicity angles for some slices of ΔE are shown in Fig. 4.12.

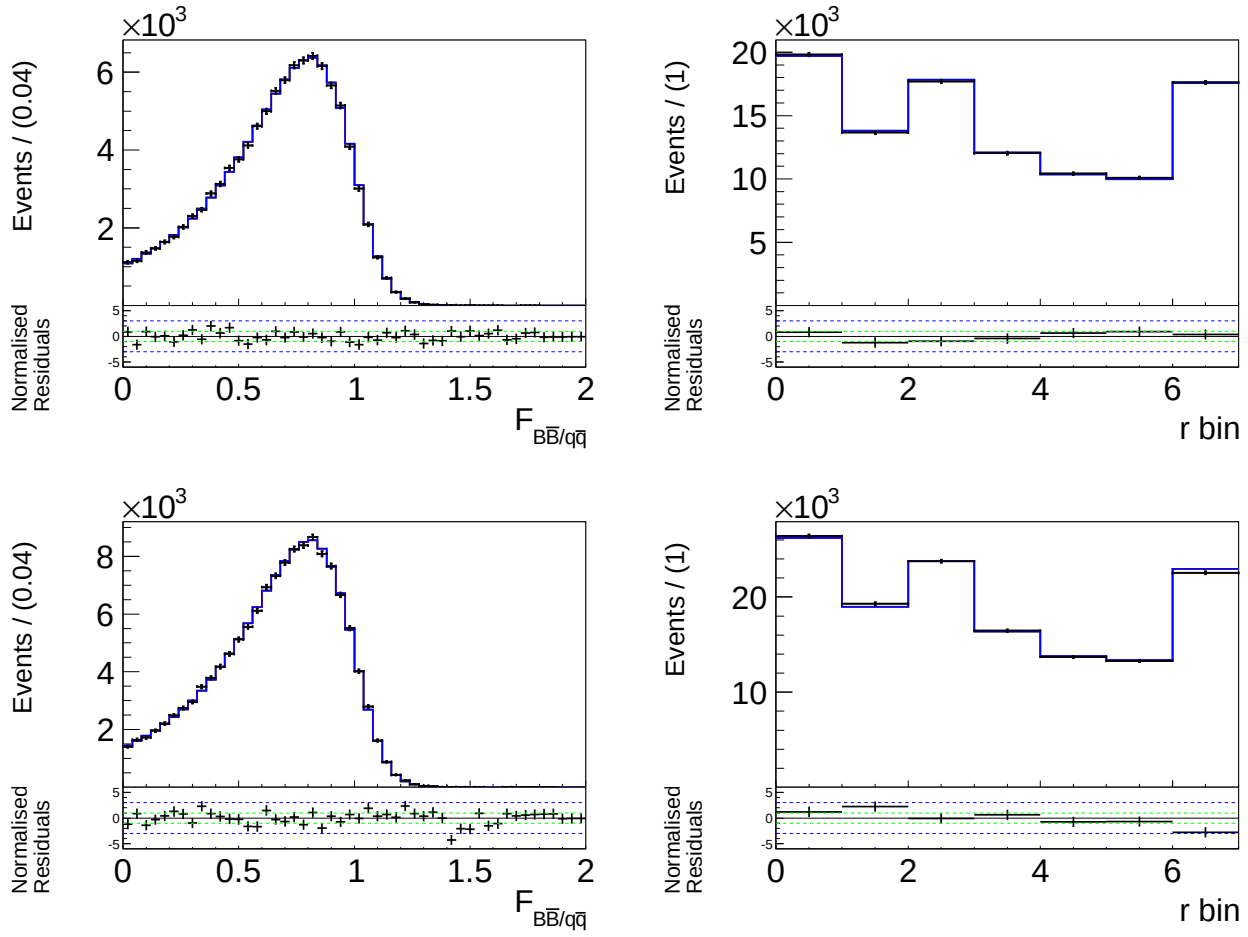

Figure 4.3: Fit projections of correctly reconstructed signal MC events for $\mathcal{F}_{B\bar{B}/q\bar{q}}$ and the r-bin fractions. LP (top row) and TP. The black points show simulated MC events and the solid line shows the fit result. The residuals are given beneath each distribution.

Each polarizations PDF for Δt is taken to be

$$\mathcal{P}^{\mathrm{LP(TP)}}_{\mathrm{truth},l,s}(\Delta t, q) \equiv \frac{e^{-|\Delta t|/\tau_{B^0}}}{4\tau_{B^0}} \Big\{ 1 - q\Delta w^{l,s} + q(1-2w^{l,s}) \times \Big[\mathcal{A}^{\mathrm{LP(TP)}}_{CP} \cos(\Delta t \Delta m) + \mathcal{S}^{\mathrm{LP(TP)}}_{CP} \sin(\Delta t \Delta m) \Big] \Big\} \otimes R^{s}_{B^0\bar{B}^0}(\Delta t), \tag{4.19}$$

where $w^{l,s}$ accounts for the CP dilution due to the probability of tagging the wrong B_{Tag} flavor q and $\Delta w^{l,s}$ accounts for the wrong tag difference between B and $\bar{B}$. Both are determined from flavor specific control samples. The B^0 lifetime, $\tau_{B^0} = (1.519 \pm 0.007)$ ps, and the mass difference between the two mass eigenstates B^0_H and B^0_L, $\Delta m = (51.0 \pm 0.4) \times 10^{10} \hbar s^{-1}$, are taken from [45]. The Δt PDF is convolved with the resolution function described in [91]. The obtained B^0 lifetimes from a fit to fully simulated signal MC events are listed in Table 4.3 and are in agreement with the generated value $\tau_{gen} = 1.534$ ps.

The full PDF for longitudinal polarization is given by

$$\mathcal{P}^{\mathrm{LP}}_{\mathrm{truth}}(\Delta E, M_{\mathrm{bc}}, m_{\pi^+\pi^0}, m_{\pi^-\pi^0}, \cos\theta^+_{\mathrm{H}}, \cos\theta^-_{\mathrm{H}}, \mathcal{F}_{B\bar{B}/q\bar{q}}, \Delta t, q) = \mathcal{P}^{\mathrm{LP}}_{\mathrm{truth}}(\Delta E) \times \mathcal{P}^{\mathrm{LP}}_{\mathrm{truth}}(M_{\mathrm{bc}}|\Delta E) \times \mathcal{P}^{\mathrm{LP}}_{\mathrm{truth}}(m_{\pi^+\pi^0}|\Delta E) \times \mathcal{P}^{\mathrm{LP}}_{\mathrm{truth}}(m_{\pi^-\pi^0}|\Delta E) \times \mathcal{P}^{\mathrm{LP}}_{\mathrm{truth}}(\cos\theta^+_{\mathrm{H}}, \cos\theta^-_{\mathrm{H}}|\Delta E) \times \mathcal{P}^{k,\mathrm{LP}}_{\mathrm{truth}}(\mathcal{F}_{B\bar{B}/q\bar{q}}) \times \mathcal{P}^{\mathrm{LP(TP}}_{\mathrm{truth}}(\Delta t, q), \tag{4.20}$$

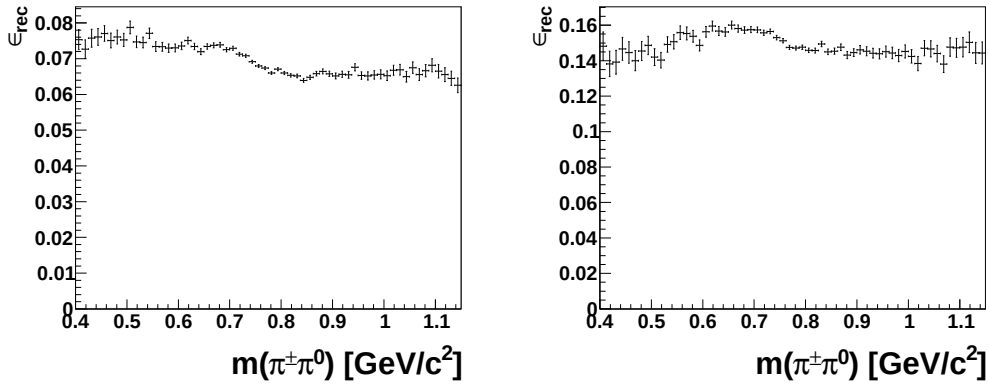

Figure 4.4: $m_{\pi^{\pm}\pi^0}$ reconstruction efficiencies obtained from fully reconstructed signal MC events for each polarization (LP left, TP right).

lifetime [ps]	$\tau_{\rm true}$ (SVD1)	$\tau_{\rm true}$ (SVD2)
$B^0 \to \rho^+\rho^-\vert_{\rm LP}$	1.527 ± 0.004	1.522 ± 0.004
$B^0 \to \rho^+\rho^-\vert_{\rm TP}$	1.527 ± 0.065	1.523 ± 0.006

Table 4.3: The B^0 lifetimes obtained from a fit to the true signal MC distributions.

and the one for tranversally polarization by

$$\begin{aligned}\mathcal{P}^{\rm TP}_{\rm truth}(\Delta E, M_{\rm bc}, m_{\pi^+\pi^0}, m_{\pi^-\pi^0}, \cos\theta^+_{\rm H}, \cos\theta^-_{\rm H}, \mathcal{F}_{B\bar{B}/q\bar{q}}, \Delta t, q) = \\ \mathcal{P}^{\rm TP}_{\rm truth}(\Delta E) \times \mathcal{P}^{\rm TP}_{\rm truth}(M_{\rm bc}) \times \mathcal{P}^{\rm TP}_{\rm truth}(m_{\pi^+\pi^0}|\Delta E) \times \mathcal{P}^{\rm TP}_{\rm truth}(m_{\pi^-\pi^0}|\Delta E) \\ \times \mathcal{P}^{\rm TP}_{\rm truth}(\cos\theta^+_{\rm H}, \cos\theta^-_{\rm H}) \times \mathcal{P}^{k,{\rm TP}}_{\rm truth}(\mathcal{F}_{B\bar{B}/q\bar{q}}) \times \mathcal{P}^{\rm LP({\rm TP}}_{\rm truth}(\Delta t, q). \qquad (4.21)\end{aligned}$$

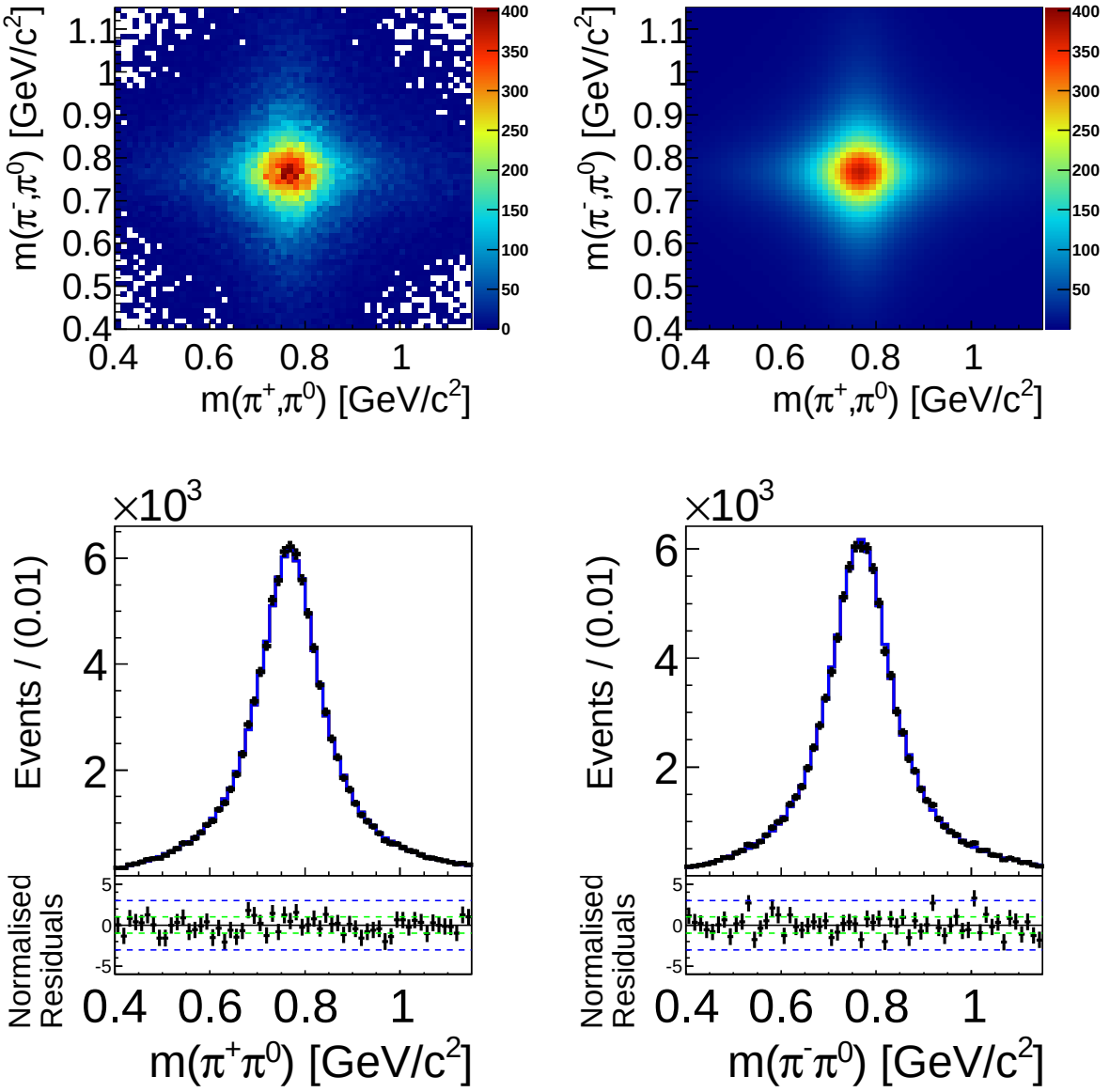

Figure 4.5: Fit projections onto $m_{\pi^{\pm}\pi^0}$ of correctly reconstructed signal MC events (LP). The top row shows the 2D projection of the data (left) and the PDF (right) and the bottom row shows projection onto each axis, where the black points show simulated MC events and the solid line shows the fit result. The residuals are given beneath each distribution.

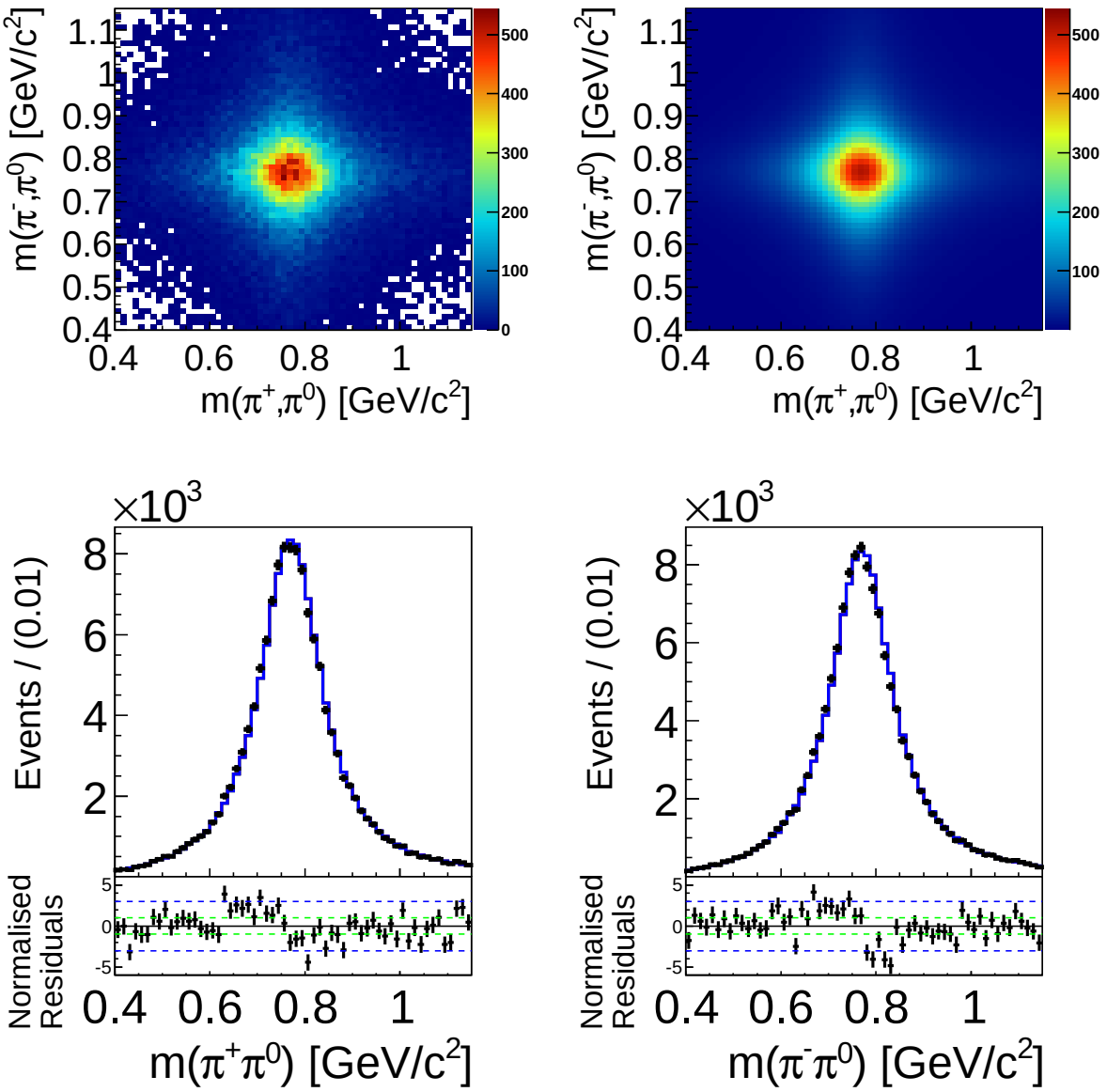

Figure 4.6: Fit projections onto $m_{\pi^{\pm}\pi^0}$ of correctly reconstructed signal MC events (TP). The top row shows the 2D projection of the data (left) and the PDF (right) and the bottom row shows projection onto each axis, where the black points show simulated MC events and the solid line shows the fit result. The residuals are given beneath each distribution.

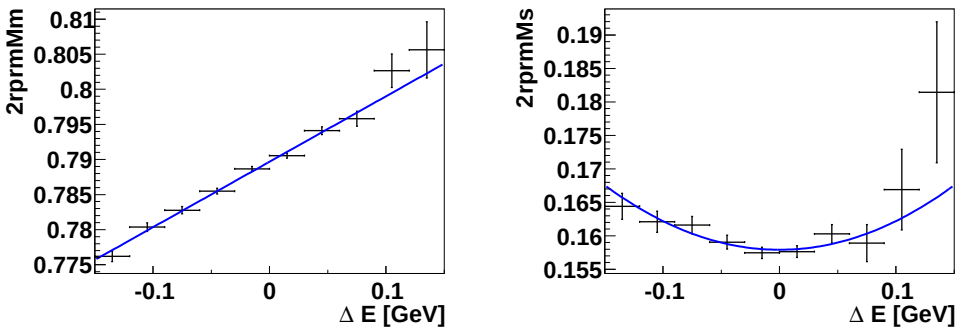

Figure 4.7: The dependence of the mean and width of the Breit-Wigner from the mass PDF on ΔE.

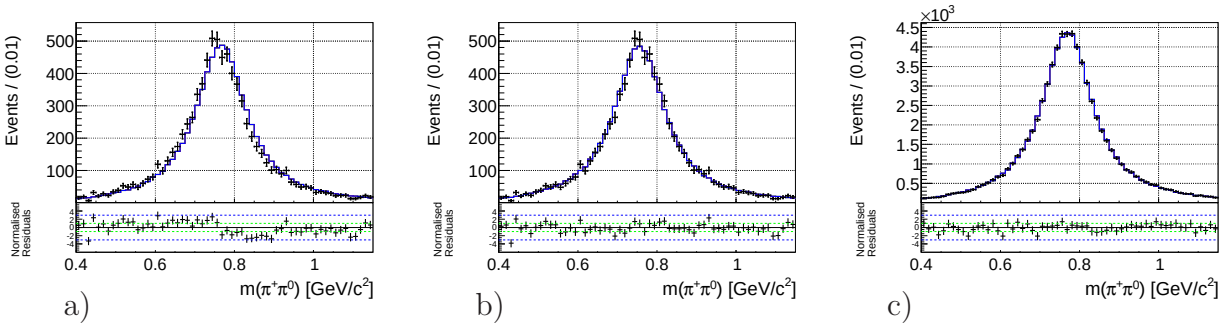

Figure 4.8: Projections onto $m_{\pi^{\pm}\pi^0}$ in different slices of ΔE. for the truth model (LP). a), b) for $\Delta E < -0.125;\mathrm{GeV}$ and c) for $-0.025 < \Delta\mathrm{E} < 0.025$ GeV. a) is plotted uncorrelated, while b) and c) are plotted including the correlation with ΔE.

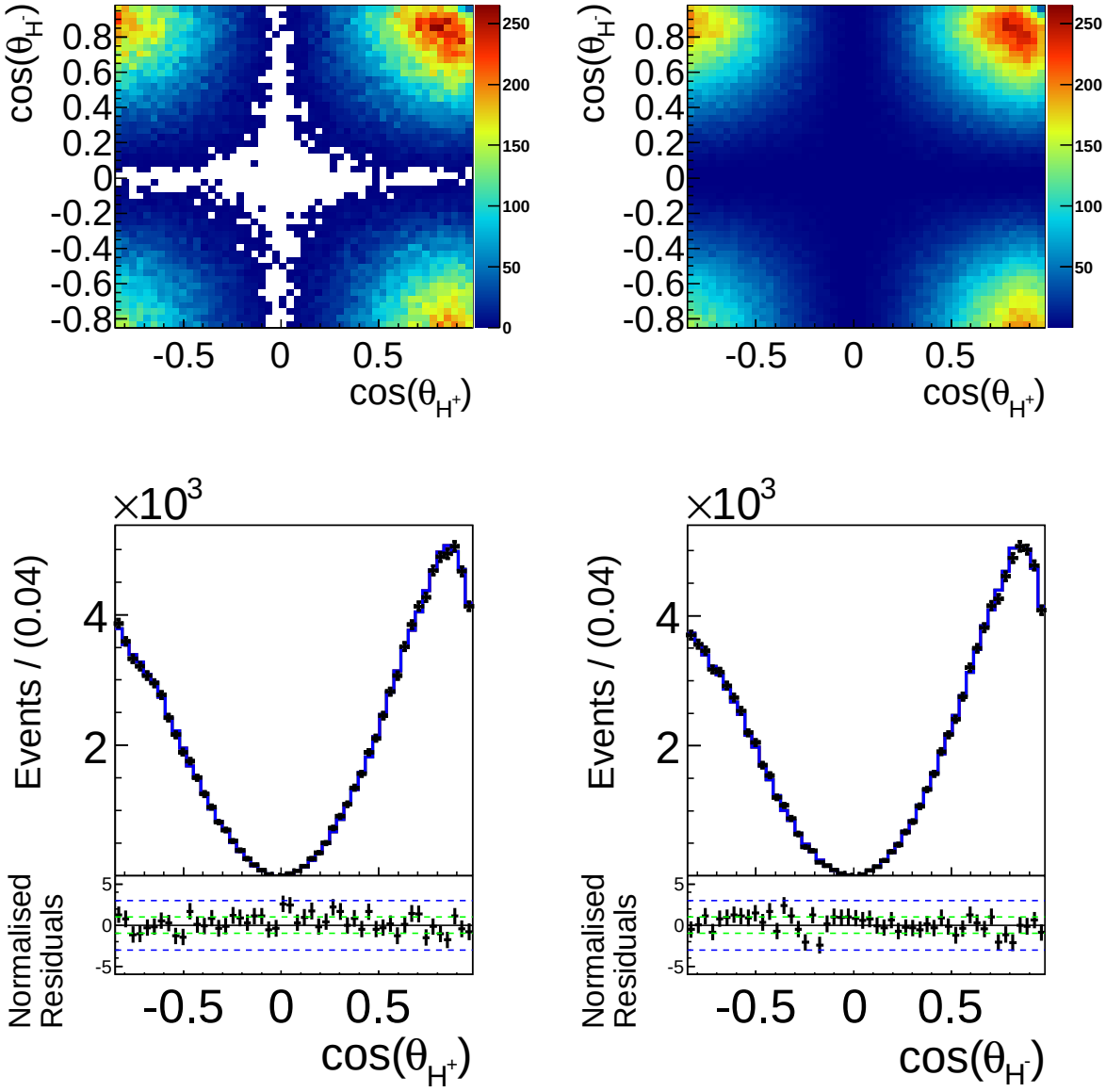

Figure 4.9: Fit projections onto $\cos\theta_{\mathrm{H}}^{+} - \cos\theta_{\mathrm{H}}^{-}$ of correctly reconstructed signal MC events (LP). The top row shows the 2D projection of the data (left) and the PDF (right) and the bottom row shows projection onto each axis, where the black points show simulated MC events and the solid line shows the fit result. The residuals are given beneath each distribution.

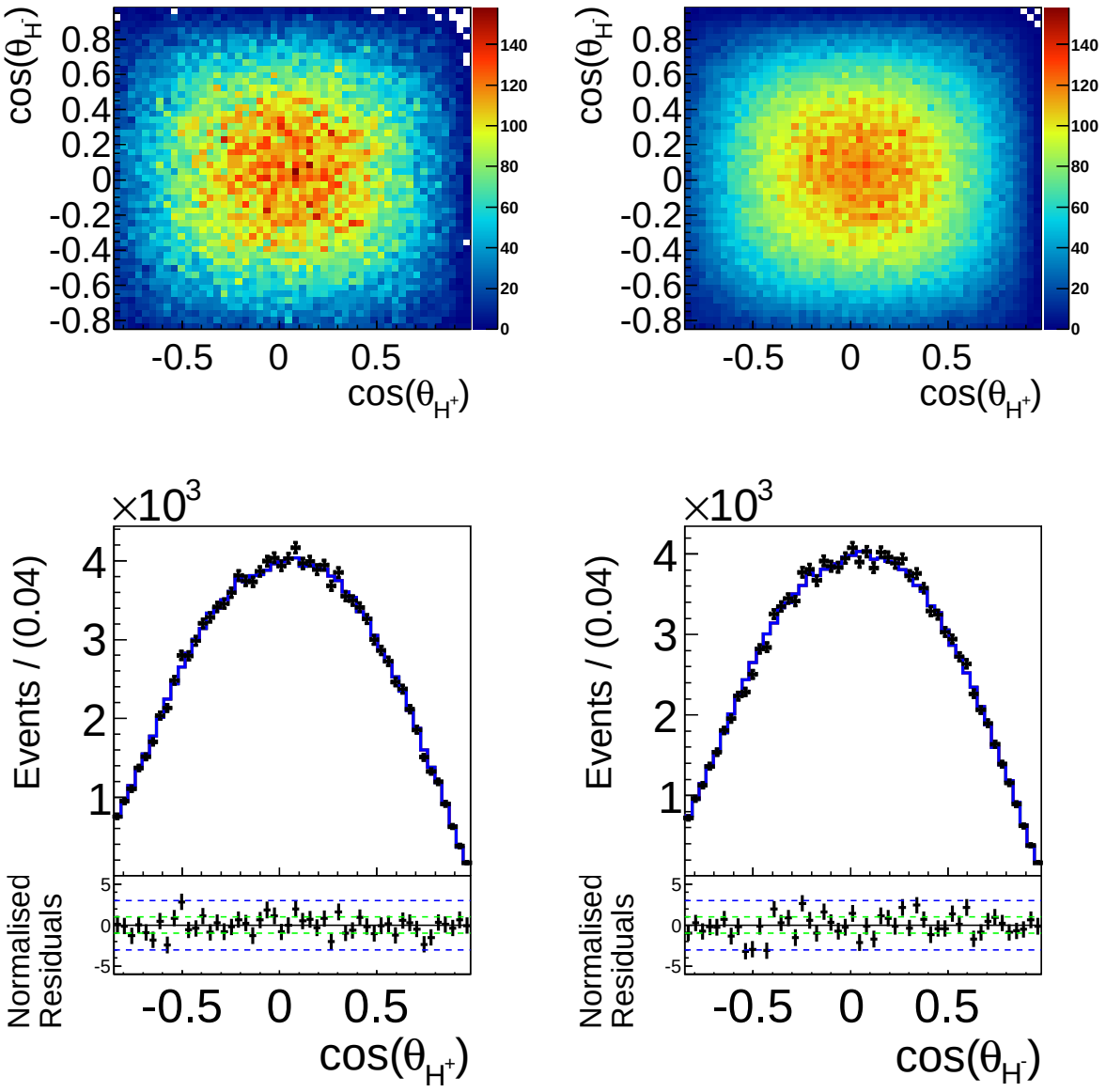

Figure 4.10: Fit projections onto $\cos\theta_{\mathrm{H}}^{+} - \cos\theta_{\mathrm{H}}^{-}$ of correctly reconstructed signal MC events (TP). The top row shows the 2D projection of the data (left) and the PDF (right) and the bottom row shows projection onto each axis, where the black points show simulated MC events and the solid line shows the fit result. The residuals are given beneath each distribution.

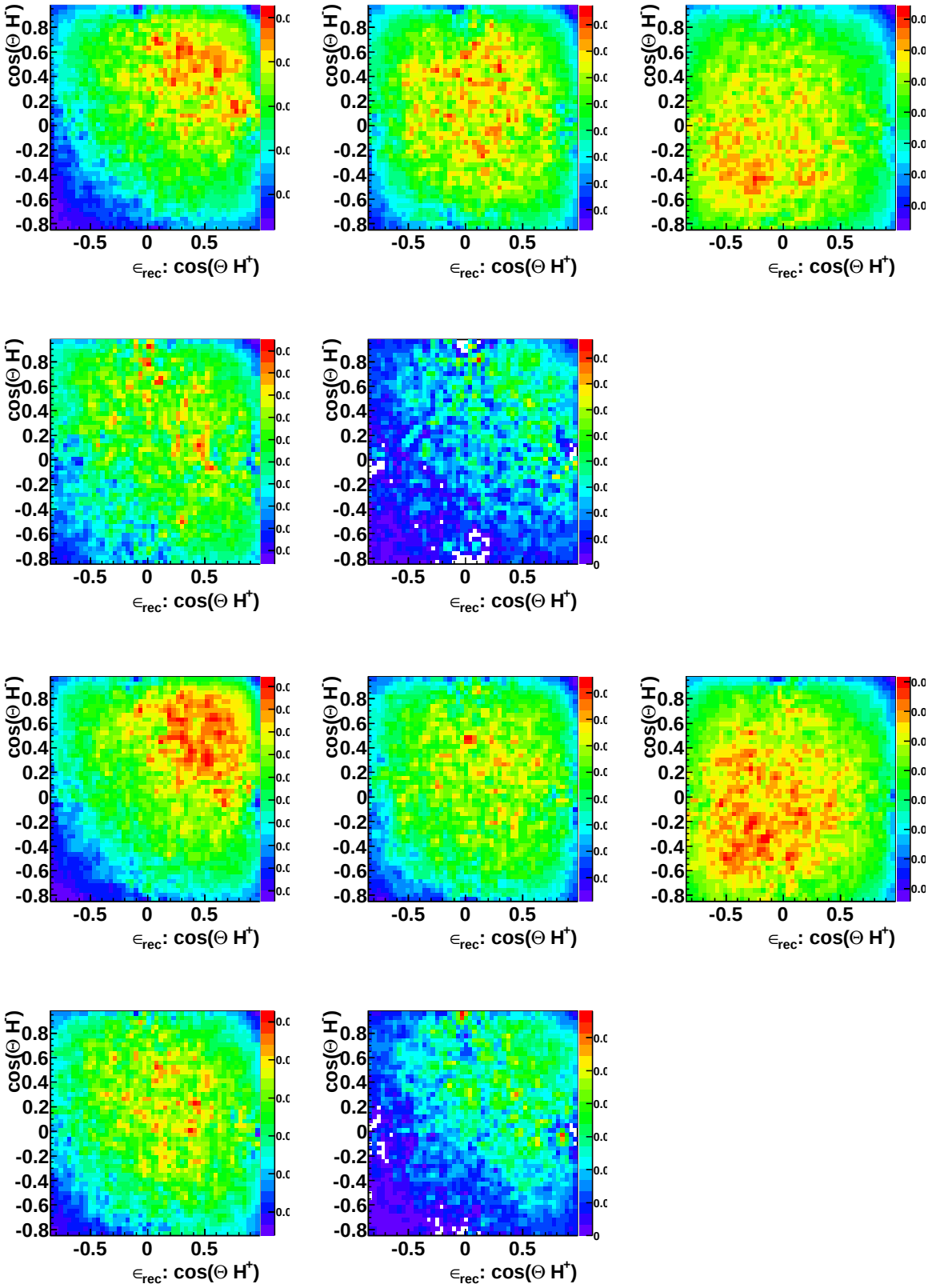

Figure 4.11: $\cos\theta_{\mathrm{H}}$-dependent reconstruction efficiencies in five bins of ΔE obtained from fully reconstructed signal MC events for detector configuration SVD1 (top) and SVD2. The bins lower and upper limits are $[-0.15, -0.6, -0.25, 0.25, 0.6, 0.15]$GeV

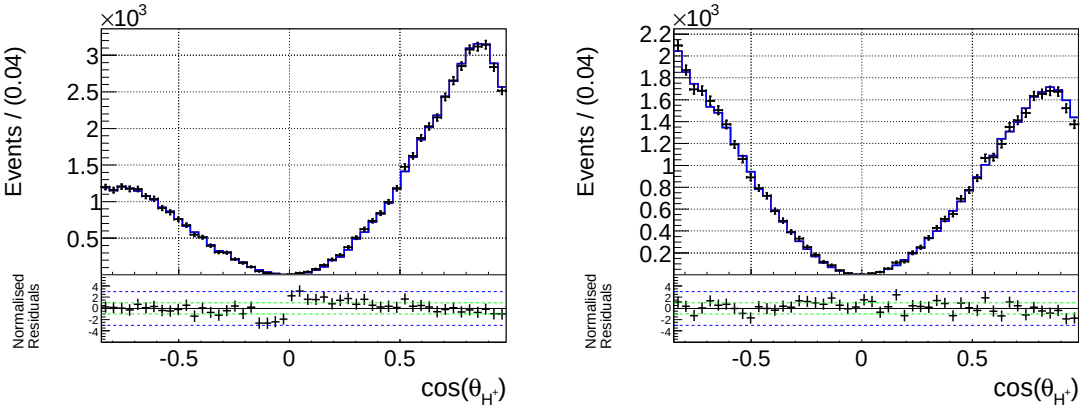

Figure 4.12: Projections onto the helicity angle in two slices of ΔE.

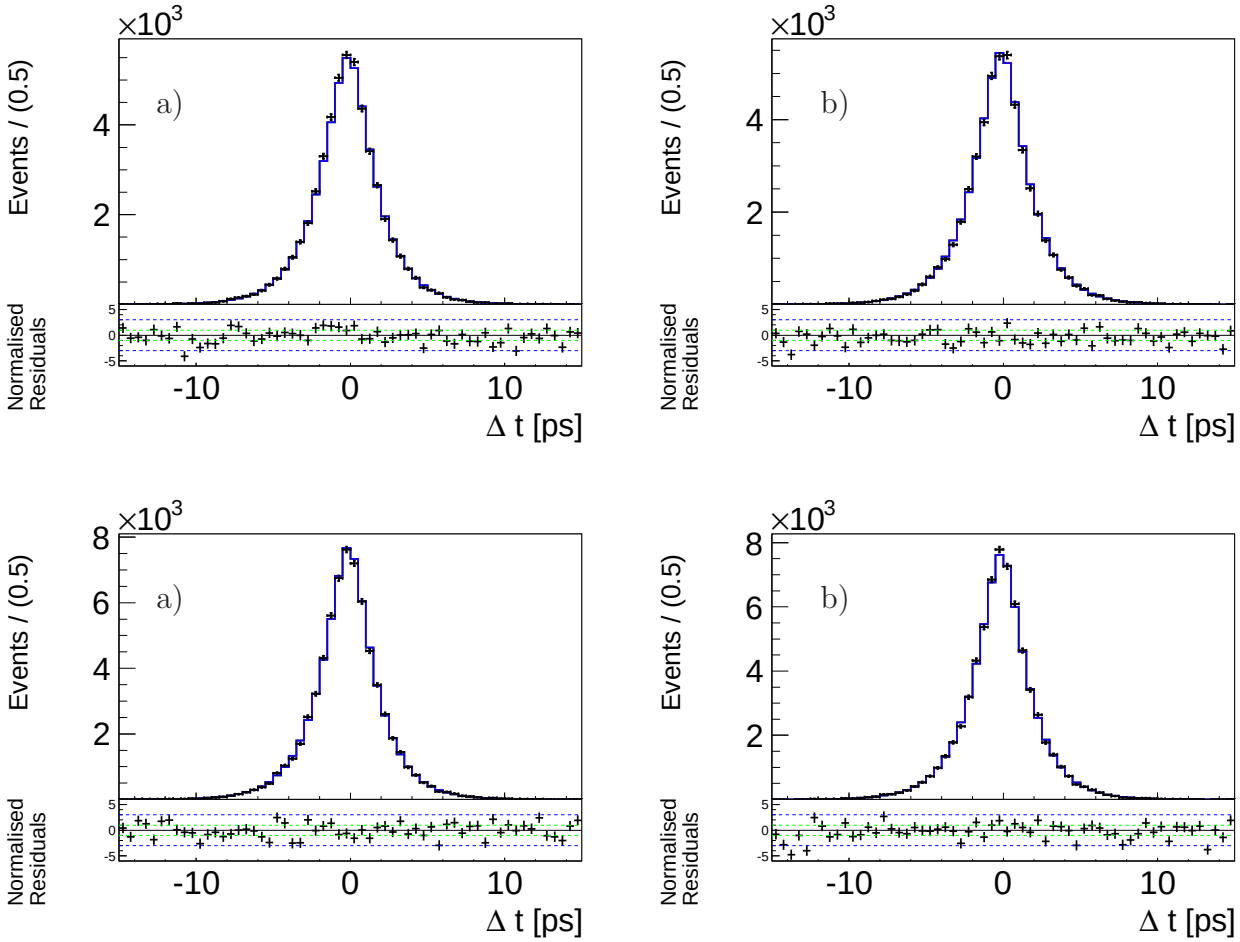

Figure 4.13: Fit projections onto Δt of the truth model (LP top, TP bottom). a) $B_{\text{tag}} = B$ and b) and $B_{\text{tag}} = \bar{B}$. The black points show simulated MC events and the solid line shows the fit result. The residuals are given beneath each distribution.

4.3.2 Two Tracks Signal Model

Signal events with both charged pions correctly reconstructed but at least one neutral pion wrongly assigned are referred to as "noπ^0". The fit results are shown in the following, the correlation matrix of the fit variables are given in Tables 4.5 and 4.6.
The ΔE distribution is modeled with the sum of a dbG and a first order Chebychev polynomial,

$$\begin{aligned}\mathcal{P}^{\mathrm{LP(TP)}}_{\mathrm{no}\pi^0}(\Delta E|\cos\theta^+_{\mathrm{H}},\cos\theta^-_{\mathrm{H}}) \equiv \\ f_{\Delta E}(\cos\theta^+_{\mathrm{H}}\cos\theta^-_{\mathrm{H}})dbG(\Delta E,\mu(\cos\theta^+_{\mathrm{H}},\cos\theta^-_{\mathrm{H}}),...) + \\ \big(1-f_{\Delta E}(\cos\theta^+_{\mathrm{H}},\cos\theta^-_{\mathrm{H}})\big)c_{\Delta E,1}(\cos\theta^+_{\mathrm{H}},\cos\theta^-_{\mathrm{H}})C_1(\Delta E). \quad (4.22)\end{aligned}$$

The dependencies of the parameters on the helicity angles are;

$$\begin{aligned}f_{\Delta E}(\cos\theta^+_{\mathrm{H}},\cos\theta^-_{\mathrm{H}}) &= f_0 + a_1\cdot(\cos\theta^+_{\mathrm{H}}+\mathrm{ll}_{\mathrm{H}})(\cos\theta^-_{\mathrm{H}}+\mathrm{ll}_{\mathrm{H}}),\\ \mu(\cos\theta^+_{\mathrm{H}},\cos\theta^-_{\mathrm{H}}) &= \mu_0 + a_2\cdot(\cos\theta^+_{\mathrm{H}}+\mathrm{ll}_{\mathrm{H}})(\cos\theta^-_{\mathrm{H}}+\mathrm{ll}_{\mathrm{H}}),\\ c_{\Delta E,1}(\cos\theta^+_{\mathrm{H}},\cos\theta^-_{\mathrm{H}}) &= c_0 + a_3\cdot(\cos\theta^+_{\mathrm{H}}+\mathrm{ll}_{\mathrm{H}})(\cos\theta^-_{\mathrm{H}}+\mathrm{ll}_{\mathrm{H}}),\end{aligned}$$

with $a_1 = 8.3\pm0.7$, $a_2 = -0.05\pm0.01$ and $a_3 = -0.1\pm0.01$. The shift of the values of the helicty angles $\mathrm{ll}_{\mathrm{H}} = 0.85$ provides the desired symmetry of the correlation, shown in Fig. 4.14.
M_{bc} is described by the sum of a dbG and an Argus function,

$$\begin{aligned}\mathcal{P}^{\mathrm{LP}}_{\mathrm{no}\pi^0}(M_{\mathrm{bc}}|\Delta E,\cos\theta^+_{\mathrm{H}},\cos\theta^-_{\mathrm{H}}) \equiv \\ f^{\mathrm{LP}}_{M_{\mathrm{bc}}}(\Delta E,\cos\theta^+_{\mathrm{H}},\cos\theta^-_{\mathrm{H}})dbG(M_{\mathrm{bc}}) + \\ \big(1-f^{\mathrm{LP}}_{M_{\mathrm{bc}}}(\Delta E,\cos\theta^+_{\mathrm{H}},\cos\theta^-_{\mathrm{H}})\big)Ar(M_{\mathrm{bc}},c^{\mathrm{LP}}_{M_{\mathrm{bc}}}). \quad (4.23)\end{aligned}$$

The dependencies of the fraction on $\Delta E, \cos\theta^+_{\mathrm{H}}$ and $\cos\theta^-_{\mathrm{H}}$,

$$\begin{aligned}f_{M_{\mathrm{bc}}}(\Delta E,\cos\theta^+_{\mathrm{H}},\cos\theta^-_{\mathrm{H}}) = f_{M_{\mathrm{bc}},0} + c_{M_{\mathrm{bc}},1}\cdot\Delta E + c_{M_{\mathrm{bc}},2}\cdot\Delta E^2 \\ + c_{M_{\mathrm{bc}},3}\cdot(\cos\theta^+_{\mathrm{H}}+\mathrm{ll}_{\mathrm{H}})(\cos\theta^-_{\mathrm{H}}+\mathrm{ll}_{\mathrm{H}}),\end{aligned}$$

with $c_{M_{\mathrm{bc}},1} = -0.07\pm0.03$, $c_{M_{\mathrm{bc}},2} = 14.3\pm0.2$ and $c_{M_{\mathrm{bc}},3} = 0.30\pm0.01$ are shown in Figs. 4.15 to 4.17. The PDF for transverse polarization reads,

$$\mathcal{P}^{\mathrm{TP}}_{\mathrm{no}\pi^0}(M_{\mathrm{bc}}) \equiv f^{\mathrm{TP}}_{M_{\mathrm{bc}}}dbG(M_{\mathrm{bc}}) + (1-f^{\mathrm{TP}}_{M_{\mathrm{bc}}})Ar(M_{\mathrm{bc}},c^{\mathrm{TP}}_{M_{\mathrm{bc}}}). \quad (4.24)$$

The $\mathcal{F}_{B\bar{B}/q\bar{q}}$ distributions are described similar to the ones used for the transverse polarized truth model (see Eq. (4.15)),

$$\mathcal{P}^{k,\mathrm{TP}}_{\mathrm{no}\pi^0}(\mathcal{F}_{B\bar{B}/q\bar{q}}) \equiv tbG^k_{\mathrm{sig}}(\mathcal{F}_{B\bar{B}/q\bar{q}}). \quad (4.25)$$

For longitudinal polarization, a correlation with ΔE has been accounted for by modifying each core Gaussian's width

$$\mathcal{P}^{k,\mathrm{LP}}_{\mathrm{no}\pi^0}(\mathcal{F}_{B\bar{B}/q\bar{q}}|\Delta E) \equiv tbG^k_{\mathrm{sig}}(\mathcal{F}_{B\bar{B}/q\bar{q}},\mu(\Delta E),...), \quad (4.26)$$

$$\text{with} \qquad \mu^k \to \mu^k(\Delta E) \equiv \mu^k_0 + c_{\mathcal{F}_{B\bar{B}/q\bar{q}},1}\Delta E + c_{\mathcal{F}_{B\bar{B}/q\bar{q}},2}\Delta E^2.$$

$c_{\mathcal{F}_{B\bar{B}/q\bar{q}},1} = 0.2\pm0.01$ and $c_{\mathcal{F}_{B\bar{B}/q\bar{q}},2} = -0.93\pm0.15$ and the correlation is shown in Fig. 4.17.
The $m_{\pi^\pm\pi^0}$ distributions of longitudinal polarized MC events are correlated with the helicity

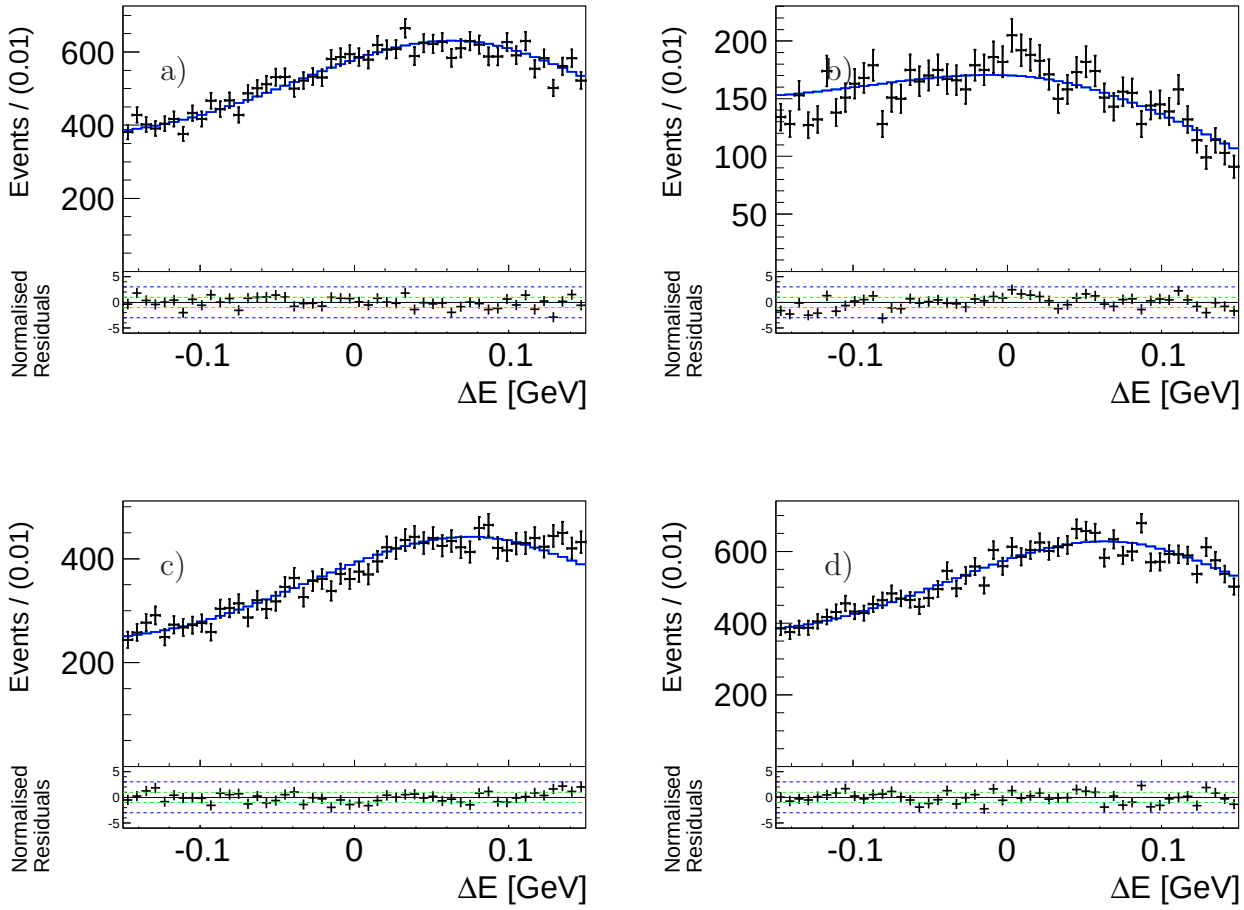

Figure 4.14: Fit projections onto ΔE for different slices of $\cos\theta_{\rm H}^{+} - \cos\theta_{\rm H}^{-}$ for noπ^0MC events. a) $\cos\theta_{\rm H}^{+} \leq -0.6$ & $\cos\theta_{\rm H}^{-} > 0.60$, b) $\cos\theta_{\rm H}^{+} > -0.6$ & $\cos\theta_{\rm H}^{-} > 0.60$, c) $\cos\theta_{\rm H}^{+} > -0.6$ & $\cos\theta_{\rm H}^{-} \leq 0.60$ and d) $\cos\theta_{\rm H}^{+} \leq -0.6$ & $\cos\theta_{\rm H}^{-} \leq 0.60$. The black points show simulated MC events and the solid line shows the fit result. The residuals are given beneath each distribution.

angles. A wrongly assigned π^0 is broaden up the resonance peak in the mass distribution and is also shifting the helicity angles towards negative values. Therefore, the mass PDF, being the product of the sum of a second order Chebychev polynomial and a Breit-Wigner function for each mass, is modeled as follows

$$\begin{aligned}\mathcal{P}^{\rm LP,A}_{{\rm no}\pi^0}(m_{\pi^\pm\pi^0}, m_{\pi^\mp\pi^0}|\cos\theta_{\rm H}^{\pm}) \equiv & \\ \big(f_1(\cos\theta_{\rm H}^{\pm})c_2C_2(m_{\pi^\pm\pi^0}) \;+\; (1-f_1(\cos\theta_{\rm H}^{\pm}))BW(m_{\pi^\pm\pi^0}, m_1, \Gamma_1)\big) \times & \\ \big(f_2(\cos\theta_{\rm H}^{\pm})\sum_{i=1}^{3} a_i(\cos\theta_{\rm H}^{\pm})C_i(m_{\pi^\pm\pi^0}) \;+\; (1-f_2(\cos\theta_{\rm H}^{\pm}))BW(m_{\pi^\mp\pi^0}, m_1, \Gamma_2(\cos\theta_{\rm H}^{\pm}))\big) & \end{aligned} \tag{4.27}$$

$$\begin{aligned}\mathcal{P}^{\rm LP,B}_{{\rm no}\pi^0}(m_{\pi^+\pi^0}, m_{\pi^-\pi^0}) \equiv & \\ \big(f_0c_2C_2(m_{\pi^+\pi^0}) \;+\; (1-f_0)BW(m_{\pi^+\pi^0}, m_1, \Gamma_1)\big) \times & \\ f_0c_2C_2(m_{\pi^-\pi^0}) \;+\; (1-f_0)BW(m_{\pi^-\pi^0}, m_1, \Gamma_1)\big) & \end{aligned} \tag{4.28}$$

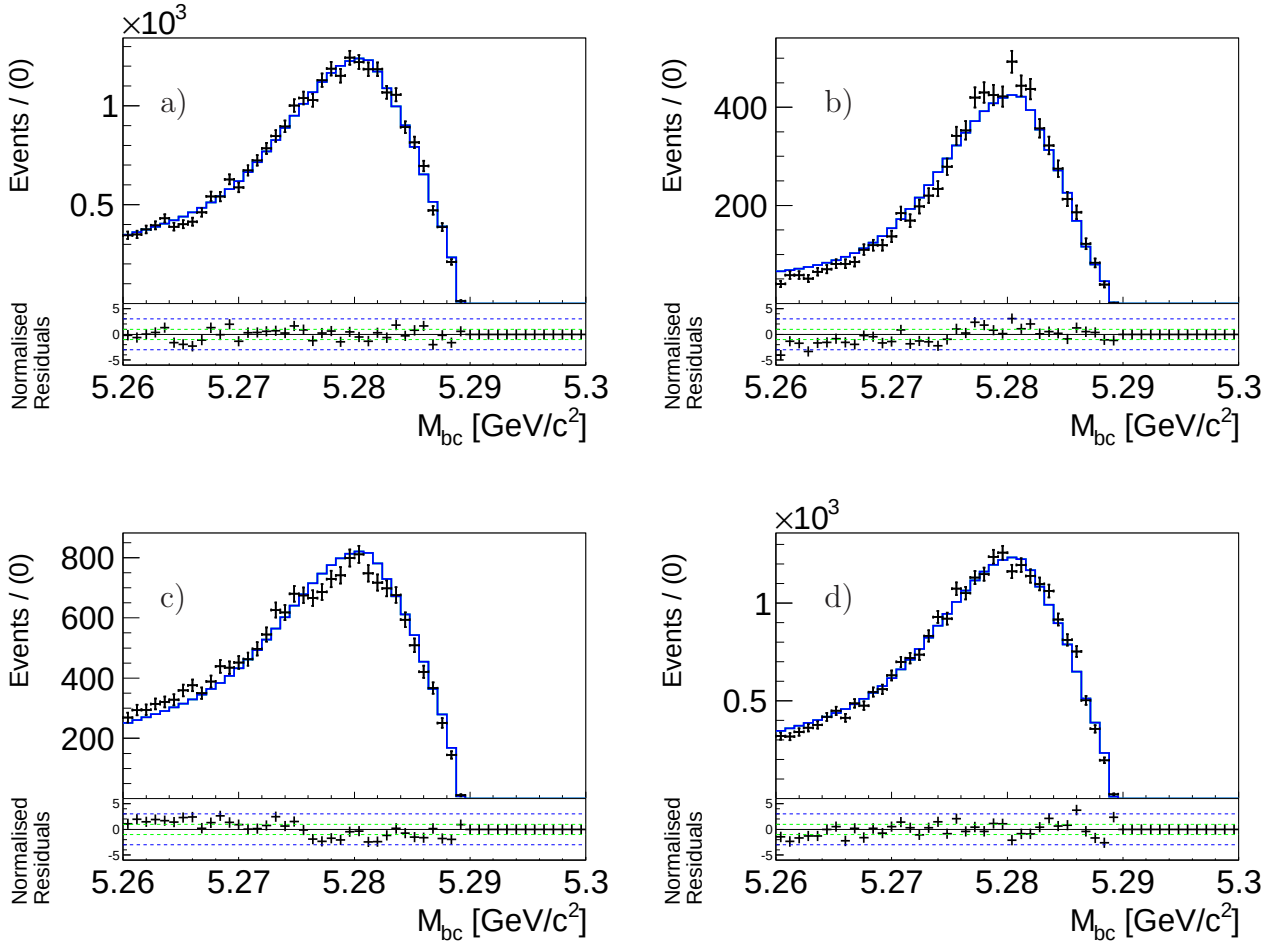

Figure 4.15: Fit projections onto $M_{\rm bc}$ for different slices of $\cos\theta_{\rm H}^{+} - \cos\theta_{\rm H}^{-}$ for noπ^0MC events. a) $\cos\theta_{\rm H}^{+} \leq -0.6$ & $\cos\theta_{\rm H}^{-} > 0.60$, b) $\cos\theta_{\rm H}^{+} > -0.6$ & $\cos\theta_{\rm H}^{-} > 0.60$, c) $\cos\theta_{\rm H}^{+} > -0.6$ & $\cos\theta_{\rm H}^{-} \leq 0.60$ and d) $\cos\theta_{\rm H}^{+} \leq -0.6$ & $\cos\theta_{\rm H}^{-} \leq 0.60$. The black points show simulated MC events and the solid line shows the fit result. The residuals are given beneath each distribution.

where the the parameters (see Table 4.4) dependencies on $\cos\theta_{\rm H}^{\pm}$ only occurs for $\cos\theta_{\rm H} \leq c_{smooth} = -0.6$ and is modeled by

$$p_j(\cos\theta_{\rm H}^{\pm}) = p_{j,0} + c_j|\cos\theta_{\rm H}^{\pm} - c_{\rm smooth}| \tag{4.29}$$

with a cut-off of $p_j(\cos\theta_{\rm H}^{\pm}) = p_j(c_{cut})$ if $\cos\theta_{\rm H}^{\pm} \leq c_{cut} = -0.81 \pm 0.02$. c_{smooth} retains the smoothness of the PDF in the transition to the uncorrelated PDF ($\cos\theta_{\rm H}^{\pm} \geq c_{smooth}$).

The PDF for the ρ masses then takes the following form

$$\begin{aligned}
&\mathcal{P}^{\rm LP}_{{\rm no}\pi^0}(m_{\pi^+\pi^0}, m_{\pi^-\pi^0}|\cos\theta_{\rm H}^{+}, \cos\theta_{\rm H}^{-}) \equiv \\
&\quad \mathcal{P}^{\rm LP,A}_{{\rm no}\pi^0}(m_{\pi^+\pi^0}, m_{\pi^-\pi^0}|\cos\theta_{\rm H}^{-}) \qquad \text{if} \quad -0.6 \leq \cos\theta_{\rm H}^{+} \;\&\; \cos\theta_{\rm H}^{-} \leq -0.6, \qquad (4.30)\\
&\quad \mathcal{P}^{\rm LP,A}_{{\rm no}\pi^0}(m_{\pi^-\pi^0}, m_{\pi^+\pi^0}|\cos\theta_{\rm H}^{+}) \qquad \text{if} \quad \cos\theta_{\rm H}^{+} \leq -0.6 \quad -0.6 \leq \cos\theta_{\rm H}^{-}, \qquad (4.31)\\
&\quad \mathcal{P}^{\rm LP,B}_{{\rm no}\pi^0}(m_{\pi^+\pi^0}, m_{\pi^-\pi^0}) \qquad \text{if} \quad -0.6 \leq \cos\theta_{\rm H}^{+} \;\&\; -0.6 \leq \cos\theta_{\rm H}^{-} \qquad (4.32)\\
&\text{and} \quad \frac{1}{2}\left(\mathcal{P}^{\rm LP,A}_{{\rm no}\pi^0}(m_{\pi^+\pi^0}, m_{\pi^-\pi^0}|\cos\theta_{\rm H}^{-}) + \mathcal{P}^{\rm LP,A}_{{\rm no}\pi^0}(m_{\pi^-\pi^0}, m_{\pi^+\pi^0}|\cos\theta_{\rm H}^{+})\right) \quad \text{else} \qquad (4.33)
\end{aligned}$$

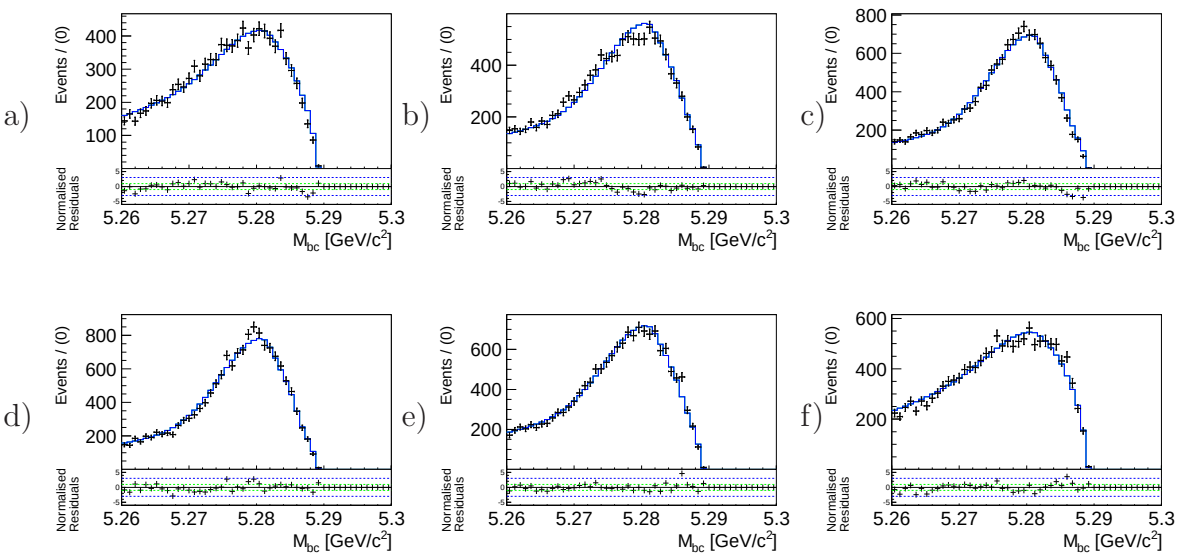

Figure 4.16: Fit projections onto $M_{\rm bc}$ for different slices of ΔE for noπ^0MC events. a) $\Delta E \leq 0.1$GeV and b)-f) increasing in steps of 0.05GeV. The black points show simulated MC events and the solid line shows the fit result. The residuals are given beneath each distribution.

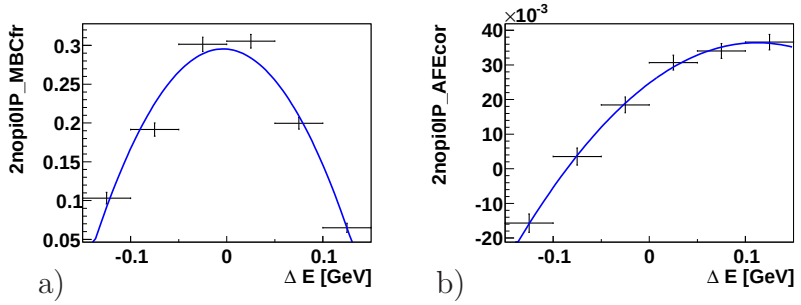

Figure 4.17: a) $M_{\rm bc}$'s dbG fraction and b) $\mathcal{F}_{B\bar{B}/q\bar{q}}$'s mean dependencies on ΔE. The plotted fit result was used as a starting guess for obtaining the full shape from a fit to the full MC sample.

Projections onto the masses for each case are shown in Fig. 4.18. A two-dimensional histogram is taken for transverse polarization.

$$\mathcal{P}^{\rm TP}_{{\rm no}\pi^0}(m_{\pi^+\pi^0}, m_{\pi^-\pi^0}) \equiv H(m_{\pi^+\pi^0}, m_{\pi^-\pi^0}). \tag{4.34}$$

The $\cos\theta^+_{\rm H}$-$\cos\theta^-_{\rm H}$ PDF for each polarization is taken to be a two-dimensional histogram.

$$\mathcal{P}^{\rm LP(TP)}_{{\rm no}\pi^0}(\cos\theta^+_{\rm H}, \cos\theta^-_{\rm H}) \equiv H(\cos\theta^+_{\rm H}, \cos\theta^-_{\rm H}). \tag{4.35}$$

Since only charged tracks contribute to the determination of Δt, its PDF is identical to the one used in the truth model (see Eq. (4.19)).

$$\mathcal{P}^{\rm LP(TP)}_{{\rm no}\pi^0}(\Delta t, q) = \mathcal{P}^{\rm LP(TP)}_{\rm truth}(\Delta t, q). \tag{4.36}$$

parameter	$p_{j,0}$	c_j^{SVD1}	c_j^{SVD2}
f_1	f_0	0.08	0.07
f_2	f_0	1.16	1.03
Γ_2	Γ_1	0.62	0.54
a_1	0	85.9	64.3
a_2	c_2	276.7	220.3
a_3	0	-161.8	-129.0

Table 4.4: Parameter correlations for the mass PDF, see Eq. (4.29).

0	ΔE	M_{bc}	$m^1_{\pi^+\pi^-}$	$m^2_{\pi^+\pi^-}$	$\mathcal{F}_{B\bar{B}/q\bar{q}}$	$\cos\theta^1_{\mathrm{H}}$	$\cos\theta^2_{\mathrm{H}}$	Δt
ΔE	1	0.00	0.06	0.06	0.05	-0.03	-0.04	0.00
M_{bc}		1	-0.03	-0.02	0.03	0.03	0.02	0.00
$m^1_{\pi^+\pi^-}$			1	-0.02	-0.01	-0.11	0.08	0.00
$m^2_{\pi^+\pi^-}$				1	-0.02	0.08	-0.12	-0.01
$\mathcal{F}_{B\bar{B}/q\bar{q}}$					1	0.02	0.02	0.00
$\cos\theta^1_{\mathrm{H}}$						1	-0.40	0.00
$\cos\theta^2_{\mathrm{H}}$							1	-0.00
Δt								1

Table 4.5: Correlation matrix for the $no\pi^0$ model (LP, SVD2).

The full PDF for the longitudinal polarized noπ^0 model is given by

$$\begin{aligned}\mathcal{P}^{\mathrm{LP}}_{no\pi^0}(\Delta E, M_{\mathrm{bc}}, m_{\pi^+\pi^0}, m_{\pi^-\pi^0}, \cos\theta^+_{\mathrm{H}}, \cos\theta^-_{\mathrm{H}}, \mathcal{F}_{B\bar{B}/q\bar{q}}, \Delta t, q) = \\ \mathcal{P}^{\mathrm{LP}}_{no\pi^0}(\Delta E|\cos\theta^+_{\mathrm{H}}, \cos\theta^-_{\mathrm{H}}) \times \mathcal{P}^{\mathrm{LP}}_{no\pi^0}(M_{\mathrm{bc}}|\Delta E, \cos\theta^+_{\mathrm{H}}, \cos\theta^-_{\mathrm{H}}) \quad \times \\ \mathcal{P}^{\mathrm{LP}}_{no\pi^0}(m_{\pi^+\pi^0}, m_{\pi^-\pi^0}|\cos\theta^+_{\mathrm{H}}, \cos\theta^-_{\mathrm{H}}) \times \mathcal{P}^{\mathrm{LP}}_{no\pi^0}(\cos\theta^+_{\mathrm{H}}, \cos\theta^-_{\mathrm{H}}) \quad \times \\ \mathcal{P}^{\mathrm{LP}}_{no\pi^0,k}(\mathcal{F}_{B\bar{B}/q\bar{q}}|\Delta E) \times \mathcal{P}^{\mathrm{LP(TP}}_{no\pi^0}(\Delta t, q) \quad , \end{aligned} \tag{4.37}$$

and for transverse polarization by

$$\begin{aligned}\mathcal{P}^{\mathrm{LP}}_{no\pi^0}(\Delta E, M_{\mathrm{bc}}, m_{\pi^+\pi^0}, m_{\pi^-\pi^0}, \cos\theta^+_{\mathrm{H}}, \cos\theta^-_{\mathrm{H}}, \mathcal{F}_{B\bar{B}/q\bar{q}}, \Delta t, q) = \\ \mathcal{P}^{\mathrm{LP}}_{no\pi^0}(\Delta E|\cos\theta^+_{\mathrm{H}}, \cos\theta^-_{\mathrm{H}}) \times \mathcal{P}^{\mathrm{LP}}_{no\pi^0}(M_{\mathrm{bc}}) \times \mathcal{P}^{\mathrm{LP}}_{no\pi^0}(m_{\pi^+\pi^0}, m_{\pi^-\pi^0}) \\ \times\mathcal{P}^{\mathrm{LP}}_{no\pi^0}(\cos\theta^+_{\mathrm{H}}, \cos\theta^-_{\mathrm{H}}) \times \mathcal{P}^{\mathrm{LP}}_{no\pi^0,k}(\mathcal{F}_{B\bar{B}/q\bar{q}}) \times \mathcal{P}^{\mathrm{LP(TP}}_{no\pi^0}(\Delta t, q). \end{aligned} \tag{4.38}$$

0	ΔE	M_{bc}	$m^1_{\pi^+\pi^-}$	$m^2_{\pi^+\pi^-}$	$\mathcal{F}_{B\bar{B}/q\bar{q}}$	$\cos\theta^1_{\mathrm{H}}$	$\cos\theta^2_{\mathrm{H}}$	Δt
ΔE	1	0.03	0.06	0.07	0.07	-0.00	0.00	-0.00
M_{bc}		1	-0.02	-0.01	0.04	0.04	0.06	-0.01
$m^1_{\pi^+\pi^-}$			1	-0.00	-0.02	-0.04	0.01	0.01
$m^2_{\pi^+\pi^-}$				1	-0.01	0.00	-0.04	-0.00
$\mathcal{F}_{B\bar{B}/q\bar{q}}$					1	0.01	-0.01	-0.02
$\cos\theta^1_{\mathrm{H}}$						1	-0.27	-0.01
$\cos\theta^2_{\mathrm{H}}$							1	-0.00
Δt								1

Table 4.6: Correlation matrix for the $no\pi^0$ model (TP, SVD2).

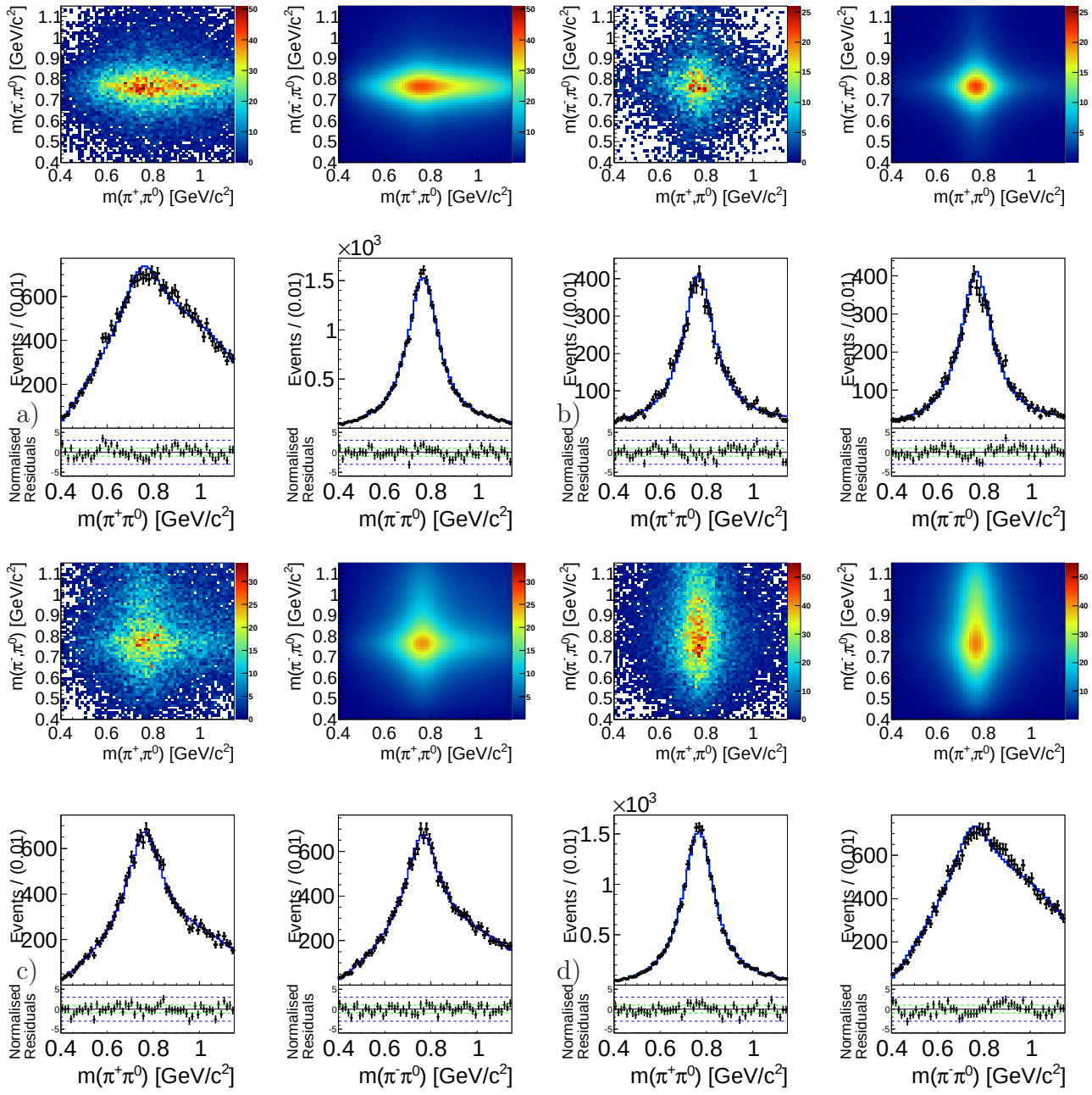

Figure 4.18: Fit projections onto $m_{\pi^{\pm}\pi^0}$for different slices of $\cos\theta_{\mathrm{H}}^{+} - \cos\theta_{\mathrm{H}}^{-}$ for noπ^0MC events. a) $\cos\theta_{\mathrm{H}}^{+} \leq -0.6$ & $\cos\theta_{\mathrm{H}}^{-} > 0.60$, b) $\cos\theta_{\mathrm{H}}^{+} > -0.6$ & $\cos\theta_{\mathrm{H}}^{-} > 0.60$, c) $\cos\theta_{\mathrm{H}}^{+} > -0.6$ & $\cos\theta_{\mathrm{H}}^{-} \leq 0.60$ and d) $\cos\theta_{\mathrm{H}}^{+} \leq -0.6$ & $\cos\theta_{\mathrm{H}}^{-} \leq 0.60$. The black points show simulated MC events and the solid line shows the fit result. The residuals are given beneath each distribution.

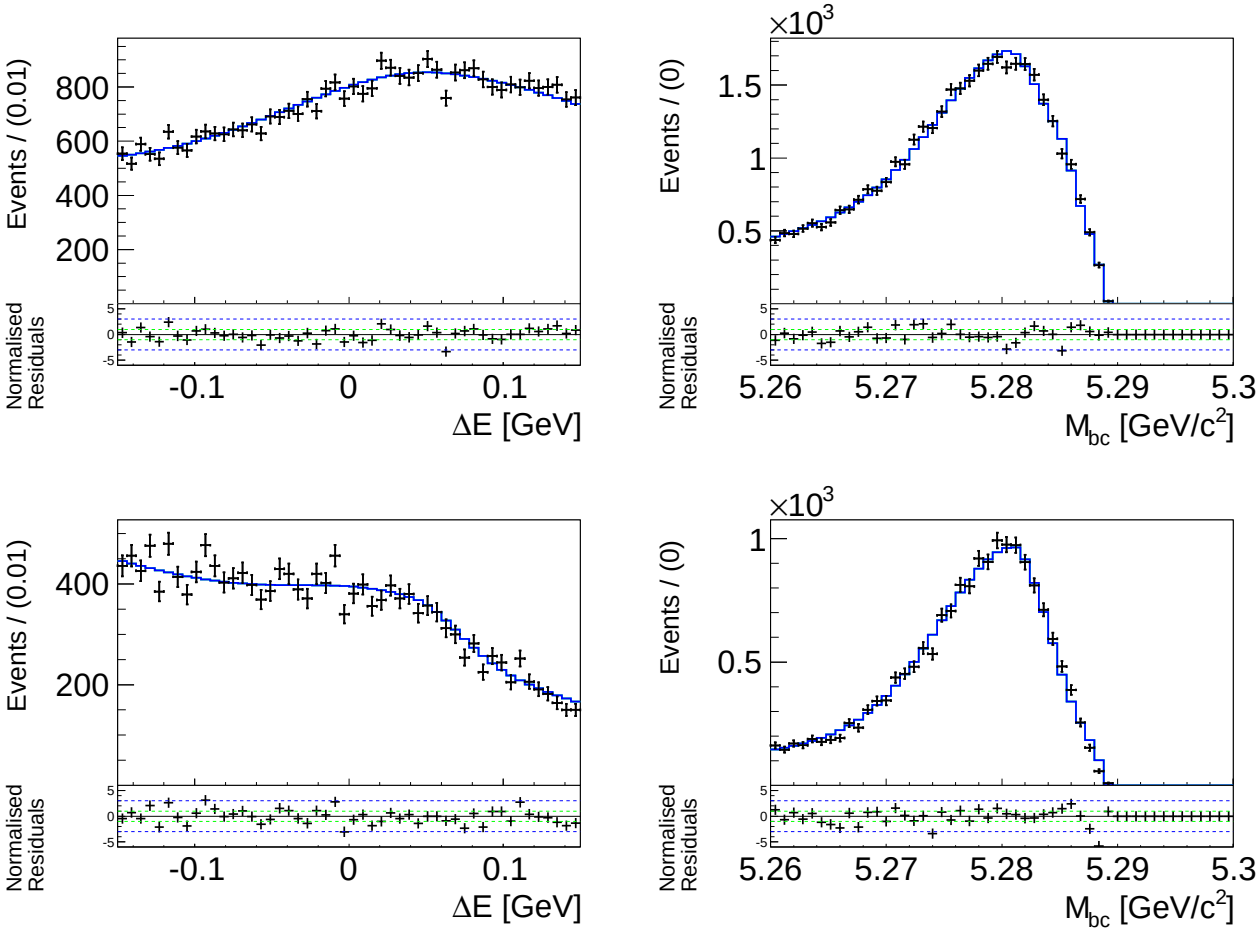

Figure 4.19: Fit projections onto ΔE and $M_{\rm bc}$ for signal MC events with both charged pion correctly reconstructed and at least one neutral pion mis-reconstructed. LP (top row) and TP. The black points show simulated MC events and the solid line shows the fit result. The residuals are given beneath each distribution.

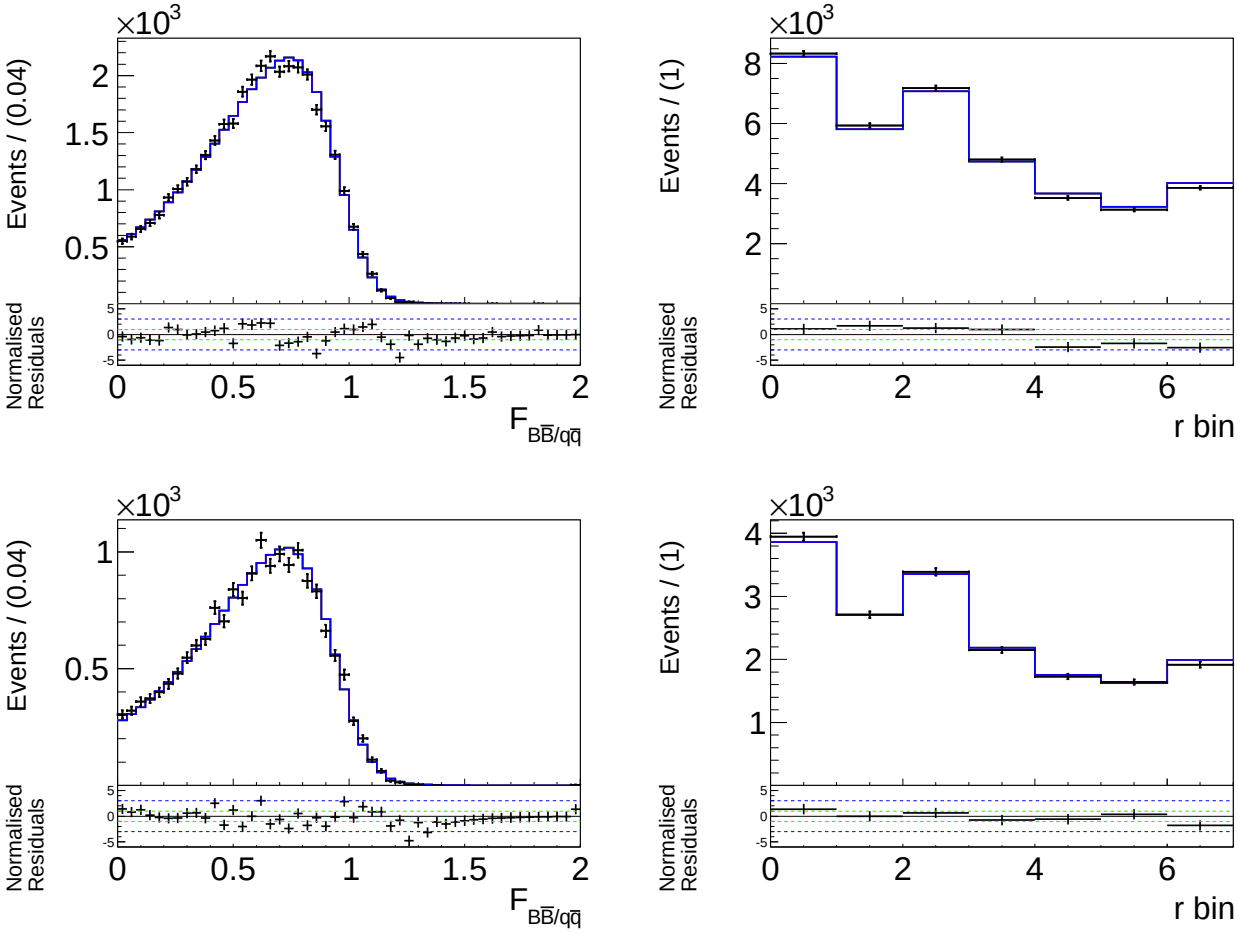

Figure 4.20: Fit projections onto $\mathcal{F}_{B\bar{B}/q\bar{q}}$ and the r-bin fractions for signal MC events with both charged pion correctly reconstructed and at least one neutral pion mis-reconstructed. LP (top row) and TP. The black points show simulated MC events and the solid line shows the fit result. The residuals are given beneath each distribution.

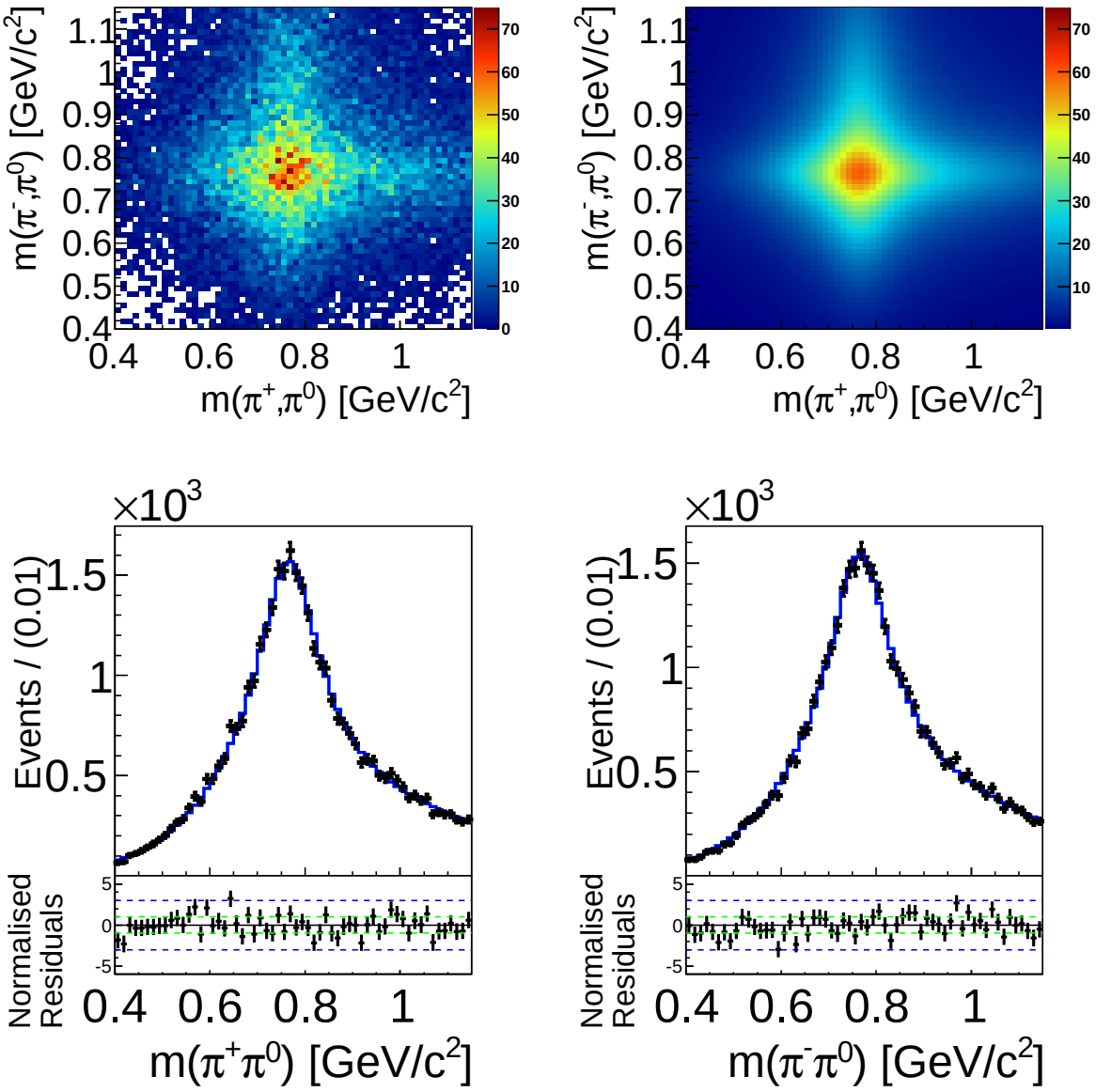

Figure 4.21: Fit projections onto $m_{\pi^{\pm}\pi^0}$ for signal events with both charged pion correctly reconstructed and at least one mis-reconstructed π^0 (LP). The top row shows the 2D projection of the data (left) and the PDF (right) and the bottom row shows projection onto each axis, where the black points show simulated MC events and the solid line shows the fit result. The residuals are given beneath each distribution.

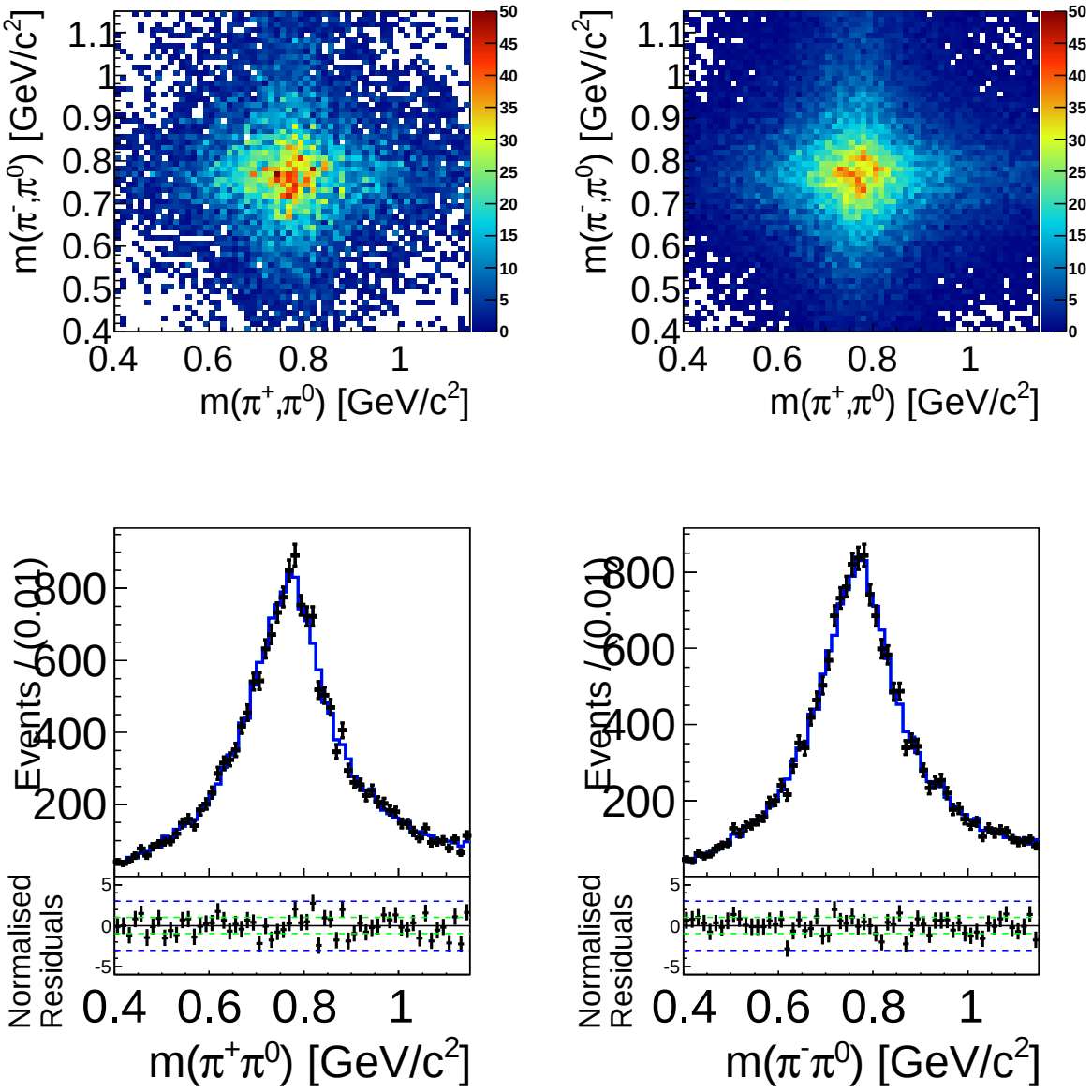

Figure 4.22: Fit projections onto $m_{\pi^{\pm}\pi^0}$ for signal events with both charged pion correctly reconstructed and at least one mis-reconstructed π^0 (TP). The top row shows the 2D projection of the data (left) and the PDF (right) and the bottom row shows projection onto each axis, where the black points show simulated MC events and the solid line shows the fit result. The residuals are given beneath each distribution.

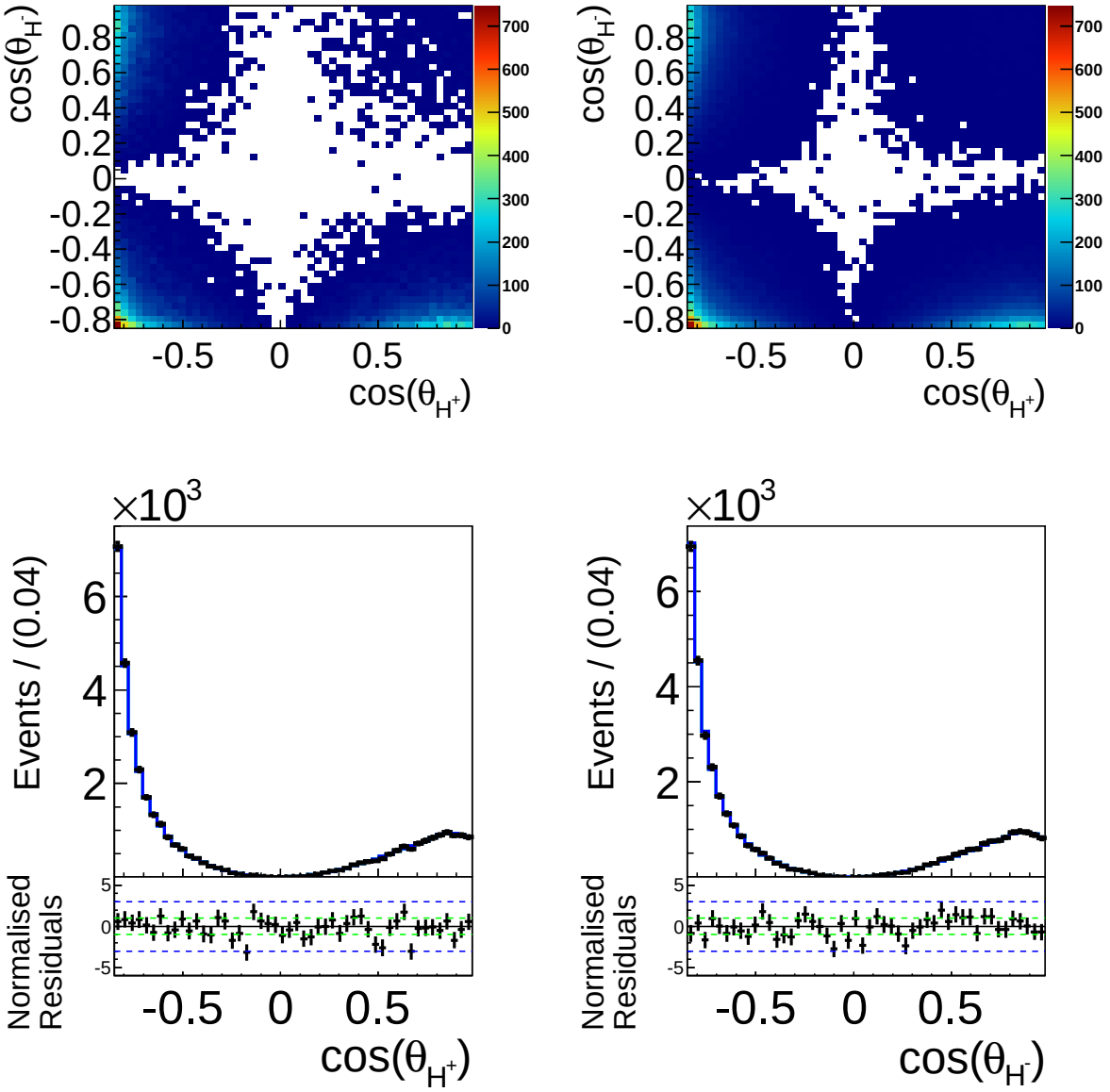

Figure 4.23: Fit projections onto $\cos\theta_{\mathrm{H}}^{+} - \cos\theta_{\mathrm{H}}^{-}$ for signal events with both charged pion correctly reconstructed and at least one mis-reconstructed π^0 (LP). The top row shows the 2D projection of the data (left) and the PDF (right) and the bottom row shows projection onto each axis, where the black points show simulated MC events and the solid line shows the fit result. The residuals are given beneath each distribution.

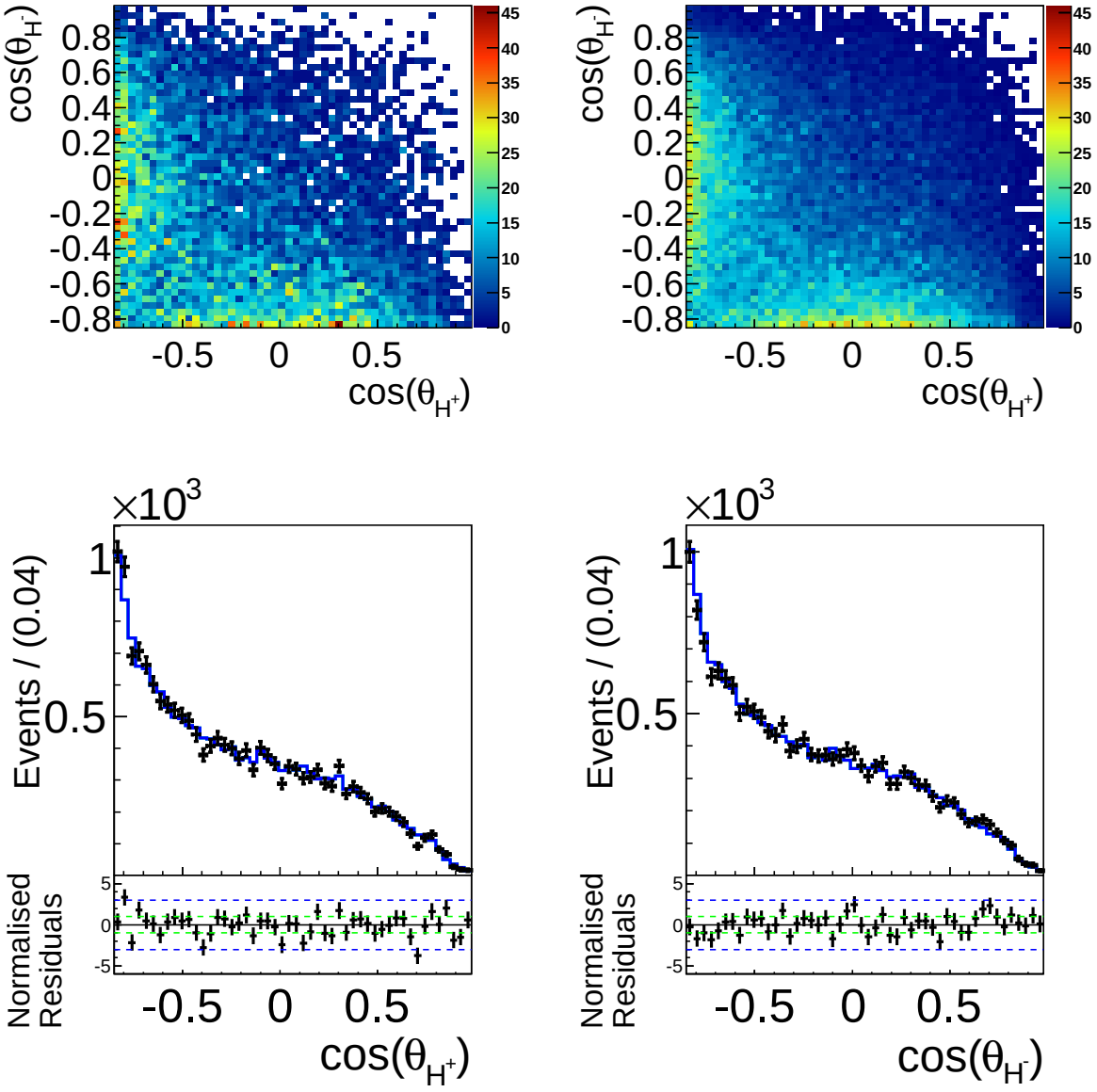

Figure 4.24: Fit projections onto $\cos\theta_{\mathrm{H}}^{+} - \cos\theta_{\mathrm{H}}^{-}$ for signal events with both charged pion correctly reconstructed and at least one mis-reconstructed π^0 (TP). The top row shows the 2D projection of the data (left) and the PDF (right) and the bottom row shows projection onto each axis, where the black points show simulated MC events and the solid line shows the fit result. The residuals are given beneath each distribution.

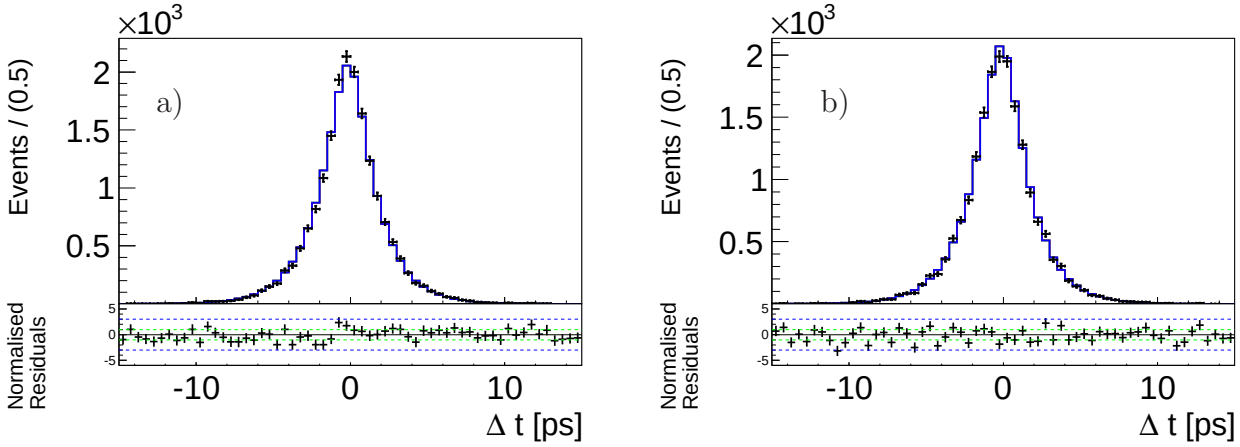

Figure 4.25: Fit projections onto Δt for signal MC (LP) for both charged pion correctly reconstructed and at least one mis-reconstructed π^0. a) $B_{\text{tag}} = B$ and b) and $B_{\text{tag}} = \bar{B}$. The black points show simulated MC events and the solid line shows the fit result. The residuals are given beneath each distribution.

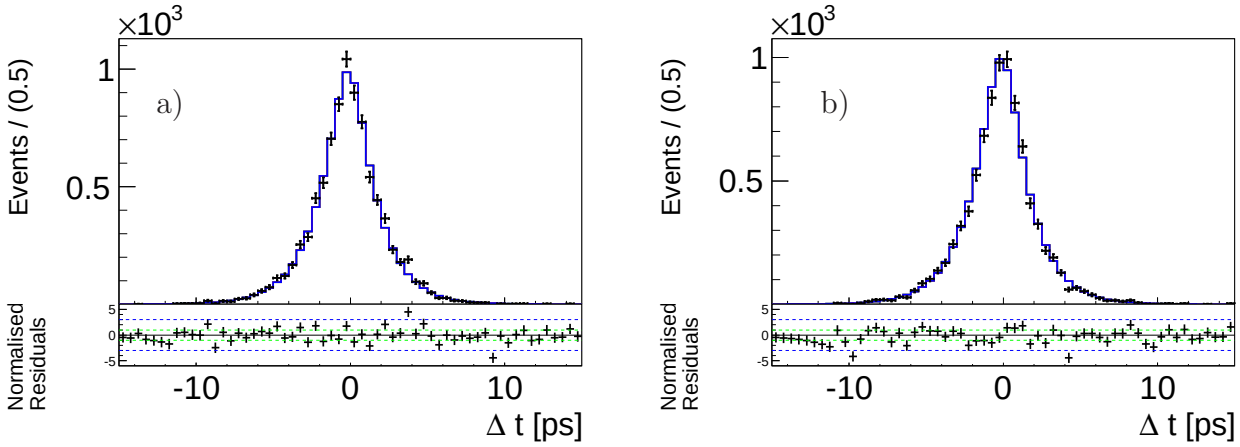

Figure 4.26: Fit projections onto Δt for signal MC (TP(for both charged pion correctly reconstructed and at least one mis-reconstructed π^0. a) $B_{\text{tag}} = B$ and b) and $B_{\text{tag}} = \bar{B}$. The black points show simulated MC events and the solid line shows the fit result. The residuals are given beneath each distribution.

4.3.3 One Track Signal Model

Signal events, where only one of the charged pions is correctly reconstructed are referred to as "$1\pi^{\pm}$".
Their ΔE distribution for longitudinal polarization is modeled with the sum of a dbG and a first order Chebychev polynomial,

$$\mathcal{P}^{\mathrm{LP}}_{1\pi^{\pm}}(\Delta E|\cos\theta^{+}_{\mathrm{H}},\cos\theta^{-}_{\mathrm{H}}) \equiv$$
$$f_{\Delta E}(\cos\theta^{+}_{\mathrm{H}},\cos\theta^{-}_{\mathrm{H}})dbG(\Delta E) + (1-f_{\Delta E}(\cos\theta^{+}_{\mathrm{H}},\cos\theta^{-}_{\mathrm{H}}))c^{\mathrm{LP}}(\cos\theta^{+}_{\mathrm{H}},\cos\theta^{-}_{\mathrm{H}})_{\Delta E,1}C_1(\Delta E), \tag{4.39}$$

where we account for a correlation with the two helicity angles by using a different fraction $f_{\Delta E}$ and two separate values for the parameter $c^{\mathrm{LP}}_{\Delta E,1}$ if $\cos\theta^{+}_{\mathrm{H}} \times \cos\theta^{-}_{\mathrm{H}} < 0$ or else (see Fig. 4.27).

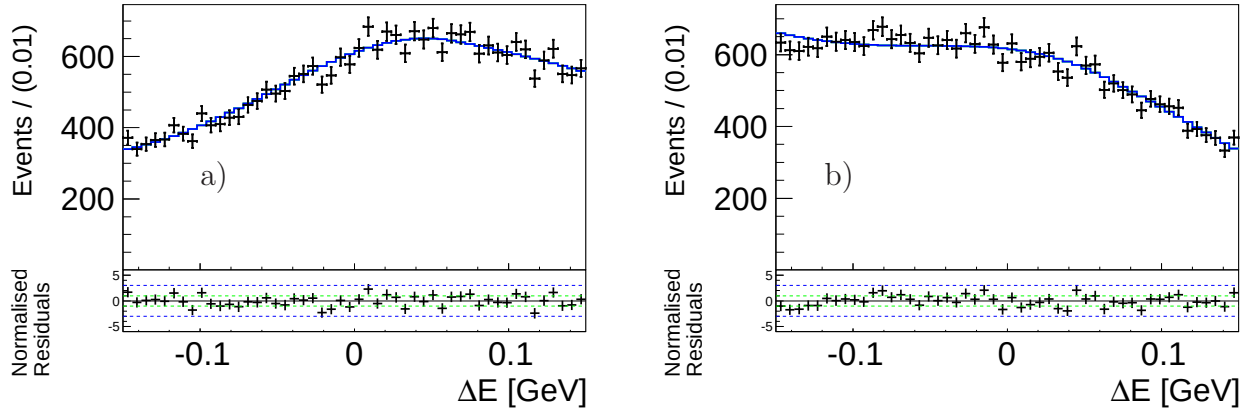

Figure 4.27: Fit projections onto ΔE for a) $\cos\theta^{+}_{\mathrm{H}} \times \cos\theta^{-}_{\mathrm{H}} < 0$ and b) else for signal MC events with only one correctly reconstructed $\pi^{\pm}$. The residuals are given beneath each distribution.

The ΔE distribution for transverse polarization is modeled with a first order Chebychev polynomial ,

$$\mathcal{P}^{\mathrm{TP}}_{1\pi^{\pm}}(\Delta E) \equiv \sum_{i=1}^{2} c^{\mathrm{TP}}_{\Delta E,i}C_i(\Delta E). \tag{4.40}$$

M_{bc} is described by the sum of a dbG and an Argus function 4.41,

$$\mathcal{P}^{\mathrm{LP(TP)}}_{1\pi^{\pm}}(M_{\mathrm{bc}}) \equiv f_{M_{\mathrm{bc}}}dbG(M_{\mathrm{bc}}) + (1-f_{M_{\mathrm{bc}}})Ar(M_{\mathrm{bc}}). \tag{4.41}$$

The distributions of the dipion masses and helicity angles depend on the charge of the correctly reconstructed $\pi^{\pm}$, see Fig 4.28. For longitudinal polarization, the $m_{\pi^{\pm}\pi^0}$ distribution including the correctly reconstructed $\pi^{\pm}$, denoted by subscript $c\pi$, is described by the sum of a Breit-Wigner function and a second order Chebychev polynomial,

$$\mathcal{P}^{c\pi}(m_{\pi^{\pm}\pi^0}) \equiv (1-f_{m_{\pi^{\pm}\pi^0}})BW(m_{\pi^{\pm}\pi^0},m_0,\Gamma_0) + f_{m_{\pi^{\pm}\pi^0}}c_{m_{\pi^{\pm}\pi^0},2}C_2(m_{\pi^{\pm}\pi^0}), \tag{4.42}$$

while the $m_{\pi^\pm\pi^0}$ distribution with the fake track from $B_{\rm tag}$, denoted by subscript $n\pi$, is modeled by the sum of Chebychev polynomials up to the fifth order;

$$\mathcal{P}^{n\pi}(m_{\pi^\pm\pi^0}) \equiv \sum_{i=1}^{5} c_{m_{\pi^\pm\pi^0},i} C_i(m_{\pi^\pm\pi^0}). \tag{4.43}$$

The helicity PDFs are taken to be two-dimensional histograms, again depending on the charge of the correctly reconstructed $\pi^\pm$.

$$\mathcal{P}^{\pm}(\cos\theta_{\rm H}^+, \cos\theta_{\rm H}^-) \equiv H^{(\pm)}(\cos\theta_{\rm H}^+, \cos\theta_{\rm H}^-). \tag{4.44}$$

The PDF of the $m_{\pi^+\pi^0}$-$m_{\pi^-\pi^0}$-$\cos\theta_{\rm H}^+$-$\cos\theta_{\rm H}^-$ distribution is then given by

$$\begin{aligned}
&\mathcal{P}^{\rm LP}_{1\pi^\pm}(m_{\pi^+\pi^0}, m_{\pi^-\pi^0}, \cos\theta_{\rm H}^+, \cos\theta_{\rm H}^-) \equiv \\
&f_+ \mathcal{P}^{c\pi}(m_{\pi^+\pi^0}) \mathcal{P}^{n\pi}(m_{\pi^-\pi^0}) \mathcal{P}^{+}(\cos\theta_{\rm H}^+, \cos\theta_{\rm H}^-) + \\
&(1-f_+) \mathcal{P}^{n\pi}(m_{\pi^+\pi^0}) \mathcal{P}^{c\pi}(m_{\pi^-\pi^0}) \mathcal{P}^{-}(\cos\theta_{\rm H}^+, \cos\theta_{\rm H}^-)
\end{aligned}$$

where the fraction of events with a correctly reconstructed π^+, $f_+ = 0.502 \pm 0.003$ is made common among the detector configurations SVD1 and SVD2. We ignore such a correlation for transverse polarization, since f_L has been measured to be close to one [75, 78]. The transverse polarized ρ masses and helicity angle distributions are modeled by the product of two two-dimensional histograms;

$$\mathcal{P}^{\rm TP}_{1\pi^\pm}(m_{\pi^+\pi^0}, m_{\pi^-\pi^0}, \cos\theta_{\rm H}^+, \cos\theta_{\rm H}^-) \equiv H(m_{\pi^+\pi^0}, m_{\pi^-\pi^0}) \times H(\cos\theta_{\rm H}^+, \cos\theta_{\rm H}^-). \tag{4.45}$$

The PDF for $\mathcal{F}_{B\bar{B}/q\bar{q}}$ is similar to the one used for the transverse polarized truth model (see Eq. (4.15)),

$$\mathcal{P}^{\rm LP(TP)}_{1\pi^\pm,{\rm k}}(\mathcal{F}_{B\bar{B}/q\bar{q}}) \equiv tbG^k_{\rm sig}(\mathcal{F}_{B\bar{B}/q\bar{q}}). \tag{4.46}$$

Even with only one correctly reconstructed track it is possible to use the Δt distribution to obtain CP violation related information. The Δt PDF is similar to one used for the truth model (see Eq. (4.19)) now with an effective lifetime, being somewhat smaller because of the contamination from the tag-side track ($B_{\rm tag}$). The effective B^0 lifetimes obtained from a fit to MC events are listed in Table 4.7.

lifetime [ps]	$\tau_{\rm eff}$ (SVD1)	$\tau_{\rm eff}$ (SVD2)
$B^0 \to \rho^+\rho^-\vert_{\rm LP}$	1.084 ± 0.008	1.038 ± 0.006
$B^0 \to \rho^+\rho^-\vert_{\rm TP}$	0.947 ± 0.026	0.978 ± 0.022

Table 4.7: The effective B^0 lifetimes obtained from a fit to the $1\pi^\pm$ signal MC distributions.

The full PDF for the longitudinal polarized $1\pi^\pm$ model is given by

$$\begin{aligned}
&\mathcal{P}^{\rm LP}_{1\pi^\pm}(\Delta E, M_{\rm bc}, m_{\pi^+\pi^0}, m_{\pi^-\pi^0}, \cos\theta_{\rm H}^+, \cos\theta_{\rm H}^-, \mathcal{F}_{B\bar{B}/q\bar{q}}, \Delta t, q) = \\
&\mathcal{P}^{\rm LP}_{1\pi^\pm}(\Delta E | \cos\theta_{\rm H}^+, \cos\theta_{\rm H}^-) \times \mathcal{P}^{\rm LP}_{1\pi^\pm}(M_{\rm bc}) \times \mathcal{P}^{\rm LP}_{1\pi^\pm,k}(\mathcal{F}_{B\bar{B}/q\bar{q}}) \times \\
&\mathcal{P}^{\rm LP}_{1\pi^\pm}(m_{\pi^+\pi^0}, m_{\pi^-\pi^0}, \cos\theta_{\rm H}^+, \cos\theta_{\rm H}^-) \times \mathcal{P}^{\rm LP}_{1\pi^\pm}(\Delta t, q),
\end{aligned} \tag{4.47}$$

and for the transverse polarized one by

$$\begin{aligned}
&\mathcal{P}^{\rm TP}_{1\pi^\pm}(\Delta E, M_{\rm bc}, m_{\pi^+\pi^0}, m_{\pi^-\pi^0}, \cos\theta_{\rm H}^+, \cos\theta_{\rm H}^-, \mathcal{F}_{B\bar{B}/q\bar{q}}, \Delta t, q) = \\
&\mathcal{P}^{\rm TP}_{1\pi^\pm}(\Delta E) \times \mathcal{P}^{\rm TP}_{1\pi^\pm}(M_{\rm bc}) \times \mathcal{P}^{\rm TP}_{1\pi^\pm,k}(\mathcal{F}_{B\bar{B}/q\bar{q}}) \times \\
&\mathcal{P}^{\rm TP}_{1\pi^\pm}(m_{\pi^+\pi^0}, m_{\pi^-\pi^0}, \cos\theta_{\rm H}^+, \cos\theta_{\rm H}^-) \times \mathcal{P}^{\rm TP}_{1\pi^\pm}(\Delta t, q).
\end{aligned} \tag{4.48}$$

0	ΔE	M_{bc}	$m^1_{\pi^+\pi^-}$	$m^2_{\pi^+\pi^-}$	$\mathcal{F}_{B\bar{B}/q\bar{q}}$	$\cos\theta^1_{\rm H}$	$\cos\theta^2_{\rm H}$	Δt
ΔE	1	0.01	0.01	0.02	0.04	-0.09	-0.09	-0.00
M_{bc}		1	-0.02	-0.02	0.03	0.02	0.03	-0.01
$m^1_{\pi^+\pi^-}$			1	-0.01	-0.00	0.04	-0.08	0.00
$m^2_{\pi^+\pi^-}$				1	-0.01	-0.08	0.06	0.00
$\mathcal{F}_{B\bar{B}/q\bar{q}}$					1	0.04	0.03	0.01
$\cos\theta^1_{\rm H}$						1	-0.39	0.01
$\cos\theta^2_{\rm H}$							1	0.01
Δt								1

Table 4.8: Correlation matrix for the $1\pi^{\pm}$ model (LP, SVD2).

0	ΔE	M_{bc}	$m^1_{\pi^+\pi^-}$	$m^2_{\pi^+\pi^-}$	$\mathcal{F}_{B\bar{B}/q\bar{q}}$	$\cos\theta^1_{\rm H}$	$\cos\theta^2_{\rm H}$	Δt
ΔE	1	-0.02	0.04	-0.01	0.02	-0.04	-0.04	-0.01
M_{bc}		1	-0.06	-0.04	0.03	0.02	-0.01	-0.01
$m^1_{\pi^+\pi^-}$			1	-0.02	-0.02	0.03	-0.03	-0.00
$m^2_{\pi^+\pi^-}$				1	-0.00	-0.03	0.04	-0.01
$\mathcal{F}_{B\bar{B}/q\bar{q}}$					1	0.02	0.06	-0.01
$\cos\theta^1_{\rm H}$						1	-0.38	0.02
$\cos\theta^2_{\rm H}$							1	-0.00
Δt								1

Table 4.9: Correlation matrix for the $1\pi^{\pm}$ model (TP, SVD2).

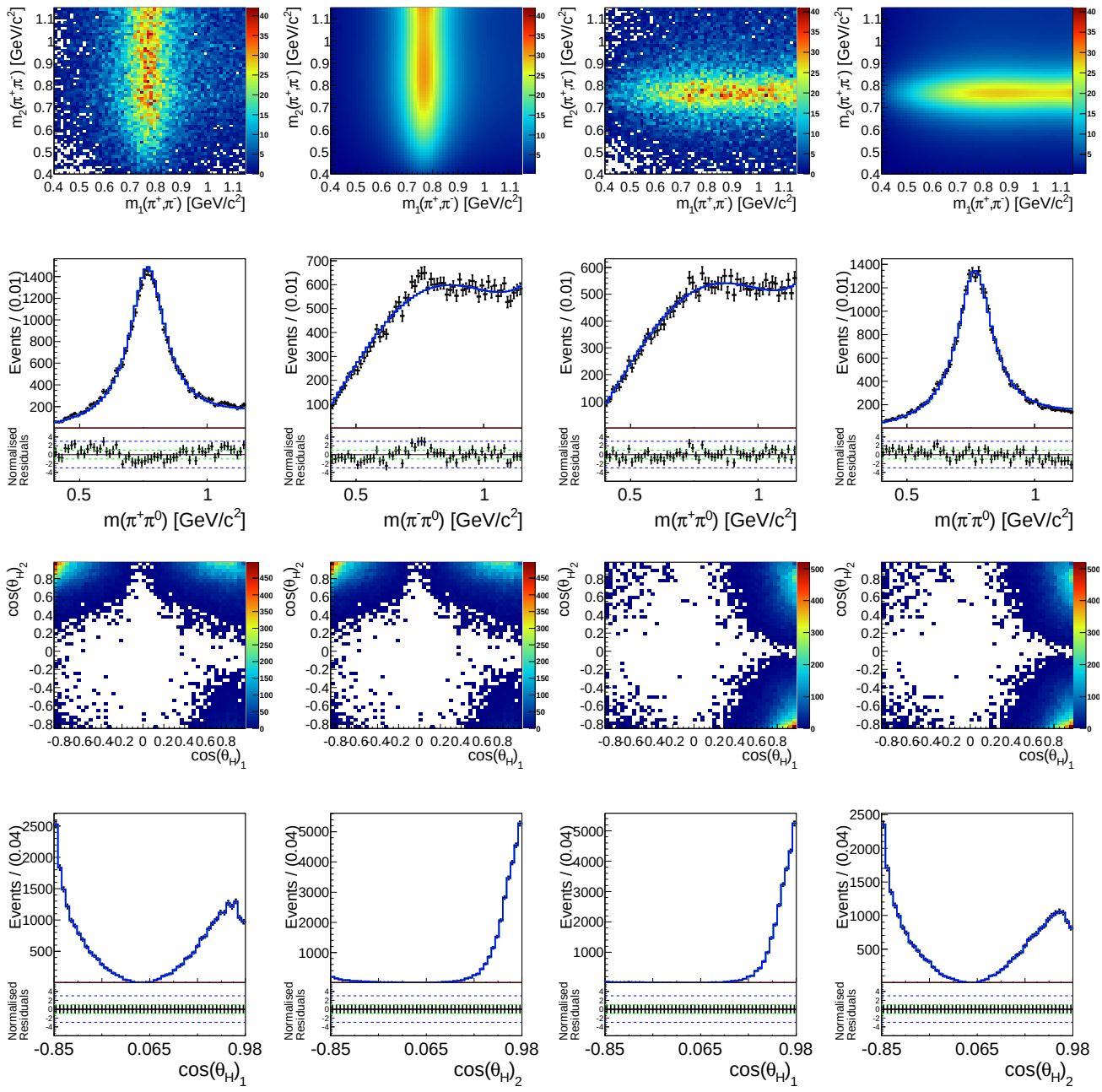

Figure 4.28: Fit projections onto the dipion masses and helicity angles for signal MC events with only one correctly reconstructed track (π^+ left and π^- right). For each set of for plots, the top row shows the 2D projection of the data (left) and the PDF (right) and the bottom row shows projection onto each axis, where the black points show simulated MC events and the solid line shows the fit result. The residuals are given beneath each distribution.

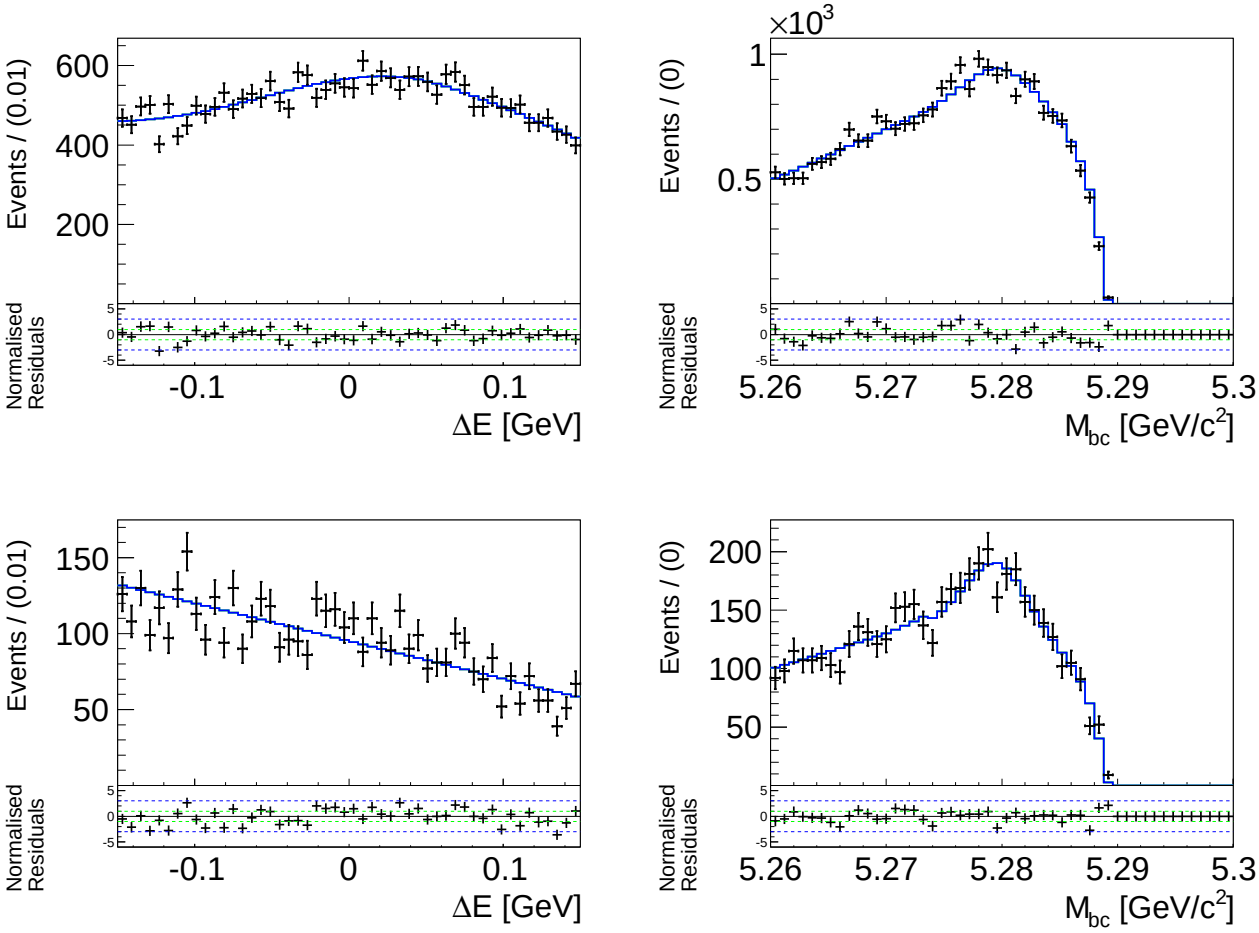

Figure 4.29: Full projections onto ΔE and $M_{\rm bc}$ of a fit to signal MC events with only one correctly reconstructed $\pi^{\mp}$. LP (top row) and TP. The black points show simulated MC events and the solid line shows the fit result. The residuals are given beneath each distribution.

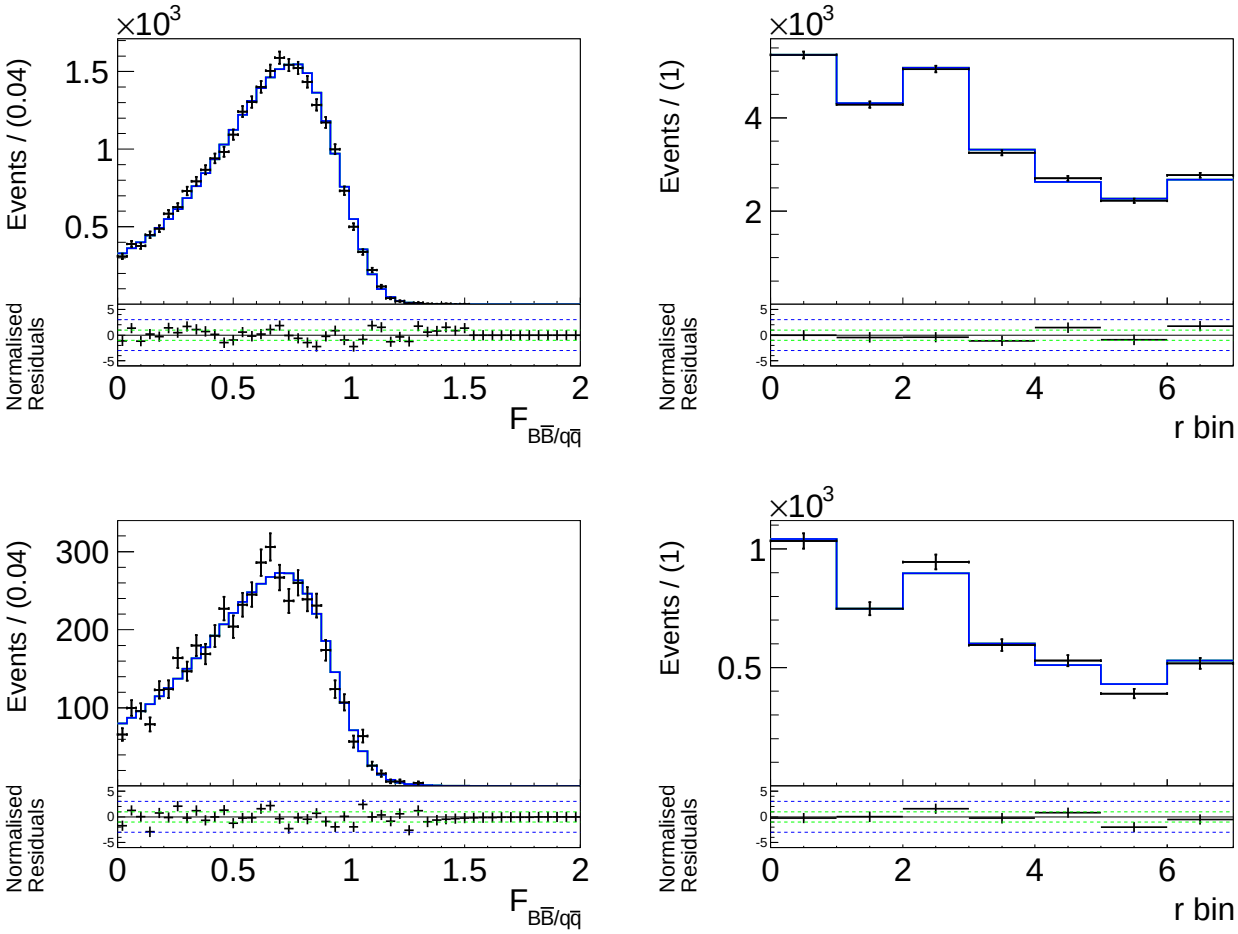

Figure 4.30: Full projections onto $\mathcal{F}_{B\bar{B}/q\bar{q}}$ and the r-bin fractions of a fit to signal MC events (LP) with only one correctly reconstructed $\pi^{\mp}$. LP (top row) and TP. The black points show simulated MC events and the solid line shows the fit result. The residuals are given beneath each distribution.

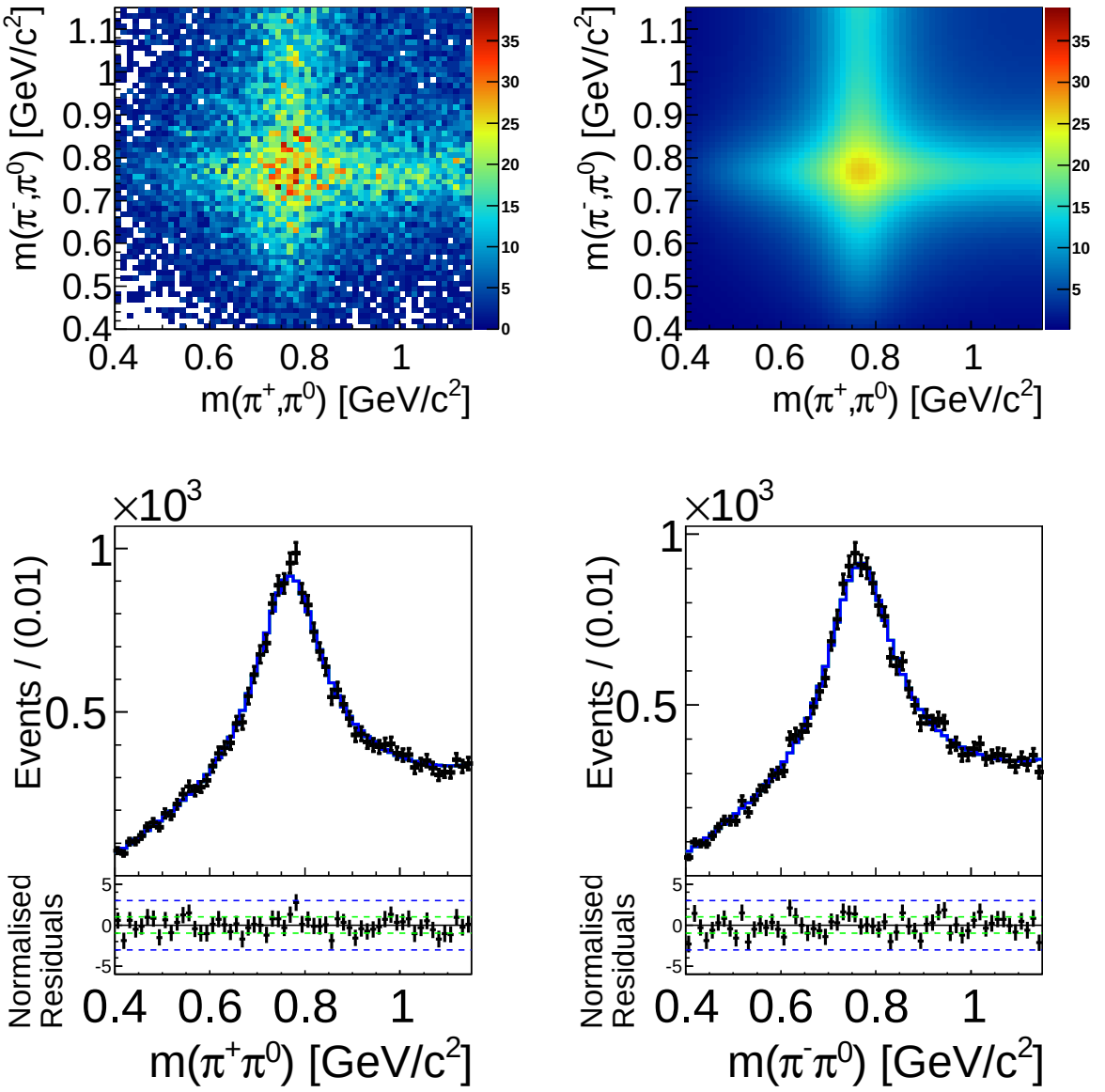

Figure 4.31: Fit projections onto $m_{\pi^{\pm}\pi^0}$ signal MC events with only one correctly reconstructed $\pi^{\mp}$ (LP). The top row shows the 2D projection of the data (left) and the PDF (right) and the bottom row shows projection onto each axis, where the black points show simulated MC events and the solid line shows the fit result. The residuals are given beneath each distribution.

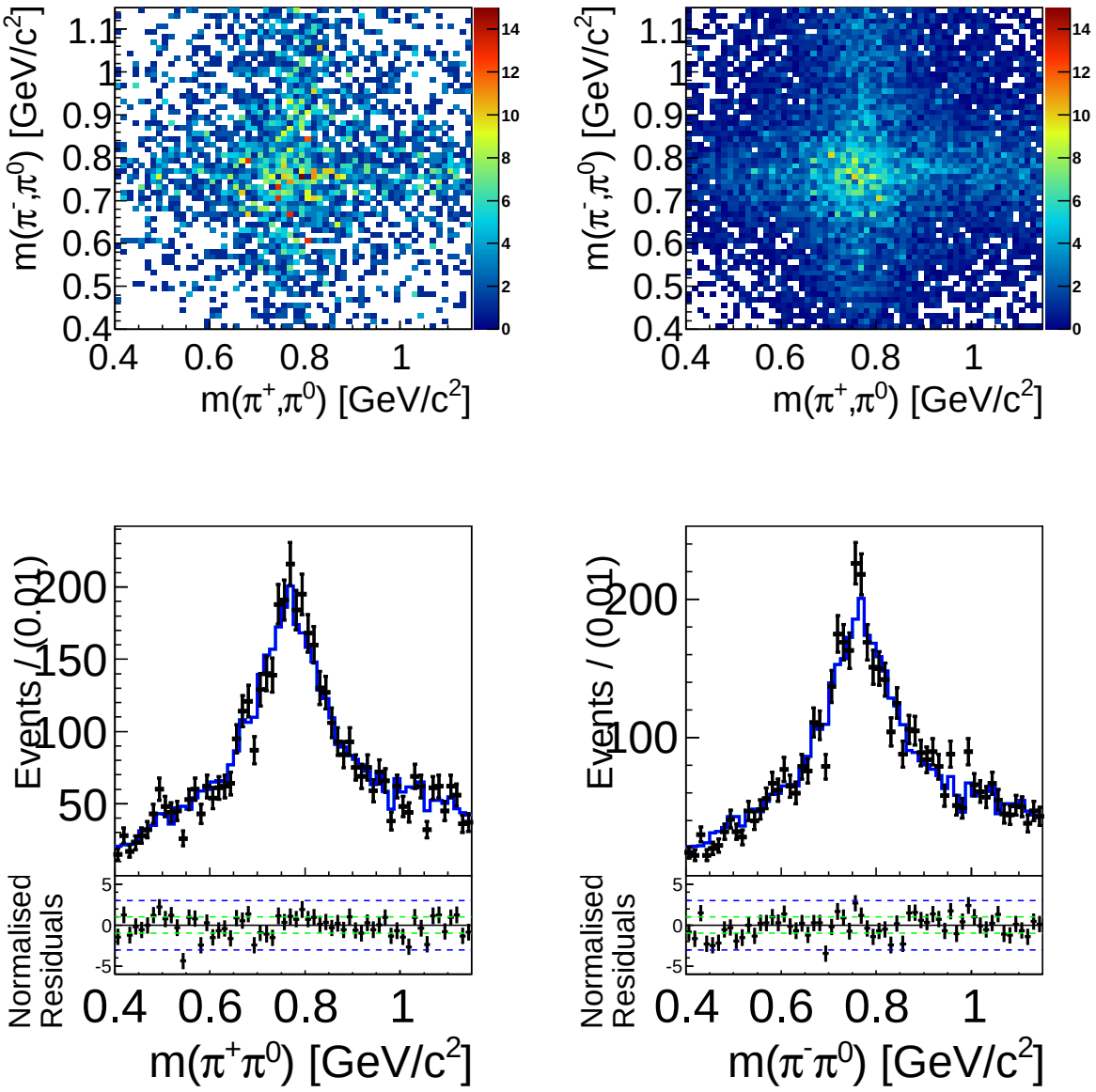

Figure 4.32: Fit projections onto $m_{\pi^{\pm}\pi^0}$ signal MC events with only one correctly reconstructed $\pi^{\mp}$ (TP). The top row shows the 2D projection of the data (left) and the PDF (right) and the bottom row shows projection onto each axis, where the black points show simulated MC events and the solid line shows the fit result. The residuals are given beneath each distribution.

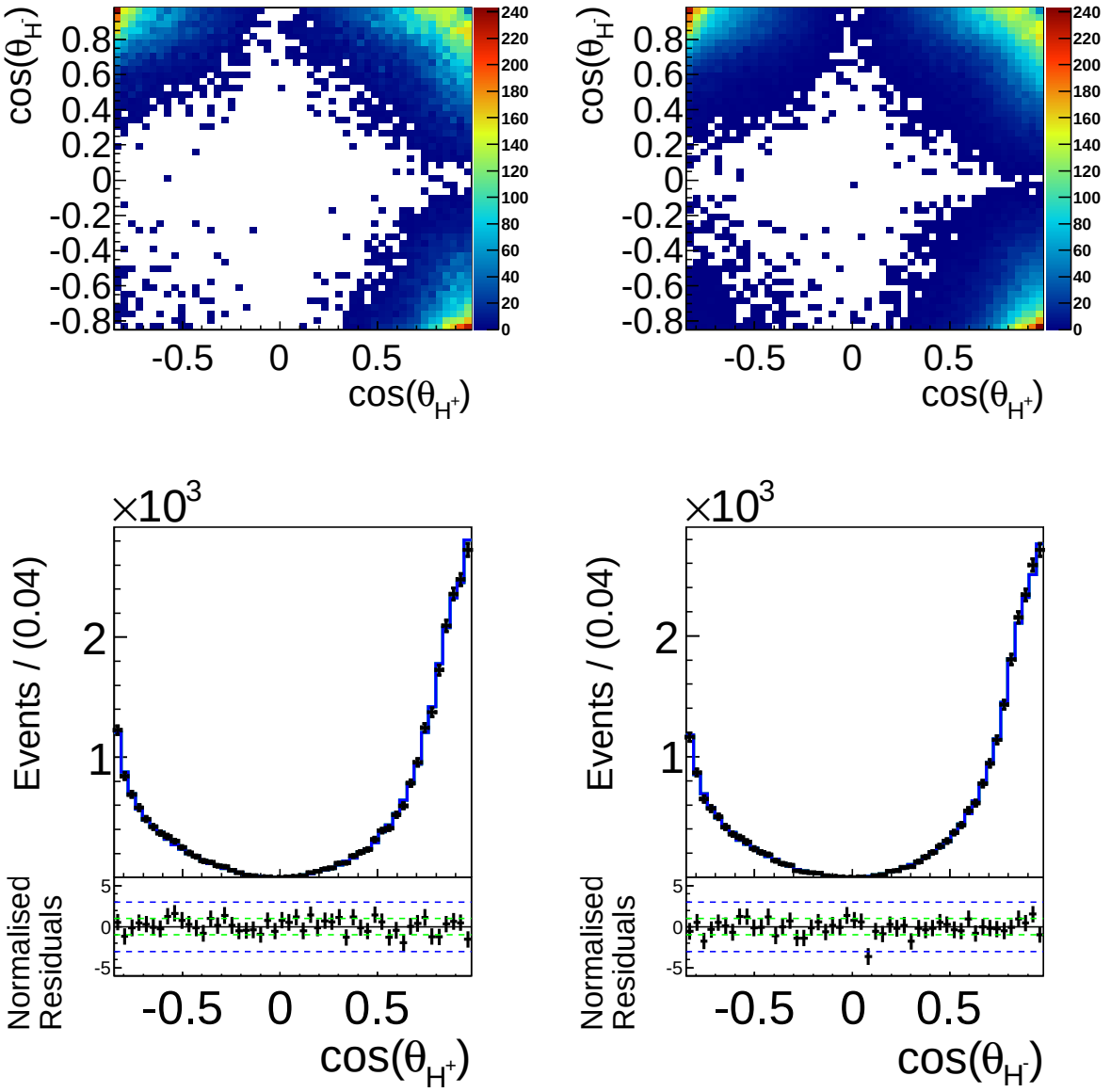

Figure 4.33: Fit projections onto $\cos\theta_{\mathrm{H}}$ signal MC events with only one correctly reconstructed $\pi^{\mp}$ (LP). The top row shows the 2D projection of the data (left) and the PDF (right) and the bottom row shows projection onto each axis, where the black points show simulated MC events and the solid line shows the fit result. The residuals are given beneath each distribution.

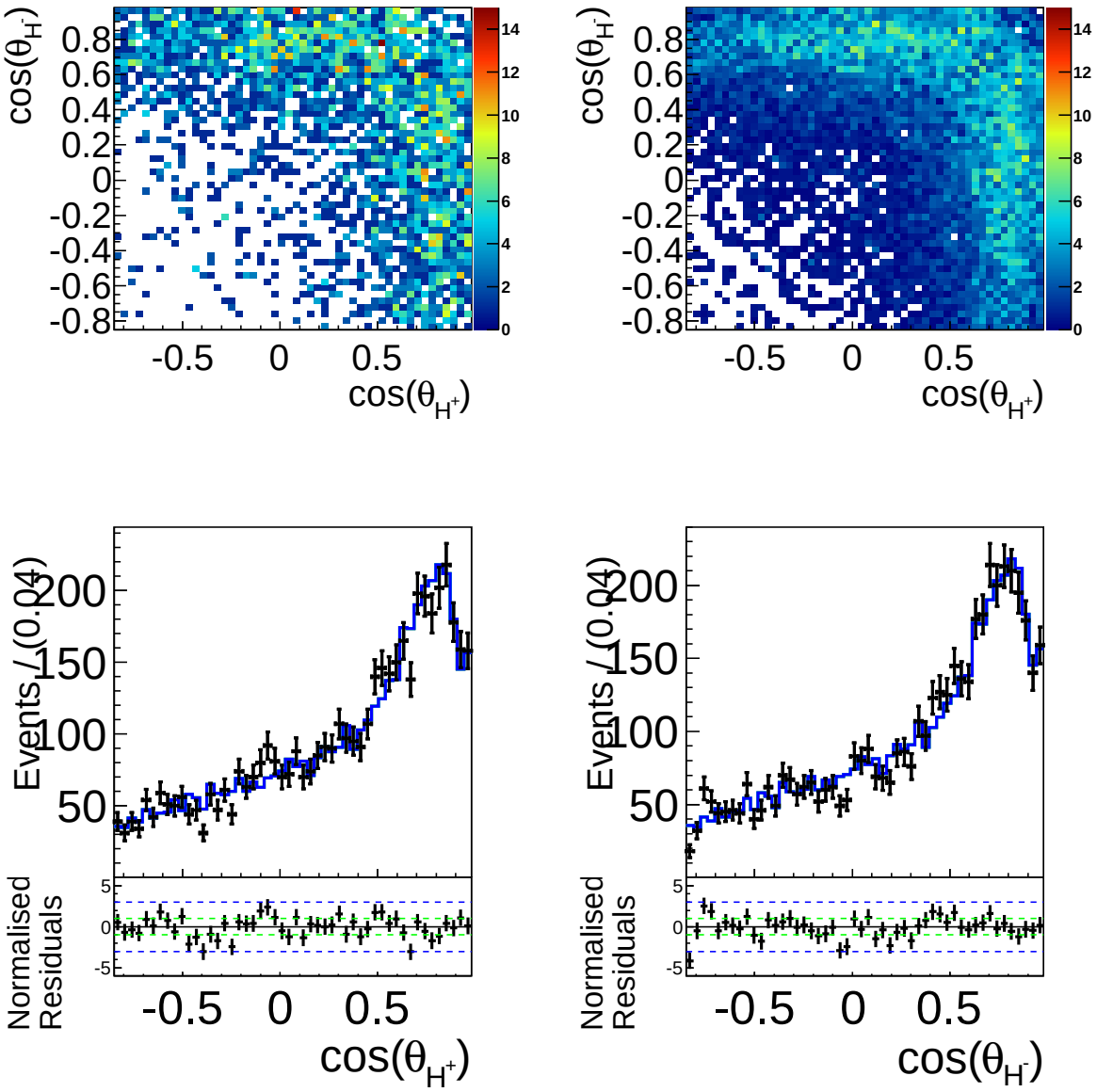

Figure 4.34: Fit projections onto $\cos\theta_{\mathrm{H}}$ signal MC events with only one correctly reconstructed $\pi^{\mp}$ (TP). The top row shows the 2D projection of the data (left) and the PDF (right) and the bottom row shows projection onto each axis, where the black points show simulated MC events and the solid line shows the fit result. The residuals are given beneath each distribution.

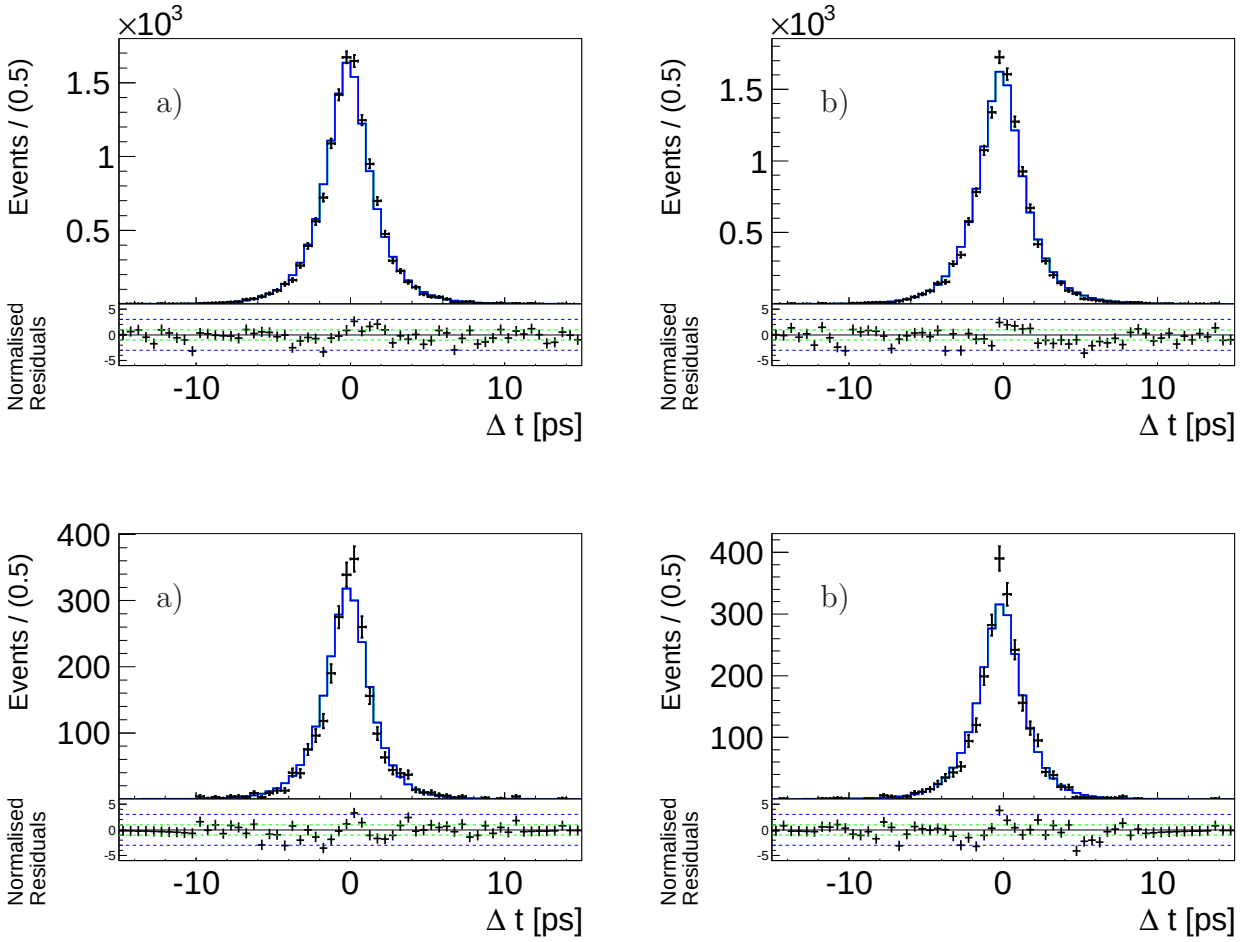

Figure 4.35: Fit projections onto Δt for signal MC events with only one correctly reconstructed $\pi^{\mp}$ (LP top, TP bottom). a) $B_{\rm tag} = B$ and b) and $B_{\rm tag} = \bar{B}$. LP (top row) and TP. The black points show simulated MC events and the solid line shows the fit result. The residuals are given beneath each distribution.

4.3.4 Self Crossfeed

Signal events without correctly reconstructed charged pions are referred to as self crossfeed (SC). Because the transverse polarization's SC fraction is negligible, see Table 3.3, we include those events in the model used for transverse polarization when one $\pi^{\pm}$ is correctly reconstructed.
The ΔE distribution of longitudinal polarized SC events is modeled with the sum of a dbG and a first order Chebychev polynomial

$$\mathcal{P}(\Delta E) \equiv f_{\Delta E} dbG(\Delta E) + (1 - f_{\Delta E}) c_{\Delta E,1} C_1(\Delta E). \tag{4.49}$$

$M_{\rm bc}$ is described by the sum of a dbG and an Argus function 4.50,

$$\mathcal{P}(M_{\rm bc}) \equiv f_{M_{\rm bc}} dbG(M_{\rm bc}) + (1 - f_{M_{\rm bc}}) Ar(M_{\rm bc}, c_{M_{\rm bc}}). \tag{4.50}$$

Each $m_{\pi^{\pm}\pi^0}$ distribution is modeled with the sum of a Breit-Wigner function, a second and a third order Chebychev polynomial.

$$\begin{aligned}\mathcal{P}(m_{\pi^{\pm}\pi^0}) \equiv \quad & (1 - f_{m_{\pi^{\pm}\pi^0}}) BW(m_{\pi^{\pm}\pi^0}, m_{0,m_{\pi^{\pm}\pi^0}}, \Gamma_{0,m_{\pi^{\pm}\pi^0}}) + \\ & f_{m_{\pi^{\pm}\pi^0}} (c_{m_{\pi^{\pm}\pi^0},2} C_2(m_{\pi^{\pm}\pi^0}) + c_{m_{\pi^{\pm}\pi^0},3} C_3(m_{\pi^{\pm}\pi^0})).\end{aligned}$$

The PDF of the $m_{\pi^+\pi^0}$-$m_{\pi^-\pi^0}$ distribution is the product

$$\mathcal{P}(m_{\pi^+\pi^0}, m_{\pi^-\pi^0}) \equiv \mathcal{P}(m_{\pi^+\pi^0}) \mathcal{P}(m_{\pi^-\pi^0}), \tag{4.51}$$

and the PDF of the $\cos\theta_{\rm H}^+$-$\cos\theta_{\rm H}^-$ distribution is taken to be a histogram.

$$\mathcal{P}(\cos\theta_{\rm H}^+, \cos\theta_{\rm H}^-) \equiv H(\cos\theta_{\rm H}^+, \cos\theta_{\rm H}^-). \tag{4.52}$$

The Δt PDF is described by an exponential decay with an effective life-time $\tau_{\rm SC}$ convoluted with a the sum of two Gaussian (see Eq. (4.70)) in order to account for detector resolution;

$$\mathcal{P}_{SC}(\Delta t) \equiv \frac{e^{-|\Delta t|/\tau_{\rm SC}}}{2\tau_{\rm SC}} \otimes R_{q\bar{q}}(\Delta t). \tag{4.53}$$

The effective B^0 lifetimes as obtained from a fit to the MC distribution are listed in Table 4.10.

lifetime [ps]	$\tau_{\rm eff}^{\rm SVD1}$	$\tau_{\rm eff}^{\rm SVD2}$	
$B^0 \to \rho^+\rho^-\vert_{\rm LP}^{\rm SC}$	1.222 ± 0.039	1.114 ± 0.034	

Table 4.10: The effective B^0 lifetimes obtained from a fit to the mis-reconstructed signal MC distributions (LP).

The full PDF for the longitudinal polarized SC model is given by

$$\begin{aligned}\mathcal{P}_{SC}(\Delta E, M_{\rm bc}, m_{\pi^+\pi^0}, m_{\pi^-\pi^0}, \cos\theta_{\rm H}^+, \cos\theta_{\rm H}^-, \mathcal{F}_{B\bar{B}/q\bar{q}}, \Delta t, q) = \\ \mathcal{P}_{SC}(\Delta E) \times \mathcal{P}_{SC}(M_{\rm bc}) \times \mathcal{P}_{SC}(m_{\pi^+\pi^0}, m_{\pi^-\pi^0}) \\ \times \mathcal{P}_{SC}(\cos\theta_{\rm H}^+, \cos\theta_{\rm H}^-) \times \mathcal{P}_{SC,k}(\mathcal{F}_{B\bar{B}/q\bar{q}}) \times \mathcal{P}_{SC}^{\rm LP(TP}(\Delta t, q).\end{aligned} \tag{4.54}$$

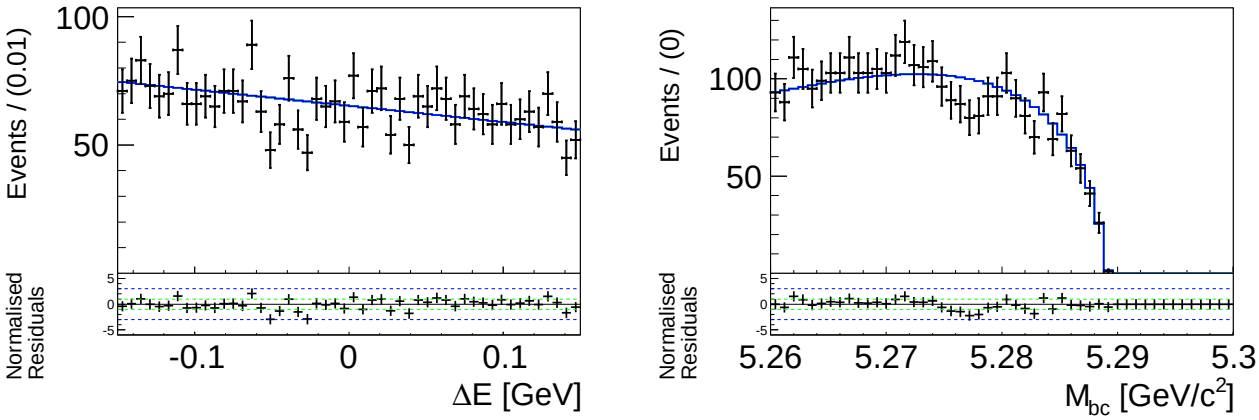

Figure 4.36: Fit projections onto ΔE and $M_{\rm bc}$ of a fit to mis-reconstructed signal MC events (LP). The black points show simulated MC events and the solid line shows the fit result. The residuals are given beneath each distribution.

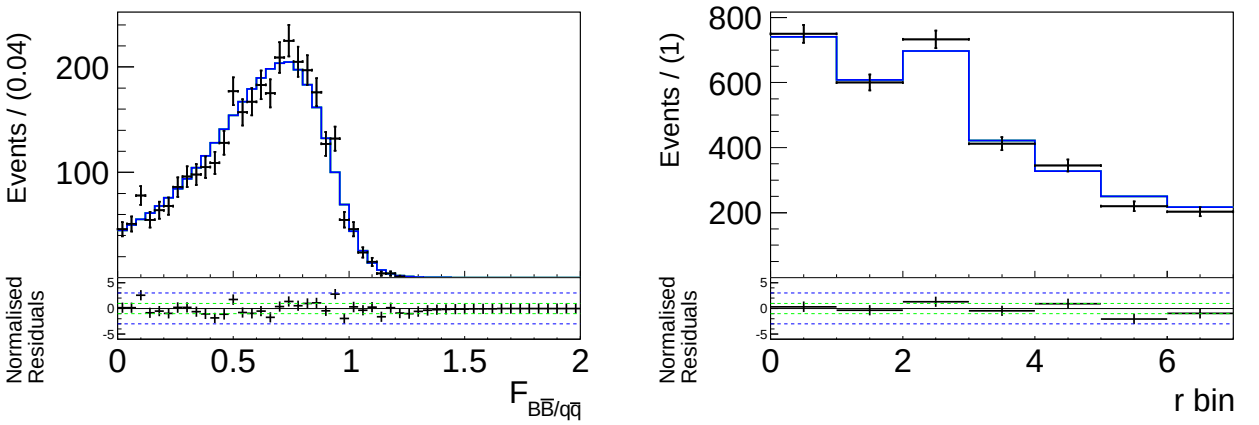

Figure 4.37: Fit projections onto $\mathcal{F}_{B\bar{B}/q\bar{q}}$ and the r-bin fractions of a fit to mis-reconstructed signal MC events (LP). The black points show simulated MC events and the solid line shows the fit result. The residuals are given beneath each distribution.

0	ΔE	M_{bc}	$m^1_{\pi^+\pi^-}$	$m^2_{\pi^+\pi^-}$	$\mathcal{F}_{B\bar{B}/q\bar{q}}$	$\cos\theta^1_{\rm H}$	$\cos\theta^2_{\rm H}$	Δt
ΔE	1	-0.01	0.00	0.03	0.06	-0.05	-0.04	-0.02
M_{bc}		1	0.00	-0.02	0.03	0.05	0.05	0.01
$m^1_{\pi^+\pi^-}$			1	0.05	0.01	0.01	-0.00	-0.01
$m^2_{\pi^+\pi^-}$				1	-0.00	0.01	-0.01	0.01
$\mathcal{F}_{B\bar{B}/q\bar{q}}$					1	0.09	0.10	-0.00
$\cos\theta^1_{\rm H}$						1	-0.01	0.00
$\cos\theta^2_{\rm H}$							1	-0.01
Δt								1

Table 4.11: Correlation matrix for the SC model (LP, SVD2).

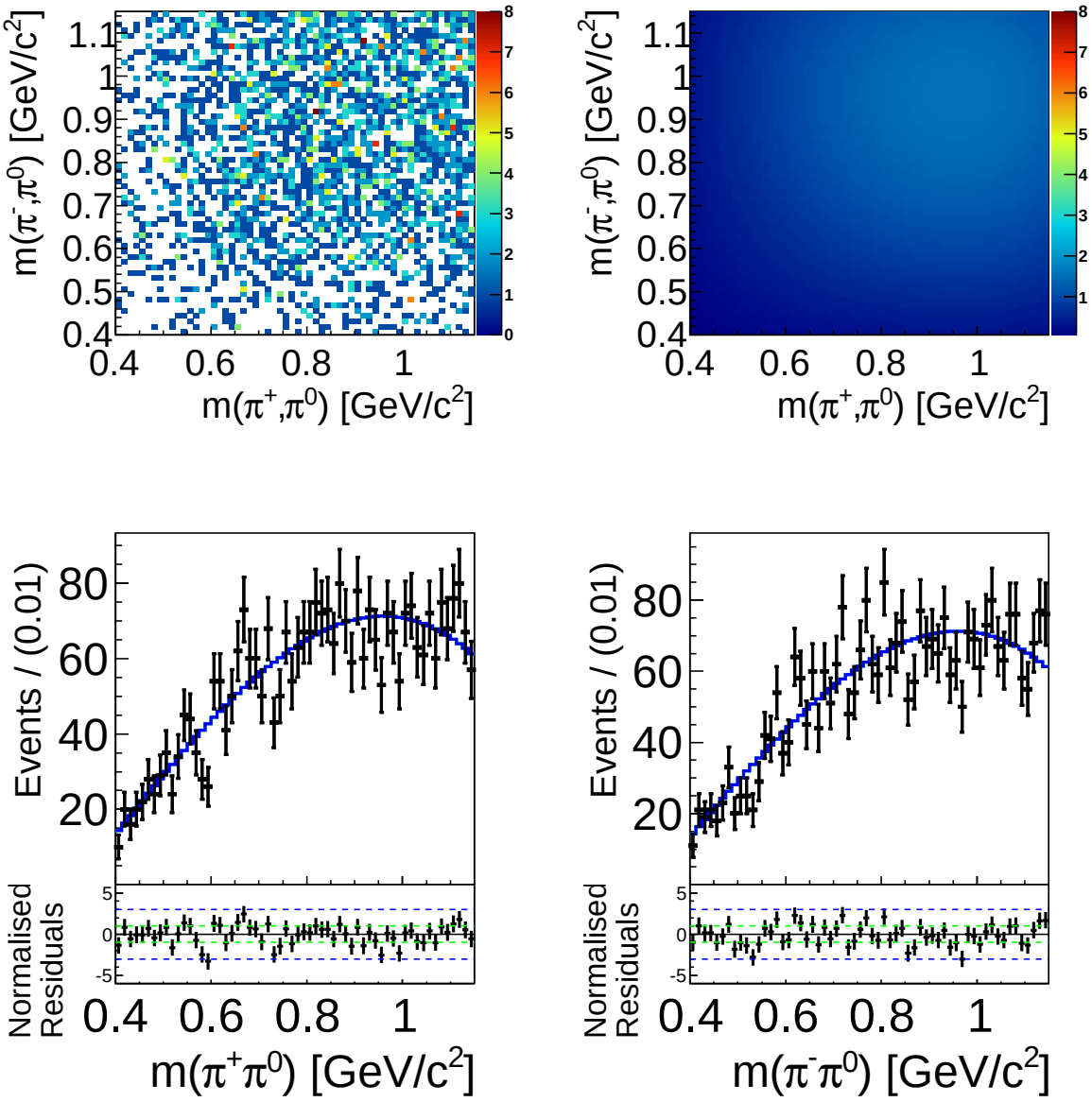

Figure 4.38: Fit projections onto $m_{\pi^{\pm}\pi^0}$ of a fit to mis-reconstructed signal MC events (LP). The top row shows the 2D projection of the data (left) and the PDF (right) and the bottom row shows projection onto each axis, where the black points show simulated MC events and the solid line shows the fit result. The residuals are given beneath each distribution.

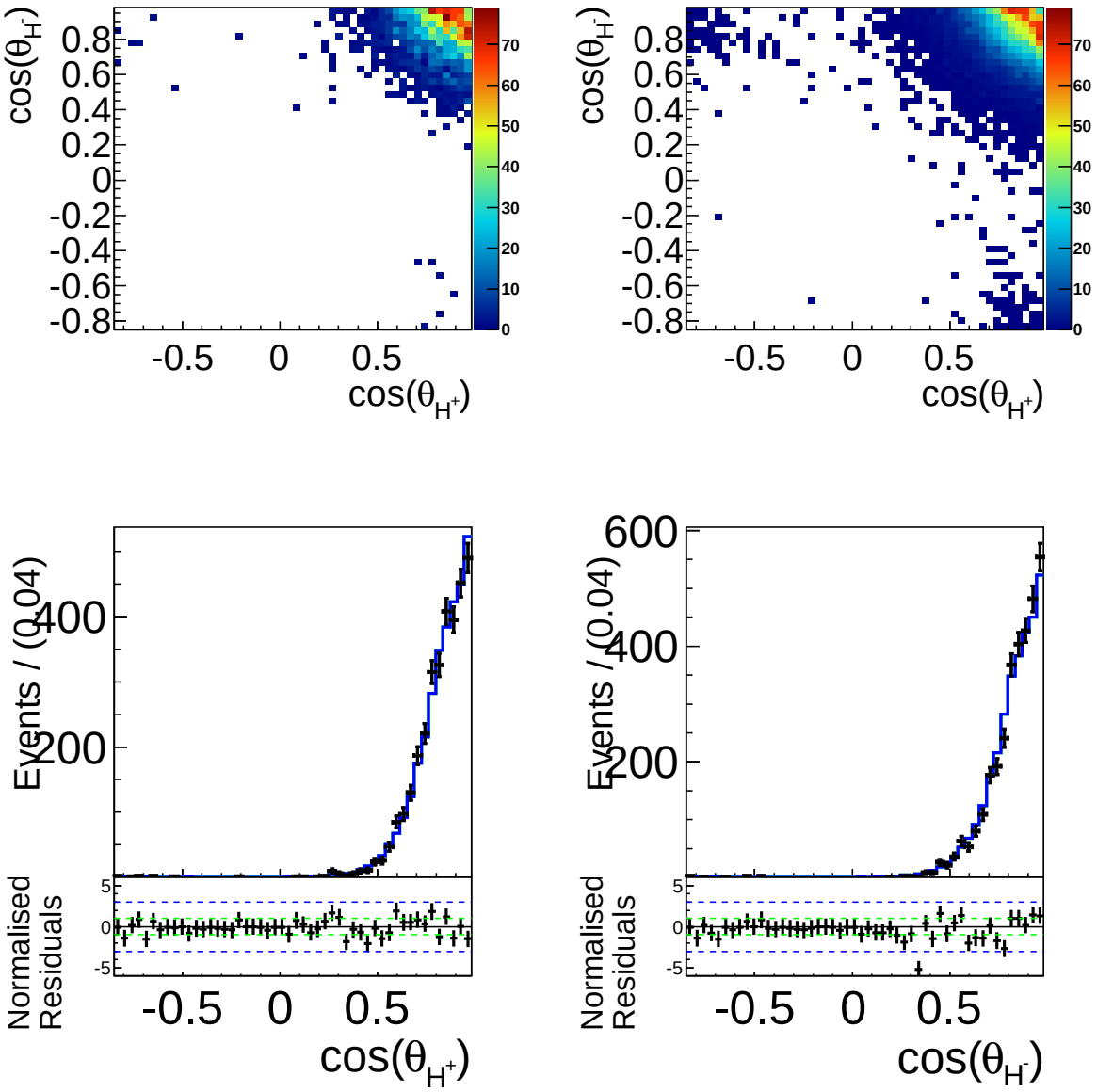

Figure 4.39: Fit projections onto $\cos\theta_{\mathrm{H}}^{+} - \cos\theta_{\mathrm{H}}^{-}$ of a fit to mis-reconstructed signal MC events (LP). The top row shows the 2D projection of the data (left) and the PDF (right) and the bottom row shows projection onto each axis, where the black points show simulated MC events and the solid line shows the fit result. The residuals are given beneath each distribution.

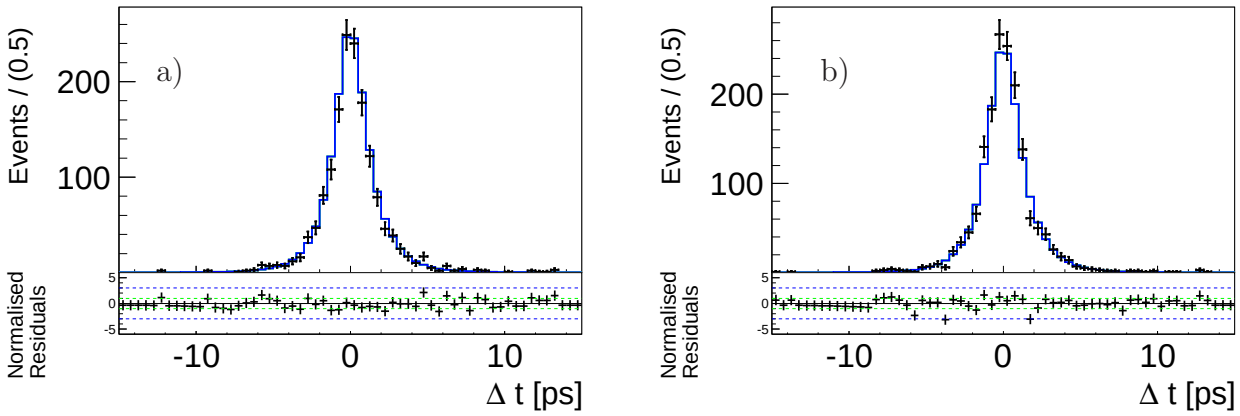

Figure 4.40: Fit projections onto Δt of a fit to mis-reconstructed signal MC events (LP). a) $B_{\text{tag}} = B$ and b) and $B_{\text{tag}} = \bar{B}$. The black points show simulated MC events and the solid line shows the fit result. The residuals are given beneath each distribution.

4.3.5 Full Signal Model

Details on how to incorporate the individual signal PDFs into the fit can be found in Section 4.6. The CP violation parameters of the signal model are made common among each polarization, except for the mis-reconstructed contribution. Projections of the fit result onto each distribution are shown in the following and the fit variables correlations from the entire signal MC sample are listed in Table 4.13.

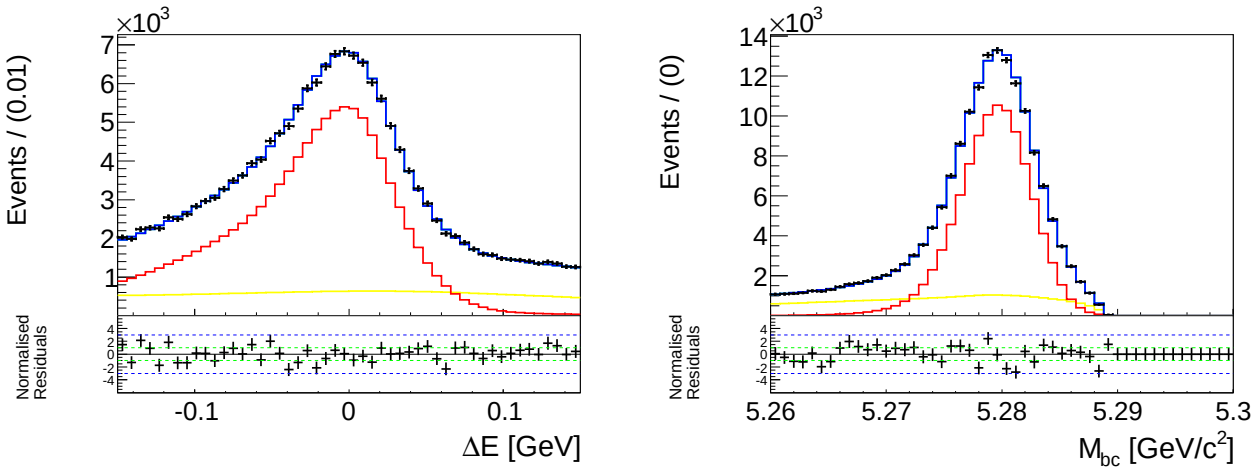

Figure 4.41: Full fit projections onto ΔE, M_{bc}, and $\mathcal{F}_{B\bar{B}/q\bar{q}}$of a fit to $B^0 \to \rho^+\rho^-$ MC events (LP). The black points show simulated MC events and the blue (solid) line shows the fit result. The "truth" and "1c$\pi^{\pm}$" contributions are shown in red and yellow, respectively. The residuals are given beneath each distribution.

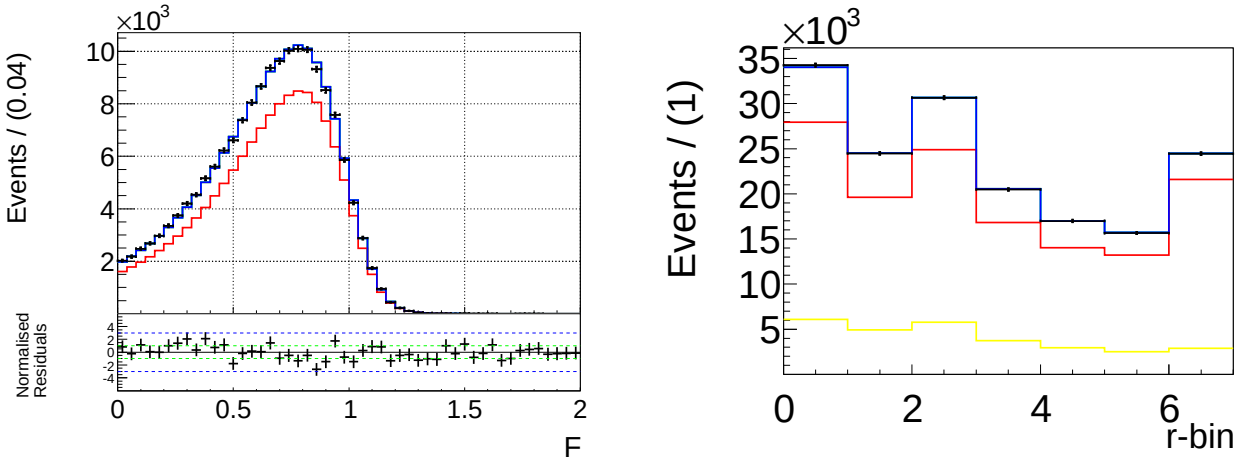

Figure 4.42: Full fit projections onto $\mathcal{F}_{B\bar{B}/q\bar{q}}$ and the r-bin fractions of a fit to $B^0 \to \rho^+\rho^-$ MC events (LP). The black points show simulated MC events and the blue (solid) line shows the fit result. The "truth" and "1c$\pi^{\pm}$" contributions are shown in red and yellow, respectively. The residuals are given beneath each distribution.

0	ΔE	M_{bc}	$m^1_{\pi^+\pi^-}$	$m^2_{\pi^+\pi^-}$	$\mathcal{F}_{B\bar{B}/q\bar{q}}$	$\cos\theta^1_{\rm H}$	$\cos\theta^2_{\rm H}$	Δt
ΔE	1	-0.08	0.06	0.06	0.01	-0.12	-0.11	0.00
M_{bc}		1	-0.05	-0.05	0.03	0.01	0.01	-0.01
$m^1_{\pi^+\pi^-}$			1	0.01	-0.04	-0.03	0.00	0.00
$m^2_{\pi^+\pi^-}$				1	-0.03	0.01	-0.03	0.00
$\mathcal{F}_{B\bar{B}/q\bar{q}}$					1	0.03	0.03	-0.00
$\cos\theta^1_{\rm H}$						1	-0.05	0.01
$\cos\theta^2_{\rm H}$							1	0.01
Δt								1

Table 4.12: Correlation matrix for the full signal model (LP, SVD1).

0	ΔE	M_{bc}	$m^1_{\pi^+\pi^-}$	$m^2_{\pi^+\pi^-}$	$\mathcal{F}_{B\bar{B}/q\bar{q}}$	$\cos\theta^1_{\rm H}$	$\cos\theta^2_{\rm H}$	Δt
ΔE	1	-0.06	0.06	0.06	0.00	-0.10	-0.10	0.00
M_{bc}		1	-0.05	-0.05	0.04	0.01	0.01	-0.01
$m^1_{\pi^+\pi^-}$			1	0.01	-0.03	-0.02	0.01	0.00
$m^2_{\pi^+\pi^-}$				1	-0.03	0.01	-0.03	0.00
$\mathcal{F}_{B\bar{B}/q\bar{q}}$					1	0.03	0.03	-0.00
$\cos\theta^1_{\rm H}$						1	-0.03	0.01
$\cos\theta^2_{\rm H}$							1	0.01
Δt								1

Table 4.13: Correlation matrix for the full signal model (LP, SVD2).

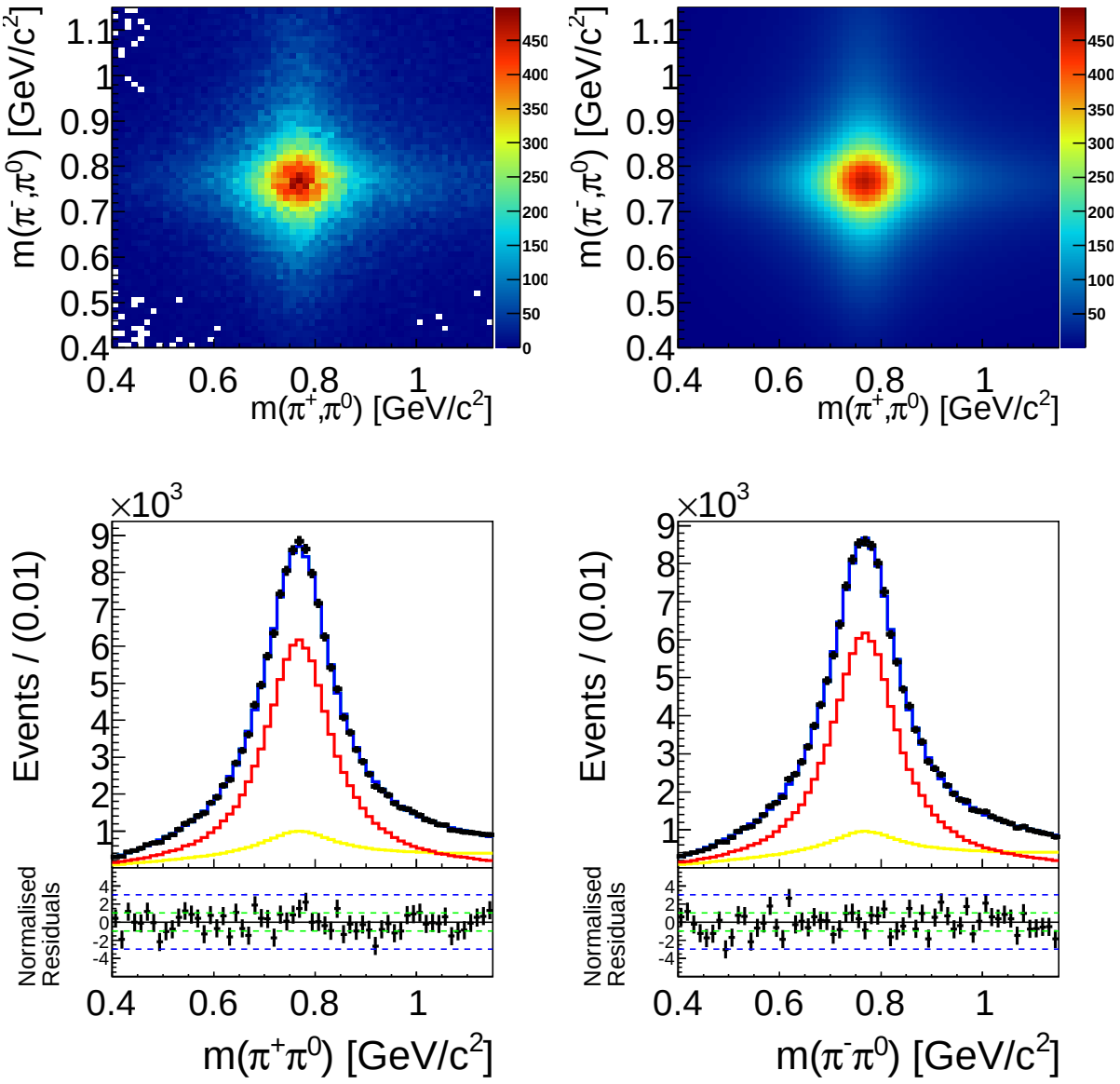

Figure 4.43: Full fit projections onto the dipion masses of a fit to $B^0 \to \rho^+\rho^-$ signal MC events (LP). The top row shows the 2D projection of the data (left) and the PDF (right) and the bottom row shows projection onto each axis, where the black points show simulated MC events and the blue (solid) line shows the fit result. The "truth" and "1c$\pi^{\pm}$" contributions are shown in red and yellow, respectively. The residuals are given beneath each distribution.

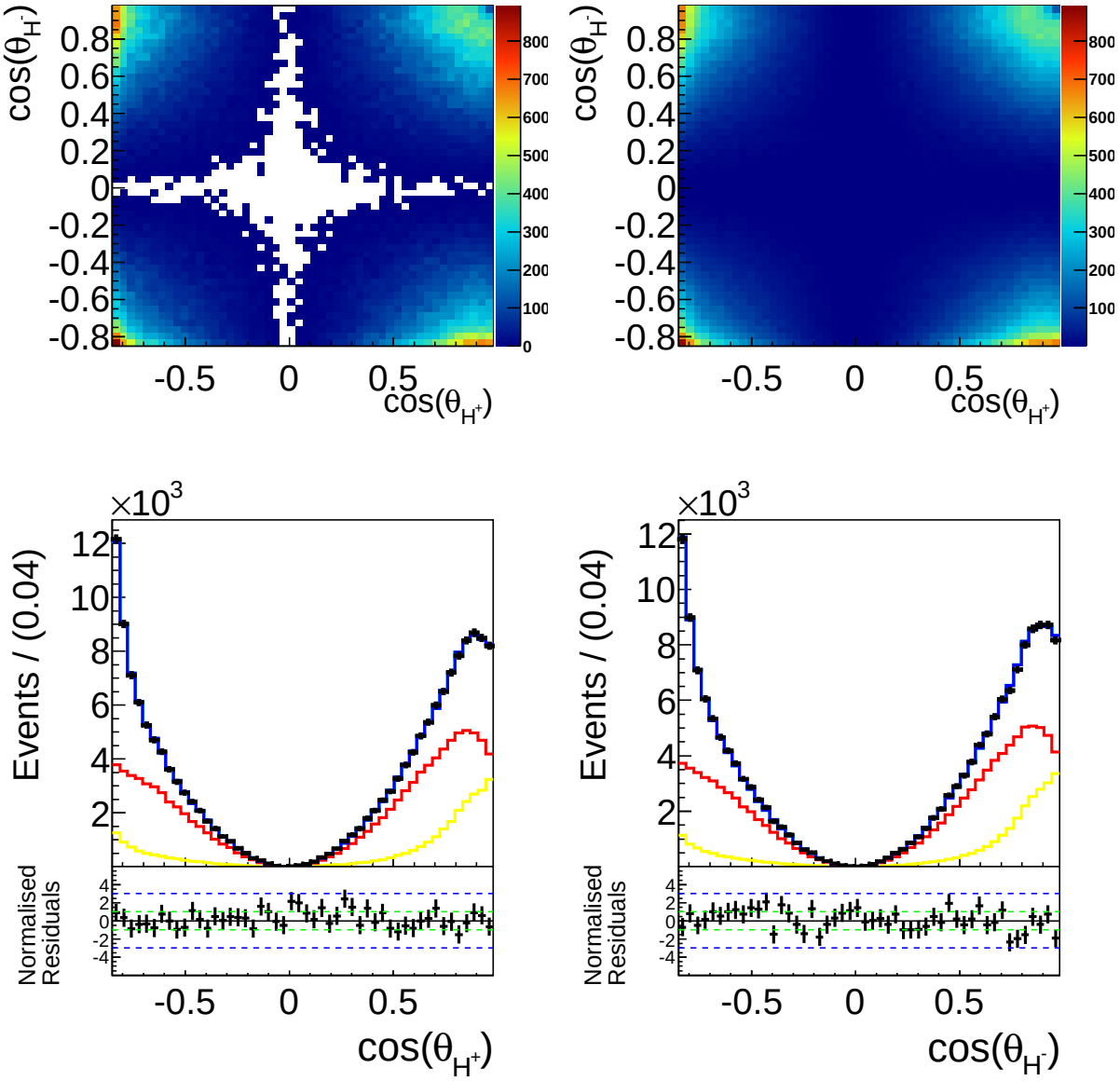

Figure 4.44: Full fit projections onto the helicity angles of a fit to $B^0 \to \rho^+\rho^-$ signal MC events (LP). The top row shows the 2D projection of the data (left) and the PDF (right) and the bottom row shows projection onto each axis, where the black points show simulated MC events and the blue (solid) line shows the fit result. The "truth" and "1c$\pi^{\pm}$" contributions are shown in red and yellow, respectively. The residuals are given beneath each distribution.

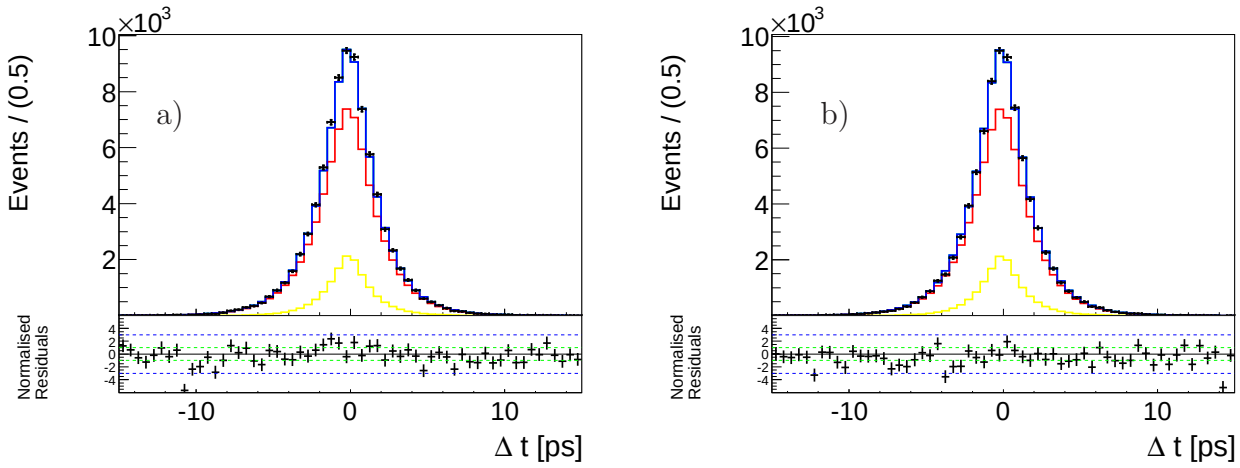

Figure 4.45: Full fit projections onto Δt of a fit to $B^0 \to \rho^+\rho^-$ signal MC events (LP). a) $B_{\text{tag}} = B$ and b) and $B_{\text{tag}} = \bar{B}$. The black points show simulated MC events and the blue (solid) line shows the fit result. The "truth" and "1c$\pi^{\pm}$" contributions are shown in red and yellow, respectively. The residuals are given beneath each distribution.

4.4 Model For Continuum

The direct production of light quarks $e^+e^- \to q\bar{q}$, $q = u, d, s, c$ gives the dominant contribution to the background. The cross-sections for continuum and $b\bar{b}$ production are given in Table 3.1. For this particular background we can study data taken 60 MeV below the $B\bar{B}$ threshold. As only 10% of the expected amount of continuum events were recorded off-resonance, the statistical precision of this data is unsatisfying. Therefore, we study fully simulated continuum MC events which also allows to obtain a description of the mass and helicity distributions depending on the numbers of reconstructed $\rho^{\pm}$s per event. We still studied off-resonance data, see Appendix C.3, which can be used for a comparison with the distributions in this section. We float the parameters of the continuum model in the fit to the data to reduce the systematic uncertainty associated with the model description and also due to a slight disagreement of the mass and helicity distributions between continuum MC and off-resonance data, see Section 4.4.1. The values obtained from studying continuum MC events are used as a starting point.

4.4.1 Continuum MC

Using fully simulated continuum MC events allows to obtain a description of continuum events that depend on the number and charge(s) of the ρ mesons being reconstructed. The fractions of the different reconstruction types, $2c, \pm, 0$, are listed in Table 4.16 and the correlation matrices are given in Tables 4.17 to 4.19. The ΔE distribution of all continuum components is described by the sum of a first and a second order Chebychev polynomial,

$$\mathcal{P}^{\pm,0}_{q\bar{q}}(\Delta E|\mathcal{F}_{B\bar{B}/q\bar{q}}) \equiv c_1^{\Delta E;\pm,0}(\mathcal{F}_{B\bar{B}/q\bar{q}})C_1(\Delta E) + c_2^{\Delta E}C_2(\Delta E), \tag{4.55}$$

where the first order one depends on $\mathcal{F}_{B\bar{B}/q\bar{q}}$,

$$c_1^{\Delta E;\pm,0}(\mathcal{F}_{B\bar{B}/q\bar{q}}) = c_a^{\Delta E;\pm,0} + c_b^{\Delta E} f(\mathcal{F}^2_{B\bar{B}/q\bar{q}}), \tag{4.56}$$

with $f(\mathcal{F}_{B\bar{B}/q\bar{q}}) = \mathcal{F}_{B\bar{B}/q\bar{q}}$ for $\mathcal{F}_{B\bar{B}/q\bar{q}} < c_{\rm cut}^{\Delta E}$ and $f(\mathcal{F}_{B\bar{B}/q\bar{q}}) = c_{\rm cut}^{\Delta E}$ else. The cutoff parameter $c_{\rm cut}^{\Delta E} = 0.93 \pm 0.01$ prevents a misbehavior of the PDF in high regions of $\mathcal{F}_{B\bar{B}/q\bar{q}}$, where the continuum contribution decreases while the one from B decays increases. Furthermore we slightly modify $c_a^{\Delta E;\pm,0}$ for the PDF for the reconstruction type 0; $c_a^{\Delta E,0} = c_{\rm mod}^{\Delta E} c_a^{\Delta E,\pm}$ with $c_{\rm mod}^{\Delta E} = -0.23 \pm 0.02$. Projections onto ΔE for different bins of $\mathcal{F}_{B\bar{B}/q\bar{q}}$ are shown in Fig. 4.46.

The $M_{\rm bc}$ distribution for all four reconstruction types is commonly described by an Argus function

$$\mathcal{P}_{q\bar{q}}(M_{\rm bc}) \equiv Ar(M_{\rm bc}). \tag{4.57}$$

Full projections onto ΔE and $M_{\rm bc}$ are shown in Fig. 4.47. Fig. 4.48 shows the projection onto $\mathcal{F}_{B\bar{B}/q\bar{q}}$ and the r-bin fractions, integrated over all reconstruction types. Because we find a small difference in the r-bin distributions of the $\pm, 0$ and $2c\pi$ components, we use different r-bin fractions for each of the three categories.

For the description of the mass and helicity angle distributions we use certain compination of two kinds of one-dimensional PDFs; one for distributions including a $\rho^{\pm}$ resonance and one otherwise. The different reconstruction types are then described by combinations of these

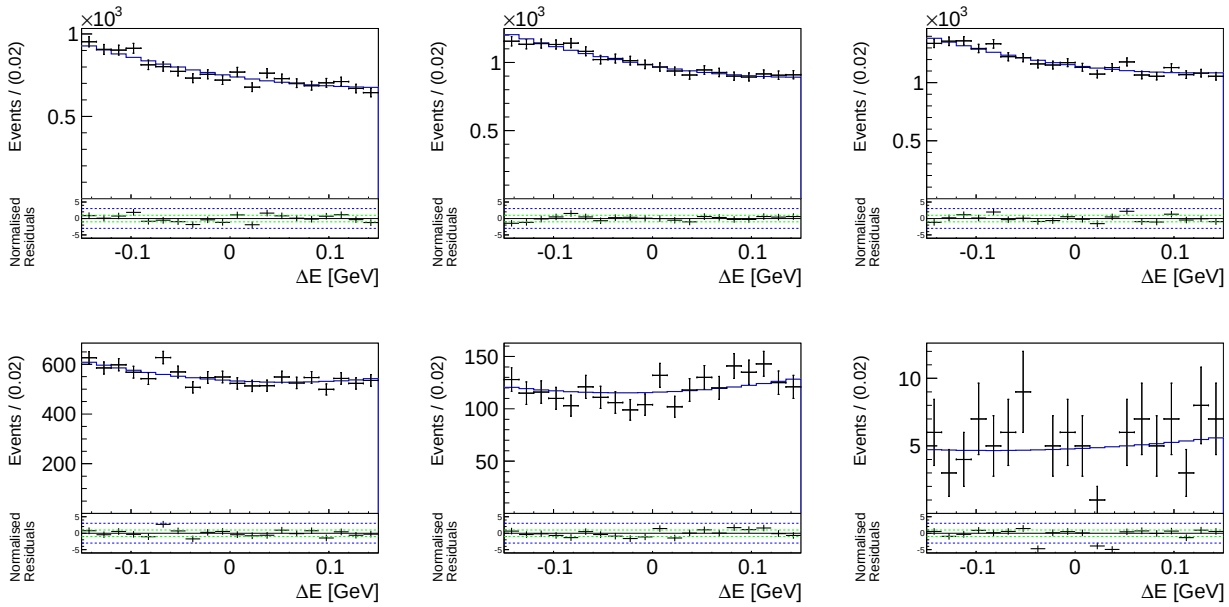

Figure 4.46: Fit projections of fully simulated continuum MC events onto ΔE for bins of $\mathcal{F}_{B\bar{B}/q\bar{q}}$; $\mathcal{F}_{B\bar{B}/q\bar{q}} \in [i, i+1]$ with $i \in \{0, 0.1, 0.25, 0.5, 0.75, 1, 2\}$. The black points show simulated MC events and the solid line shows the fit result. The residuals are given beneath each distribution.

PDFs. This reduces the degrees of freedom in the fit to data, where the parameters of the continuum model are floated. The mass PDF for the distributions including a $\rho^{\pm}$ resonance is given by a sum of a Breit-Wigner function with Chebychev polynomials

$$\mathcal{P}^{\mathrm{cr}}_{q\bar{q}}(m_{\pi^{\pm}\pi^0}) \equiv f_1 BW(m_{\pi^{\pm}\pi^0}, m, \Gamma) + (1 - f_1) \sum_{i=1}^{3} c_i^{M,\mathrm{cr}} C_i(m_{\pi^{\pm}\pi^0}), \tag{4.58}$$

and a the sum of a bifurcated Gaussian and Chebychev polynomials is describing the entirely combinatorial background

$$\mathcal{P}^{\mathrm{bkg}}_{q\bar{q}}(m_{\pi^{\pm}\pi^0}) \equiv f_2 bG(m_{\pi^{\pm}\pi^0}, ..) + (1 - f_2) \sum_{j=1}^{3} c_j^{M,\mathrm{bkg}} C_j(m_{\pi^{\pm}\pi^0}). \tag{4.59}$$

The helicity PDFs for each kind are given by the sums of Chebychev polynomials up to the ninth order

$$\mathcal{P}^{\mathrm{cr}}_{q\bar{q}}(\cos\theta^{\pm}_{\mathrm{H}} | m_{\pi^{\pm}\pi^0}) \equiv \sum_{i=1}^{2} c_i^{H,\mathrm{cr}}(m_{\pi^{\pm}\pi^0}) C_i(\cos\theta^{\pm}_{\mathrm{H}}) + \sum_{i=3}^{9} c_i^{H,\mathrm{cr}} C_i(\cos\theta^{\pm}_{\mathrm{H}}), \tag{4.60}$$

and

$$\mathcal{P}^{\mathrm{bkg}}_{q\bar{q}}(\cos\theta^{\pm}_{\mathrm{H}} | m_{\pi^{\pm}\pi^0}) \equiv \sum_{i=1}^{3} c_i^{H,\mathrm{bkg}}(m_{\pi^{\pm}\pi^0}) C_i(\cos\theta^{\pm}_{\mathrm{H}}) + \sum_{i=4}^{9} c_i^{H,\mathrm{bkg}} C_i(\cos\theta^{\pm}_{\mathrm{H}}), \tag{4.61}$$

where we account for correlations with the dipion masses via the coefficients

$$c_i^{H,\mathrm{cr,bkg}}(m_{\pi^{\pm}\pi^0}) = c_{i,a}^{H,\mathrm{cr,bkg}} + c_{i,b}^{H,\mathrm{cr,bkg}} m_{\pi^{\pm}\pi^0} + c_{i,c}^{H,\mathrm{cr,bkg}} m^2_{\pi^{\pm}\pi^0} + c_{i,d}^{H,\mathrm{cr,bkg}} m^3_{\pi^{\pm}\pi^0}. \tag{4.62}$$

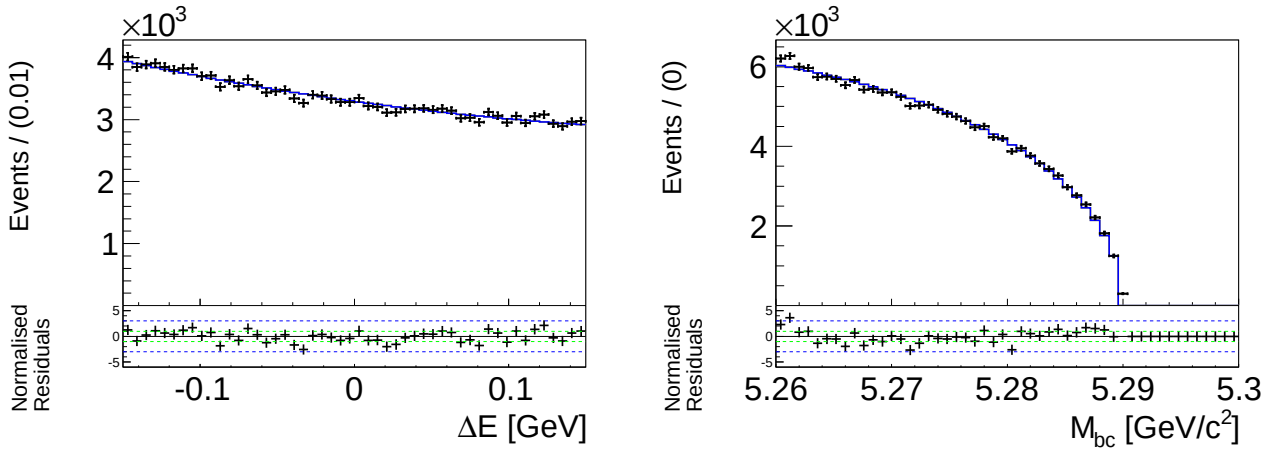

Figure 4.47: Full projections onto ΔE and M_{bc} of fully simulated continuum MC events. The black points show simulated MC events and the solid line shows the fit result. The residuals are given beneath each distribution.

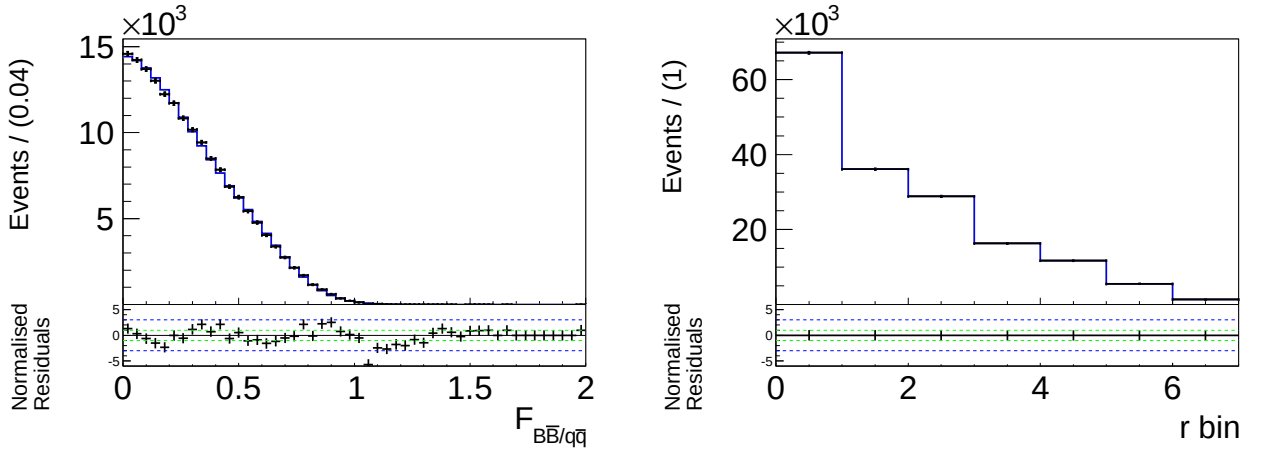

Figure 4.48: Full projections onto $\mathcal{F}_{B\bar{B}/q\bar{q}}$ and the r-bin fractions of fully simulated continuum MC events. The black points show simulated MC events and the solid line shows the fit result. The residuals are given beneath each distribution.

Due to small differences in the distributions, we incorporate modification factors for the reconstruction types $'0, 2c'$, where we add a constant to the right width of the Gaussian of Eq. (4.59) and similarly to the parameters $c^{M,\mathrm{cr}}_{[1,2],a}$ and $c^{H\mathrm{cr,bkg}}_{[1,3],a}$.

Because a difference in the distributions from MC simulation and real data can have a strong impact on the correlations between the masses and helicity angles, we compare the distribution of continuum MC simulation, off and on-resonance data (almost entirely continuum events) in slices of the masses/angles. Fig. C.100 and Fig. C.101 in Appendix C.5 show a good agreement of the behaviour of the correlation between continuum MC simulation and on-resonance data. The values obtained from the fit to continuum MC simulation are listed in Table 4.14 and projections onto the masses (angles) for different slices of the angles (masses) are shown in Appendix C.5.1.

The PDFs of the $m_{\pi^\pm\pi^0}$ distribution of the different continuum components are then given

	c_a	c_b	c_c	c_d
cr1	-3.33 ± 0.03	5.30 ± 0.04	-2.70 ± 0.04	-0.05 ± 0.05
cr2	1.81 ± 0.04	-4.6 ± 0.06	5.6 ± 0.08	-2.3 ± 0.08
bkg1	0.82 ± 0.01	-4.17 ± 0.01	2.44 ± 0.01	0.07 ± 0.01
bkg2	0.51 ± 0.01	0.37 ± 0.01	0.32 ± 0.01	-0.14 ± 0.01
bkg3	-0.25 ± 0.01	0.16 ± 0.01	1.25 ± 0.01	0.88 ± 0.01

Table 4.14: The parameters that describe the correlations of the helicity PDFs with the dipion masses.

by

$$\mathcal{P}^{2c\pi}_{q\bar{q}}(m_{\pi^+\pi^0}, m_{\pi^-\pi^0}) \equiv \mathcal{P}^{\rm cr}_{q\bar{q}}(m_{\pi^+\pi^0}) \times \mathcal{P}^{\rm cr}_{q\bar{q}}(m_{\pi^-\pi^0}), \tag{4.63}$$

$$\mathcal{P}^{\pm}_{q\bar{q}}(m_{\pi^\pm\pi^0}, m_{\pi^\mp\pi^0})\mathcal{P}^{\rm cr}_{q\bar{q}}(m_{\pi^\pm\pi^0}) \times \mathcal{P}^{\rm bkg}_{q\bar{q}}(m_{\pi^\mp\pi^0}) \tag{4.64}$$

and

$$\mathcal{P}^{0}_{q\bar{q}}(m_{\pi^+\pi^0}, m_{\pi^-\pi^0})\mathcal{P}^{\rm bkg}_{q\bar{q}}(m_{\pi^+\pi^0}) \times \mathcal{P}^{\rm bkg}_{q\bar{q}}(m_{\pi^-\pi^0}). \tag{4.65}$$

The distributions of the helicity angles are modeled with

$$\mathcal{P}^{2c\pi}_{q\bar{q}}(\cos\theta^+_{\rm H}, \cos\theta^-_{\rm H}|m_{\pi^+\pi^0}, m_{\pi^-\pi^0}) \equiv \mathcal{P}^{\rm cr}_{q\bar{q}}(\cos\theta^+_{\rm H}|m_{\pi^+\pi^0}) \times \mathcal{P}^{\rm cr}_{q\bar{q}}(\cos\theta^-_{\rm H}|m_{\pi^-\pi^0}), \tag{4.66}$$

$$\mathcal{P}^{\pm}_{q\bar{q}}(\cos\theta^\pm_{\rm H}, \cos\theta^\mp_{\rm H}|m_{\pi^\pm\pi^0}, m_{\pi^\mp\pi^0}) \equiv \mathcal{P}^{\rm cr}_{q\bar{q}}(\cos\theta^\pm_{\rm H}|m_{\pi^\pm\pi^0}) \times \mathcal{P}^{\rm bkg}_{q\bar{q}}(\cos\theta^\mp_{\rm H}|m_{\pi^\mp\pi^0}), \tag{4.67}$$

and

$$\mathcal{P}^{0}_{q\bar{q}}(\cos\theta^+_{\rm H}, \cos\theta^-_{\rm H}|m_{\pi^+\pi^0}, m_{\pi^-\pi^0}) \equiv \mathcal{P}^{\rm bkg}_{q\bar{q}}(\cos\theta^+_{\rm H}|m_{\pi^+\pi^0}) \times \mathcal{P}^{\rm bkg}_{q\bar{q}}(\cos\theta^-_{\rm H}|m_{\pi^-\pi^0}). \tag{4.68}$$

Projections onto the dipion masses and the helicity angles of the "±,0" and "2c" components are shown in Figs. 4.49 to 4.51, and the full projections are shown in Figs. 4.52 and 4.53. The lifetime PDF consists out of two parts, where the exponential life-time describes $e^+e^- \to c\bar{c}$ processes with an effective life-time $\tau_{q\bar{q}}$ and the time evolution of light quarks is described by a prompt contribution from a δ-function;

$$\mathcal{P}_{q\bar{q}}(\Delta t) \equiv \left[(1-f_\delta)\frac{e^{-|\Delta t|/\tau_{q\bar{q}}}}{2\tau_{q\bar{q}}} + f_\delta\delta(\Delta t - \mu_{q\bar{q}})\right] \otimes R_{q\bar{q}}(\Delta t). \tag{4.69}$$

The Δt PDF is convoluted with the sum of two Gaussians

$$R_{q\bar{q}}(\Delta t) \equiv (1-f_{\rm tail})G(\Delta t, \mu, S_{\rm core}\sigma) + f_{\rm tail}G(\Delta t, \mu, S_{\rm core}S_{\rm tail}). \tag{4.70}$$

where the scale factor $S_{\rm core} \equiv \sqrt{\sigma^2_{\rm Rec} + \sigma^2_{\rm Tag}}/\beta\gamma c$ is the event-dependent Δt error constructed from the vertex resolution. We use a different set of Gaussians if at least one of the B vertices is obtained from only one track. Projections onto each flavor are shown in Fig. 4.54 and the effective lifetimes as obtained from a fit to the MC distribution are listed in Table 4.15.

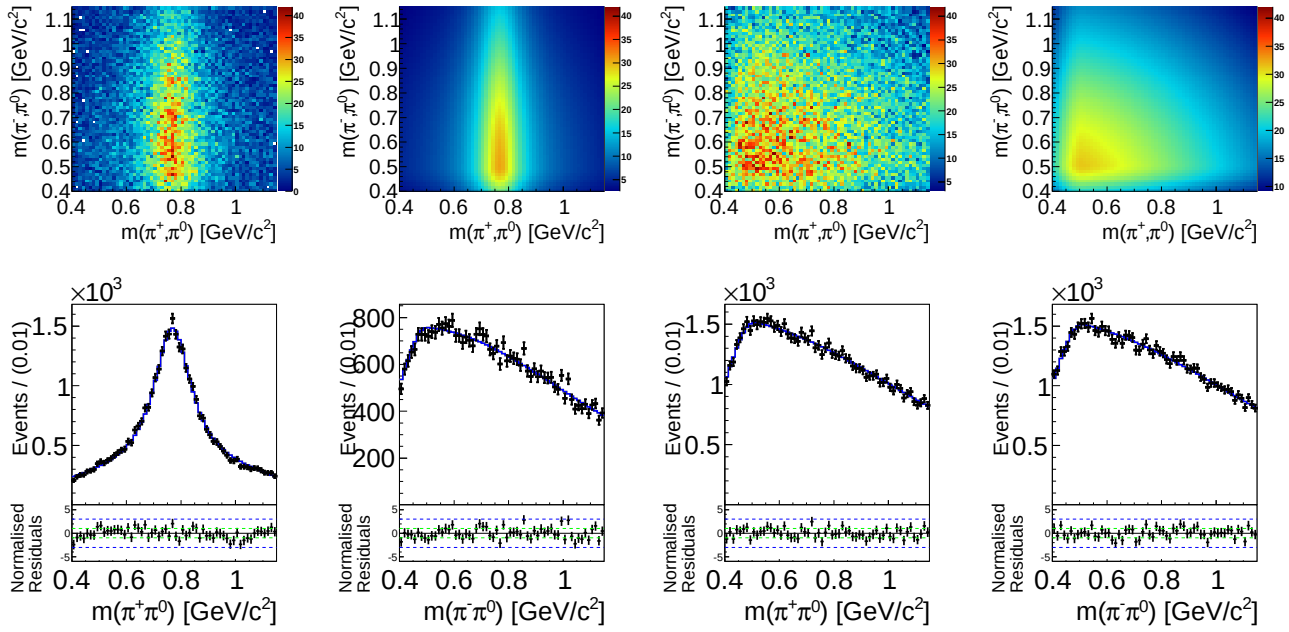

Figure 4.49: Fit projections onto $m_{\pi^{\pm}\pi^0}$ of fully simulated continuum MC events for the components $\pm$ (left) and 0. The top row shows the 2D projection of the data (left) and the PDF (right) and the bottom row shows projection onto each axis, where the black points show simulated MC events and the solid line shows the fit result. The residuals are given beneath each distribution.

lifetime [ps]	SVD1	SVD2
$\tau_{B^0}^{\text{eff}}$	0.55 ± 0.04	0.61 ± 0.02

Table 4.15: The effective B^0 lifetimes obtained from a fit to the continuum MC distributions.

The full PDF for continuum events is given by

$$\begin{aligned}
&\mathcal{PDF}_{q\bar{q}}(\Delta E, M_{\text{bc}}, m_{\pi^+\pi^0}, m_{\pi^-\pi^0}, \cos\theta_{\text{H}}^+, \cos\theta_{\text{H}}^-, \mathcal{F}_{B\bar{B}/q\bar{q}}, \Delta t, q) \equiv \\
&\Big((1-f_0) \times \mathcal{P}_{q\bar{q}}^{\pm}(\Delta E|\mathcal{F}_{B\bar{B}/q\bar{q}}) \times \Big((1-f_{2c}) \\
&\times\big(f_+ \times \mathcal{PDF}_{q\bar{q}}^{+}(m_{\pi^+\pi^0}, m_{\pi^-\pi^0}) \times \mathcal{PDF}_{q\bar{q}}^{+}(\cos\theta_{\text{H}}^+, \cos\theta_{\text{H}}^-|m_{\pi^+\pi^0}, m_{\pi^-\pi^0}) + \\
&(1-f_+) \times \mathcal{PDF}_{q\bar{q}}^{-}(m_{\pi^+\pi^0}, m_{\pi^-\pi^0}) \times \mathcal{PDF}_{q\bar{q}}^{-}(\cos\theta_{\text{H}}^-, \cos\theta_{\text{H}}^+|m_{\pi^-\pi^0}, m_{\pi^+\pi^0})\big) + \\
&f_{2c} \times \mathcal{PDF}_{q\bar{q}}^{2c}(m_{\pi^+\pi^0}, m_{\pi^-\pi^0}) \times \mathcal{PDF}_{q\bar{q}}^{2c}(\cos\theta_{\text{H}}^+, \cos\theta_{\text{H}}^-|m_{\pi^+\pi^0}, m_{\pi^-\pi^0})\Big) + \\
&f_0 \times \mathcal{P}_{q\bar{q}}^{0}(\Delta E|\mathcal{F}_{B\bar{B}/q\bar{q}}) \times \mathcal{PDF}_{q\bar{q}}^{0}(m_{\pi^+\pi^0}, m_{\pi^-\pi^0}) \times \mathcal{PDF}_{q\bar{q}}^{0}(\cos\theta_{\text{H}}^+, \cos\theta_{\text{H}}^-|m_{\pi^+\pi^0}, m_{\pi^-\pi^0})\Big) \\
&\times \mathcal{PDF}_{q\bar{q}}(M_{\text{bc}}) \times \mathcal{PDF}_{q\bar{q}}^{l}(\mathcal{F}_{B\bar{B}/q\bar{q}}) \times \mathcal{PDF}_{q\bar{q}}(\Delta t, q).
\end{aligned} \tag{4.71}$$

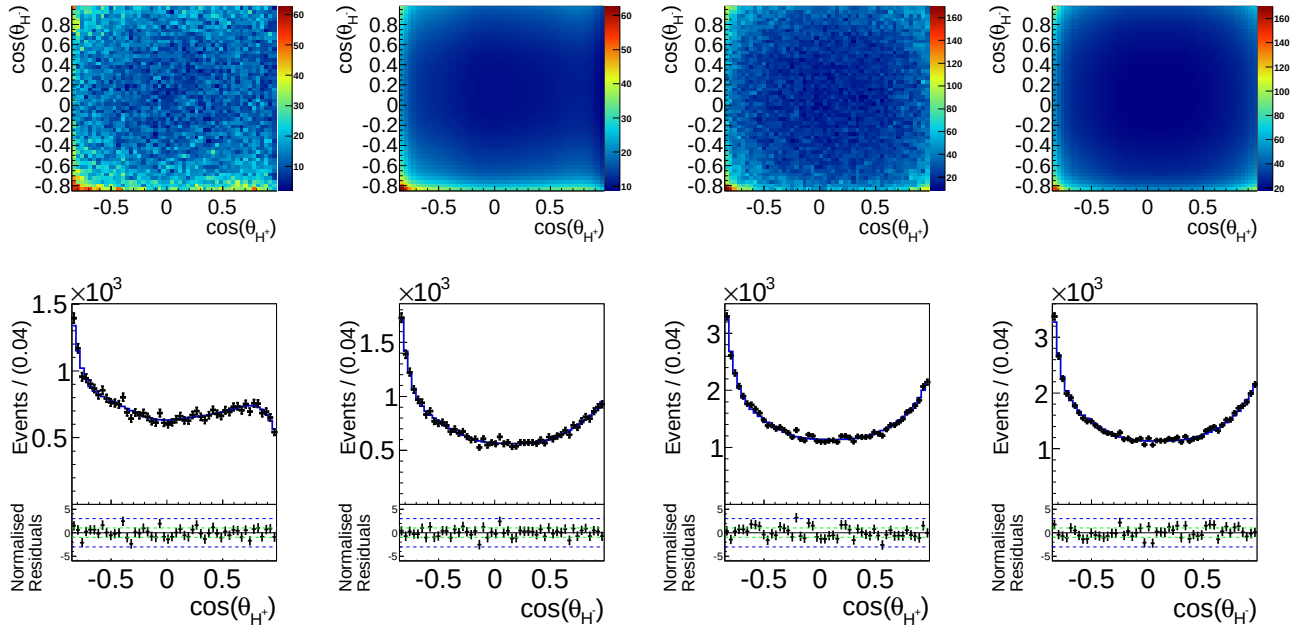

Figure 4.50: Fit projections onto $m_{\pi^\pm\pi^0}$ of fully simulated continuum MC events for the reconstruction types + (left) and 0. The top row shows the 2D projection of the data (left) and the PDF (right) and the bottom row shows projection onto each axis, where the black points show simulated MC events and the solid line shows the fit result. The residuals are given beneath each distribution.

	f_+	f_0	f_{2c}
continuum	0.50 ± 0.01	0.44 ± 0.01	0.23 ± 0.02

Table 4.16: The fractions of the different reconstruction types obtained from fully simulated continuum MC events as used in Eq. (4.71).

0	ΔE	M_{bc}	$m^1_{\pi^+\pi^-}$	$m^2_{\pi^+\pi^-}$	$\mathcal{F}_{B\bar{B}/q\bar{q}}$	$\cos\theta^1_{\rm H}$	$\cos\theta^2_{\rm H}$	Δt
ΔE	1	0.01	0.00	0.01	0.03	-0.00	-0.00	-0.00
M_{bc}		1	0.00	-0.00	-0.00	0.01	0.00	0.00
$m^1_{\pi^+\pi^-}$			1	-0.00	-0.01	0.08	-0.00	0.00
$m^2_{\pi^+\pi^-}$				1	0.00	0.00	0.03	0.00
$\mathcal{F}_{B\bar{B}/q\bar{q}}$					1	0.02	-0.01	0.00
$\cos\theta^1_{\rm H}$						1	-0.03	0.00
$\cos\theta^2_{\rm H}$							1	-0.00
Δt								1

Table 4.17: Correlation matrix for fully simulated continuum MC events (+, SVD2).

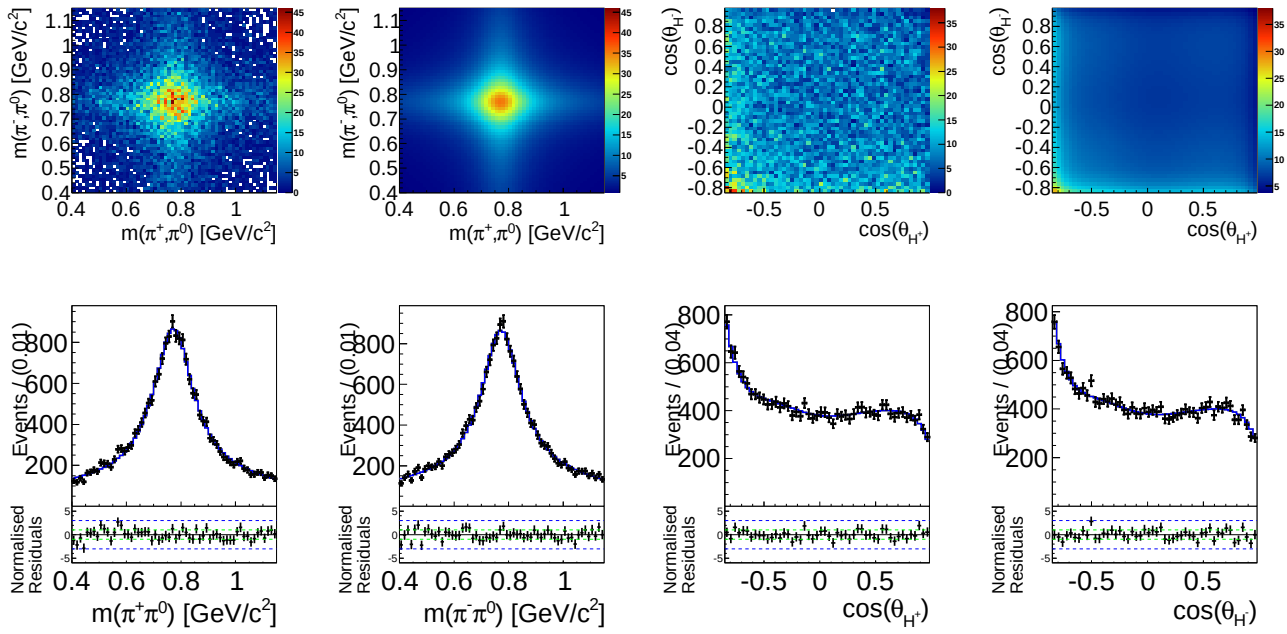

Figure 4.51: Fit projections onto $m_{\pi^\pm\pi^0}$ and $\cos\theta_{\rm H}^{\pm}$ of fully simulated continuum MC events for the component $2c$. The top row shows the 2D projection of the data (left) and the PDF (right) and the bottom row shows projection onto each axis, where the black points show simulated MC events and the solid line shows the fit result. The residuals are given beneath each distribution.

0	ΔE	M_{bc}	$m^1_{\pi^+\pi^-}$	$m^2_{\pi^+\pi^-}$	$\mathcal{F}_{B\bar{B}/q\bar{q}}$	$\cos\theta^1_{\rm H}$	$\cos\theta^2_{\rm H}$	Δt
ΔE	1	0.00	0.01	0.01	0.02	-0.00	0.00	0.00
M_{bc}		1	-0.00	-0.00	-0.01	0.00	0.00	-0.00
$m^1_{\pi^+\pi^-}$			1	-0.01	-0.00	0.04	-0.00	0.00
$m^2_{\pi^+\pi^-}$				1	0.01	-0.00	0.04	0.00
$\mathcal{F}_{B\bar{B}/q\bar{q}}$					1	0.01	0.01	0.00
$\cos\theta^1_{\rm H}$						1	-0.00	0.00
$\cos\theta^2_{\rm H}$							1	0.00
Δt								1

Table 4.18: Correlation matrix for fully simulated continuum MC events (0, SVD2).

0	ΔE	M_{bc}	$m^1_{\pi^+\pi^-}$	$m^2_{\pi^+\pi^-}$	$\mathcal{F}_{B\bar{B}/q\bar{q}}$	$\cos\theta^1_{\rm H}$	$\cos\theta^2_{\rm H}$	Δt
ΔE	1	-0.00	0.01	0.01	0.03	0.00	-0.00	0.00
M_{bc}		1	0.01	-0.00	0.01	0.01	0.01	-0.00
$m^1_{\pi^+\pi^-}$			1	-0.01	-0.01	0.07	-0.00	0.00
$m^2_{\pi^+\pi^-}$				1	0.01	-0.00	0.07	0.00
$\mathcal{F}_{B\bar{B}/q\bar{q}}$					1	0.01	0.02	-0.00
$\cos\theta^1_{\rm H}$						1	-0.03	0.00
$\cos\theta^2_{\rm H}$							1	0.00
Δt								1

Table 4.19: Correlation matrix for fully simulated continuum MC events (2c, SVD2). As this components fraction is tiny, correlations are ignored.

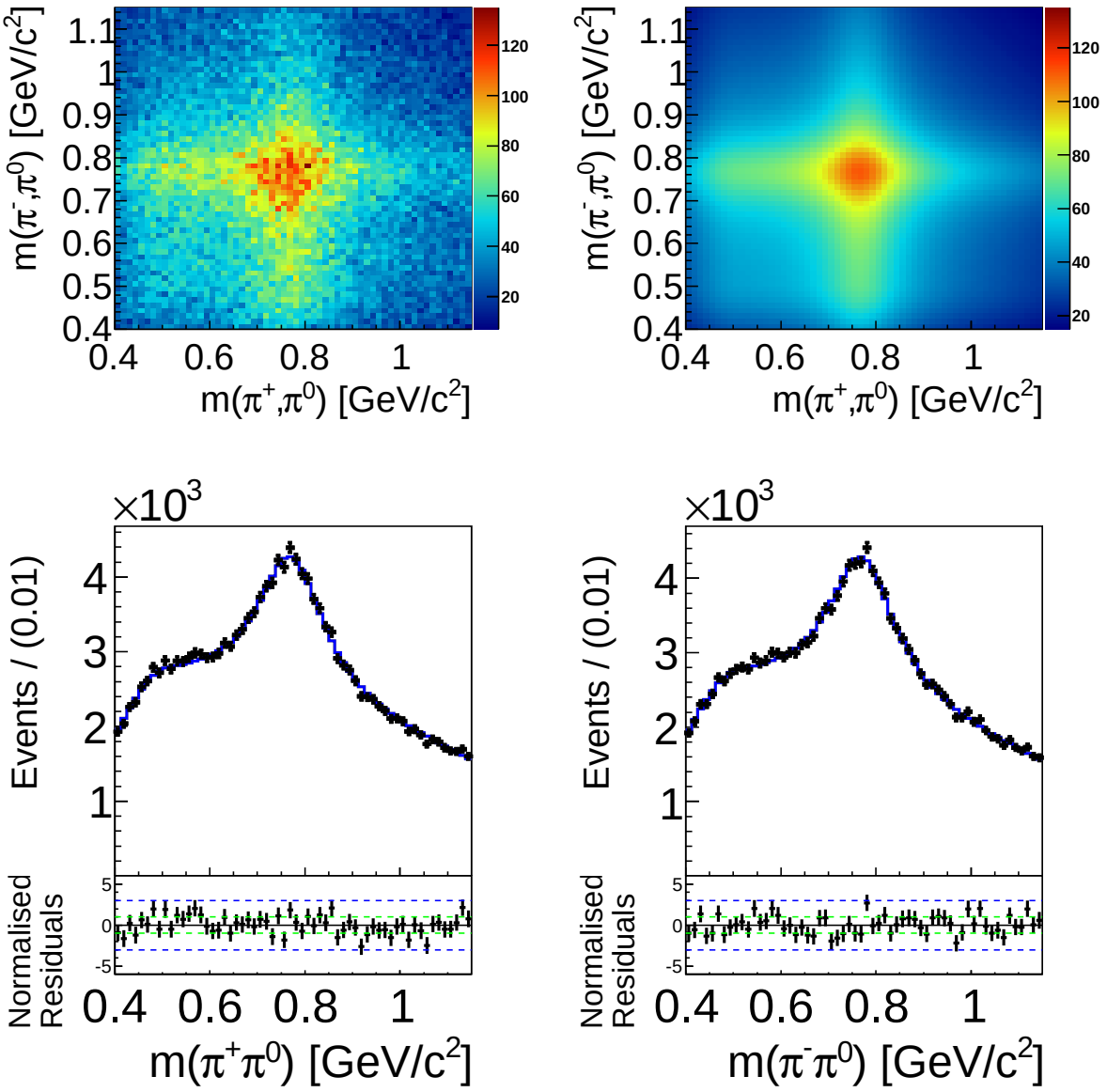

Figure 4.52: Full projections onto $m_{\pi^{\pm}\pi^0}$ of fully simulated continuum MC events. The top row shows the 2D projection of the data (left) and the PDF (right) and the bottom row shows projection onto each axis, where the black points show simulated MC events and the solid line shows the fit result. The residuals are given beneath each distribution.

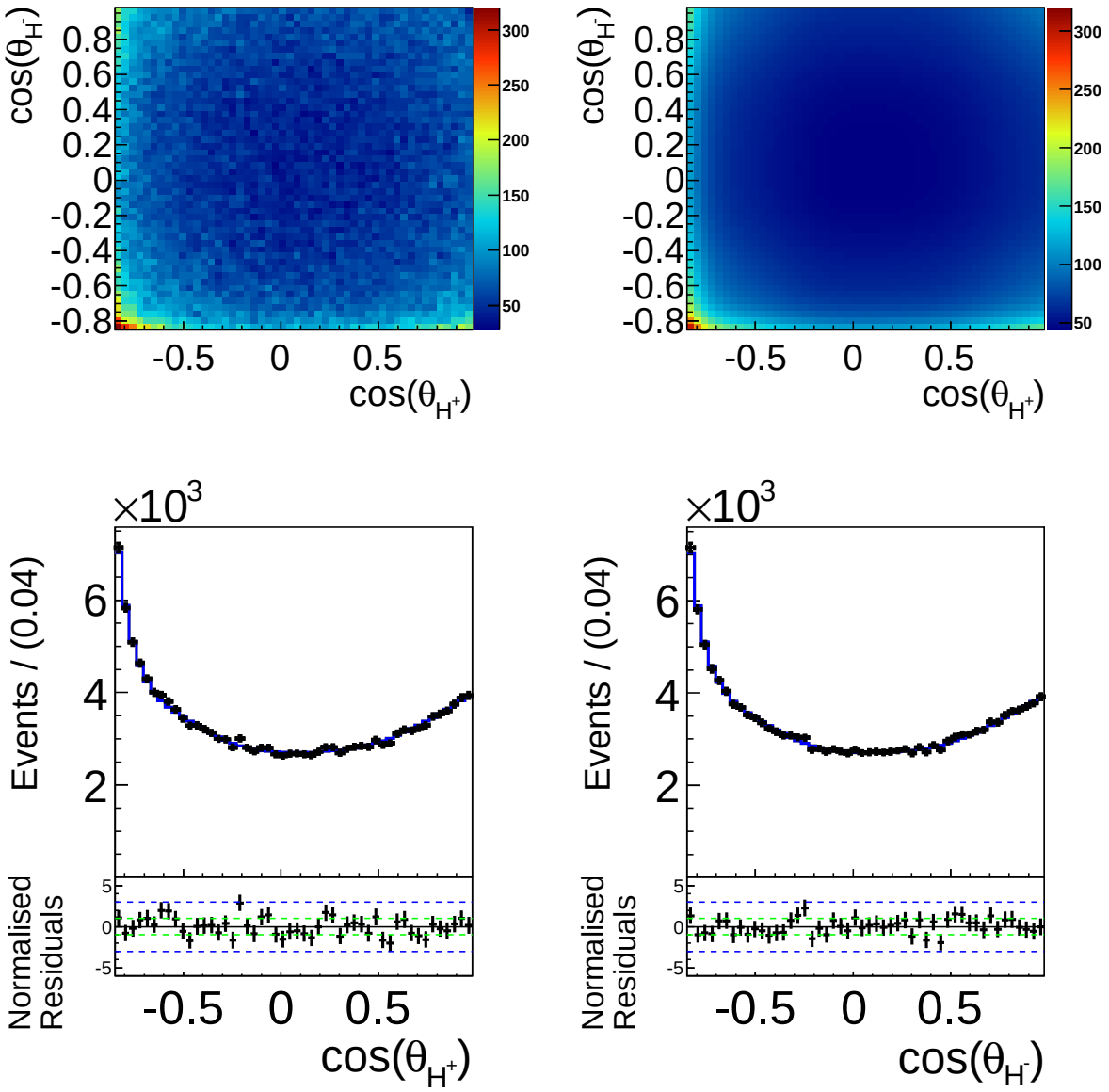

Figure 4.53: Full projections onto the helcicity angles of fully simulated continuum MC events. The top row shows the 2D projection of the data (left) and the PDF (right) and the bottom row shows projection onto each axis, where the black points show simulated MC events and the solid line shows the fit result. The residuals are given beneath each distribution.

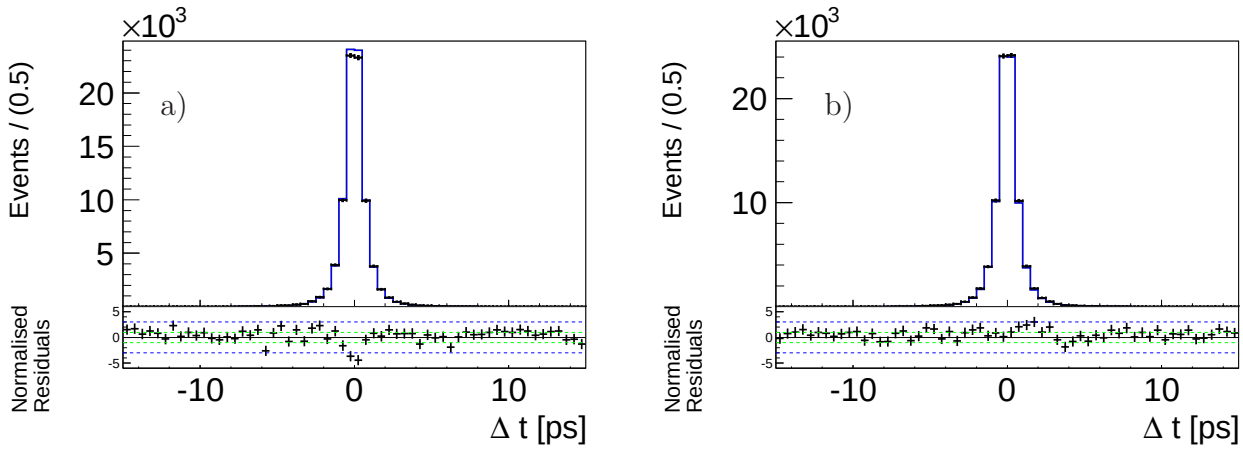

Figure 4.54: Full projections onto Δt of fully simulated continuum MC events. a) $B_{\rm tag} = B$ and b) and $B_{\rm tag} = \bar{B}$. The black points show simulated MC events and the solid line shows the fit result. The residuals are given beneath each distribution.

Comparison of Continuum MC with Off-Resonance Data

The following plots show the shapes obtained from studying continuum MC simulation normalized to the off-resonance data and demonstrate a small mis-agreement in the mass and helicity distributions. We assume that this is caused by some simplifications in the description of the hadronisation and we account for this effect by floating the parameters of the continuum model in the fit to data. This reduces the systematic uncertainty related to fixed parameters of the model description as already mentioned before. All other fit variables and also the behavior of the correlations between the mass and helicity angle distributions, see Appendix C.5, agree reasonably well.

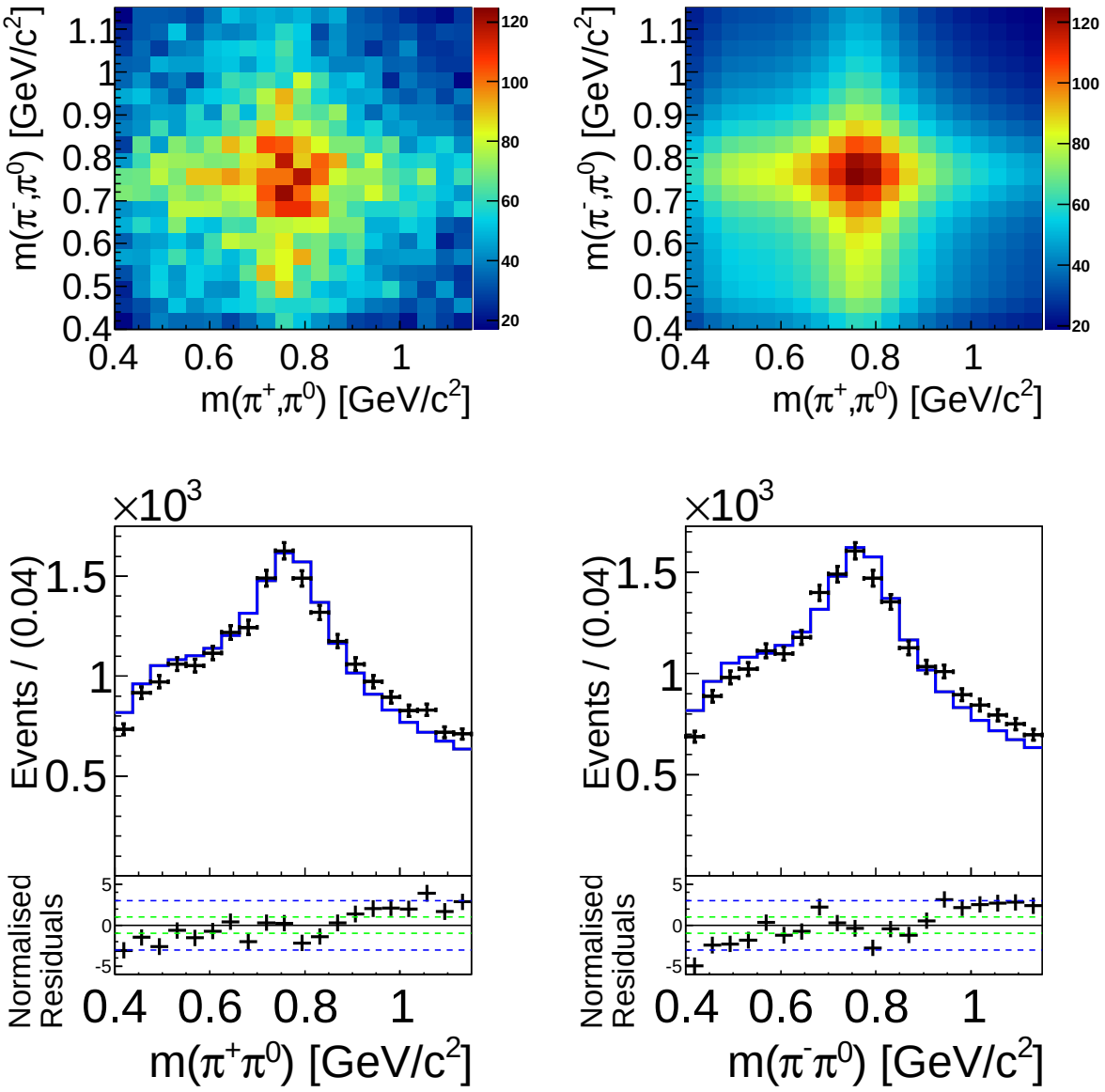

Figure 4.55: The shape obtained from studying continuum MC simulation superimposed on off-resonance data for the dipion masses. The top row shows the 2D projection of the data (left) and the PDF (right) and the bottom row shows projection onto each axis, where the black points show simulated MC events and the solid line shows the fit result. The residuals are given beneath each distribution.

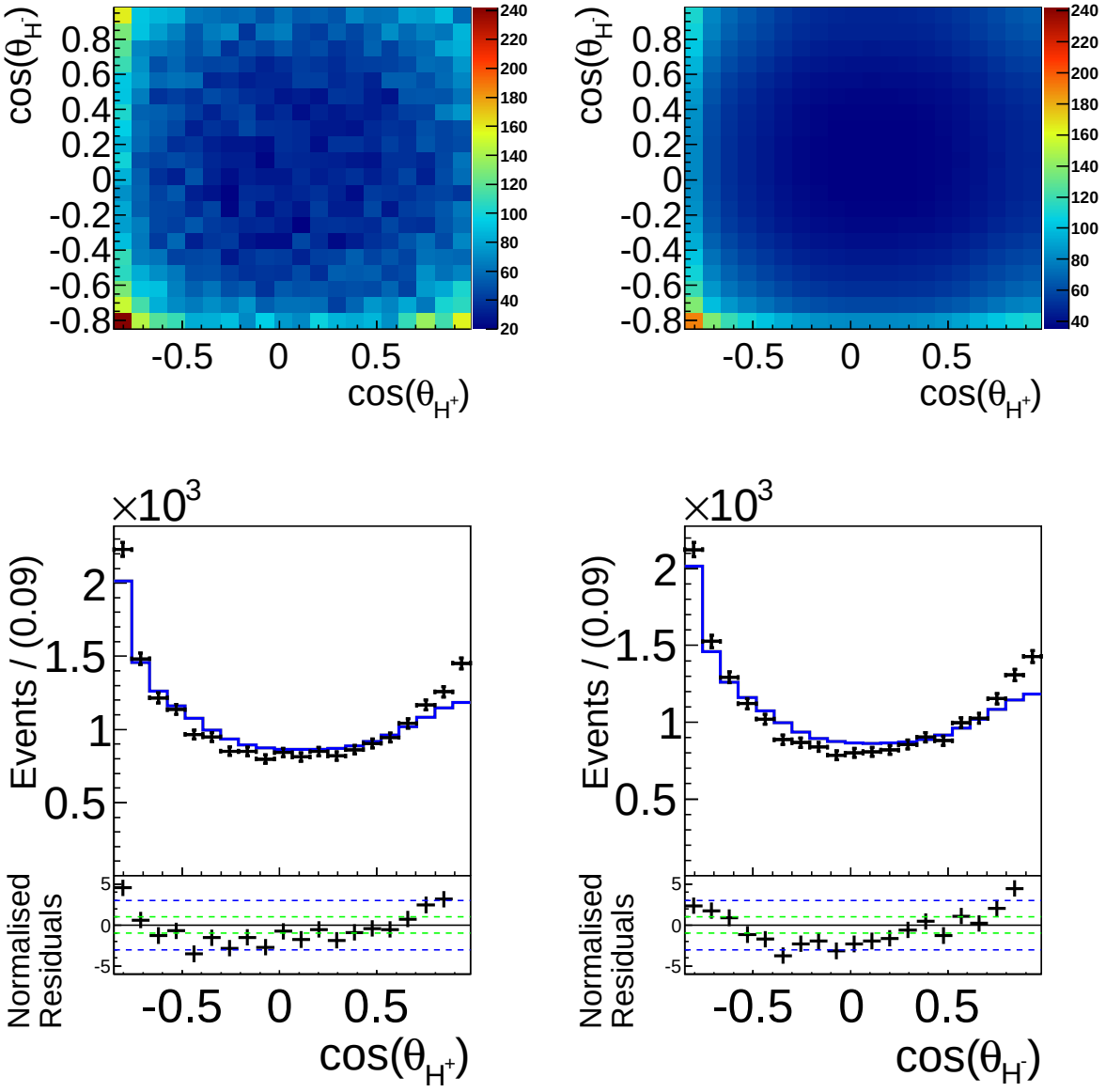

Figure 4.56: The shape obtained from studying continuum MC simulation superimposed on off-resonance data for the helicity angles. The top row shows the 2D projection of the data (left) and the PDF (right) and the bottom row shows projection onto each axis, where the black points show simulated MC events and the solid line shows the fit result. The residuals are given beneath each distribution.

4.5 Model Summary

This section provides a summary of the fit model used in this measurement. The fit components were shortly introduced in Section 3.3, their PDFs are described in detail in Chapter 4 and Appendix C.
Table 4.20 lists an overview of all components including their (simplified) parametrization and the considered correlations.
Figs. 4.57 to 4.63 show the fit projections onto each fit variable and the r-bin fractions for each component.
The distributions of the two ρ masses and the helicity angles are both symmetric under the exchange $\rho^+ \leftrightarrow \rho^-$ in the full projection, thus we only show the distributions of ρ^+. The plots show the distributions of $B^0 \to \rho^+\rho^-$ (LP) and (TP, truth), continuum, $B^0 \to$ charm, $B^\pm \to$ charm, $B^0 \to$ charmless, $B^\pm \to$ charmless, $B \to a_1^0[\rho^\pm\pi^\mp]\pi^0$, $B \to a_1^0[\rho^0\pi^0]\pi^0$, $B \to a_1^\pm\pi^\mp$, $B \to \rho^\pm\pi^\mp\pi^0$, $B \to \rho^0\pi^0\pi^0$,$B \to \pi^+\pi^0\pi^-\pi^0$, $B \to \omega\pi^0$ and $B \to f_0\pi^0\pi^0$ from left to right and from bottom to top and as labeled.
Signal with longitudinal polarization include also the "truth" component in red and the "1c$\pi^\pm$"component in yellow.

mode	ΔE	M_{bc}	$m(\pi^{\pm}\pi^0)$	$\cos\theta_{\mathrm{H}}^{\pm}$	$\mathcal{F}_{B\bar{B}/q\bar{q}}$	Δt
truth (LP)	dbG	$\mathrm{dbG}|_{\Delta E}$	$\mathrm{BW}|_{\Delta E}$	Eq. (4.17)$|_{\Delta E}$	tbG_l	$\exp_{\mathcal{R}}^{CP}$
$no\pi^0$ (LP)	$(\mathrm{dbG+C})|_{\cos\theta_{\mathrm{H}}}$	$(\mathrm{dbG+A})|_{\Delta E\cos\theta_{\mathrm{H}}}$	$(\mathrm{BW+C})|_{\cos\theta_{\mathrm{H}}}$	H	$dbG_l^{\mathrm{sig}}|_{\Delta E}$	truth (LP)
$1C\pi$ (LP)	$(\mathrm{dbG+C})|_{\cos\theta_{\mathrm{H}}}$	(dbG+A)	$(\mathrm{BW+C})^{\pm}$	$\mathrm{H}^{\pm}$	dbG_l^{sig}	$\exp_{\mathcal{R}}^{CP}|_{\mathrm{eff.}}^{\mathrm{truth}}$
mr (LP)	(dbG+C)	(dbG+A)	(BW+C)	H	dbG_l^{sig}	$\exp_{\mathcal{R}}$
truth (TP)	dbG	dbG	$\mathrm{BW}|_{\Delta E}$	Eq. (4.18)	dbG_l^{sig}	$\exp_{\mathcal{R}}^{CP}$
$no\pi^0$ (TP)	$(\mathrm{dbG+C})|_{\cos\theta_{\mathrm{H}}}$	(dbG+A)	H	H	dbG_l^{sig}	truth (TP)
$1C\pi$ (TP)	C	(dbG+A)	H	H	dbG_l^{sig}	$\exp_{\mathcal{R}}^{CP}|_{\mathrm{eff.}}^{\mathrm{truth}}$
4π	(dbG +C)	(dbG + A)	C	C	dbG_l^{sig}	$\exp_{\mathcal{R}}^{CP}$
$a_1^{\pm}\pi^{\mp}$	(dbG +C)	(dbG + A)	$(\mathrm{BW+C})^{\pm,0}$	$\mathrm{H}^{\pm,0}$	dbG_l^{sig}	$\exp_{\mathcal{R}}^{CP}$
$a_1^0[\rho^{\pm}\pi^{\mp}]\pi^0$	(dbG +C)	(dbG + A)	$\mathrm{H}^{\pm,0}$	$\mathrm{H}^{\pm,0}$	dbG_l^{sig}	$\exp_{\mathcal{R}}^{CP}$
$a_1^0[\rho^0\pi^0]\pi^0$	(dbG +C)	(dbG + A)	$(\mathrm{C})|_{\cos\theta_{\mathrm{H}}}$	(G+C)	dbG_l^{sig}	$\exp_{\mathcal{R}}^{CP}$
$\rho^{\pm}\pi^{\mp}\pi^0$	$(\mathrm{dbG}+\mathrm{C})^{\pm,0}|_{M_{\mathrm{bc}},\cos\theta_{\mathrm{H}}}$	$(\mathrm{dbG}+\mathrm{A})_{\cos\theta_{\mathrm{H}}}$	$(\mathrm{BW+C})^{\pm,0}|_{\cos\theta_{\mathrm{H}}}$	$\mathrm{H}^{\pm,0}$	dbG_l^{sig}	$\exp_{\mathcal{R}}^{CP}$
$\rho^0\pi^0\pi^0$	(dbG +C)	(dbG + A)	C	H	dbG_l^{sig}	$\exp_{\mathcal{R}}^{CP}$
$f_0\pi^0\pi^0$	(dbG +C)	(dbG + A)	C	H	dbG_l^{sig}	$\exp_{\mathcal{R}}^{CP}$
$\omega\pi^0$	(dbG +C)	(dbG + A)	$(\mathrm{G+C})|_{\cos\theta_{\mathrm{H}}}$	(G+C)	dbG_l^{sig}	$\exp_{\mathcal{R}}^{CP}$
continuum	$C^{\pm,0,2c}|_{\mathcal{F}_{B\bar{B}/q\bar{q}}}$	A	$(\mathrm{BW+C})^{\pm,0,2c}$	$C^{\pm,0,2c}|_{m(\pi^{\pm}\pi^0)}$	dbG_l	$\exp_{\mathcal{R}}$
B^0_{charm}	$\mathrm{C}^{\pm,0}$	A	$(\mathrm{BW+C})^{\pm,0}|_{\cos\theta_{\mathrm{H}}}$	$C^{\pm,0}$	dbG_l^{sig}	$\exp_{\mathcal{R}}$
B^+_{charm}	$\mathrm{C}^{\pm,0,2c}$	A	$(\mathrm{BW+C})^{\pm,0,2c}|_{\cos\theta_{\mathrm{H}}}$	$C^{\pm,0,2c}$	dbG_l^{sig}	$\exp_{\mathcal{R}}$
$B^0_{\mathrm{charmless}}$	$\mathrm{C}^{\pm,0}|_{\cos\theta_{\mathrm{H}}}$	$(\mathrm{dbG+A})|_{\Delta E}$	$(\mathrm{BW+C})^{\pm,0}|_{\cos\theta_{\mathrm{H}},\Delta E}$	$C^{\pm,0}|_{\Delta E}$	dbG_l^{sig}	$\exp_{\mathcal{R}}$
$B^+_{\mathrm{charmless}}$	$\mathrm{C}^{\pm,0,2c}|_{\cos\theta_{\mathrm{H}}}$	A	$(\mathrm{BW+C})^{\pm,0,2c}|_{\cos\theta_{\mathrm{H}}}$	$C^{\pm,0,2c}$	dbG_l^{sig}	$\exp_{\mathcal{R}}$

Table 4.20: Summary of the parametrization for each component of the fit model. This table gives only a rough overview, most components are further divided into up to four categories $(\pm, 0, 2c)$ with individual descriptions, being indicated by a superscript. The variables in the subscript list the considered correlations. The PDFs for the masses and helicity angles are usually higher dimensional ones, here we only show a one-dimensional simplification. C stands for sums of Chebychev polynomials, H for histograms, A is an Argus function, (t/db)G is a (triple/double-bifurcated) Gaussian, BW is a relativistic Breit-Wigner function and $\exp_{\mathcal{R}}$ is an exponential function convoluted with a resolution function. The superscript CP labels an included asymmetry.

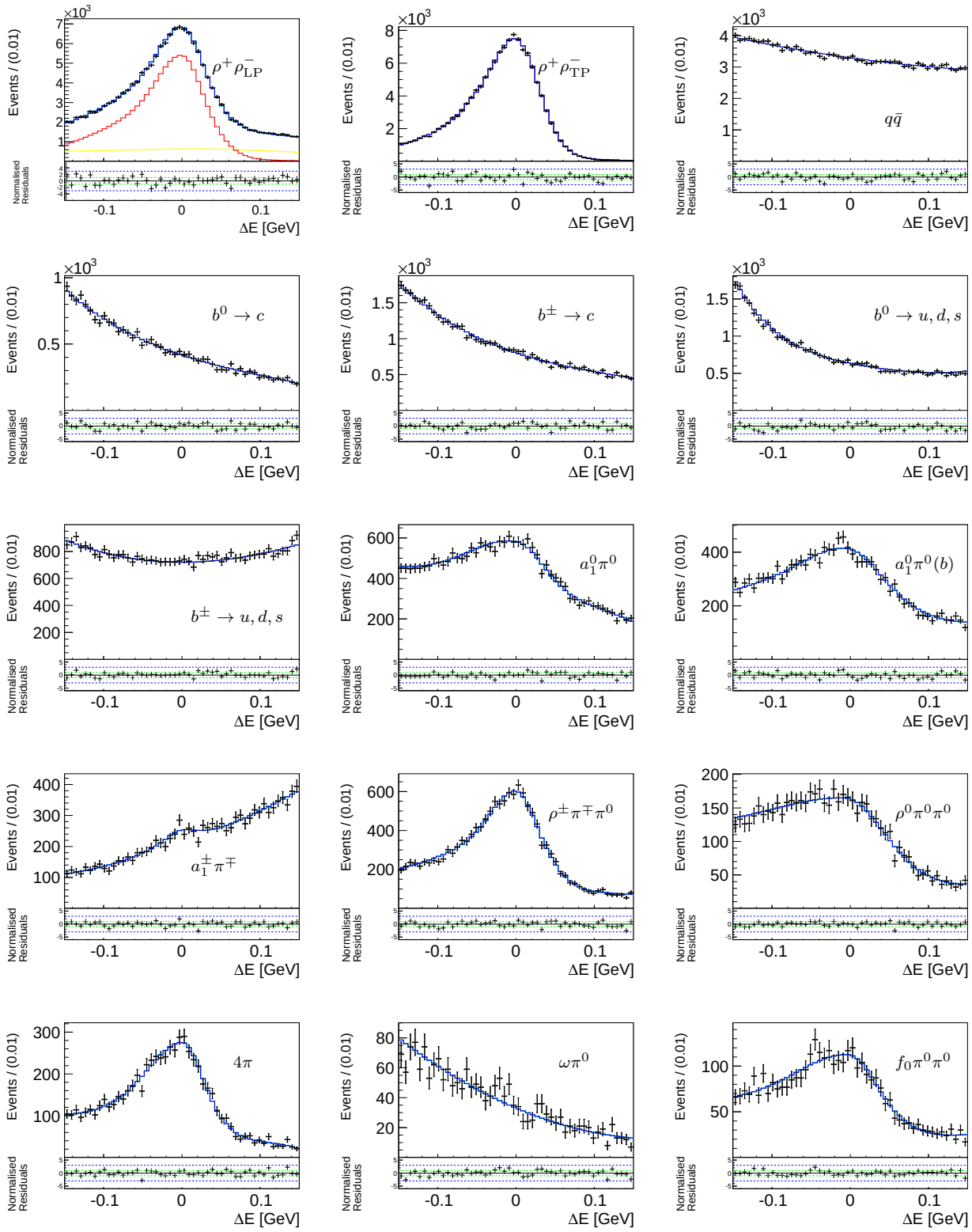

Figure 4.57: Full projections onto ΔE with fit result on top for all components as explained in the text.

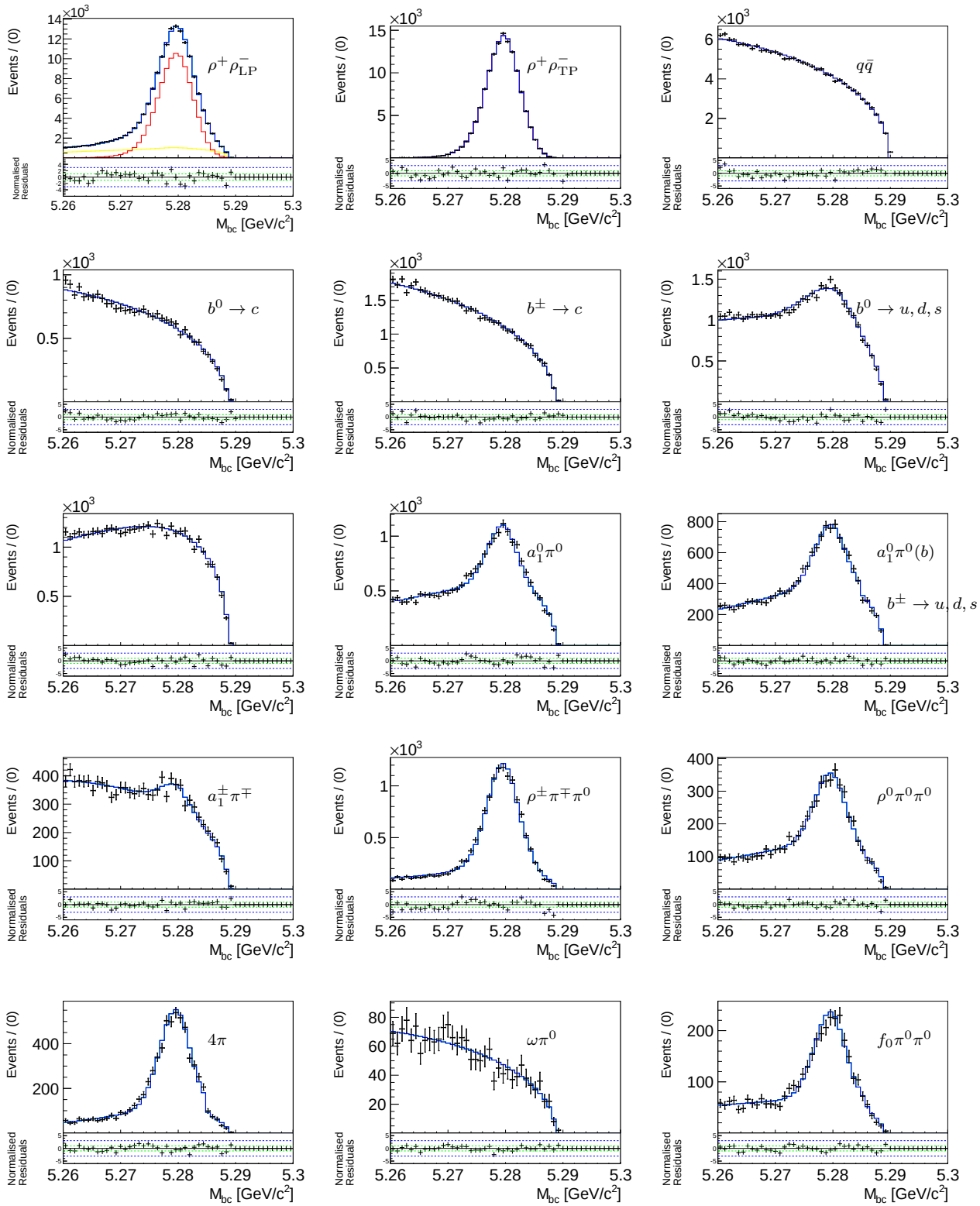

Figure 4.58: Full projections onto $M_{\rm bc}$ with fit result on top for all components as explained in the text.

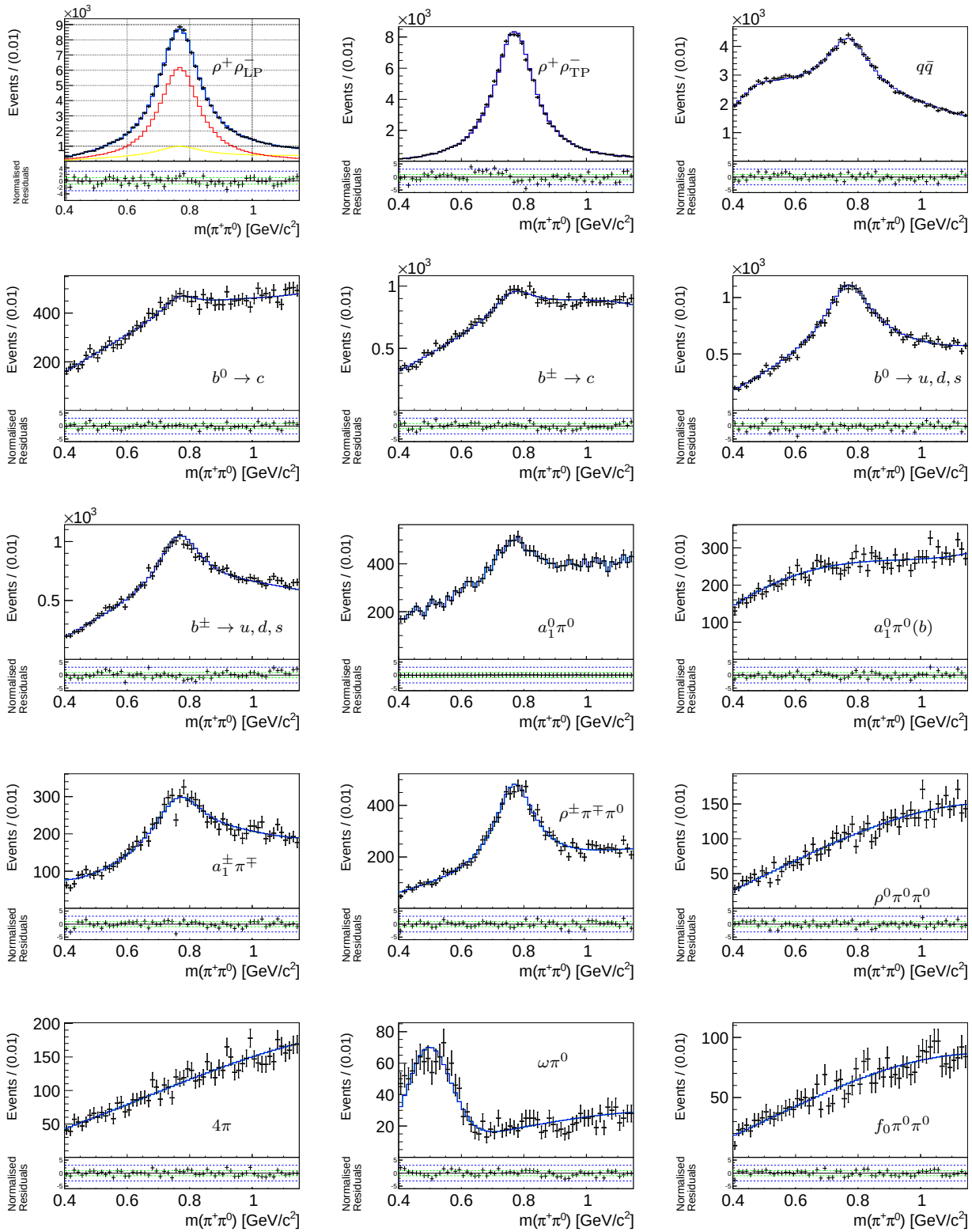

Figure 4.59: Full projections onto $m(\pi^+\pi^0)$ with fit result on top for all components as explained in the text.

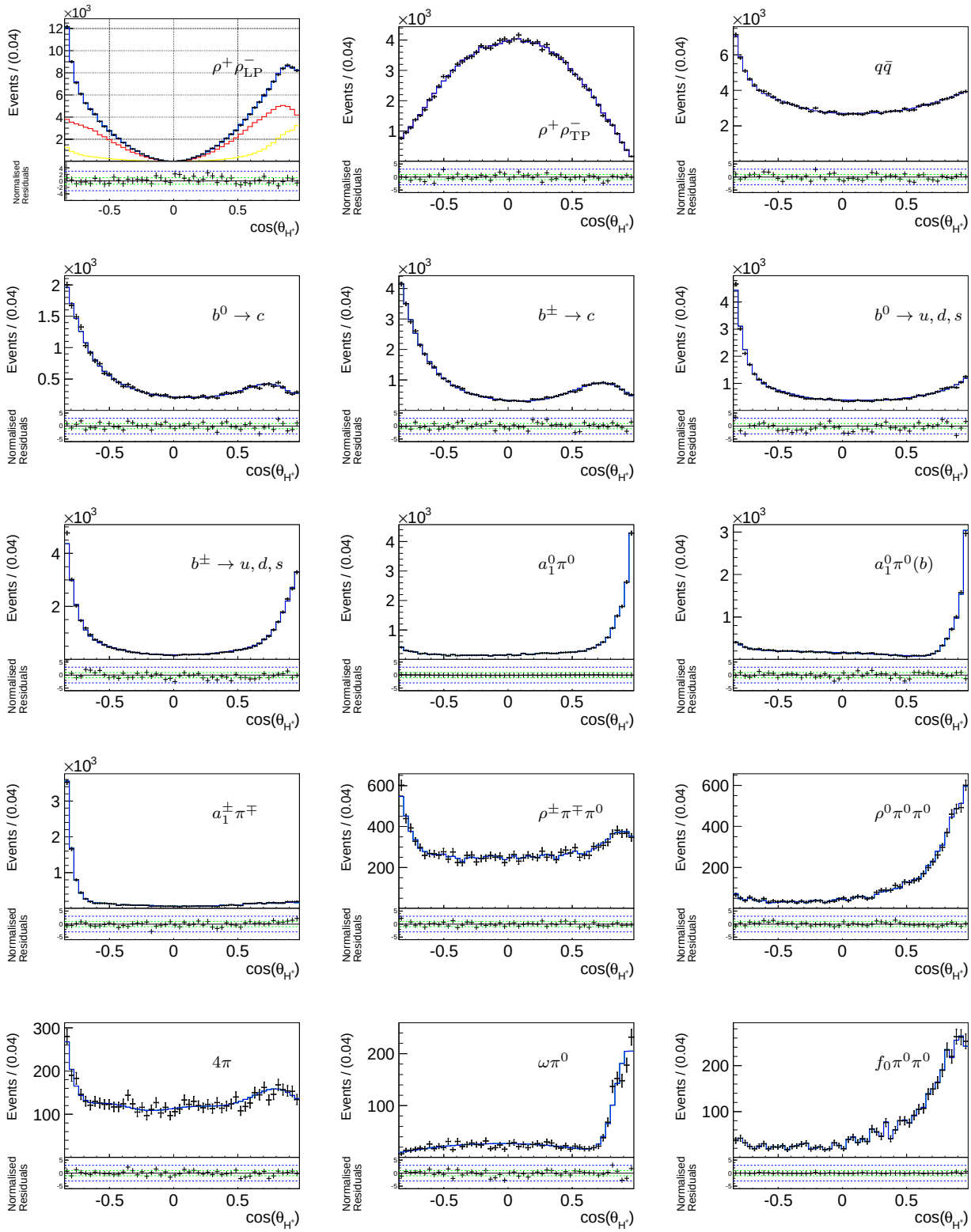

Figure 4.60: Full projections onto $\cos\theta_{\rm H}^+$ with fit result on top for all components as explained in the text.

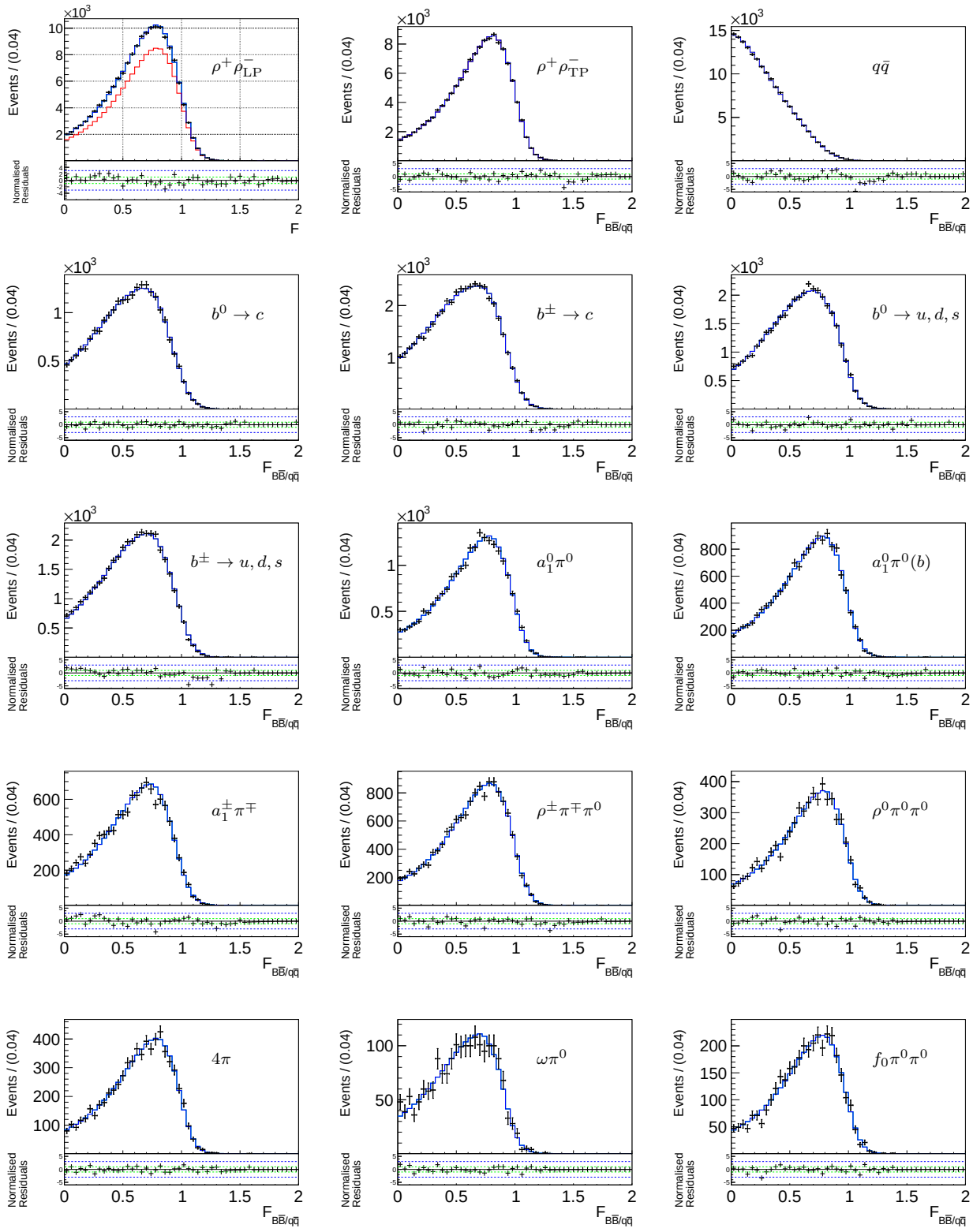

Figure 4.61: Full projections onto $\mathcal{F}_{B\bar{B}/q\bar{q}}$ with fit result on top for all components as explained in the text.

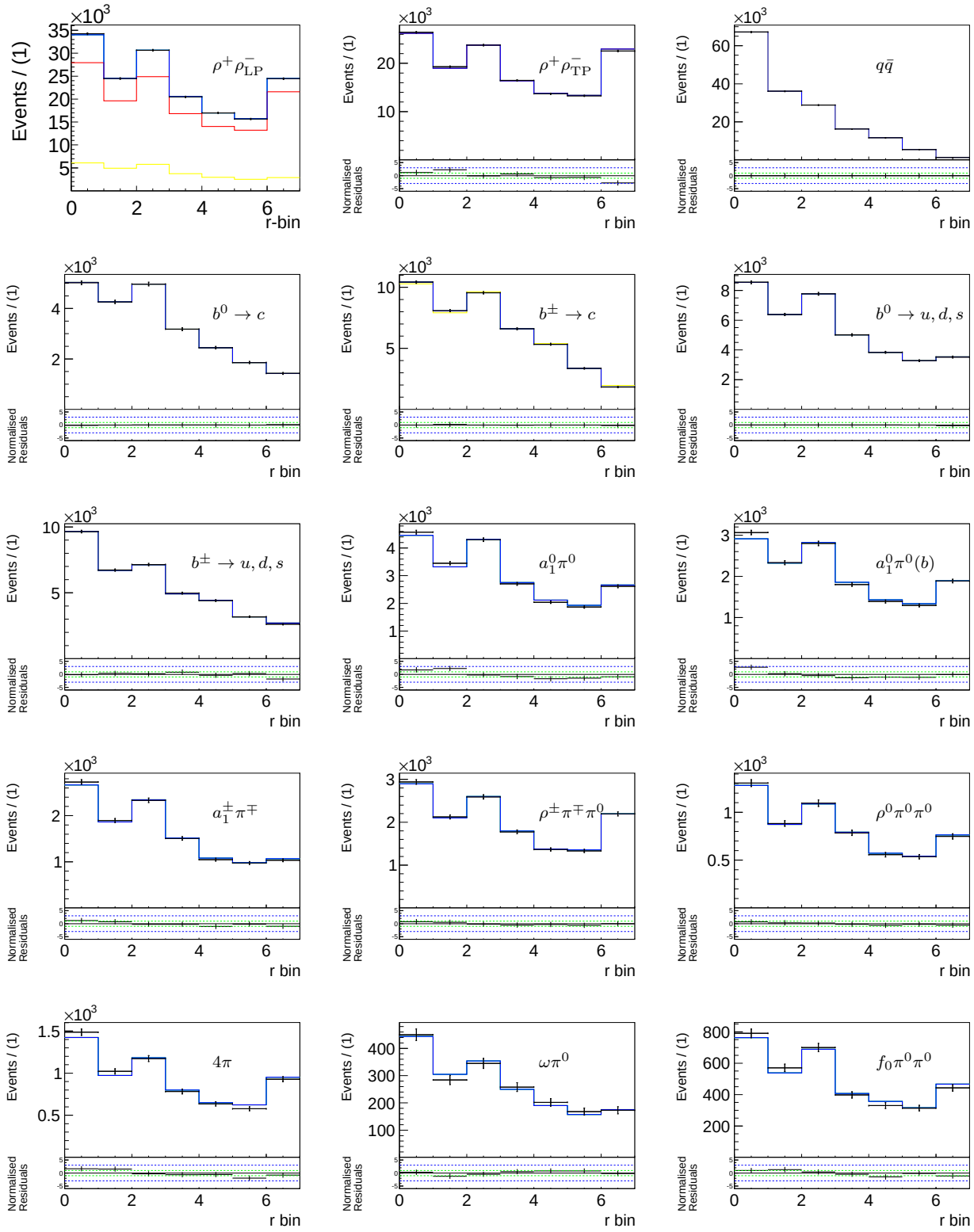

Figure 4.62: r-bin distribution with fit result on top for all components as explained in the text.

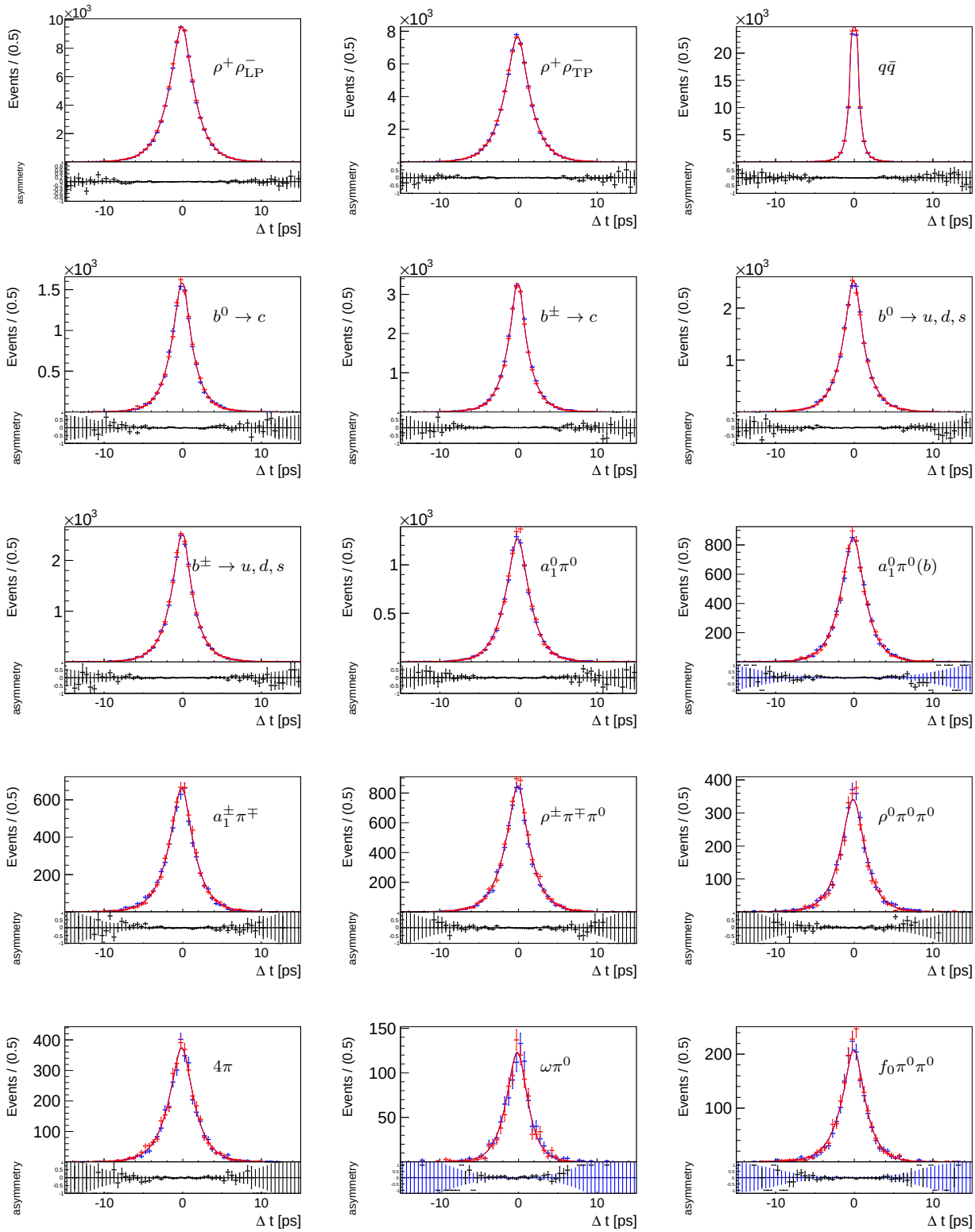

Figure 4.63: Full projections onto Δt for both flavors of $B_{\rm tag}$ with fit result on top for all components as explained in the text.

4.6 Total PDF

The total likelihood for 216176 signal candidate events in the fit region is

$$\mathcal{L} \equiv \prod_{l,s} \frac{e^{-\sum_j N_j^s \sum_{l,s} f_j^{l,s}}}{N_{l,s}!} \prod_{i=1}^{N_{l,s}} \sum_j N_j^s f_j^{l,s} \mathcal{P}_j^{l,s}(\Delta E^i, M_{\rm bc}^i, M_1^i, M_2^i, H_1^i, H_2^i, \mathcal{F}_{B\bar{B}/q\bar{q}}^i, \Delta t^i, q^i), \quad (4.72)$$

which runs over event i, component j, r-bin l and SVD configuration s.
Instead of two free signal yields $N_{\rm Sig}^s$ for each detector configuration, branching fractions for the four-pion final states (j) are chosen as single free parameters $\mathcal{B}(B \to X)$ and incorporated into the fit with

$$N_j^s = \mathcal{B}(B^0 \to f) N_{B\bar{B}}^s \epsilon_j^s \eta_\pi, \quad (4.73)$$

where ϵ_j^s are the reconstruction efficiencies as described in Sec. 3.2.10 and $\eta_\pi = \eta_{\pi^\pm} \cdot \eta_{\pi^0}$ is a correction factor to account for differences between data and MC simulation for charged particle identification ($\eta_{\pi^\pm}$) and π^0 reconstruction (η_{π^0}). The correction for charged particles is obtained from a two-dimensional look-up table depending on the momentum and polar angle of the track, see Ref. [101]. For π^0s a one-dimensional momentum dependent one is used, see [102,103]. Both tables are provided by the Belle collaboration and the uncertainties on the corrections are included in the systematic error. There is no significant difference between the several four pion final states, consequently we take the ones obtained from LP signal MC simulation, $\eta_{\pi^\pm} = 0.93 \pm 0.03$ and $\eta_{\pi^0} = 0.91 \pm 0.03$.
Because of the two possible polarizations in $B^0 \to \rho^+\rho^-$ decays, Eq. (4.73) takes the distinct forms; for example, for 'truth' $B^0 \to \rho^+\rho^-$ component with longitudinal polarization:

$$N_{\rm LP,truth}^s = \mathcal{B}(B^0 \to \rho^+\rho^-) f_L N_{B\bar{B}}^s \epsilon_{\rm LP,truth}^s \eta_{\rm PID}, \quad (4.74)$$

and similarly with $(1 - f_L)$ replacing f_L for the signal components with transverse polarization. The fraction of events in each r-bin l, for component j, is denoted by $f_j^{l,s}$. The fractions of all $B\bar{B}$ components, $f_{\rm B\bar{B}}^{l,s}$, have been calibrated with the $B^+ \to \bar{D}^0\rho^+$ control sample (see Sec. A). In the fit to data, we also float f_L, the branching ratios of the unknown four-pion final states, the yields $N_{q\bar{q}}^s$, $N_{B^0\bar{B}^0}^{{\rm charm},s}$ and $N_{B^0\bar{B}^0}^{{\rm charmless},s}$ and the parameters of the shape of the continuum model. The remaining yields and parameters are fixed to the values determined from MC simulation.

4.7 Validation Studies

We validate the fitting procedure and search for a possible fit bias with a sufficiently large number of pseudo-experiments. Each pseudo-experiments exists of MC events from all considered components, generated according to our expectation of the composition of the recorded data set. We fit each pseudo-experiment and plot the results of the observables of interest ($\mathcal{B}, f_L, \mathcal{S}_{CP}$ and $\mathcal{A}_{CP}$ of $B^0 \to \rho^+\rho^-$ decays).
Each distribution of the fit results is then fitted with with a Gaussian, whose mean should match the generated value and whose width corresponds to one statistical standard deviation. We also provide pull distributions, being defined as

$$x_p = \frac{x_{\text{observed}} - x_{\text{true}}}{\sigma_{x,\text{observed}}}, \tag{4.75}$$

where x_{observed} is the observed value from a fit, x_{true} its true value and $\sigma_{x,\text{observed}}$ the uncertainty on x_{observed}. Ideally, the pull should be Gaussian distributed with a mean of 0 and a width of 1. A shift of the mean corresponds to a bias expressed in units of the statistical uncertainty, whose reliablilty can be check from the width of the pull distribution.
Two separate validation studies (A and B) are performed.

A) For the first test of the fitter, we generate all events per experiment (almost) entirely from PDF. Component-wise, we generate random numbers for each fit variable and accept events according to the PDFs from the respective fit model. $q \cdot r$, event-dependent (for example the beam energy) and vertex-related variables needed for the calculation of the Δt PDF are distributed from fully simulated MC events. We pull the variables for continuum events from on-resonance data in order to have enough statistic.
A Gaussian fit to the distributions of the fitted physics parameters are shown in Fig. 4.64. No noticeable bias can be seen, except for $\mathcal{A}_{CP}$ where the observed bias origins from a imperfect parametrization. This bias becomes visible in this study because we use event dependent variables from fully-simulated MC events for the calculation of Δt. It is tolerable due to its small size. This study is not sensitive to correlations between the fit variables that are not accounted for in the model.

B) In the second study, randomly selected events are distributed from fully simulated MC samples (the samples we used for studying each component for the data model). Because the number of available off-resonance events is only a fraction of the continuum events in the data, continuum events are generated from PDF (like in study A).
This study provides a check of how well the fit model describes the distributions used to obtain the model, which becomes more difficult with more fit dimensions (due to mentioned correlations) and practically can only been done approximately. Especially when dealing with many backgrounds and including two often correlated (broad) masses and helicity angles in the fit, we cannot expect to be completely bias free. Hence, a bias has to be sufficiently small as it will contribute to the systematical uncertainty of the fit result.
We choose to accept a bias of $\sim$ 50% of the expected statistical uncertainty: assuming $\mathcal{B}(B^0 \to \rho^+\rho^-) = 25 \times 10^{-6}$ with an expected statistical uncertainty of $\delta\mathcal{B}(B^0 \to \rho^+\rho^-) = 1 \times 10^{-6}$ and a bias of the order of half of that size corresponds to an conservative (taken the full bias as an uncertainty) systematic uncertainty of 2%, which is acceptable. Similar arguments hold for the remaining observables of interest; $f_L, \mathcal{S}_{CP}$ and $\mathcal{A}_{CP}$.

We scan the physics parameters in a range that covers the expected values in a reasonable

way [75,76,78]. The fit results, the error and pull distributions of an example (GSIM) ensemble test are shown in Figs. 4.65 to 4.67. The full scans of the physics parameters of $B^0 \to \rho^+\rho^-$ are shown in Figs. 4.68 and 4.69. Each point corresponds to 300 pseudo-experiments and their errors to the statistical uncertainty of the fitted mean. The corresponding distributions are given in Appendix D.
While $\mathcal{S}_{CP}$ and f_L show no noteworthy bias, we notice a small and therefore acceptable bias of $\sim 0.5\sigma$ for the branching fraction and also for $\mathcal{A}_{CP}$, both originating from unaccounted correlations in the model description. The bias of $\mathcal{A}_{CP}$ is consistent within the two studies and since the measured $\mathcal{A}_{CP}$ is consistent with zero, the increase of the bias with larger direct CP violation can be overlooked. We correct the branching fraction by -0.5×10^{-6} and $\mathcal{A}_{CP}$ by -0.04 in the fit result. The corrections are obtained from an ensemble test with large statistic, generated according to the fit result. The systematic uncertainties due to fit biases are estimated in Chapter 6.

4.7.1 Lifetime Fit

We check the Δt PDF by extracting the B^0 lifetime from the data, where we fix $\mathcal{S}_{CP} = 0$ and $\mathcal{A}_{CP} = 0$ of $B^0 \to \rho^+\rho^-$. We obtain

$$\tau_{B^0} = 1.41 \pm 0.11 \text{ ps}, \tag{4.76}$$

being in good agreement with the current world average; $\tau_{B^0} = 1.52 \pm 0.07$ ps [45].

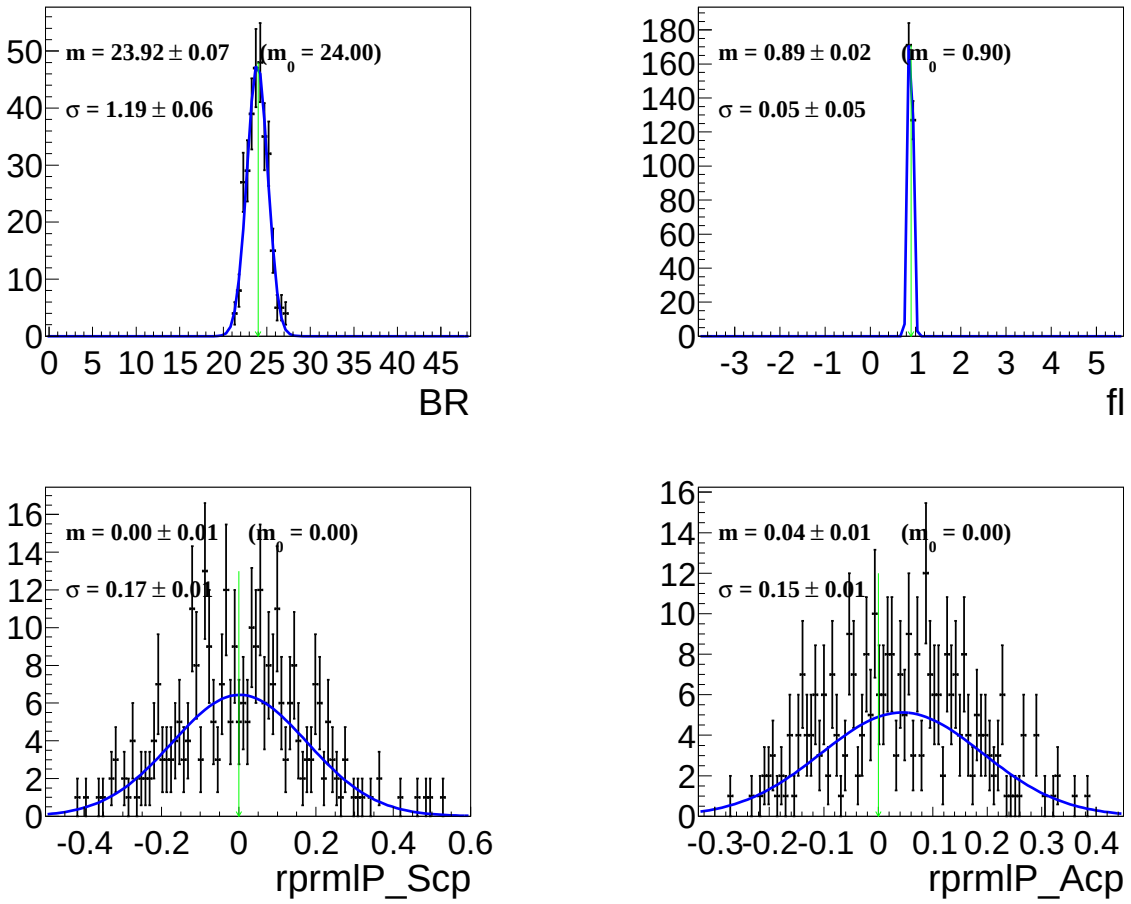

Figure 4.64: Fit results from pseudo experiments generated from PDF (A) and fitted with a Gaussian. The generated values are indicated by the green arrow.

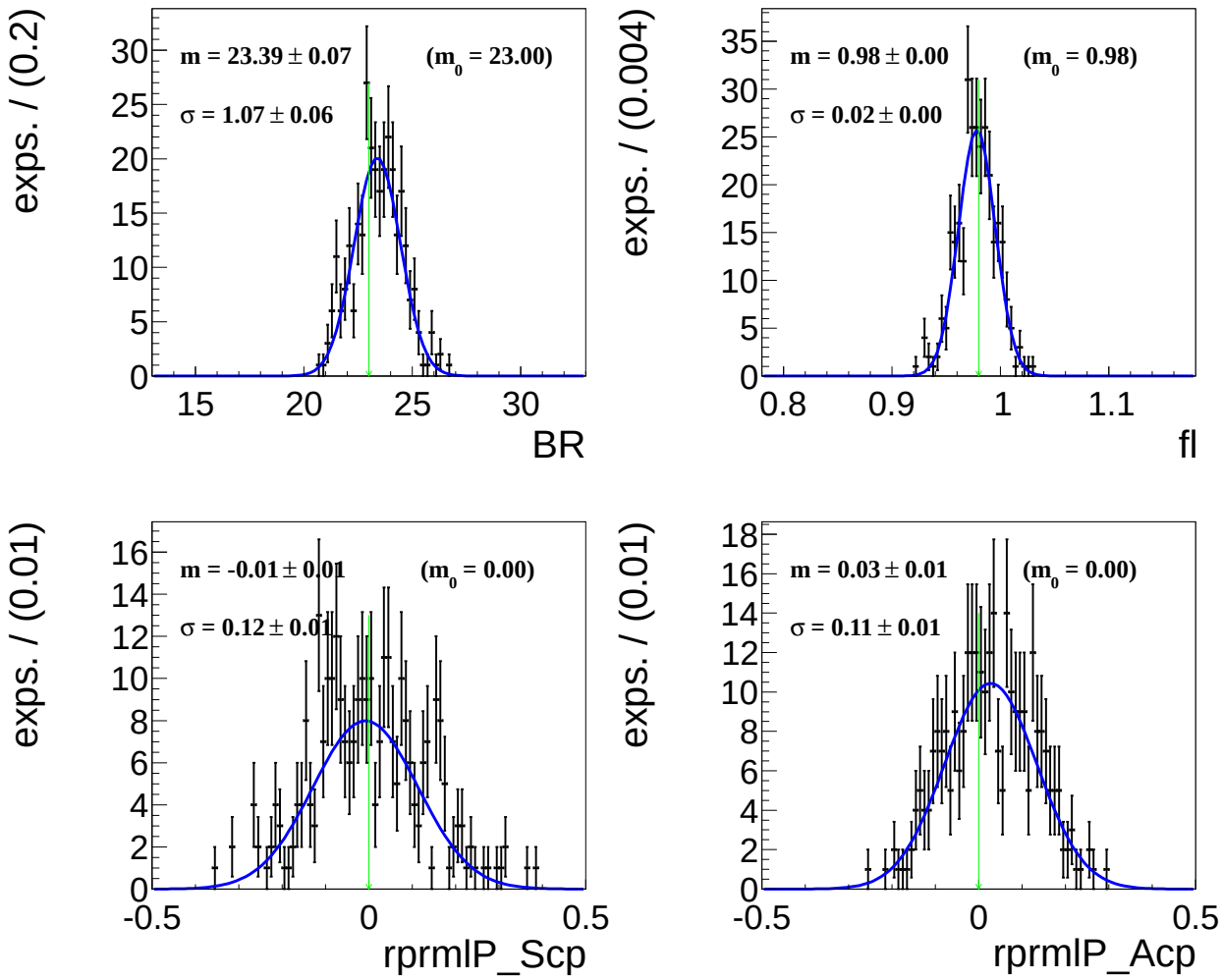

Figure 4.65: Fit results from pseudo experiments generated from fully simulated MC events (B) fitted with a Gaussian. The generated values are indicated by the green arrow.

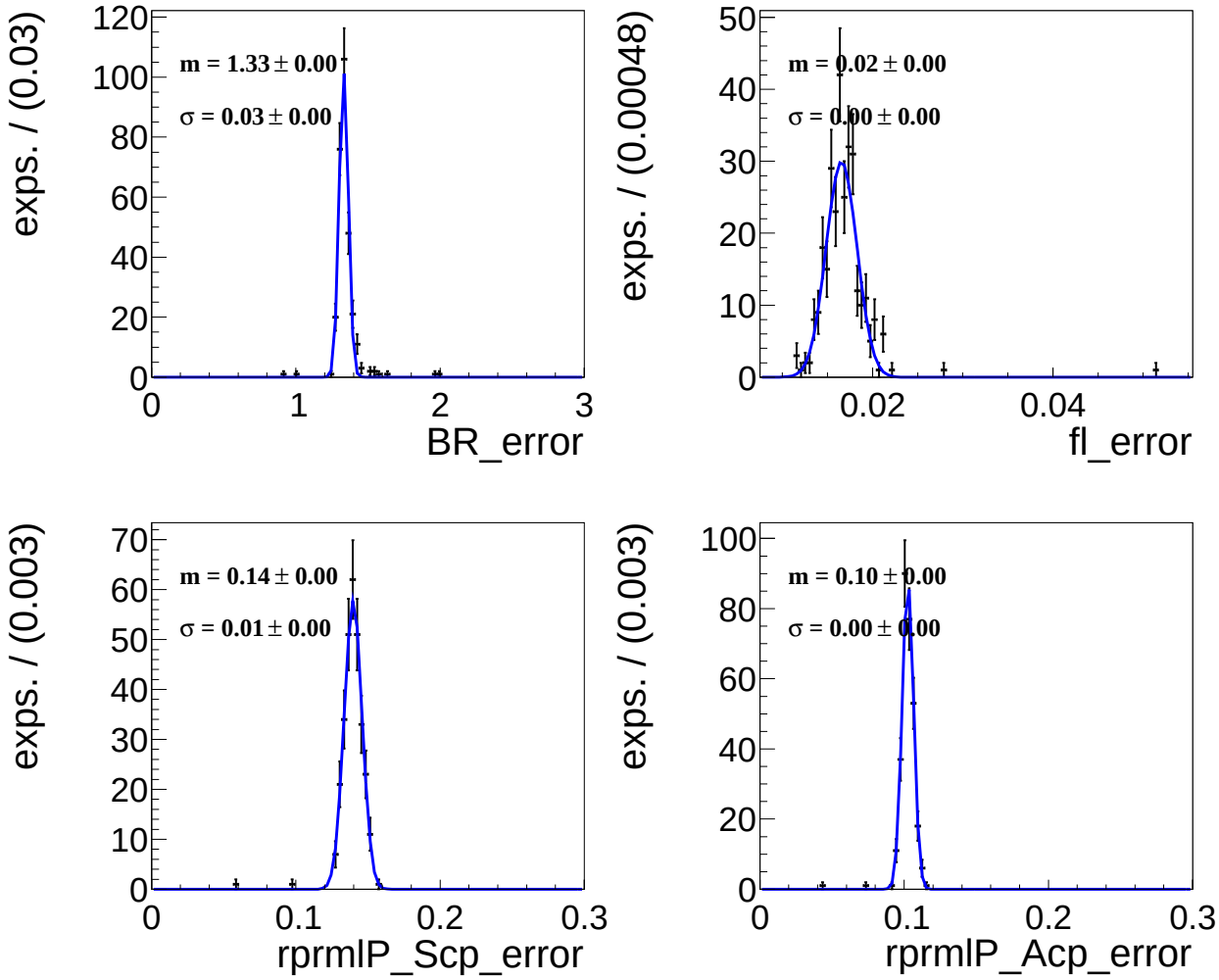

Figure 4.66: Error distributions from the fits to pseudo experiments generated from fully simulated MC events (B) fitted with a Gaussian.

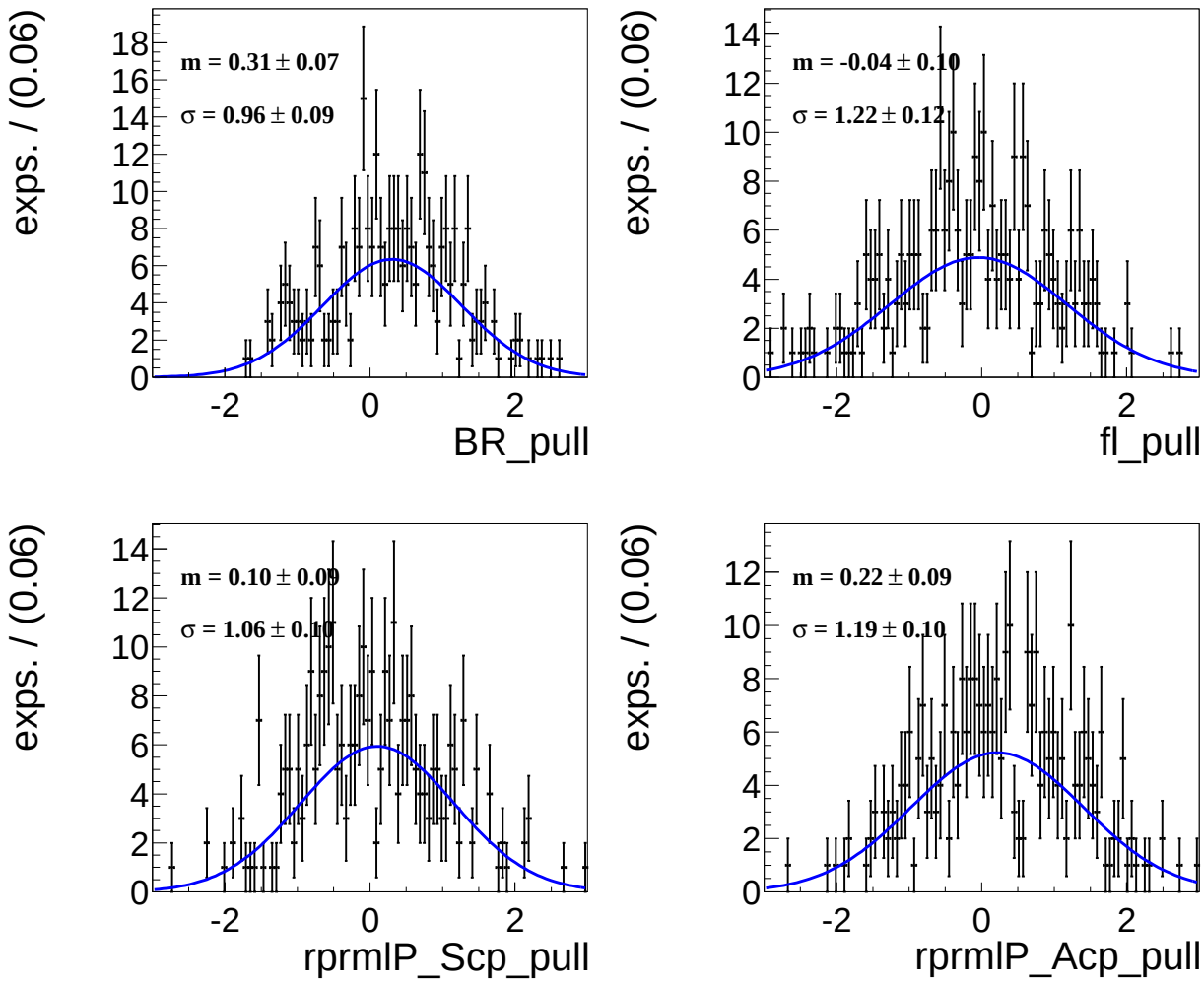

Figure 4.67: Pull distributions from the toy MC studies (B) fitted with a Gaussian.

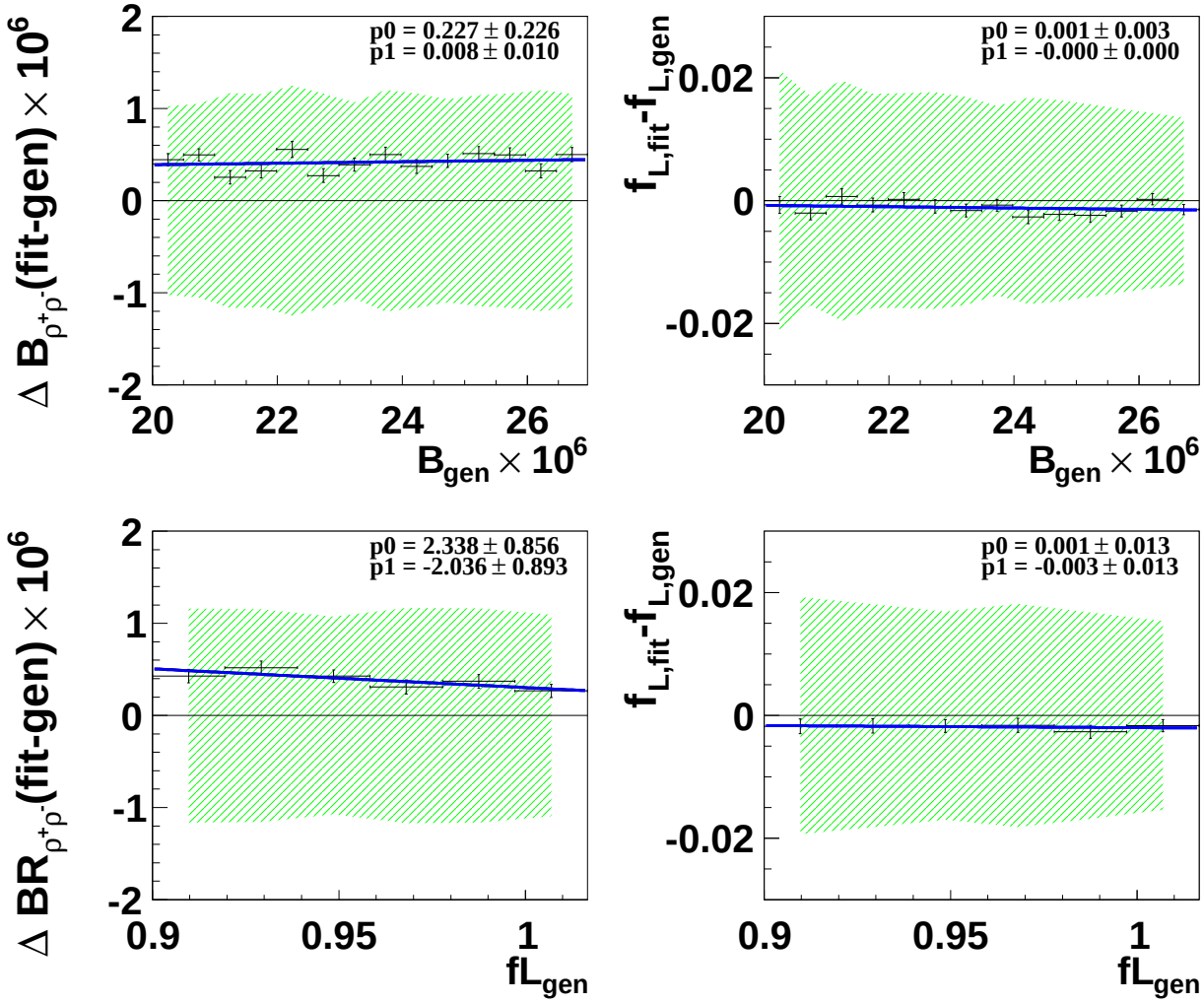

Figure 4.68: The difference of the fitted and the generated value versus generated values of either $\mathcal{B}(B^0 \to \rho^+\rho^-)$ or f_L from fitting fully simulated MC events (B). The green shaded area corresponds to the statistical uncertainty in each point. Remark: we performed this study without using the efficiency correction factors η_π in the yield calculation from the branching fraction, see expression Eq. (4.73). Thefore the the observed yield is included in the range of considered branching fractions.

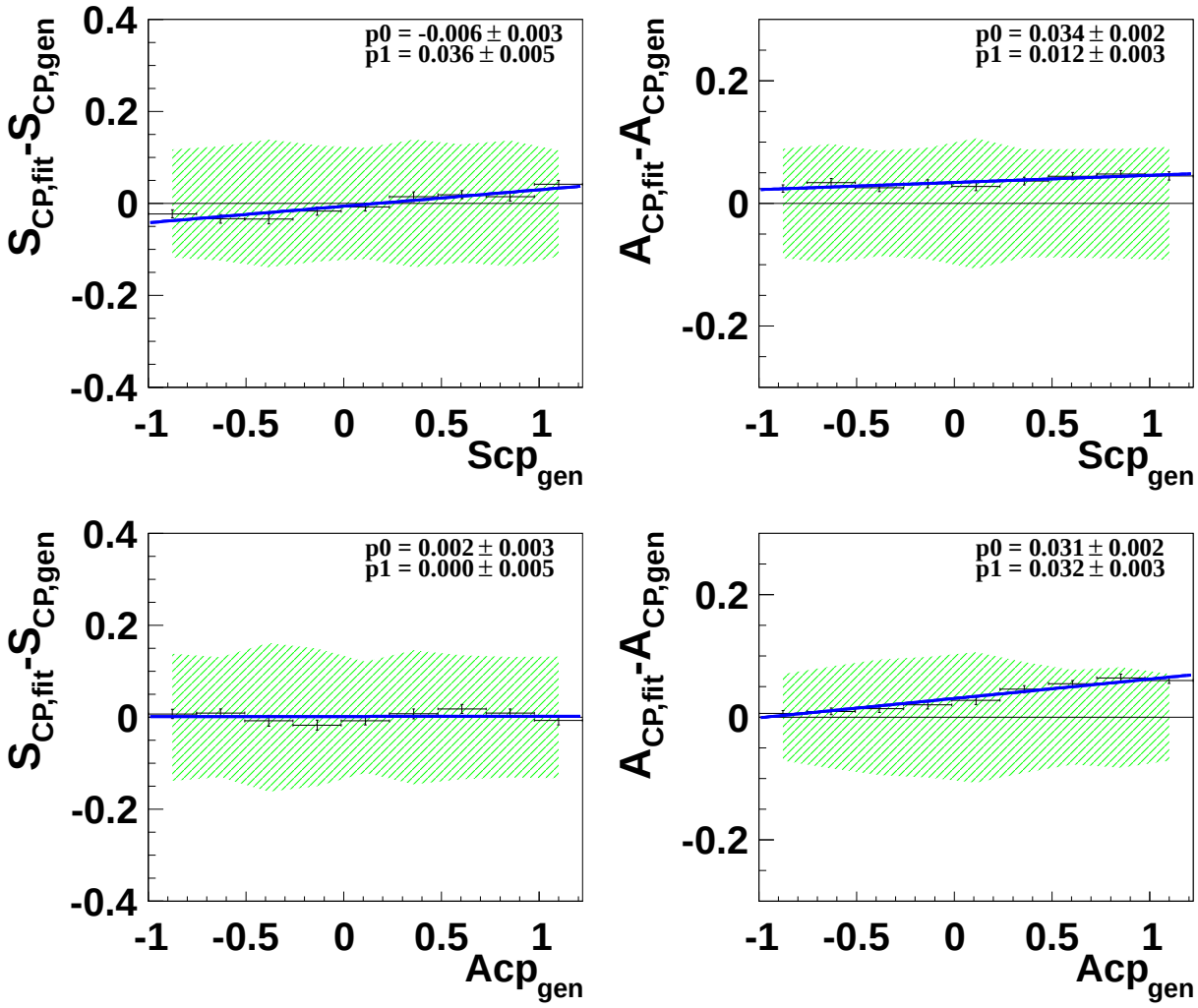

Figure 4.69: The difference of the fitted and the generated value versus the generated values of either $\mathcal{S}_{CP}$ or $\mathcal{A}_{CP}$ from fitting fully simulated MC samples (B). The green shaded area corresponds to the statistical uncertainty in each point.

Chapter 5

Fit Result

We perform a fit to Belle's final data set of 772×10^6 $B\bar{B}$ pairs yielding in 216176 signal candidates after the reconstruction. We obtain the following result

$$\begin{aligned} \mathcal{B}(B^0 \to \rho^+\rho^-) &= (28.3 \pm 1.5\ (\text{stat}) \pm 1.5\ (\text{syst})) \times 10^{-6}, & (5.1)\\ f_L &= 0.988 \pm\ 0.012\ (\text{stat}) \pm 0.02\ (\text{syst}), & (5.2)\\ \mathcal{S}_{CP} &= -0.13 \pm 0.15\ (\text{stat}) \pm 0.06\ (\text{syst}), & (5.3)\\ \mathcal{A}_{CP} &= 0.00 \pm 0.10\ (\text{stat}) \pm 0.08\ (\text{syst}). & (5.4) \end{aligned}$$

This corresponds to 1754 ± 94 and 21 ± 22 $B^0 \to \rho^+\rho^-$ events with longitudinal and transverse polarization, respectively. The correlations of the observables are given in Table 5.1. Full and signal enhanced projections onto the fit variables are shown in Figs. 5.1 to 5.4 and Figs. 5.5 to 5.8, respectively. The data is well described by the model. Asymmetric statistical uncertainties are obtained with MINOS [99] (see Section 4.1.1). Assuming Gaussian distributed variables, the likelihood function behaves like a χ^2 distribution [104]. All statistical upper and lower errors are identical in the quoted precision and therefore symmetrized. The systematic uncertainties are evaluated as described in Sect. 6.
Our result is in good agreement with previous measurements [75, 76, 78] and significantly improves the uncertainties of all four observables, see Table 1.3 for a comparison. This is currently the most precise measurement of the branching fraction and polarization fraction as well as the tightest constraint on CP violation in this mode.

Furthermore, we obtain 224 ± 113 $B^0 \to \pi^+\pi^0\pi^-\pi^0$, 175 ± 129 $B^0 \to \rho^\pm\pi^\mp\pi^0$ and -138 ± 68 $B^0 \to a_1^0\pi^0$ events, where the uncertainties are statistical only. None of these modes give a significant contribution, even without including systematic uncertainties, which are estimated to be significantly larger compared to the one from $B^0 \to \rho^+\rho^-$. We also exclude a significant contribution from $B^0 \to \rho^0\pi^0\pi^0$ as explained in Section 5.2.

	$\mathcal{B}(B^0 \to \rho^+\rho^-)$	f_L	$\mathcal{A}_{CP}$	$\mathcal{S}_{CP}$
$\mathcal{B}(B^0 \to \rho^+\rho^-)$	1	-0.228	-0.031	-0.015
f_L		1	0.003	0.026
$\mathcal{A}_{CP}$			1	0.018
$\mathcal{S}_{CP}$				1

Table 5.1: Correlation matrix as obtained from the fit to data.

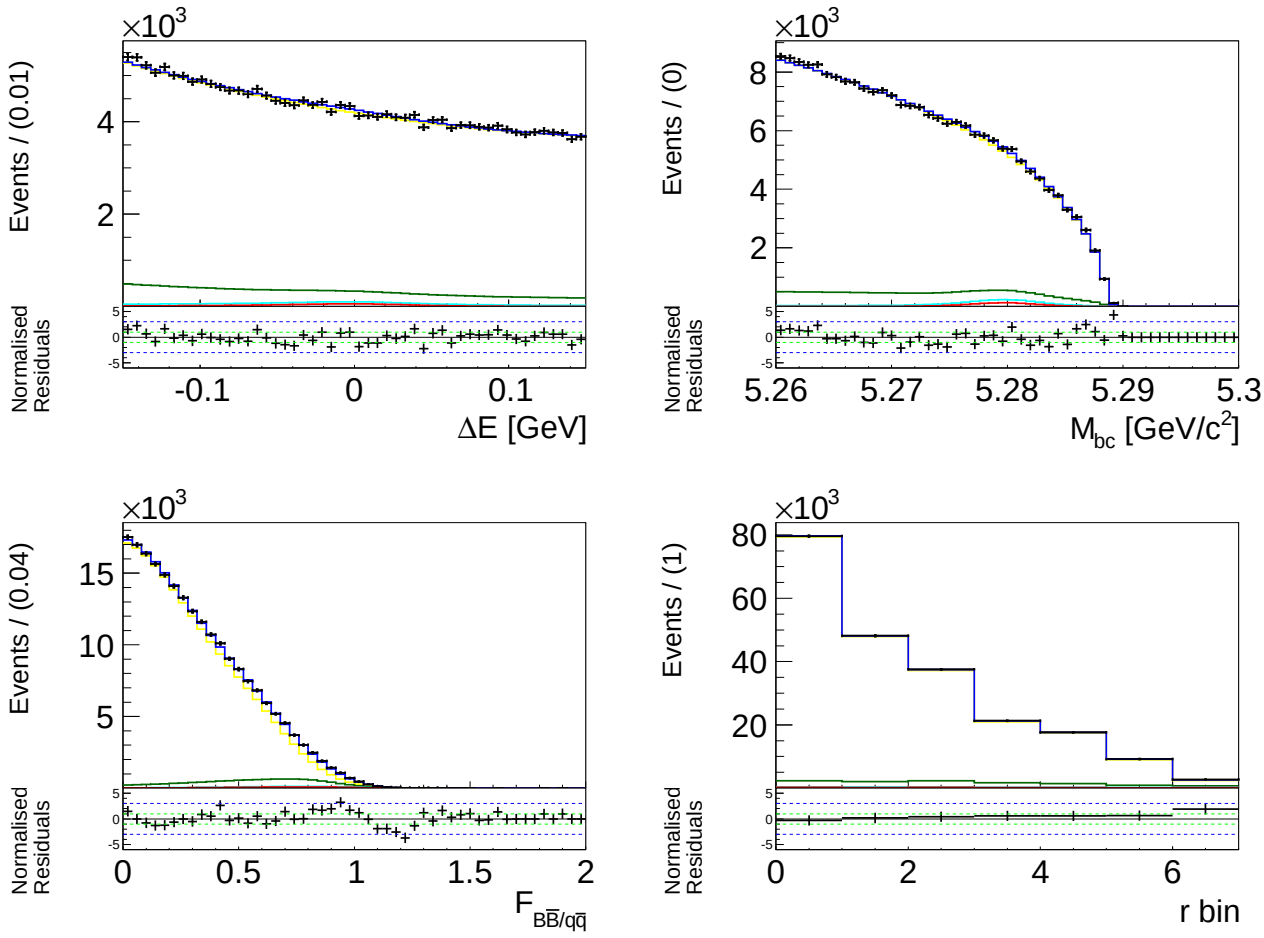

Figure 5.1: Full projections onto ΔE and $M_{\rm bc}$ (top) and $\mathcal{F}_{B\bar{B}/q\bar{q}}$ as well as the r-bin fractions (bottom) from the fit to data. Signal is shown in red, the $B\bar{B}$ background in green, the combined backgrounds in yellow and the total PDF in blue. Data are shown as black points.

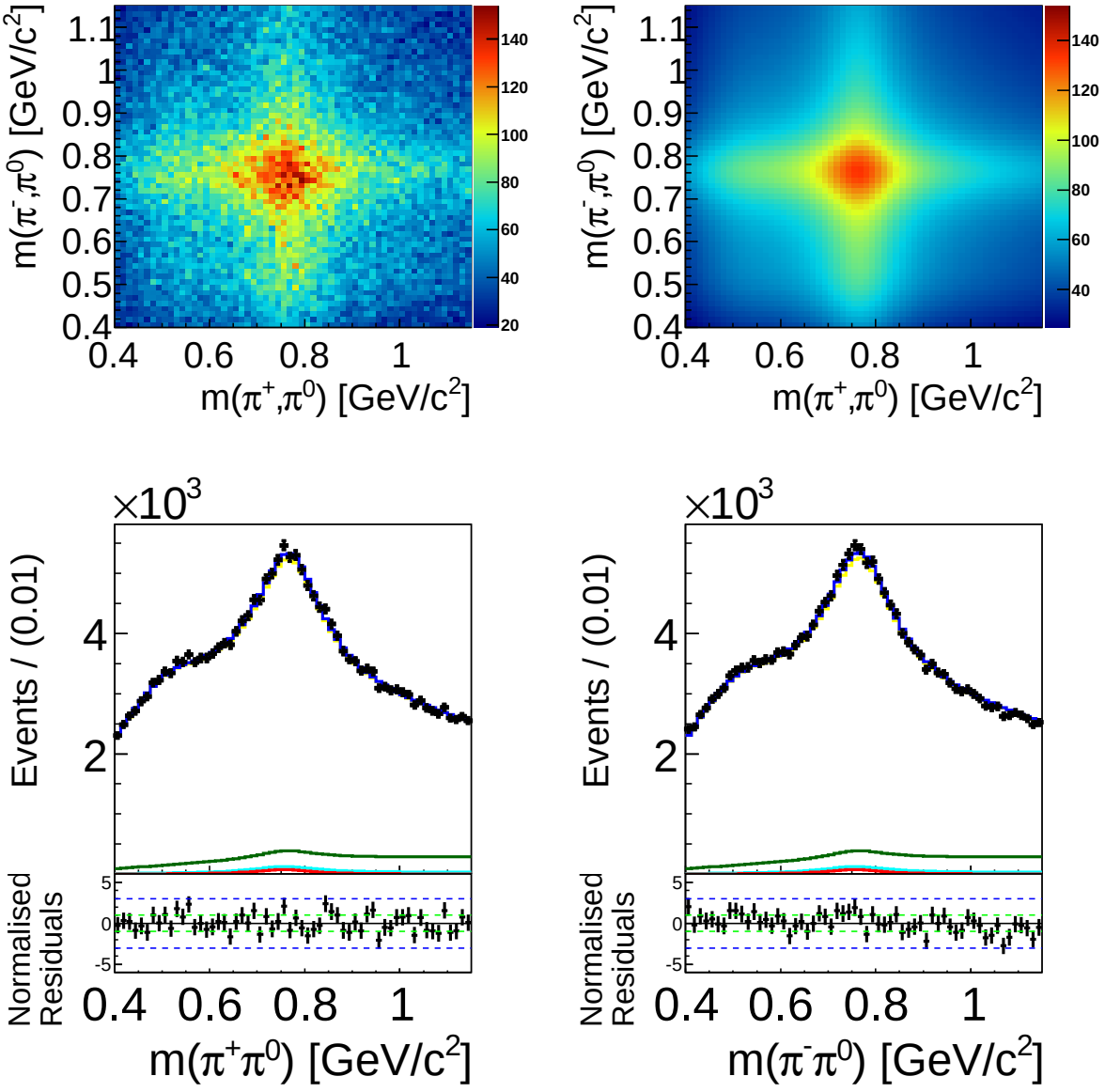

Figure 5.2: Full projections onto the dipion masses from the fit to data. Signal is shown in red, the $B\bar{B}$ background in green, the combined backgrounds in yellow and the total PDF in blue. Data are shown as black points.

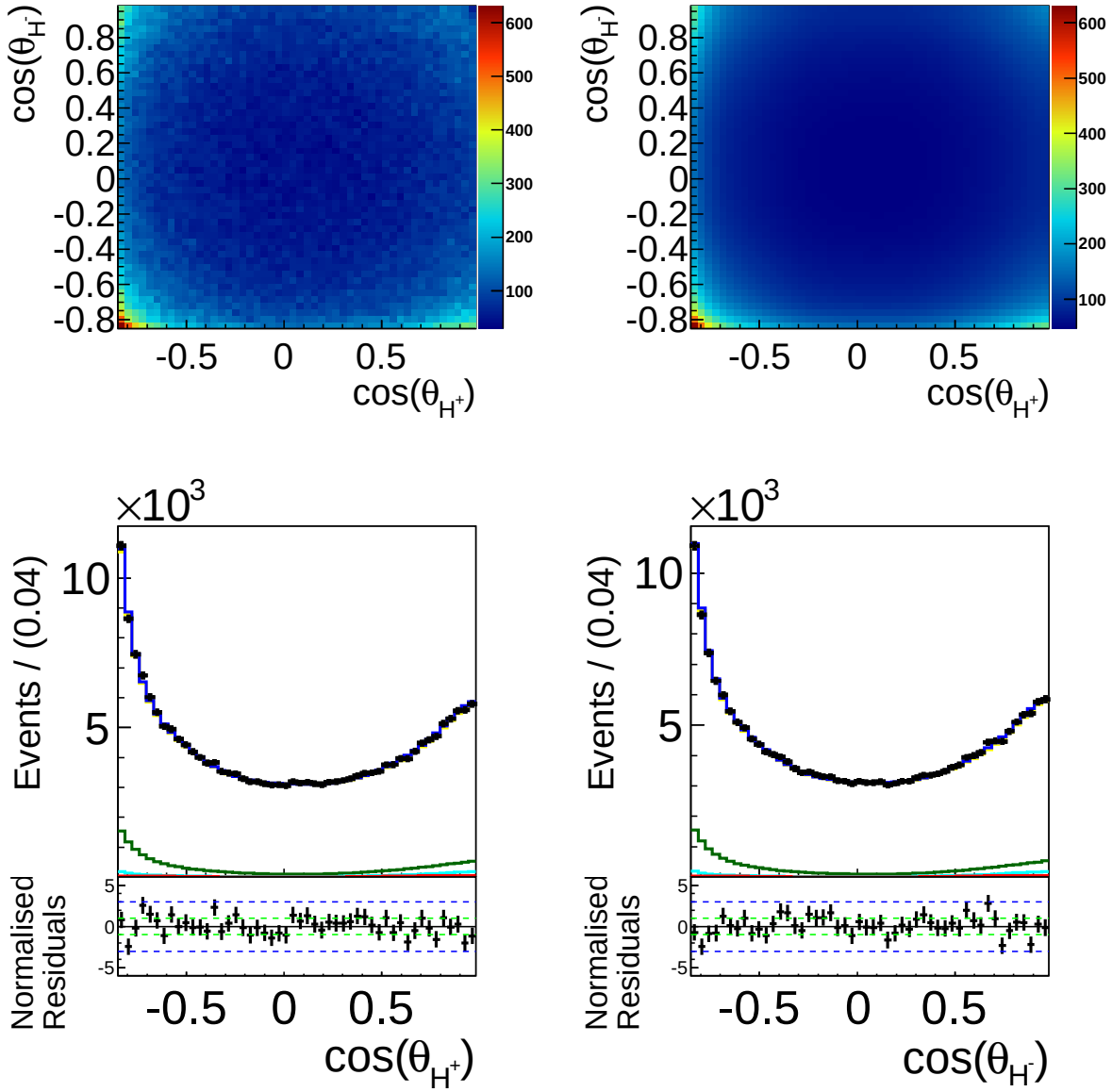

Figure 5.3: Full projections onto the helicity angles from the fit to data. Signal is shown in red, the $B\bar{B}$ background in green, the combined backgrounds in yellow and the total PDF in blue. Data are shown as black points.

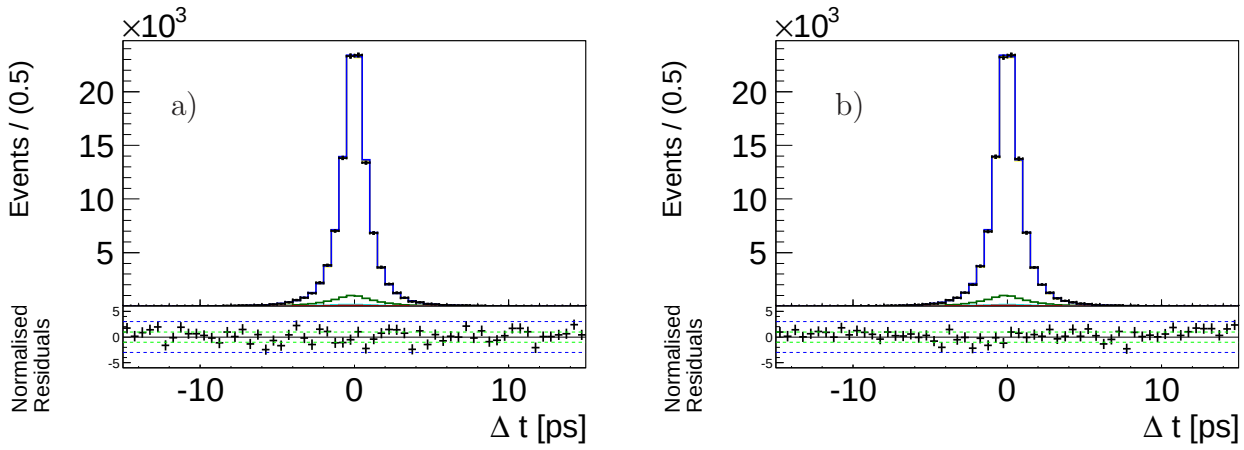

Figure 5.4: Full projections onto Δt for a) $B_{\rm tag} = B^0$ and b) $B_{\rm tag} = \bar{B}^0$ from the fit to data. Signal is shown in red, the $B\bar{B}$ background in green, the combined backgrounds in yellow and the total PDF in blue. Data are shown as black points.

5.1 Signal Enhanced Fit Projections

We project onto the fit variables while drastically reducing the background contributions with hard cuts on other variables. This allows to visualize the signal contribution in the distributions. The signal enhanced region is defined as

$$\begin{aligned} |\Delta E| < 0.1 \text{ GeV}, \quad M_{\text{bc}} > 5.275 \text{ GeV/c}^2, \\ 0.62 < m_{\pi^+\pi^0}, m_{\pi^-\pi^0} < 0.92 \text{ GeV/c}^2, \\ \mathcal{F}_{B\bar{B}/q\bar{q}} > 0.5, \quad r-\text{bin} > 2, \end{aligned} \tag{5.5}$$

where each projected variable is accepted in its entire analysis region. We retain $10\% - 16\%$ of signal, being visible especially in the distributions of ΔE and M_{bc}. Because the CP violating parameters are consistent with zero, no asymmetry can be observed, see Fig. 5.5.

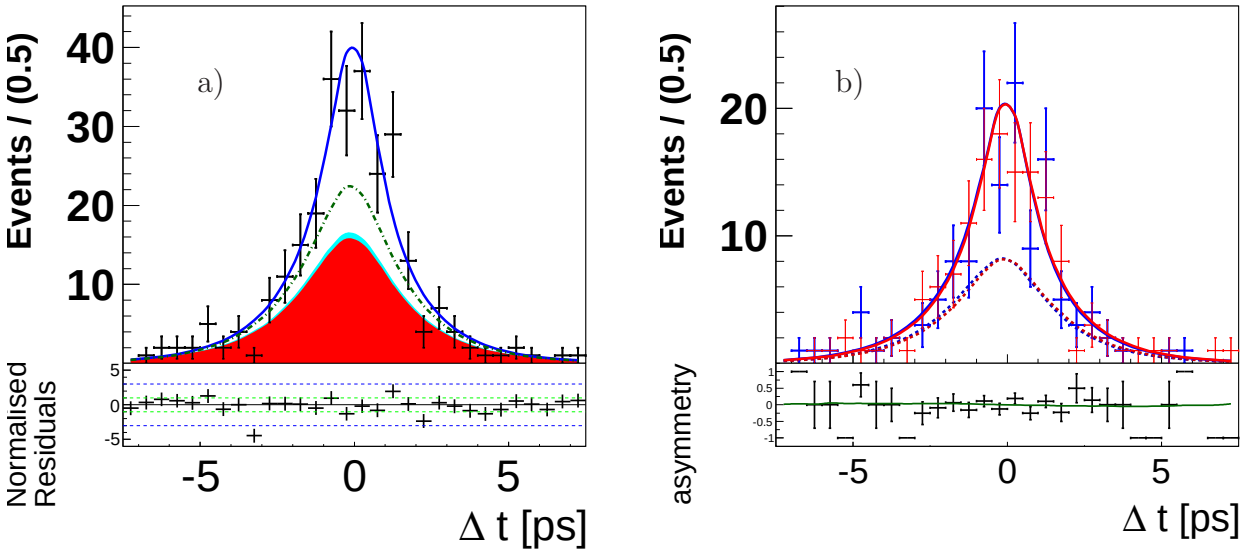

Figure 5.5: Signal enhanced projections (see text) onto Δt from the fit to data. a) flavor integrated projection, where signal is shown in red, the $B\bar{B}$ background in green, the combined backgrounds in yellow and the total PDF in blue, while data is shown as black points. The residuals are given below. b) shows the data distributions in red for $B_{\text{tag}} = B^0$ and in blue for $B_{\text{tag}} = \bar{B}^0$ with the fit results on top. The $B^0 \to \rho^+\rho^-$ contribution is shown as dashed lines and the resulting asymmetry is plotted below.

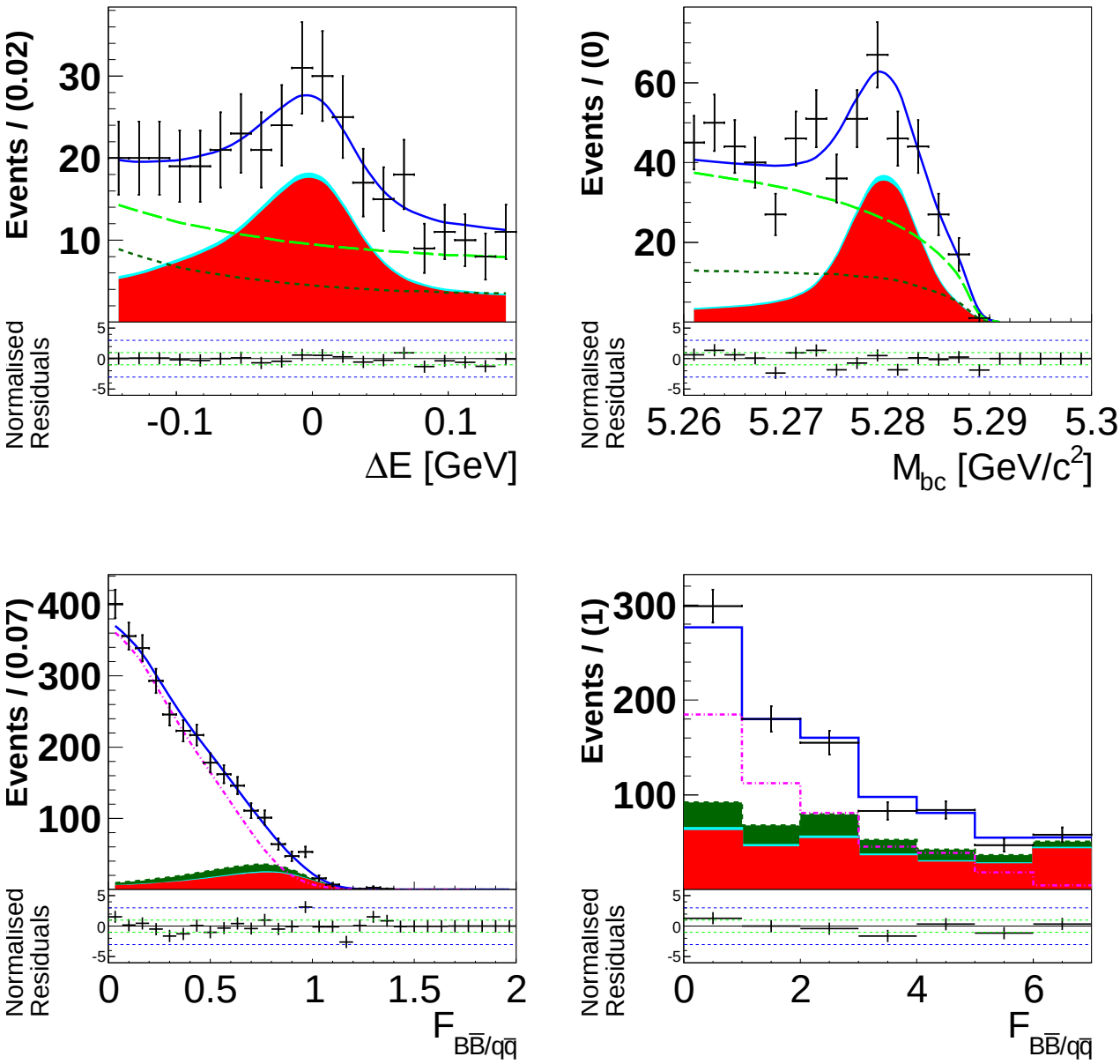

Figure 5.6: Signal enhanced projections (see text) onto ΔE and $M_{\rm bc}$ (top) and $\mathcal{F}_{B\bar{B}/q\bar{q}}$ (bottom) from the fit to data. Signal is shown in red, all four pion final states in cyan, the $B\bar{B}$ background in green and the total PDF in blue. The non-peaking background is shown as a dashed light green line and continuum is shown separately in magenta. Data are shown as black points.

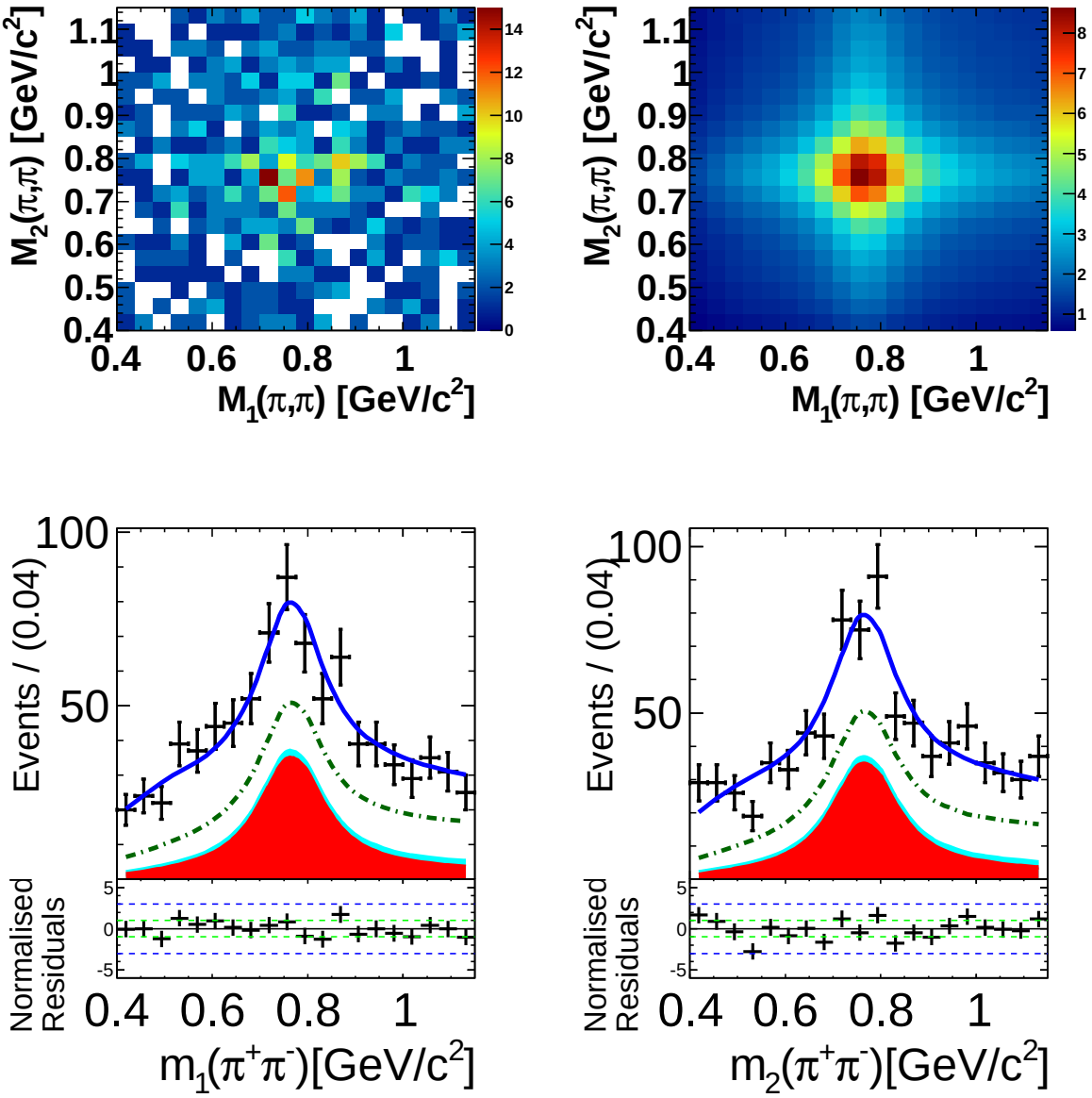

Figure 5.7: Signal enhanced projections (see text) onto the dipion masses from the fit to data. Signal is shown in red, all four pion final states in cyan, the $B\bar{B}$ background in green and the total PDF in blue.

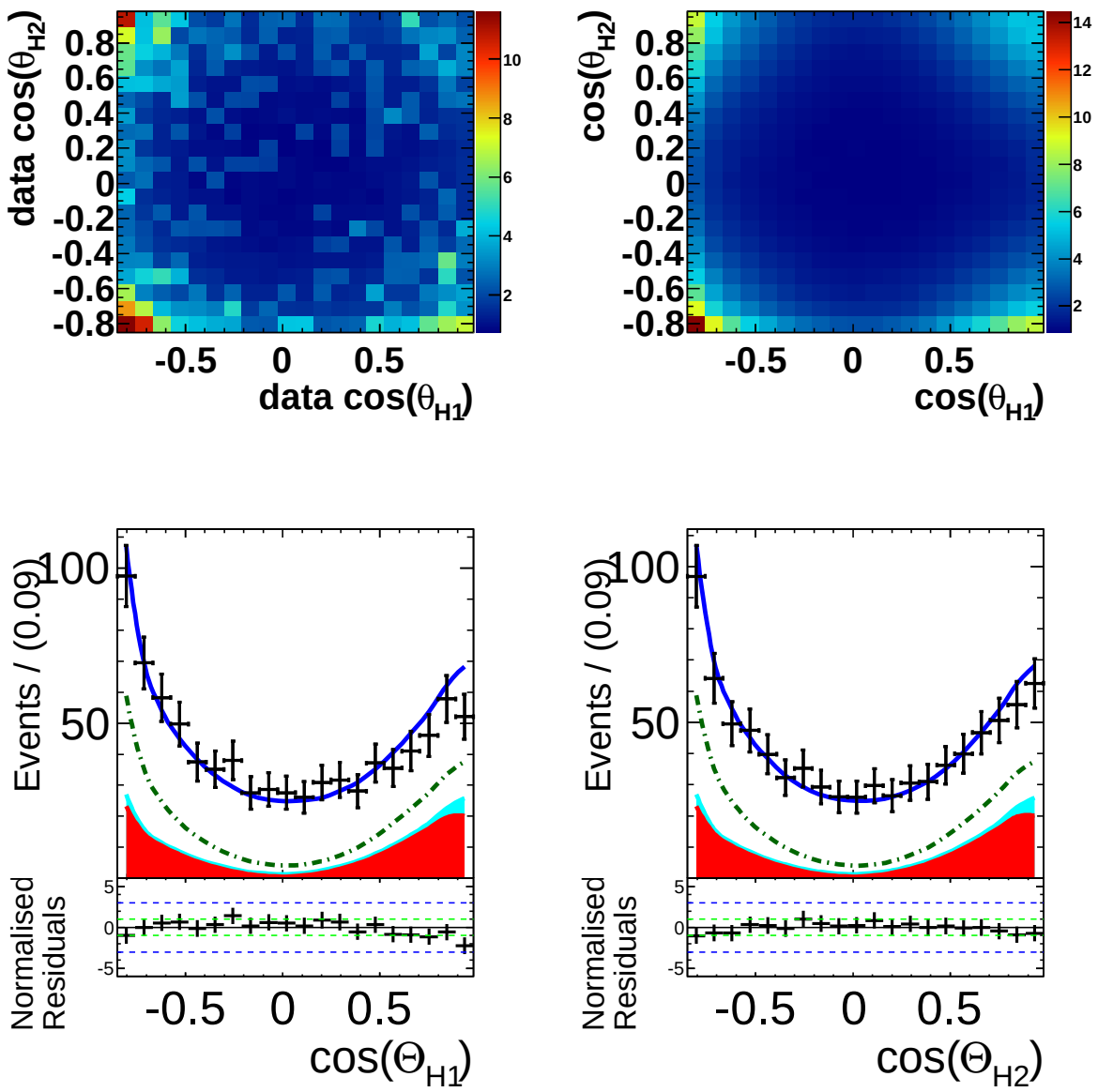

Figure 5.8: Signal enhanced projections (see text) onto the helicity angles from the fit to data. Signal is shown in red, all four pion final states in cyan, the $B\bar{B}$ background in green and the total PDF in blue.

5.2 Additional Contributions

We find an unexpected high yield of 625 ± 90 $B \to \rho^0\pi^0\pi^0$ events in the fit to data. Isospin allows to relate the amplitude of $B \to \rho^0\pi^0\pi^0$ decays to the one of $B \to \rho^0\pi^+\pi^-$, being unobserved up to date, hence only an upper limit of $\mathcal{B}(B \to \rho^0\pi^+\pi^-) < 12 \times 10^{-6}$ [5] exists. Using Clebsh-Gordan coefficients yields in half the rate, which conflicts with the seen excess. As a first check, we fix the yield of $B \to \rho^0\pi^0\pi^0$ to zero in the fit to data, which gives an increase of only $+64$ $B^0 \to \rho^+\rho^-$ events corresponding to $\sim 0.6\times$ statistical standard deviations. Consequently, no strong correlation with the signal component is present.

When reconstructing $B^0 \to \rho^+\rho^-$ from $B \to \rho^0\pi^0\pi^0$ decays the resulting helicity distribution is mainly driven by the kinematics of the decay. Constraining the charged pions within a ρ^0 mass window, results in a very distinct signature in the helicity angle distribution, as shown in Fig. 5.9. This correlation is also found in the $B\bar{B}$ and continuum backgrounds, see Figs. 5.10 and 5.11. The fraction of these events is 3-5% in $B\bar{B}$ decay MC simulation and off-resonance data. In this region, $B\bar{B}$ background events can only be distinguished from $B \to \rho^0\pi^0\pi^0$ decays in the ΔE and $M_{\rm bc}$ distributions. Because either $\cos\theta_{\rm H}^+$ or $\cos\theta_{\rm H}^-$ is always close to $+1$, the helictiy distribution provides a powerfull separation. Therefore, events in this kinamtic region have a higher probability to be identified as $B \to \rho^0\pi^0\pi^0$ events by the fit, if the correlation is not appropriately accounted for or the contribution is underestimated in other backgrounds.

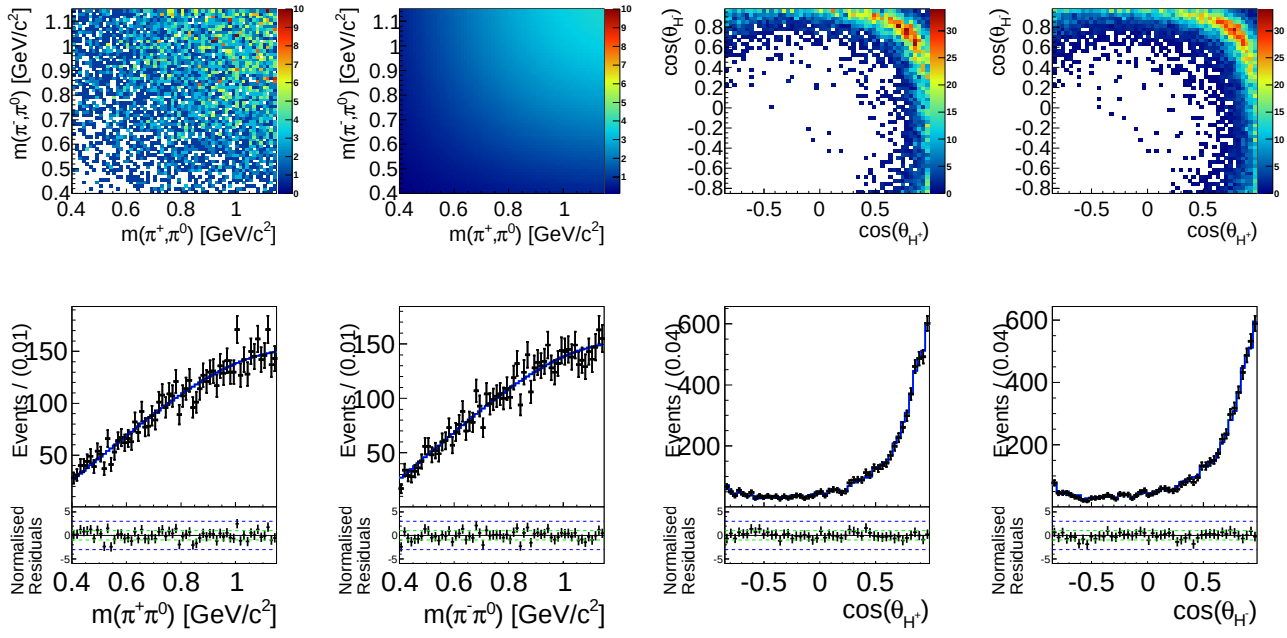

Figure 5.9: The dipion mass and helicity angle distributions from $B \to \rho^0\pi^0\pi^0$ MC siumlation.

We introduce a new component similar to $B \to \rho^0\pi^0\pi^0$ decays, where we substitute the PDFs for ΔE,$M_{\rm bc}$,$\mathcal{F}_{B\bar{B}/q\bar{q}}$ and Δt with those obtained from studying the $B\bar{B}$ backgrounds,

$$\begin{aligned}\mathcal{PDF}_{\rm kin}(\Delta E, M_{\rm bc}, m_{\pi^+\pi^0}, m_{\pi^-\pi^0}, \cos\theta_{\rm H}^+, \cos\theta_{\rm H}^-, \mathcal{F}_{B\bar{B}/q\bar{q}}, \Delta t, q) = \\ \mathcal{P}_{B\bar{B}}(\Delta E) \times \mathcal{P}_{B\bar{B}}(M_{\rm bc}) \;\times\; \mathcal{P}^k_{B\bar{B}}(\mathcal{F}_{B\bar{B}/q\bar{q}}) \times \mathcal{P}_{B\bar{B}}(\Delta t, q) \times \\ \mathcal{P}_{\rho^0\pi^0\pi^0}(\cos\theta_{\rm H}^+, \cos\theta_{\rm H}^-) \times \mathcal{P}_{\rho^0\pi^0\pi^0}(m_{\pi^+\pi^0}) \times \mathcal{P}_{\rho^0\pi^0\pi^0}(m_{\pi^-\pi^0}). \end{aligned} \tag{5.6}$$

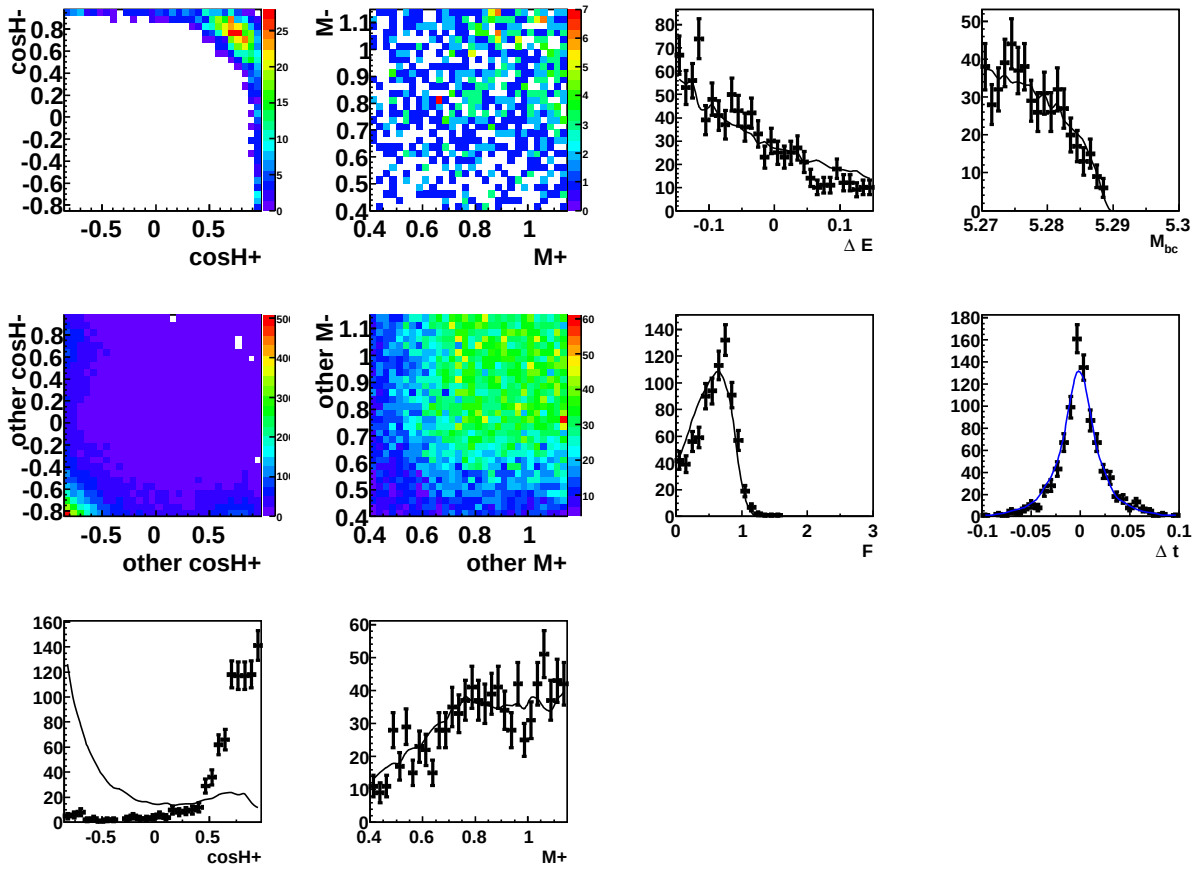

Figure 5.10: Constraining the invariant mass $m(\pi^+\pi^-)$ to be inside or outside (other) of $0.57\text{GeV/c}^2 < m(\pi^+\pi^-) < 0.97\text{GeV/c}^2$ yields in the shown distributions of the fit variables of generic B decay MC simulation. Events from within (outside) the $m(\pi^+\pi^-)$ constraint are shown as black points (line) in the one-dimensional projections.

We relate the yield of this component to the one of $B \to \rho^0\pi^0\pi^0$ decays via

$$N_{\text{new}} = f_{\text{kin}} N_0, \quad \text{and} \quad N_{\rho^0\pi^0\pi^0} = (1 - f_{\text{kin}}) N_0, \tag{5.7}$$

where N_0 is the original yield of $B \to \rho^0\pi^0\pi^0$ decays and floating the fraction f_{kin} in the fits allows to determine the source of this unexpected yield. We obtain $f_{\text{kin}} = 1.12 \pm 0.16$ from a fit to the data, so clearly the $B\bar{B}$ background hypothesis is favored over $B \to \rho^0\pi^0\pi^0$.

In a similar manner we test a continuum hypothesis where we substitute the PDFs with those from the continuum model. Because of the additional separation power from $\mathcal{F}_{B\bar{B}/q\bar{q}}$ and Δt, the overlapp is smaller. We obtain $f_{\text{kin}}^{q\bar{q}} = 0.04 \pm 0.12$ and therefore exclude the continuum hypothesis.

We use the $B\bar{B}$ background hypothesis and fix $f_{\text{kin}} = 1$ in the final fit to data. Compared to our original fit, the fit result is rather stable. We notice a small difference of $+0.6 \times 10^{-6}$, -0.001, $+0.002$ and $+0.004$ of the branching fraction of $B^0 \to \rho^+\rho^-$, f_L, $\mathcal{A}_{CP}$ and $\mathcal{S}_{CP}$, respectively, and update the fit result accordingly.

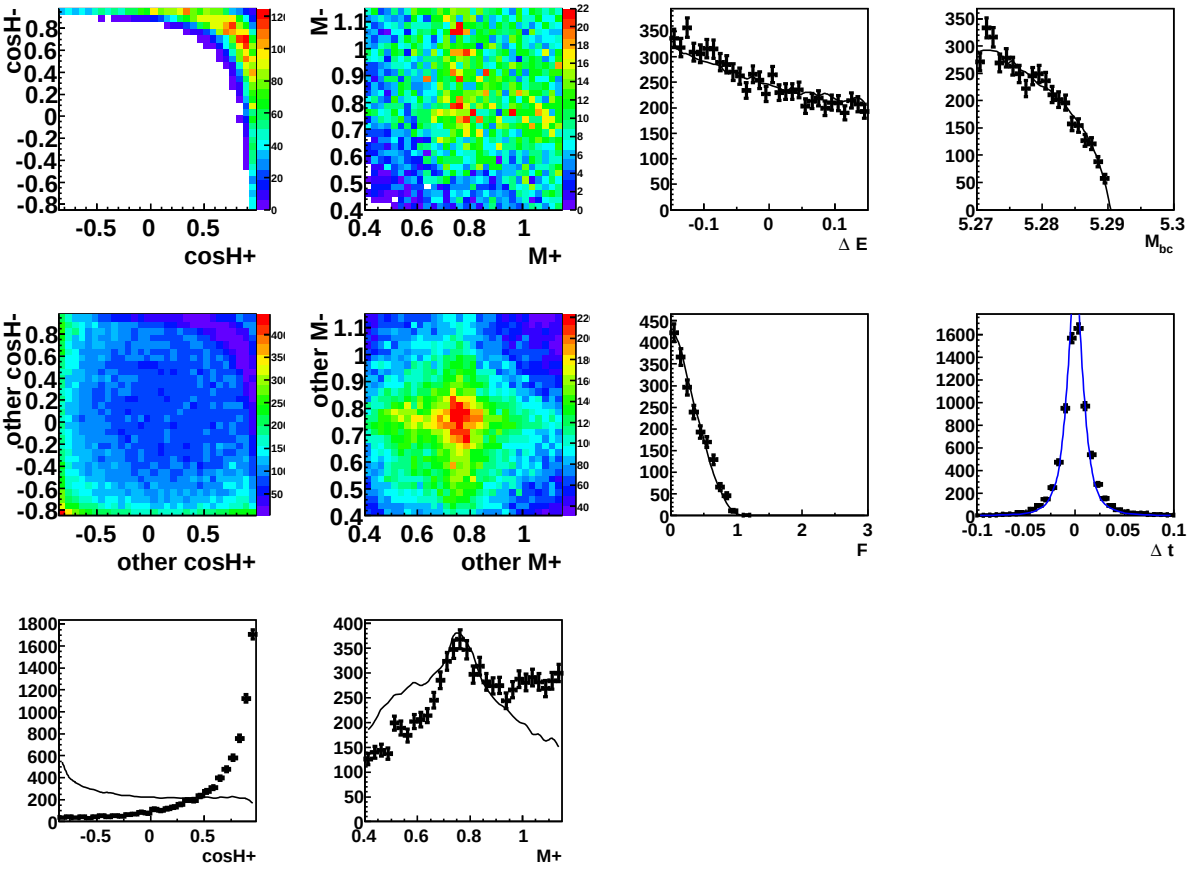

Figure 5.11: Constraining the invariant mass $m(\pi^+\pi^-)$ to be inside or outside (other) of $0.57\text{GeV/c}^2 < m(\pi^+\pi^-) < 0.97\text{GeV/c}^2$ yields in the shown distributions of the fit variables of off-resonance data. Events from within (outside) the $m(\pi^+\pi^-)$ constraint are shown as black points (line) in the one-dimensional projections.

Chapter 6

Systematic Uncertainties

This section describes the evaluation of the systematic uncertainty. The errors from various sources are summarized in Table 6.1 and added in quadrature.

6.1 Vertex Related Systematics

All variations in this section are standard within Belle and were obtained for the time-dependent measurement of $B \to c\bar{c}K^0$ decays.

The Δt Resolution Function

The fixed parameters of the Δt resolution function [91] are varied one by one in the fit to data. The variations are within one or two standard deviations depending on whether the parameter is obtained from MC or real data events. However, the quadratic sum of all differences to the nominal fit result is zero in the quoted precision.

IP Profile

Requiring that our reconstructed B meson origins from the interaction point (IP) allows to obtain the B vertex from a single track. Therefore, the single track is fitted to the IP, which is approximated by a ellipsoid, whose center is the measured IP and the uncertainty on the exact position corresponds the volume of the ellipsoid. As the z position of the track is hardly constraint only the uncertainty in $r-\phi$, $\delta_{\rm IP}^{r-\phi} = 21$ μm is conservatively varied by ± 10 μm. The difference to our nominal fit result gives the uncertainty.

Track Helix Error

Due to imperfections of the detector the track resolution is too optimistic. Consequently, the errors of the track parametrization are rescaled before the reconstruction. The corrections

are obtained from studies with cosmic rays and MC simulation [105]. A conservative systematic error is usually obtained from comparing the fit result from reconstructed data with and without scaling. However, we follow [54] and exploit the high correlation of the helix parameters with the B lifetime, τ_{B^0} and mass difference Δm. It is sufficient to compare the fit results with τ_B^0 and Δm set to the PDG values and with τ_{B^0} and Δm set to values obtained from a high statistics control sample without helix error modification, $\tau_{B^0} = (1.5299 \pm 0.0029)$ps and $\Delta m = (0.5088 \pm 0.0019)\text{ps}^{-1}$ (taken from [106]).

Δt Selection Criteria

We vary our nominal Δt range of $|\Delta t| < 70$ ps by ± 30 ps and add the differences of each fit result to our nominal result in quadrature.

Vertex Fit Quality

We vary the requirements on the quality of the B_{CP} vertex, $\chi^2/\text{ndf} < 50$ by $^{+50}_{-25}$ and $\delta_z < 0.2(0.5)$ mm by ± 0.1 mm, and add the differences of each fit result to our nominal result in quadrature.

Tag-side Track Selection

The requirement on tracks used for the vertex fit of B_{tag}, $d_r, d_z < 0.5$ mm are varied by $\pm 10\%$ and the fit to data repeated. The differences to our nominal result are added in quadrature.

Δz Bias And Misalignment

Despite a regular correction of the data due to alignment, a possible misalignment can bias the Δz distribution. This effect is considered to be mode independent, therefore the error is taken from Ref. [54] and is the difference of the results of studies of $B^0 \to J\Psi K_S$ decays; either without accounting for this effect or including a correction function in the Δt PDF. In addition, a relative misalignment of the SVD with respect to the CDC is account for by a study of MC samples where the position of the sub-detectors is altered in the simulation.

Flavor Tagging

The uncertainties on the fraction of wrongly tagged events are varied in each r-bin according to the uncertainties provided by the Belle flavor tagging group [92], see Table 3.2 in Section 3.2.4. We add the differences to our nominal fit result in quadrature.

Tag-side Interference

The tagging algorithm uses decays that are only approximately flavor specific. An example is the decay $B \to D\pi$, where the final state of the CKM-favored decay $\bar{B} \to D^+\pi^-$ ($b \to c\bar{u}d$) can also be realized via the double CKM-suppressed $\bar{b} \to \bar{u}c\bar{d}$ transition. Due to the suppression this effect is expected to be small and the corresponding uncertainty is estimated from a pseudo-MC ensemble test. Events including tag-side interference [107] are generated according to the procedure described in Ref. [108], while this effect is neglected in the fits to the MC samples. The largest deviation is taken as the systematic uncertainty.

6.2 Reconstruction Related Systematics

Number of $B\bar{B}$ pairs

The uncertainty arises from estimating the contribution of continuum events, which has to be subtracted from the data set in order to determine the number of recorded $B\bar{B}$ pairs, as described in Section 3.1.2.

Charged Particle Identification and Tracking

We correct the reconstruction efficiency for differences between the performance of particle identification in data and MC [101] and include the uncertainty of this correction in the systematic error. The efficiency correction of charged pions has an error $0.8\% - 1.8\%$ per track, depending on the track's momentum and direction and are estimated from a study of an inclusive D^* control sample provided by the PID group. We add the errors of both tracks quadratically.
The track finding efficiency is almost perfect for tracks with a momentum $|p| > 200$ MeV and therefore not included in the branching ratio calculation, but treated entirely as a systematic uncertainty. For tracks above 200 MeV the error is 0.35% per track while the averaged error per track with a momentum below 200 MeV is 2% for SVD1 and 1.4% for SVD2 [109, 110]. The errors are obtained from partial reconstructed D^* events and added linearly for both charged tracks.

π^0 Reconstruction Efficiency

We correct for the difference in the π^0 reconstruction efficiency between data and MC simulation (see Section 4.6) and include an error of 1.49% per π^0. This number is determined from studying $\tau^- \to \pi^-\pi^0\nu$ decays, see [102, 103].

6.3 Fit Related Systematics

Misreconstruction Fraction

We vary the the fractions of the signal components $1c\pi^{\pm}$ and $no\pi^0$ within $\pm 20\%$ and the fraction of the mr component within $\pm 30\%$ in turn and add the differences in quadrature.

Fit Bias

The fitters bias is estimated from fully simulated GEANT toy MC ensemble test, where we observe a small and stable deviation from the generated value of 0.50×10^{-6} for $\mathcal{B}(B^0 \to \rho^+\rho^-)$ and 0.04 for $\mathcal{A}_{CP}$. We fully correct for this bias and include the uncertainty of the correction in the systematics. The correction is obtained from studying fully simulated MC events generated according to the fit result. The generated values of $\mathcal{B}(B^0 \to \rho^+\rho^-)$ and $\mathcal{A}_{CP}$ are varied by $\pm 1\sigma_{\rm stat}$, in turn. The largest deviations from the results with nominal values are taken for each observable. For f_L and $\mathcal{S}_{CP}$ the full deviation of the result from the ensemble test is taken and no correction is applied.

Model Shape

The parametric and non-parametric PDFs are varied within their uncertainties and the fixed fractions of charm and charmless $B^{\pm}$ decays are varied within $\pm 10\%$ in turn. The differences to the nominal fit result are added in quadrature. The fixed branching ratio of $B^0 \to \omega\pi^0$ gives a negligible uncertainty under the variation of $\pm 100\% = \pm 1$ event and the uncertainty related to $B^0 \to a_1^{\pm}\pi^{\mp}$ is described separately.

Description Of $B^0 \to a_1^{\pm}\pi^{\mp}$ Decays

Because the reconstruction quality of $B^0 \to a_1\pi$ decays is very sensitive to the selection criteria, especially the dipion mass window, we account for a possible difference of data and MC simulation for $B^0 \to a_1^{\pm}\pi^{\mp}$ decays by increasing its reconstruction efficiency by a factor of two, while simultaneously increasing the peaking contributions in ΔE,$M_{\rm bc}$ and the dipion masses. This change is motivated by fully simulated MC events with an alternative event generator, see Appendix B.1. The differences to our fit result are taken as a systematic uncertainty.

Physics Parameters

We vary the the mass and the width of the $\rho^{\pm}$, the B^0 lifetime and the mass difference between the heavy and light B mass eigenstate within one standard deviation as fixed to

their world averages [45].

$$m_{\rho^\pm} = 775.11 \pm 0.34 \text{ MeV}, \qquad \Gamma_{\rho^\pm} = 149.1 \pm 0.8 \text{ MeV},$$
$$\tau_{B^0} = 1.519 \pm 0.005 \text{ ps}, \qquad \Delta m = 0.510 \pm 0.004 \text{ ps}^{-1}.$$

MC Composition

We vary the fractions of the '0' component of each $B\bar{B}$ background by $\pm 10\%$ in turn and add the differences to our nominal fit result in quadrature. This variation mimics the in/decrease of combinatorial background with respect to peaking structures and accounts for a possible difference between the data and MC distributions.

Helicity Model Of $B^0 \to \rho^\pm\pi^\mp\pi^0$

We vary the helicity PDF for $B^0 \to \rho^\pm\pi^\mp\pi^0$ decays as described in Appendix B.2 and take the largest deviation from our fit result as an uncertainty.

Background CP Violation

We conservatively allow for CP violation up to 20% for B decays into charm final states and up to 50% for decays into charmless final states, in turn, and consider only direct CP violation for $B^\pm$ decays. A CP asymmetry term is included in the Δt PDFs of the inclusive $B\bar{B}$ backgrounds for this purpose. The deviations are added in quadrature and give the dominant contribution to the uncertainty of the CP violation parameters. The contribution from charged B decays leads to an even larger uncertainty on $\mathcal{A}_{CP}$.

6.4 Interference

The uncertainty from neglecting possible interference between the four-pion final states in the fit model is estimated to be small as described in detail in Appendix B.1.

Category	$\delta\mathcal{B}(\%)$	δf_L	$\delta\mathcal{A}_{CP}[10^{-2}]$	$\delta\mathcal{S}_{CP}[10^{-2}]$
Resolution function	0.00	0.000	0.00	0.00
IP profile	0.01	0.001	0.68	0.94
Track helix error	0.00	0.000	0.02	0.01
Δt selection	0.00	0.001	0.04	0.06
Vertex quality	0.16	0.000	1.20	0.60
Tagside track selection	0.01	0.001	0.84	0.95
Δz bias	-	-	0.50	0.40
Misalignement	-	-	0.40	0.20
Flavor tagging	0.07	0.002	0.71	0.51
Tagside interference	-	-	1.02	0.08
$N(B\overline{B})$	1.38	-	-	-
Tracking	0.70	-	-	-
PID	2.50	-	-	-
π^0 reconstruction	2.98	-	-	-
Misreconstructed fraction	0.01	0.001	0.60	0.50
Fit bias	0.53	0.002	0.50	0.74
Model shape	3.47	0.003	0.30	0.60
Histogram shape	0.17	0.002	0.19	0.31
Fixed background yields	0.00	0.001	0.04	0.08
Physics parameters	0.00	0.000	0.02	0.02
$B \to a_1^{\pm}\pi^{\mp}$ description	0.01	0.002	0.09	0.20
$\rho^{\pm}\pi^{\mp}\pi^0$ helicity	0.04	0.020	0.12	0.77
MC composition	0.04	0.007	0.64	1.34
Background CP violation	0.00	0.000	6.66	3.23
$B \to 4\pi$ CP violation	0.03	0.006	3.03	3.65
Interference	0.01	0.002	0.12	0.15
Total	5.47	0.023	7.79	5.68
(abs[$\times 10^{-6}$])	1.55			

Table 6.1: Systematic uncertainties.

Chapter 7

Constraints on the Unitarity Triangle

We combine our fit results with other (Belle) measurements to obtain new constraints on two of the angles from the unitarity triangle, ϕ_2 and ϕ_3, and on the magnitude of the CKM matrix element V_{ub}. First, flavor symmetries are used for an estimation of the true value of ϕ_2. The obtained results are then used to determine ϕ_3 and $|V_{ub}|$ by exploiting the the unitarity of the CKM triangle.

7.1 ϕ_2 Constraints

We provide two alternative constraints on ϕ_2 using either the SU(2) or the SU(3) isospin symmetry. Both methods use isospin related decays for an estimate of the penguin pollution $\Delta\phi_2$ in the observed mixing-induced CP asymmetry parameter of $B^0 \to \rho^+\rho^-$ decays, $\mathcal{S}_{CP} = \sqrt{1-\mathcal{A}_{CP}^2}\sin(2(\phi_2+\Delta\phi_2))$, see Section 1.4.3.

7.1.1 SU(2) Isospin analysis

The ρ meson has an isospin of $I = 1$. In general, a total isospin of $I = 0, 1, 2$ of the $\rho\rho$ system would be possible, but Bose-Einstein statistics forbids $I = 1$. Consequently, the two ρ mesons can only carry a total isospin of $I = 0, 2$ ($\Delta I = \frac{1}{2}, \frac{3}{2}$ transitions). Gluonic loop contributions (penguins) can only yield in a final state with $I = 0$ ($\Delta I = \frac{1}{2}$ transition), because the gluon doesn't carry isospin.
This can be used to relate the complex $B \to \rho\rho$ (A_{ij}) and $\bar{B} \to \rho\rho$ ($\bar{A}_{ij}$) amplitudes with Clebsch-Gordan coefficients to [111]

$$\frac{1}{\sqrt{2}}A_{+-} + A_{00} = A_{+0}, \qquad \frac{1}{\sqrt{2}}\bar{A}_{+-} + \bar{A}_{00} = \bar{A}_{-0}, \tag{7.1}$$

where the subscript identifies the charges of the ρ mesons and electroweak contributions, $\rho-\omega$ mixing or isospin breaking are neglected. These relations can be visualized as two triangles in the complex plane. Being a $\Delta I = \frac{3}{2}$ transition, the charged B decay $B^\pm \to \rho^\pm\rho^0$ arises only at tree level. Consequently, the two isospin triangles can be aligned to share the same base,

$$A^{+0} = \bar{A}^{-0}, \tag{7.2}$$

as illustrated in Fig. 7.1.
The angle between the two sides of the decay providing also $\mathcal{S}_{CP}$ (here A_{+-} and $\bar{A}_{+-}$) corresponds to the shift $2\Delta\phi_2$ due to higher order contributions with different weak phases. In general, this method results in an eight-fold ambiguity in the determination of ϕ_2 that arises from the four possible orientations of the two triangles and from measuring $\sin(\phi_2^{\text{eff}})$, see Section 1.4.3.

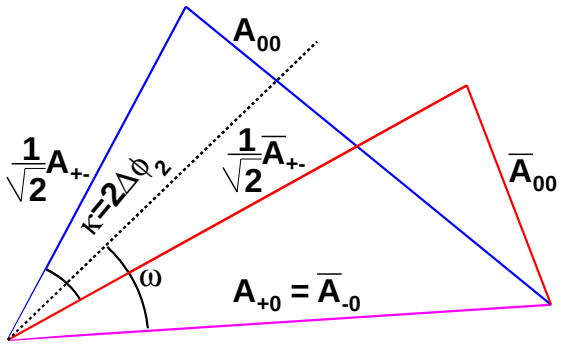

Figure 7.1: A sketch of the two isospin triangles as explained in the text.

We construct the amplitudes from Eq. (7.1) from hypothetical values for the branching fractions for the two decays involving charged ρ mesons a_{+-}, a_{+0}, the angles w, κ as shown in Fig. 7.1 and the direct CP asymmetries of $B^0 \to \rho^+\rho^-$, $\mathcal{A}_{CP}$,

$$A_{+-} = \sqrt{a_{+-}(1-\mathcal{A}_{CP})}, \tag{7.3}$$
$$\bar{A}_{+-} = \sqrt{a_{+-}(1+\mathcal{A}_{CP})}, \tag{7.4}$$
$$A_{\pm 0} = \sqrt{a_{+0}}, \tag{7.5}$$
$$A_{00} = \big(\frac{A_{+-}^2}{2} + A_{+0}^2 - \sqrt{2}A_{+-}A_{+0}\cos(w-\frac{\kappa}{2})\big)^{\frac{1}{2}}, \tag{7.6}$$
$$\bar{A}_{00} = \big(\frac{\bar{A}_{+-}^2}{2} + A_{+0}^2 - \sqrt{2}\bar{A}_{+-}\bar{A}_{+0}\cos(w+\frac{\kappa}{2})\big)^{\frac{1}{2}}. \tag{7.7}$$

and use them to calculate the theoretical predictions of

$$\mathcal{B}(\rho^+\rho^-)_{\text{theo}} = \frac{1}{2}(A_{+-}^2 + \bar{A}_{+-}^2), \tag{7.8}$$
$$\mathcal{B}(\rho^0\rho^0)_{\text{theo}} = \frac{1}{2}(A_{00}^2 + \bar{A}_{00}^2), \tag{7.9}$$
$$\mathcal{B}(\rho^\pm\rho^0)_{\text{theo}} = \frac{\tau_{B^+}}{\tau_{B^0}}A_{+0}^2, \tag{7.10}$$
$$\mathcal{A}_{CP}(\rho^+\rho^-)_{\text{theo}} = \mathcal{A}_{CP}, \tag{7.11}$$
$$\mathcal{S}_{CP}(\rho^+\rho^-)_{\text{theo}} = \sqrt{1-\mathcal{A}_{CP}^2}\sin(2\phi_2+\kappa). \tag{7.12}$$

A χ^2 distribution is obtained from minimizing a $-2\log(\mathcal{L})$, as the likelihood $\mathcal{L}$ takes the from of a multivariate normal distribution

$$\begin{aligned}\chi^2 &= -2\log\mathcal{L} \\ &\equiv -2\log\big[\frac{1}{(2\pi)^{n/2}\det\Sigma^{1/2}}exp[\frac{1}{2}(\vec{x}_{\text{theo}}-\vec{x}_{\text{data}})^T\Sigma^{-1}(\vec{x}_{\text{theo}}-\vec{x}_{\text{data}})]\big].\end{aligned} \tag{7.13}$$

The covariance matrix Σ includes also available correlations between the measured parameters $\vec{x}_{\rm data} = \{\mathcal{B}(\rho^+\rho^-), \mathcal{B}(\rho^0\rho^0), \mathcal{B}(\rho^\pm\rho^0), \mathcal{A}_{CP}(\rho^+\rho^-)\mathcal{S}_{CP}(\rho^+\rho^-), \}|_{\rm LP}$.

We use our result (see Chapter 5) and the branching fraction and the longitudinally polarized fraction from our measurement of $B^0 \to \rho^0\rho^0$ decays [5]; $f_L^{00} \times \mathcal{B}(B^0 \to \rho^0\rho^0) = (0.21 \pm 0.34) \times 10^{-6}$. For $B^\pm \to \rho^\pm\rho^0$, the branching fraction $\mathcal{B}(B^\pm \to \rho^\pm\rho^0) = (31.7 \pm 8.8) \times 10^{-5}$ and longitudinal polarization fraction $f_L^{+0} = 0.95 \pm 0.11$ are taken from an early Belle measurement [77].
We vary $\phi_2 \in [0°, 90°]$ in steps of 1° and minimize the $-2\log\mathcal{L}$ with the fixed value of ϕ_2 in order to obtain the probability scan shown in Fig. 7.2. The solution being most consistent with other SM constraints on the unitarity triangle is

$$\phi_2 = (93.6 \pm 10.7)°. \tag{7.14}$$

The other solution is $\phi_2 = (176.4 \pm 10.7)°$. We are improving the knowledge of ϕ_2 in the $B \to \rho\rho$ system by 2.8° compared to previous Belle measurements. Belle's ϕ_2 constraint is still worse than BaBar's, because $B^\pm \to \rho^\pm\rho^0$ decays are only measured with $\sim 10\%$ of the available data. An update of this mode is therefore highly desired, an extrapolations to Belle's final data set and to Belle II are shown in Section 7.3.
The size of the penguin contributions is small: $\Delta\phi_2 = (0.0 \pm 9.6)°$. Because of the very small $B^0 \to \rho^0\rho^0$ branching fraction relative to the other two $B \to \rho\rho$ decays, the four solutions from the isospin analysis degenerate into the apparent solution (two-fold). This makes the isospin analysis with $B \to \rho\rho$ less ambiguous compared to $B \to \pi\pi$. There the decay into two neutral pions is relatively stronger [112–116], currently resulting in eight solutions for ϕ_2. In the future this could be reduced to a two-fold ambiguity, when the measurement of the unknown mixing-induced CP violation parameter of $B^0 \to \pi^0\pi^0$ will be included in the isospin analysis of $B \to \pi\pi$ decays.

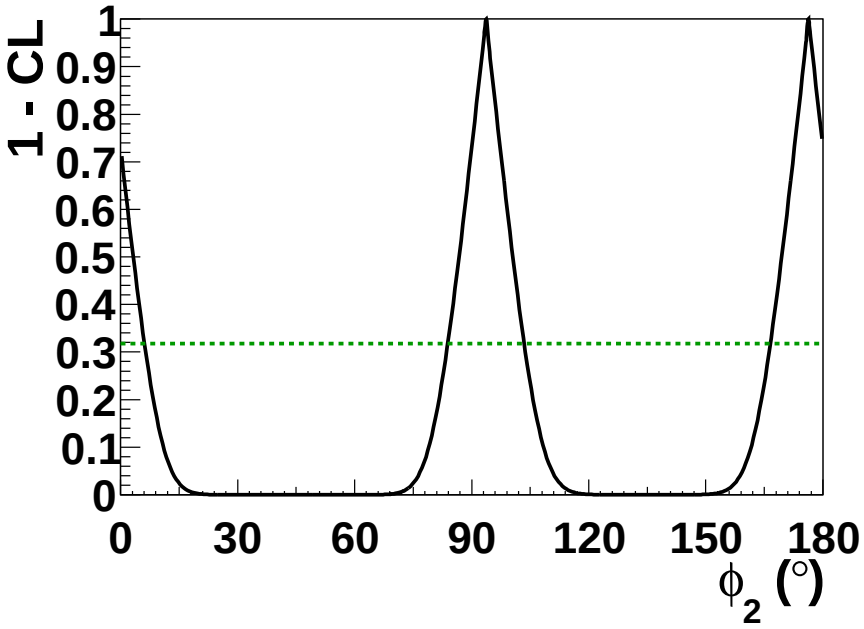

Figure 7.2: 1−CL versus ϕ_2 obtained from an isospin analysis from $B \to \rho\rho$ decays. The horizontal line shows the 68% CL.

7.1.2 SU(3) Symmetry

Exploiting the SU(3) symmetry provides an alternative way to determine the penguin contribution in $\mathcal{S}_{CP}$. The amplitude of $B^0 \to \rho^+\rho^-$ can be written as the sum of tree and penguin contributions

$$\mathcal{A}_{B^0\to\rho^+\rho^-} = Te^{i\phi_3} + Pe^{i\delta_{PT}}, \tag{7.15}$$

where ϕ_i are the internal angle from the unitarity triangle. T and P are the magnitudes of the tree and penguin amplitude and δ_{PT} is their phase difference. Being a pure penguin mode, we can use the branching fraction and longitudinal polarization fraction of the SU(3) related decay $B^+ \to K^{*0}\rho^+$ to estimate the penguin contribution in $B^0 \to \rho^+\rho^-$ up to SU(3) breaking effects. Following [117] we can write

$$-\mathcal{A}_{CP} = \frac{2r_{PT}\sin\delta_{PT}\sin(\phi_1+\phi_2)}{1-2r_{PT}\cos\delta_{PT}\cos(\phi_1+\phi_2)+r_{PT}^2} \tag{7.16}$$

$$\mathcal{S}_{CP} = \frac{\sin 2\phi_2 + 2r_{PT}\cos\delta_{PT}\sin(\phi_1-\phi_2) - r_{PT}^2\sin 2\phi_1}{1-2r_{PT}\cos\delta_{PT}\cos(\phi_1+\phi_2)+r_{PT}^2} \tag{7.17}$$

and

$$\frac{\mathcal{B}_{\mathrm{LP}}(B^+\to K^{*0}\rho^+)}{\mathcal{B}_{\mathrm{LP}}(B^0\to\rho^+\rho^-)} = \frac{\tau_{B^\pm}}{\tau_{B^0}}\left(\frac{|V_{cs}|f_{K^*}}{|V_{cd}|f_\rho}\right)^2 \frac{Fr_{PT}^2}{1-2r_{PT}\cos\delta_{PT}\cos(\phi_1+\phi_2)+r_{PT}^2}, \tag{7.18}$$

with the decay constants f_{ρ,K^*} and the ratio of penguin to tree amplitude, $r_{PT} = |P/T|$. $\tau_{B^{0/\pm}}$ are the $B^{0/\pm}$ lifetimes [45] and $F \neq 1$ allow for SU(3) breaking effects. It turns out that the determination of ϕ_2 is rather stable even if strong SU(3) breaking is considered as it comes with the very small quantity r_{PT}^2. We set $F = 0.9 \pm 0.6$ [117] to its mean value and take the difference of the result on ϕ_2 when varying F within the quoted error as an additional uncertainty due to possible SU3 breaking.
Besides the branching fractions and longitudinal polarization fractions of the two decays, we furthermore need the CP violating parameters $\mathcal{S}_{CP}$, $\mathcal{A}_{CP}$ from $B^0 \to \rho^+\rho^-$ decays and ϕ_1 as inputs. Inputs related to $B^0 \to \rho^+\rho^-$ are taken from this measurement, $\mathcal{B}(B^+ \to K^{*0}\rho^+) = (8.9 \pm 1.7\ (\mathrm{stat}) \pm 1.2\ (\mathrm{syst})) \times 10^{-6}$ and $f_L^{K^{*0}\rho^+} = 0.43 \pm 0.11; (\mathrm{stat}) \pm 0.05; (\mathrm{syst})$ are taken from Ref. [118] and $\phi_1 = (21.88^{+0.81}_{-0.71})^\circ$ is taken from [50].
Fig. 7.3 shows a similar scan as for the SU(2) isospin analysis. For the theoretical motivated condition $|\delta_{PT}| < 90^\circ$, we obtain

$$\phi_2 = (89.3 \pm 4.9\ (\mathrm{scan})\ ^{+1.0}_{-3.4}\ (\mathrm{SU3}))^\circ, \tag{7.19}$$

as the solution best compatible with other SM fits. The other solution with $|\delta_{PT}| < 90^\circ$ is $\phi_2 = 174.9(\pm 4.3\ (\mathrm{scan}))^\circ$. The result should only be used for comparison with the result from the SU(2) analysis, as same inputs were used.
We furthermore obtain $r_{PT} = 0.09 \pm 0.02\ (\mathrm{scan})\ ^{+0.06}_{-0.02}\ (\mathrm{SU3})$ and $\delta_{PT} = (0.0 \pm 48.7\ (\mathrm{scan}) \pm 0.0\ (\mathrm{SU3}))^\circ$. Comparing our result with the numerically calculated values $r_{PT}^{\mathrm{theo}} = 0.038 \pm 0.005^{+0.019}_{-0.026}$ and $\delta_{PT}^{\mathrm{theo}} = 0.23 \pm 0.09^{+0.74}_{-0.73}$ [119] shows a fair agreement, although the amplitude ratio is marginally larger. The penguin contribution decreases with larger values for F, which are also favored when floating F in the fit.
The results are also in good agreement with those from the isospin analysis, see Eq. (1.100)

for the relation of $r_{PT}, \cos\delta_{PT}$ and $\Delta\phi_2$. Although SU(3) breaking is considered, this method gives currently a smaller uncertainty on ϕ_2. But an update of $B^{\pm} \to \rho^{\pm}\rho^0$ is expected to improve the SU(2) analysis to a comparable level. It is common to quote the result from the SU(2) isospin analysis, as it is the more exact symmetry (strange quarks are considerably heavier than the unflavored ones: $m_u \sim m_d < m_s$).

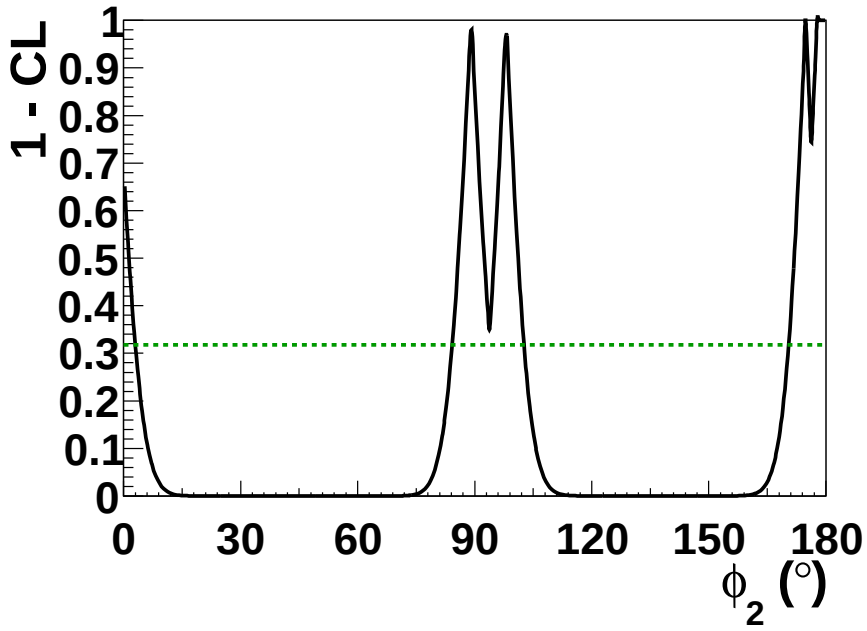

Figure 7.3: 1−CL versus ϕ_2 obtained from relating $B \to \rho\rho$ decays to $B^+ \to K * \rho^+$ decays with SU3. Each double peak consists out of one solution for $|\delta_{PT}| < 90°$ and one else. The horizontal line shows the 68% CL.

7.2 ϕ_3 Constraint

The unitarity of the CKM triangle can be used to calculate a solution for the CKM angle ϕ_3 from $\mathcal{S}_{CP}$ of $B^0 \to \rho^+\rho^-$ decays and ϕ_1. We follow the discussion in [119]. With

$$\tau \equiv \cot\phi_1, \tag{7.20}$$

the unitarity triangle is fully determined by

$$\bar{\rho} = 1 - \tau\bar{\eta}, \tag{7.21}$$

where $\bar{\rho}$ and $\bar{\eta}$ define the apex of the CKM triangle in the improved Wolfenstein parametrization [49] (see Section 1.2.3). The CKM angles ϕ_2 and ϕ_3 are then given by

$$\phi_2 = \pi - \phi_1 - \phi_3 \quad \text{with} \quad \phi_3 = \arctan\frac{\bar{\eta}}{1-\tau\bar{\eta}}. \tag{7.22}$$

$\bar{\eta}$ can be written in terms of $\phi_1, \mathcal{S}_{\rho^+\rho^-}$ as well as the magnitude (r_{PT}) and phase (δ_{PT}) of the penguin-to-tree ratio amplitude

$$\bar{\eta} = \frac{1}{1+\tau^2 \cdot \mathcal{S}_{\rho^+\rho^-}} \Big[(1+\tau \cdot \mathcal{S}_{\rho^+\rho^-})(1 + r_{PT}\cos\delta_{PT}) - \sqrt{(1-\mathcal{S}^2_{\rho^+\rho^-})(1+r_{PT}\cos\delta_{PT})^2 - \mathcal{S}_{\rho^+\rho^-}(1+\tau^2)(\mathcal{S}_{\rho^+\rho^-} + \sin 2\phi_1) r^2_{PT}\sin^2\delta_{PT}} \Big], \quad (7.23)$$

which is an exact equality. We use our fit result of $\mathcal{S}_{CP}$ and the values for r_{PT} and δ_{PT} obtained from the SU(3) scan, see Section 7.1.2, to calculate ϕ_3. We obtain

$$\phi_3 = (77^{+7}_{-11})^\circ, \quad (7.24)$$

The errors are obtained by varying each input by its error in turn and adding the differences in quadrature. It is possible to approximate Eq. (7.22) to first order in the small quantities $\mathcal{S}^{\rho^+\rho^-}_{CP}$ and r_{PT}

$$\phi_3 \approx \arctan\tau + \frac{\mathcal{S}_{\rho^+\rho^-}}{2} + \tau \cdot r_{PT} \cdot \cos\delta_{PT}. \quad (7.25)$$

Both results are identical in the quoted precision and are in good agreement with other determinations, e.g. Belle's measurement of $B \to DK$ decays; $\phi_3 = (68^{+15}_{-14})^\circ$ [120].
Because the unitarity condition has been used to express ϕ_3 in terms of the other two angles, the result should only be used to check for consistency through a comparison with direct measurements. The uncertainty of this method is dominated by the uncertainty on r_{PT} due to possible $SU3$ breaking, but is remarkably small. The current world average is $\phi_3 = (70^{+8}_{-9})^\circ$ [50].

7.3 V_{ub}

In a similar manner it is possible to determine the magnitude of the CKM element $|V_{ub}|$ [119]. Because of a small ($\sim 3\sigma$) tension of the results of $|V_{ub}|$ from inclusive and exclusive semi-leptonic decays, this observable has recently gained more attention. The current values are $|V_{ub}|_{\text{inclusive}} = (4.40 \pm 0.15 \pm 0.20) \times 10^{-3}$ and $|V_{ub}|_{\text{exclusive}} = (3.23 \pm 0.30) \times 10^{-3}$ [121]. Also because of a sensitivity to new physics contribution in $B^0 \to \rho^+\rho^-$ or $B \to J/\Psi K_s$, it is interesting to compare results on $|V_{ub}|$ from the method presented here with those from semi-leptonic measurements, which are regarded as pure SM processes.
The magnitude of V_{ub} is proportional to the side $R_b \equiv \sqrt{\bar{\rho}^2 + \bar{\eta}^2}$ of the unitarity triangle, which can be expressed in terms of $\phi_1, \mathcal{S}^{\rho^+\rho^-}_{CP}$, r_{PT} and δ_{PT},

$$R_b = \sin\phi_1 \big[1 + \frac{1}{2}\big(\frac{1}{2}\mathcal{S}_{CP} + \tau \cdot r_{PT}\cos\delta_{PT}\big)^2\big]. \quad (7.26)$$

With

$$|V_{ub}| = \frac{|V_{cb}V_{cd}|}{|V_{ud}|} R_b = \frac{|V_{us}||V_{cb}|}{1 - \frac{1}{2}|V_{us}|^2} R_b, \quad (7.27)$$

we obtain

$$|V_{ub}| = (3.60^{+0.16}_{-0.22}) \times 10^{-3}, \quad (7.28)$$

being in good agreement with the $|V_{ub}|$ measurement from exclusive semi-leptonic decays. We notice a small tension ($< 3\sigma$) with $|V_{ub}|_{\text{inclusive}}$, although our mean value is larger than the

exclusive one. We use the CKM elements from [50] as additional inputs and the uncertainty is obtained by varying each input by its error in turn and adding the differences in quadrature. It is interesting to note, that the contribution of $\sin\phi_1$ to the uncertainty is significantly larger than $\mathcal{S}_{CP}^{\rho^+\rho^-}$'s (as indicated by Eq. (7.26)), hence the small uncertainty.

Conclusion

We presented a measurement of the branching fraction of the decay $B^0 \to \rho^+\rho^-$, the fraction of longitudinally polarized final state ρ mesons and the time-dependent CP violation parameters in this decay. The following results are obtained from Belle's final data set of 772×10^6 $B\bar{B}$ pairs:

$$\begin{aligned}
\mathcal{B}(B^0 \to \rho^+\rho^-) &= (28.3 \pm 1.5\ (\text{stat}) \pm 1.5\ (\text{syst})) \times 10^{-6}, \\
f_L &= 0.988 \pm\ 0.012\ (\text{stat}) \pm\ 0.023(\text{syst}), \\
\mathcal{S}_{CP} &= -0.13 \pm 0.15(\text{stat}) \pm 0.06\ (\text{syst}), \\
\mathcal{A}_{CP} &= 0.00 \pm 0.10(\text{stat}) \pm 0.08\ (\text{syst}).
\end{aligned}$$

The results are in excellent agreement with previous measurements [75,76,78] and currently the most precise measurement of the branching fraction and the longitudinal polarization fraction as well as the tightest constraint on CP violation in this mode. We use this result together with our published measurement of the branching fraction and the longitudinal polarization fraction of $B^0 \to \rho^0\rho^0$ [5]

$$\begin{aligned}
\mathcal{B}(B^0 \to \rho^0\rho^0) &= (1.02 \pm 0.30\ (\text{stat}) \pm 0.15\ (\text{syst})) \times 10^{-6}, \\
f_L^{00} &= 0.21^{+0.18}_{-0.22}\ (\text{stat}) \pm\ 0.15(\text{syst}),
\end{aligned}$$

and an early Belle measurement of $B^\pm \to \rho^\pm\rho^0$ to obtain a constraint on the internal angle ϕ_2 of CKM unitarity triangle with an SU(2) isospin analysis. We obtain two solutions with

$$\phi_2 = (93.6 \pm 10.7)^\circ, \tag{7.29}$$

being the one best compatible with other SM-based fits to the existing experimental data. The other solution is $\phi_2 = (176.4 \pm 10.7)^\circ$. We improve the knowledge of ϕ_2 from Belle measurements by 2.8°, while the statistical uncertainty of $B^\pm \to \rho^\pm\rho^0$ decays provides room for further improvement to a level well compatible with BaBar's constraint [50]. Being only measured with $\sim 10\%$ of Belle's existing data, an update of $\mathcal{B}(B^\pm \to \rho^\pm\rho^0)$ is highly desired.

Furthermore we provide an alternative constraint on ϕ_2 by exploiting the SU(3) symmetry, being in excellent agreement with the result from the isospin analysis. We use our result together with the experimental knowledge on ϕ_1 and CKM matrix elements to calculate ϕ_3 and $|V_{ub}|$. We find good agreement with direct measurements.
In the global fit of the unitarity triangle, the constraint of $(\bar{\rho}, \bar{\eta})$ with ϕ_2 currently (excluding our result) exhibits an tendency for a possible tension with other constraints: the band from the ϕ_2 constraint might be slightly to high, see Fig. 7.4. As our result on ϕ_2 is larger than the previous, including this measurement in the constraint will slightly decrease the radius

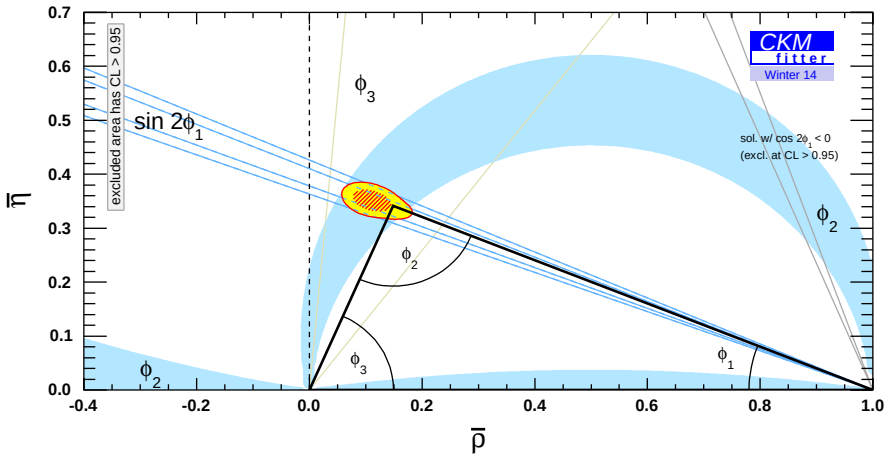

Figure 7.4: The current status of the unitarity triangle. The red (yellow) shaded area shows the one (two) sigma constraints from the internal angles (excluding our result) on the apex [50].

of the band. But the uncertainty will be reduced as well, which might compensate the shift. Within the given precision, all results contribute to a consistent picture of the SM.

We would like to add a remark to our measurement of $B^0 \to \rho^0\rho^0$ decays: although it is currently the most significant one, with 3.4 standard deviations, we can only claim evidence. It is worth mentioning that as we are dealing with a complex structure of a decay of a pseudoscalar particle into two vector particles, two almost independent signal components are considered: one for each polarization. The significance, however, is obtained from the total yield, being the sum of both polarizations. The unexpected low longitudinal polarization fraction is only 2.1σ different from BaBar's measurement [79] and therefore could be an unlucky statistical fluctuation. Nevertheless, the result is systematically stable. In addition, the theoretical predictions [65,70] do not exclude an enhancement of the transverse polarized component for the color-suppressed $B^0 \to \rho^0\rho^0$ decay. Future measurements with more data will provide a clearer picture. Higher statistics will allow to optimize for a pure sample instead of focusing only on a high signal yield. A four-body Dalitz analysis should be performed to have the interference among the four-pion final states under control. This is currently the dominant systematic uncertainty. If f_L remains small, the transversity basis allows to disentangle the CP-even and odd components for transverse polarization. The measurement of the CP violating parameters of $B^0 \to \rho^0\rho^0$, so far only performed by BaBar, would provide an important input for the isospin analysis.

Future results from measurements of $B^0 \to \rho^+\rho^-$ will be limited by their systematical uncertainties. Aiming for signal purity will be useful to reduce the systematic uncertainty associated with the likelihood parametrization and also other background related ones. An individual treatment of the dominant irreducible $B\bar{B}$ backgrounds can be helpful, especially to further reduce uncertainties from CP violation in the background. Tag-side interference could be included in the PDF of Δt. The particle identification and π^0 reconstruction efficiencies should be better understood, as the branching fraction is an important input for the ϕ_2 constraint. Interference is estimated to be small, consequently a similar treatment could be considered. Nevertheless, a full partial wave analysis could provide interesting information on the final state interactions. Other final states might become more important as well, for example the full set of $B \to a_1\pi$ decays.

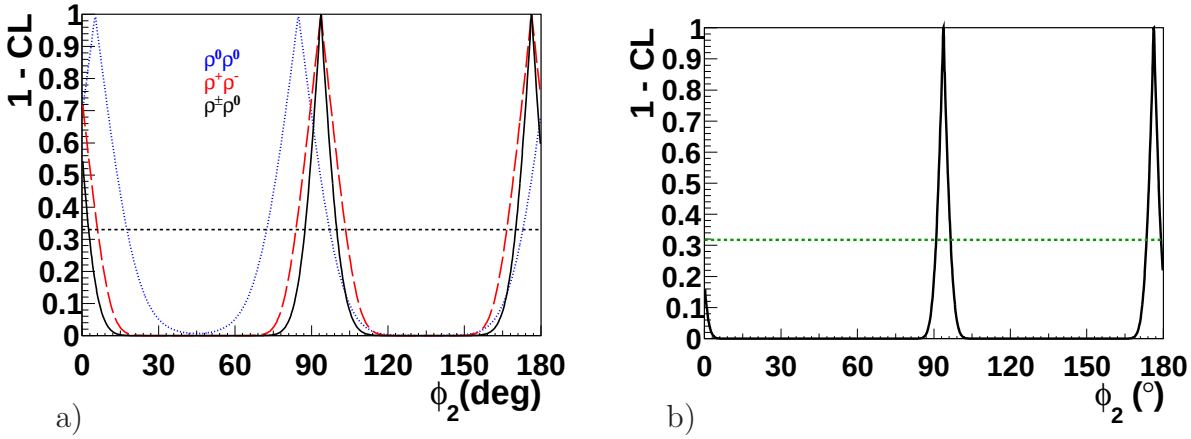

Figure 7.5: 1−CL versus ϕ_2 obtained from extrapolated toy SU(2) isospin analysis from $B \to \rho\rho$ decays as explained in the text. a) the black solid line is the extrapolation of $B^{\pm} \to \rho^{\pm}\rho^0$ to 1ab^{-1}, the dashed red line shows the result from this measurement and the blue dotted line is with previous Belle results. b) shows the extrapolation to Belle II. The horizontal line shows the 68% CL.

The SU(2) isospin analyzes in Fig. 7.5 show what to expect for ϕ_2 in the future from the $B \to \rho\rho$ system. We assume the current mean values from Belle and scale the errors according to several expectations:
One toy analysis is extrapolated to Belle's final data set of 1ab^{-1}, where we assume the uncertainty of $B^{\pm} \to \rho^{\pm}\rho^0$ to be similar to the one of $B^0 \to \rho^+\rho^-$. The current and the previous scans are also included for a comparison.
The other scan is extrapolated to Belle II's expected final data set of 50ab^{-1}. The statistical uncertainties are scaled according to the luminosity and the systematical ones are conservatively multiplied by 0.7. Under these assumptions we obtain uncertainties on ϕ_2 of 6° for 1 ab^{-1} and 3° for 50 ab^{-1}, where $\mathcal{S}_{CP}$ of $B^0 \to \rho^0\rho^0$ is not included in the scans.
The decay $B^0 \to \rho^+\rho^-$ has two π^0 mesons in the final state and is therefore rather difficult to study at LHCb, the experiment at the LHC primarily dedicated to flavor physics and CP violation. There, the experimental environment is better suited for analyzing final states with charged particles, hence, interesting results for the decay $B^0 \to \rho^0\rho^0$ can be expected in the near future.
This toy example shows that, although the CKM mechanism is describing the current data well, the next generation B experiments will push the constraints on the unitarity triangle to a new level of precision. We need to look carefully at a variety of observables, e.g. branching fractions of rare decays or (a)symmetries and study processes that are not allowed in the SM to find its limitations.

The first generation B factories were built to test the CKM mechanism. This is nowadays an accepted theory and a great example of the success of the SM among many others. The recent discovery of a Higgs particle [19,20] makes the SM internally consistent. But we know that there must be more. Even though the LHC experiments did not discover any phenomena beyond the SM, yet, the LHC is only about to operate at the design center-of-mass energy. If there will be no sign of a direct production of new particles, high luminosity experiments, such as Belle II or LHCb, are a complementary approach to challenge the SM and are sensitive to energies orders of magnitude higher then the LHC's center-of-mass energy. There are still

many areas to explore, the future of particle physics has exciting prospects. This will be challenging, but what would pushing boundaries be without a challenge?

Appendix A

Appendix Control Sample

One has to account for differences between the distributions of data and MC simulation, used to obtain the data model. For that purpose, we analyze a control channel with sufficiently high statistics and a similar final state topology as $B^0 \to \rho^+\rho^-$. We perform a branching fraction measurement and obtain MC/data correction factors for the shape of ΔE, $M_{\rm bc}$and $\mathcal{F}_{B\bar{B}/q\bar{q}}$ as well as for the fractions of events in each r-bin from a fit to data. We then apply the corrections to the model for the $B^0 \to \rho^+\rho^-$ analysis. There, the signal to background ratio makes a direct extraction of such a difference not feasible. The correction factors of ΔE and $M_{\rm bc}$, $cf^{\Delta E}$ and $cf^{M_{\rm bc}}$, will be included in all peaking PDFs, the ones of $\mathcal{F}_{B\bar{B}/q\bar{q}}$ and the r-bin fractions $cf^{\mathcal{F}_{B\bar{B}/q\bar{q}},r}$ and $cf^{r-\rm bin}$ in all $B\bar{B}$ PDFs. The explicit incorporation of the correction factors of ΔE,$M_{\rm bc}$ and $\mathcal{F}_{B\bar{B}/q\bar{q}}$ is described in Appendix E.3 Eq. (E.7) and the correction factors of the r-bin fraction are multiplicative.

We choose $(B^+ \to \bar{D}^0\rho^+) \times (\bar{D}^0 \to K^+\pi^-\pi^0)$ as our control sample, because it has only one additional charged Kaon in the final state. The subsequent D decay provides the second π^0 and has a very high probability of $(13.9 \pm 0.5)\%$ [45].

In the reconstruction, we apply the same selection criteria as for $B^0 \to \rho^+\rho^-$(Section 3.2) decays, in addition, a PID likelihood for kaon candidates of $\mathcal{L}_{K/\pi} > 0.6$ as well as a mass window for D candidates, $1.82\ \mathrm{GeV}/c^2 < m(K\pi\pi) < 1.90\ \mathrm{GeV}/c^2$, are included. Accounting for the non-negligible flight length of the D, the vertex fit is modified. First, the D vertex is obtained by adding its charged daughters ($K^\pm\pi^\mp$) to a prior vertex fit. We force the π^0 from the D meson to origin from the D vertex and update its four-momentum and error matrix accordingly, requiring also a π^0 mass-constraint. Then the B vertex, the common vertex of the D and the remaining charged π, coming from the ρ resonance, is determined in a second step. An IP constraint is used for the determination of the B vertex.

A simultaneous extraction of the branching fraction as well as the correction factors is performed in a three-dimensional fit to ΔE, $M_{\rm bc}$and $\mathcal{F}_{B\bar{B}/q\bar{q}}$ in each r-bin. In addition, we also include the invariant mass ($m_{\rho^\pm}$) and the helicity angle of the $\rho^\pm$ as well as Δt in the fit, allowing an extension up to six fit dimensions. This allows to compare the mass and helicity distributions derived from MC simulation with the data. A correction of the corresponding efficiency-dependencies would require two charged ρ mesons in the final state and preferable less background. Most backgrounds contain a $\rho^\pm$ resonance, resulting in similar shapes of the ρ mass and helicity angle distributions. We validate the time-dependent part of the fitter

by measuring the $B^{\pm}$ lifetime from the Δt distribution.

We consider backgrounds from continuum and charm $B\bar{B}$ decays. Other backgrounds from charmless B decays are insignificant and no peaking background is found (e.g. the momentum of a charged pion from a D^* in $B^+ \to \bar{D}^{0*}\pi^+$ decays is two low for the standard tracking, slow charged pions require a SVD-only tracking).

A.1 Likelihood Parametrization

Each components' shape is determined from a fit to fully simulated MC events (all B decays) or off-resonance data (continuum). For $D^0 \to K\pi^+\pi^0$ decays, we use the EvtGEN decay model *D_DALITZ* [97] for the generation of one million signal MC events. All backgrounds shapes are obtained from the same MC/data samples as analyzed for $B^0 \to \rho^+\rho^-$. We give the total PDF in six dimension (for each component), for a dimension reduction the excluded PDFs are set to one. All $\mathcal{F}_{B\bar{B}/q\bar{q}}$ distributions are modeled in a similar way as in the $B^0 \to \rho^+\rho^-$ model, see Chapter 4.

A.1.1 Signal Model

In analogy to the model of $B^0 \to \rho^+\rho^-$, we distinguish three different kinds of reconstruction for $B^+ \to \bar{D}^0\rho^+$ decays. We consider a truth (all particles correctly reconstructed), a $no\pi^0$ (only charged tracks correctly reconstructed) and a mis-reconstructed (mr) signal component separately. The reconstruction efficiencies for each signal component and both detector configurations are given together with the PID correction factors in Table A.1. We fix the relative fractions of the signal components in the fit. The parameter correlations are given in Tables A.3 to A.5.
The ΔE-$M_{\rm bc}$ distribution of the truth signal component is likewise modeled as described in 4.3.1, the ΔE ($M_{\rm bc}$) tail Gaussians are taken over from the $B^0 \to \rho^+\rho^-$ truth signal model and a similar correlation between ΔE and $M_{\rm bc}$ is included. The PDFs of the invariant dipion mass and helicity angle are one-dimensional versions of the corresponding PDFs from Eqs. (4.16) and (4.17).
Two-dimensional histograms are used for the description of the ΔE-$M_{\rm bc}$ and the $m_{\rho^\pm}$-$\cos\theta_{\rm H}$ distributions of the remaining signal components. The truth and $no\pi^0$ component share the same Δt PDF, see Eq. (4.19). The MC B^+ lifetime for each detector configuration, as obtained from a fit to signal MC events, are listed in Table A.2 and are in good agreement with the generated value of $\tau^{\rm gen}_{B^+} = 1.65$ ps. The Δt PDF of the misreconstructed component takes a similar form as Eq. (4.53) with an effective life time $\tau^{\rm mr}_{B^\pm{\rm eff}}$, see Table A.2. The total PDF for the truth signal component takes the from

$$\begin{aligned}\mathcal{P}_{\rm truth}(\Delta E, M_{\rm bc}, \mathcal{F}_{B\bar{B}/q\bar{q}}, m_{\rho^\pm}, \cos\theta_{\rm H}, \Delta t) \equiv \\ \mathcal{P}_{\rm truth}(\Delta E, M_{\rm bc}) \times \mathcal{P}_{\rm truth}(\mathcal{F}_{B\bar{B}/q\bar{q}}) \times \mathcal{P}_{\rm truth}(m_{\rho^\pm}) \times \mathcal{P}_{\rm truth}(\cos\theta_{\rm H}) \times \mathcal{P}_{\rm truth}(\Delta t), \qquad \text{(A.1)}\end{aligned}$$

and for the remaining signal (sig = $no\pi^0$, mr) components

$$\mathcal{P}_{\rm sig}(\Delta E, M_{\rm bc}, \mathcal{F}_{B\bar{B}/q\bar{q}}, m_{\rho^\pm}, \cos\theta_{\rm H}, \Delta t) \equiv$$
$$\mathcal{P}_{\rm sig}(\Delta E) \times \mathcal{P}_{\rm sig}(M_{\rm bc}) \times \mathcal{P}_{\rm sig}(\mathcal{F}_{B\bar{B}/q\bar{q}}) \times \mathcal{P}_{\rm sig}(m_{\rho^\pm}, \cos\theta_{\rm H}) \times \mathcal{P}_{\rm sig}(\Delta t). \quad \text{(A.2)}$$

Projections onto each signal components' fit variable are shown in Figs. A.1 to A.3.

SVD	$\epsilon_{\rm Rec}^{\rm truth}(\%)$	$\epsilon_{\rm Rec}^{\rm no\pi^0}(\%)$	$\epsilon_{\rm Rec}^{\rm mr}(\%)$	$\eta_{\rm PID}$
1	1.85	0.77	0.30	0.93 ± 0.02
2	2.76	1.24	0.44	0.92 ± 0.03

Table A.1: Reconstruction efficiencies and PID correction factor for the control channel measurement for the three signal components introduced in the text.

	$\tau_{B^\pm}^{\rm truth}$ [ps]	$\tau_{B^\pm{\rm eff}}^{\rm mr}$ [ps]
SVD1	1.67 ± 0.01	1.28 ± 0.04
SVD2	1.65 ± 0.01	1.17 ± 0.03

Table A.2: $B^\pm$ life times for the truth and the mis-reconstructed signal component obtained from a fit to signal MC events.

0	ΔE	M_{bc}	$\mathcal{F}_{B\bar{B}/q\bar{q}}$	$m^1_{\pi^+\pi^-}$	$\cos\theta^1_{\rm H}$	Δt
ΔE	1	-0.03	0.00	0.06	-0.13	-0.00
M_{bc}		1	0.01	-0.01	-0.02	0.01
$\mathcal{F}_{B\bar{B}/q\bar{q}}$			1	-0.02	0.01	0.00
$m^1_{\pi^+\pi^-}$				1	-0.03	-0.00
$\cos\theta^1_{\rm H}$					1	-0.00
Δt						1

Table A.3: Correlation matrix for the truth component of $B^+ \to \bar{D}0\rho^+$ decays.

0	ΔE	M_{bc}	$\mathcal{F}_{B\bar{B}/q\bar{q}}$	$m^1_{\pi^+\pi^-}$	$\cos\theta^1_{\rm H}$	Δt
ΔE	1	0.03	0.04	0.08	-0.10	0.02
M_{bc}		1	0.03	-0.03	0.06	-0.00
$\mathcal{F}_{B\bar{B}/q\bar{q}}$			1	-0.02	0.01	-0.01
$m^1_{\pi^+\pi^-}$				1	-0.09	0.01
$\cos\theta^1_{\rm H}$					1	-0.00
Δt						1

Table A.4: Correlation matrix for the $no\pi^0$ component of $B^+ \to \bar{D}0\rho^+$ decays.

0	ΔE	M_{bc}	$\mathcal{F}_{B\bar{B}/q\bar{q}}$	$m^1_{\pi^+\pi^-}$	$\cos\theta^1_{\rm H}$	Δt
ΔE	1	0.03	0.05	0.04	0.09	0.00
M_{bc}		1	0.04	-0.04	0.06	0.00
$\mathcal{F}_{B\bar{B}/q\bar{q}}$			1	-0.02	0.08	0.01
$m^1_{\pi^+\pi^-}$				1	0.02	-0.01
$\cos\theta^1_{\rm H}$					1	-0.01
Δt						1

Table A.5: Correlation matrix for the mis-reconstructed component of $B^+ \to \bar{D}0\rho^+$ decays.

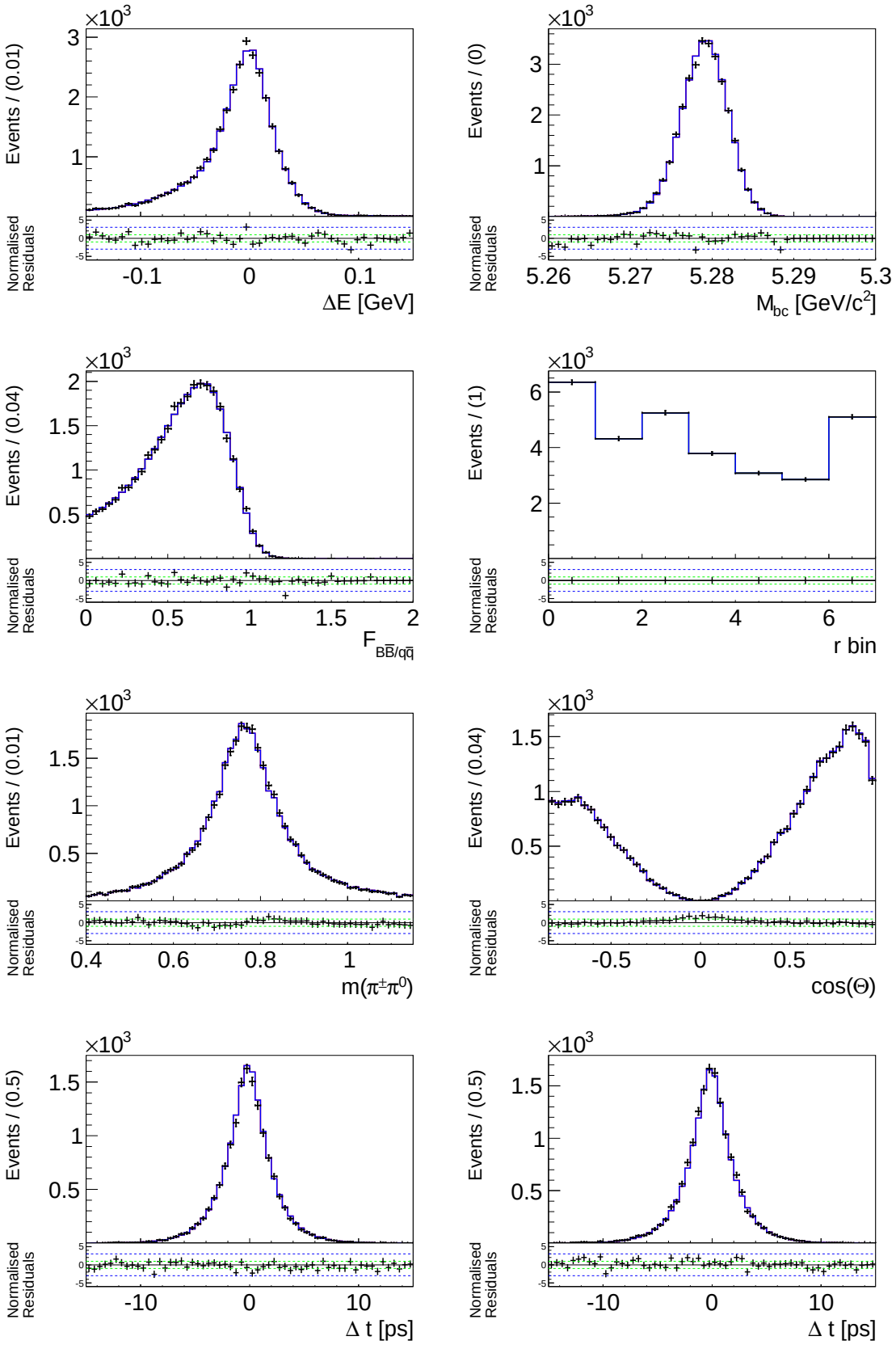

Figure A.1: Fit results for correctly reconstructed $B^{\pm} \to D^0\rho^{\pm}$ MC events.

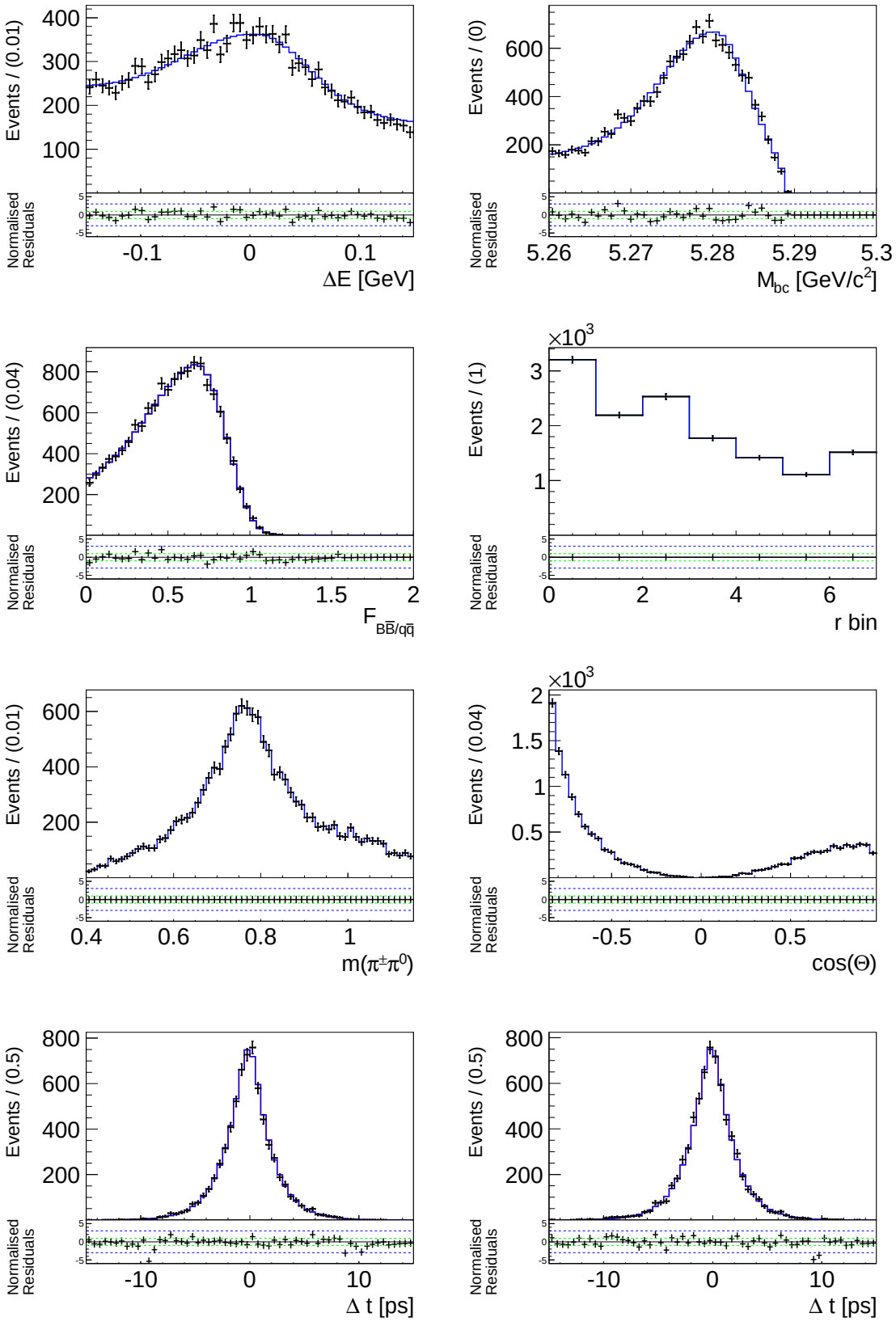

Figure A.2: Fit results for the $no\pi^0$ component of $B^{\pm} \to D^0\rho^{\pm}$ MC events.

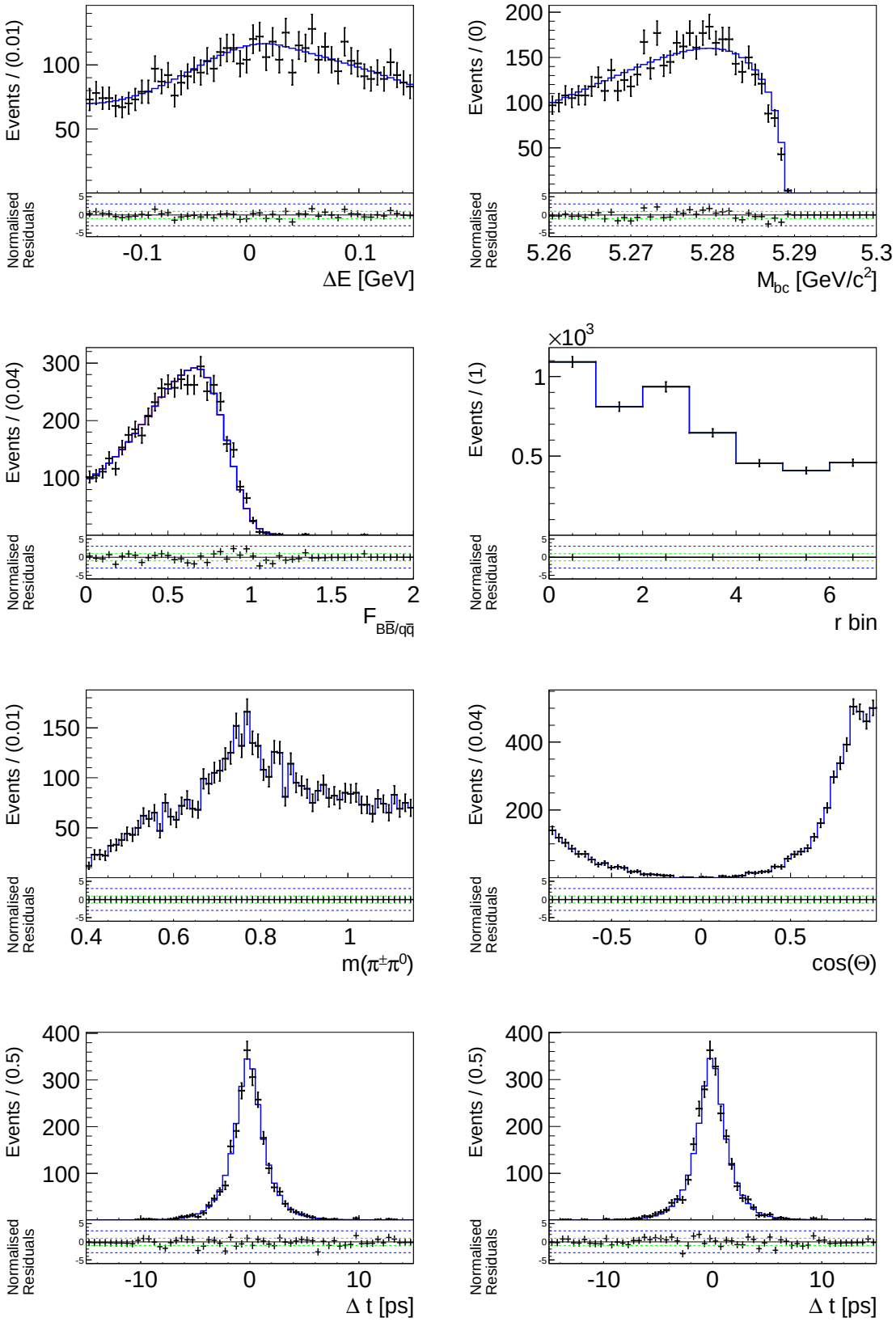

Figure A.3: Fit results for mis-reconstructed $B^{\pm} \to D^0\rho^{\pm}$ MC events.

A.1.2 $B\bar{B}$ Model

We build separate models for neutral and charged B decays into final states including a charm quark. The distributions are obtained from fully simulated MC.
Each components' ΔE distribution is described the sum of Chebychev polynomials up to the fifth order

$$\mathcal{P}^{\mathrm{CF}}_{B\bar{B}}(\Delta E) = \sum_{i=1}^{5} c_i C_i(\Delta E). \tag{A.3}$$

The PDF of M_{bc} of neutral B decays takes the smooth form

$$\mathcal{P}^{\mathrm{CF}}_{B^0\bar{B}^0}(M_{\mathrm{bc}}) = \begin{cases} Arg(M_{\mathrm{bc}}) & \text{if } M_{\mathrm{bc}} > c_{M_{\mathrm{bc}},\mathrm{cut}} \\ Arg(c_{M_{\mathrm{bc}},\mathrm{cut}}) + c_{M_{\mathrm{bc}},1}(M_{\mathrm{bc}} - c_{M_{\mathrm{bc}},\mathrm{cut}}) & \text{else,} \end{cases} \tag{A.4}$$

with $c_{M_{\mathrm{bc}},\mathrm{cut}} \sim 5.28\mathrm{GeV/c^2}$. The M_{bc} distribution of $B^{\pm}$ decays is modeled by the sum of an Argus function and a double-bifurcated Gaussian

$$\mathcal{P}^{\mathrm{CF}}_{B^{\pm}}(M_{\mathrm{bc}}) = f dbG(M_{\mathrm{bc}}) + (1-f) Arg(M_{\mathrm{bc}}). \tag{A.5}$$

We use two-dimensional histograms to model the $m_{\rho^{\pm}}$-$\cos\theta_{\mathrm{H}}$ distribution of each $B\bar{B}$ background. The Δt PDFs are similar described as in the $B^0 \to \rho^+\rho^-$ analysis, the effective life times are obtained from a fit to fully simulated MC samples and are listed in Table A.6. Projections onto the fit variables are shown in Figs. A.4 and A.5. The r-bin fractions and relative fractions of the $B\bar{B}$ components, obtained from MC simulation, are listed in Table A.7 and are fixed in the fit to data.
Thus the total PDF for each ($B\bar{B} = B^0\bar{B}^0$ or $B^{\pm}$) background takes the form

$$\begin{aligned} &\mathcal{P}_{B\bar{B}}(\Delta E, M_{\mathrm{bc}}, \mathcal{F}_{B\bar{B}/q\bar{q}}, m_{\rho^{\pm}}, \cos\theta_{\mathrm{H}}, \Delta t) \equiv \\ &\mathcal{P}_{B\bar{B}}(\Delta E) \times \mathcal{P}_{B\bar{B}}(M_{\mathrm{bc}}) \times \mathcal{P}_{B\bar{B}}(\mathcal{F}_{B\bar{B}/q\bar{q}}) \times \mathcal{P}_{B\bar{B}}(m_{\rho^{\pm}}, \cos\theta_{\mathrm{H}}) \times \mathcal{P}_{B\bar{B}}(\Delta t). \end{aligned} \tag{A.6}$$

	SVD1	SVD2
$\tau_{B^0\bar{B}^0}$; $[ps]$	1.40 ± 0.01	1.42 ± 0.01
$\tau_{B^{\pm}}$; $[ps]$	1.57 ± 0.01	1.55 ± 0.01

Table A.6: Effective life times of the background from B decays obtained from a fit fully simulated MC samples.

SVD	$R_{B^{\pm}/B^0}$
1	2.110 ± 0.013
2	2.067 ± 0.004

Table A.7: Relative fraction of B^+ to B^0 background events, $R_{B^{\pm}/B^0}$, as obtained from background MC samples.

0	ΔE	M_{bc}	$\mathcal{F}_{B\bar{B}/q\bar{q}}$	$m^1_{\pi^+\pi^-}$	$\cos\theta^1_{\rm H}$	Δt
ΔE	1	-0.05	0.03	0.02	-0.02	0.00
M_{bc}		1	0.03	-0.01	0.06	-0.00
$\mathcal{F}_{B\bar{B}/q\bar{q}}$			1	-0.02	0.04	0.00
$m^1_{\pi^+\pi^-}$				1	-0.08	-0.00
$\cos\theta^1_{\rm H}$					1	0.01
Δt						1

Table A.8: Correlation matrix for backgrounds from B^0 decays for the control channel measurement.

0	ΔE	M_{bc}	$\mathcal{F}_{B\bar{B}/q\bar{q}}$	$m^1_{\pi^+\pi^-}$	$\cos\theta^1_{\rm H}$	Δt
ΔE	1	-0.13	-0.02	0.06	-0.13	0.00
M_{bc}		1	0.05	-0.03	0.08	-0.00
$\mathcal{F}_{B\bar{B}/q\bar{q}}$			1	-0.02	0.03	0.00
$m^1_{\pi^+\pi^-}$				1	-0.09	0.00
$\cos\theta^1_{\rm H}$					1	0.01
Δt						1

Table A.9: Correlation matrix for backgrounds from $B^\pm$ decays for the control channel measurement.

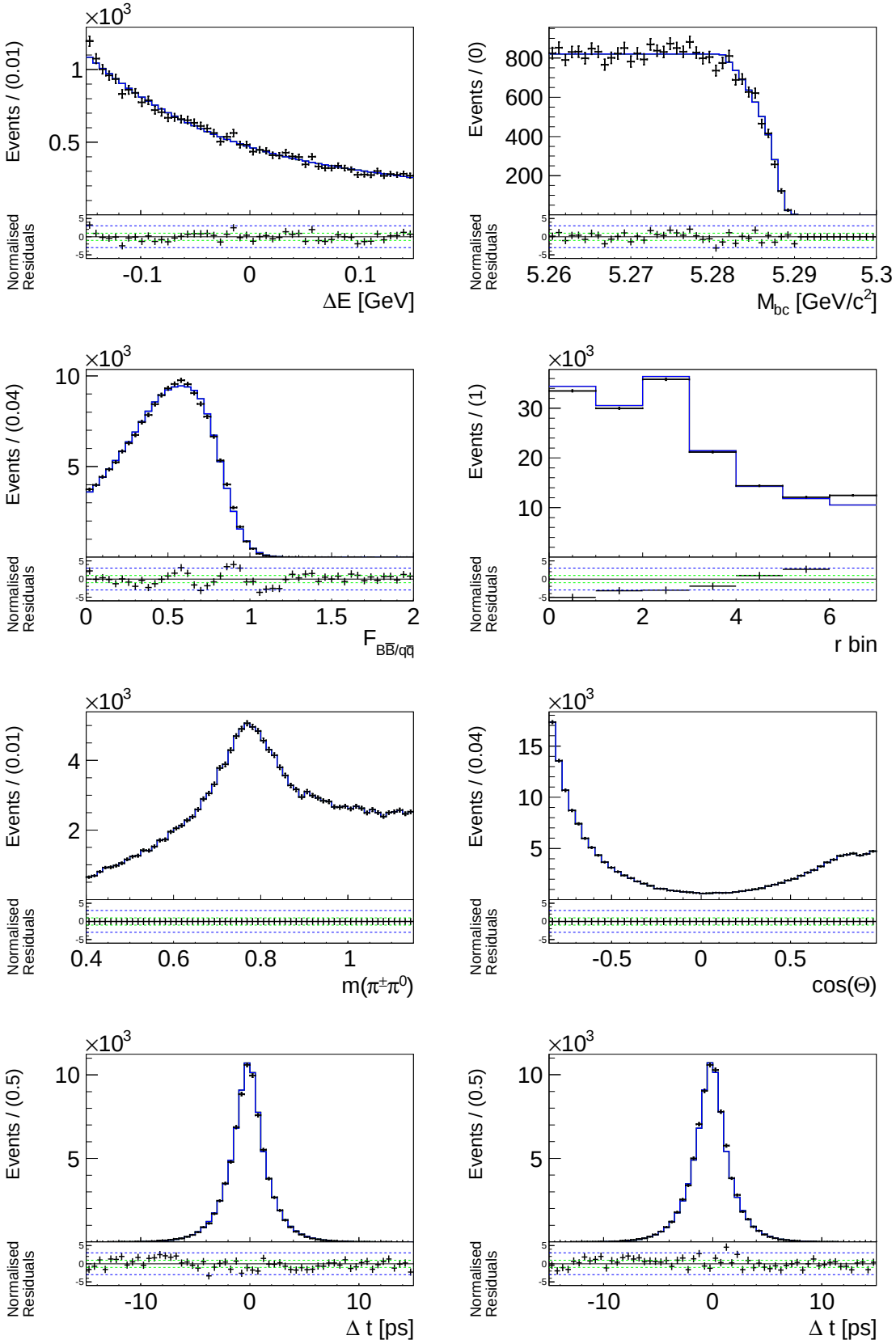

Figure A.4: Results of a fit to fully simulated MC events for B^0 decays to charm final states for the control sample measurement.

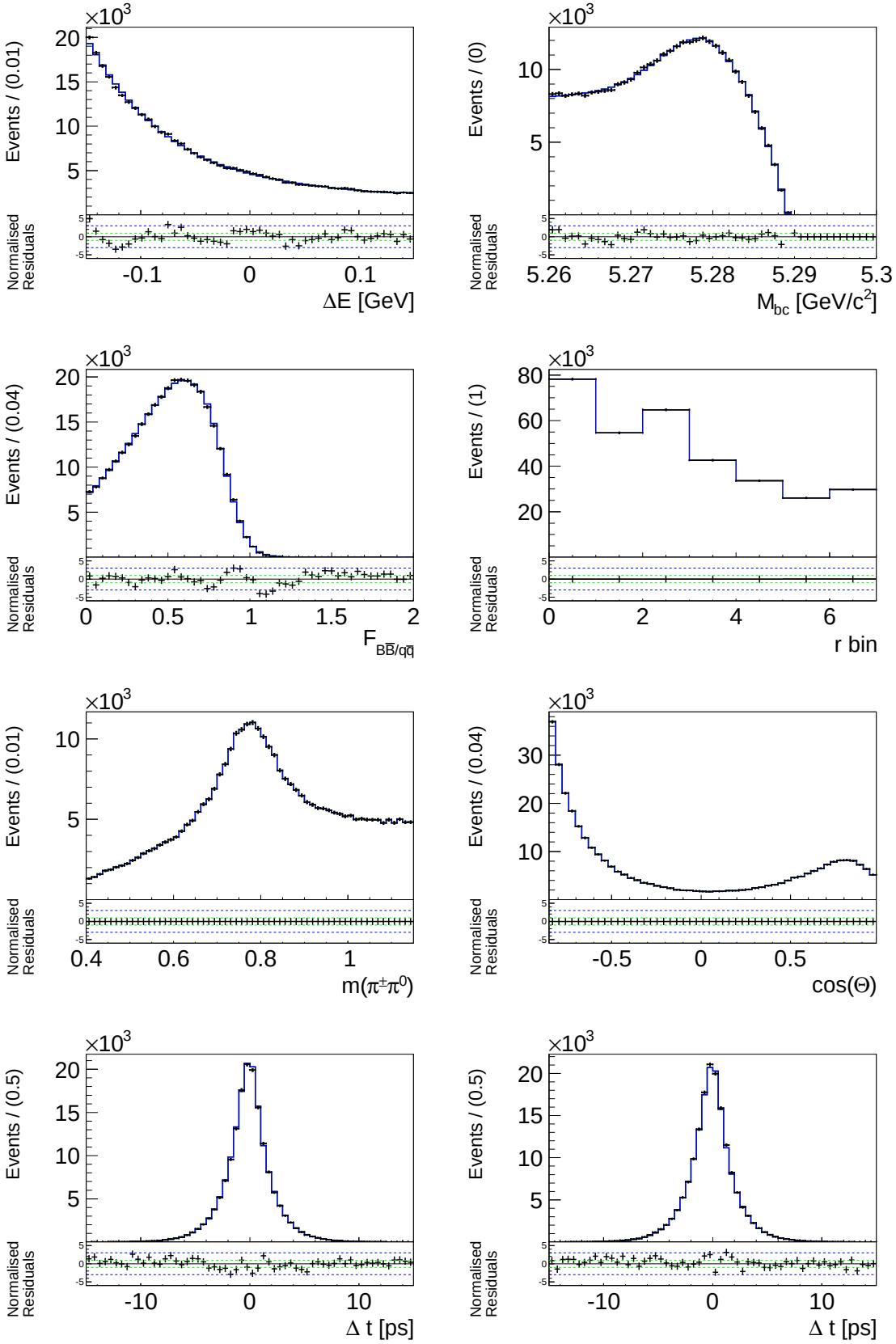

Figure A.5: Results of a fit to fully simulated MC events for $B^{\pm}$ decays to charm final states for the control sample measurement.

A.1.3 Continuum Model

The shape of the continuum component is finalized in the fit to on-resonance data, we use off-resonance data to obtain a parametrization of the PDFs beforehand.
The ΔE shape is described by a sum of Chebychev polynomials up to the third order,

$$\mathcal{P}^{\mathrm{CS}}_{q\bar{q}}(\Delta E) \equiv \sum_{i=1}^{3} c_i C_i(\Delta E), \tag{A.7}$$

and the M_{bc} distribution is modeled by an Argus function

$$\mathcal{P}^{\mathrm{CS}}_{q\bar{q}}(M_{\mathrm{bc}}) \equiv Ar(M_{\mathrm{bc}}). \tag{A.8}$$

We model the $\mathcal{F}_{B\bar{B}/q\bar{q}}$ distribution with a double Gaussian in each r-bin;

$$\mathcal{P}^{\mathrm{CS}}_{q\bar{q},k}(\mathcal{F}_{B\bar{B}/q\bar{q}}) \equiv dG_k(\mathcal{F}_{B\bar{B}/q\bar{q}}). \tag{A.9}$$

The invariant dipion mass distribution is described by a sum of two Breit-Wigner functions and polynomials ($P_i(x)$) up to the fifth order

$$\begin{aligned}\mathcal{P}^{\mathrm{CS}}_{q\bar{q}}(m_{\rho^\pm}) \equiv f_{q\bar{q},1} BW(m_{\rho^\pm}, \mu_{q\bar{q},1}, \sigma_{q\bar{q},1}) + \\ f_{q\bar{q},2} BW(m_{\rho^\pm}, \mu_{q\bar{q},2}, \sigma_{q\bar{q},2}) + (1 - f_{q\bar{q},1} - f_{q\bar{q},2}) \sum_{i=1}^{5} P_i(m_{\rho^\pm}),\end{aligned} \tag{A.10}$$

and the helicity angle distribution by the sum of Chebychev polynomials up to the eighth order

$$\mathcal{P}^{\mathrm{CS}}_{q\bar{q}}(\cos\theta_{\mathrm{H}}) \equiv \sum_{i=1}^{8} c_i C_i(\cos\theta_{\mathrm{H}}). \tag{A.11}$$

The Δt PDF is similar to the one used to describe the continuum component in the $B^0 \to \rho^+\rho^-$ analysis Eq. (4.69), the effective life time is found to be $\tau^{q\bar{q}}_{B^\pm,\mathrm{eff}} = 0.76 \pm 0.02$ ps for detector configuration SVD1 and $\tau^{q\bar{q}}_{B^\pm,\mathrm{eff}} = 0.54 \pm 0.02$ ps for SVD2. Fig. A.6 shows the results from a fit to off-resonance data and the fit parameter correlations, as found in the off-resonance data, are listed in Table A.10.
The total PDF for continuum events is given by

$$\begin{aligned}\mathcal{P}^{\mathrm{CS}}_{q\bar{q}}(\Delta E, M_{\mathrm{bc}}, \mathcal{F}_{B\bar{B}/q\bar{q}}, m_\rho, \cos\theta_{\mathrm{H}}, \Delta t) \equiv \\ \mathcal{P}^{\mathrm{CS}}_{q\bar{q}}(\Delta E) \times \mathcal{P}^{\mathrm{CS}}_{q\bar{q}}(M_{\mathrm{bc}}) \times \mathcal{P}^{\mathrm{CS}}_{q\bar{q}}(\mathcal{F}_{B\bar{B}/q\bar{q}}) \times \mathcal{P}^{\mathrm{CS}}_{q\bar{q}}(m_\rho) \times \mathcal{P}^{\mathrm{CS}}_{q\bar{q}}(\cos\theta_{\mathrm{H}}) \times \mathcal{P}^{\mathrm{CS}}_{q\bar{q}}(\Delta t, q).\end{aligned} \tag{A.12}$$

0	ΔE	M_{bc}	$\mathcal{F}_{B\bar{B}/q\bar{q}}$	$m^1_{\pi^+\pi^-}$	$\cos\theta^1_{\rm H}$	Δt
ΔE	1	0.00	-0.00	0.01	0.03	0.00
M_{bc}		1	-0.02	-0.00	0.02	-0.01
$\mathcal{F}_{B\bar{B}/q\bar{q}}$			1	0.00	0.03	0.00
$m^1_{\pi^+\pi^-}$				1	0.05	0.00
$\cos\theta^1_{\rm H}$					1	-0.01
Δt						1

Table A.10: Continuum correlation matrix for the control channel measurement.

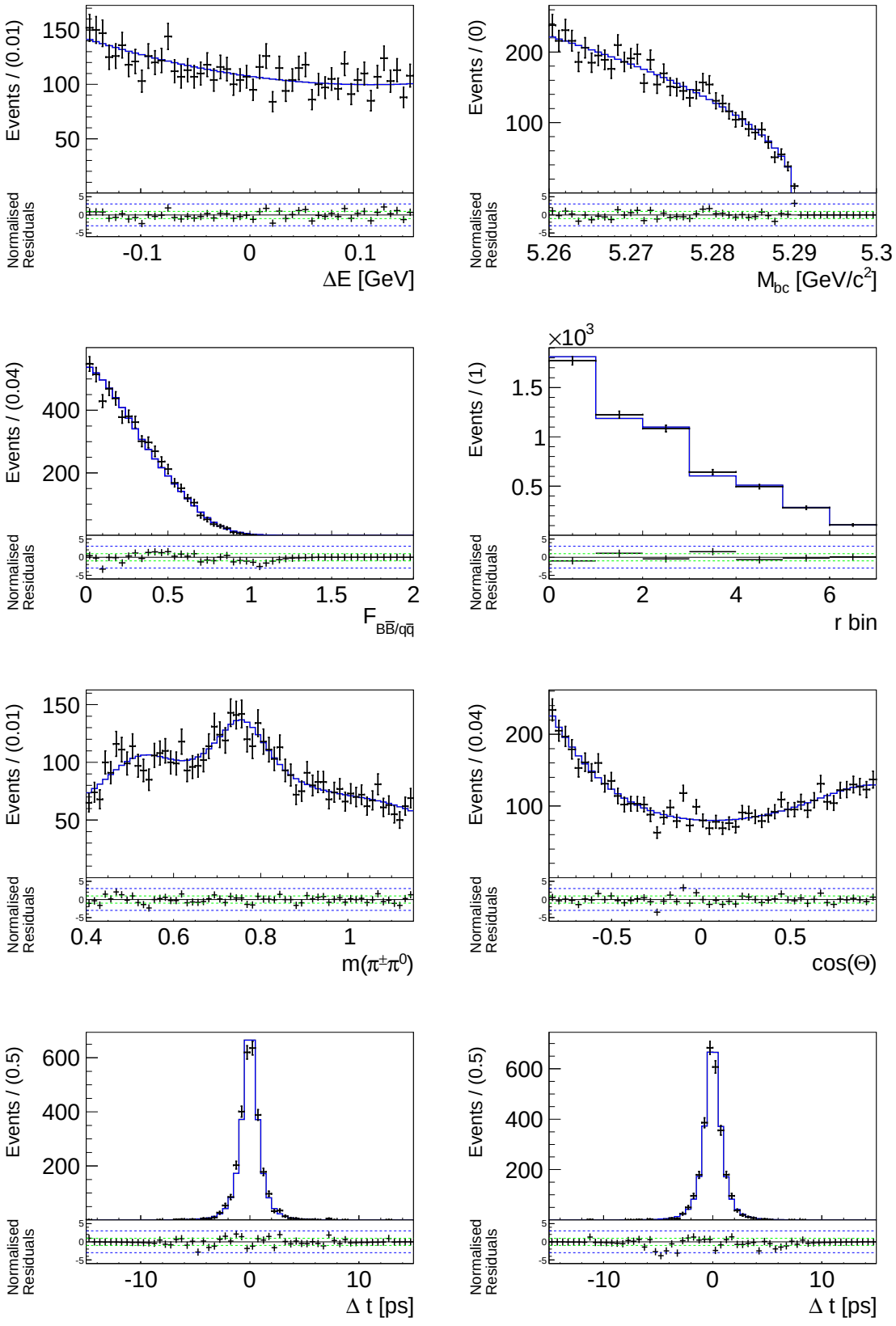

Figure A.6: Results from a fit to off-resonance data for the control sample measurement.

A.2 Fit Result

The total PDF of the control sample for $N = 161283$ events takes the form

$$\mathcal{L}^{\mathrm{CS}} = \frac{e^{-\sum_j N_j \sum_l f_{j,k}}}{N!} \prod_{i=1}^{N} \sum_j N_j \times P_j(\Delta E^i, M^i_{\mathrm{bc}}, \mathcal{F}^i_{B\bar{B}/q\bar{q}}, m^i_{\rho^\pm}, \cos\theta^i_{\mathrm{H}}, \Delta t^i), \tag{A.13}$$

where N_j is the yield of the jth component and $f_{j,k}$, its r-bin fractions. Again $N_{\mathrm{D}\rho}$ is replaced with the branching ratio, see Section 4.6. We do not apply a π^0 efficiency correction in the branching fraction calculation. Other free parameters are the continuum shape and yield in each r-bin and the $B\bar{B}$ yield. We perform a three-dimensional fit (ΔE, M_{bc}, $\mathcal{F}_{B\bar{B}/q\bar{q}}$) to the data and obtain a branching fraction of

$$\mathcal{B}(B^+ \to \bar{D}^0\rho^+) \times \mathcal{B}(\bar{D}^0 \to K^+\pi^-\pi^0) = (1.11 \pm 0.01\ (\mathrm{stat})) \times 10^{-3}; \tag{A.14}$$

the fit result is shown in Fig. A.7 and can be compared with the result without correction, see Fig. A.8. The obtained correction factors are given in Table A.11. Our result is in agreement the exclusive measurement performed by the CLEO collaboration [122]

$$\mathcal{B}(B^+ \to \bar{D}^0\rho^+) \times \mathcal{B}(\bar{D}^0 \to K^+\pi^-\pi^0) = (1.26 \pm 0.23) \times 10^{-3}, \tag{A.15}$$

assuming $\mathcal{B}(\bar{D}^0 \to K^+\pi^-\pi^0) = (12.1 \pm 1.1)\%$. Although the CLEO measurement is dominating the current world average, averaging the measurements of $B^+ \to \bar{D}^0[K\mathrm{n}\pi]\rho^+$ decays (n=1,2,3) is shifting the value up. As a consequence, the current world average [45],

$$\mathcal{B}(B^0 \to \bar{D}^0\rho^+) \times \mathcal{B}(\bar{D}^0 \to K^+\pi^-\pi^0)_{\mathrm{WA}} = (1.86 \pm 0.18) \times 10^{-3}, \tag{A.16}$$

is by $\sim 3\sigma$ different from our result as systematic uncertainties are typically of the order 10%. An independent, yet in-official, study performed by Belle is also observing less $B^+ \to \bar{D}^0\rho^+$ events than expected from the world averages. They reconstruct $D \to K^-\pi^+$ and use the full reconstruction method in the measurement of the ratio $\frac{\mathcal{B}(B^+\to\bar{D}^0\rho^+)}{\mathcal{B}(B^+\to\bar{D}^0\pi^+)} = 2.13 \pm 0.12$ and the branching fraction of $\mathcal{B}(B^+ \to \bar{D}^0\pi^+) = (4.87 \pm 0.16) \times 10^{-3}$. We translate their result to $\mathcal{B}(B^+ \to \bar{D}^0\rho^+) \times \mathcal{B}(\bar{D}^0 \to K^+\pi^-\pi^0) = (1.44 \pm 0.11) \times 10^{-3}$ using the current world average for $\mathcal{B}(\bar{D}^0 \to K^+\pi^-\pi^0)$. It is noteworthy that their deviation from the W.A. mainly arises from the ratio of the branching fractions being lower than expected, while $\mathcal{B}(B^+ \to \bar{D}^0\pi^+)$ is in good agreement.

A.2.1 5D Fit Result

We add the ρ mass and the helicity angle to the fit and obtain

$$\mathcal{B}(B^+ \to \bar{D}^0\rho^+)_{\mathrm{5D}} \times \mathcal{B}(\bar{D}^0 \to K^+\pi^-\pi^0) = (1.13 \pm 0.01\ (\mathrm{stat})) \times 10^{-3}, \tag{A.17}$$

being in agreement with our baseline (3D) result. Projections onto the mass and the helicity angle are shown in Fig. A.9, where the mass-distribution is well described while the small but noticeable disagreement in the helicity distribution can be tolerated as it does not exceed 3σ in any bin and even more important, it does not bias the fit result. We identify the $B\bar{B}$ background as its source and expect only 10% of the amount of events being present here

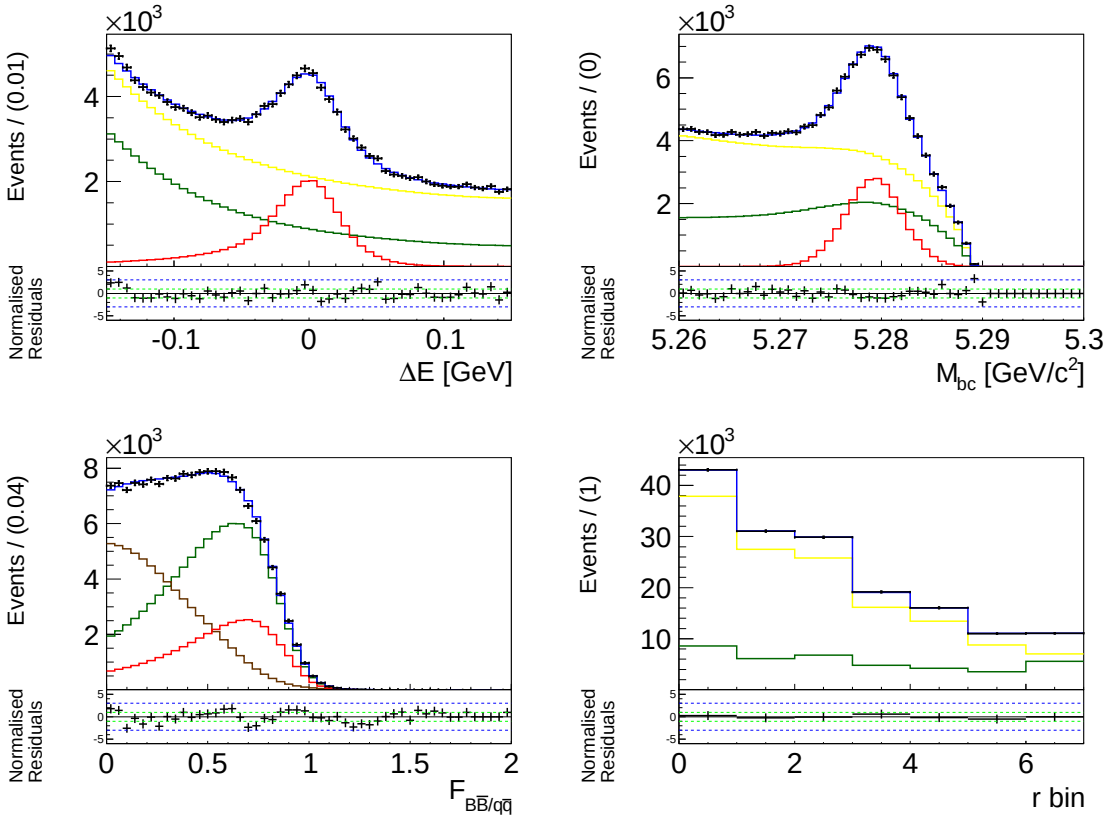

Figure A.7: Control sample result from the fit to data. Signal is shown in red, the $B\bar{B}$ background in green, the combined backgrounds in yellow and the total PDF in blue. Data is shown as black points.

in the $B^0 \to \rho^+\rho^-$ analysis. There, other events contribute and we describe the method of accounting for differences in the data/MC distribution in Chapter 6.
In $S \to SV$ decays the SM predicts the vector particle to be purely longitudinal polarized, which is confirmed by measurement [64]. We use the helicity information to validate our helicity measurement by extracting the fraction of longitudinal polarized $\rho^\pm$ mesons, f_L, from the fit to data. Therefore, we add another signal component with a transverse polarized $\rho^\pm$ to the fit. Its entire PDF is taken from the truth model with the exception of the helicity PDF, being substituted by a one-dimensional version of the PDF for transversely polarized $B^0 \to \rho^+\rho^-$ decays (truth model). We obtain

$$f_L = 1.003 \pm 0.003 \text{ (stat)}, \tag{A.18}$$

being in perfect agreement with the prediction and previous measurements.

A.2.2 6D Fit Result

We furthermore add Δt to the fit and obtain

$$\mathcal{B}(B^+ \to \bar{D}^0\rho^+)_{\text{6D}} \times \mathcal{B}(\bar{D}^0 \to K^+\pi^-\pi^0) = (1.15 \pm 0.01 \text{ (stat)}) \times 10^{-3}, \tag{A.19}$$

being in good agreement with our baseline (3D) fit result.
We perform a fit to the $B^\pm$ lifetime and obtain $\tau_{B^\pm}^{\text{SVD1}} = 1.63 \pm 0.03$ ps and $\tau_{B^\pm}^{\text{SVD1}} = 1.67 \pm$

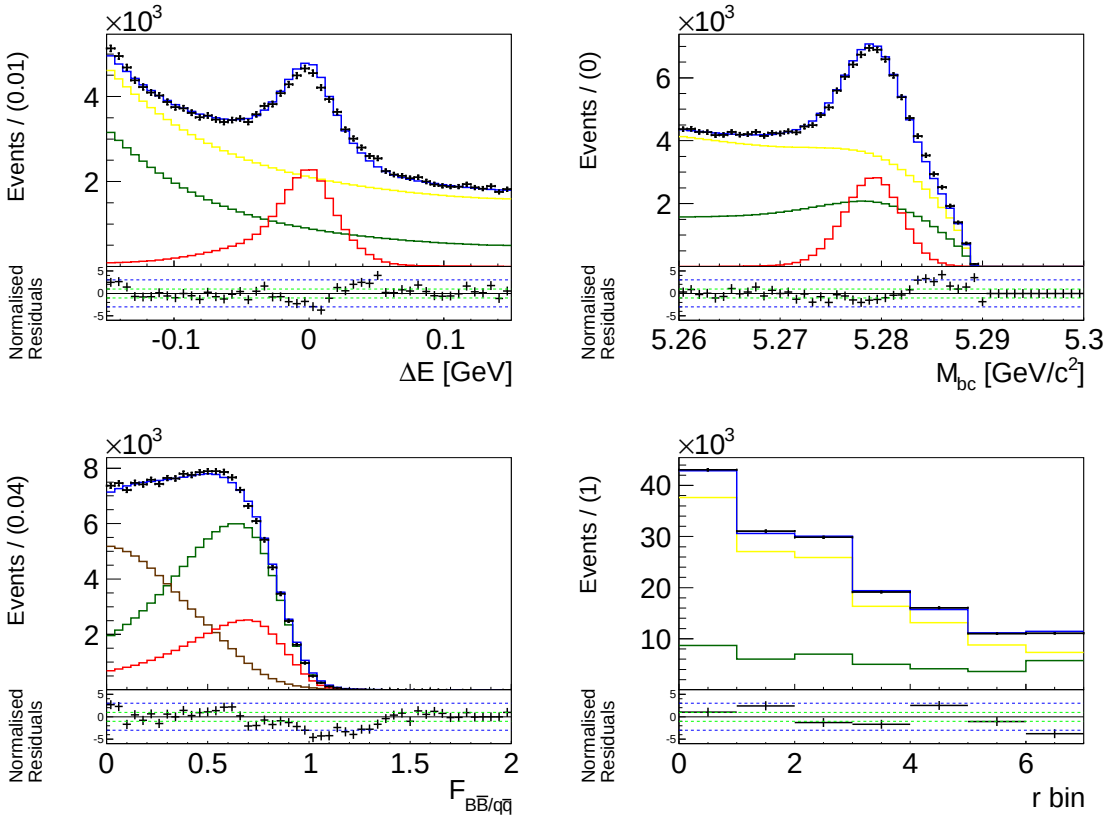

Figure A.8: Control sample result from the fit to data. Here, the model shape is fixed from MC studies and no correction has been applied. Signal is shown in red, the $B\bar{B}$ background in green, the combined backgrounds in yellow and the total PDF in blue. Data is shown as black points.

0.01 ps for each detector configuration, being in good agreement with the current world average $\tau_{B^\pm}^{\text{W.A.}} = 1.64 \pm 0.01$ ps [45]. Projections onto Δt for both $B^\pm$ charges are shown in Fig. A.10.

A.3 Validation Study

We validate the control channel fitting procedure by analyzing a small but sufficient number of 20 pseudo experiments, generated entirely from fully simulated events. We generate according to our fit result, except for continuum. There only a fraction of $\sim$ 10% of the amount of observed continuum events is used, because not enough off-resonance data is available. The number of events per component and detector configuration are listed in Table A.12. An example fit result is shown in Figs. A.11 and A.12. The ensemble test shows that the fitter is able to reproduce the generated value of the branching fraction Fig. A.13 .

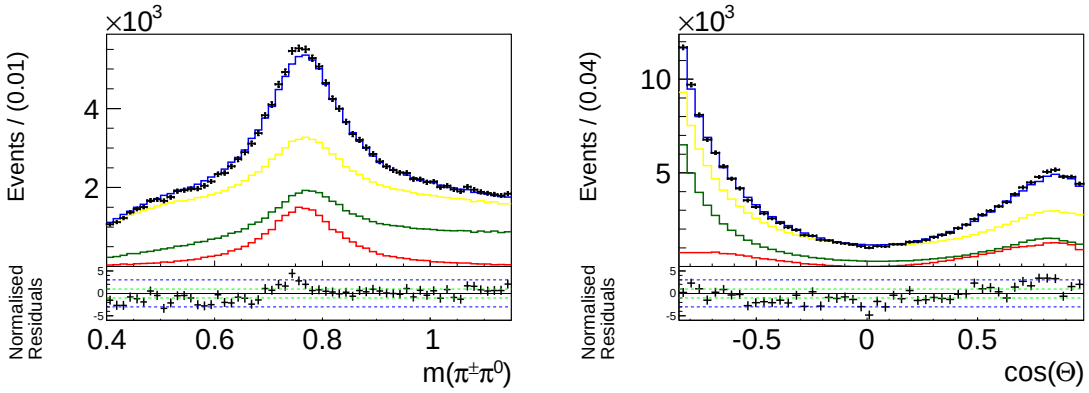

Figure A.9: Control sample result from the (5D) fit to data. Signal is shown in red, the $B\bar{B}$ background in green, the combined backgrounds in yellow and the total PDF in blue. Data is shown as black points.

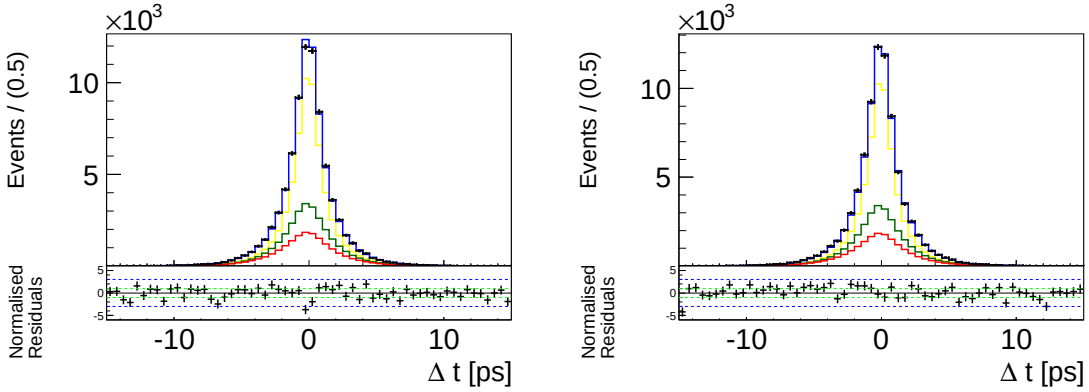

Figure A.10: Control sample result from the (6D) fit to data for B^+ (left) and B^-. Signal is shown in red, the $B\bar{B}$ background in green, the combined backgrounds in yellow and the total PDF in blue. Data is shown as black points.

A.4 Consequences For The Signal Reconstruction Efficiency

Because the reconstruction efficiencies are obtained from MC simulation, a difference in the shape in data can alter these. We estimate this effect by comparing two large samples of $B^0 \to \rho^+\rho^-$ signal MC events, generated from PDF. In one sample the shape is corrected with the factors obtained from the control channel measurement, while the other shape remains uncorrected. For each set we generate 38000 events in a broader range of $\Delta E \in [-0.18, 0.18]$GeV and $\mathcal{F}_{B\bar{B}/q\bar{q}} \in [-2, 3]$ and compare the number of events that make it into our fit region defined in Section 3.2.9. $M_{\rm bc}$ is sufficiently covered by the signal region and therefore ignored. We obtain a negligible correction of

$$\epsilon_{\rm CF}^{\rm rec.eff.} \equiv \frac{N_{\rm corrected}}{N_{\rm uncorrected}} = 0.996 \pm 0.010. \tag{A.20}$$

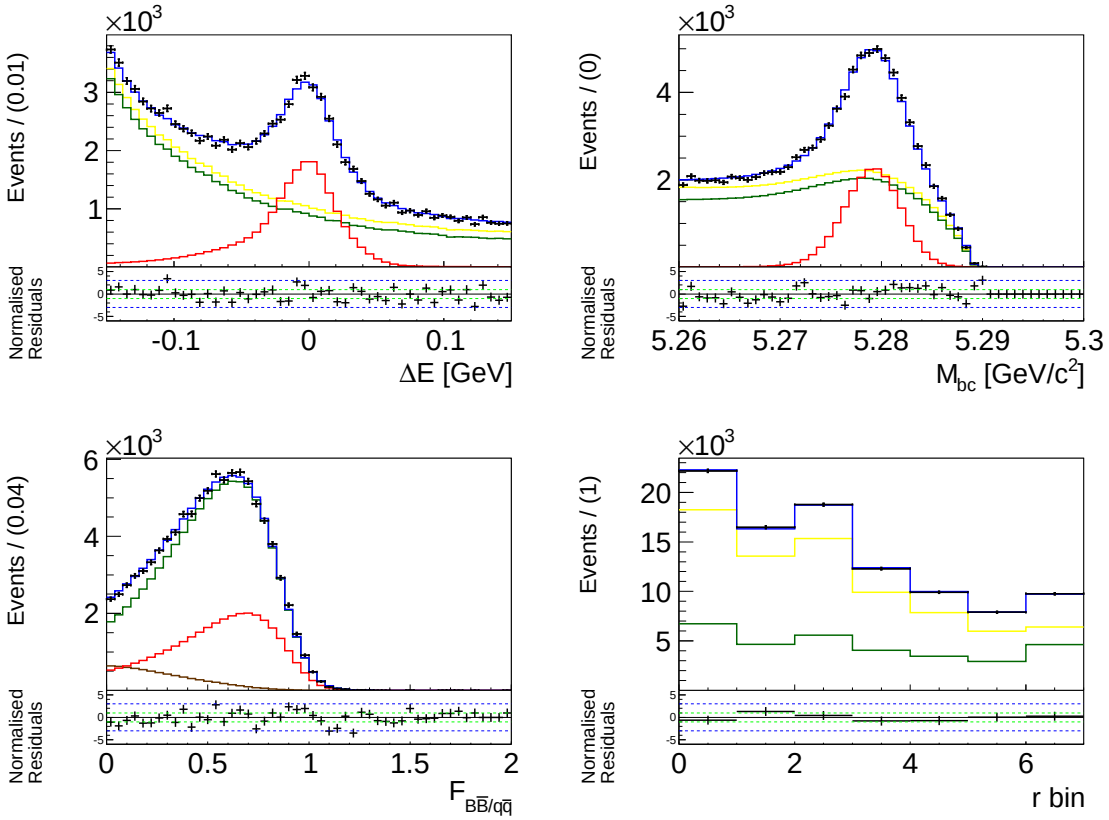

Figure A.11: Control sample result from the fit to an example toy experiment. Signal is shown in red, the $B\bar{B}$ background in green, the combined backgrounds in yellow and the total PDF in blue. MC events are shown as black points.

	SVD1	SVD2
$\mu^{CF\Delta E}$	-0.006 ± 0.001	$0.002 \pm \mathit{0.001}$
$\sigma_l^{CF\Delta E}$	0.725 ± 0.054	1.276 ± 0.055
$\sigma_r^{CF\Delta E}$	1.090 ± 0.072	1.276 ± 0.051
$f^{CF\Delta E}$	0.582 ± 0.138	1.154 ± 0.037
$\mu^{CFM_{\rm bc}}$	0.000 ± 0.001	$0.000 \pm \mathit{0.001}$
$\sigma_l^{CFM_{\rm bc}}$	0.922 ± 0.042	1.040 ± 0.030
$\sigma_r^{CFM_{\rm bc}}$	1.088 ± 0.034	1.023 ± 0.020
$f^{CFM_{\rm bc}}$	1.088 ± 0.065	1.141 ± 0.034
f_1^{CFr}	1.047 ± 0.021	0.994 ± 0.009
f_2^{CFr}	1.046 ± 0.024	1.020 ± 0.010
f_3^{CFr}	0.973 ± 0.022	0.992 ± 0.009
f_4^{CFr}	0.941 ± 0.027	0.982 ± 0.011
f_5^{CFr}	1.046 ± 0.028	1.032 ± 0.013
f_6^{CFr}	0.935 ± 0.030	1.009 ± 0.014
μ_1^{CFF}	-0.013 ± 0.012	0.001 ± 0.006
σ_{l1}^{CFF}	0.911 ± 0.065	1.065 ± 0.034
σ_{r1}^{CFF}	0.961 ± 0.043	0.937 ± 0.021
μ_2^{CFF}	0.013 ± 0.013	0.000 ± 0.006
σ_{l2}^{CFF}	0.951 ± 0.062	1.018 ± 0.033
σ_{r2}^{CFF}	0.866 ± 0.052	0.971 ± 0.024
μ_3^{CFF}	0.014 ± 0.013	0.002 ± 0.006
σ_{l3}^{CFF}	0.867 ± 0.059	1.020 ± 0.034
σ_{r3}^{CFF}	0.840 ± 0.062	0.942 ± 0.027
μ_4^{CFF}	0.040 ± 0.017	0.005 ± 0.007
σ_{l4}^{CFF}	1.213 ± 0.100	0.957 ± 0.036
σ_{r4}^{CFF}	0.791 ± 0.067	0.942 ± 0.031
μ_5^{CFF}	0.010 ± 0.015	0.021 ± 0.008
σ_{l5}^{CFF}	0.924 ± 0.078	0.972 ± 0.040
σ_{r5}^{CFF}	0.842 ± 0.060	0.86 ± 0.035
μ_6^{CFF}	-0.022 ± 0.016	-0.010 ± 0.007
σ_{l6}^{CFF}	0.77 ± 0.053	0.982 ± 0.038
σ_{r6}^{CFF}	1.063 ± 0.087	1.0145 ± 0.030
μ_7^{CFF}	0.003 ± 0.014	-0.009 ± 0.006
σ_{l7}^{CFF}	0.950 ± 0.073	1.009 ± 0.029
σ_{r7}^{CFF}	0.972 ± 0.050	1.007 ± 0.027

Table A.11: Control sample correction factors for SVD1 obtained from the fit to data.

	# signal	# continuum	#gm	#gc
SVD1	4445	1000	2867	6053
SVD2	27486	5000	16449	34003

Table A.12: Number of generated events per component for the validation of the control channel measurement. The signal component is composed out of three types as explained in the text.

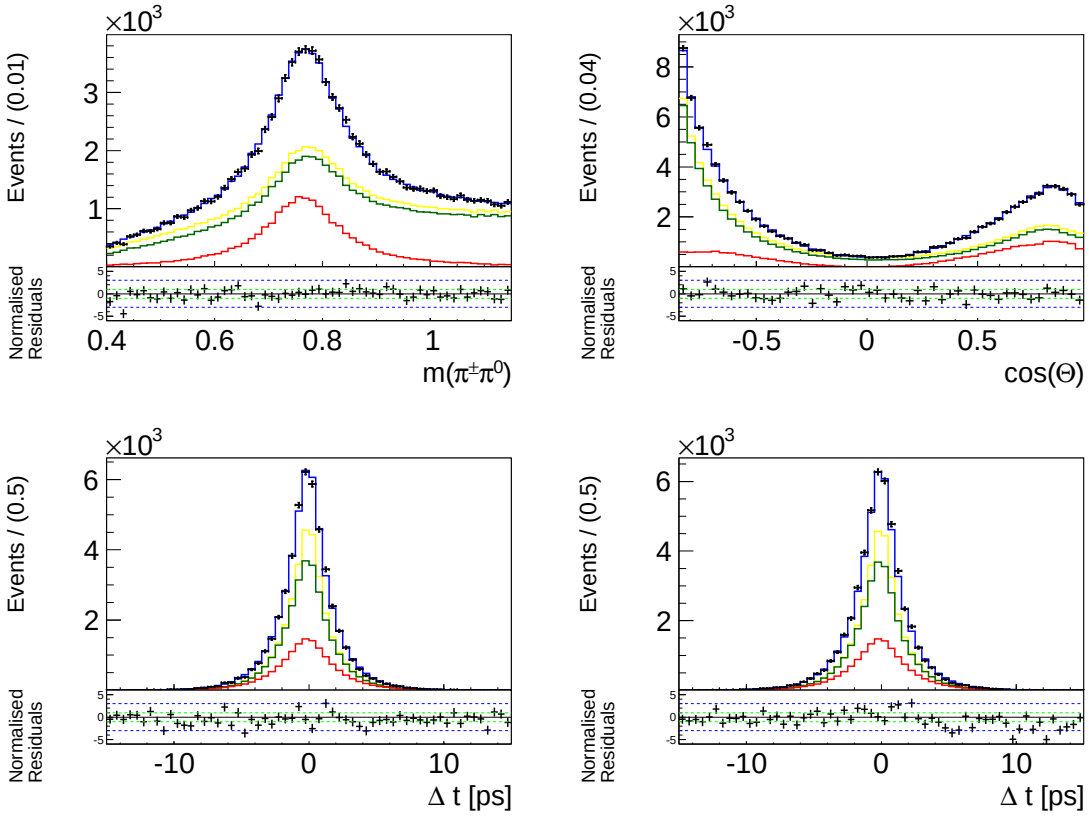

Figure A.12: Control sample result from the fit to an example toy experiment. Signal is shown in red, the $B\bar{B}$ background in green, the combined backgrounds in yellow and the total PDF in blue. MV events are shown as black points.

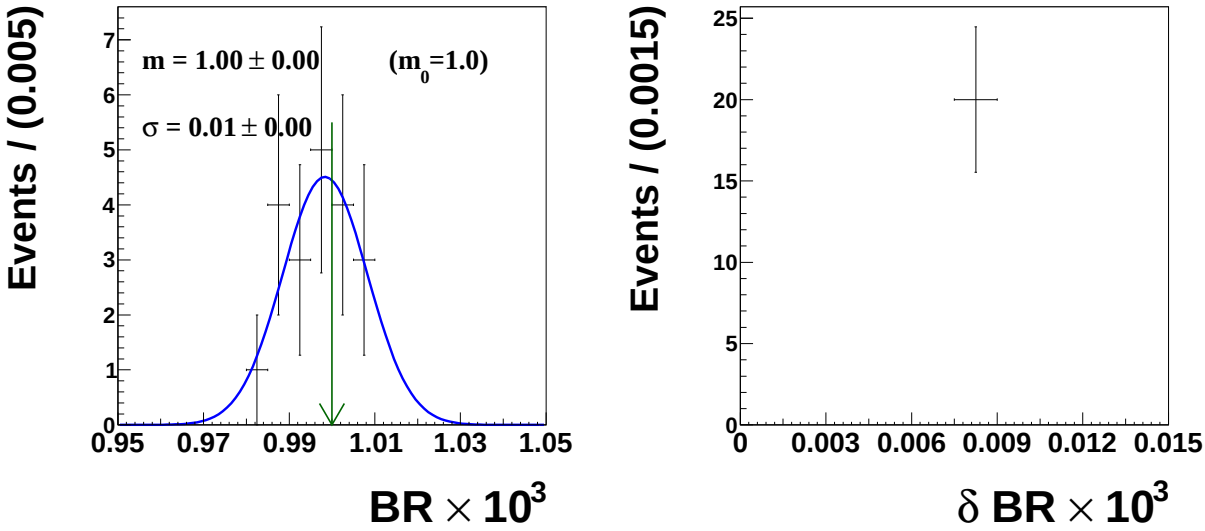

Figure A.13: Control sample fit results and error distribution from 20 example toy experiments. The generated branching fraction is indicated by the green arrow.

Appendix B

Appendix Systematics

This section provides a more detailed description of the estimation of the systematical uncertainties related to four-pion final state interference and the helicity PDF of $B \to \rho\pi\pi$ decays.

B.1 Interference

Possible interference between the four-pion final states is not accounted for in the incoherent fit model. We study this effect with a $B^0 \to \pi^+\pi^0\pi^-\pi^0$ isobar amplitude model, being capable of generating interference between the four pion final states. We include this model in the EvtGen [97] MC event generator and generate one million single component events to build an incoherent fit model. This fit model is then used to study generated interference between two coherent components in the second step. B mixing and CP violation are included in the description of the amplitudes and all samples include full detector simulation and the same reconstruction procedure as described in Chapter 3.
We generate MC samples where $B^0 \to \rho^+\rho^-$ interferes with another component and scan their relative phase. A five-dimensional fit is performed on each sample to obtain the branching fraction, the longitudinal polarization fraction and the CP violating parameters. The fit model consists out of a two-dimensional histogram for the dipion masses, atwo-dimensional histogram for the helicity angles and the previously introduced signal Δt PDF, see Eq. (4.19). The amplitude model is introduced in the following.

B.1.1 Amplitude Model

The amplitudes consist out of three terms: $\mathcal{A}_i = C_i \times L_i \times H_i$ with a complex damping factor $C_i = c_i e^{i\phi_i}$, the line-shape L_i and the angular distribution H_i. The B meson decays into four pion, $B^0 \to \pi_1^+\pi_2^0\pi_3^-\pi_4^0$, and we label the intermediate resonances according to their daughters: e.g. $\mathcal{A}_{1234}$: $B \to X_{123}\pi_4^0$, $X_{123} \to Y_{12}\pi_3^-$, $Y_{12} \to \pi_1^+\pi_2^0$. In the following $\rho^\pm$ decays exclusively into $\pi^\pm\pi^0$ and f_0 as well as ρ^0 into $\pi^+\pi^-$. The following figures show the generated distributions with the corresponding PDF.

$B^0 \to \rho^+\rho^-$

We describe line-shape of $B^0 \to \rho^+\rho^-$ decays with the product of two BWs (see Appendix E.2), one for each ρ. We use the world averages of the mass $m_\rho = 775$ MeV/c^2 and width $\Gamma_\rho = 149$ MeV/c^2 [45].
The angular distributions are modeled with the following helicity amplitudes in the transversity base formalism

$$H_0 = \cos\theta_1 \cos\theta_2, \tag{B.1}$$

$$H_\parallel = \frac{1}{\sqrt{2}} \cos\phi \sin\theta_1 \sin\theta_2, \tag{B.2}$$

$$H_\perp = \frac{i}{\sqrt{2}} \sin\phi \sin\theta_1 \sin\theta_2, \tag{B.3}$$

where $\theta_{1,2}$ are the helicity angles as defined in Section 1.4.1 and the acoplanarity angle ϕ, is the angle between $\vec{p}(p_2) \times \vec{p}(p_1)$ and $\vec{p}(p_4) \times \vec{p}(p_3)$. Integrating over ϕ gives the helicity base used in our measurement.
The amplitude for each polarization is then given by the sum over both $\rho^\pm$ combinations.

$$\mathcal{A}_{\rho^\pm\rho^\mp} = C_{\mathrm{LP(TP)}} \times \left(\mathcal{A}^{\mathrm{LP(TP)}}_{1234} + \mathcal{A}^{\mathrm{LP(TP)}}_{1432}\right), \tag{B.4}$$

where

$$\mathcal{A}^{LP}_{ijkl} = BW(m_{ij}, m_{\rho^0}, \Gamma_{\rho^0}) \times BW(m_{kl}, m_{\rho^0}, \Gamma_{\rho^0}) \times \frac{9}{4} H_0 \quad \text{and} \tag{B.5}$$

$$\mathcal{A}^{TP}_{ijkl} = BW(m_{ij}, m_{\rho^0}, \Gamma_{\rho^0}) \times BW(m_{kl}, m_{\rho^0}, \Gamma_{\rho^0}) \times \frac{9}{16} \Big(H_\parallel + H_\perp \Big). \tag{B.6}$$

Projections onto the masses and helicity angles are shown in Fig. B.1 and Fig. B.2. Projections onto Δt are shown in Fig. B.3.

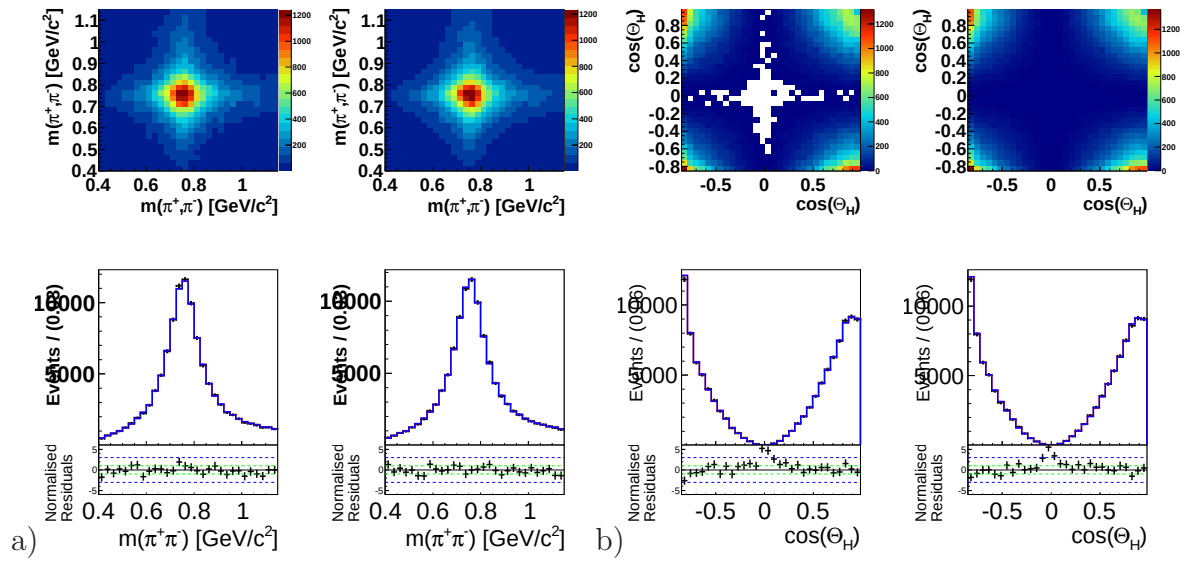

Figure B.1: Projections onto (a) the dipion masses and (b) the helicity angles for longitudinal polarized $B^0 \to \rho^+\rho^-$fully simulated MC events generated with the amplitude model.

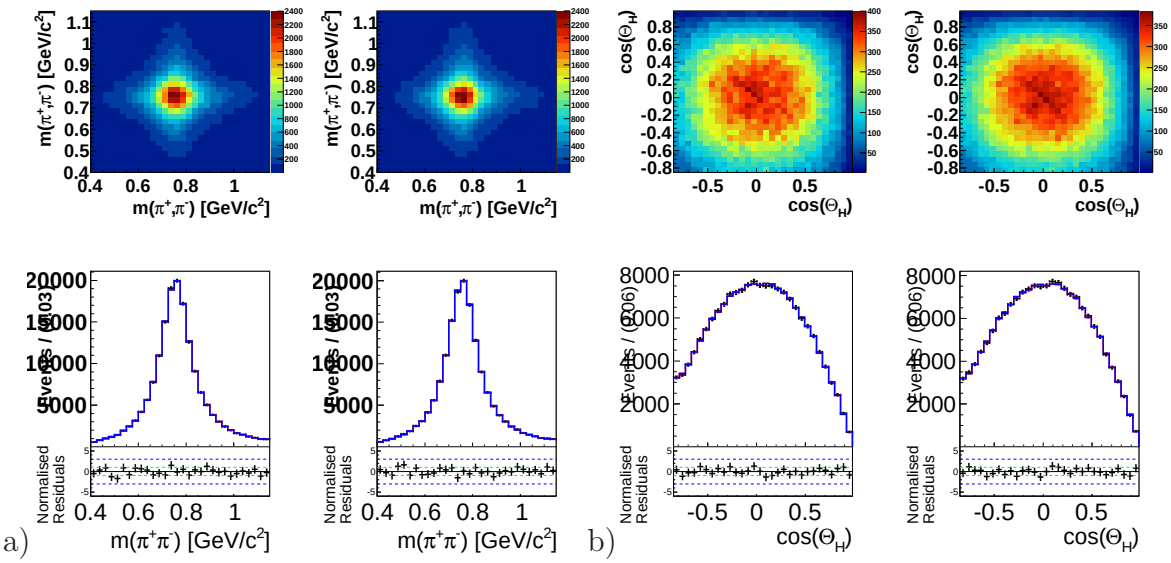

Figure B.2: Projections onto (a) the dipion masses and (b) the helicity angles for transversely polarized $B^0 \to \rho^+\rho^-$fully simulated MC events generated with the amplitude model.

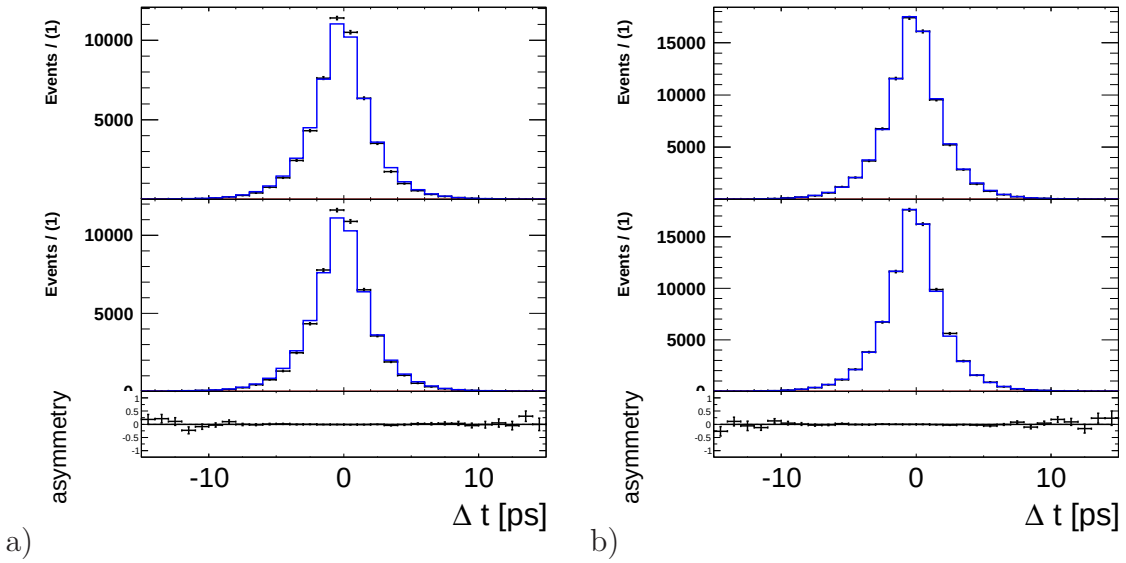

Figure B.3: Projections onto the Δt distributions for $q = \pm 1$ for (a) longitudinal and (b) traversal polarized $B^0 \to \rho^+\rho^-$fully simulated MC events generated with the amplitude model

$B \to \pi^+\pi^0\pi^-\pi^0$

The non-resonant decay only depends on the available phase-space, hence

$$\mathcal{A}_{\pi^+\pi^0\pi^-\pi^0} = 1. \tag{B.7}$$

Projections onto the fit variables are shown in Fig. B.4.

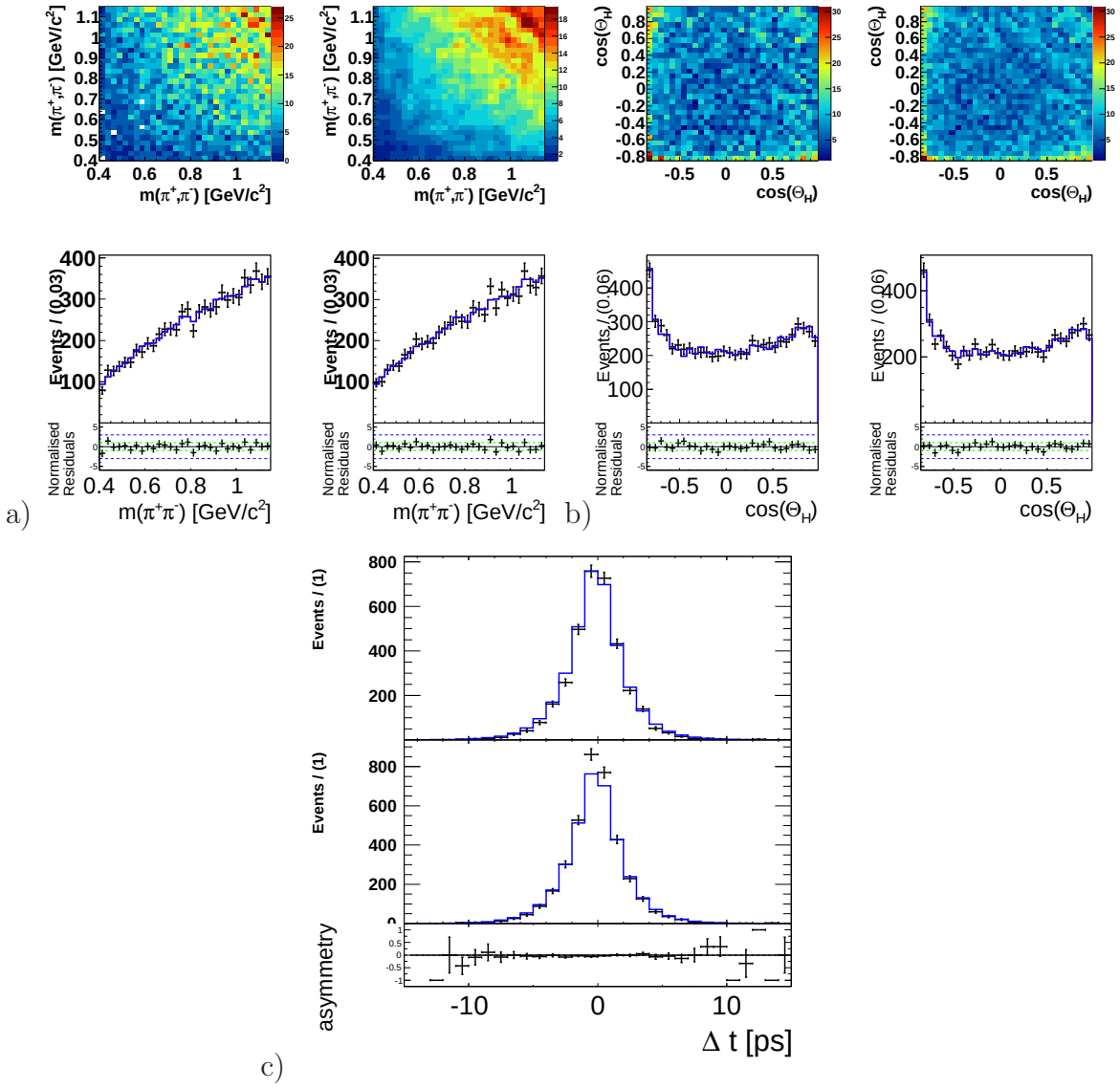

Figure B.4: Projections onto (a) the dipion masses and (b) the helicity angles for $B \to \pi^+\pi^0\pi^-\pi^0$ fully simulated MC events generated with the amplitude model. c) shows the projections onto the Δt distributions for $q = \pm 1$.

$B \to a_1\pi$

$B \to a_1[\rho\pi]\pi$ decays are described as a sequence of three two-body decays

$$B \to a_1\pi$$
$$a_1 \to \rho\pi$$
$$\rho \to \pi\pi$$

and the amplitude is the product of the amplitudes in each step,

$$\mathcal{A}_{a_1\pi} = C_{a_1\pi}(L_{B\to a_1\pi}H_{B\to a_1\pi} \times L_{a_1\to\rho\pi}H_{a_1\to\rho\pi} \times L_{\rho\to\pi\pi}H_{\rho\to\pi\pi}). \tag{B.8}$$

The line-shapes of the a_1 and the ρ are both described by a Breit-Wigner function. We generate the a_1 with a mass of 1.23 GeV/c^2 and a width of 400 MeV/c^2. The width is the average of the range given in [45].
The spin factors H_i are described by Lorentz-scalars. Therefore we have to contract available four-vectors (four-momenta p_μ and polarization vectors ϵ_ν) at each point of the decay. The normalized and mutually orthogonal polarization vectors for a massive spin-1 particle in its own rest-frame, e.g.

$$\begin{aligned}\epsilon_1^\mu &= (0,1,0,0),\\ \epsilon_2^\mu &= (0,0,1,0),\\ \epsilon_3^\mu &= (0,0,0,1),\end{aligned} \tag{B.9}$$

form a complete set;

$$\sum_i \epsilon_i^{*\mu}\epsilon_i^\nu = g^{\mu\nu} - p^\mu p^\nu/m^2, \tag{B.10}$$

where sum goes over all three helicity states and the right-hand side is the propagator for a spin-1 resonance with mass m decaying into two scalar particles with four-momenta p^κ. $g^{\mu\nu}$ is the metric tensor. The amplitude for a scalar particle decaying into a vector particle with polarization vector ϵ^ν and a scalar particle with momentum k^μ can be expressed by

$$\mathcal{A}_{SVS} = \epsilon_\mu^* k^\nu. \tag{B.11}$$

The amplitude for a spin-1 resonance with polarization vector ϵ_1^μ decaying into a vector particle with polarization vector ϵ_2^μ and a scalar particle, can be written as

$$\mathcal{A}_{VVS} = \epsilon_{1\mu}^*\epsilon_2^\nu, \tag{B.12}$$

and the amplitude for a spin-1 resonance with polarization vector ϵ_μ decaying into two scalar particles with momenta $p_{1,2}^\nu$ is

$$\mathcal{A}_{VSS} = \epsilon_\mu^*(p_1 - p_2)^\nu. \tag{B.13}$$

Assuming only S-wave contribution, the $B \to a_1\pi$ decay sequence can be written as

$$H_{B\to a_1\pi_l} = (p_{\pi_l})_\mu(\epsilon_{a_1})^\nu, \tag{B.14}$$
$$H_{a_1\to\rho\pi_k} = (\epsilon_{a_1})_\mu(\epsilon_\rho)^\nu, \tag{B.15}$$
$$H_{\rho\to\pi_i\pi_j} = (\epsilon_\rho)_\mu(p_{\pi_i} - p_{\pi_j})^\nu, \tag{B.16}$$

where the subscript labels the corresponding particle. The total spin factor is then the sum over all possible spin configurations,

$$H_{ijkl} = \sum_{\text{spins}} H_{B\to a_1\pi_l} H_{a_1\to\rho\pi_j} H_{\rho\to\pi_k\pi_l}, \tag{B.17}$$

which can be simplified with Eq. (B.10). Thus the amplitude is given by

$$\mathcal{A}_{ijkl} = BW(m_{ijk}, m_{a_1}, \Gamma_{a_1}) \times BW(m_{ij}, m_{\rho^\pm}, \Gamma_\rho) \times H_{ijkl}, \tag{B.18}$$

Considering all possible pion combinations the total amplitude for decays into a charged $a_1^\pm$ takes the form

$$\mathcal{A}_{a_1^\pm\pi^\mp} = C_{a_1^\pm\pi^\mp} \times (\mathcal{A}_{1243} + \mathcal{A}_{1423} + \mathcal{A}_{3241} + \mathcal{A}_{3421}). \tag{B.19}$$

Another sum of combinations,

$$\mathcal{A}_{a_1^0\pi^0} = C_{a_1^0\pi^0} \times (\mathcal{A}_{1234} + \mathcal{A}_{1432} + \mathcal{A}_{3214} + \mathcal{A}_{3412} + \mathcal{A}_{1324}, + \mathcal{A}_{1342}). \tag{B.20}$$

describe decays into a neutral a_1^0, where we combine the two possible decays of the a_1^0; $a_1^0 \to \rho^\pm\pi^\mp$ and $a_1^0 \to \rho^0\pi^0$ (last two terms). Projections onto the masses and angles are shown for in Fig. B.5 and Fig. B.6 for $B \to a_1^\pm\pi^\mp$ and onto Δt in Fig. B.7.

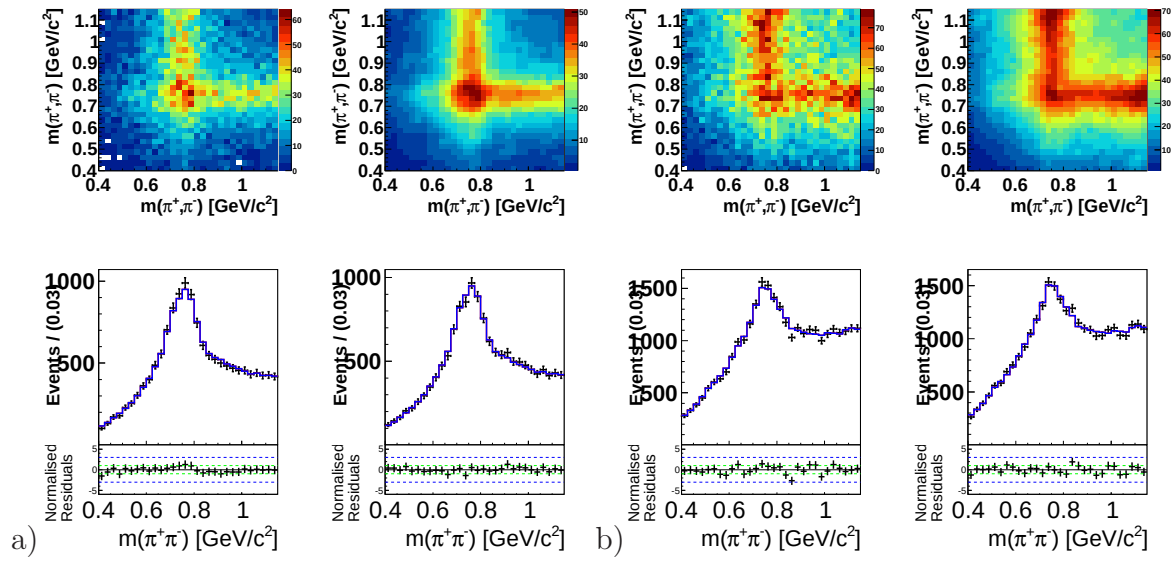

Figure B.5: Projections onto the dipion masses for a) $B \to a_1^\pm\pi^\mp$ and b) $B \to a_1^0\pi^0$ decays generated with the amplitude model.

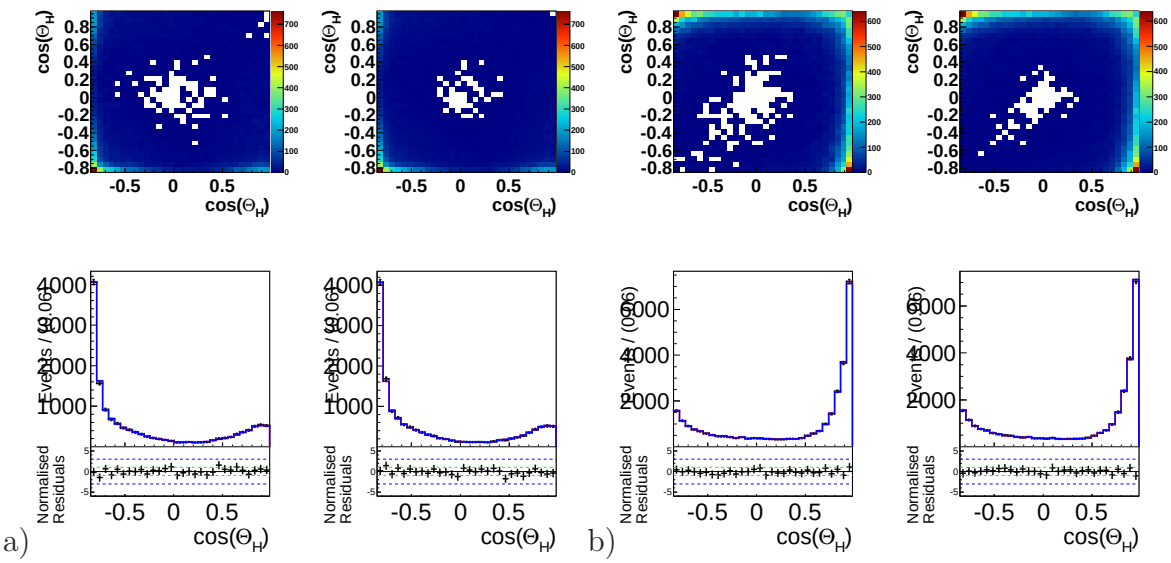

Figure B.6: Projections onto the helicity angles for a) $B \to a_1^{\pm}\pi^{\mp}$ and b) $B \to a_1^0\pi^0$ decays generated with the amplitude model.

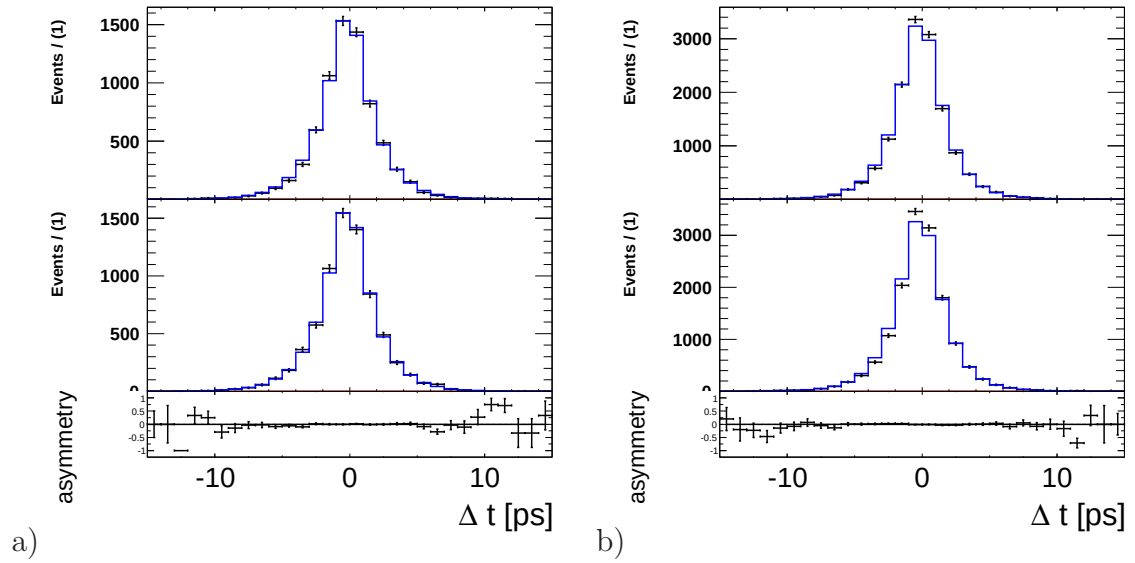

Figure B.7: Projections onto the Δt distributions for $q = \pm 1$ for $B \to a_1\pi$ fully simulated MC events generated with the amplitude model. (a) shows $B \to a_1^{\pm}\pi^{\mp}$ and (b) shows $B \to a_1^0\pi^0$.

$B \to \rho\pi\pi$

Opposite to $B^0 \to \rho^+\rho^-$ the wave function of $B \to \rho\pi\pi$ is asymmetric, consequently no interference effects are expected over four π. Since the Belle detector does not completely cover the full range, small effects still might occur. This decay's line-shape is described by a Breit-Wigner and no helicity dependency is applied for the interference study as this agrees with the generated MC events used for the model description.

$$\mathcal{A}_{ij} = BW(m_{ij}, m_{\rho^0}, \Gamma_{\rho^0}). \tag{B.21}$$

Thus, the amplitude for $B \to \rho^\pm\pi^\mp\pi^0$ takes the form

$$\mathcal{A}_{\rho^\pm\pi^\mp\pi^0} = C_{\rho^\pm\pi^\mp\pi^0}(\mathcal{A}_{12} + \mathcal{A}_{34} + \mathcal{A}_{14} + \mathcal{A}_{32}), \tag{B.22}$$

while for $B \to \rho^0\pi^0\pi^0$ the amplitude is

$$\mathcal{A}_{\rho^0\pi^0\pi^0} = C_{\rho^0\pi^0\pi^0}\mathcal{A}_{13}. \tag{B.23}$$

Fit projections onto the masses and angles are shown in Figs. B.8 and B.9 and onto Δt in Fig. B.10. Furthermore, we can use one-dimensional versions of Eq. (B.1)-Eq. (B.3) to generate $B \to \rho\pi\pi$ decays with longitudinal or transverse polarization and test the phase-space assumption used in the generation of the nominal MC events (see next section).

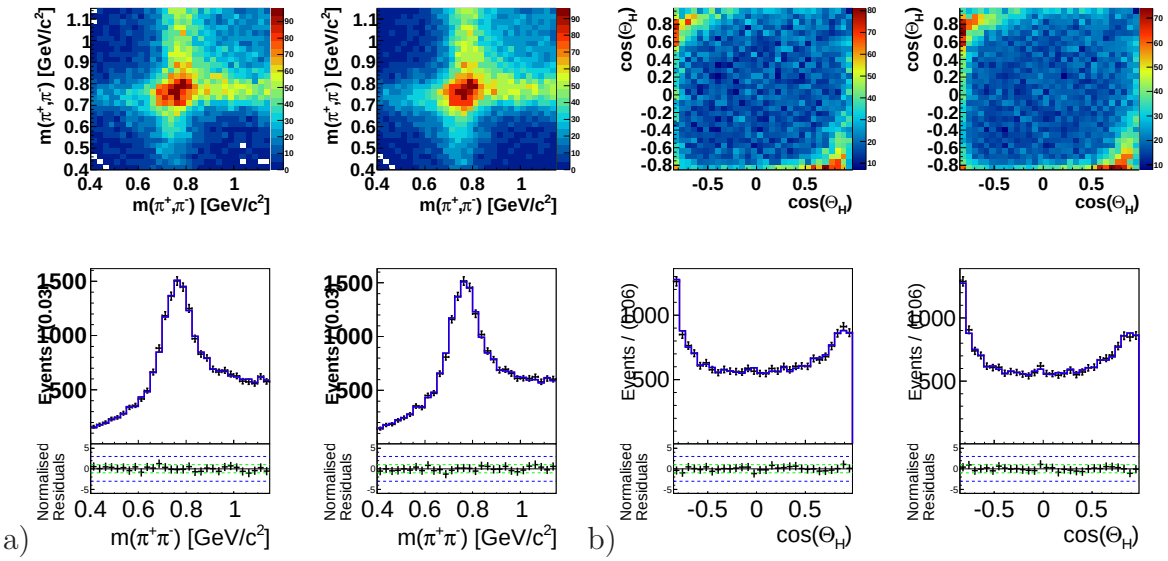

Figure B.8: Projections onto (a) the dipion masses and (b) the helicity angles for $B \to \rho^\pm\pi^\mp\pi^0$ fully simulated MC events generated with the amplitude model (phase-space).

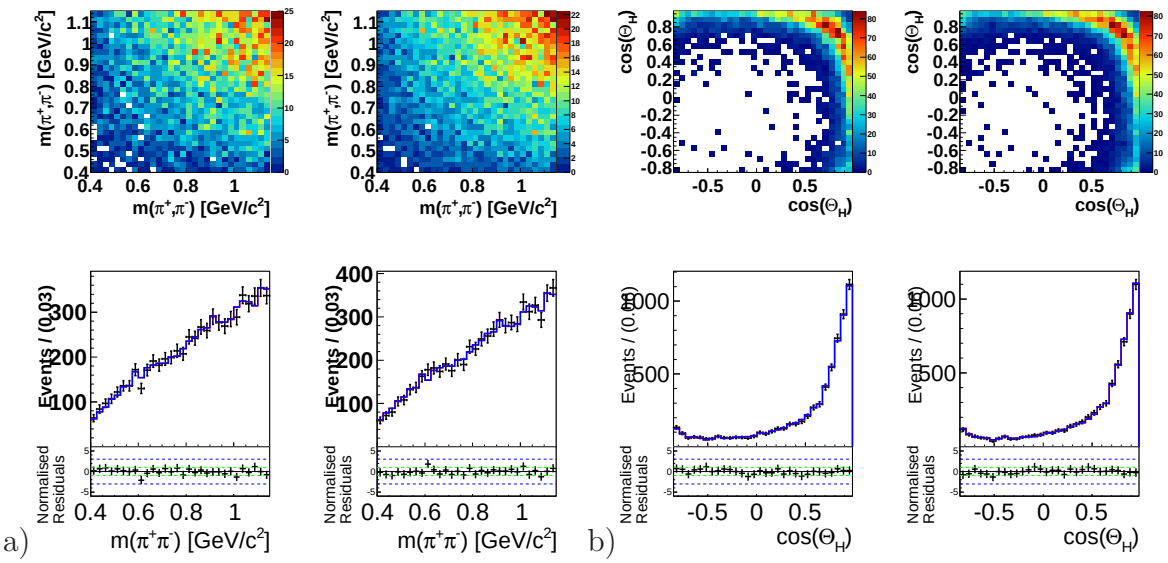

Figure B.9: Projections onto (a) the dipion masses and (b) the helicity angles for $B \to \rho^0\pi^0\pi^0$ fully simulated MC events generated with the amplitude model.

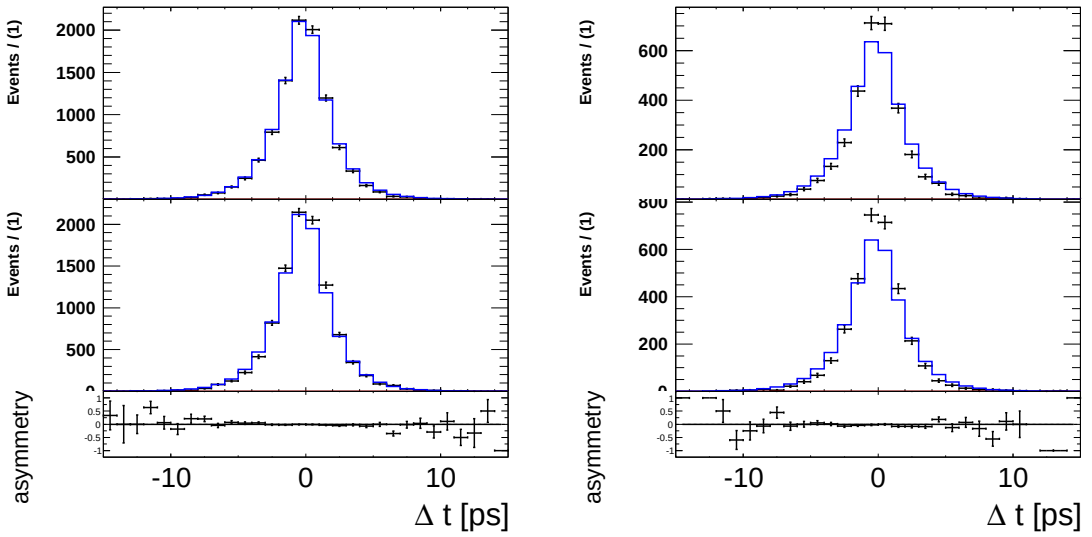

Figure B.10: Projections onto the Δt distributions for $q = \pm 1$ for $B \to \rho^+\pi^-\pi^0$ and $B \to \rho^0\pi^0\pi^0$ fully simulated MC events generated with the amplitude model.

B.1.2 Interference Study

We generate several MC samples with two components: the first component is $B^0 \to \rho^+\rho^-$ and the second one is either $B \to a_1\pi$, $B \to \pi^+\pi^0\pi^-\pi^0$ or $B \to \rho\pi\pi$. Each sample consists of 5×10^5 events. Because the measured longitudinal polarization fraction is consistent with one, we only generate $B^0 \to \rho^+\rho^-$ events with longitudinal polarization but still float f_L in the fit to the MC events, where a $B^0 \to \rho^+\rho^-$ component with transverse polarization is included and we do not generate CP violation.
The amplitude takes the form

$$\mathcal{A} = \mathcal{A}_{\rho^+\rho^-} + \mathcal{A}_j = C_{\rho^+\rho^-} L_{\rho^+\rho^-} H_{\rho^+\rho^-} + C_j L_j H_j. \tag{B.24}$$

For simplicity we set $C_{\rho^+\rho^-} = 1$,

$$\mathcal{A} = L_{\rho^+\rho^-} H_{\rho^+\rho^-} + c_j e^{i\phi} L_j H_j. \tag{B.25}$$

For each background component j, we vary the relative phase ϕ from 0°-180° in steps of 10° in the generation. The factor c_j is chosen such that the respective yield fraction in the data is obtained from the fit to data when generating events with a relative phase of 90°.
We then perform a five-dimensional fit to $2 \times m_{\pi^+\pi^-}$, $2 \times \cos\theta_{\mathrm{H}}$ and Δt to extract a yield fraction $f_N = N_{\rho^+\rho^-}/(N_{\rho^+\rho^-} + N_j) = N_{\rho^+\rho^-}/N_{tot}$, $f_L^{\rho^+\rho^-}$, $\mathcal{A}_{CP}^{\rho^+\rho^-}$ and $\mathcal{S}_{CP}^{\rho^+\rho^-}$. We plot the results and take the standard deviation of each observable as the systematic uncertainty. Figs. B.11 and B.13 show scans of the four observables for the considered backgrounds $B \to a_1^\pm\pi^\mp, \pi^+\pi^0\pi^-\pi^0$ and $\rho^+\pi^-\pi^0$ and Table B.1 lists the obtained systematic uncertainties. The largest one is included in the total systematic uncertainty (Chapter 6), as it is extremely unlikely that all modes are equally coherent. We conclude that interference effects are almost negigible. The pure effect may be even (partly) hidden under the statistical fluctuations of this study, epsecially for other observables than the branching fraction.

mode	$f_{\mathrm{N_{sig}/N}}$	f_l(abs.)	$\mathcal{S}_{CP}^{\rho^+\rho^-}$	$\mathcal{A}_{CP}^{\rho^+\rho^-}$
$a_1^\pm\pi^\mp$	0.01%	0.001	0.012	0.007
4π	0.00%	0.002	0.015	0.012
$\rho^+\pi^+\pi^-$	0.00%	0.002	0.013	0.010

Table B.1: Systematic uncertainties arising from interference for the listed modes. The largest number (marked as red) is taken to be the systematic uncertainty.

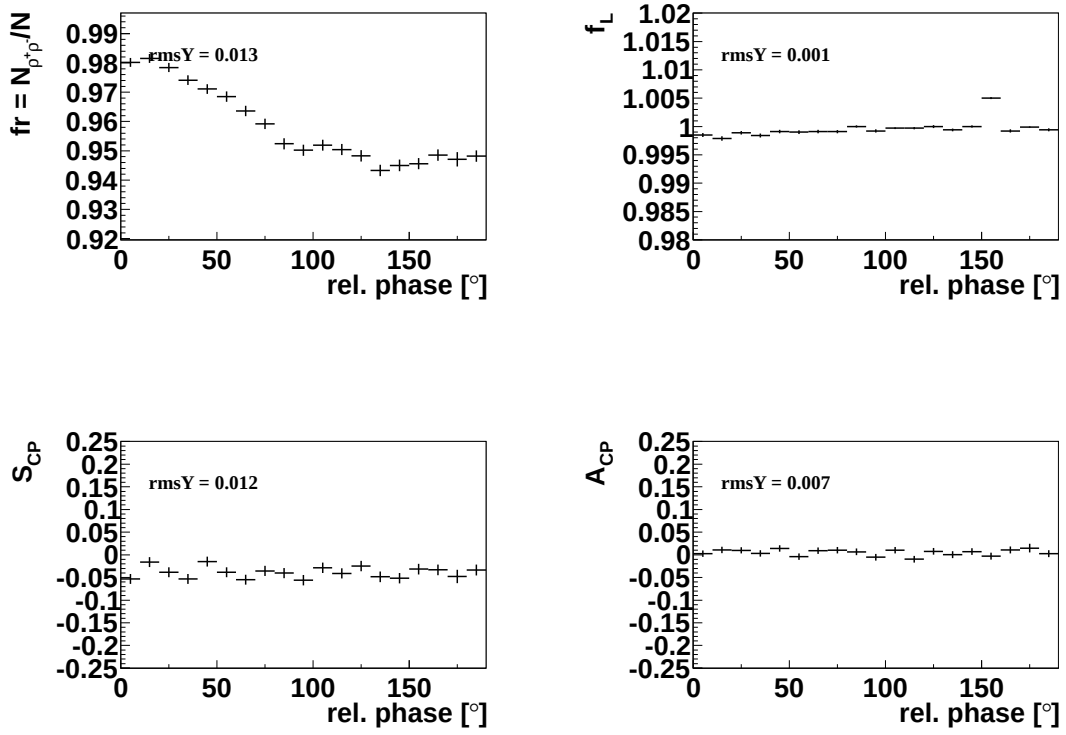

Figure B.11: Scans of the observables for $B^0 \to \rho^+\rho^-$interfering with $B \to a_1^{\pm}\pi^{\mp}$.

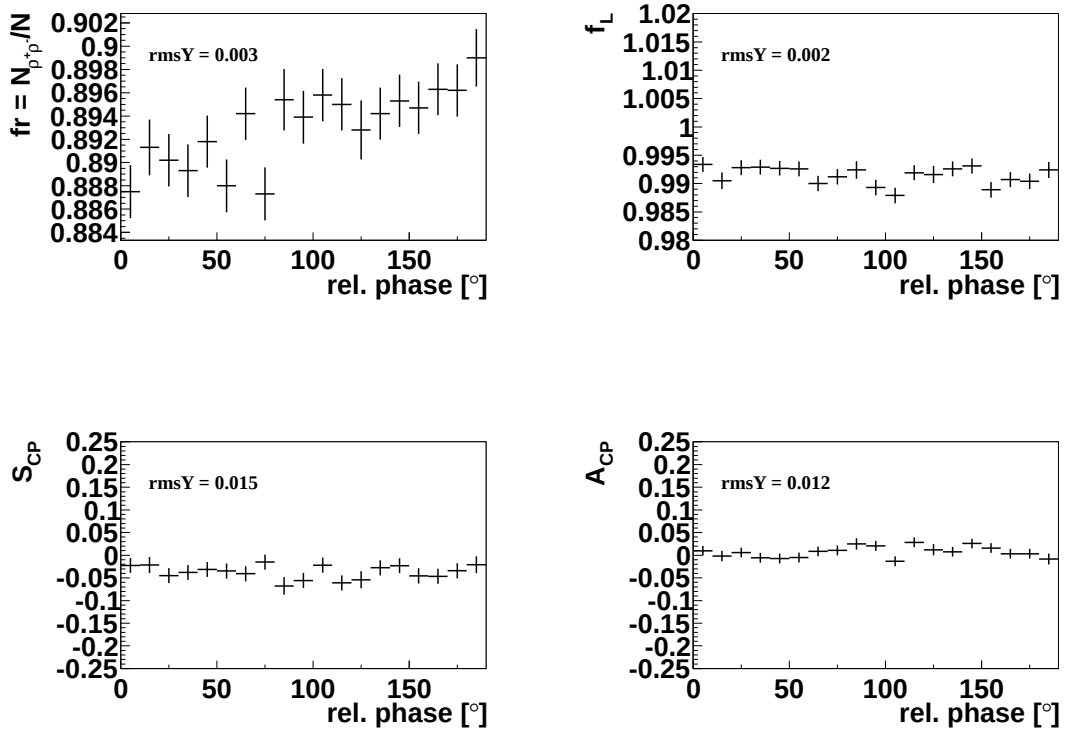

Figure B.12: Scans of the observables for $B^0 \to \rho^+\rho^-$interfering with $B \to \pi^+\pi^0\pi^-\pi^0$.

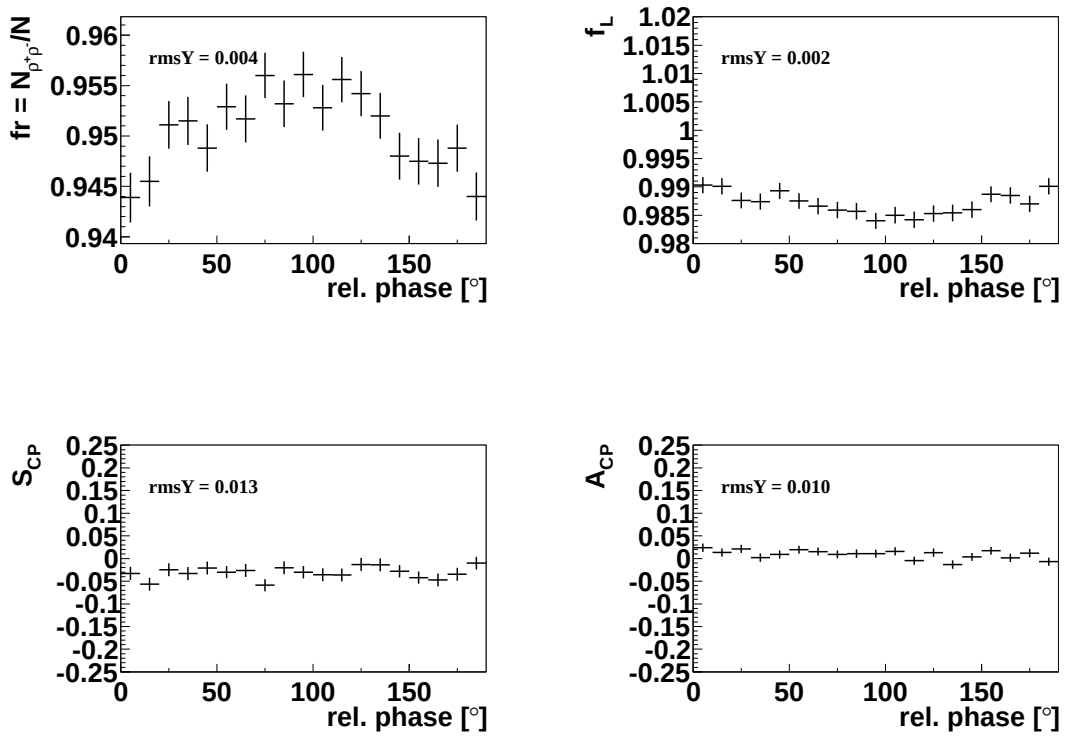

Figure B.13: Scans of the observables for $B^0 \to \rho^+\rho^-$interfering with $B \to \rho^\pm\pi^\mp\pi^0$.

B.2 Helicity Model of $B^0 \to \rho^\pm\pi^\mp\pi^0$

We use the EvtGen decay model PHSP (phase-space) to model the decay $B^0 \to \rho^\pm\pi^\mp\pi^0$ in our nominal fit model, but it is not unlikely that this decay has a different helicity dependence. To account for this, we provide three alternative descriptions of the PDF of the helicity angles. The two non-resonant pions can either be in a S- or P-wave configuration. In the ladder case, we consider either a longitudinal or a transverse polarized $\rho^\pm$. In the fit to the data, we substitute the helicity PDF of $B \to \rho^\pm\pi^\mp\pi^0$ with those obtained from the alternative distributions.

In a S-wave H_S is simliar to Eq. (B.11) with a scalar particle $p = p_k + p_l$, the amplitude of $B^0 \to \rho^\pm\pi^\mp\pi^0$ is given by

$$\mathcal{A}_{ij}^{\mathrm{S}} = BW(m_{ij}, m_{\rho^0}, \Gamma_{\rho^0}) \times H_S. \tag{B.26}$$

We use the corresponding description from $B^0 \to \rho^+\rho^-$ for the P-wave with the longitudinal or transverse polarization

$$\mathcal{A}_{ij}^{rmP,LP(TP)} = BW(m_{ij}, m_{\rho^0}, \Gamma_{\rho^0}) \times H_{LP(TP),\rho^+\rho^-}. \tag{B.27}$$

The phase space model is described in Appendix B.1.1.
Projections onto the alternative helicity angles distributions are shown in Fig. B.14 and the differences to our nominal (phase-space) fit result are listed in Table B.2. We conservatively select the largest error for each variable. Except for f_L, we observe the largest but still negligible deviation to the nominal fit result in the case of pions being in a P-wave with transverse polarization. For f_L, the LP configuration results in the largest deviation, as the helicity PDF is very similar to the signal PDF for longitudinal polarization. This is a dominant contribution to the total uncertainty of f_L.

Variation	$\Delta\mathcal{B}(B^0 \to \rho^+\rho^-)[\%]$	Δf_L	$\Delta\mathcal{A}_{CP}[\times 10^{-2}]$	$\Delta\mathcal{S}_{CP}[\times 10^{-2}]$
PLP	0.033	0.020	0.036	0.033
PTP	0.035	0.004	0.117	0.77
S	0.023	0.014	0.049	0.265
Total				

Table B.2: Absolute differences of the fit result for the various assumptions on the helicity dependency of $B \to \rho^\pm\pi^\mp\pi^0$. The largest ones, marked as red, are taken as a systematic uncertainty.

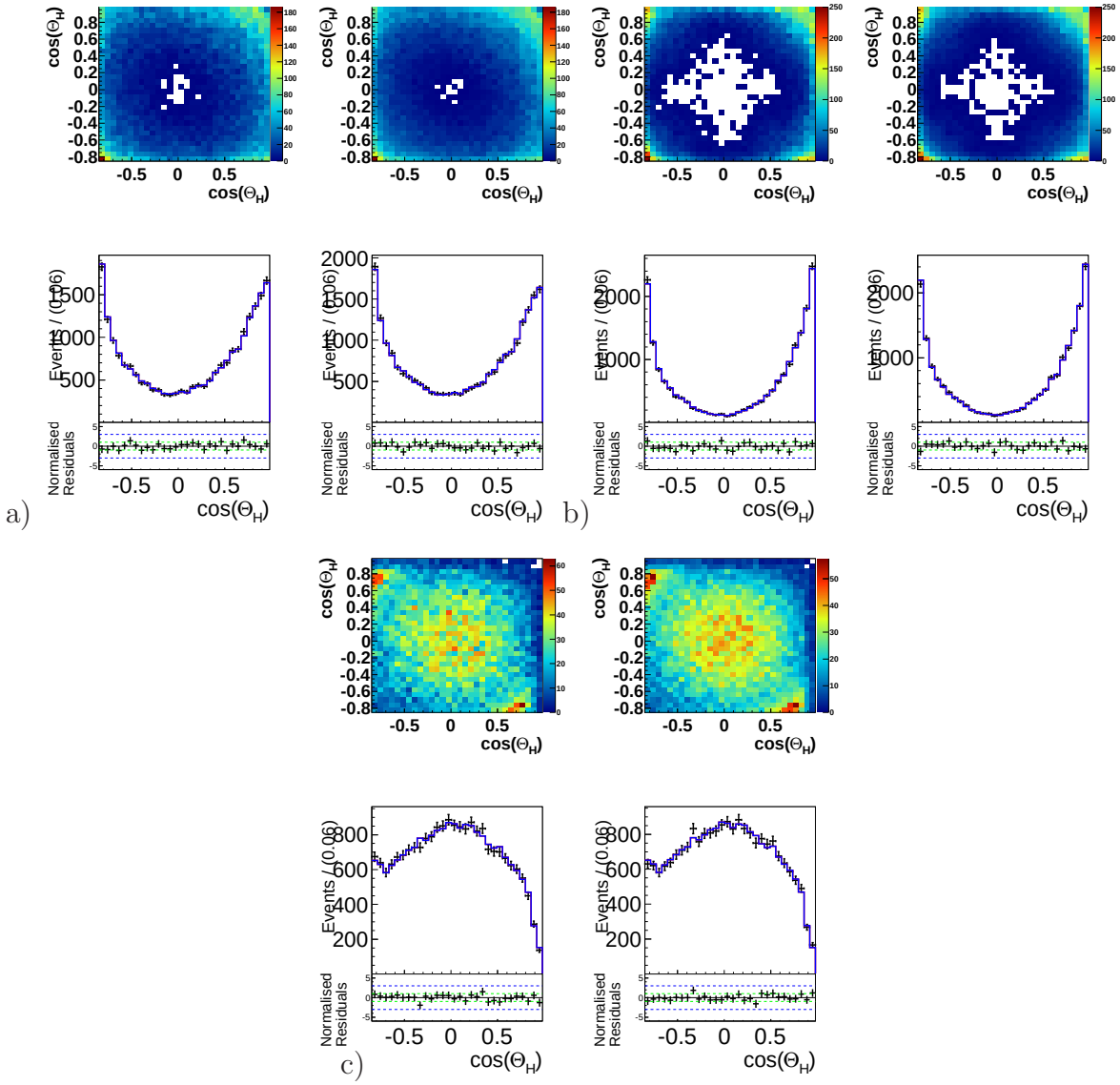

Figure B.14: Projections onto the helicity angles for $B \to \rho^{\pm}\pi^{\mp}\pi^{0}$ fully simulated MC events generated with the amplitude model for the different helicity dependencies. a) S-wave, b) P-wave (LP) and c) P-wave (TP).

Appendix C

Appendix Model

C.1 Model For Backgrounds From $B\bar{B}$ Decays

The model for combinatorial background from other B meson decays is divided into four components: charm and charmless decays of neutral and charged B mesons. Each (charm or charmless) fraction of charged B decays is fixed relative to the yield of the respective neutral B decays. The fractions are obtained from fully simulated MC events and are given in Table C.1. B decays into final states with a charm quark yield in almost identical distributions for charged and neutral B mesons after reconstruction. We consider two separate models, nevertheless.

$B^{\pm}/B^0(B^0)$	SVD1	SVD2
c	1.78 ± 0.02	2.02 ± 0.01
u, d, s	1.04 ± 0.02	1.00 ± 0.01

Table C.1: Fractions of the yields of charged B meson decays into charm and charmless final states relatively to the corresponding neutral B decays.

$\rho^{\pm}$ resonances contribute to each $B\bar{B}$ component and we subdivide each component's model into up to four parts, depending on the $\rho^{\pm}$'s charge and whether the resonance is correctly reconstructed. We denote events including both, one and no correctly reconstructed $\rho^{\pm}$ with the superscript $2c, +, -, 0$, respectively, where we only require that the charged pion is correctly assigned to the $\rho^{\pm}$ to be correctly reconstructed. The distributions of $+$ and $-$ are identical when interchanging $\rho^+ \leftrightarrow \rho^-$ and the fraction of the yields $N_{\pm}$ of the $\pm$ components $f_+ = N_+/(N_+ + N_-)$ is consistent with 0.5 for all components and detector configurations (SVD1/2). In order to increase the statistics for the model building, we combine the $+$ and $-$ components by interchanging $m_{\pi^+\pi^0} \leftrightarrow m_{\pi^-\pi^0}$ and $\cos\theta_{\mathrm{H}}^+ \leftrightarrow \cos\theta_{\mathrm{H}}^-$ for events from the $-$ component. When a group of components (no classification at all) is given, the PDF is made common among the group (all). Variables that are not sensitive to this classification are made common among the sub-components. For example, each component's $\mathcal{F}_{B\bar{B}/q\bar{q}}$ distribution is described by a double bifurcated Gaussian in each r-bin, k,

$$\mathcal{P}^k_{B\bar{B}}(\mathcal{F}_{B\bar{B}/q\bar{q}}) \equiv dbG^k(\mathcal{F}_{B\bar{B}/q\bar{q}}). \tag{C.1}$$

Each component's lifetime PDF is given by an exponential decay convoluted with the sum of two Gaussian,

$$\mathcal{P}_{B\bar{B}}(\Delta t) \equiv \frac{e^{-|\Delta t|/\tau_{B\bar{B}}}}{2\tau_{B\bar{B}}} \otimes R_{B\bar{B}}(\Delta t), \tag{C.2}$$

similar to the one introduced for the self crossfed model, see Section 4.3.4 and Eq. (4.53). The subscript $B\bar{B}$ stands for either one of the following four $B\bar{B}$ components.

C.1.1 Charm B^0 Backgrounds

The subscript nc labels neutral B meson decays into charm final states, e.g. including a $D^{(*)}$, J/Ψ etc. The fractions of the $\pm, 0$ components are listed in Table C.3, the correlation matrices are given in Tables C.4 to C.6 and the fit results are shown in the following. Here, the fraction of $2c$ is negligible and is therefore not treated separately.
The ΔE distributions of charm B decays are described by the sum of Chebychev polynomials up to the second order,

$$\mathcal{P}_{nc}^{\pm,0}(\Delta E) \equiv \sum_{i=1}^{2} c_i^{\pm,0} C_i(\Delta E), \tag{C.3}$$

the projections onto ΔE for each reconstruction category are shown in Fig. C.1.

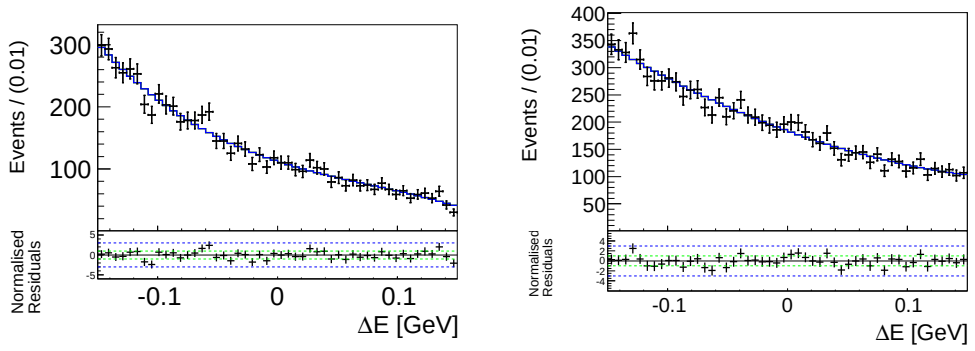

Figure C.1: Fit projections onto ΔE of $b \to c$ transitions in neutral B decays for the components $-$ (left) and 0. The black points show simulated MC events and the solid line shows the fit result. The residuals are given beneath each distribution.

The $M_{\rm bc}$ distribution for all three reconstruction categories is described by an Argus function,

$$\mathcal{P}_{nc}(M_{\rm bc}) \equiv Ar(M_{\rm bc}), \tag{C.4}$$

and is shown together with the full projection onto ΔE in Fig. C.2.

The $\mathcal{F}_{B\bar{B}/q\bar{q}}$ distribution is described by Eq. (C.1) and shown in Fig. C.3

The PDF of the $m_{\pi^+\pi^0}$-$m_{\pi^-\pi^0}$ distribution including one correctly reconstructed $\rho^\pm$ meson is given by the sum of a Breit-Wigner, a second and a third order Chebychev polynomial for the part with the resonance, multiplied with the sum of Chebychev polynomial up to the

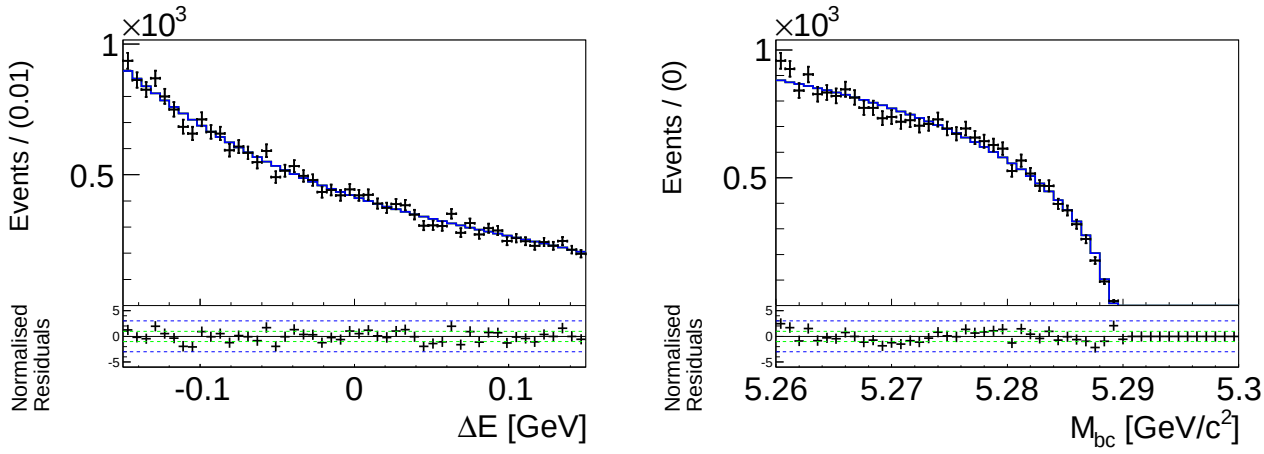

Figure C.2: Full projections of $b \to c$ transitions in neutral B meson decays for ΔE and $M_{\rm bc}$. The black points show simulated MC events and the solid line shows the fit result. The residuals are given beneath each distribution.

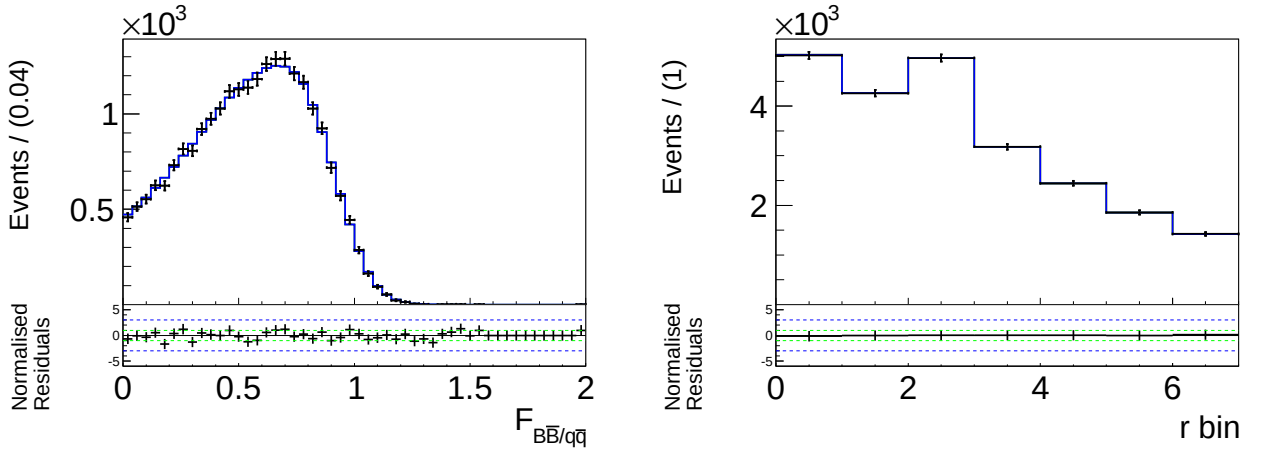

Figure C.3: Full projections of $b \to c$ transitions in neutral B meson decays for $\mathcal{F}_{B\bar{B}/q\bar{q}}$ and the r-bin fractions. The black points show simulated MC events and the solid line shows the fit result. The residuals are given beneath each distribution.

fifth order for the other mass,

$$\mathcal{P}^{\pm}_{nc}(m_{\pi^{\pm}\pi^0}, m_{\pi^{\mp}\pi^0}|\cos\theta^{\pm}_{\rm H}, \cos\theta^{\mp}_{\rm H}) \equiv$$
$$\Big(f_{nc}(\cos\theta^{\pm}_{\rm H}, \cos\theta^{\mp}_{\rm H}))BW(m_{\pi^{\pm}\pi^0}, m, \Gamma) + (1 - f_{nc}(\cos\theta^{\pm}_{\rm H}, \cos\theta^{\mp}_{\rm H}))\sum_{i=2}^{3} c_i^{M\pm} C_i(m_{\pi^{\pm}\pi^0})\Big)$$
$$\times \sum_{i=1}^{5} c_i^{M,{\rm mr}} C_i(m_{\pi^{\mp}\pi^0}). \qquad \text{(C.5)}$$

The fraction of the resonance depends on the helicity angles

$$f_{nc}(\cos\theta^{\pm}_{\rm H}, \cos\theta^{\mp}_{\rm H}) = c_{0,M} + c_{1,M}\cos\theta^{\pm}_{\rm H} + c_{2,M}(\cos\theta^{\pm}_{\rm H})^2 + c_{3,M}(\cos\theta^{\pm}_{\rm H})^4 + c_{4,M}(\cos\theta^{\mp}_{\rm H})^2$$
$$+c_{5,M}(\cos\theta^{\mp}_{\rm H})^4 + c_{6,M}(\cos\theta^{\pm}_{\rm H})^2\cos\theta^{\mp}_{\rm H}.$$

In the case of no correctly reconstructed $\rho^{\pm}$ resonance, the PDF is taken to be the product

of two sums of Chebychev polynomials for up to the fifth order, one for each mass

$$\mathcal{P}^0_{nc}(m_{\pi^+\pi^0}, m_{\pi^-\pi^0}) \equiv \sum_{i=1}^{5} c_i^{M,0} C_i(m_{\pi^+\pi^0}) \times \sum_{i=1}^{5} c_i^{M,0} C_i(m_{\pi^-\pi^0}), \tag{C.6}$$

Projections onto the masses of the "+" and "0" components are shown in Fig. C.4, projections onto the masses of the "+" component in different slices of the helicity angles are shown in Fig. C.5 and the full projection is shown in Fig. C.6.

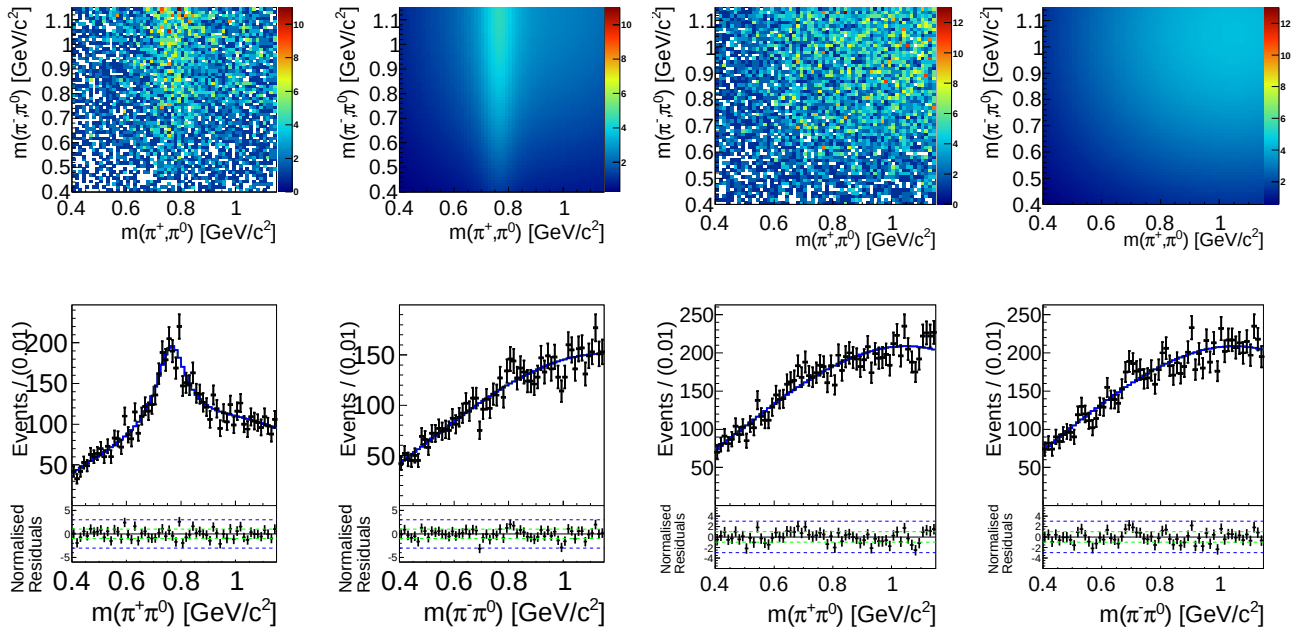

Figure C.4: Fit projections onto the dipion masses of $b \to c$ transitions in neutral B decays for the components + (left) and 0. The top row shows the 2D projection of the data (left) and the PDF (right) and the bottom row shows projection onto each axis, where the black points show simulated MC events and the solid line shows the fit result. The residuals are given beneath each distribution.

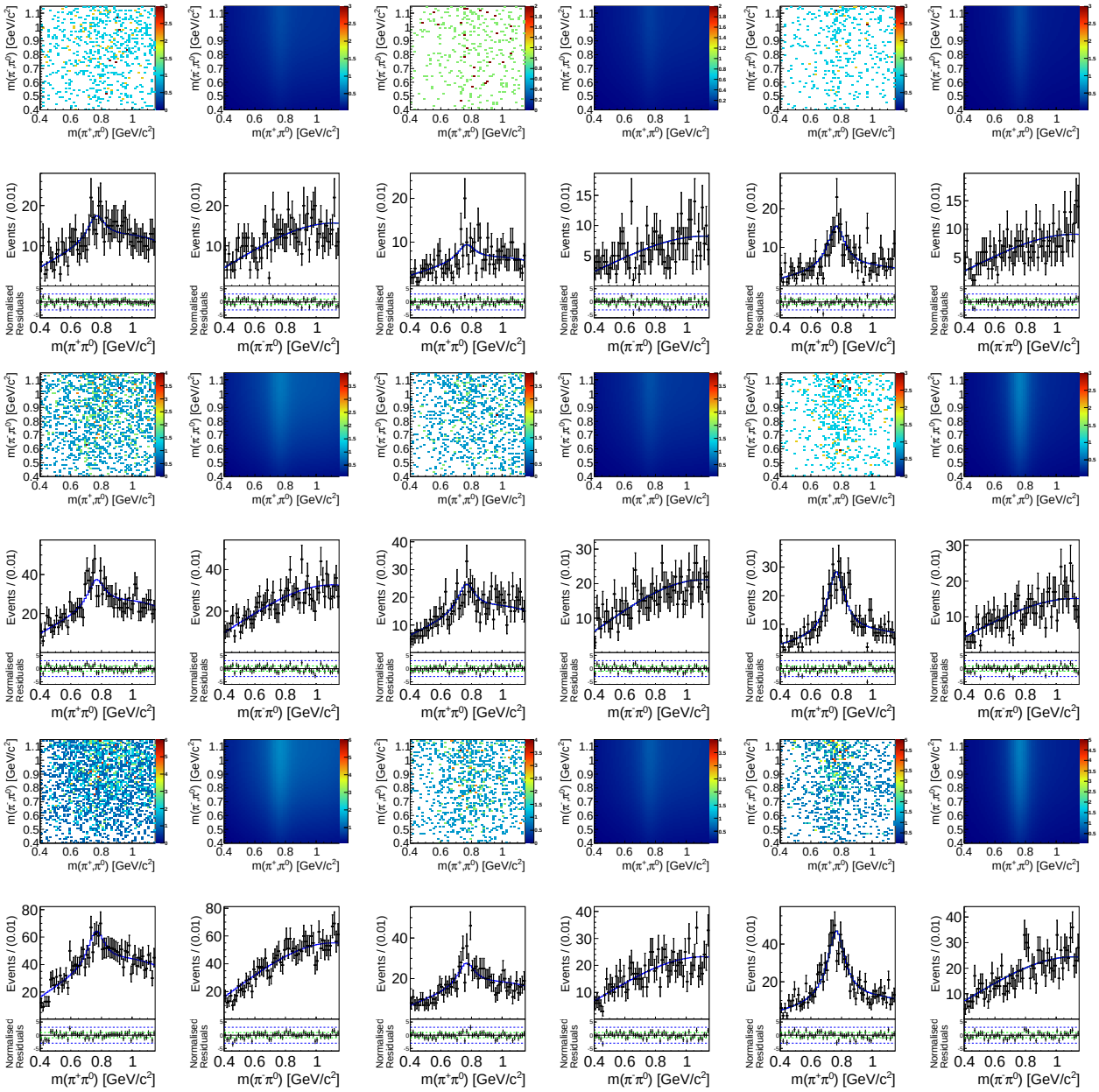

Figure C.5: Fit projections onto the dipion masses of the "+" component of nc in different bins of $\cos\theta_{\mathrm{H}}^{+}$-$\cos\theta_{\mathrm{H}}^{-}$ (lower and upper limits $\in \{-0.85, -0.6, 0.6, 0.98\}$). The top row shows the 2D projection of the data (left) and the PDF (right) and the bottom row shows projection onto each axis, where the black points show simulated MC events and the solid line shows the fit result. The residuals are given beneath each distribution.

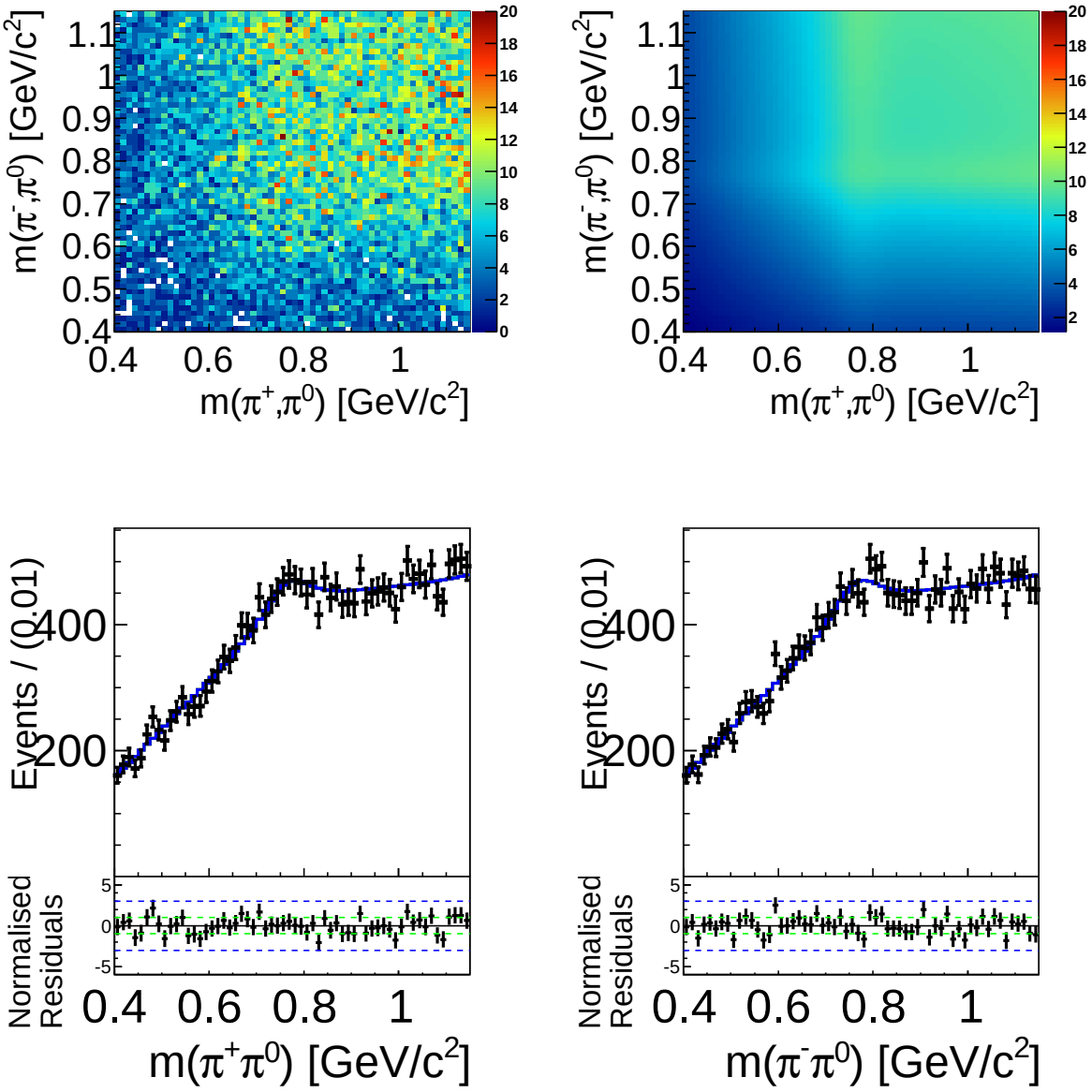

Figure C.6: Full projections onto the dipion masses of $b \to c$ transitions . The top row shows the 2D projection of the data (left) and the PDF (right) and the bottom row shows projection onto each axis, where the black points show simulated MC events and the solid line shows the fit result. The residuals are given beneath each distribution.

The distributions of the helicity angles are modeled by the products of sums of Chebychev polynomials up to the eigth order, where the PDFs for the ± parts take the form

$$\mathcal{P}^{\pm}_{nc}(\cos\theta^{\pm}_{\rm H}, \cos\theta^{\mp}_{\rm H}) \equiv \sum_{i=1}^{8} c_i^{H,+} C_i(\cos\theta^{\pm}_{\rm H}) \times \sum_{i=1}^{8} c_i^{H,-} C_i(\cos\theta^{\mp}_{\rm H}), \tag{C.7}$$

while the PDF for the '0' part is symmetric,

$$\mathcal{P}^{0}_{nc}(\cos\theta^{+}_{\rm H}, \cos\theta^{-}_{\rm H}) \equiv \sum_{i=1}^{8} c_i^{H,0} C_i(\cos\theta^{+}_{\rm H}) \times \sum_{i=1}^{8} c_i^{H,0} C_i(\cos\theta^{-}_{\rm H}). \tag{C.8}$$

Projections onto both distributions are shown in Fig. C.7 and the full projection is shown in Fig. C.8.

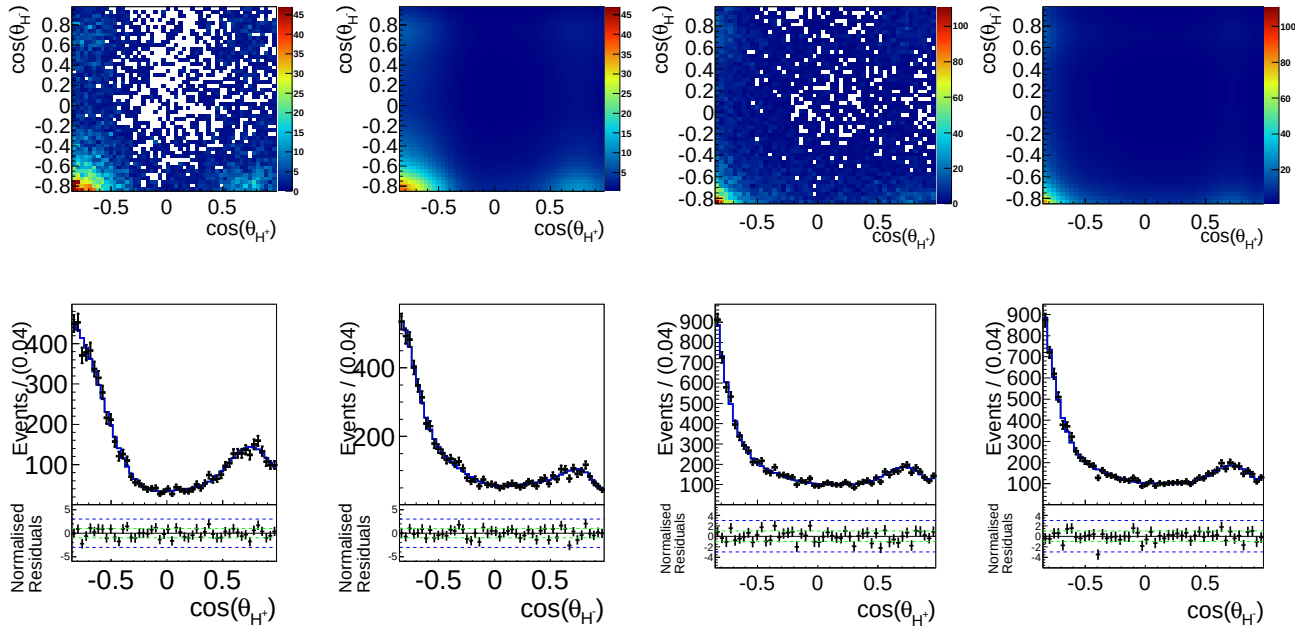

Figure C.7: Fit projections onto the helicity angles of $b \to c$ transitions in neutral B decays for the components + (left) and 0. The top row shows the 2D projection of the data (left) and the PDF (right) and the bottom row shows projection onto each axis, where the black points show simulated MC events and the solid line shows the fit result. The residuals are given beneath each distribution.

The Δt distributions are described by Eq. (C.2), projections onto each flavor are shown in Fig. C.9. The effective lifetimes, obtained from fits to the corresponding MC distributions, are listed in Table C.2.

lifetime [ps]	$\tau^{\rm SVD1}$	$\tau^{\rm SVD2}$	
$B^0\bar{B}^0$	1.36 ± 0.04	1.35 ± 0.02	

Table C.2: The B^0 lifetimes obtained from a fit to the $B^0, b \to c$ MC distributions.

The full PDF for neutral B mesons decaying into charm final states is given by

$$\begin{aligned}
&\mathcal{PDF}_{nc}(\Delta E, M_{\rm bc}, m_{\pi^+\pi^0}, m_{\pi^-\pi^0}, \cos\theta_{\rm H}^+, \cos\theta_{\rm H}^-, \mathcal{F}_{B\bar{B}/q\bar{q}}, \Delta t, q) \equiv \\
&\Big((1-f_0)\mathcal{PDF}_{nc}^{\pm}(\Delta E) \\
&\times\big(f_+ \times \mathcal{PDF}_{nc}^{+}(m_{\pi^+\pi^0}, m_{\pi^-\pi^0}|\cos\theta_{\rm H}^+, \cos\theta_{\rm H}^-) \times \mathcal{PDF}_{nc}^{+}(\cos\theta_{\rm H}^+, \cos\theta_{\rm H}^-) + \\
&(1-f_+) \times \mathcal{PDF}_{nc}^{-}(m_{\pi^+\pi^0}, m_{\pi^-\pi^0}|\cos\theta_{\rm H}^+, \cos\theta_{\rm H}^-) \times \mathcal{PDF}_{nc}^{-}(\cos\theta_{\rm H}^+, \cos\theta_{\rm H}^-)\big) \\
&+f_0 \times \mathcal{PDF}_{nc}^{0}(\Delta E) \times \mathcal{PDF}_{nc}^{0}(m_{\pi^+\pi^0}, m_{\pi^-\pi^0}) \times \mathcal{PDF}_{nc}^{0}(\cos\theta_{\rm H}^+, \cos\theta_{\rm H}^-)\Big) \\
&\times\mathcal{PDF}_{nc}(M_{\rm bc}) \times \mathcal{PDF}_{nc}(\mathcal{F}_{B\bar{B}/q\bar{q}}) \times \mathcal{PDF}_{nc}(\Delta t, q), \qquad \text{(C.9)}
\end{aligned}$$

the fractions $f_{+,0}$ are given in Table C.3.

	f_+	f_0
$B^0 \to c$	0.49 ± 0.02	0.6 ± 0.02

Table C.3: The fractions of the different reconstruction categories used in Eq. (C.9).

0	ΔE	M_{bc}	$m^1_{\pi^+\pi^-}$	$m^2_{\pi^+\pi^-}$	$\mathcal{F}_{B\bar{B}/q\bar{q}}$	$\cos\theta^1_{\rm H}$	$\cos\theta^2_{\rm H}$	Δt
ΔE	1	-0.02	0.01	0.00	0.02	-0.04	0.00	-0.02
M_{bc}		1	0.03	0.06	0.01	-0.04	0.04	0.01
$m^1_{\pi^+\pi^-}$			1	-0.00	-0.01	-0.00	0.00	0.01
$m^2_{\pi^+\pi^-}$				1	0.03	0.00	-0.01	-0.00
$\mathcal{F}_{B\bar{B}/q\bar{q}}$					1	0.00	-0.01	-0.00
$\cos\theta^1_{\rm H}$						1	0.04	-0.01
$\cos\theta^2_{\rm H}$							1	-0.01
Δt								1

Table C.4: Correlation matrix for charm $B^0(\bar{B}^0)$ decays (+, SVD2).

0	ΔE	M_{bc}	$m^1_{\pi^+\pi^-}$	$m^2_{\pi^+\pi^-}$	$\mathcal{F}_{B\bar{B}/q\bar{q}}$	$\cos\theta^1_{\rm H}$	$\cos\theta^2_{\rm H}$	Δt
ΔE	1	-0.03	-0.03	-0.01	-0.04	0.02	-0.05	-0.01
M_{bc}		1	0.02	0.01	0.04	-0.01	-0.05	0.02
$m^1_{\pi^+\pi^-}$			1	0.00	0.01	-0.04	0.05	0.00
$m^2_{\pi^+\pi^-}$				1	-0.02	0.01	-0.02	0.01
$\mathcal{F}_{B\bar{B}/q\bar{q}}$					1	-0.02	0.04	-0.01
$\cos\theta^1_{\rm H}$						1	0.08	-0.02
$\cos\theta^2_{\rm H}$							1	0.00
Δt								1

Table C.5: Correlation matrix for charm $B^0(\bar{B}^0)$ decays (-, SVD2).

0	ΔE	M_{bc}	$m^1_{\pi^+\pi^-}$	$m^2_{\pi^+\pi^-}$	$\mathcal{F}_{B\bar{B}/q\bar{q}}$	$\cos\theta^1_{\rm H}$	$\cos\theta^2_{\rm H}$	Δt
ΔE	1	0.01	-0.02	-0.00	0.01	-0.02	-0.02	-0.01
M_{bc}		1	-0.00	0.00	0.03	0.01	-0.01	-0.02
$m^1_{\pi^+\pi^-}$			1	0.03	0.02	-0.05	0.02	0.01
$m^2_{\pi^+\pi^-}$				1	0.01	0.01	-0.05	-0.01
$\mathcal{F}_{B\bar{B}/q\bar{q}}$					1	0.01	0.01	-0.01
$\cos\theta^1_{\rm H}$						1	0.09	0.04
$\cos\theta^2_{\rm H}$							1	0.03
Δt								1

Table C.6: Correlation matrix for charm $B^0(\bar{B}^0)$ decays (0, SVD2).

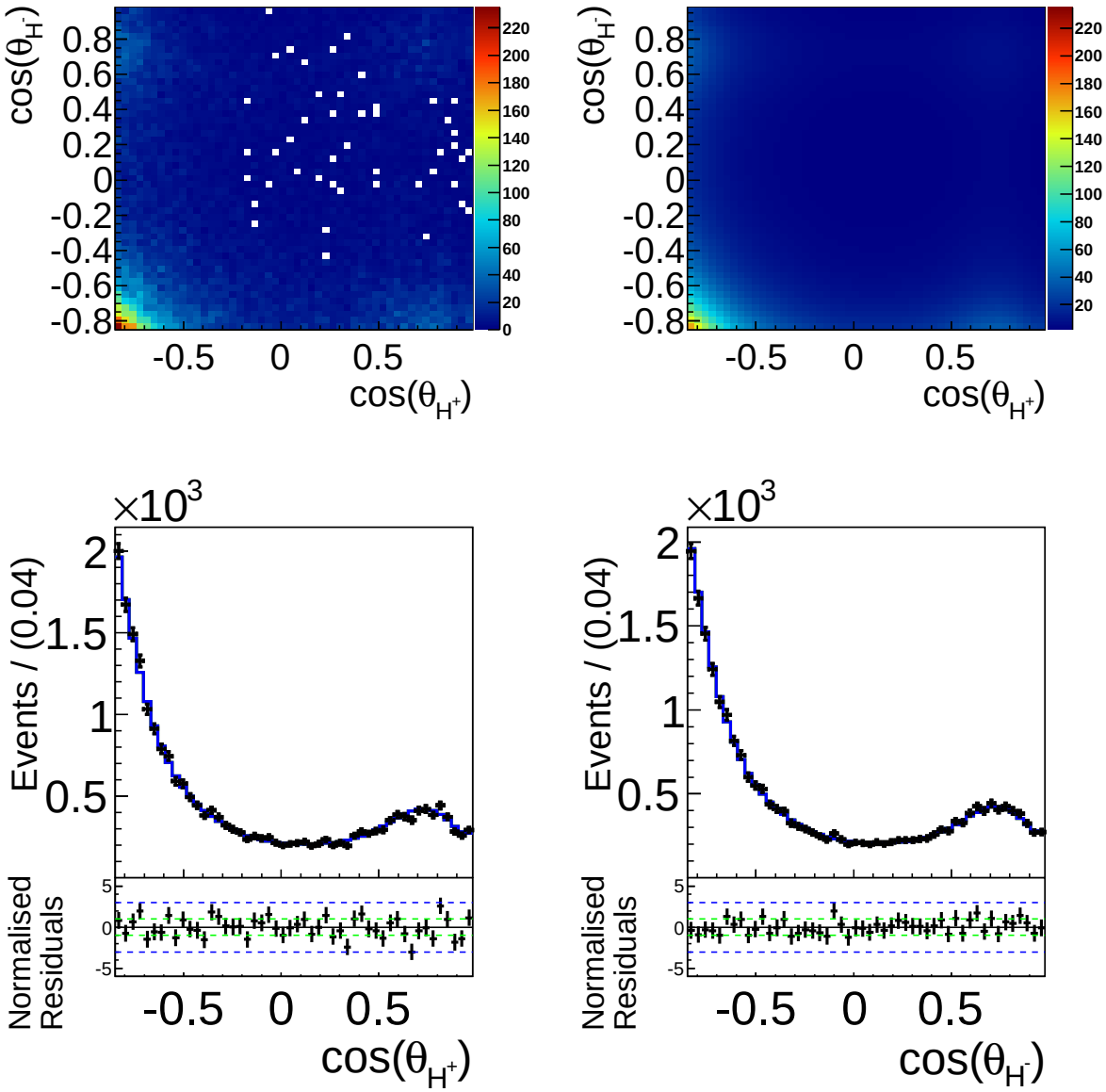

Figure C.8: Full projections onto the helicity angles of $b \to c$ transitions . The top row shows the 2D projection of the data (left) and the PDF (right) and the bottom row shows projection onto each axis, where the black points show simulated MC events and the solid line shows the fit result. The residuals are given beneath each distribution.

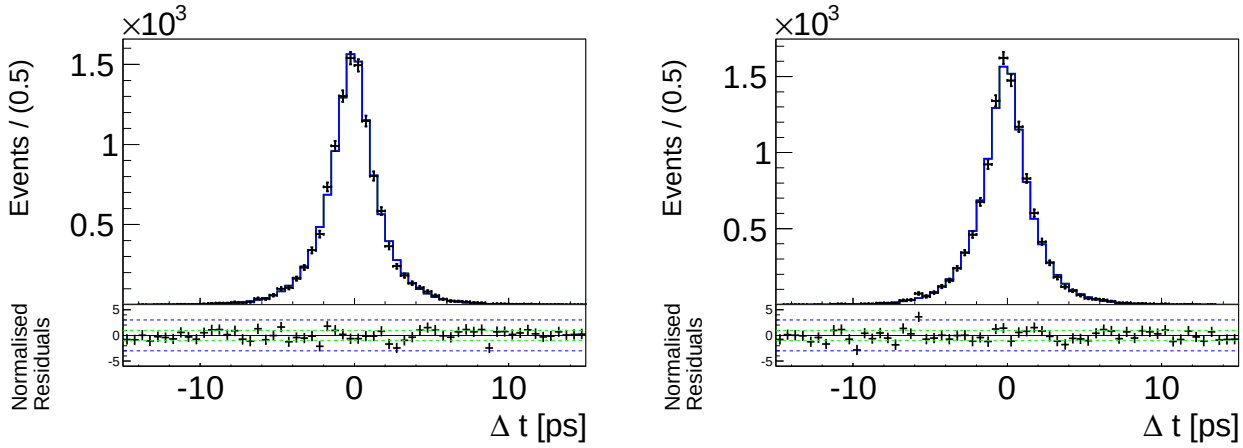

Figure C.9: Full projections onto Δt for $q = +1$ (left) and $q = -1$. The black points show simulated MC events and the solid line shows the fit result. The residuals are given beneath each distribution.

C.1.2 Charm $B^{\pm}$ Backgrounds

The subscript cc labels charged B meson decays into charm final states. The fractions of the $\pm, 0, 2c$ components are listed in Table C.8 and the correlation matrices are given in Tables C.9 to C.12.
The ΔE distributions of charm B decays are each described by the sum of Chebychev polynomials up to the second order,

$$\mathcal{P}_{cc}^{\pm,0,2c}(\Delta E) \equiv \sum_{i=1}^{2} c_i^{\pm,0,2c} C_i(\Delta E). \tag{C.10}$$

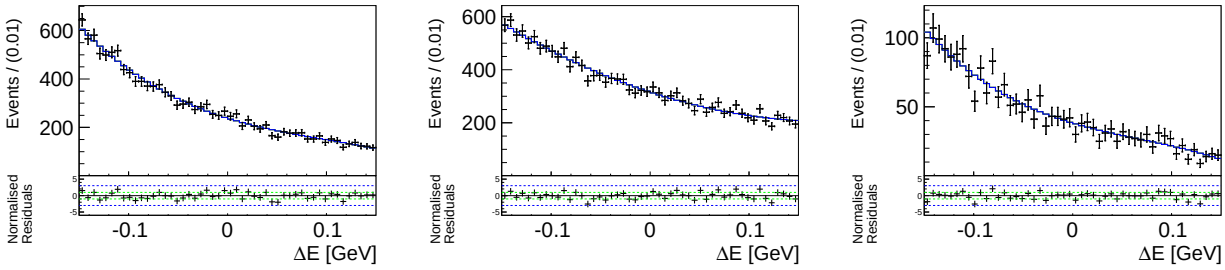

Figure C.10: Fit projections of $b \to c$ transitions for charge B decays onto ΔE for the three reconstruction categories $+, 0$ and $2c$ (from left to right). The black points show simulated MC events and the solid line shows the fit result. The residuals are given beneath each distribution.

The $M_{\rm bc}$ distribution for all four reconstruction categories is described by an Argus function

$$\mathcal{P}_{cc}(M_{\rm bc}) \equiv Ar(M_{\rm bc}), \tag{C.11}$$

and is shown together with the full projection onto ΔE in Fig. C.11. Fig. C.12 shows the projection onto $\mathcal{F}_{B\bar{B}/q\bar{q}}$ and the r-bin fractions and Fig. C.19 shows the projection onto Δt for each flavor q.

The PDFs of the $m_{\pi^{\pm}\pi^0}$ distributions of the $\pm, 0$ components are similar to those used for neutral B decays into charm final states Eqs. (C.5) and (C.6). For the $\pm$ component, the dependence on the helicity angles of the fraction in the mass PDF of the correctly reconstructed $\rho^{\pm}$ resonance is:

$$f_{cc}(\cos\theta_{\rm H}^{\pm}, \cos\theta_{\rm H}^{\mp}) = c_{0,M} + c_{1,M}\cos\theta_{\rm H}^{\pm} + c_{2,M}\cos\theta_{\rm H}^{\pm}(\cos\theta_{\rm H}^{\mp})^2 + c_{3,M}(\cos\theta_{\rm H}^{\pm})^2(\cos\theta_{\rm H}^{\mp})^3 + c_{4,M}(\cos\theta_{\rm H}^{\mp})^2 + c_{5,M}(\cos\theta_{\rm H}^{\mp})^4.$$

The mass distribution of the remaining component, $2c$, is the product of the PDF for each mass $m_{\pi^{\pm}\pi^0}$, taken to be the sum of a BreitWigner and a second order Chebychev polynomial;

$$\mathcal{P}_{cc}^{2c}(m_{\pi^{\pm}\pi^0}) \equiv \big(f_{2c} BW(m_{\pi^{\pm}\pi^0}, m, \Gamma) + (1 - f_{2c}) c_2^M C_2(m_{\pi^{\pm}\pi^0})\big). \tag{C.12}$$

The distributions the $\pm, 0$ components of the helicity angles are similar to those used for neutral B decays into charm final states Eqs. (C.7) and (C.8), the additional PDF for the component $2c$ is similar to the one used for reconstruction category 0. Projections onto the masses of the "+" component in different slices of the helicity angles are shown in Fig. C.14,

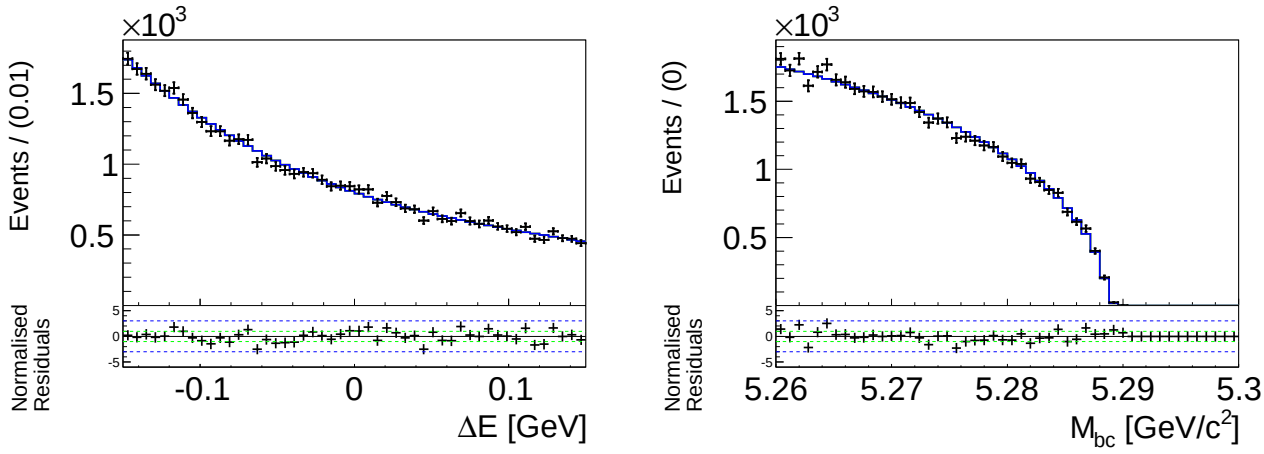

Figure C.11: Full projections onto ΔE and $M_{\rm bc}$ of $b \to c$ transitions in charged B decays. The black points show simulated MC events and the solid line shows the fit result. The residuals are given beneath each distribution.

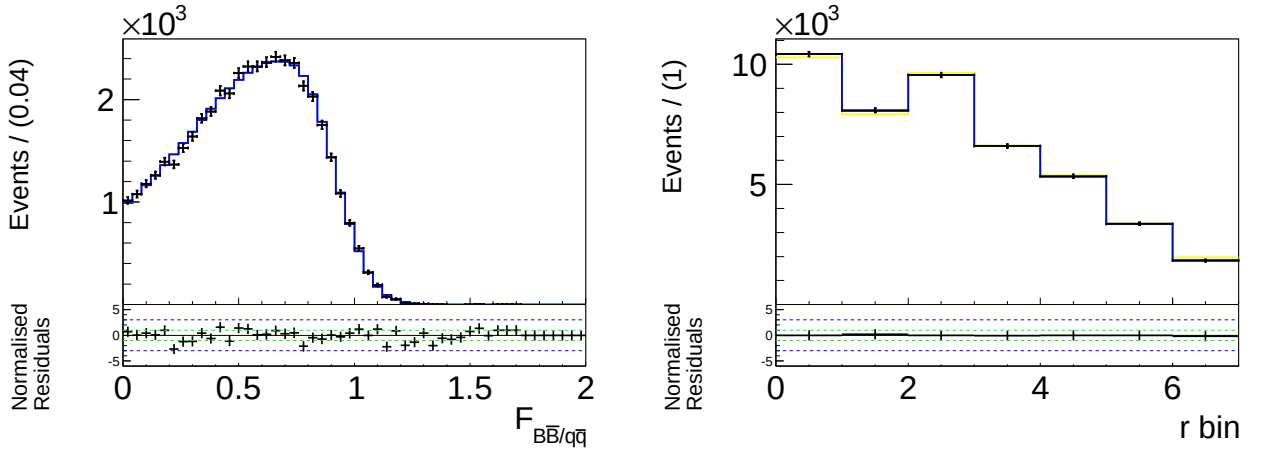

Figure C.12: Full projections onto $\mathcal{F}_{B\bar{B}/q\bar{q}}$ and the r-bin fractions of $b \to c$ transitions in charged B decays. The black points show simulated MC events and the solid line shows the fit result. The residuals are given beneath each distribution.

projections onto the masses of the "+" and "2c" components are shown in Fig. C.16 and the full projection is shown in Fig. C.15.
The Δt distributions are described by Eq. (C.2), projections onto each flavor are shown in Fig. C.19 and the effective lifetimes as obtained from a fit to the MC distribution are listed in Table C.7.

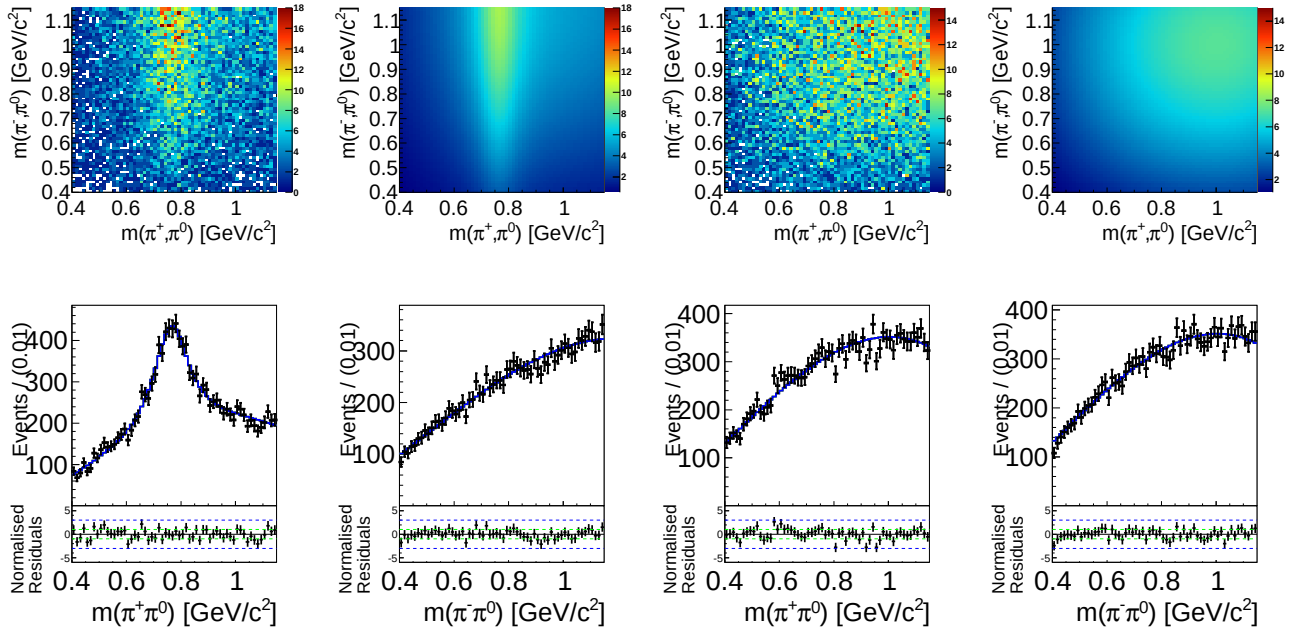

Figure C.13: Fit projections onto the dipion masses of $b \to c$ transitions in neutral B decays for the components + (left) and 0. The top row shows the 2D projection of the data (left) and the PDF (right) and the bottom row shows projection onto each axis, where the black points show simulated MC events and the solid line shows the fit result. The residuals are given beneath each distribution.

lifetime [ps]	τ^{SVD1}	τ^{SVD2}	
$B^{\pm}$	1.36 ± 0.03	1.29 ± 0.01	

Table C.7: The B^0 lifetimes obtained from a fit to the $B^{\pm}, b \to c$ MC distributions.

The full PDF for charged B mesons decaying into charm final states is given by

$$\begin{aligned}
&\mathcal{PDF}_{cc}(\Delta E, M_{\text{bc}}, m_{\pi^+\pi^0}, m_{\pi^-\pi^0}, \cos\theta_{\text{H}}^+, \cos\theta_{\text{H}}^-, \mathcal{F}_{B\bar{B}/q\bar{q}}, \Delta t, q) \equiv \\
&\Big((1-f_0) \times \Big((1-f_{2c}) \times \mathcal{PDF}_{cc}^{\pm}(\Delta E) \\
&\times \big(f_+ \times \mathcal{PDF}_{cc}^{+}(m_{\pi^+\pi^0}, m_{\pi^-\pi^0} | \cos\theta_{\text{H}}^+, \cos\theta_{\text{H}}^-) \times \mathcal{PDF}_{cc}^{+}(\cos\theta_{\text{H}}^+, \cos\theta_{\text{H}}^-) + \\
&(1-f_+) \times \mathcal{PDF}_{cc}^{-}(m_{\pi^+\pi^0}, m_{\pi^-\pi^0} | \cos\theta_{\text{H}}^+, \cos\theta_{\text{H}}^-) \times \mathcal{PDF}_{cc}^{-}(\cos\theta_{\text{H}}^+, \cos\theta_{\text{H}}^-) \big) + \\
&f_{2c} \times \mathcal{PDF}_{cc}^{2c}(\Delta E) \times \mathcal{PDF}_{cc}^{2c}(m_{\pi^+\pi^0}) \times \mathcal{PDF}_{cc}^{2c}(m_{\pi^-\pi^0}) \times \mathcal{PDF}_{cc}^{2c}(\cos\theta_{\text{H}}^+, \cos\theta_{\text{H}}^-) \Big) + \\
&f_0 \times \mathcal{PDF}_{cc}^{0}(\Delta E) \times \mathcal{PDF}_{cc}^{0}(m_{\pi^+\pi^0}, m_{\pi^-\pi^0}) \times \mathcal{PDF}_{cc}^{0}(\cos\theta_{\text{H}}^+, \cos\theta_{\text{H}}^-) \Big) \\
&\times \mathcal{PDF}_{cc}(M_{\text{bc}}) \times \mathcal{PDF}_{cc}(\mathcal{F}_{B\bar{B}/q\bar{q}}) \times \mathcal{PDF}_{cc}(\Delta t, q), \quad \text{(C.13)}
\end{aligned}$$

and the fractions f_i are given in Table C.8.

	f_+	f_0	f_{2c}
$B^0 \to c$	0.50 ± 0.02	0.48 ± 0.01	0.08 ± 0.03

Table C.8: The fractions of the different reconstruction categories used in Eq. (C.13).

0	ΔE	M_{bc}	$m^1_{\pi^+\pi^-}$	$m^2_{\pi^+\pi^-}$	$\mathcal{F}_{B\bar{B}/q\bar{q}}$	$\cos\theta^1_{\rm H}$	$\cos\theta^2_{\rm H}$	Δt
ΔE	1	-0.02	-0.01	-0.02	-0.02	-0.05	-0.01	-0.00
M_{bc}		1	0.01	0.03	0.04	-0.01	-0.01	0.00
$m^1_{\pi^+\pi^-}$			1	0.02	-0.00	-0.05	0.00	0.01
$m^2_{\pi^+\pi^-}$				1	0.03	0.02	-0.02	0.00
$\mathcal{F}_{B\bar{B}/q\bar{q}}$					1	0.04	-0.00	-0.02
$\cos\theta^1_{\rm H}$						1	-0.02	0.02
$\cos\theta^2_{\rm H}$							1	-0.00
Δt								1

Table C.9: Correlation matrix for charm $B^\pm$ decays (+, SVD2).

0	ΔE	M_{bc}	$m^1_{\pi^+\pi^-}$	$m^2_{\pi^+\pi^-}$	$\mathcal{F}_{B\bar{B}/q\bar{q}}$	$\cos\theta^1_{\rm H}$	$\cos\theta^2_{\rm H}$	Δt
ΔE	1	-0.01	-0.02	0.01	-0.00	-0.01	-0.06	0.00
M_{bc}		1	0.03	0.02	0.02	-0.02	-0.04	-0.00
$m^1_{\pi^+\pi^-}$			1	0.02	0.05	-0.03	0.02	-0.02
$m^2_{\pi^+\pi^-}$				1	0.00	0.04	-0.04	0.02
$\mathcal{F}_{B\bar{B}/q\bar{q}}$					1	0.00	0.05	0.00
$\cos\theta^1_{\rm H}$						1	-0.05	0.01
$\cos\theta^2_{\rm H}$							1	0.01
Δt								1

Table C.10: Correlation matrix for charm $B^\pm$ decays (-, SVD2).

0	ΔE	M_{bc}	$m^1_{\pi^+\pi^-}$	$m^2_{\pi^+\pi^-}$	$\mathcal{F}_{B\bar{B}/q\bar{q}}$	$\cos\theta^1_{\rm H}$	$\cos\theta^2_{\rm H}$	Δt
ΔE	1	0.00	-0.01	-0.01	0.02	-0.02	-0.02	-0.01
M_{bc}		1	0.00	0.02	0.01	-0.01	-0.00	-0.00
$m^1_{\pi^+\pi^-}$			1	0.02	0.01	-0.04	0.03	0.01
$m^2_{\pi^+\pi^-}$				1	0.01	0.04	-0.03	0.00
$\mathcal{F}_{B\bar{B}/q\bar{q}}$					1	0.03	0.01	0.02
$\cos\theta^1_{\rm H}$						1	0.03	0.02
$\cos\theta^2_{\rm H}$							1	0.02
Δt								1

Table C.11: Correlation matrix for charm $B^\pm$ decays (0, SVD2).

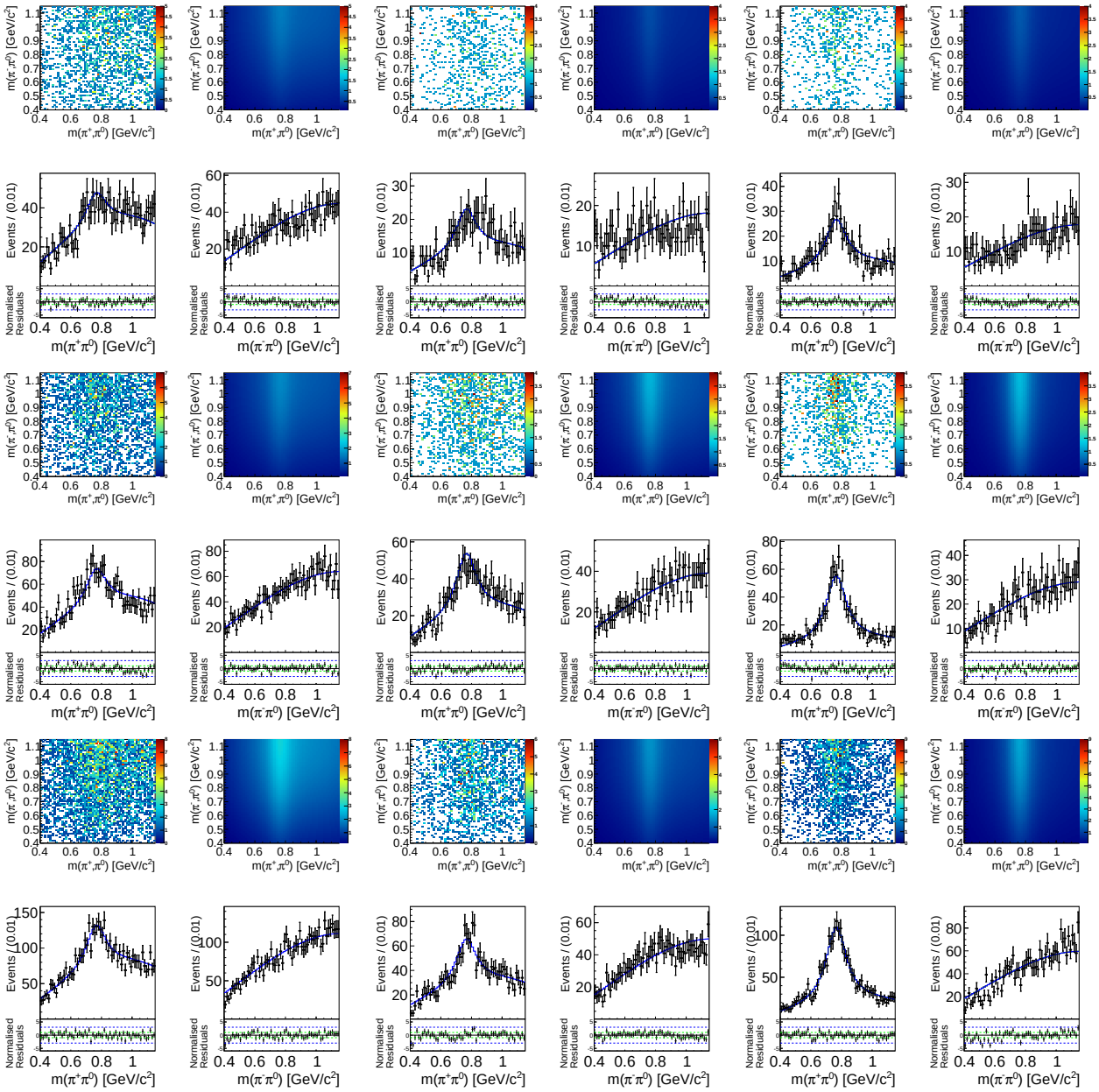

Figure C.14: Fit projections onto the dipion masses of the "+" component of $b \to c$ transitions in charged B decays in different bins of $\cos\theta_{\rm H}^{+}$-$\cos\theta_{\rm H}^{-}$ (lower and upper limits $\in \{-0.85, -0.6, 0.6\ , 0.98\}$). The top row shows the 2D projection of the data (left) and the PDF (right) and the bottom row shows projection onto each axis, where the black points show simulated MC events and the solid line shows the fit result. The residuals are given beneath each distribution.

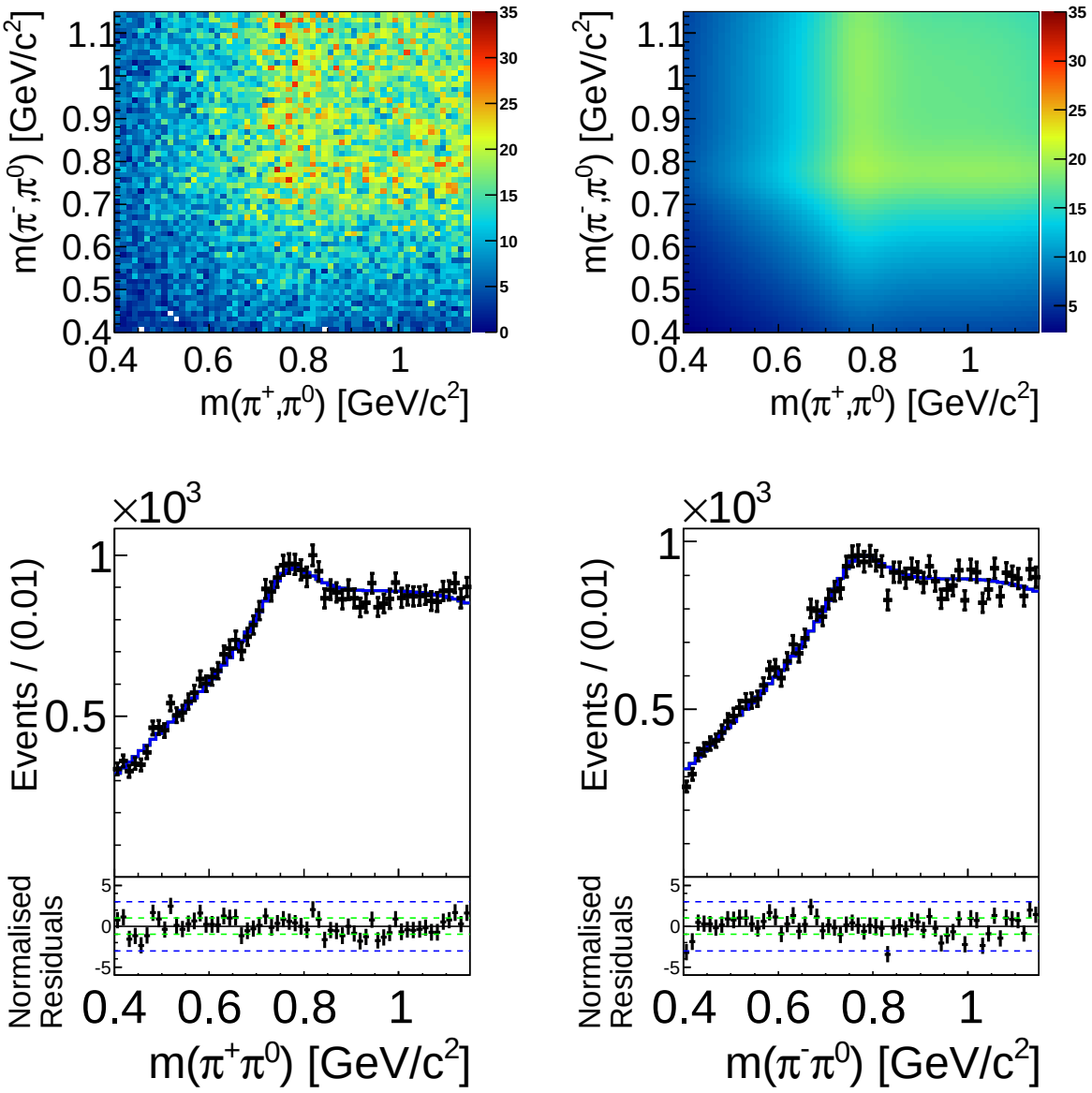

Figure C.15: Full projections onto the dipion masses of $b \to c$ transitions in charged B decays. The top row shows the 2D projection of the data (left) and the PDF (right) and the bottom row shows projection onto each axis, where the black points show simulated MC events and the solid line shows the fit result. The residuals are given beneath each distribution.

0	ΔE	M_{bc}	$m^1_{\pi^+\pi^-}$	$m^2_{\pi^+\pi^-}$	$\mathcal{F}_{B\bar{B}/q\bar{q}}$	$\cos\theta^1_{\mathrm{H}}$	$\cos\theta^2_{\mathrm{H}}$	Δt
ΔE	1	-0.05	0.00	-0.02	-0.01	-0.02	0.01	0.01
M_{bc}		1	0.04	0.02	0.03	-0.05	-0.02	-0.04
$m^1_{\pi^+\pi^-}$			1	0.03	0.02	-0.03	0.02	-0.00
$m^2_{\pi^+\pi^-}$				1	0.00	0.01	0.01	0.02
$\mathcal{F}_{B\bar{B}/q\bar{q}}$					1	0.02	0.01	0.01
$\cos\theta^1_{\mathrm{H}}$						1	0.00	0.00
$\cos\theta^2_{\mathrm{H}}$							1	0.02
Δt								1

Table C.12: Correlation matrix for charm $B^{\pm}$ decays (2c, SVD2). As this components fraction is tiny, correlations are ignored.

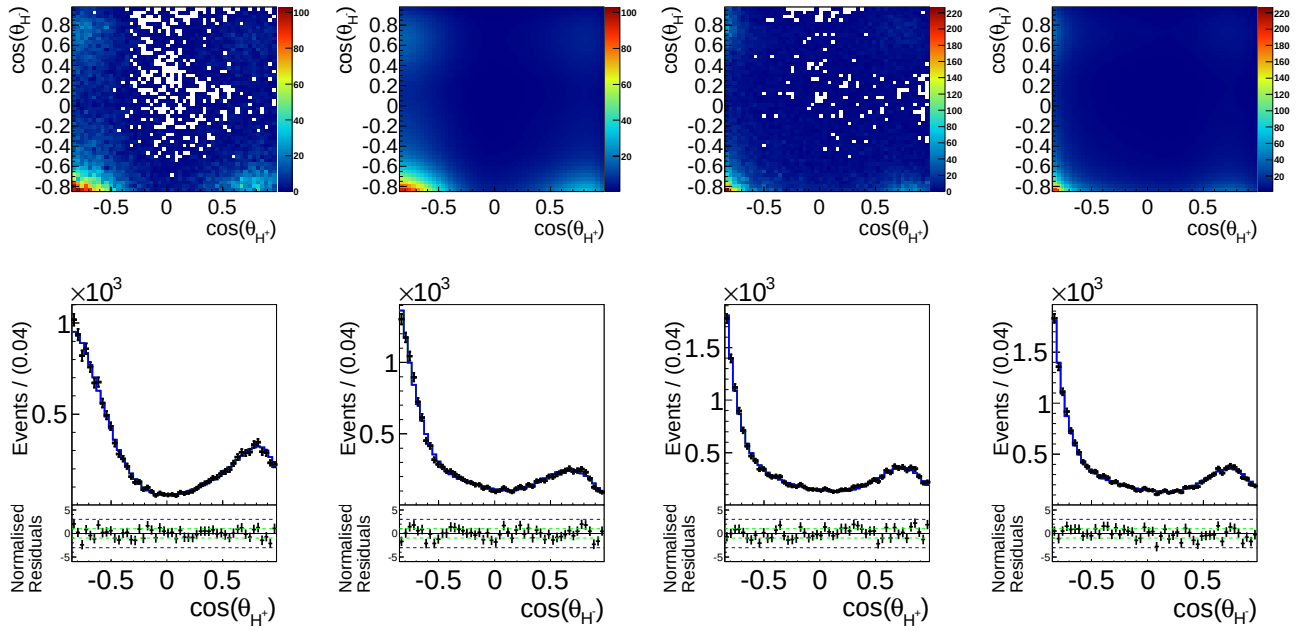

Figure C.16: Fit projections onto the dipion masses of $b \to c$ transitions in charged B decays for the reconstruction categories + (left) and 0. The top row shows the 2D projection of the data (left) and the PDF (right) and the bottom row shows projection onto each axis, where the black points show simulated MC events and the solid line shows the fit result. The residuals are given beneath each distribution.

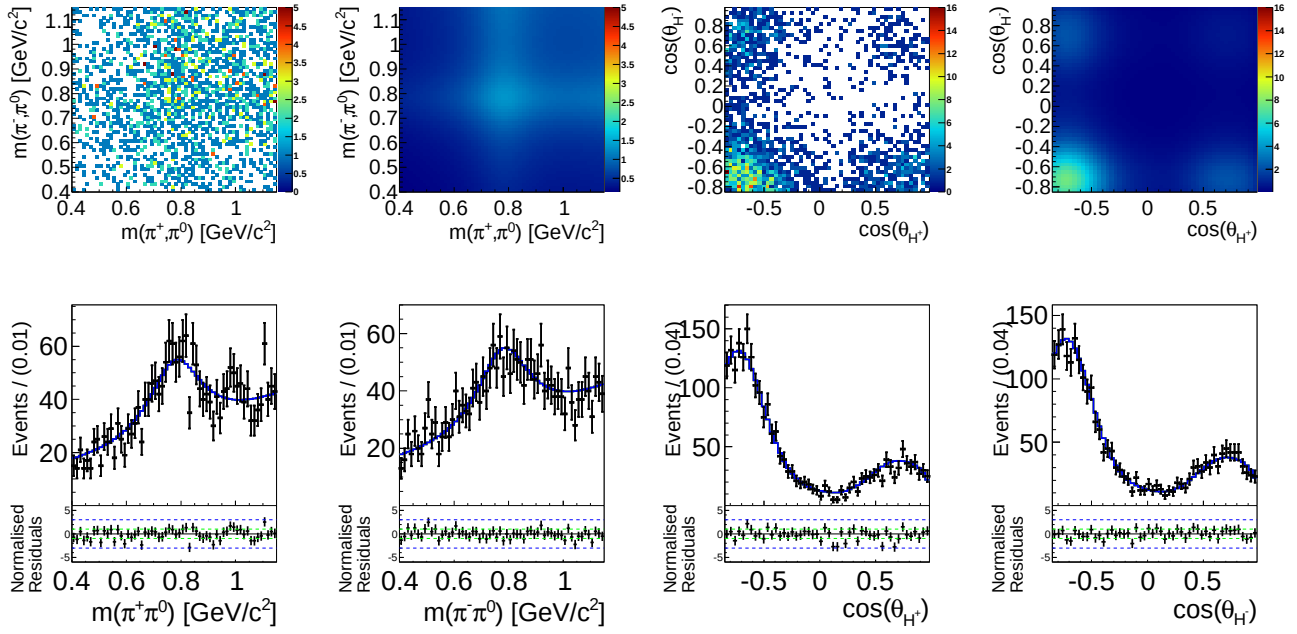

Figure C.17: Fit projections onto the dipion masses and $\cos\theta_{\mathrm{H}}^{\pm}$ of $b \to c$ transitions in charged B decays for the component $2c$. The top row shows the 2D projection of the data (left) and the PDF (right) and the bottom row shows projection onto each axis, where the black points show simulated MC events and the solid line shows the fit result. The residuals are given beneath each distribution.

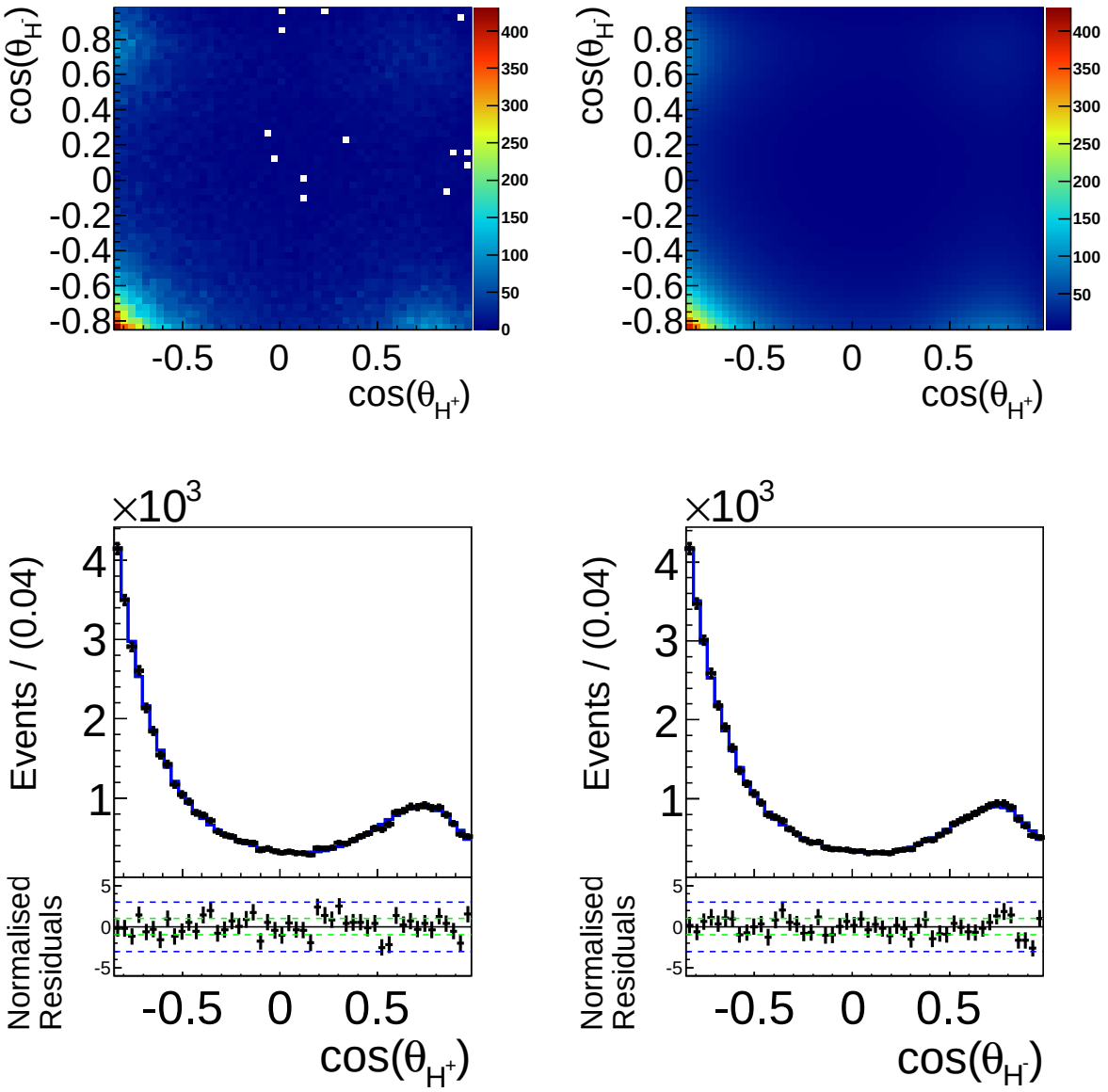

Figure C.18: Full projections onto the helicity angles of $b \to c$ transitions . The top row shows the 2D projection of the data (left) and the PDF (right) and the bottom row shows projection onto each axis, where the black points show simulated MC events and the solid line shows the fit result. The residuals are given beneath each distribution.

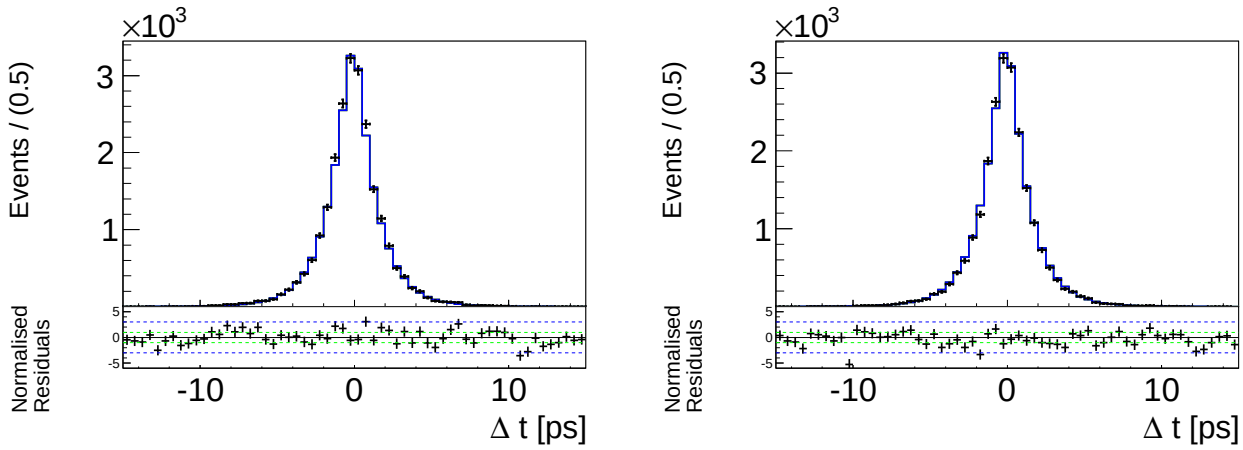

Figure C.19: Full projections onto Δt for $q = +1$ (left) and $q = -1$. The black points show simulated MC events and the solid line shows the fit result. The residuals are given beneath each distribution.

C.1.3 Charmless B^0 Backgrounds

The subscript rn refers to neutral B meson decays into charmless final states. We consider the cases $\pm$ and 0 separately.
The ΔE distributions are described by the sum of Chebychev polynomials up to the forth (second) order for the reconstruction categories $\pm$ (0).

$$\mathcal{P}^0_{\rm rn}(\Delta E) \equiv \sum_{i=1}^{2} c_i^0 C_i(\Delta E), \tag{C.14}$$

For the category $\pm$ we account a for a correlation with the helicity angles by using three different sets of $c_i^{\pm}(\cos\theta_{\rm H}^+, \cos\theta_{\rm H}^-)$: i) if $\cos\theta_{\rm H}^{\pm} < -0.5$, ii) if $|\cos\theta_{\rm H}^{\pm}| < 0.5$ and iii) else.

$$\mathcal{P}^{\pm}_{\rm rn}(\Delta E|\cos\theta_{\rm H}^+, \cos\theta_{\rm H}^-) \equiv \sum_{i=1}^{4} c_i^{\pm}(\cos\theta_{\rm H}^+, \cos\theta_{\rm H}^-) C_i(\Delta E), \tag{C.15}$$

Projections for the three cases for category $\pm$ are shown in Fig. C.20 and the full projections for each reconstruction category are shown in Fig. C.21.

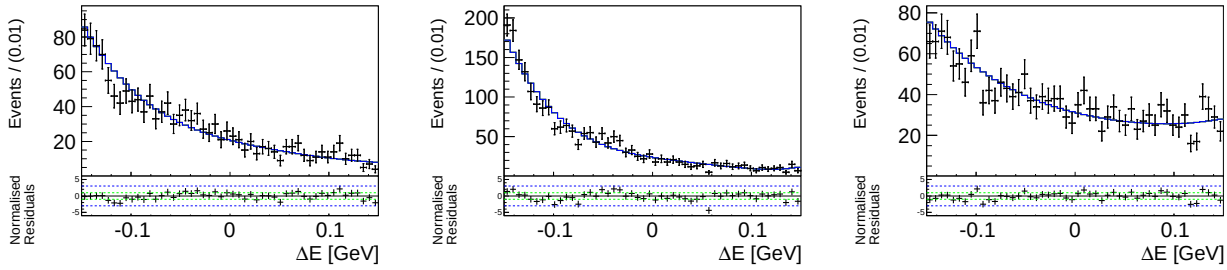

Figure C.20: Fit projections onto ΔE of $b \to u, d, s$ transitions in neutral B decays (category $\pm$) for different slices of $\cos\theta_{\rm H}^+ \cos\theta_{\rm H}^-$. a)$\cos\theta_{\rm H}^+ < -0.5 \& -0.5 < \cos\theta_{\rm H}^- < 0.5$, b) $-0.85 < \cos\theta_{\rm H}^+, \cos\theta_{\rm H}^- < -0.5$ and c) $|cH^+, \cos\theta_{\rm H}^-| < 0.5$. The residuals are given beneath each distribution.

The $M_{\rm bc}$ distribution for reconstruction category 0 is described by an Argus function

$$\mathcal{P}^0_{\rm rn}(M_{\rm bc}) \equiv Ar(M_{\rm bc}). \tag{C.16}$$

For the reconstruction categories $\pm$ a dbG is added, its fraction

$$f_G(\Delta E) = f_{G0} + c_{M_{\rm bc},1}\Delta E + c_{M_{\rm bc},2}\Delta E^2$$

depends on ΔE and the helicity angles with $c_{M_{\rm bc},1} = c_{M_{\rm bc},2} = 0$ for $-0.85 < \cos\theta_{\rm H}^{\pm} < 0.5$ and $c_{M_{\rm bc},1} = -1.35 \pm 0.07$ and $c_{M_{\rm bc},2} = 4.20 \pm 0.6$ else;

$$\mathcal{P}^{\pm}_{\rm rn}(M_{\rm bc}|\Delta E) \equiv f_G(\Delta E) dbG(M_{\rm bc}) + (1 - f_G(\Delta E)) Ar(M_{\rm bc}). \tag{C.17}$$

Projections onto $M_{\rm bc}$ in slices of the helicity angles or ΔE are shown in Fig. C.22 and the full projections for each reconstruction category are shown in Fig. C.23.

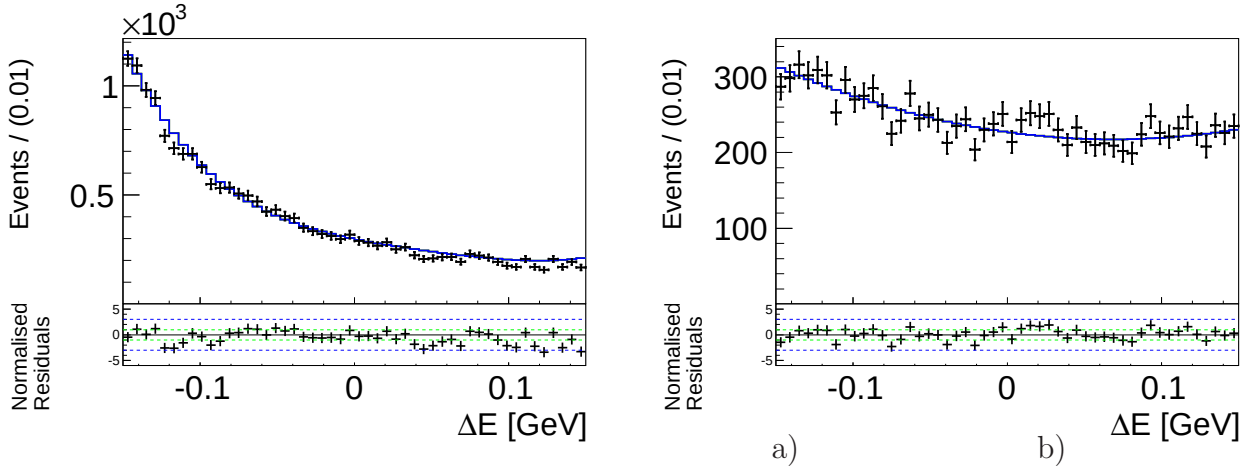

Figure C.21: Fit projections onto ΔE of $b \to u, d, s$ transitions in neutral B decays for reconstruction category $\pm$ (left) and 0. The residuals are given beneath each distribution.

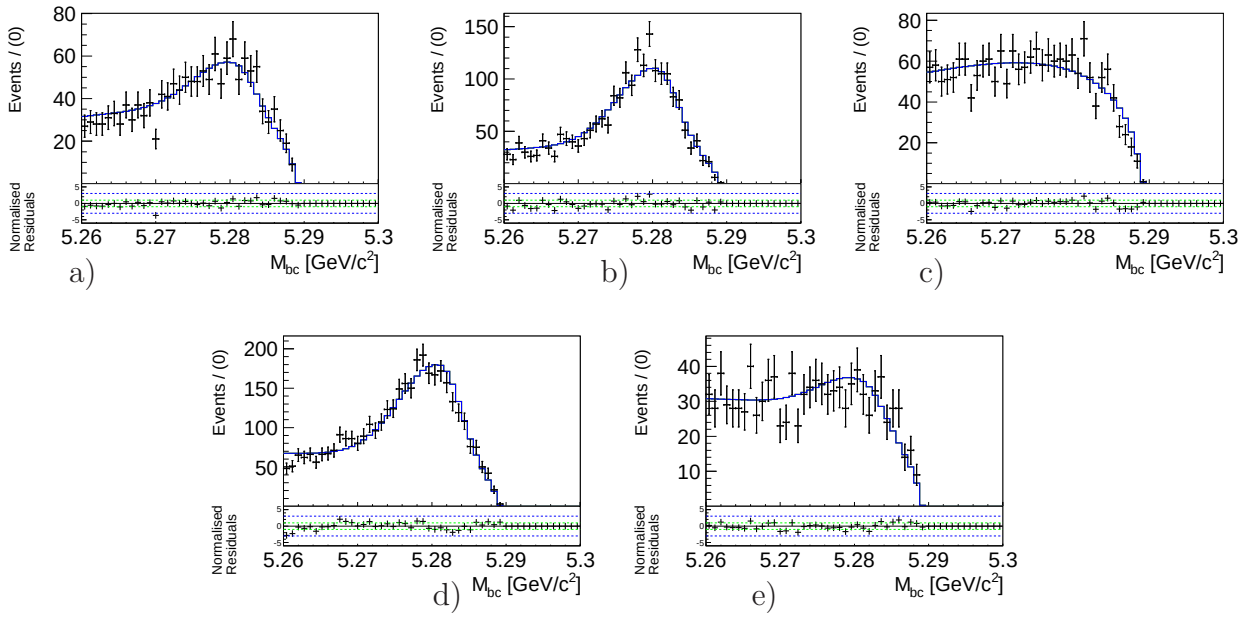

Figure C.22: Fit projections onto $M_{\rm bc}$ of $b \to u, d, s$ transitions in neutral B decays (category $\pm$) for different slices of $\cos\theta_{\rm H}^{+}\cos\theta_{\rm H}^{-}$: a)-c). And for different slices of ΔE: d) -0.15 GeV $< \Delta E < -0.1$ GeV and e) 0 GeV $< \Delta E <$ 0.05 GeV. The residuals are given beneath each distribution.

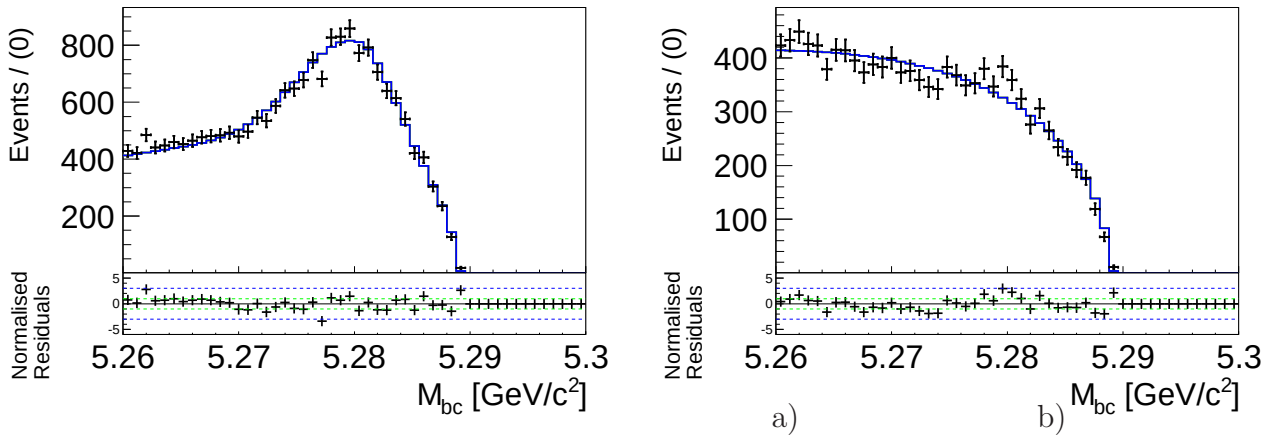

Figure C.23: Fit projections onto $M_{\rm bc}$ of $b \to u, d, s$ transitions in neutral B decays for reconstruction categories $\pm$ and 0. The residuals are given beneath each distribution.

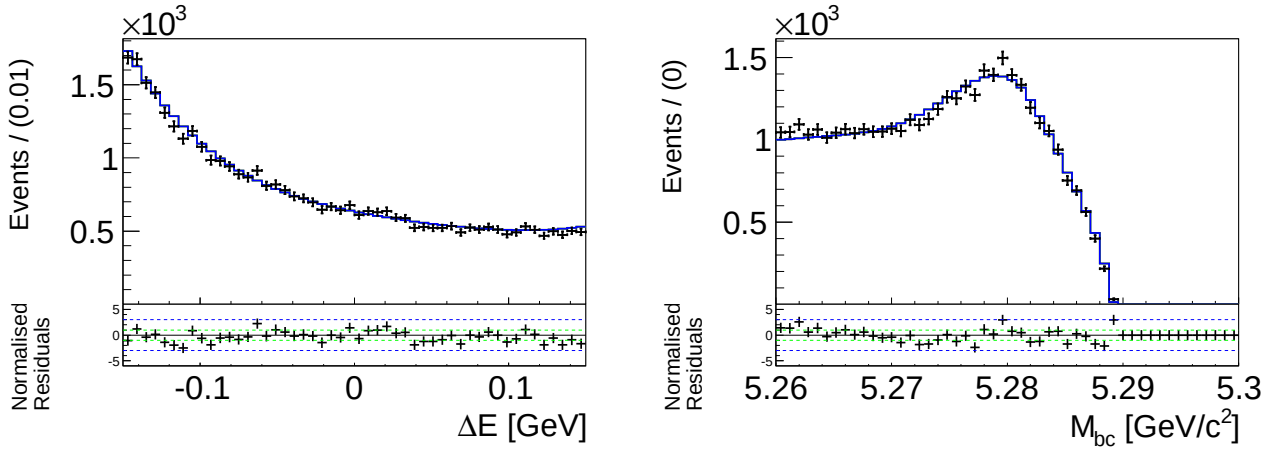

Figure C.24: Full projections onto ΔE and $M_{\rm bc}$of $b \to u, d, s$ transitions in neutral B decays. The black points show simulated MC events and the solid line shows the fit result. The residuals are given beneath each distribution.

The PDF of the $m_{\pi^+\pi^0}$-$m_{\pi^-\pi^0}$ distribution for category $\pm$ is given by the the product of a Breit-Wigner added to the sum of Chebychev polynomials up to the third order for each dipion mass,

$$\mathcal{P}^{\pm}_{\rm rn}(m_{\pi^+\pi^0}, m_{\pi^-\pi^0}|\cos\theta^+_{\rm H}, \cos\theta^-_{\rm H}) \equiv \tag{C.18}$$

$$(f_+(\cos\theta^+_{\rm H}, \cos\theta^-_{\rm H})BW(m_{\pi^+\pi^0}, m^+, \Gamma^+) + (1 - f_+(\cos\theta^+_{\rm H}, \cos\theta^-_{\rm H}))\sum_{i=1}^{3} c^+_{M,i}C_i(m_{\pi^+\pi^0}))$$

$$\times (f_-BW(m_{\pi^-\pi^0}, m^-, \Gamma^-) + (1 - f_-)\sum_{i=1}^{3} c^-_{M,i}C_i(m_{\pi^-\pi^0})), \tag{C.19}$$

where for the + part the fraction of the Breit-Wigner depends on the helicity angles:

$$f_+(\cos\theta^+_{\rm H}, \cos\theta^-_{\rm H}) = c_{H,1}(\cos\theta^+_{\rm H} + \cos\theta^-_{\rm H}) + c_{H,2}((\cos\theta^+_{\rm H})^2 + (\cos\theta^-_{\rm H})^2) + c_{H,3}\cos\theta^+_{\rm H}\cos\theta^-_{\rm H},$$

with $c_{H,1} = 0.07 \pm 0.2$, $c_{H,2} = -0.40 \pm 0.1$ and $c_{H,3} = -0.13 \pm 0.3$. We restrict $0 \leq f_+(\cos\theta^+_{\rm H}, \cos\theta^-_{\rm H}) \leq 1$. Projections onto $m_{\pi^+\pi^0}$-$m_{\pi^-\pi^0}$ for different slices of $\cos\theta^+_{\rm H} - \cos\theta^-_{\rm H}$ are shown in Fig. C.26 and the fraction's dependency is shown in Fig. C.25;
The product of a sum of Chebychev polynomial up to the fifth order is taken if no $\rho^{\pm}$ resonance has been correctly reconstructed;

$$\begin{aligned}\mathcal{P}^0_{\rm rn}(m_{\pi^+\pi^0}, m_{\pi^-\pi^0}|\Delta E) \equiv \\ \Big(\sum_{i=1,i\neq3}^{5} c^0_{M,i}C_i(m_{\pi^+\pi^0}) + c^0_{M,3}(\Delta E)C_3(m_{\pi^+\pi^0})\Big) \\ \times\Big(\sum_{i=1,i\neq3}^{5} c^0_{M,i}C_i(m_{\pi^-\pi^0}) + c^0_{M,3}(\Delta E)C_3(m_{\pi^-\pi^0})\Big)\end{aligned} \quad , \tag{C.20}$$

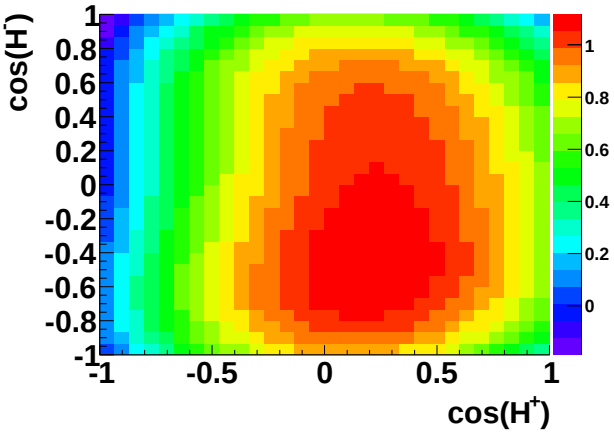

Figure C.25: The fraction of the Breit-Wigner, $f_+(\cos\theta^+_{\rm H}, \cos\theta^-_{\rm H})$, of the + part of the PDF for $m_{\pi^+\pi^0}$-$m_{\pi^-\pi^0}$ for neutral B decays into charmless final states depending on the helicity angles.

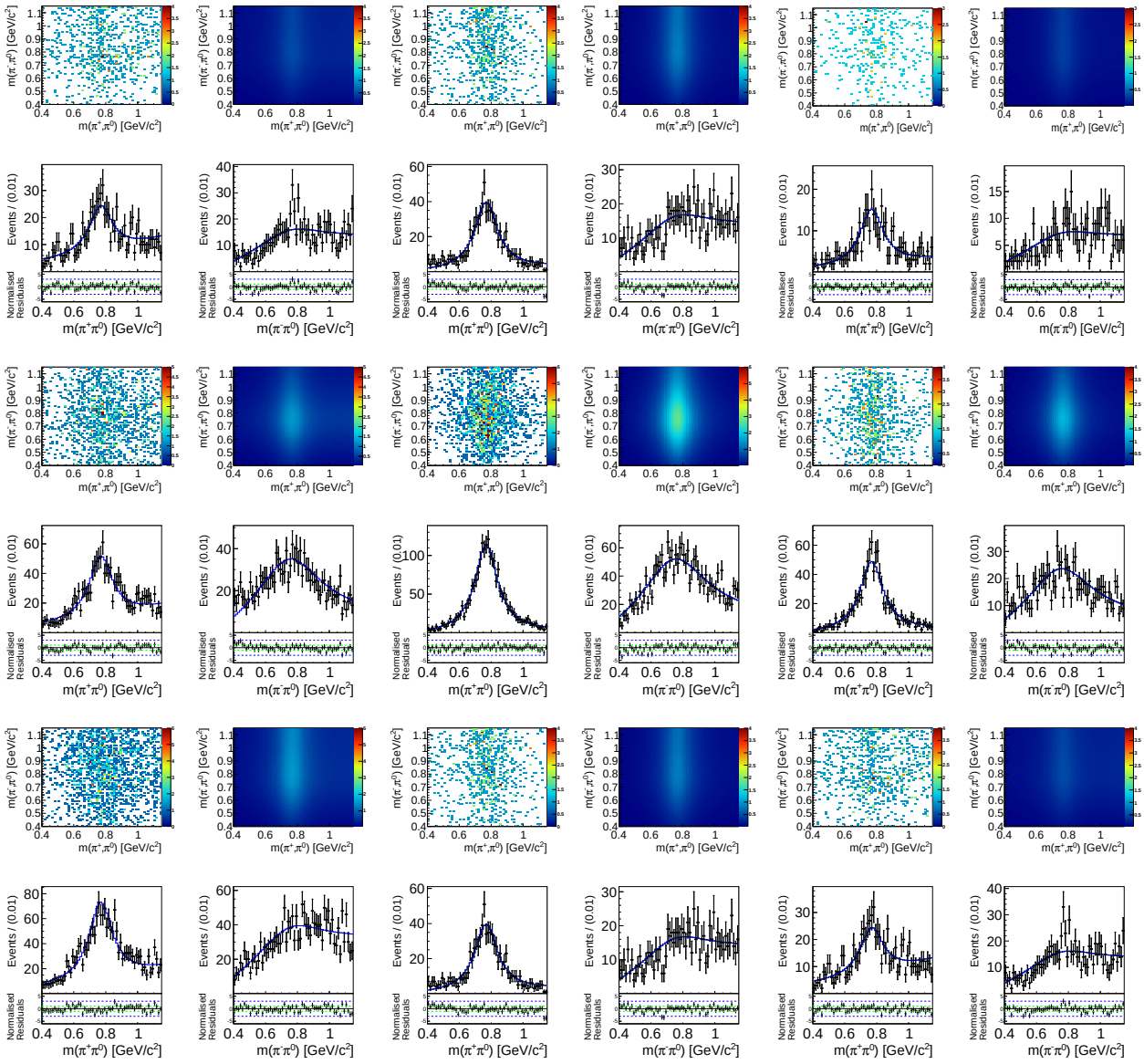

Figure C.26: Fit projections onto $m_{\pi^{\mp}\pi^0}$ of $b \to u, d, s$ transitions in neutral B decays (category +) for different slices of $\cos\theta_{\rm H}^{+}\cos\theta_{\rm H}^{-}$. a) -0.15 GeV $< \Delta E < -0.1$ GeV and b) 0 GeV $< \Delta E <$ 0.05 GeV. The residuals are given beneath each distribution.

The distribution of the helicity angles is modeled by the product of sums of Chebychev polynomials up to the eigth order. The PDF for the ± part takes the form

$$\mathcal{P}^{\pm}_{\rm rn}(\cos\theta_{\rm H}^{+}, \cos\theta_{\rm H}^{-}|\Delta E) \equiv \sum_{i=1}^{8} c^{\pm}_{H,i}(\Delta E) C_i(\cos\theta_{\rm H}^{\pm}) \times \sum_{i=1}^{8} c^{\rm mr}_{H,i}(\Delta E) C_i(\cos\theta_{\rm H}^{\mp}), \qquad \text{(C.21)}$$

where a correlation with ΔE is accounted for via

$$c^{\pm,\rm mr}_{H,i} = a^{\pm,\rm mr}_{1H,i} + a^{\pm,\rm mr}_{2H,i}\Delta E + a^{\pm,\rm mr}_{3H,i}\Delta E^2.$$

The PDF for the '0' part is symmetric

$$\mathcal{P}^{0}_{\rm rn}(\cos\theta_{\rm H}^{+}, \cos\theta_{\rm H}^{-}) \equiv \sum_{i=1}^{8} c^{0}_{H,i} C_i(\cos\theta_{\rm H}^{+}) \times \sum_{i=1}^{8} c^{0}_{H,i} C_i(\cos\theta_{\rm H}^{-}), \qquad \text{(C.22)}$$

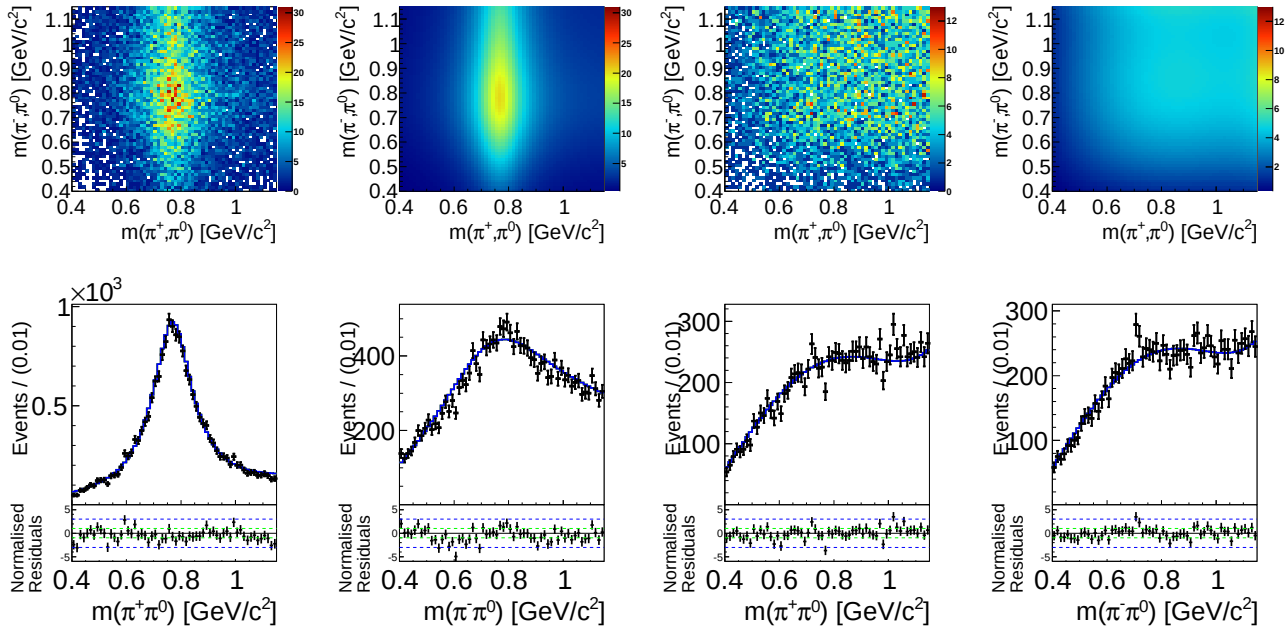

Figure C.27: Fit projections onto the dipion masses of $b \to c$ transitions in neutral B decays for the reconstruction categories + (left) and 0. The top row shows the 2D projection of the data (left) and the PDF (right) and the bottom row shows projection onto each axis, where the black points show simulated MC events and the solid line shows the fit result. The residuals are given beneath each distribution.

Projections onto the helicity angles for different slices of ΔE are shown in Fig. C.29, projections for each reconstruction category and the full projection are shown in Figs. C.30 and C.31.
The results from a fit to the Δt MC distributions are shown in Fig. C.33 and the obtained effective lifetimes are listed in Table C.13.

lifetime [ps]	τ^{SVD1}	τ^{SVD2}
$B^0\bar{B}^0$	1.42 ± 0.06	1.44 ± 0.03

Table C.13: The B^0 lifetimes obtained from a fit to the $B^0, b \to u, d, s$ MC distributions.

The full PDF for neutral B mesons decaying into charmless final states is given by

$$\begin{aligned}
&\mathcal{PDF}_{\text{rn}}(\Delta E, M_{\text{bc}}, m_{\pi^+\pi^0}, m_{\pi^-\pi^0}, \cos\theta_{\text{H}}^+, \cos\theta_{\text{H}}^-, \mathcal{F}_{B\bar{B}/q\bar{q}}, \Delta t, q) \equiv \\
&\Big((1-f_0) \times \mathcal{PDF}^{\pm}_{\text{rn}}(\Delta E) \times \mathcal{PDF}^{\pm}_{\text{rn}}(M_{\text{bc}}) \\
&\big(f_+ \times \mathcal{PDF}^{+}_{\text{rn}}(m_{\pi^+\pi^0}, m_{\pi^-\pi^0} | \cos\theta_{\text{H}}^+, \cos\theta_{\text{H}}^-) \times \mathcal{PDF}^{+}_{\text{rn}}(\cos\theta_{\text{H}}^+, \cos\theta_{\text{H}}^-) + \\
&(1-f_+) \times \mathcal{PDF}^{-}_{\text{rn}}(m_{\pi^+\pi^0}, m_{\pi^-\pi^0} | \cos\theta_{\text{H}}^+, \cos\theta_{\text{H}}^-) \times \mathcal{PDF}^{-}_{\text{rn}}(\cos\theta_{\text{H}}^+, \cos\theta_{\text{H}}^-) \big) \\
&+ f_0 \times \mathcal{PDF}^{0}_{\text{rn}}(\Delta E) \times \mathcal{PDF}^{0}_{\text{rn}}(M_{\text{bc}}) \times \mathcal{PDF}^{0}_{\text{rn}}(m_{\pi^+\pi^0}, m_{\pi^-\pi^0}) \times \mathcal{PDF}^{0}_{\text{rn}}(\cos\theta_{\text{H}}^+, \cos\theta_{\text{H}}^-) \Big) \\
&\times \mathcal{PDF}_{\text{rn}}(\mathcal{F}_{B\bar{B}/q\bar{q}}) \times \mathcal{PDF}_{\text{rn}}(\Delta t, q)
\end{aligned} \tag{C.23}$$

and the fractions $f_{+,0}$ are given in Table C.17.

0	ΔE	M_{bc}	$m^1_{\pi^+\pi^-}$	$m^2_{\pi^+\pi^-}$	$\mathcal{F}_{B\bar{B}/q\bar{q}}$	$\cos\theta^1_{\rm H}$	$\cos\theta^2_{\rm H}$	Δt
ΔE	1	-0.13	-0.01	0.05	-0.03	-0.01	-0.13	0.01
M_{bc}		1	0.01	-0.04	0.07	0.03	0.04	-0.00
$m^1_{\pi^+\pi^-}$			1	-0.01	-0.02	-0.06	0.02	0.00
$m^2_{\pi^+\pi^-}$				1	0.00	0.01	-0.02	-0.00
$\mathcal{F}_{B\bar{B}/q\bar{q}}$					1	0.03	0.01	-0.01
$\cos\theta^1_{\rm H}$						1	-0.04	0.01
$\cos\theta^2_{\rm H}$							1	0.02
Δt								1

Table C.14: Correlation matrix for charmless $B^0(\bar{B}^0)$ decays (+, SVD2).

0	ΔE	M_{bc}	$m^1_{\pi^+\pi^-}$	$m^2_{\pi^+\pi^-}$	$\mathcal{F}_{B\bar{B}/q\bar{q}}$	$\cos\theta^1_{\rm H}$	$\cos\theta^2_{\rm H}$	Δt
ΔE	1	-0.13	0.06	-0.00	-0.04	-0.16	0.00	0.01
M_{bc}		1	-0.03	0.00	0.08	0.04	0.03	-0.00
$m^1_{\pi^+\pi^-}$			1	-0.02	-0.04	-0.04	0.00	0.00
$m^2_{\pi^+\pi^-}$				1	-0.00	0.03	-0.06	0.01
$\mathcal{F}_{B\bar{B}/q\bar{q}}$					1	0.02	0.02	-0.00
$\cos\theta^1_{\rm H}$						1	-0.03	0.01
$\cos\theta^2_{\rm H}$							1	-0.00
Δt								1

Table C.15: Correlation matrix for charmless $B^0(\bar{B}^0)$ decays (-, SVD2).

0	ΔE	M_{bc}	$m^1_{\pi^+\pi^-}$	$m^2_{\pi^+\pi^-}$	$\mathcal{F}_{B\bar{B}/q\bar{q}}$	$\cos\theta^1_{\rm H}$	$\cos\theta^2_{\rm H}$	Δt
ΔE	1	0.01	0.04	0.05	0.03	-0.04	-0.05	0.01
M_{bc}		1	-0.00	-0.01	0.06	0.03	0.01	-0.00
$m^1_{\pi^+\pi^-}$			1	-0.01	0.00	-0.04	0.00	-0.00
$m^2_{\pi^+\pi^-}$				1	0.01	0.02	-0.04	0.01
$\mathcal{F}_{B\bar{B}/q\bar{q}}$					1	-0.00	-0.01	0.01
$\cos\theta^1_{\rm H}$						1	0.02	0.03
$\cos\theta^2_{\rm H}$							1	0.03
Δt								1

Table C.16: Correlation matrix for charmless $B^0(\bar{B}^0)$ decays (0, SVD2).

	f_+	f_0
rn	0.49 ± 0.01	0.37 ± 0.01

Table C.17: The fractions of the different reconstruction categories used in Eq. (C.23).

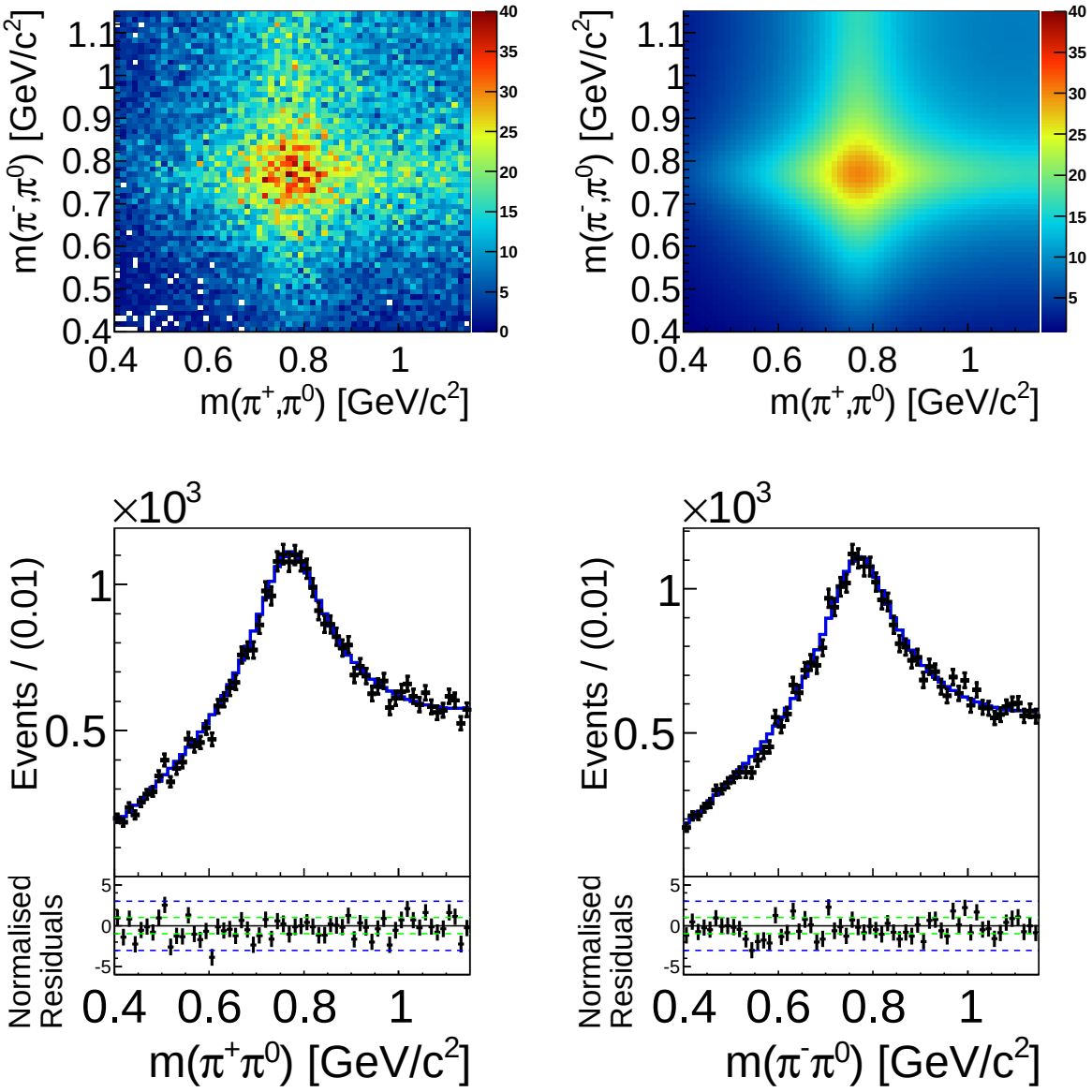

Figure C.28: Full projections onto the dipion masses of $b \to c$ transitions in neutral B decays. The top row shows the 2D projection of the data (left) and the PDF (right) and the bottom row shows projection onto each axis, where the black points show simulated MC events and the solid line shows the fit result. The residuals are given beneath each distribution.

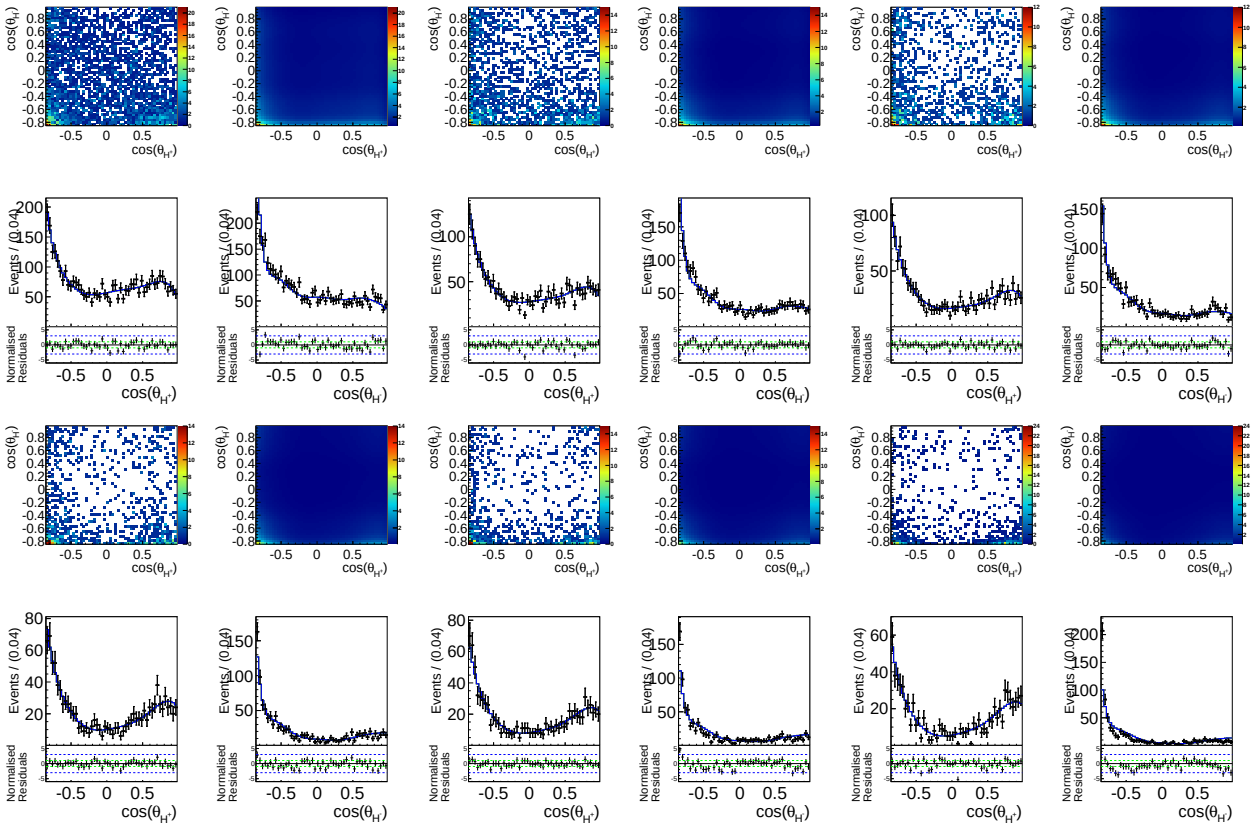

Figure C.29: Fit projections onto $\cos\theta_{\rm H}^{+} - \cos\theta_{\rm H}^{-}$ of $b \to u, d, s$ transitions in neutral B decays (category +) for different slices of ΔE; $[-0.15, -0.1]$, $[-0.1, -0.05]$, $[-0.05, 0]$, $[0, 0.05]$, $[0.05, 0.1]$ and $[0.1, 0.15]$ GeV. The residuals are given beneath each distribution.

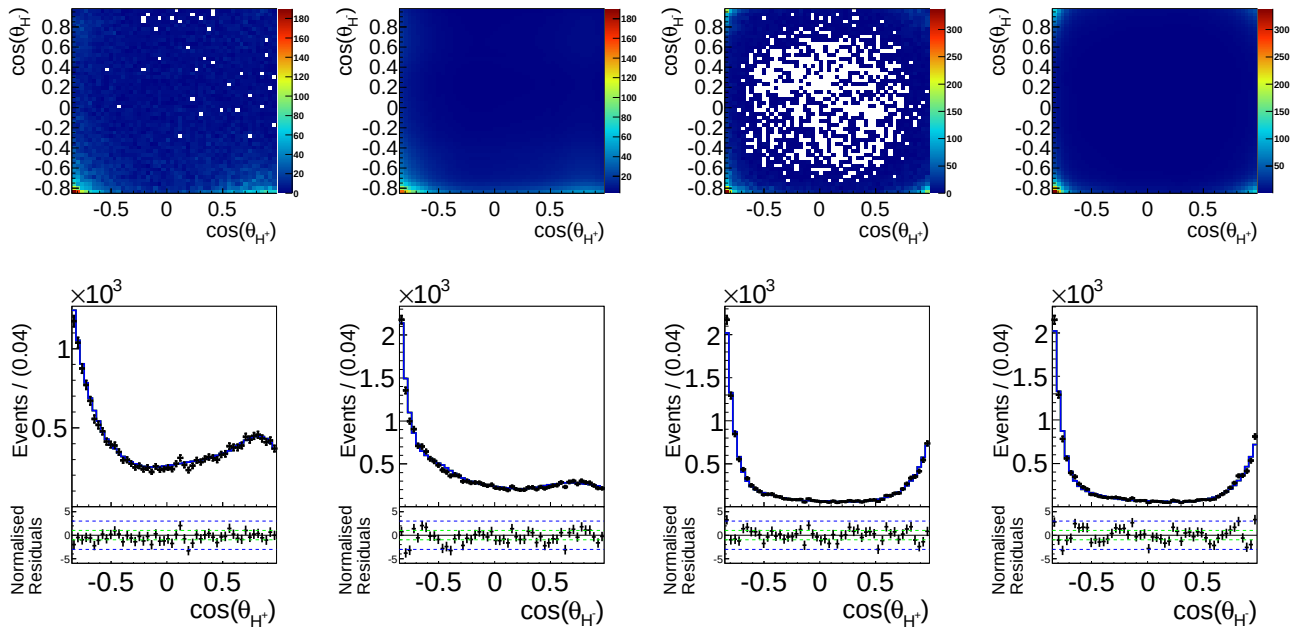

Figure C.30: Fit projections onto $\cos\theta_{\rm H}^{+} - \cos\theta_{\rm H}^{-}$ of $b \to u, d, s$ transitions in neutral B decays for reconstruction categories + (left) and 0. The top row shows the 2D projection of the data (left) and the PDF (right) and the bottom row shows projection onto each axis, where the black points show simulated MC events and the solid line shows the fit result. The residuals are given beneath each distribution.

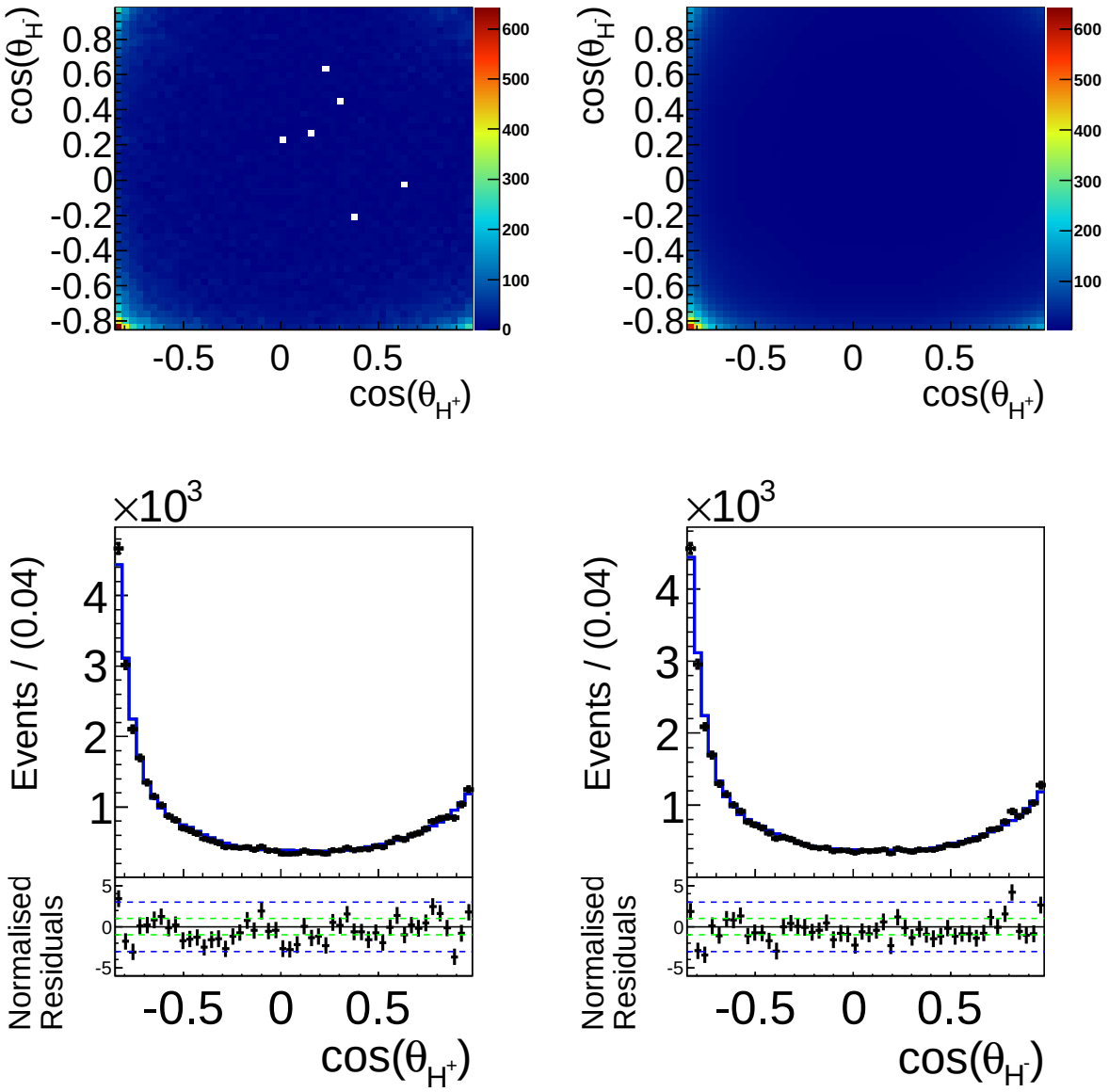

Figure C.31: Full projections onto the helicity angles of $b \to c$ transitions in neutral B decays. The top row shows the 2D projection of the data (left) and the PDF (right) and the bottom row shows projection onto each axis, where the black points show simulated MC events and the solid line shows the fit result. The residuals are given beneath each distribution.

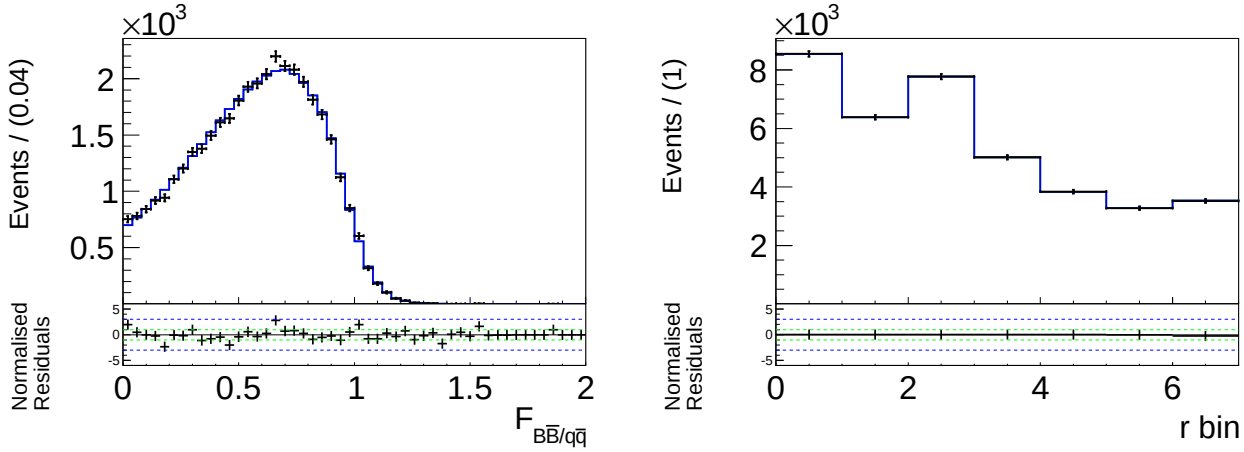

Figure C.32: Full projections onto $\mathcal{F}_{B\bar{B}/q\bar{q}}$ and the r-bin fractions of $b \to u, d, s$ transitions in neutral B decays. The black points show simulated MC events and the solid line shows the fit result. The residuals are given beneath each distribution.

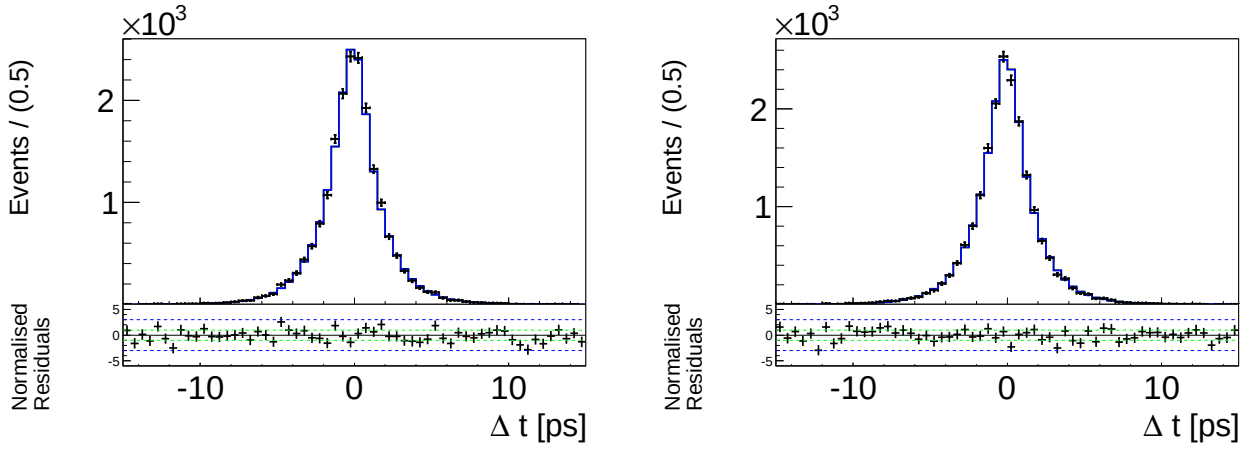

Figure C.33: Full projections onto Δt of $b \to u, d, s$ transitions in neutral B decays for $q = +1$ (left) and $q = -1$. The black points show simulated MC events and the solid line shows the fit result. The residuals are given beneath each distribution.

C.1.4 Charmless $B^{\pm}$ Backgrounds

The subscript rc refers to charged B meson decays into charmless final states. We consider the cases 2c, $\pm$ and 0 separately.
The ΔE distribution for the reconstruction categories $\pm$ of charged B decays into charmless final states is depending on the helicity angles and is given by

$$\mathcal{P}^{\pm}_{\rm rc}(\Delta E|\cos\theta^{+}_{\rm H},\cos\theta^{-}_{\rm H}) \equiv$$
$$c^{\pm}_{1}C_1(\Delta E) + c^{\pm}_{2}(\cos\theta^{+}_{\rm H},\cos\theta^{-}_{\rm H})C_2(\Delta E) + c^{\pm}_{3}(\cos\theta^{+}_{\rm H},\cos\theta^{-}_{\rm H})C_3(\Delta E) \quad , \tag{C.24}$$

where

$$c^{\pm}_{2}(\cos\theta^{+}_{\rm H},\cos\theta^{-}_{\rm H}) = a_0 + a_1(\cos\theta^{\pm}_{\rm H})^2 + a_2(\cos\theta^{\mp}_{\rm H})^4,$$
$$c^{\pm}_{3}(\cos\theta^{+}_{\rm H},\cos\theta^{-}_{\rm H}) = b_0 + b_1(\cos\theta^{\mp}_{\rm H})^2.$$

The remaining two reconstruction categories are described by sum of Chebychev polynomials up to the third order,

$$\mathcal{P}^{2c,0}_{\rm rc}(\Delta E) \equiv \sum_{i=1}^{3} c^{2c,0}_{i} C_i(\Delta E). \tag{C.25}$$

The PDF for $M_{\rm bc}$ takes the from

$$\mathcal{P}^{2c\pm,0}_{\rm rc}(M_{\rm bc}) \equiv Ar(M_{\rm bc}). \tag{C.26}$$

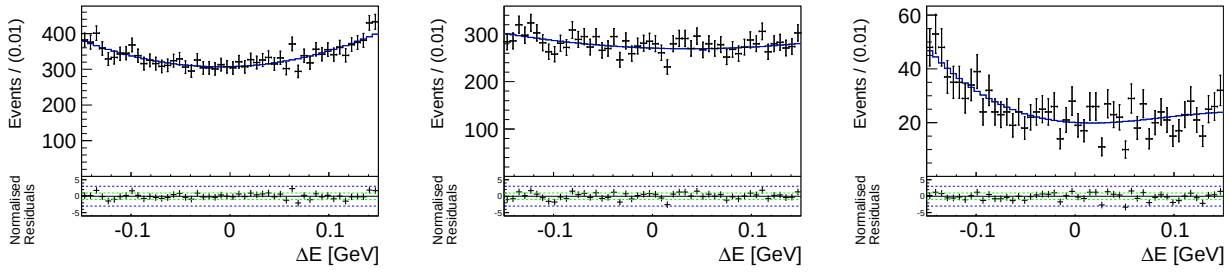

Figure C.34: Fit projections onto ΔE of $b \to u, d, s$ transitions in charged B decays for reconstruction category $+, 0$ and $2c$ (from left to right). The residuals are given beneath each distribution.

The distributions of the invariant dipion masses is described similar to the previous components,

$$\mathcal{P}^{\pm}_{\rm rc}(m_{\pi^{\pm}\pi^0}, m_{\pi^{-}\pi^0}|\cos\theta^{\pm}_{\rm H},\cos\theta^{\mp}_{\rm H}) \equiv$$
$$\big(f_{\rm rc}(\cos\theta^{\pm}_{\rm H},\cos\theta^{\mp}_{\rm H}) \times BW(m_{\pi^{\pm}\pi^0}, m, \Gamma)$$
$$+ (1 - f_{\rm rc}(\cos\theta^{\pm}_{\rm H},\cos\theta^{\mp}_{\rm H})) \times \sum_{i=2}^{3} c^{M,\pm}_{i}(\cos\theta^{\pm}_{\rm H},\cos\theta^{\mp}_{\rm H}) C_i(m_{\pi^{\pm}\pi^0})\big)$$
$$\times \sum_{i=1}^{5} c^{M,\rm mr}_{i}(\cos\theta^{\pm}_{\rm H},\cos\theta^{\mp}_{\rm H}) C_i(m_{\pi^{\mp}\pi^0}), \tag{C.27}$$

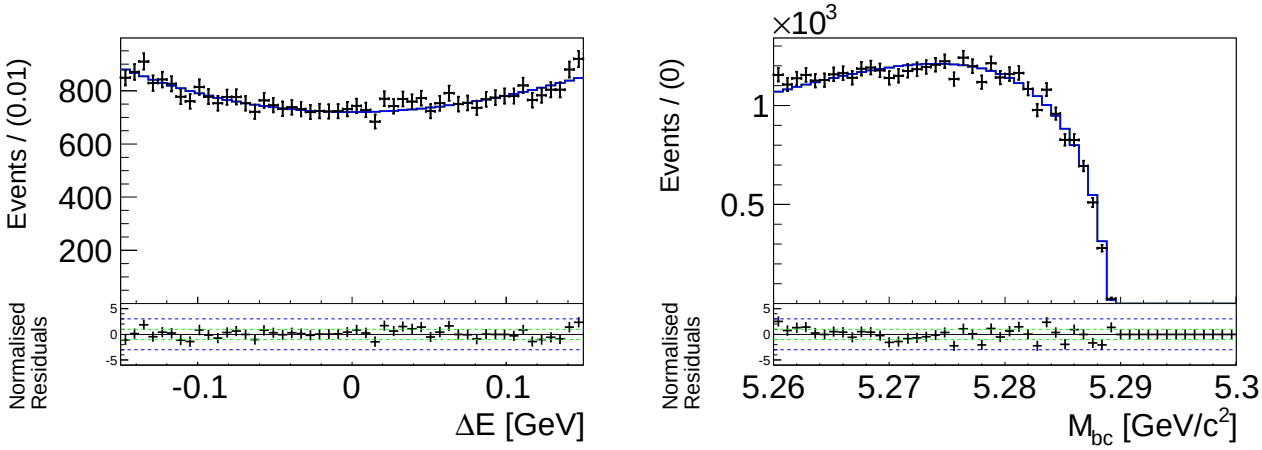

Figure C.35: Full projections onto ΔE and $M_{\rm bc}$ of $b \to u, d, s$ transitions in charged B decays. The black points show simulated MC events and the solid line shows the fit result. The residuals are given beneath each distribution.

where the fraction of the resonance depends on the helicity angles:

$$f_{\rm rc}(\cos\theta_{\rm H}^{\pm}, \cos\theta_{\rm H}^{\mp}) = c_{0,M} + c_{1,M}\cos\theta_{\rm H}^{\pm} + c_{2,M}(\cos\theta_{\rm H}^{\pm})^2 + c_{3,M}\cos\theta_{\rm H}^{\mp} + c_{4,M}\cos\theta_{\rm H}^{\pm}(\cos\theta_{\rm H}^{\mp})^2 + c_{5,M}(\cos\theta_{\rm H}^{\pm})^4 + c_{6,M}(\cos\theta_{\rm H}^{\mp})^4,$$

and in addition also the Chebychev polynomials are correlated with the helicity angles via the following parameters of the polynomial underneath the BreitWigner

$$c_2^{M,\pm} = c_{2,0} + c_{2,1}(\cos\theta_{\rm H}^{\pm})^2, c_3^{M,\pm} = c_{3,0} + c_{3,1}(\cos\theta_{\rm H}^{\pm})^2,$$

and similar for the combinatorial part (mr). The mass PDF for events without a correctly reconstructed $\rho^{\pm}$ also depends on the helicity angles,

$$\mathcal{P}_{\rm rc}^0(m_{\pi^{\pm}\pi^0}, m_{\pi^-\pi^0}|\cos\theta_{\rm H}^{\pm}, \cos\theta_{\rm H}^{\mp}) \equiv \Big(\sum_{i=1}^{4} c_i^{M,0}(\cos\theta_{\rm H}^{+})C_i(m_{\pi^+\pi^0})\Big) \times \Big(\sum_{i=1}^{4} c_i^{M,0}(\cos\theta_{\rm H}^{-})C_i(m_{\pi^-\pi^0})\Big). \quad \text{(C.28)}$$

with

$$c_2^{M,0}(\cos\theta_{\rm H}) = c_{2,0b} + c_{2,1b}(\cos\theta_{\rm H})^2 + c_{2,2b}(\cos\theta_{\rm H})^4.$$

In the case of two correctly reconstructed $\rho^{\pm}$ resonances the PDF for each invariant mass is similar to Eq. (C.12) and the PDF for the helicity angles takes a similar form as those used for charged B decays into charm final states, see Appendix C.1.2.

The results from a fit to the Δt distribution are shown in Fig. C.43 and the obtained effective lifetimes are listed in Table C.18.

lifetime [ps]	τ^{SVD1}	τ^{SVD2}	
$B^0\bar{B}^0$	1.42 ± 0.05	1.50 ± 0.02	

Table C.18: The B^0 lifetimes obtained from a fit to the $B^{\pm}, b \to u, d, s$ MC distributions.

The full PDF for charged B mesons decaying into charmless final states is given by

$$\begin{aligned}
&\mathcal{PDF}_{\mathrm{rc}}(\Delta E, M_{\mathrm{bc}}, m_{\pi^+\pi^0}, m_{\pi^-\pi^0}, \cos\theta_{\mathrm{H}}^+, \cos\theta_{\mathrm{H}}^-, \mathcal{F}_{B\bar{B}/q\bar{q}}, \Delta t, q) \equiv \\
&\Bigg((1-f_0) \times \Bigg((1-f_{2c}) \times \mathcal{PDF}_{\mathrm{rc}}^{\pm}(\Delta E) \times \mathcal{PDF}_{\mathrm{rc}}^{\pm}(M_{\mathrm{bc}}) \\
&\big(f_+ \times \mathcal{PDF}_{\mathrm{rc}}^{+}(m_{\pi^+\pi^0}, m_{\pi^-\pi^0}|\cos\theta_{\mathrm{H}}^+, \cos\theta_{\mathrm{H}}^-) \times \mathcal{PDF}_{\mathrm{rc}}^{+}(\cos\theta_{\mathrm{H}}^+, \cos\theta_{\mathrm{H}}^-) + \\
&(1-f_+) \times \mathcal{PDF}_{\mathrm{rc}}^{-}(m_{\pi^+\pi^0}, m_{\pi^-\pi^0}|\cos\theta_{\mathrm{H}}^+, \cos\theta_{\mathrm{H}}^-) \times \mathcal{PDF}_{\mathrm{rc}}^{-}(\cos\theta_{\mathrm{H}}^+, \cos\theta_{\mathrm{H}}^-)\big) + \\
&f_{2c} \times \mathcal{PDF}_{\mathrm{rc}}^{2c}(\Delta E) \times \mathcal{PDF}_{\mathrm{rc}}^{2c}(M_{\mathrm{bc}}) \times \mathcal{PDF}_{\mathrm{rc}}^{2c}(m_{\pi^+\pi^0}) \times \\
&\mathcal{PDF}_{\mathrm{rc}}^{2c}(m_{\pi^-\pi^0}) \times \mathcal{PDF}_{\mathrm{rc}}^{2c}(\cos\theta_{\mathrm{H}}^+, \cos\theta_{\mathrm{H}}^-)\Bigg) + \\
&f_0 \times \mathcal{PDF}_{\mathrm{rc}}^{0}(\Delta E) \times \mathcal{PDF}_{\mathrm{rc}}^{2c}(M_{\mathrm{bc}}) \times \mathcal{PDF}_{\mathrm{rc}}^{0}(m_{\pi^+\pi^0}, m_{\pi^-\pi^0}) \times \mathcal{PDF}_{\mathrm{rc}}^{0}(\cos\theta_{\mathrm{H}}^+, \cos\theta_{\mathrm{H}}^-)\Bigg) \\
&\times \mathcal{PDF}_{\mathrm{rc}}(\mathcal{F}_{B\bar{B}/q\bar{q}}) \times \mathcal{PDF}_{\mathrm{rc}}(\Delta t, q),
\end{aligned} \tag{C.29}$$

and the fractions f_i are given in Table C.19.

	f_+	f_0	f_{2c}
rc	0.49 ± 0.01	0.40 ± 0.01	0.05 ± 0.01

Table C.19: The fractions of the different reconstruction categories used in Eq. (C.29).

0	ΔE	M_{bc}	$m^1_{\pi^+\pi^-}$	$m^2_{\pi^+\pi^-}$	$\mathcal{F}_{B\bar{B}/q\bar{q}}$	$\cos\theta^1_{\mathrm{H}}$	$\cos\theta^2_{\mathrm{H}}$	Δt
ΔE	1	0.05	0.01	0.07	0.06	0.00	0.06	-0.00
M_{bc}		1	-0.00	-0.00	0.06	0.00	0.05	-0.00
$m^1_{\pi^+\pi^-}$			1	-0.01	-0.06	0.03	-0.05	-0.01
$m^2_{\pi^+\pi^-}$				1	0.03	-0.01	0.08	-0.01
$\mathcal{F}_{B\bar{B}/q\bar{q}}$					1	0.04	0.06	0.01
$\cos\theta^1_{\mathrm{H}}$						1	-0.09	0.02
$\cos\theta^2_{\mathrm{H}}$							1	-0.01
Δt								1

Table C.20: Correlation matrix for charmless $B^{\pm}$ decays (+, SVD2).

0	ΔE	M_{bc}	$m^1_{\pi^+\pi^-}$	$m^2_{\pi^+\pi^-}$	$\mathcal{F}_{B\bar{B}/q\bar{q}}$	$\cos\theta^1_{\rm H}$	$\cos\theta^2_{\rm H}$	Δt
ΔE	1	0.06	0.07	-0.02	0.06	0.08	0.01	-0.01
M_{bc}		1	-0.02	-0.04	0.05	0.06	0.01	0.00
$m^1_{\pi^+\pi^-}$			1	-0.01	0.02	0.07	-0.00	-0.01
$m^2_{\pi^+\pi^-}$				1	-0.06	-0.07	0.02	0.01
$\mathcal{F}_{B\bar{B}/q\bar{q}}$					1	0.07	0.05	0.01
$\cos\theta^1_{\rm H}$						1	-0.09	-0.01
$\cos\theta^2_{\rm H}$							1	0.02
Δt								1

Table C.21: Correlation matrix for charmless $B^\pm$ decays (-, SVD2).

0	ΔE	M_{bc}	$m^1_{\pi^+\pi^-}$	$m^2_{\pi^+\pi^-}$	$\mathcal{F}_{B\bar{B}/q\bar{q}}$	$\cos\theta^1_{\rm H}$	$\cos\theta^2_{\rm H}$	Δt
ΔE	1	0.04	-0.01	0.01	0.06	0.00	-0.01	-0.00
M_{bc}		1	0.00	0.02	0.03	0.04	0.05	-0.01
$m^1_{\pi^+\pi^-}$			1	-0.03	-0.00	-0.00	0.00	-0.00
$m^2_{\pi^+\pi^-}$				1	-0.00	-0.00	-0.01	-0.01
$\mathcal{F}_{B\bar{B}/q\bar{q}}$					1	0.00	0.01	-0.00
$\cos\theta^1_{\rm H}$						1	-0.05	0.02
$\cos\theta^2_{\rm H}$							1	0.01
Δt								1

Table C.22: Correlation matrix for charmless $B^\pm$ decays (0, SVD2).

0	ΔE	M_{bc}	$m^1_{\pi^+\pi^-}$	$m^2_{\pi^+\pi^-}$	$\mathcal{F}_{B\bar{B}/q\bar{q}}$	$\cos\theta^1_{\rm H}$	$\cos\theta^2_{\rm H}$	Δt
ΔE	1	-0.06	0.06	-0.00	0.05	0.13	0.14	-0.01
M_{bc}		1	-0.03	0.02	0.09	0.02	0.03	0.00
$m^1_{\pi^+\pi^-}$			1	-0.08	0.04	0.09	-0.09	0.04
$m^2_{\pi^+\pi^-}$				1	-0.03	-0.08	0.11	-0.04
$\mathcal{F}_{B\bar{B}/q\bar{q}}$					1	0.05	0.01	-0.01
$\cos\theta^1_{\rm H}$						1	-0.21	-0.02
$\cos\theta^2_{\rm H}$							1	0.02
Δt								1

Table C.23: Correlation matrix for charmless $B^\pm$ decays (2c, SVD2).

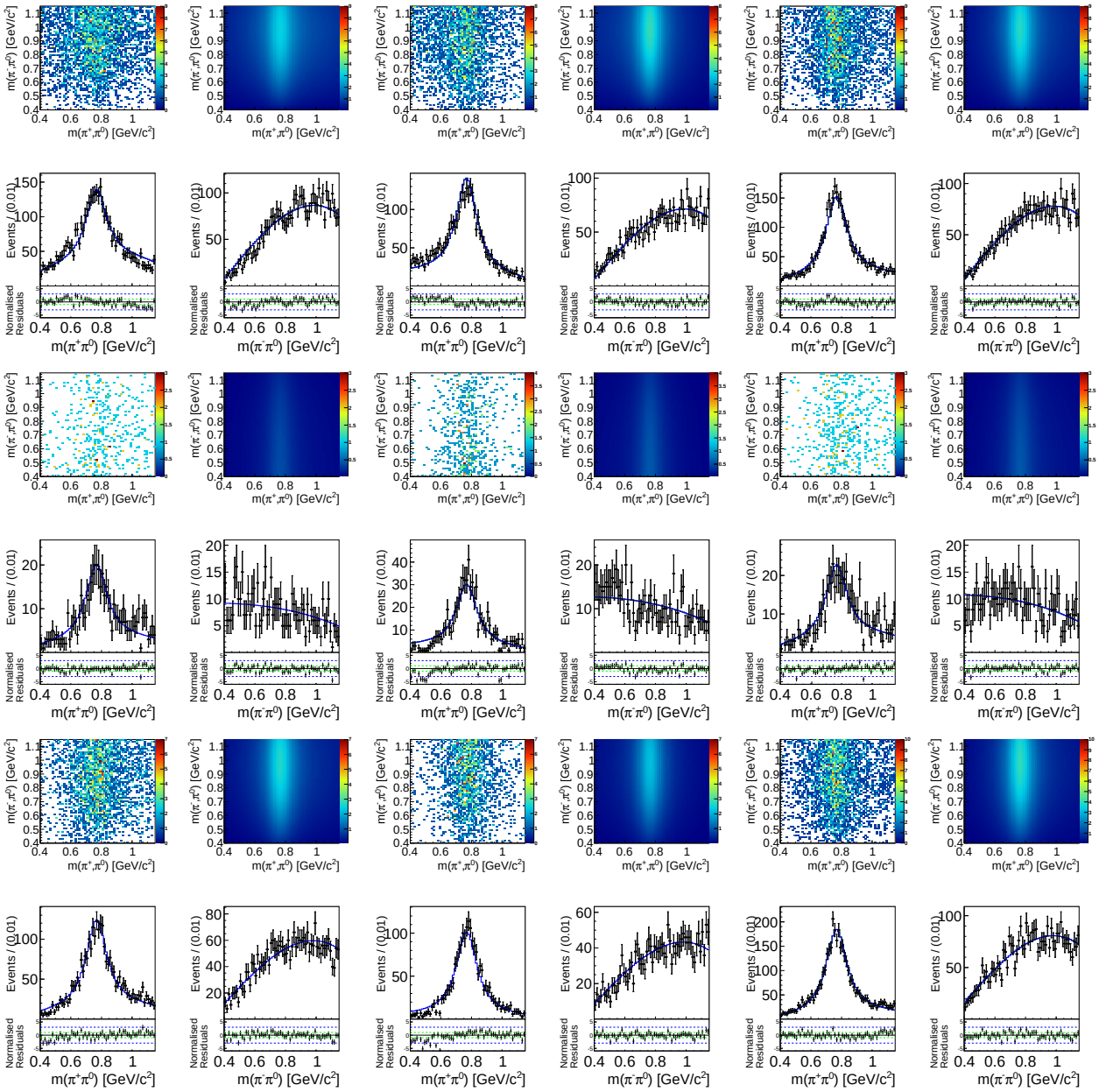

Figure C.36: Fit projections onto the dipion masses of the "+" component of $b \to u, d, s$ transitions in charged B decays in different bins of $\cos\theta_{\rm H}^{+}$-$\cos\theta_{\rm H}^{-}$ (lower and upper limits $\in \{-0.85, -0.6, 0.6, 0.98\}$). The top row shows the 2D projection of the data (left) and the PDF (right) and the bottom row shows projection onto each axis, where the black points show simulated MC events and the solid line shows the fit result. The residuals are given beneath each distribution.

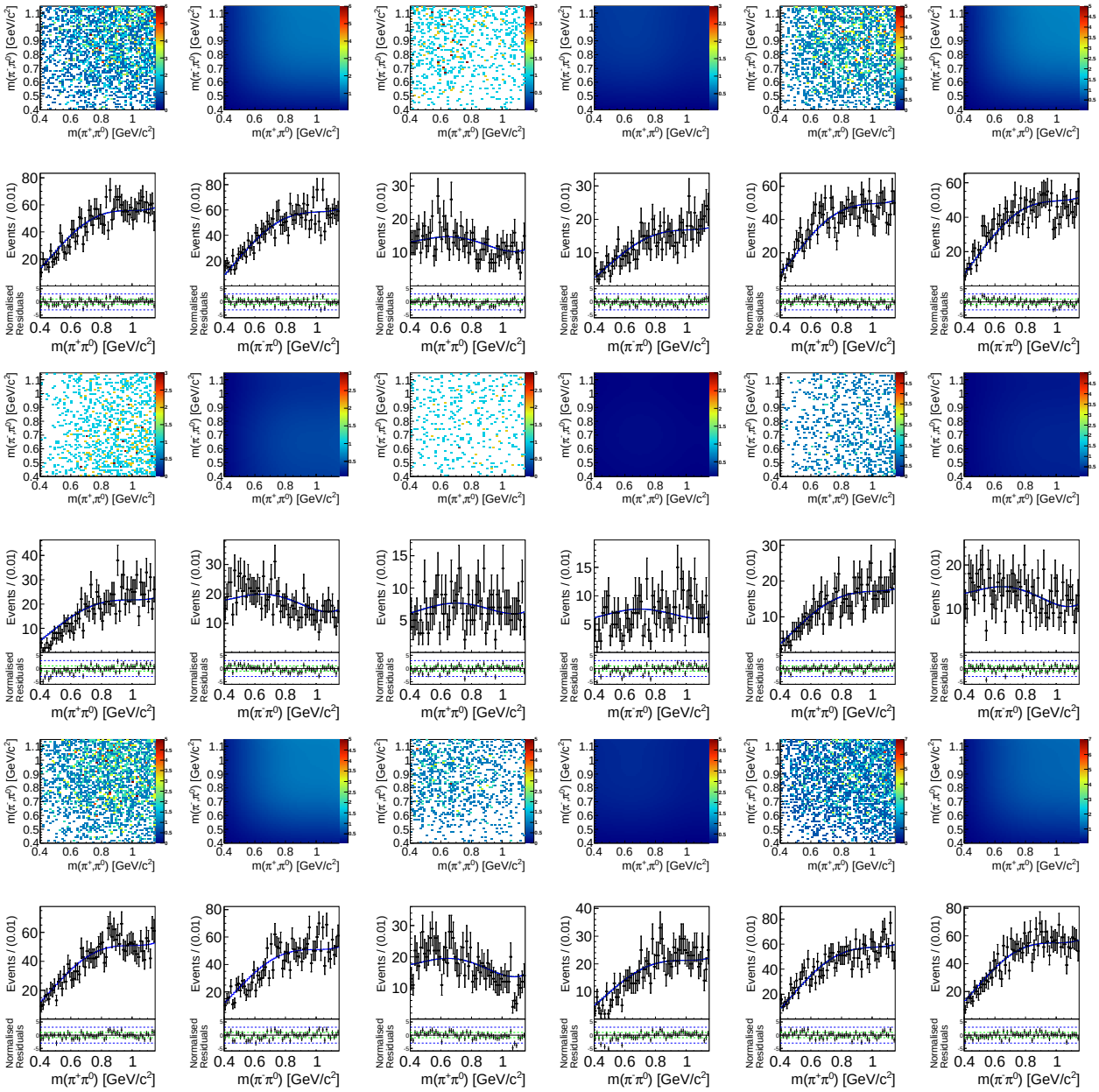

Figure C.37: Fit projections onto the dipion masses of the "0" component of $b \to u, d, s$ transitions in charged B decays in different bins of $\cos\theta_{\rm H}^{+}$-$\cos\theta_{\rm H}^{-}$ (lower and upper limits $\in \{-0.85, -0.6, 0.6, 0.98\}$). The top row shows the 2D projection of the data (left) and the PDF (right) and the bottom row shows projection onto each axis, where the black points show simulated MC events and the solid line shows the fit result. The residuals are given beneath each distribution.

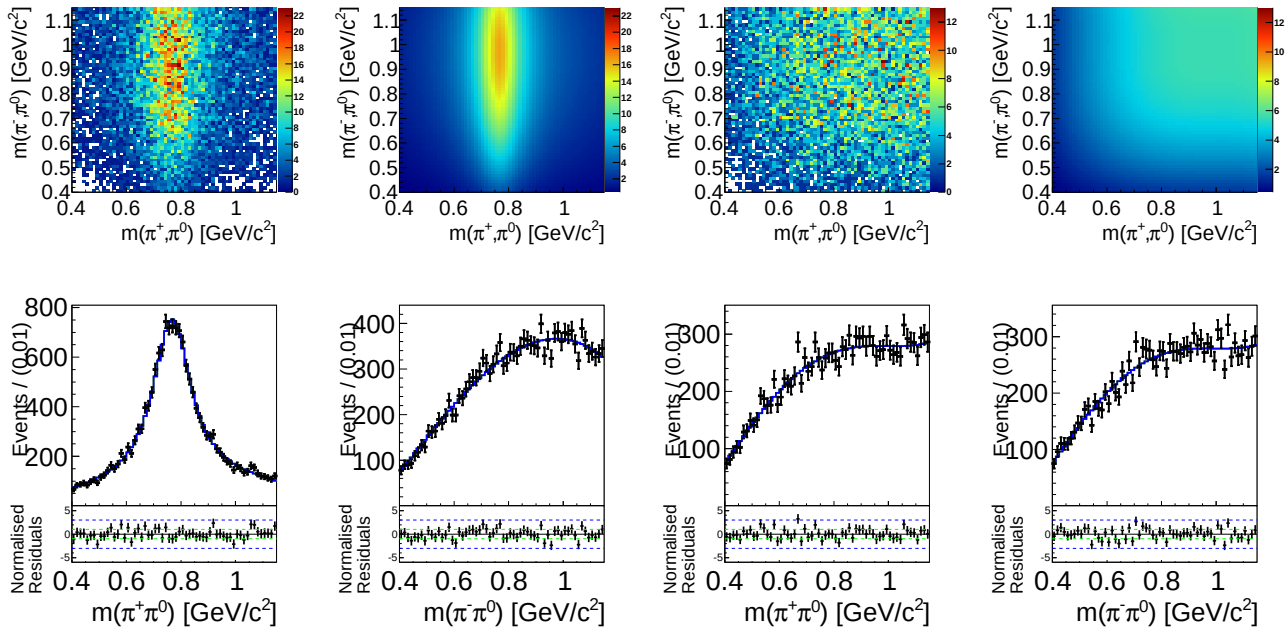

Figure C.38: Fit projections onto the dipion masses of $b \to u, d, s$ transitions in charged B decays for reconstruction category + (left) and 0. The top row shows the 2D projection of the data (left) and the PDF (right) and the bottom row shows projection onto each axis, where the black points show simulated MC events and the solid line shows the fit result. The residuals are given beneath each distribution.

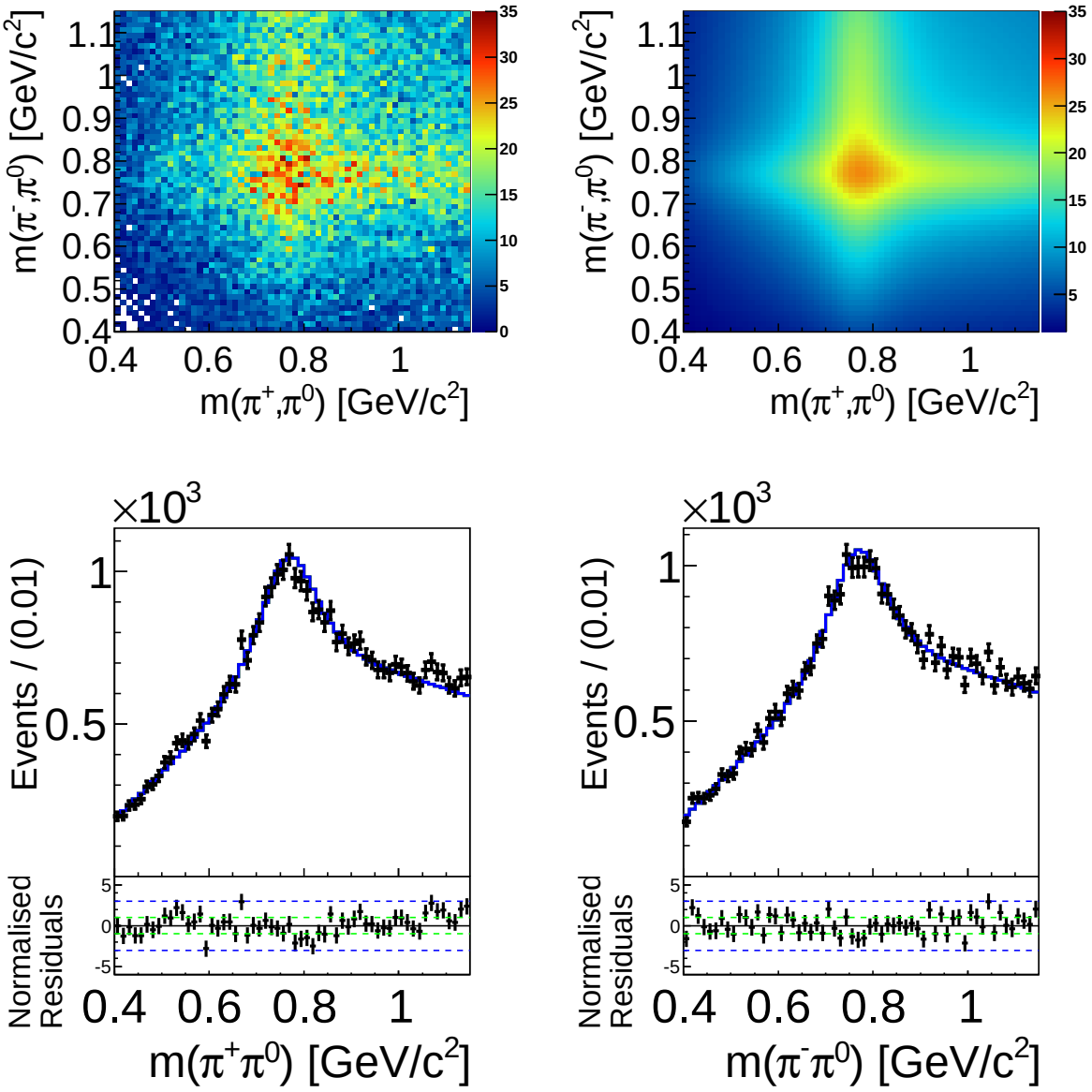

Figure C.39: Full projections onto the dipion masses of $b \to u, d, s$ transitions in charged B decays. The top row shows the 2D projection of the data (left) and the PDF (right) and the bottom row shows projection onto each axis, where the black points show simulated MC events and the solid line shows the fit result. The residuals are given beneath each distribution.

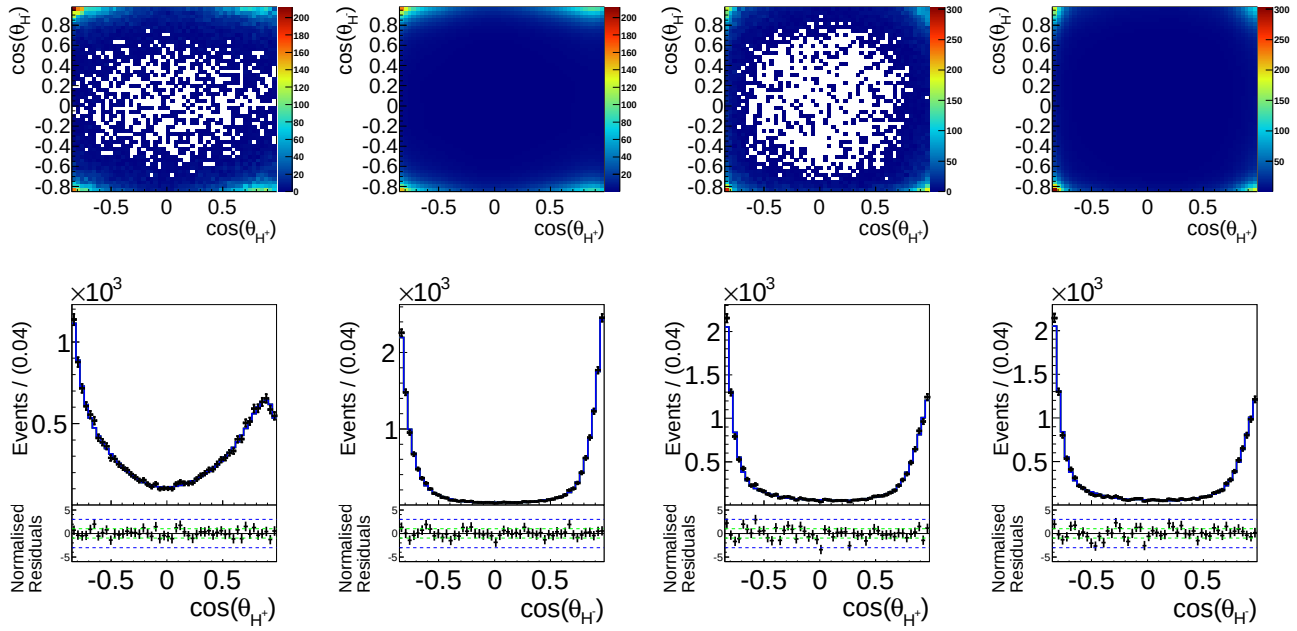

Figure C.40: Fit projections onto $\cos\theta_{\rm H}^{\pm}$ of $b \to u, d, s$ transitions in charged B decays for reconstruction category + (left) and 0. The top row shows the 2D projection of the data (left) and the PDF (right) and the bottom row shows projection onto each axis, where the black points show simulated MC events and the solid line shows the fit result. The residuals are given beneath each distribution.

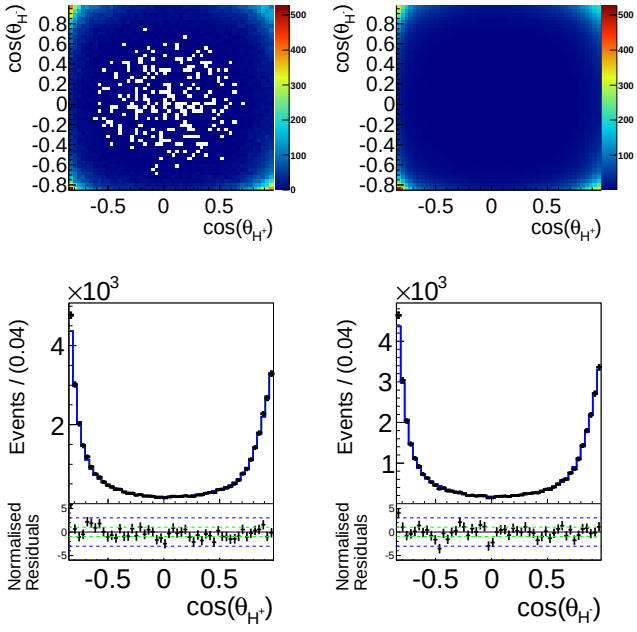

Figure C.41: Full projections onto $\cos\theta_{\rm H}^{\pm}$ of $b \to u, d, s$ transitions in charged B decays. The top row shows the 2D projection of the data (left) and the PDF (right) and the bottom row shows projection onto each axis, where the black points show simulated MC events and the solid line shows the fit result. The residuals are given beneath each distribution.

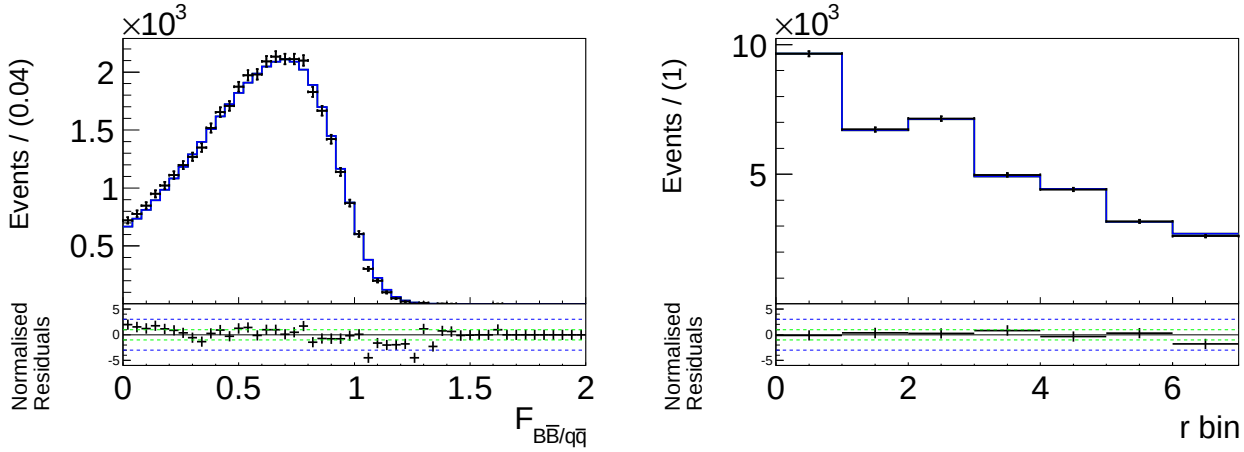

Figure C.42: Full projections onto $\mathcal{F}_{B\bar{B}/q\bar{q}}$ and the r-bin fractions of $b \to u, d, s$ transitions in charged B decays. The black points show simulated MC events and the solid line shows the fit result. The residuals are given beneath each distribution.

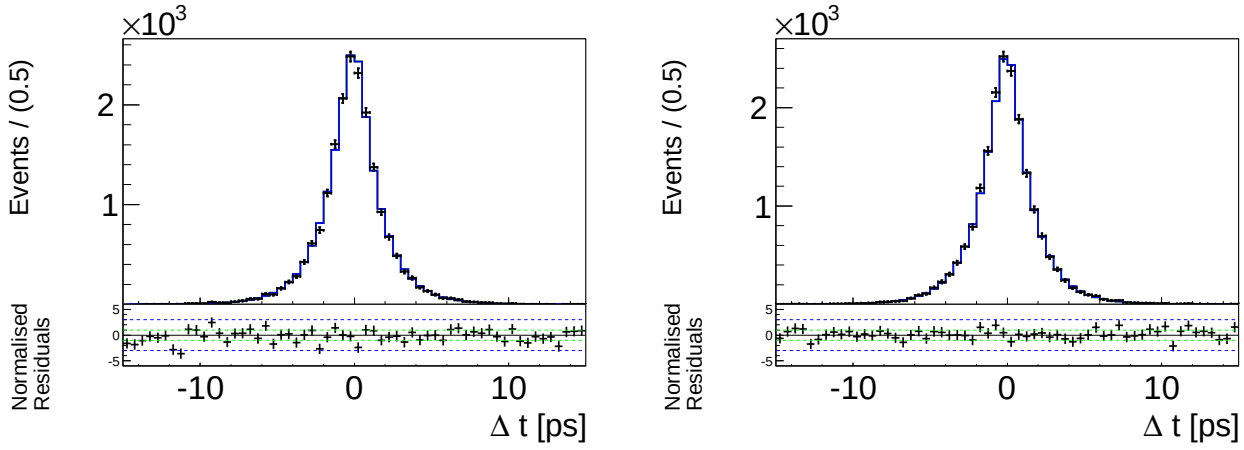

Figure C.43: Full projections onto Δt of $b \to u, d, s$ transitions in charged B decays for $q = +1$ (left) and $q = -1$. The black points show simulated MC events and the solid line shows the fit result. The residuals are given beneath each distribution.

C.2 Model For Other Four-Pion Final States

We have to consider a variety of decays with the same final state (peaking background) as $B^0 \to \rho^+\rho^-$, some of them are poorly known. Interference of the four-pion final states has to be considered (see Appendix B.1). Because of the same final state, the B meson can be correctly reconstructed from four pions and the ΔE and $M_{\rm bc}$ distributions show similar peaks as for $B^0 \to \rho^+\rho^-$ decays. If no other description is explicitly mentioned, we use a double-bifurcated Gaussian (*dbG*, Eq. (E.7)) to model the ΔE distributions of all peaking backgrounds. The tail Gaussian is obtained from correctly reconstructed Brprm MC events (truth, see Section 4.3.1) and is made common among all four-pion final states. The sum of Chebychev polynomials up to the third order is added in order to describe underlying combinatorial background from wrongly assigned tracks, where usually a first order one is sufficient.

$$\mathcal{P}_{B\to 4\pi}(\Delta E) \equiv (1-f_{\rm G})dbG(\Delta E, \mu_1, \sigma_{1l}, \sigma_{1r}, \mu_2^{\rm truth,LP}, \sigma_{2l}^{\rm truth,LP}, \sigma_{2r}^{\rm truth,LP}, \mu_{\rm CF}, \sigma_{l,\rm CF}, \sigma_{r,\rm CF}, f^{\rm truth,LP}) + f_{\rm G}\sum_{i=1}^{3} c_i C_i(\Delta E). \tag{C.30}$$

The $M_{\rm bc}$ distributions of the four-pion final states are described by a double bifurcated Gaussian for correctly reconstructed tracks plus an Argus function for the combinatorial background.

$$\mathcal{P}_{B\to 4\pi}(M_{\rm bc}) \equiv (1-f_{\rm A})dbG(M_{\rm bc}, \mu_1, \sigma_{1l}, \sigma_{1r}, \mu_2^{\rm truthLP}, \sigma_{2l}^{\rm truthLP}, \sigma_{2r}^{\rm truthLP}, \mu_{\rm CF}, \sigma_{l,\rm CF}, \sigma_{r,\rm CF}, f^{\rm truthLP}) + f_{\rm A}Ar(M_{\rm bc}). \tag{C.31}$$

The $\mathcal{F}_{B\bar{B}/q\bar{q}}$ distribution of all four-pion states is described by a triple bifurcated Gaussian in each r-bin,

$$\mathcal{P}_k^{\rm four\pi f.s.}(\mathcal{F}_{B\bar{B}/q\bar{q}}) \equiv tbG_k^{\rm sig}(\mathcal{F}_{B\bar{B}/q\bar{q}}). \tag{C.32}$$

where analogously to ΔE,$M_{\rm bc}$ the two tail Gaussians in each r-bin are obtained from correctly reconstructed signal MC events and are made common among all four-pion final states, see Eq. (4.15).

C.2.1 Model For $B^0 \to \pi^+\pi^0\pi^-\pi^0$ Decays

The ΔE, $M_{\rm bc}$ and $\mathcal{F}_{B\bar{B}/q\bar{q}}$ distributions for B^0 mesons decaying into non-resonant $\pi^+\pi^0\pi^-\pi^0$ are described as mentioned above, the projections onto the distributions are shown in Figs. C.44 and C.45. The projections onto the remaining distributions are shown in Figs. C.46 to C.48.

The distribution of each mass is modeled by the sum of a second and a third order Chebychev polynomial

$$\mathcal{P}_{B\to 4\pi}(m_{\pi^\pm\pi^0}) \equiv \sum_{i=2}^{3} c_i C_i(m_{\pi^\pm\pi^0}), \tag{C.33}$$

and the distribution of each helicity angle is described by the sum of Chebychev polynomials up to the eighth order

$$\mathcal{P}_{B\to 4\pi}(\cos\theta_{\rm H}^\pm) \equiv \sum_{i=1}^{8} c_i^{\cos\theta_{\rm H}} C_i(\cos\theta_{\rm H}^\pm). \tag{C.34}$$

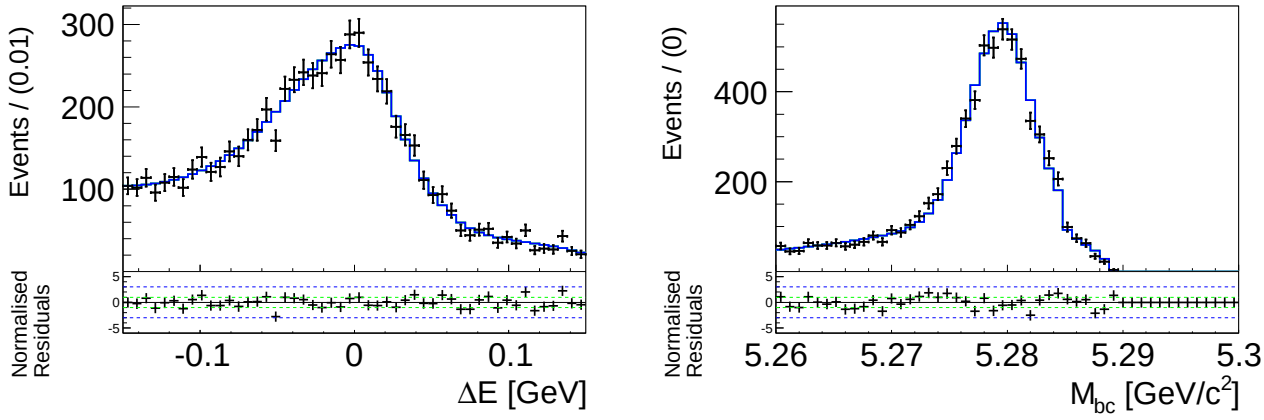

Figure C.44: Full projections onto ΔE and $M_{\rm bc}$ of $B^0 \to \pi^+\pi^0\pi^-\pi^0$ decays. The black points show simulated MC events and the solid line shows the fit result. The residuals are given beneath each distribution.

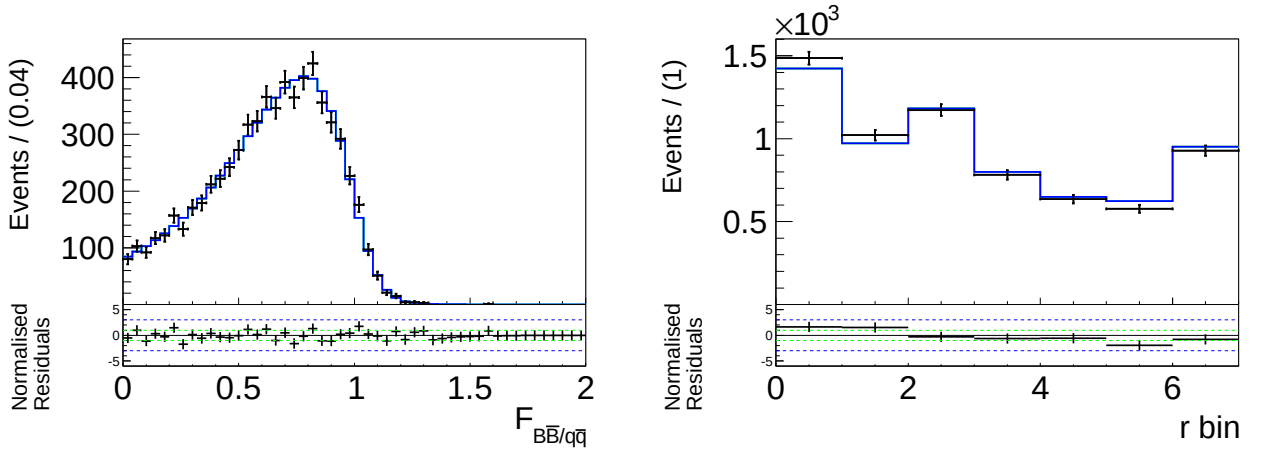

Figure C.45: Full projections onto $\mathcal{F}_{B\bar{B}/q\bar{q}}$ and the r-bin fractions of $B^0 \to \pi^+\pi^0\pi^-\pi^0$ decays. The black points show simulated MC events and the solid line shows the fit result. The residuals are given beneath each distribution.

The Δt distribution is modeled by Eq. (4.19) with an effective lifetime due to contamination of tracks from the accompanied $B_{\rm tag}$, $\tau^{\rm eff}_{B\to 4\pi} = (1.46 \pm 0.02)$ ps as determined from fully simulated MC events.
Correlations between the fit variables are shown in Table C.24, the full PDF for $B \to \pi^+\pi^0\pi^-\pi^0$ decays is given by the product of the individual PDFs for each variable,

$$\begin{aligned}\mathcal{P}_{B\to 4\pi}(\Delta E, M_{\rm bc}, m_{\pi^+\pi^0}, m_{\pi^-\pi^0}, \cos\theta^+_{\rm H}, \cos\theta^-_{\rm H}, \mathcal{F}_{B\bar{B}/q\bar{q}}, \Delta t, q) = \\ \mathcal{P}_{B\to 4\pi}(\Delta E) \times \mathcal{P}_{B\to 4\pi}(M_{\rm bc}) \times \mathcal{P}_{B\to 4\pi}(m_{\pi^+\pi^0}) \times \mathcal{P}_{B\to 4\pi}(m_{\pi^-\pi^0}) \times \\ \mathcal{P}_{B\to 4\pi}(\cos\theta^+_{\rm H}) \times \mathcal{P}_{B\to 4\pi}(\cos\theta^-_{\rm H}) \times \mathcal{P}^k_{B\to 4\pi}(\mathcal{F}_{B\bar{B}/q\bar{q}}) \times \mathcal{P}_{B\to 4\pi}(\Delta t, q). \end{aligned} \quad \text{(C.35)}$$

0	ΔE	M_{bc}	$m^1_{\pi^+\pi^-}$	$m^2_{\pi^+\pi^-}$	$\mathcal{F}_{B\bar{B}/q\bar{q}}$	$\cos\theta^1_{\rm H}$	$\cos\theta^2_{\rm H}$	Δt
ΔE	1	0.00	0.00	0.00	0.02	-0.06	-0.07	0.01
M_{bc}		1	0.01	0.00	0.03	0.01	0.02	0.01
$m^1_{\pi^+\pi^-}$			1	0.01	-0.01	-0.02	0.00	-0.01
$m^2_{\pi^+\pi^-}$				1	-0.01	0.03	-0.02	0.01
$\mathcal{F}_{B\bar{B}/q\bar{q}}$					1	0.02	0.00	0.02
$\cos\theta^1_{\rm H}$						1	-0.03	0.01
$\cos\theta^2_{\rm H}$							1	0.02
Δt								1

Table C.24: Correlation matrix of the fit variables of $B^0 \to \pi^+\pi^0\pi^-\pi^0$ decays.

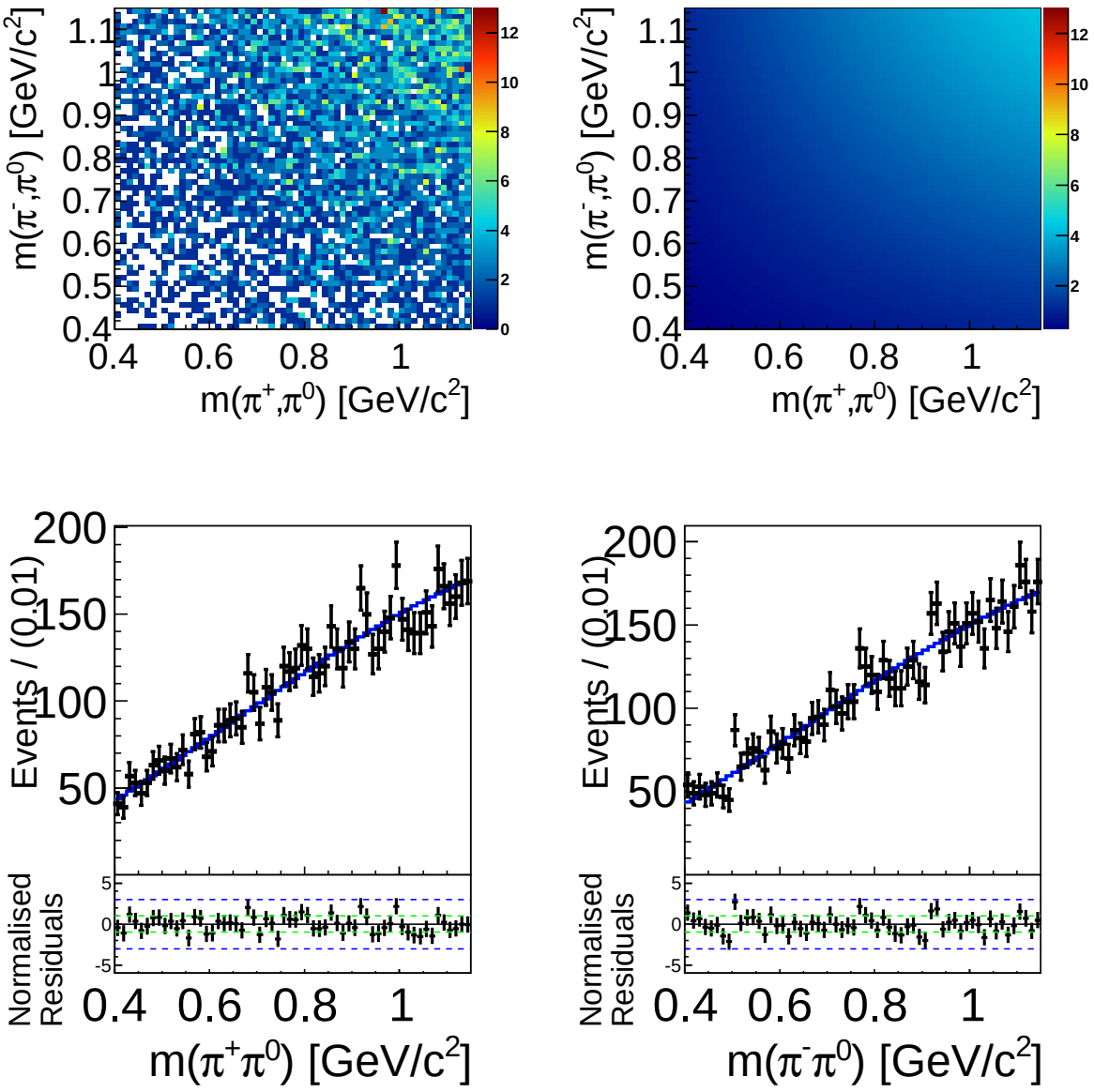

Figure C.46: Full projections onto $m_{\pi^+\pi^0} - m_{\pi^-\pi^0}$ of $B^0 \to \pi^+\pi^0\pi^-\pi^0$ decays. The black points show simulated MC events and the solid line shows the fit result. The residuals are given beneath each distribution.

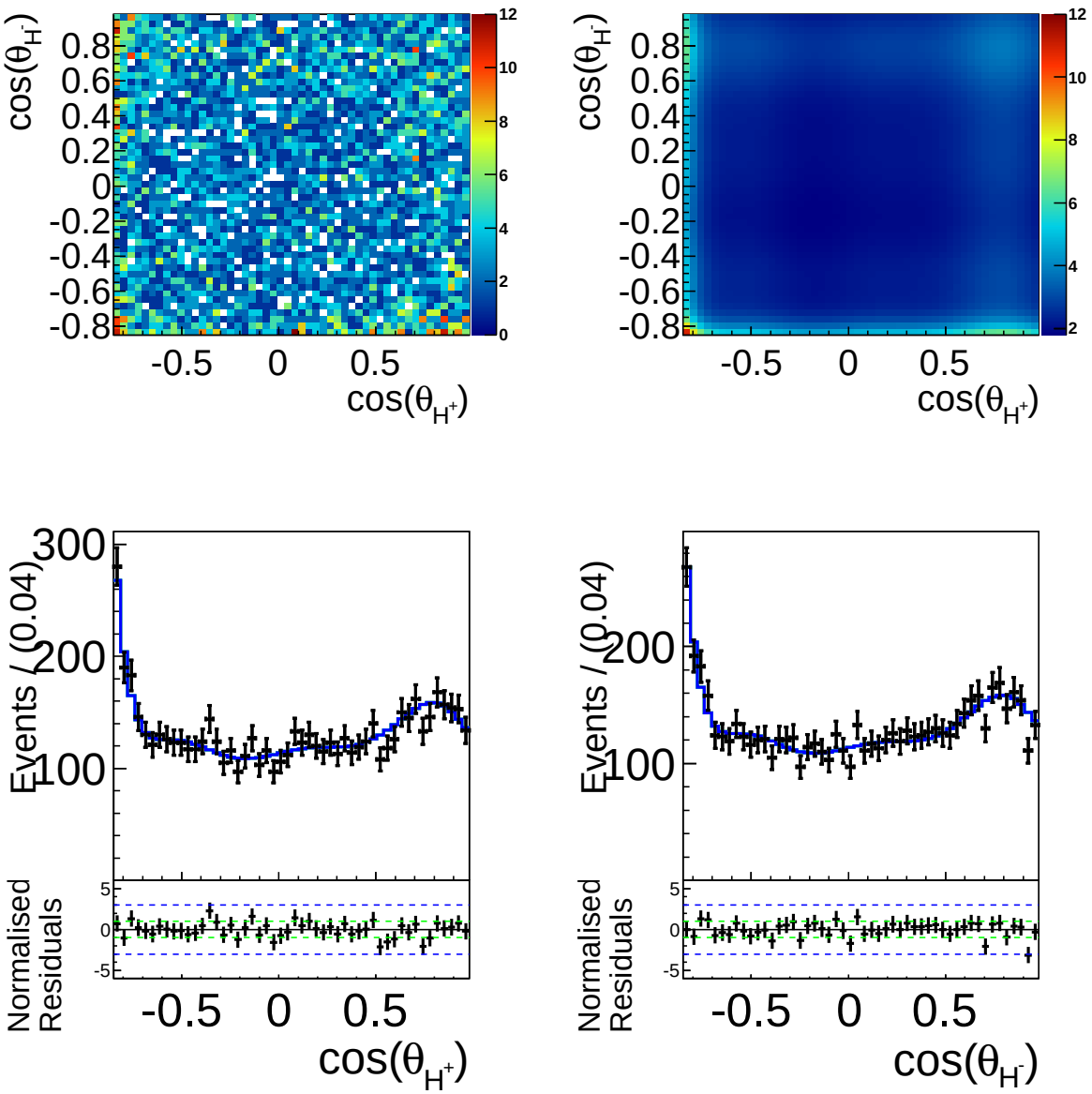

Figure C.47: Full projections onto $\cos\theta_{\rm H}^{+} - \cos\theta_{\rm H}^{-}$ of $B^0 \to \pi^+\pi^0\pi^-\pi^0$ decays. The black points show simulated MC events and the solid line shows the fit result. The residuals are given beneath each distribution.

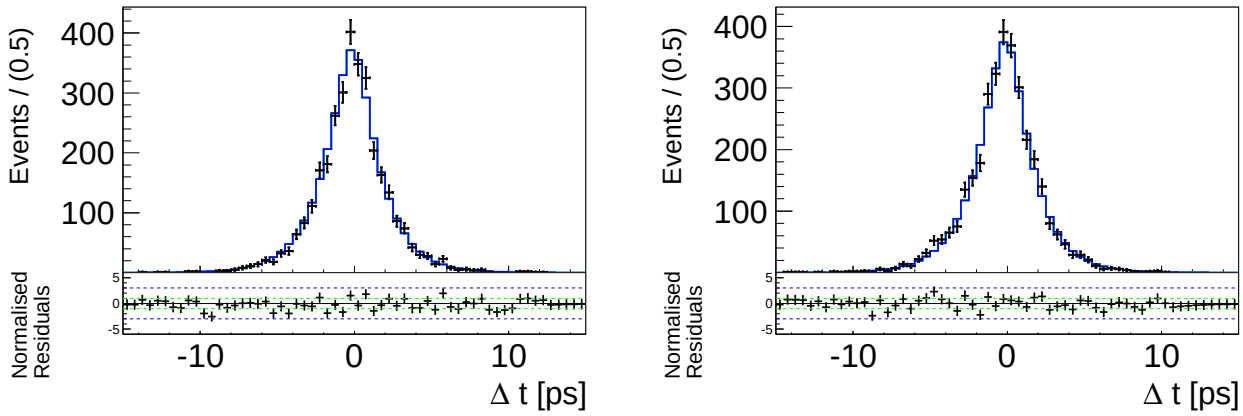

Figure C.48: Full projections onto Δt of $B^0 \to \pi^+\pi^0\pi^-\pi^0$ decays for $q = +1$ (left) and $q = -1$. The black points show simulated MC events and the solid line shows the fit result. The residuals are given beneath each distribution.

C.2.2 Model For $B^0 \to a_1\pi$ Decays

A dominant decay of the a_1 meson is $a_1 \to \rho\pi$, and therefore $B^0 \to a_1\pi$ decays can yield in the same final state as our signal. We consider both decays $B^0 \to a_1^\pm\pi^\mp$ and $B^0 \to a_1^0\pi^0$ individually, where the latter decay is further separated into two different possible decays of the a_1^0: $a_1^0 \to \rho^\pm\pi^\mp$ and $a_1^0 \to \rho^0\pi^0$. Each components $\Delta E, M_{\rm bc}$ and $\mathcal{F}_{B\bar{B}/q\bar{q}}$ distribution is described by Eqs. (C.30) to (C.32), respectively, if not mentioned otherwise.

Model for $B^0 \to a_1^\pm\pi^\mp$ Decays

Here, we consider only the subsequent decay $a_1^\pm \to \rho^\pm\pi^0$ as the decay $B^0 \to a_1^\pm[\rho^0\pi^\pm]\pi^\mp$ yields in a different final state and is included in the non-peaking B^0 decays into charmless final states. We assume isospin symmetry and set the fraction of $a_1^\pm$ decaying to $\rho^\pm\pi^0$ to be 50%. Again, we treat the reconstruction categories "+, -" and " 0" separately in the description of the mass and helicity distributions, projections onto the different categories are shown in Figs. C.49 and C.50. The $\rho^\pm$ contribution is visible in the mass distributions of the $\pm$ components and the helicity angle associated with a $\pi^\pm\pi^0$ pair reconstructed with the $\pi^\mp$ from the B decay peaks sharply at $\cos\theta_{\rm H} = -1$, because of the high momentum of the $\pi^\mp$. Therefore, the helicity angles are especially usefull in sparating this component from others.
The mass PDF for the part containing a correctly reconstructed $\rho^\pm$ meson depend on its charge and takes the form

$$\mathcal{P}^\pm_{a_1^\pm\pi^\mp}(m_{\pi^\pm\pi^0}, m_{\pi^\mp\pi^0}) \equiv \big((1-f_{m_{\pi^\pm\pi^0}})BW(m_{\pi^\pm\pi^0}, m_0, \Gamma_0) + f_{m_{\pi^\pm\pi^0}} c_{m_{\pi^\pm\pi^0},2} C_2(m_{\pi^\pm\pi^0})\big) \times \big(\sum_{i=1}^{5} c_i C_i(m_{\pi^\mp\pi^0})\big). \tag{C.36}$$

while the mass distribution without a correctly reconstructed ρ resonance is described by the sum of Chebychev polynomials up to the fifth order

$$\mathcal{P}^0_{a_1^\pm\pi^\mp}(m_{\pi^\pm\pi^0}, m_{\pi^\mp\pi^0}) \equiv \sum_{i=1}^{5} c_i C_i(m_{\pi^\pm\pi^0}) \times \sum_{i=1}^{5} c_i C_i(m_{\pi^\mp\pi^0}). \tag{C.37}$$

The helicity PDFs for all three cases of reconstruction are histograms from fully simulated MC events,

$$\mathcal{P}^{+,-,0}_{a_1^\pm\pi^\mp}(\cos\theta^+_{\rm H}, \cos\theta^-_{\rm H}) \equiv H^{+,-,0}(\cos\theta^+_{\rm H}, \cos\theta^-_{\rm H}). \tag{C.38}$$

The Δt distribution is modeled by Eq. (4.19) with an effective lifetime due to contamination of tracks from the accompanied $B_{\rm tag}$, $\tau^{\rm eff}_{B\to a_1^\pm\pi^\mp} = (1.51 \pm 0.02)$ ps as determined from fully simulated MC events.
Full projections onto the individual fit variables are shown in Figs. C.51 to C.55 and correlations between the fit variables are shown in Tables C.25 to C.27. The full PDF for

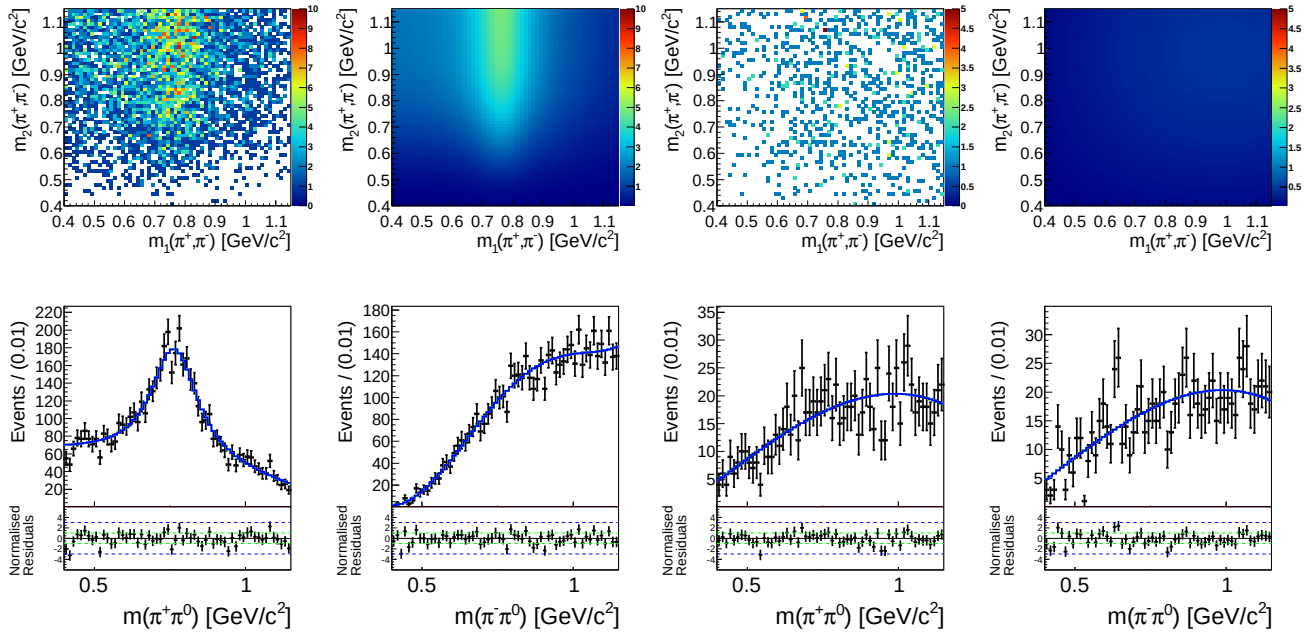

Figure C.49: Fit projections onto $m_{\pi^+\pi^0} - m_{\pi^-\pi^0}$ of $B \to a_1^{\pm}\pi^{\mp}$ decays for the components + (left) and 0. The black points show simulated MC events and the solid line shows the fit result. The residuals are given beneath each distribution.

$B^0 \to a_1^{\pm}\pi^{\mp}$ decays is given by,

$$\mathcal{P}^{\mathrm{LP(TP)}}_{B\to a_1^{\pm}\pi^{\mp}}(\Delta E, M_{\mathrm{bc}}, m_{\pi^+\pi^0}, m_{\pi^-\pi^0}, \cos\theta_{\mathrm{H}}^{+}, \cos\theta_{\mathrm{H}}^{-}, \mathcal{F}_{B\bar{B}/q\bar{q}}, \Delta t, q) =$$
$$\left(\sum_{v=+,-,0} f_v \mathcal{P}^{v}_{B\to a_1^{\pm}\pi^{\mp}}(m_{\pi^+\pi^0}, m_{\pi^-\pi^0}) \times \mathcal{P}^{v}_{B\to a_1^{\pm}\pi^{\mp}}(\cos\theta_{\mathrm{H}}^{+}, \cos\theta_{\mathrm{H}}^{-})\right) \times$$
$$\mathcal{P}_{B\to a_1^{\pm}\pi^{\mp}}(\Delta E) \times \mathcal{P}_{B\to a_1^{\pm}\pi^{\mp}}(M_{\mathrm{bc}}) \times \mathcal{P}^{k}_{B\to a_1^{\pm}\pi^{\mp}}(\mathcal{F}_{B\bar{B}/q\bar{q}}) \times \mathcal{P}_{B\to a_1^{\pm}\pi^{\mp}}(\Delta t, q). \quad \text{(C.39)}$$

We parametrize the fractions of the different reconstruction categories, f_v, as follows;

$$\sum f_v \mathcal{P}^v \to (1. - f_0)(f_{\pm}\mathcal{P}^{+} + (1. - f_{\pm})\mathcal{P}^{-}) + f_0\mathcal{P}^0, \quad \text{(C.40)}$$

and obtain $f_{\pm} = 0.51 \pm 0.02$ and $f_0 = 0.06 \pm 0.01$ from a fit to simulated MC events.

0	ΔE	M_{bc}	$m^1_{\pi^+\pi^-}$	$m^2_{\pi^+\pi^-}$	$\mathcal{F}_{B\bar{B}/q\bar{q}}$	$\cos\theta^1_{\mathrm{H}}$	$\cos\theta^2_{\mathrm{H}}$	Δt
ΔE	1	0.08	-0.01	-0.07	0.04	-0.08	-0.03	-0.00
M_{bc}		1	-0.02	0.06	0.06	0.07	0.03	0.00
$m^1_{\pi^+\pi^-}$			1	0.01	-0.06	0.03	0.04	0.04
$m^2_{\pi^+\pi^-}$				1	0.01	-0.01	0.00	0.01
$\mathcal{F}_{B\bar{B}/q\bar{q}}$					1	0.03	0.02	0.01
$\cos\theta^1_{\mathrm{H}}$						1	0.07	-0.01
$\cos\theta^2_{\mathrm{H}}$							1	0.00
Δt								1

Table C.25: $B \to a1^{\pm}pi^{\mp}$ correlation matrix for reconstruction category +.

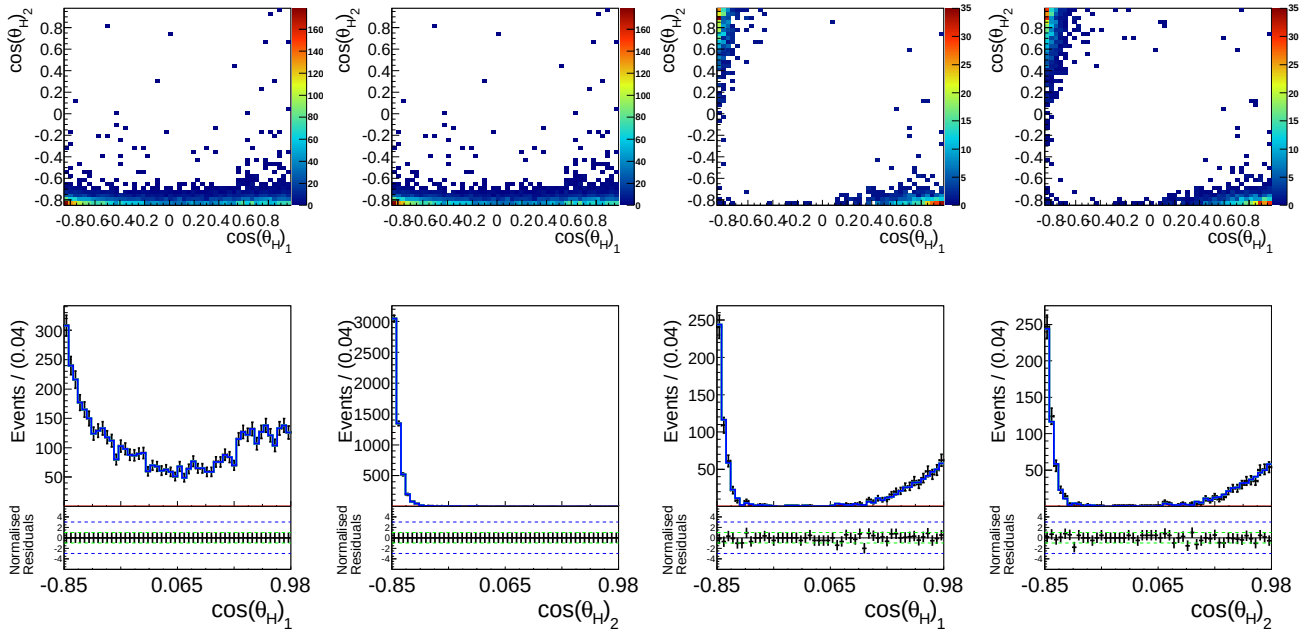

Figure C.50: Fit projections onto $\cos\theta_{\rm H}^{+} - \cos\theta_{\rm H}^{-}$ of $B \to a_1^{\pm}\pi^{\mp}$ decays for the components + (left) and 0. The black points show simulated MC events and the solid line shows the fit result. The residuals are given beneath each distribution.

0	ΔE	M_{bc}	$m^1_{\pi^+\pi^-}$	$m^2_{\pi^+\pi^-}$	$\mathcal{F}_{B\bar{B}/q\bar{q}}$	$\cos\theta^1_{\rm H}$	$\cos\theta^2_{\rm H}$	Δt
ΔE	1	0.12	-0.06	-0.00	0.06	-0.05	-0.09	-0.00
M_{bc}		1	0.05	-0.02	0.05	0.02	0.07	-0.00
$m^1_{\pi^+\pi^-}$			1	-0.00	-0.00	0.01	0.01	-0.00
$m^2_{\pi^+\pi^-}$				1	-0.03	0.05	0.04	0.01
$\mathcal{F}_{B\bar{B}/q\bar{q}}$					1	0.04	0.05	0.00
$\cos\theta^1_{\rm H}$						1	0.07	0.01
$\cos\theta^2_{\rm H}$							1	-0.00
Δt								1

Table C.26: $B \to a1^{\pm}pi^{\mp}$ correlation matrix for reconstruction category -.

0	ΔE	M_{bc}	$m^1_{\pi^+\pi^-}$	$m^2_{\pi^+\pi^-}$	$\mathcal{F}_{B\bar{B}/q\bar{q}}$	$\cos\theta^1_{\rm H}$	$\cos\theta^2_{\rm H}$	Δt
ΔE	1	0.09	0.02	-0.08	0.09	-0.04	0.01	-0.03
M_{bc}		1	-0.01	0.02	0.03	0.02	0.00	-0.01
$m^1_{\pi^+\pi^-}$			1	-0.05	-0.02	-0.33	0.33	-0.03
$m^2_{\pi^+\pi^-}$				1	-0.08	0.32	-0.31	-0.01
$\mathcal{F}_{B\bar{B}/q\bar{q}}$					1	-0.03	0.09	-0.03
$\cos\theta^1_{\rm H}$						1	-0.92	-0.03
$\cos\theta^2_{\rm H}$							1	0.02
Δt								1

Table C.27: $B \to a1^{\pm}pi^{\mp}$ correlation matrix for reconstruction category 0.

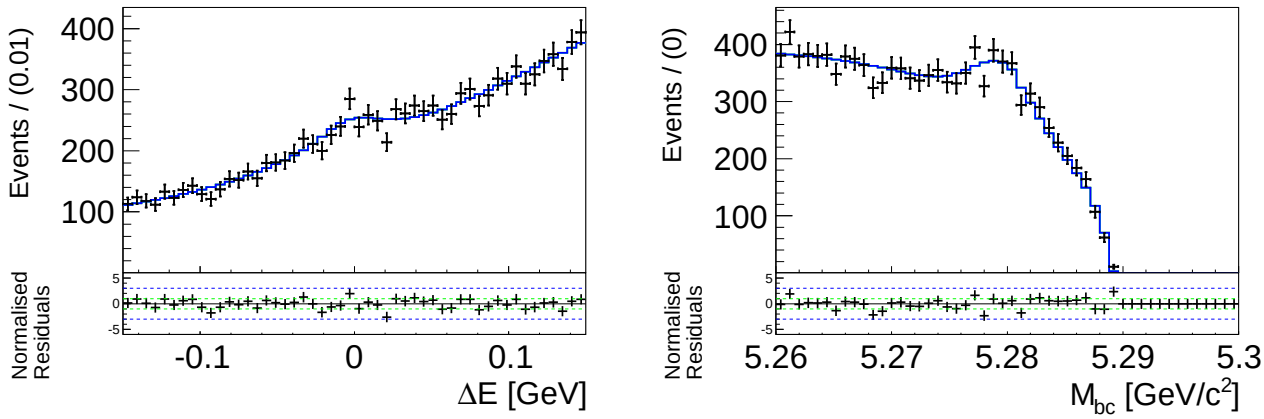

Figure C.51: Full projections onto ΔE and $M_{\rm bc}$ of $B \to a_1^{\pm}\pi^{\mp}$ decays. The black points show simulated MC events and the solid line shows the fit result. The residuals are given beneath each distribution.

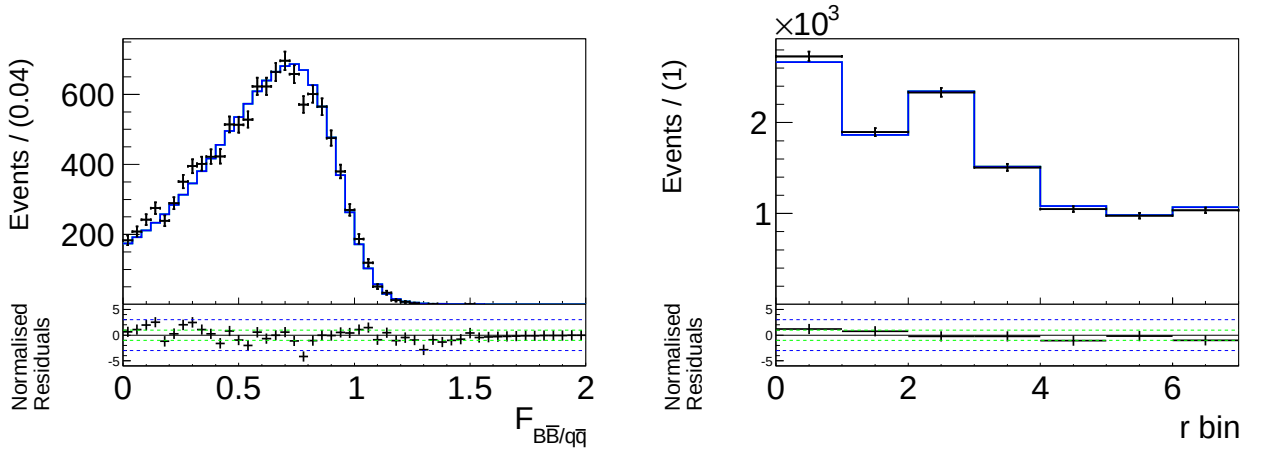

Figure C.52: Full projections onto $\mathcal{F}_{B\bar{B}/q\bar{q}}$ and the r-bin fractions of $B \to a_1^{\pm}\pi^{\mp}$ decays. The black points show simulated MC events and the solid line shows the fit result. The residuals are given beneath each distribution.

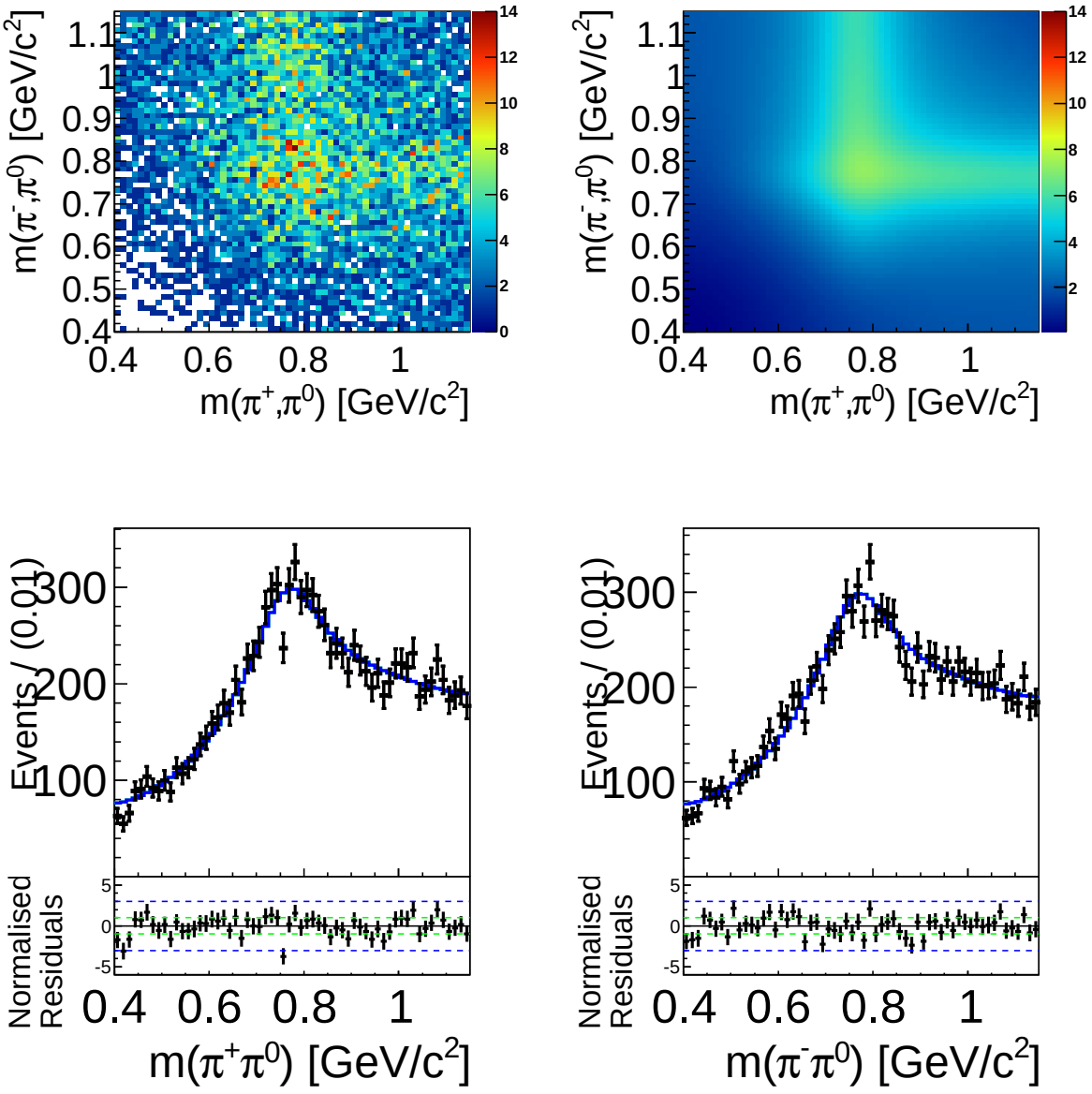

Figure C.53: Full projections onto $m_{\pi^+\pi^0} - m_{\pi^-\pi^0}$ of $B \to a_1^{\pm}\pi^{\mp}$ decays. The black points show simulated MC events and the solid line shows the fit result. The residuals are given beneath each distribution.

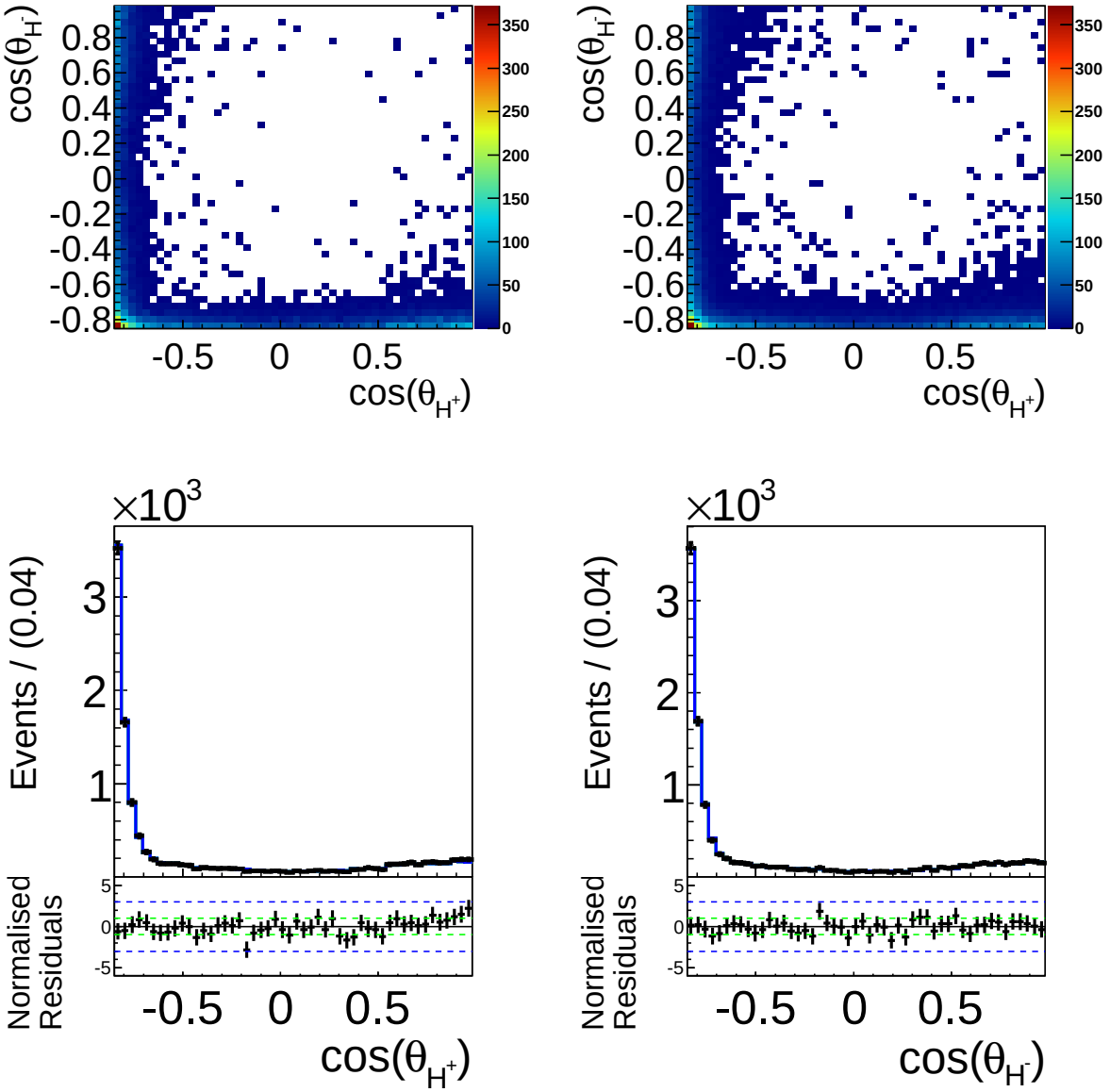

Figure C.54: Full projections onto $\cos\theta_{\rm H}^{+} - \cos\theta_{\rm H}^{-}$ of $B \to a_1^{\pm}\pi^{\mp}$ decays. The black points show simulated MC events and the solid line shows the fit result. The residuals are given beneath each distribution.

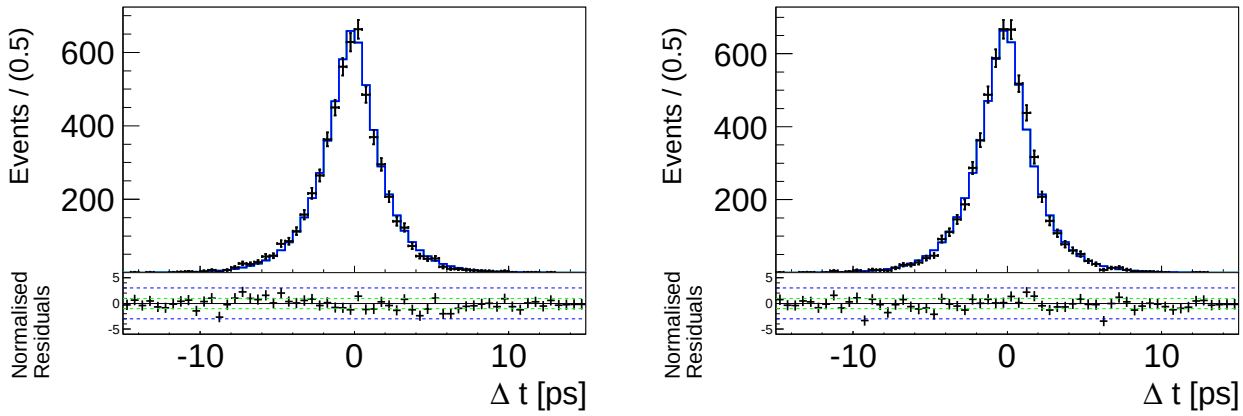

Figure C.55: Full projections onto Δt of $B \to a_1^{\pm}\pi^{\mp}$ decays for $q = +1$ (left) and $q = -1$. The black points show simulated MC events and the solid line shows the fit result. The residuals are given beneath each distribution.

Model For $B^0 \to a_1^0\pi^0$ Decays

Here, three dominant subsequent decays of the $a_1^0 \to \rho\pi$ lead to the same final state as our signal, $a_1^0 \to \rho^+\pi^-, \rho^-\pi^+, \rho^0\pi^0$. We assume that their amplitudes are of similar size, because of isospin arguments. We have a common model for $a_1^0 \to \rho^\pm\pi^\mp$ decays, where we furthermore distinguish between the different reconstruction categories $+, -$ and 0, due to misreconstruction. Opposite to $B^0 \to a_1^\pm\pi^\mp$ decays, the fast pion is neutral, therefore the corresponding helicity distributions peak at $\cos\theta_{\rm H} = +1$.

$B^0 \to a_1^0[\rho^\pm\pi^\mp]\pi^0$

The ΔE PDF for $\pm$ is taken to be the sum of a bifurcated Gaussian and a second order Chebychev polynomial

$$\mathcal{P}^{\pm}_{a_1^0\pi^0}(\Delta E) \equiv f_{\Delta E} G(\Delta E) + (1 - f_{\Delta E}) c_2 C_2(m_{\pi^\pm\pi^0}), \tag{C.41}$$

and for 0 the sum of Chebychev polynomials of the order two, three and four are used

$$\mathcal{P}^{0}_{a_1^0\pi^0}(\Delta E) \equiv \sum_{i=2}^{4} c_i C_i(\Delta E). \tag{C.42}$$

The PDF for $M_{\rm bc}$ of reconstruction category $\pm$ takes the form of Eq. (C.31) and the PDF for "0" is an Argus function

$$\mathcal{P}^{0}_{a_1^0\pi^0}(M_{\rm bc}) \equiv Ar(M_{\rm bc}). \tag{C.43}$$

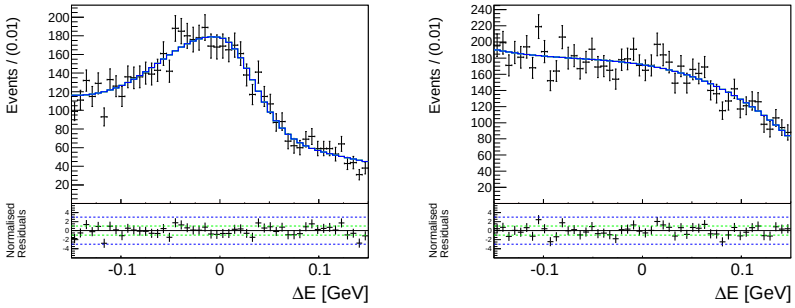

Figure C.56: Fit projections onto ΔE of $B \to a_1^0[\rho^\pm\pi^\mp]\pi^0$ decays for the components $\pm$ (left) and 0. The black points show simulated MC events and the solid line shows the fit result. The residuals are given beneath each distribution.

The mass and helicity PDFs for all reconstruction categories are individual two-dimensional histograms

$$\mathcal{P}^{+,-,0}_{a_1^0\pi^0}(m_{\pi^\pm\pi^0}, m_{\pi^\mp\pi^0}) \equiv H^{+,-,0}(m_{\pi^\pm\pi^0}, m_{\pi^\mp\pi^0}), \tag{C.44}$$

and

$$\mathcal{P}^{+,-,0}_{a_1^0\pi^0}(\cos\theta_{\rm H}^+, \cos\theta_{\rm H}^-) \equiv H^{+,-,0}(\cos\theta_{\rm H}^+, \cos\theta_{\rm H}^-). \tag{C.45}$$

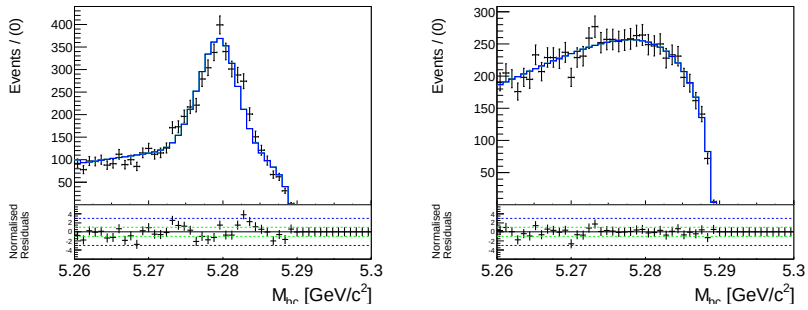

Figure C.57: Fit projections onto $M_{\rm bc}$ of $B \to a_1^0[\rho^\pm\pi^\mp]\pi^0$ decays for the components $\pm$ (left) and 0. The black points show simulated MC events and the solid line shows the fit result. The residuals are given beneath each distribution.

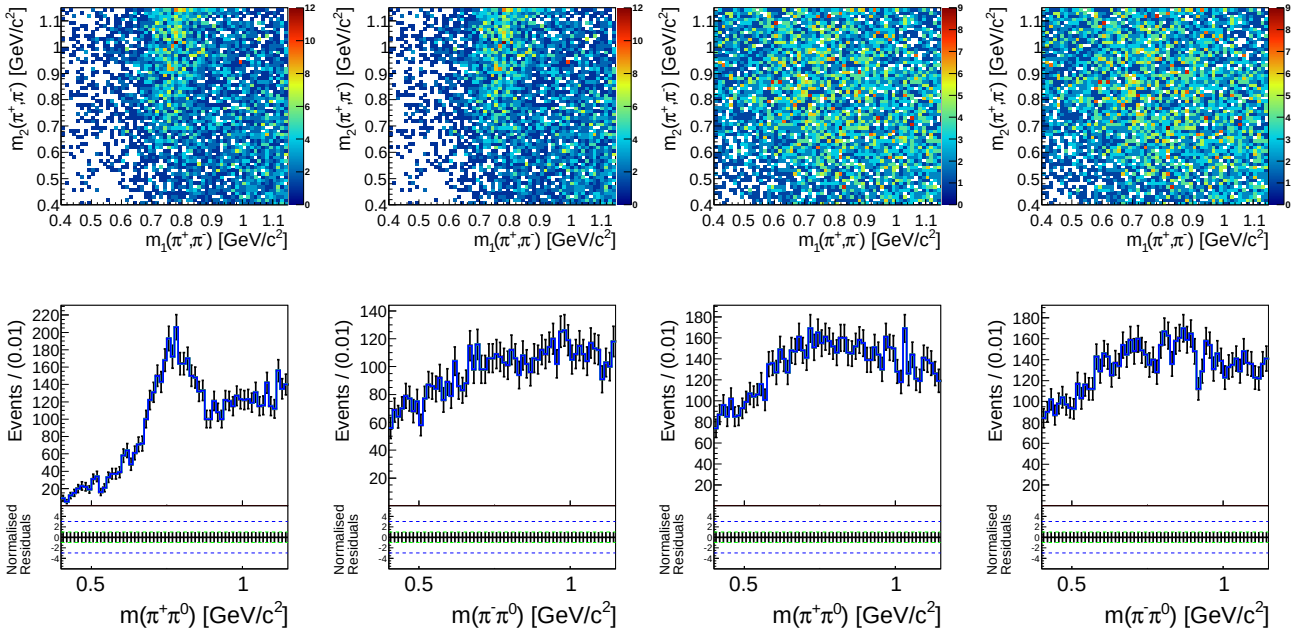

Figure C.58: Fit projections onto $m_{\pi^+\pi^0} - m_{\pi^-\pi^0}$ of $B \to a_1^0[\rho^\pm\pi^\mp]\pi^0$ decays for the components + (left) and 0. The black points show simulated MC events and the solid line shows the fit result. The residuals are given beneath each distribution.

Projection onto ΔE,$M_{\rm bc}$, the masses and helicity angles for the cases + and 0 are shown in Figs. C.56 to C.59 and full projections onto the fit variables are shown in Figs. C.60 to C.64. The parameter correlations are given in Tables C.28 to C.30.

The Δt distribution for the reconstruction category $\pm$ ($\mathcal{PDF}^{\pm}_{a_1^0\pi^0}(\Delta t, q)$) is modeled similar to Eq. (4.19) with an effective lifetime $\tau_{\rm eff}^{a_1^0\pi^0,\pm} = (1.40 \pm 0.02)$ ps. Another PDF similar to Eq. (4.69) ($\mathcal{PDF}^{0}_{a_1^0\pi^0}(\Delta t)$) with an effective lifetime $\tau_{\rm eff}^{a_1^0\pi^0,0} = (1.29 \pm 0.03)$ ps is accounting for the contamination from wrong side tracks for reconstruction category 0. Consequently,

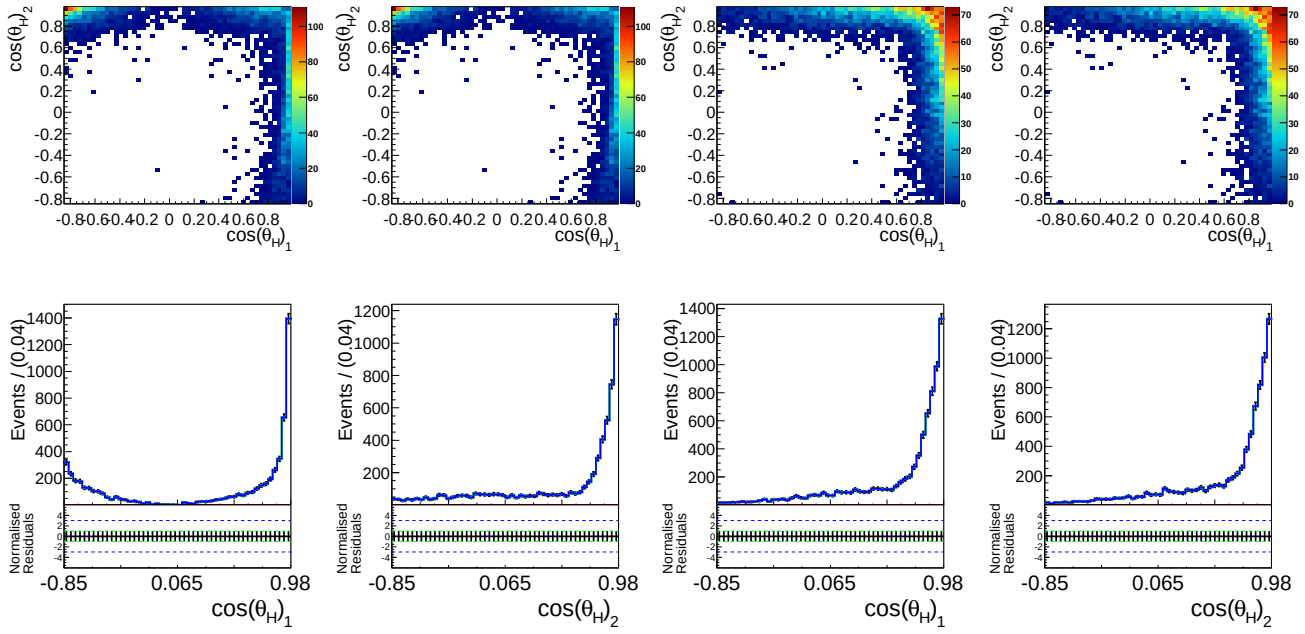

Figure C.59: Fit projections onto $\cos\theta_{\rm H}^{+} - \cos\theta_{\rm H}^{-}$ of $B \to a_1^0[\rho^{\pm}\pi^{\mp}]\pi^0$ decays for the components + (left) and 0. The black points show simulated MC events and the solid line shows the fit result. The residuals are given beneath each distribution.

the full PDF for $B^0 \to a_1^0[\rho^{\pm}\pi^{\mp}]\pi^0$ decays is given by

$$\mathcal{P}^{\rm LP(TP)}_{B\to a_1^0\pi^0}(\Delta E, M_{\rm bc}, m_{\pi^+\pi^0}, m_{\pi^-\pi^0}, \cos\theta_{\rm H}^{+}, \cos\theta_{\rm H}^{-}, \mathcal{F}_{B\bar{B}/q\bar{q}}, \Delta t, q) =$$
$$\Bigg(\sum_{v=+,-,0} \big(f_v \mathcal{P}^{v}_{B\to a_1^0\pi^0}(\Delta E) \times \mathcal{P}^{v}_{B\to a_1^0\pi^0}(M_{\rm bc}) \times \mathcal{P}^{v}_{B\to a_1^0\pi^0}(m_{\pi^+\pi^0}, m_{\pi^-\pi^0})$$
$$\times \mathcal{P}^{v}_{B\to a_1^0\pi^0}(\cos\theta_{\rm H}^{+}, \cos\theta_{\rm H}^{-}) \times \mathcal{P}^{v}_{B\to a_1^0\pi^0}(\Delta t, q) \big) \Bigg) \times \mathcal{P}^{k}_{B\to a_1^0\pi^0}(\mathcal{F}_{B\bar{B}/q\bar{q}}), \qquad \text{(C.46)}$$

where the PDFs for ΔE, $M_{\rm bc}$ and also Δt are identical for reconstruction categories + and -. The fractions f_v are parametrized according to Eq. (C.40) and are: $f_{\pm} = 0.50 \pm 0.02$ and $f_0 = 0.39 \pm 0.02$.

0	ΔE	M_{bc}	$m^1_{\pi^+\pi^-}$	$m^2_{\pi^+\pi^-}$	$\mathcal{F}_{B\bar{B}/q\bar{q}}$	$\cos\theta^1_{\rm H}$	$\cos\theta^2_{\rm H}$	Δt
ΔE	1	-0.03	-0.05	-0.01	0.02	-0.07	0.01	0.01
M_{bc}		1	0.13	-0.08	0.06	0.18	-0.17	-0.01
$m^1_{\pi^+\pi^-}$			1	-0.22	0.00	0.32	-0.30	-0.02
$m^2_{\pi^+\pi^-}$				1	-0.07	-0.32	0.35	0.02
$\mathcal{F}_{B\bar{B}/q\bar{q}}$					1	0.10	-0.05	-0.02
$\cos\theta^1_{\rm H}$						1	-0.53	-0.01
$\cos\theta^2_{\rm H}$							1	0.02
Δt								1

Table C.28: Correlation matrix for $B \to a_1^0[\rho^+\pi^-]\pi^0$ decays.

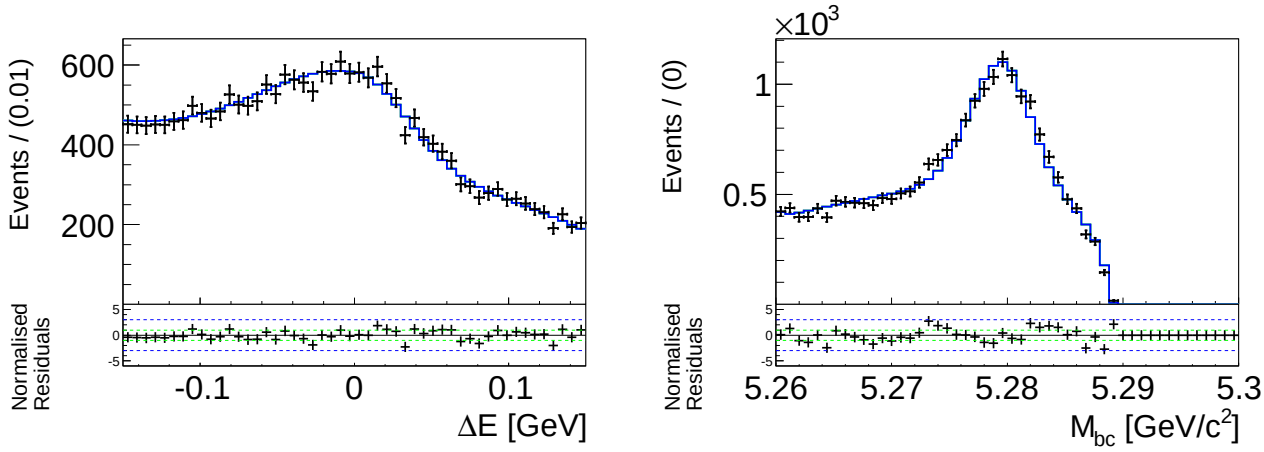

Figure C.60: Full projections onto ΔE and $M_{\rm bc}$ of $B \to a_1^0[\rho^\pm\pi^\mp]\pi^0$ decays. The black points show simulated MC events and the solid line shows the fit result. The residuals are given beneath each distribution.

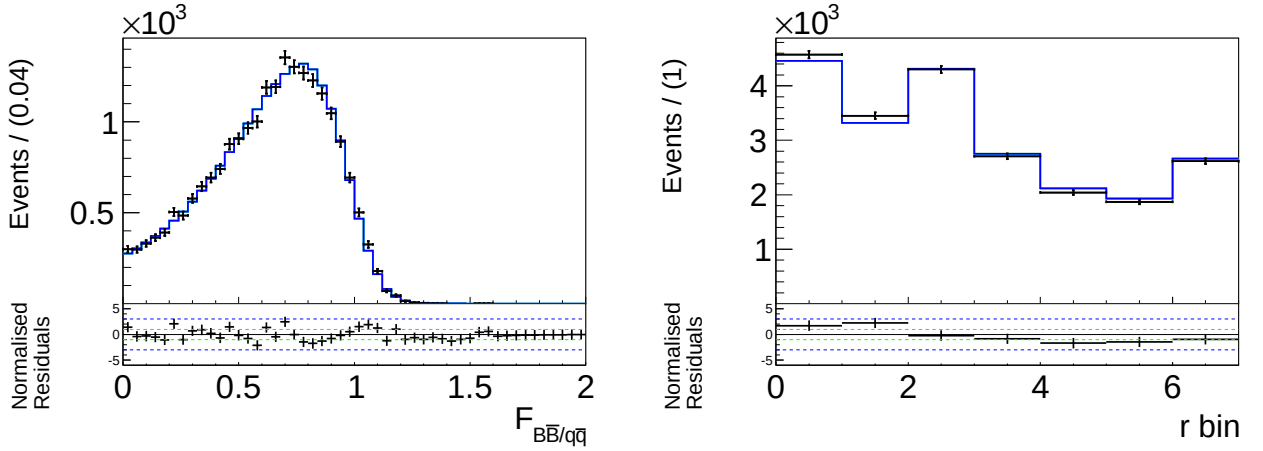

Figure C.61: Full projections onto $\mathcal{F}_{B\bar{B}/q\bar{q}}$ and the r-bin fractions of $B \to a_1^0[\rho^\pm\pi^\mp]\pi^0$ decays. The black points show simulated MC events and the solid line shows the fit result. The residuals are given beneath each distribution.

0	ΔE	M_{bc}	$m^1_{\pi^+\pi^-}$	$m^2_{\pi^+\pi^-}$	$\mathcal{F}_{B\bar{B}/q\bar{q}}$	$\cos\theta^1_{\rm H}$	$\cos\theta^2_{\rm H}$	Δt
ΔE	1	-0.04	-0.01	-0.05	0.02	-0.01	-0.08	0.00
M_{bc}		1	-0.08	0.12	0.05	-0.13	0.18	-0.03
$m^1_{\pi^+\pi^-}$			1	-0.22	-0.03	0.33	-0.32	0.01
$m^2_{\pi^+\pi^-}$				1	-0.03	-0.26	0.30	-0.01
$\mathcal{F}_{B\bar{B}/q\bar{q}}$					1	-0.02	0.06	-0.00
$\cos\theta^1_{\rm H}$						1	-0.52	0.01
$\cos\theta^2_{\rm H}$							1	-0.01
Δt								1

Table C.29: Correlation matrix for $B \to a_1^0[\rho^-\pi^+]\pi^0$ decays.

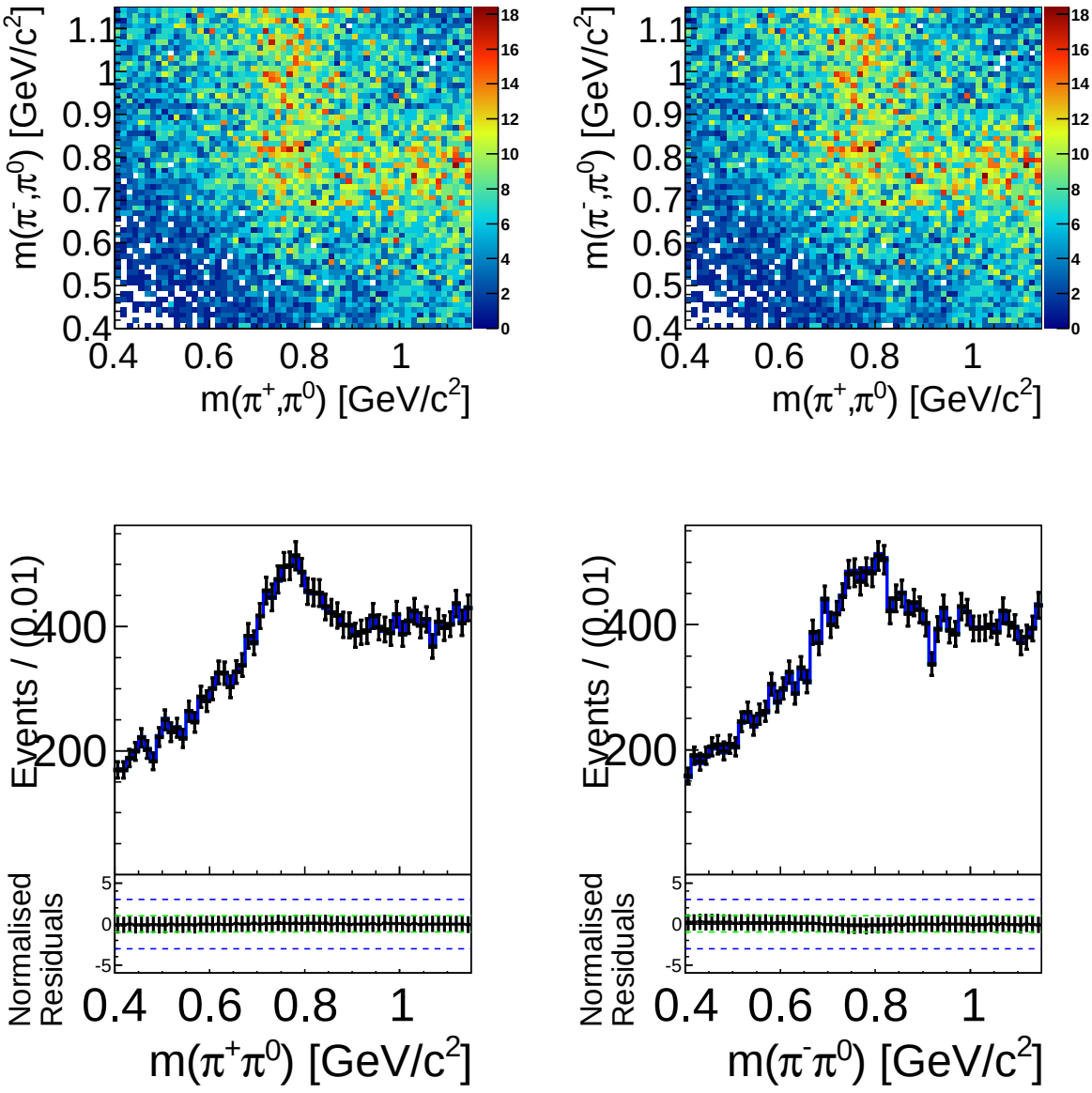

Figure C.62: Full projections onto $m_{\pi^+\pi^0} - m_{\pi^-\pi^0}$ of $B \to a_1^0[\rho^\pm\pi^\mp]\pi^0$ decays. The black points show simulated MC events and the solid line shows the fit result. The residuals are given beneath each distribution.

0	ΔE	M_{bc}	$m^1_{\pi^+\pi^-}$	$m^2_{\pi^+\pi^-}$	$\mathcal{F}_{B\bar{B}/q\bar{q}}$	$\cos\theta^1_{\rm H}$	$\cos\theta^2_{\rm H}$	Δt
ΔE	1	-0.01	-0.02	-0.01	0.02	-0.02	-0.02	0.00
M_{bc}		1	-0.00	-0.02	0.03	0.00	0.02	-0.02
$m^1_{\pi^+\pi^-}$			1	-0.15	-0.01	0.27	-0.23	0.01
$m^2_{\pi^+\pi^-}$				1	-0.04	-0.25	0.28	-0.00
$\mathcal{F}_{B\bar{B}/q\bar{q}}$					1	0.02	-0.00	-0.02
$\cos\theta^1_{\rm H}$						1	-0.39	0.02
$\cos\theta^2_{\rm H}$							1	0.00
Δt								1

Table C.30: Correlation matrix for mis-reconstructed $B \to a_1^0[\rho^\pm\pi^\mp]\pi^0$ decays.

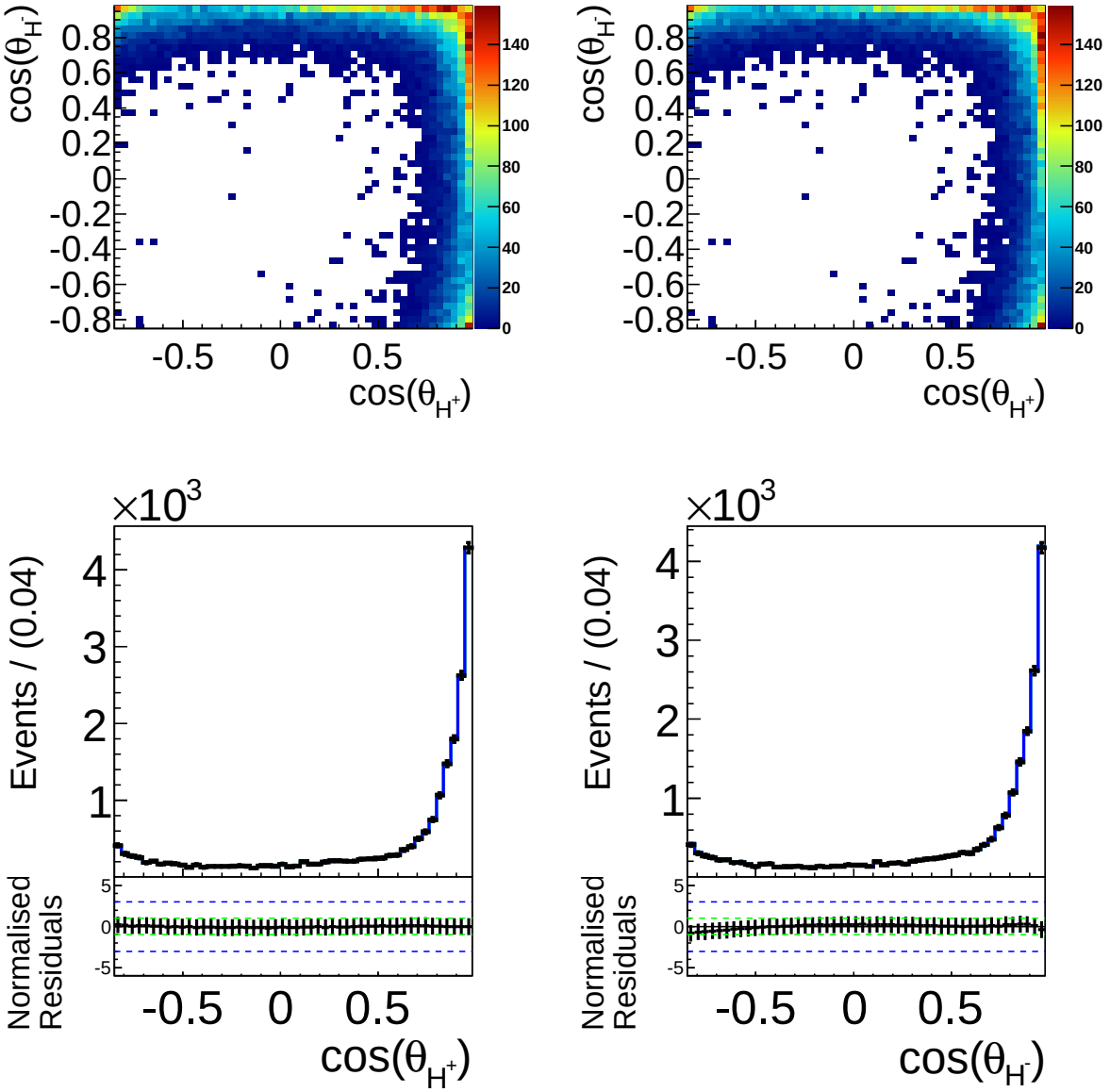

Figure C.63: Full projections onto $\cos\theta_{\rm H}^{+} - \cos\theta_{\rm H}^{-}$ of $B \to a_1^0[\rho^{\pm}\pi^{\mp}]\pi^0$ decays. The black points show simulated MC events and the solid line shows the fit result. The residuals are given beneath each distribution.

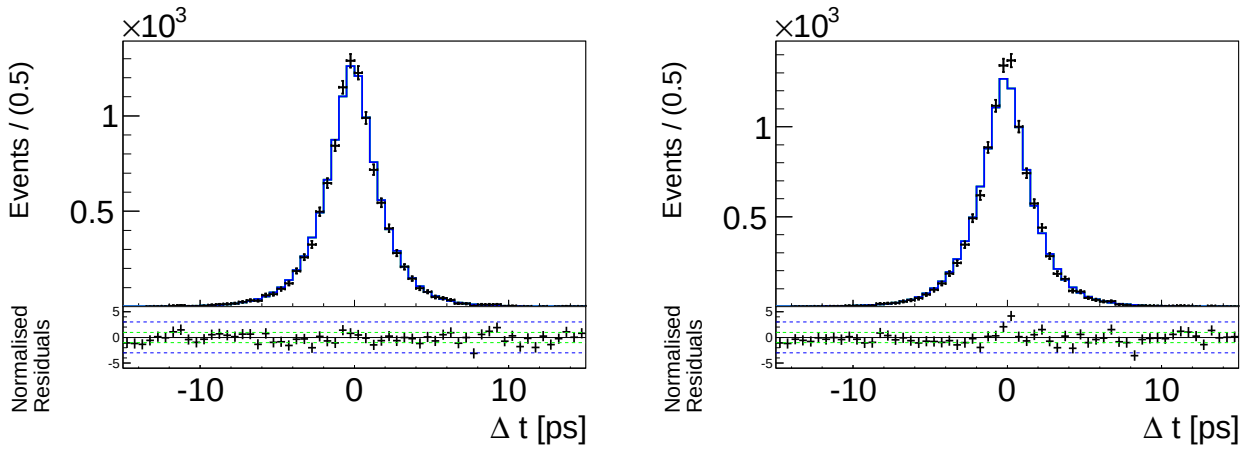

Figure C.64: Full projections onto Δt of $B \to a_1^0[\rho^{\pm}\pi^{\mp}]\pi^0$ decays for $q = +1$ (left) and $q = -1$. The black points show simulated MC events and the solid line shows the fit result. The residuals are given beneath each distribution.

Model For $B^0 \to a_1^0[\rho^0\pi^0]\pi^0$ Decays

This decay does not contain a $\rho^\pm$ resonance, hence no separate treatment is needed. We account for a correlation of the mass with the helicity distribution via

$$\mathcal{P}^{a_1^0\to\rho^0\pi^0}_{a_1^0\pi^0}(m_A, m_B|\cos\theta_{\rm H}^+, \cos\theta_{\rm H}^-) \equiv \sum_{i=1}^{5} c_i^A C_i(m_A) \times \sum_{i=1}^{5} c_i^B C_i(m_B), \tag{C.47}$$

where $m_{A(B)} = m(\pi^{+(-)}\pi^0)$ if $\cos\theta_{\rm H}^+ > \cos\theta_{\rm H}^-$ and $m_{A(B)} = m(\pi^{-(+)}\pi^0)$ else. The PDF for the helicity angles is the product of sums of Gaussians and a second order Chebychev polynomial

$$\begin{aligned}
&\mathcal{P}^{a_1^0\to\rho^0\pi^0}_{a_1^0\pi^0}(\cos\theta_{\rm H}^+, \cos\theta_{\rm H}^-) \equiv \\
&\frac{1}{2}\Bigg(\big(fr_+ G(\cos\theta_{\rm H}^+, m_0, \sigma_0) + (1-fr_+)c_2 C_2(\cos\theta_{\rm H}^+)\big) \times \sum_{i=1}^{3} f_{i-} G(\cos\theta_{\rm H}^+, m_i, \sigma_i) \Bigg) \times \\
&\frac{1}{2}\Bigg(\big(fr_+ G(\cos\theta_{\rm H}^-, m_0, \sigma_0) + (1-fr_+)c_2 C_2(\cos\theta_{\rm H}^-)\big) \times \sum_{i=1}^{3} f_{i-} G(\cos\theta_{\rm H}^+, m_i, \sigma_i) \Bigg).
\end{aligned} \tag{C.48}$$

The PDF for Δt is identical to $\mathcal{PDF}^{\pm}_{a_1^0\pi^0}(\Delta t, q)$ from $B^0 \to a_1^0[\rho^\pm\pi^\mp]\pi^0$ decays. Full projections onto the fit variables are shown in Figs. C.65 to C.69, the correlations among them are given in Table C.31. The full PDF takes the form

$$\begin{aligned}
&\mathcal{P}_{B\to a_1^0[\rho^0\pi^0]\pi^0}(\Delta E, M_{\rm bc}, m_{\pi^+\pi^0}, m_{\pi^-\pi^0}, \cos\theta_{\rm H}^+, \cos\theta_{\rm H}^-, \mathcal{F}_{B\bar{B}/q\bar{q}}, \Delta t, q) = \\
&\mathcal{P}_{B\to a_1^0[\rho^0\pi^0]\pi^0}(\Delta E) \times \mathcal{P}_{B\to a_1^0[\rho^0\pi^0]\pi^0}(M_{\rm bc}) \times \mathcal{P}_{B\to a_1^0[\rho^0\pi^0]\pi^0}(m_{\pi^\pm\pi^0}, m_{\pi^\mp\pi^0}|\cos\theta_{\rm H}^+, \cos\theta_{\rm H}^-) \times \\
&\mathcal{P}_{B\to a_1^0[\rho^0\pi^0]\pi^0}(\cos\theta_{\rm H}^+, \cos\theta_{\rm H}^-) \times \mathcal{P}^k_{B\to a_1^0[\rho^0\pi^0]\pi^0}(\mathcal{F}_{B\bar{B}/q\bar{q}}) \times \mathcal{P}_{B\to a_1^0[\rho^0\pi^0]\pi^0}(\Delta t, q).
\end{aligned} \tag{C.49}$$

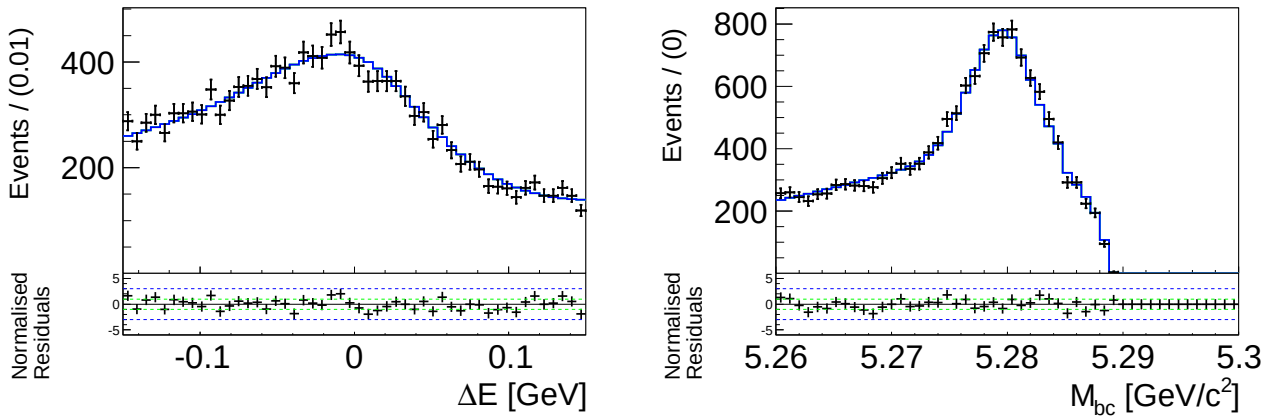

Figure C.65: Full projections onto ΔE and $M_{\rm bc}$ of $B \to a_1^0[\rho^0\pi^0]\pi^0$ decays. The black points show simulated MC events and the solid line shows the fit result. The residuals are given beneath each distribution.

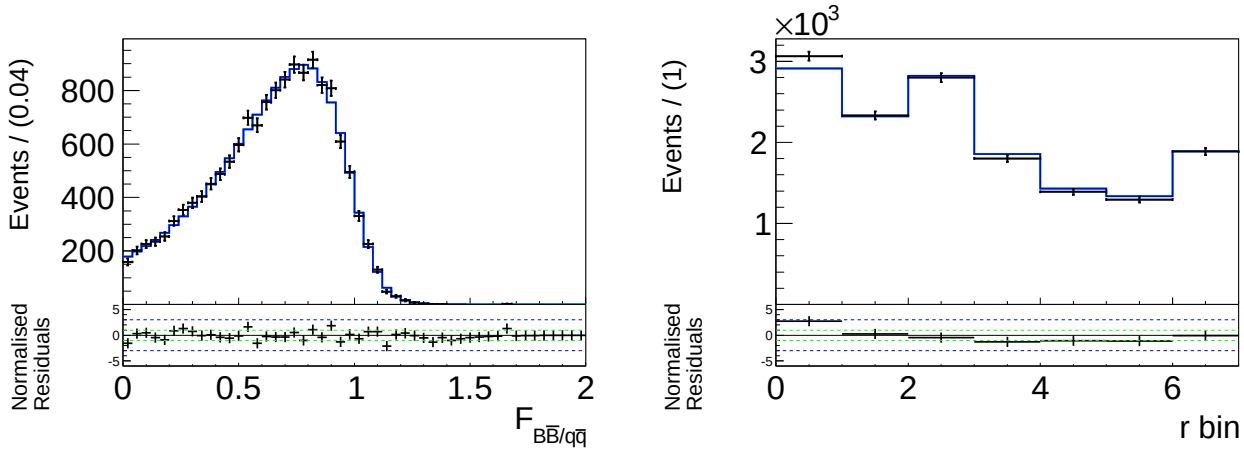

Figure C.66: Full projections onto $\mathcal{F}_{B\bar{B}/q\bar{q}}$ and the r-bin fractions of $B \to a_1^0[\rho^0\pi^0]\pi^0$ decays. The black points show simulated MC events and the solid line shows the fit result. The residuals are given beneath each distribution.

0	ΔE	M_{bc}	$m^1_{\pi^+\pi^-}$	$m^2_{\pi^+\pi^-}$	$\mathcal{F}_{B\bar{B}/q\bar{q}}$	$\cos\theta^1_{\rm H}$	$\cos\theta^2_{\rm H}$	Δt
ΔE	1	-0.04	-0.01	-0.00	0.02	-0.03	-0.04	-0.01
M_{bc}		1	0.03	0.03	0.02	0.05	0.05	-0.02
$m^1_{\pi^+\pi^-}$			1	-0.22	-0.03	0.38	-0.42	0.02
$m^2_{\pi^+\pi^-}$				1	-0.03	-0.42	0.38	0.00
$\mathcal{F}_{B\bar{B}/q\bar{q}}$					1	0.03	0.01	0.00
$\cos\theta^1_{\rm H}$						1	-0.76	0.01
$\cos\theta^2_{\rm H}$							1	-0.01
Δt								1

Table C.31: Correlation matrix for $B \to a_1^0[[\rho^0\pi^0]\pi^0$ decays.

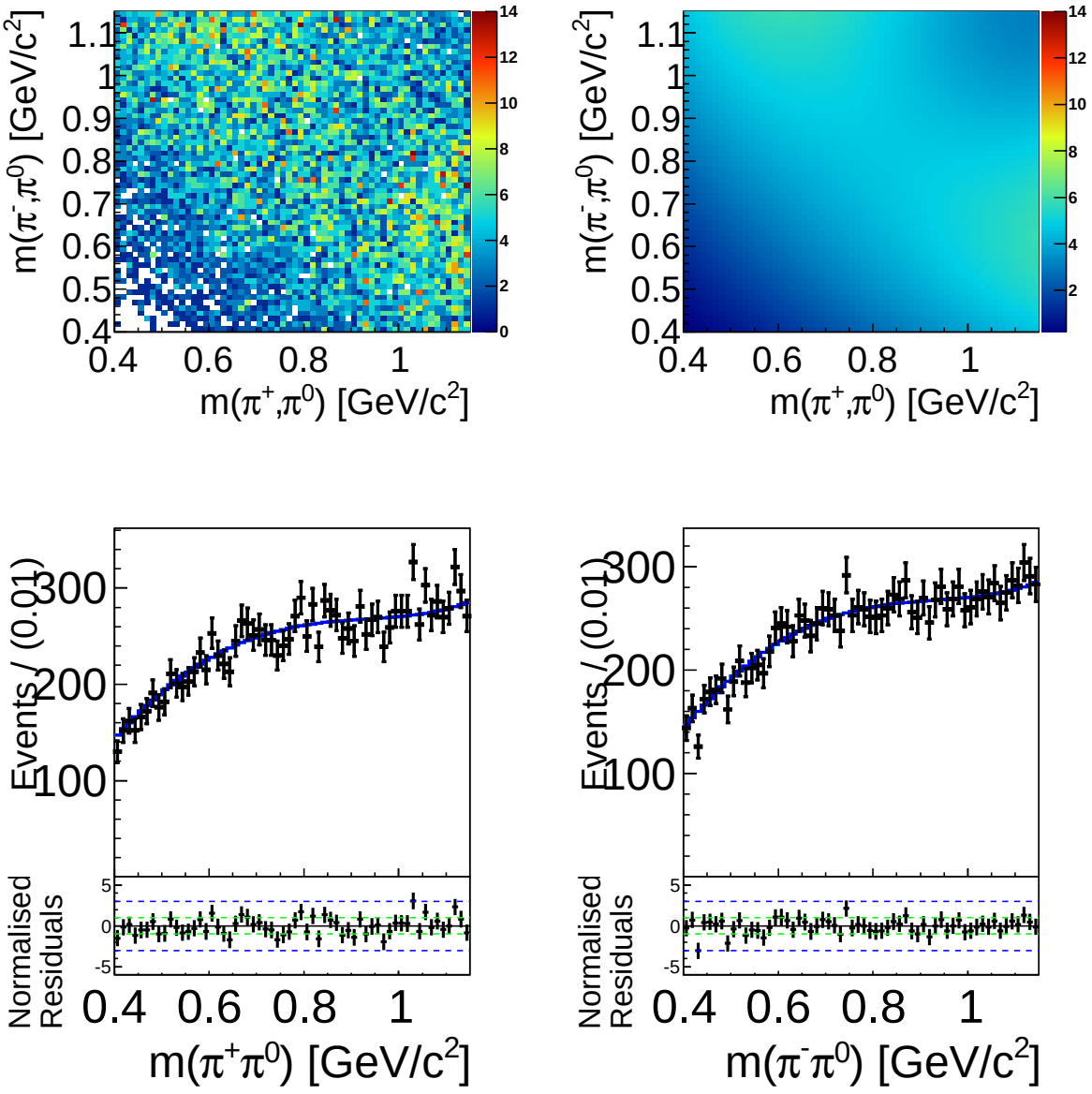

Figure C.67: Full projections onto $m_{\pi^+\pi^0} - m_{\pi^-\pi^0}$ of $B \to a_1^0[\rho^0\pi^0]\pi^0$ decays. The black points show simulated MC events and the solid line shows the fit result. The residuals are given beneath each distribution.

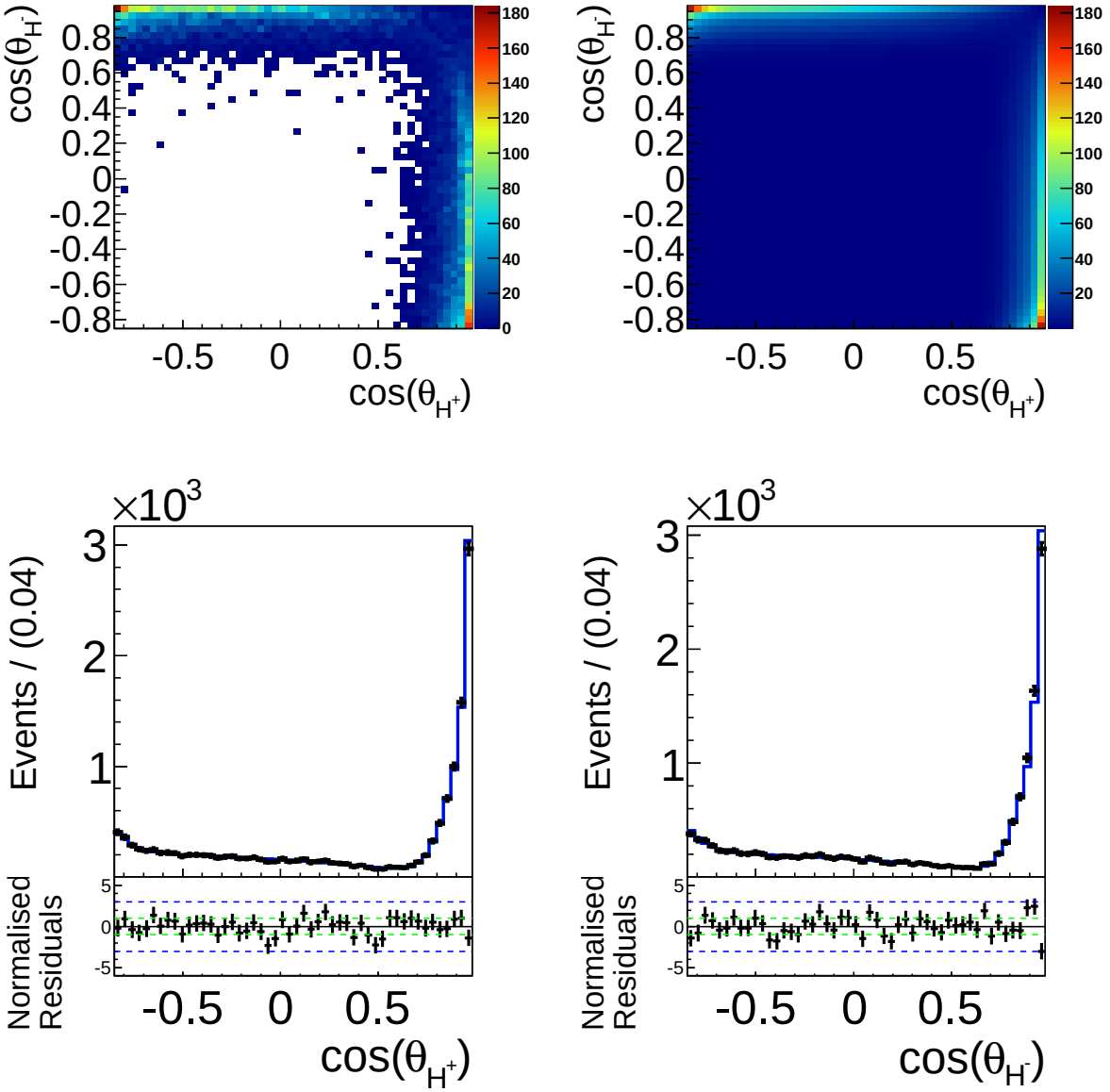

Figure C.68: Full projections onto $\cos\theta_{\rm H}^{+} - \cos\theta_{\rm H}^{-}$ of $B \to a_1^0[\rho^0\pi^0]\pi^0$ decays. The black points show simulated MC events and the solid line shows the fit result. The residuals are given beneath each distribution.

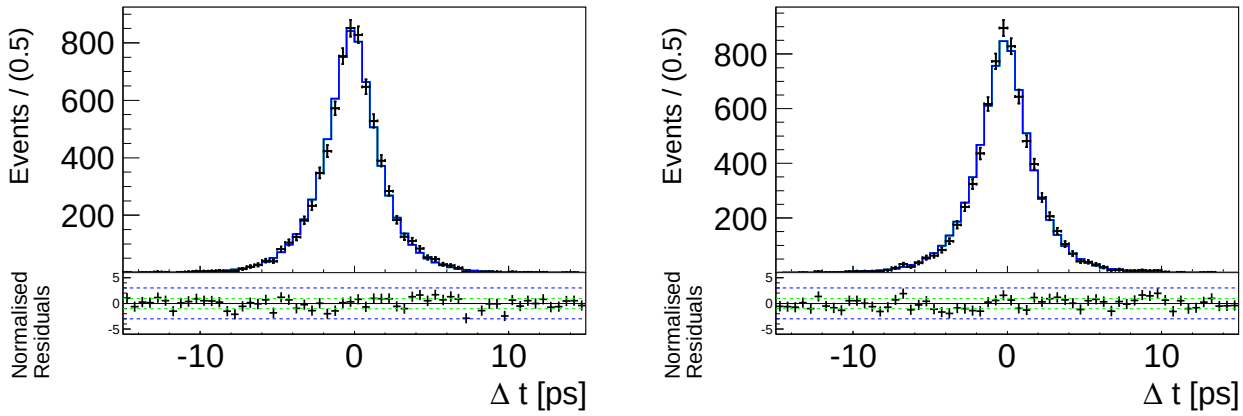

Figure C.69: Full projections onto Δt of $B \to a_1^0[\rho^0\pi^0]\pi^0$ decays for $q = +1$ (left) and $q = -1$. The black points show simulated MC events and the solid line shows the fit result. The residuals are given beneath each distribution.

C.2.3 Model For $B^0 \to \rho^{\pm}\pi^{\mp}\pi^0$ Decays

Since there is no suitable decay model for a pseudo-scalar decaying into a vector particle and two pseudo-scalars, we assume a phase-space model and account for that assumption in the systematic uncertainty. Again, we consider the three cases +,- and 0 separately, with the fraction of events of category 0 being $f_0 = (0.08 \pm 0.01)\%$. The ΔE distribution for $\pm$ MC events is described similar to Eq. (C.30),

$$\begin{aligned}\mathcal{P}^{\pm}_{\rho^{\pm}\pi^{\mp}\pi^0}(\Delta E|M_{\rm bc}, \cos\theta^+_{\rm H}, \cos\theta^-_{\rm H}) \equiv (1 - f_{\rm G}(M_{\rm bc}, \cos\theta^+_{\rm H}, \cos\theta^-_{\rm H}))\\ \times dbG(\Delta E, \mu_1, \sigma_{1l}, \sigma_{1r}, \mu_2^{\rm truthLP}, \sigma_{2l}^{\rm truthLP}, \sigma_{2r}^{\rm truthLP}, \mu_{\rm CF}, \sigma_{l,\rm CF}, \sigma_{r,\rm CF}, f^{\rm truthLP})\\ + f_{\rm G}(M_{\rm bc}, \cos\theta^+_{\rm H}, \cos\theta^-_{\rm H}) \sum_{i=1}^{3} c_i C_i(\Delta E),\end{aligned} \tag{C.50}$$

with a modified fraction of the Gaussian to account for a correlation with $M_{\rm bc}$ and the helicity angles:

$$f_{\rm G}(M_{\rm bc}, \cos\theta^+_{\rm H}, \cos\theta^-_{\rm H}) = f_{\Delta E} + + c_{\Delta E,1}|M_{\rm bc} - c_{\Delta E,0}| + c_{\Delta E,2}|\cos\theta^+_{\rm H}\cos\theta^-_{\rm H}|^3.$$

The ΔE distribution for reconstruction category 0 is described by a first order Chebychev polynomial,

$$\mathcal{P}^{0}_{\rho^{\pm}\pi^{\mp}\pi^0}(\Delta E) \equiv c_1 C_1(\Delta E). \tag{C.51}$$

Projections onto ΔE for different slices are shown in Fig. C.70.
The PDF for $M_{\rm bc}$ for events of category $\pm$ is correlated with the helicity angles and takes the form

$$\mathcal{P}^{\pm}_{\rho^{\pm}\pi^{\mp}\pi^0}(M_{\rm bc}|\cos\theta^+_{\rm H}, \cos\theta^-_{\rm H}) \equiv f_{M_{\rm bc}}(\cos\theta^+_{\rm H}, \cos\theta^-_{\rm H}) dbG(M_{\rm bc}) + (1 - f_{M_{\rm bc}}(\cos\theta^+_{\rm H}, \cos\theta^-_{\rm H}) Ar(M_{\rm bc}), \tag{C.52}$$

where the fraction of the dbG takes the form $f_{M_{\rm bc}}(\cos\theta^+_{\rm H}, \cos\theta^-_{\rm H}) = f_{M_{\rm bc}} + c_{M_{\rm bc},1}|(\tilde{\cos\theta_{\rm H}}^{+}\tilde{\cos\theta_{\rm H}}^{-})^3|$ with $\tilde{\cos\theta_{\rm H}}^{\pm} = c_{M_{\rm bc},0}$ if $\cos\theta^{\pm}_{\rm H} > c_{M_{\rm bc},0}$ and $\tilde{\cos\theta_{\rm H}}^{\pm} = \cos\theta^{\pm}_{\rm H}$ else. Projections onto $M_{\rm bc}$ for different slices are presented in Fig. C.71 and the parameters c_j of ΔE and $M_{\rm bc}$ are given in table Table C.32.

c_j	SVD1	SVD2
$c_{\Delta E,0}$	-5.28 ± 0.01	-5.28 ± 0.01
$c_{\Delta E,1}$	101.59 ± 2.78	101.80 ± 1.47
$c_{\Delta E,2}$	2.59 ± 0.14	2.56 ± 0.13
$c_{M_{\rm bc},0}$	0.70 ± 0.01	0.73 ± 0.01
$c_{M_{\rm bc},1}$	-1.47 ± 0.09	-1.5 ± 0.08
$c_{m_{\pi^{\pm}\pi^0},0}$	0.71 ± 0.01	0.73 ± 0.01
$c_{m_{\pi^{\pm}\pi^0},1}$	-1.47 ± 0.09	-1.42 ± 0.08

Table C.32: Correlation parameters included in the PDF of $M_{\rm bc}$ for $B \to \rho^+\pi^-\pi^0$ decays.

The mass distributions for reconstruction categories $\pm$ and 0 are described similar to Eq. (C.36) and Eq. (C.37), respectively, where for the category $\pm$ the fraction of the resonant part depends on the helicity angles in addition;

$$f_{m_{\pi^{\pm}\pi^0}}(\cos\theta^+_{\rm H}, \cos\theta^-_{\rm H}) = f_{m_{\pi^{\pm}\pi^0},0} + c_{m_{\pi^{\pm}\pi^0},1}(\tilde{\cos\theta_{\rm H}}^{+} \times \tilde{\cos\theta_{\rm H}}^{-})^2 \tag{C.53}$$

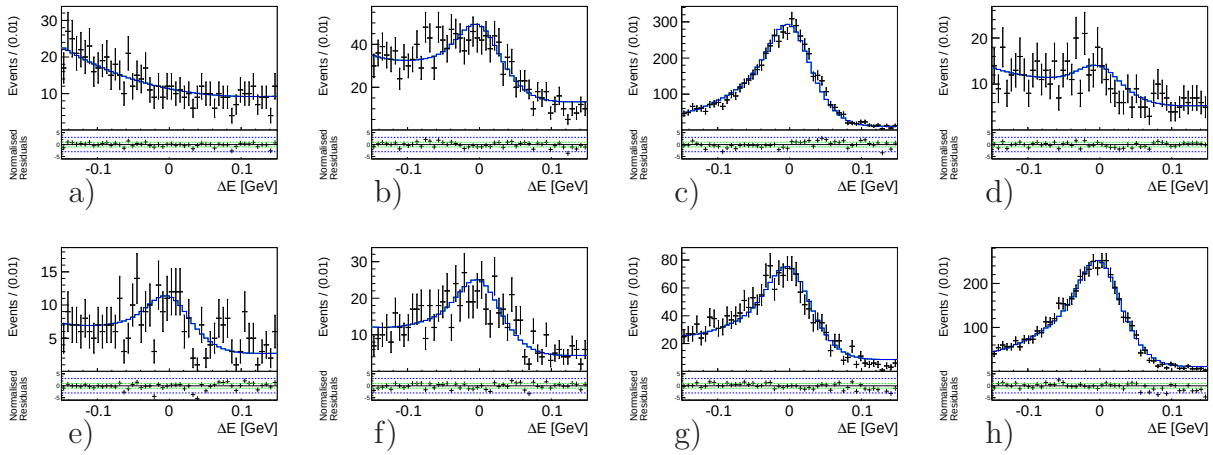

Figure C.70: Sliced fit projections onto ΔE of $B^0 \to \rho^{\pm}\pi^{\mp}\pi^0$ decays for the components $\pm$. The top row shows projections for *a)* $M_{\rm bc} < 5.27;\text{GeV}$, *b)* $5.27\ \text{GeV} < M_{\rm bc} < 5.275;\text{GeV}$, *c)* $5.275\ \text{GeV} < M_{\rm bc} < 5.285;\text{GeV}$ and *d)* $M_{\rm bc} > 5.285\ \text{GeV}$ and the bottom row shows *e)* $\cos\theta_{\rm H}^{\pm} < -0.6$, *f)* $\cos\theta_{\rm H}^{+} > 0.6 \& \cos\theta_{\rm H}^{-} < -0.6$ *g)* $\cos\theta_{\rm H}^{+} > 0.6 \& -0.6\cos\theta_{\rm H}^{-} < 0.6$ and *h)* $\cos\theta_{\rm H}^{\pm} > 0.6$. The black points show simulated MC events and the solid line shows the fit result. The residuals are given beneath each distribution.

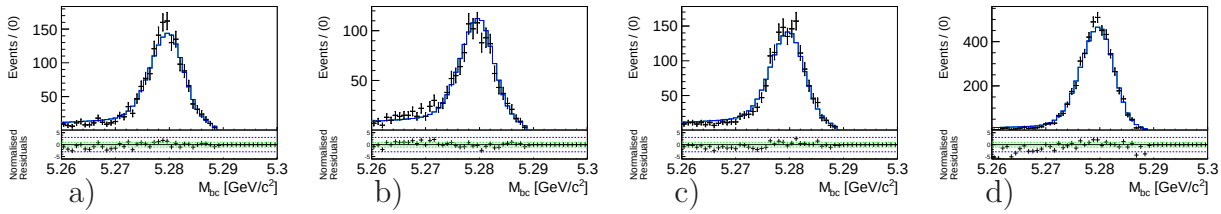

Figure C.71: Sliced fit projections onto $M_{\rm bc}$ of $B^0 \to \rho^{\pm}\pi^{\mp}\pi^0$ decays for the components $\pm$. The row shows projections for *a)* $\cos\theta_{\rm H}^{\pm} < -0.6$, *b)* $\cos\theta_{\rm H}^{+} > 0.6 \& \cos\theta_{\rm H}^{-} < -0.6$ *c)* $\cos\theta_{\rm H}^{+} > 0.6 \& -0.6\cos\theta_{\rm H}^{-} < 0.6$ and *d)* $\cos\theta_{\rm H}^{\pm} > 0.6$. The black points show simulated MC events and the solid line shows the fit result. The residuals are given beneath each distribution.

where $\tilde{\cos\theta_{\rm H}}^{\pm} = \cos\theta_{\rm H}^{\pm}$ for $\cos\theta_{\rm H}^{\pm} < c_{m_{\pi^{\pm}\pi^0},0}$ and $\tilde{\cos\theta_{\rm H}}^{\pm} = c_{m_{\pi^{\pm}\pi^0},0}$ else. The fraction is restricted to be within $f_{m_{\pi^{\pm}\pi^0}}(\cos\theta_{\rm H}^{+}, \cos\theta_{\rm H}^{-}) \in [0,1]$. The parameters $c_{m_{\pi^{\pm}\pi^0},i}$ are listed in Table C.32 and projections onto different slices are presented in Fig. C.73.
The PDF for the helicity distribution is taken to be two-dimensional histogram for each reconstruction category

$$\mathcal{P}^{+,-,0}_{\rho^{\pm}\pi^{\mp}\pi^0}(\cos\theta_{\rm H}^{+}, \cos\theta_{\rm H}^{-}) = H^{+,-,0}(\cos\theta_{\rm H}^{+}, \cos\theta_{\rm H}^{-}). \tag{C.54}$$

The $\mathcal{F}_{B\bar{B}/q\bar{q}}$ and Δt distributions are described according to Eq. (C.32) and Eq. (4.19), respectively, where an effective life of the B meson accounts for wrong assigned tracks (only the tracks from the $\rho^{\pm}$ are required to be correct for the reconstruction category $\pm$) and is determined from fully simulated MC events: $\tau^{\rm eff}_{\rho^{\pm}\pi^{\mp}\pi^0} = (1.48 \pm 0.02)\text{ps}$.

Full projections onto the fit variables are shown in Figs. C.76 to C.80, the correlations among them are given in Tables C.33 to C.35 for each reconstruction category. The full PDF for

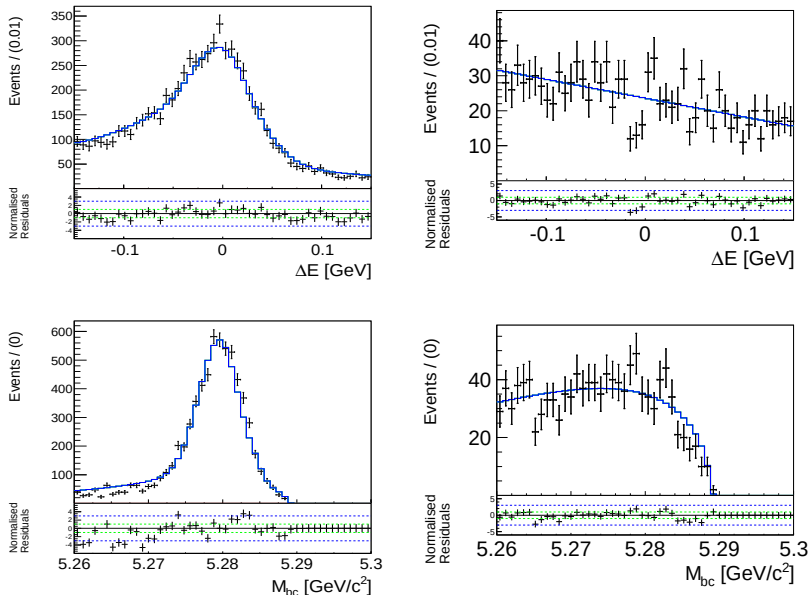

Figure C.72: Fit projections onto ΔE and $M_{\rm bc}$ of $B^0 \to \rho^\pm\pi^\mp\pi^0$ decays for the components $\pm$ (left) and 0. The black points show simulated MC events and the solid line shows the fit result. The residuals are given beneath each distribution.

$B^0 \to \rho^\pm\pi^\mp\pi^0$ decays takes the form

$$\begin{aligned}
&\mathcal{PDF}_{\rho^\pm\pi^\mp\pi^0}(\Delta E, M_{\rm bc}, m_{\pi^+\pi^0}, m_{\pi^-\pi^0}, \cos\theta_{\rm H}^+, \cos\theta_{\rm H}^-, \mathcal{F}_{B\bar{B}/q\bar{q}}, \Delta t, q) \equiv \\
&\Big((1-f_0)\times\mathcal{PDF}^{\pm}_{\rho^\pm\pi^\mp\pi^0}(\Delta E|M_{\rm bc}, \cos\theta_{\rm H}^+, \cos\theta_{\rm H}^-)\times\mathcal{PDF}^{\pm}_{\rho^\pm\pi^\mp\pi^0}(M_{\rm bc}|\cos\theta_{\rm H}^+, \cos\theta_{\rm H}^-)\times \\
&\big(f_+\times\mathcal{PDF}^{+}_{\rho^\pm\pi^\mp\pi^0}(m_{\pi^+\pi^0}, m_{\pi^-\pi^0}|\cos\theta_{\rm H}^+, \cos\theta_{\rm H}^-)\times\mathcal{PDF}^{+}_{\rho^\pm\pi^\mp\pi^0}(\cos\theta_{\rm H}^+, \cos\theta_{\rm H}^-)+ \\
&(1-f_+)\times\mathcal{PDF}^{-}_{\rho^\pm\pi^\mp\pi^0}(m_{\pi^+\pi^0}, m_{\pi^-\pi^0}|\cos\theta_{\rm H}^+, \cos\theta_{\rm H}^-)\times\mathcal{PDF}^{-}_{\rho^\pm\pi^\mp\pi^0}(\cos\theta_{\rm H}^+, \cos\theta_{\rm H}^-)\big)+ \\
&f_0\times\mathcal{PDF}^{0}_{\rho^\pm\pi^\mp\pi^0}(\Delta E)\times\mathcal{PDF}^{0}_{\rho^\pm\pi^\mp\pi^0}(M_{\rm bc})\times\mathcal{PDF}^{0}_{\rho^\pm\pi^\mp\pi^0}(m_{\pi^+\pi^0}, m_{\pi^-\pi^0})\times \\
&\mathcal{PDF}^{0}_{\rho^\pm\pi^\mp\pi^0}(\cos\theta_{\rm H}^+, \cos\theta_{\rm H}^-)\Big) \\
&\mathcal{PDF}_{\rho^\pm\pi^\mp\pi^0}(\mathcal{F}_{B\bar{B}/q\bar{q}})\times\mathcal{PDF}_{\rho^\pm\pi^\mp\pi^0}(\Delta t, q)
\end{aligned} \tag{C.55}$$

0	ΔE	M_{bc}	$m^1_{\pi^+\pi^-}$	$m^2_{\pi^+\pi^-}$	$\mathcal{F}_{B\bar{B}/q\bar{q}}$	$\cos\theta^1_{\rm H}$	$\cos\theta^2_{\rm H}$	Δt
ΔE	1	0.00	0.04	-0.01	0.01	-0.07	-0.04	0.01
M_{bc}		1	-0.03	-0.01	0.05	0.04	0.01	0.01
$m^1_{\pi^+\pi^-}$			1	-0.02	-0.01	0.04	-0.04	-0.01
$m^2_{\pi^+\pi^-}$				1	-0.01	0.00	-0.01	-0.00
$\mathcal{F}_{B\bar{B}/q\bar{q}}$					1	0.03	0.01	-0.02
$\cos\theta^1_{\rm H}$						1	-0.10	0.00
$\cos\theta^2_{\rm H}$							1	0.00
Δt								1

Table C.33: Correlation matrix for $B \to \rho^+\pi^-\pi^0$ decays.

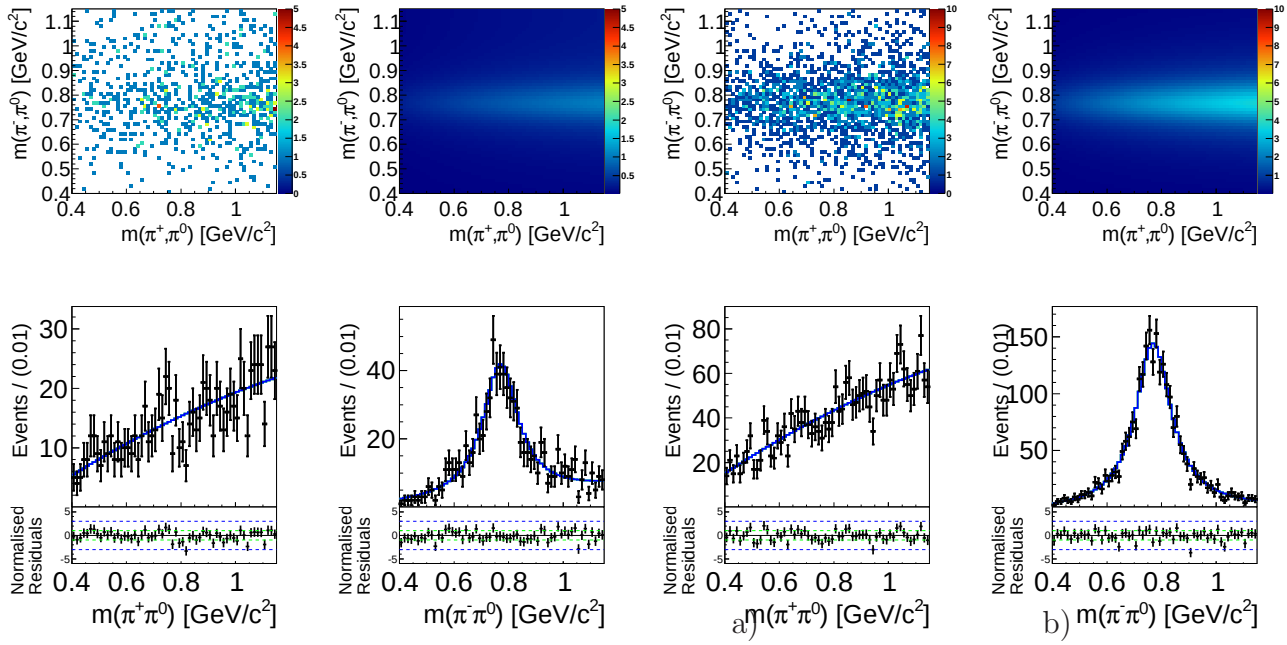

Figure C.73: Fit projections onto $m_{\pi^{\pm}\pi^0}$ of $B^0 \to \rho^{\pm}\pi^{\mp}\pi^0$ decays for the component − onto two different slices of the helicity distribution. The black points show simulated MC events and the solid line shows the fit result. The residuals are given beneath each distribution.

0	ΔE	M_{bc}	$m^1_{\pi^+\pi^-}$	$m^2_{\pi^+\pi^-}$	$\mathcal{F}_{B\bar{B}/q\bar{q}}$	$\cos\theta^1_{\rm H}$	$\cos\theta^2_{\rm H}$	Δt
ΔE	1	-0.00	0.01	0.03	0.01	-0.08	-0.04	-0.01
M_{bc}		1	-0.02	-0.04	0.05	0.04	0.03	-0.01
$m^1_{\pi^+\pi^-}$			1	-0.00	-0.05	-0.04	0.00	0.00
$m^2_{\pi^+\pi^-}$				1	-0.02	-0.05	0.02	0.02
$\mathcal{F}_{B\bar{B}/q\bar{q}}$					1	0.03	-0.00	-0.02
$\cos\theta^1_{\rm H}$						1	-0.10	-0.03
$\cos\theta^2_{\rm H}$							1	-0.00
Δt								1

Table C.34: Correlation matrix for $B \to \rho^-\pi^+\pi^0$ decays.

0	ΔE	M_{bc}	$m^1_{\pi^+\pi^-}$	$m^2_{\pi^+\pi^-}$	$\mathcal{F}_{B\bar{B}/q\bar{q}}$	$\cos\theta^1_{\rm H}$	$\cos\theta^2_{\rm H}$	Δt
ΔE	1	-0.00	-0.06	-0.02	0.05	0.01	-0.01	-0.01
M_{bc}		1	0.04	0.04	0.06	0.07	0.02	-0.02
$m^1_{\pi^+\pi^-}$			1	0.03	0.02	-0.03	0.07	-0.03
$m^2_{\pi^+\pi^-}$				1	-0.01	0.01	0.01	0.01
$\mathcal{F}_{B\bar{B}/q\bar{q}}$					1	0.04	0.03	-0.03
$\cos\theta^1_{\rm H}$						1	-0.50	0.02
$\cos\theta^2_{\rm H}$							1	-0.02
Δt								1

Table C.35: Correlation matrix for mis-reconstructed $B \to \rho^{\pm}\pi^{\mp}\pi^0$ decays.

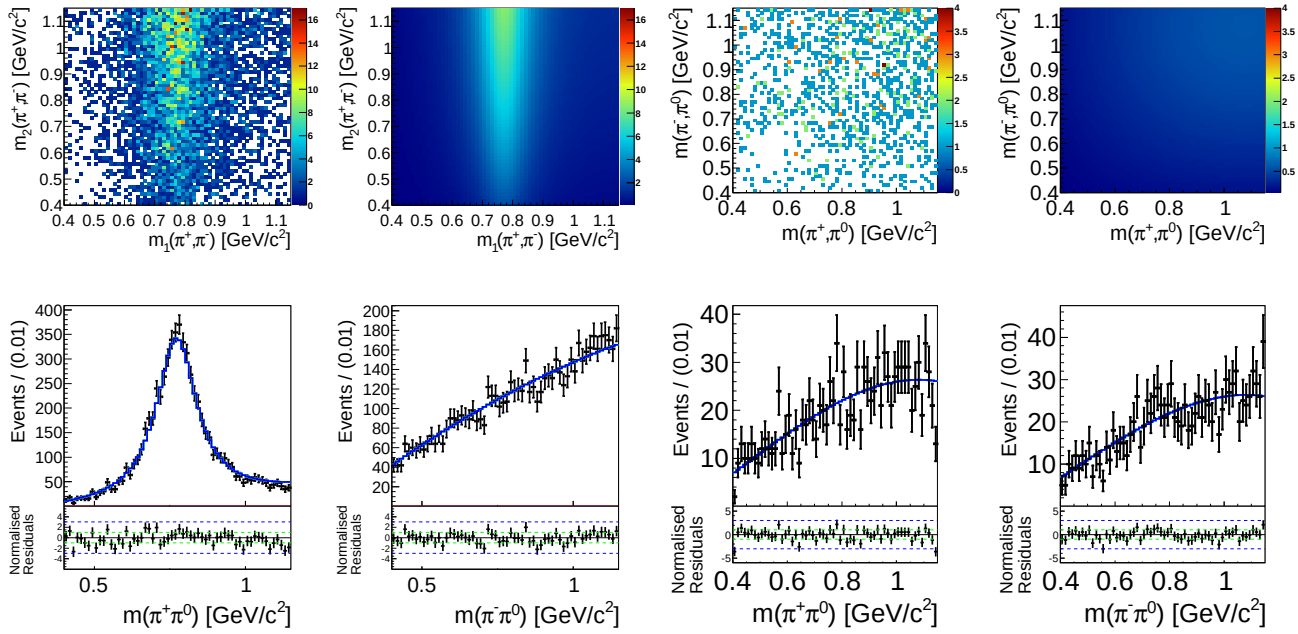

Figure C.74: Fit projections onto $m_{\pi^+\pi^0} - m_{\pi^-\pi^0}$ of $B^0 \to \rho^\pm\pi^\mp\pi^0$ decays for the components $\pm$ (left) and 0. The black points show simulated MC events and the solid line shows the fit result. The residuals are given beneath each distribution.

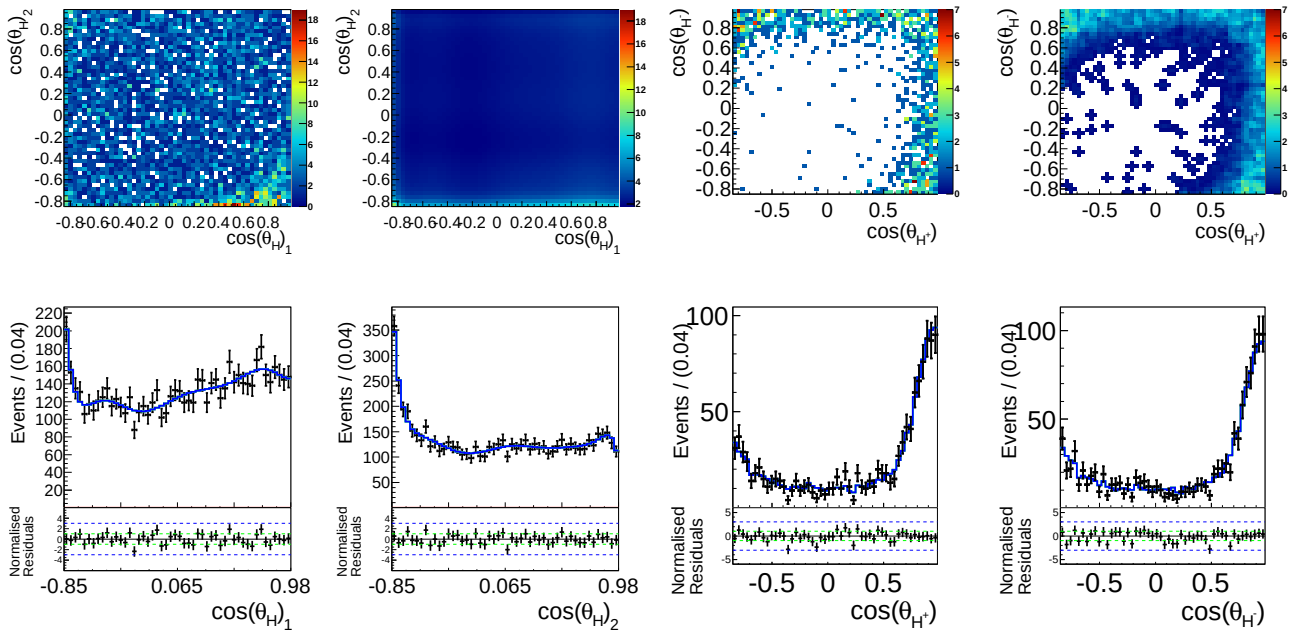

Figure C.75: Fit projections onto $\cos\theta_{\rm H}^+ - \cos\theta_{\rm H}^-$ of $B^0 \to \rho^\pm\pi^\mp\pi^0$ decays for the components $\pm$ (left) and 0. The black points show simulated MC events and the solid line shows the fit result. The residuals are given beneath each distribution.

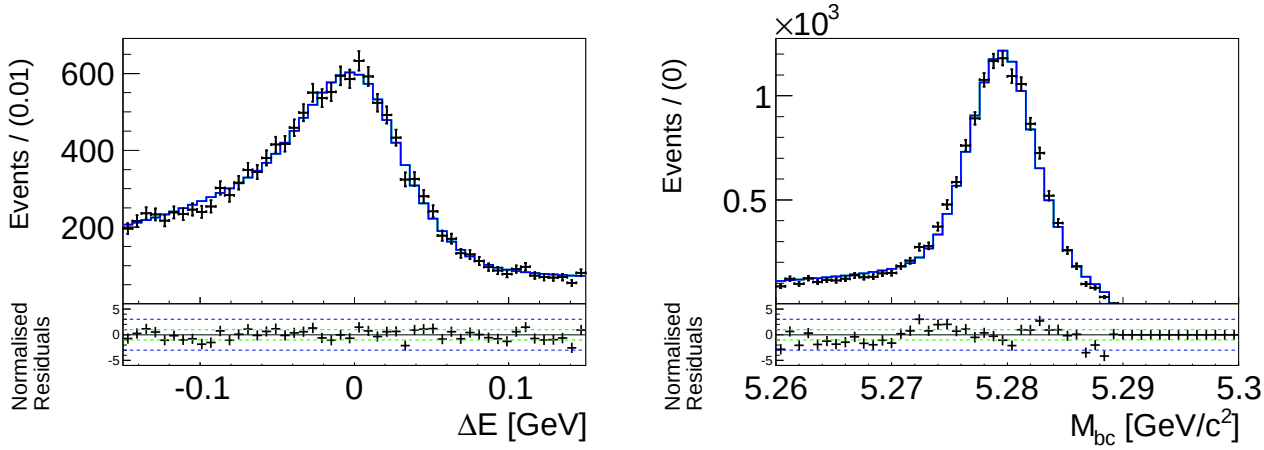

Figure C.76: Full projections onto ΔE and $M_{\rm bc}$ of $B^0 \to \rho^{\pm}\pi^{\mp}\pi^0$ decays. The black points show simulated MC events and the solid line shows the fit result. The residuals are given beneath each distribution.

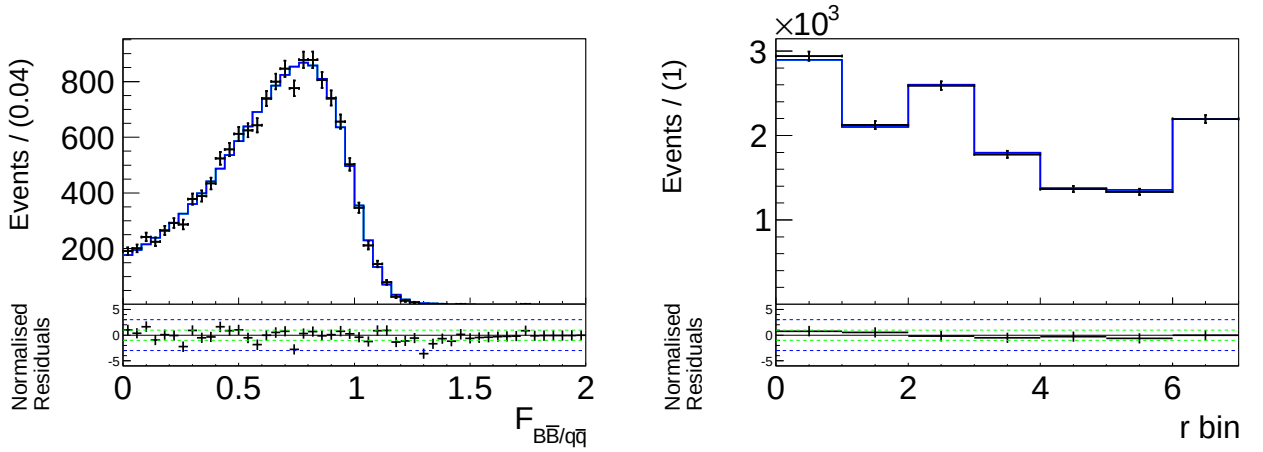

Figure C.77: Full projections onto $\mathcal{F}_{B\bar{B}/q\bar{q}}$ and the r-bin fractions of $B^0 \to \rho^{\pm}\pi^{\mp}\pi^0$ decays. The black points show simulated MC events and the solid line shows the fit result. The residuals are given beneath each distribution.

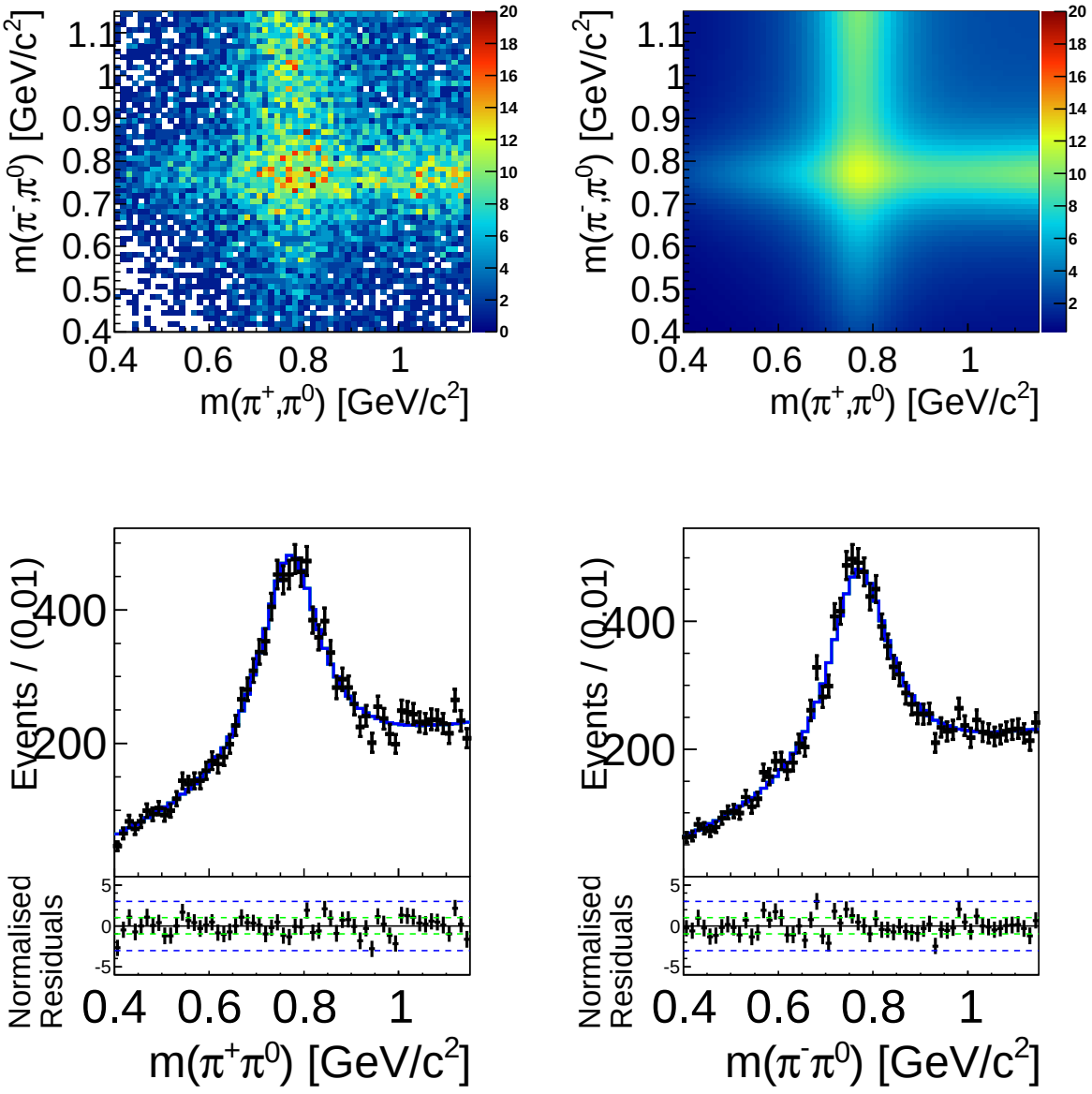

Figure C.78: Full projections onto $m_{\pi^+\pi^0} - m_{\pi^-\pi^0}$ of $B^0 \to \rho^{\pm}\pi^{\mp}\pi^0$ decays. The black points show simulated MC events and the solid line shows the fit result. The residuals are given beneath each distribution.

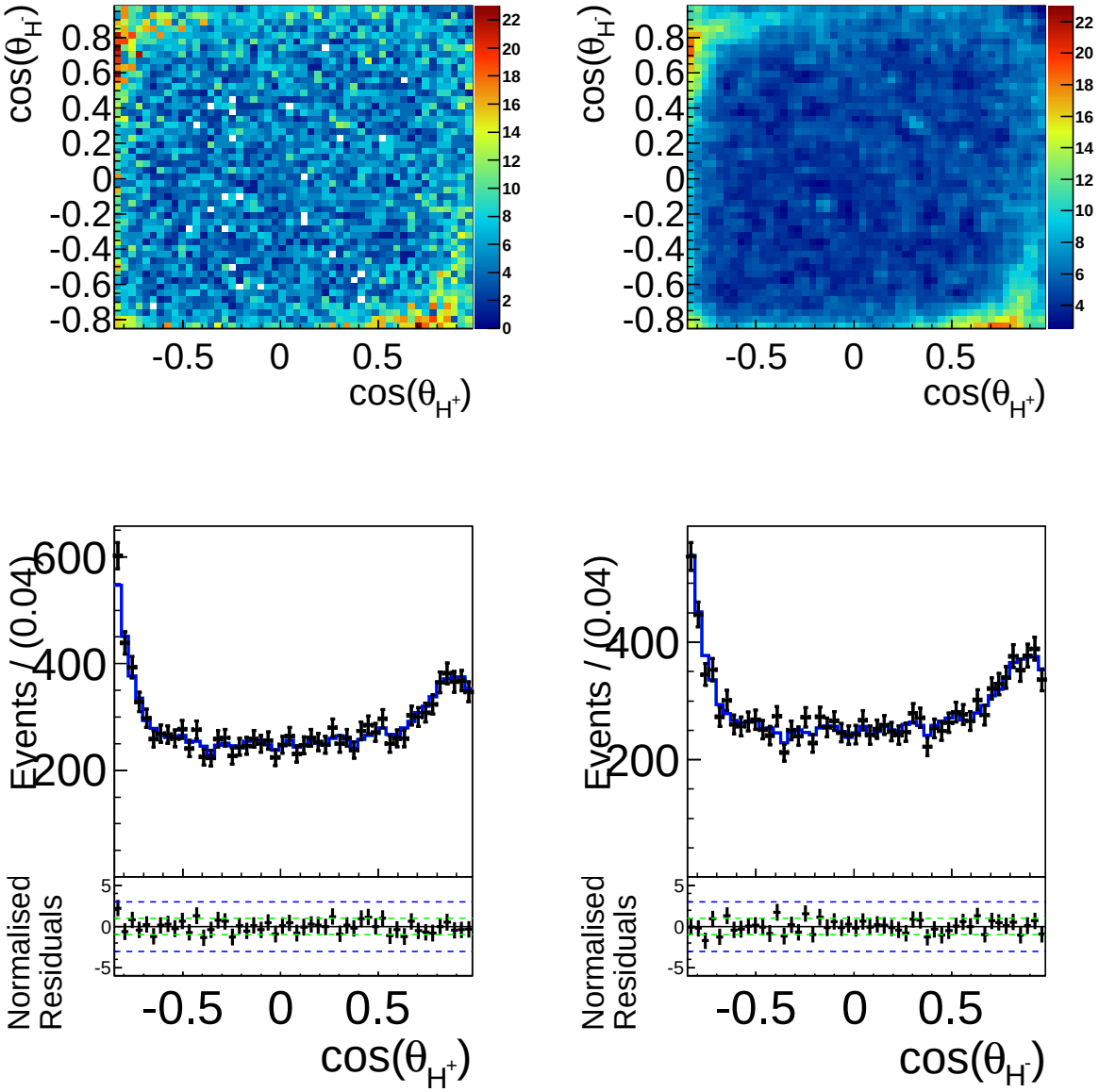

Figure C.79: Full projections onto $\cos\theta_{\rm H}^{+} - \cos\theta_{\rm H}^{-}$ of $B^0 \to \rho^{\pm}\pi^{\mp}\pi^0$ decays. The black points show simulated MC events and the solid line shows the fit result. The residuals are given beneath each distribution.

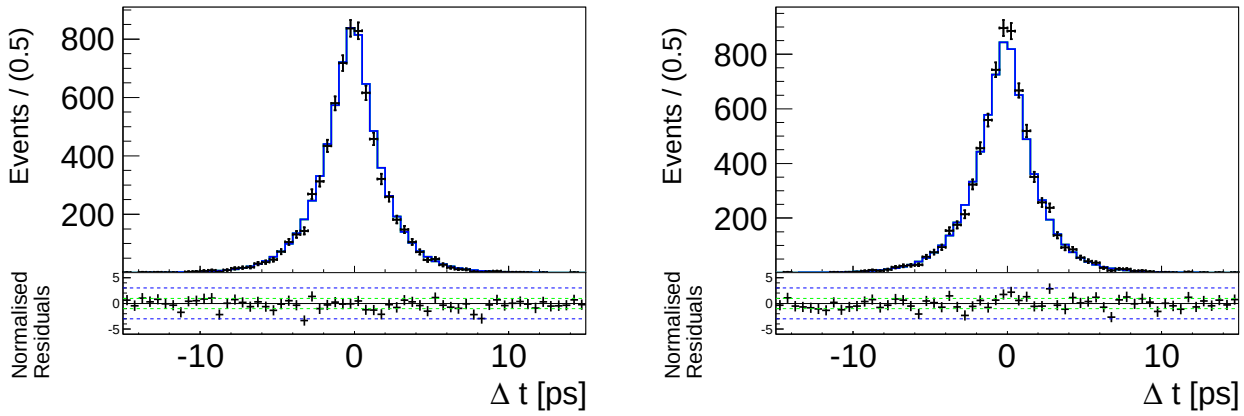

Figure C.80: Full projections onto Δt of $B^0 \to \rho^{\pm}\pi^{\mp}\pi^0$ decays for $q = +1$ (left) and $q = -1$. The black points show simulated MC events and the solid line shows the fit result. The residuals are given beneath each distribution.

C.2.4 Model For $B^0 \to \rho^0\pi^0\pi^0$ And $B^0 \to f_0\pi^0\pi^0$ Decays

Both components are parametrized with similar PDFs, the subscript $\rho^0\pi^0\pi^0$ has to be substituted with $f_0\pi^0\pi^0$ to obtain the PDF for $B^0 \to f_0\pi^0\pi^0$ decays. The agreement between the distributions of both decays is good enough to safely neglect $B^0 \to f_0\pi^0\pi^0$ in the fit. The expected yield is less then 24 events when we conservatively assume the branching fraction to be the measured upper limit of its isospin partner decay $B^0 \to f_0\pi^+\pi^-$, with $\mathcal{B}(B^0 \to f_0\pi^+\pi^-) < 3 \times 10^{-6}$ [5].
The ΔE, $M_{\rm bc}$ and $\mathcal{F}_{B\bar{B}/q\bar{q}}$ distributions are described as mentioned in Appendix C.2, the projections onto them for both decays are shown in Figs. C.81 and C.82 and Figs. C.86 and C.87. The projections onto the remaining distributions are shown in Figs. C.83 to C.85 and Figs. C.88 to C.90. The PDF for the mass distribution is take to be the product of a sum of a second and third order Chebychev polynomial for each dipion mass

$$\mathcal{P}_{\rho^0\pi^0\pi^0}(m_{\pi^\pm\pi^0}) \equiv \sum_{i=2}^{3} c_i C_i(m_{\pi^\pm\pi^0}). \tag{C.56}$$

The helicity PDF is taken to be a two-dimensional histogram

$$\mathcal{P}_{\rho^0\pi^0\pi^0}(\cos\theta_{\rm H}^+, \cos\theta_{\rm H}^-) \equiv H(\cos\theta_{\rm H}^+, \cos\theta_{\rm H}^-). \tag{C.57}$$

Because the π^0 momenta are usually higher then those of the charged ρ^0 daughters, the helicity angles peak at $\cos\theta_{\rm H} = +1$.
Δt is modeled according to Eq. (4.19) with an effective life time, $\tau^{\rm eff}_{\rho^0\pi^0\pi^0} = (1.23 \pm 0.02)$ ps. The correlations between the fit variables are listed in Tables C.36 and C.37 and the full PDF for $B^0 \to \rho^0\pi^0\pi^0$ decays takes the form

$$\begin{aligned}\mathcal{P}_{\rho^0\pi^0\pi^0}(\Delta E, M_{\rm bc}, m_{\pi^+\pi^0}, m_{\pi^-\pi^0}, \cos\theta_{\rm H}^+, \cos\theta_{\rm H}^-, \mathcal{F}_{B\bar{B}/q\bar{q}}, \Delta t, q) = \\ \mathcal{P}_{\rho^0\pi^0\pi^0}(\Delta E) \times \mathcal{P}_{\rho^0\pi^0\pi^0}(M_{\rm bc}) \times \mathcal{P}_{\rho^0\pi^0\pi^0}(m_{\pi^+\pi^0}) \times \mathcal{P}_{\rho^0\pi^0\pi^0}(m_{\pi^-\pi^0}) \\ \mathcal{P}_{\rho^0\pi^0\pi^0}(\cos\theta_{\rm H}^+, \cos\theta_{\rm H}^-) \times \mathcal{P}^k_{\rho^0\pi^0\pi^0}(\mathcal{F}_{B\bar{B}/q\bar{q}}) \times \mathcal{P}_{\rho^0\pi^0\pi^0}(\Delta t, q).\end{aligned} \tag{C.58}$$

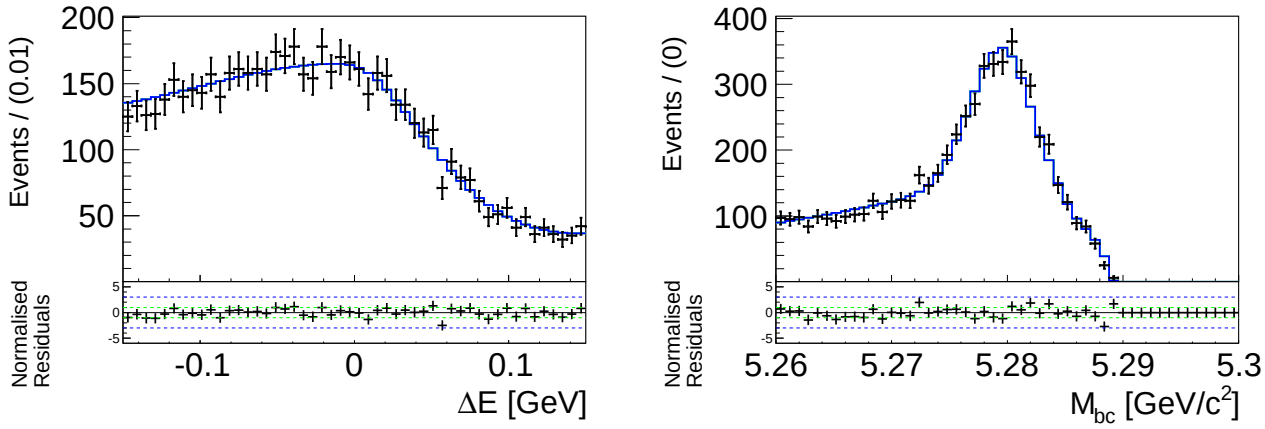

Figure C.81: Full projections onto ΔE and $M_{\rm bc}$ of $B^0 \to \rho^0\pi^0\pi^0$ decays. The black points show simulated MC events and the solid line shows the fit result. The residuals are given beneath each distribution.

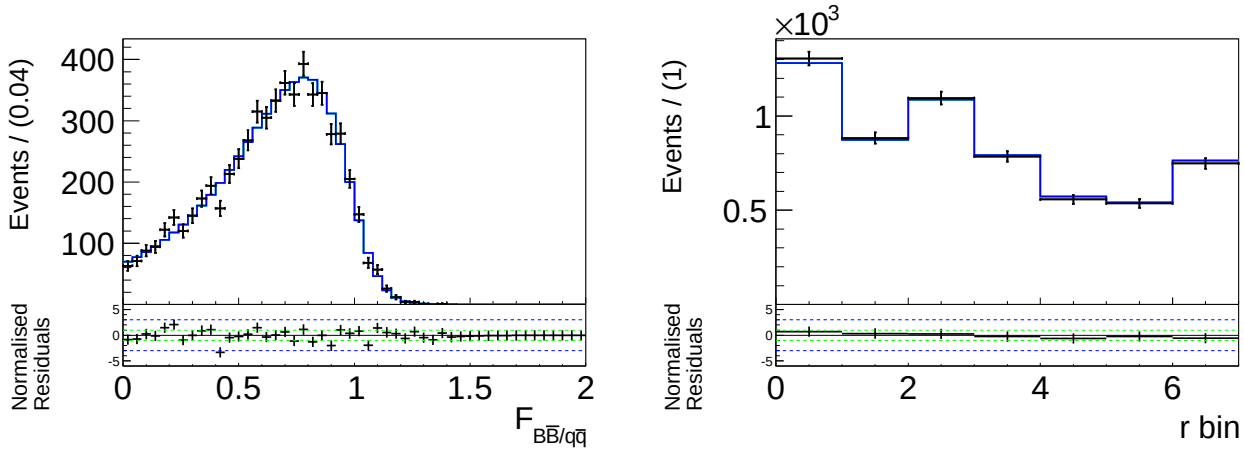

Figure C.82: Full projections onto $\mathcal{F}_{B\bar{B}/q\bar{q}}$ and the r-bin fractions of $B^0 \to \rho^0\pi^0\pi^0$ decays. The black points show simulated MC events and the solid line shows the fit result. The residuals are given beneath each distribution.

0	ΔE	M_{bc}	$m^1_{\pi^+\pi^-}$	$m^2_{\pi^+\pi^-}$	$\mathcal{F}_{B\bar{B}/q\bar{q}}$	$\cos\theta^1_{\rm H}$	$\cos\theta^2_{\rm H}$	Δt
ΔE	1	-0.01	-0.00	0.00	0.02	-0.04	-0.05	0.01
M_{bc}		1	0.06	0.04	0.03	0.06	0.09	0.00
$m^1_{\pi^+\pi^-}$			1	-0.02	-0.01	0.04	-0.09	0.00
$m^2_{\pi^+\pi^-}$				1	-0.03	-0.10	0.04	-0.01
$\mathcal{F}_{B\bar{B}/q\bar{q}}$					1	0.02	0.06	0.00
$\cos\theta^1_{\rm H}$						1	-0.47	-0.01
$\cos\theta^2_{\rm H}$							1	0.02
Δt								1

Table C.36: Correlation matrix for $B^0 \to \rho^0\pi^0\pi^0$ decays.

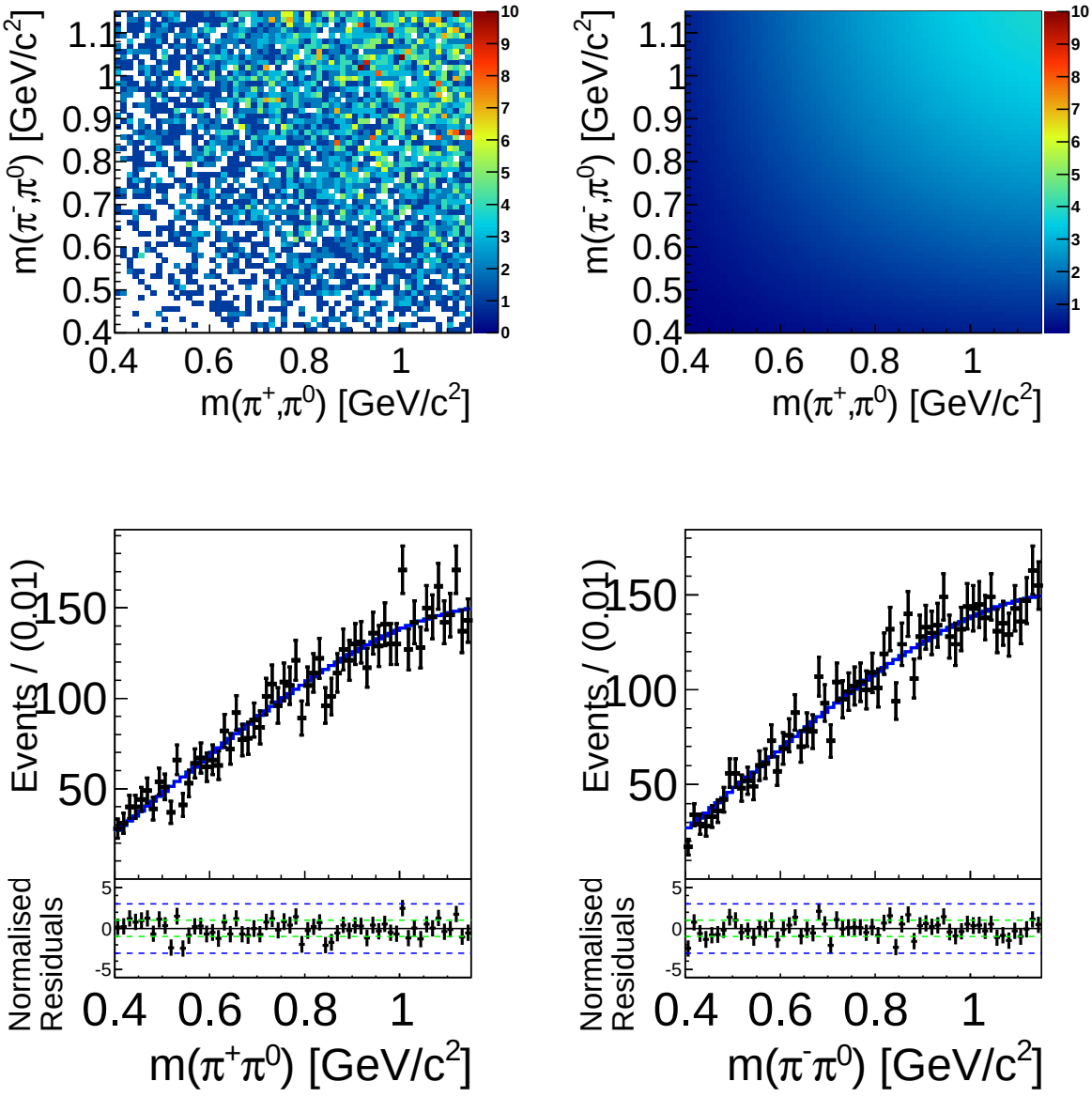

Figure C.83: Full projections onto $m_{\pi^+\pi^0} - m_{\pi^-\pi^0}$ of $B^0 \to \rho^0\pi^0\pi^0$ decays. The black points show simulated MC events and the solid line shows the fit result. The residuals are given beneath each distribution.

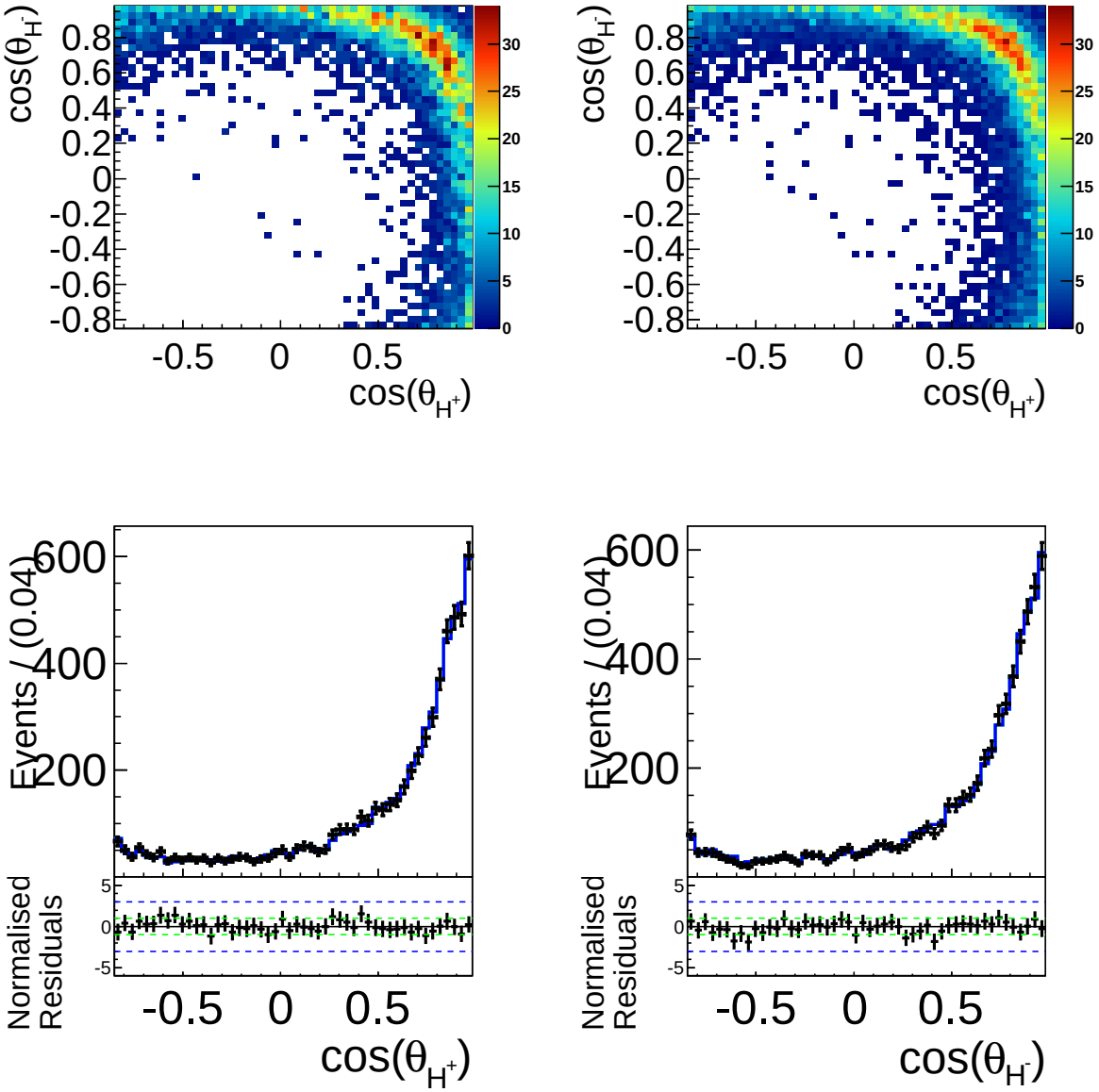

Figure C.84: Full projections onto $\cos\theta_{\rm H}^{+} - \cos\theta_{\rm H}^{-}$ of $B^0 \to \rho^0\pi^0\pi^0$ decays. The black points show simulated MC events and the solid line shows the fit result. The residuals are given beneath each distribution.

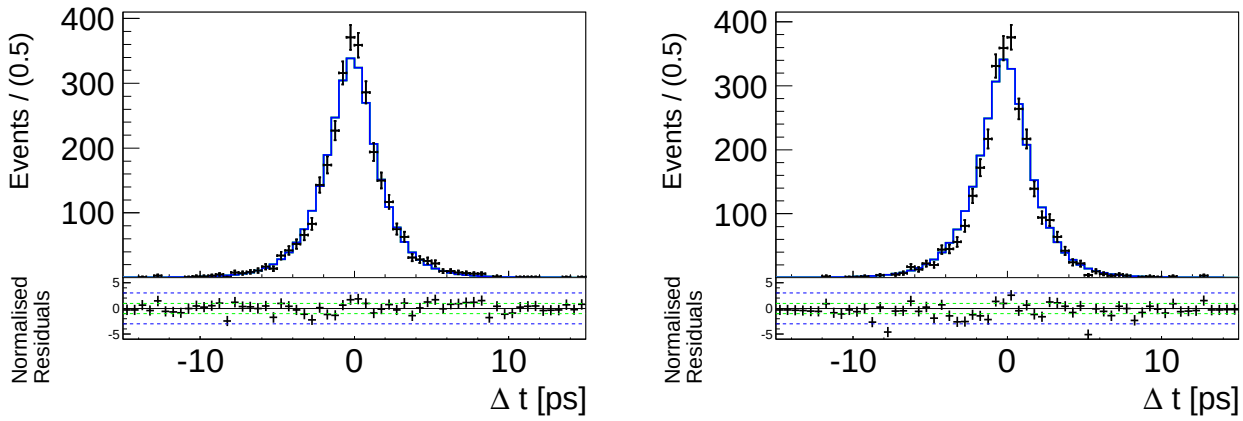

Figure C.85: Full projections onto Δt of $B^0 \to \rho^0\pi^0\pi^0$ decays for $q = +1$ (left) and $q = -1$. The black points show simulated MC events and the solid line shows the fit result. The residuals are given beneath each distribution.

Figs. C.86 to C.90 shows the distributions for $B^0 \to f_0\pi^0\pi^0$ decays and Table C.37 the parameter correlations.

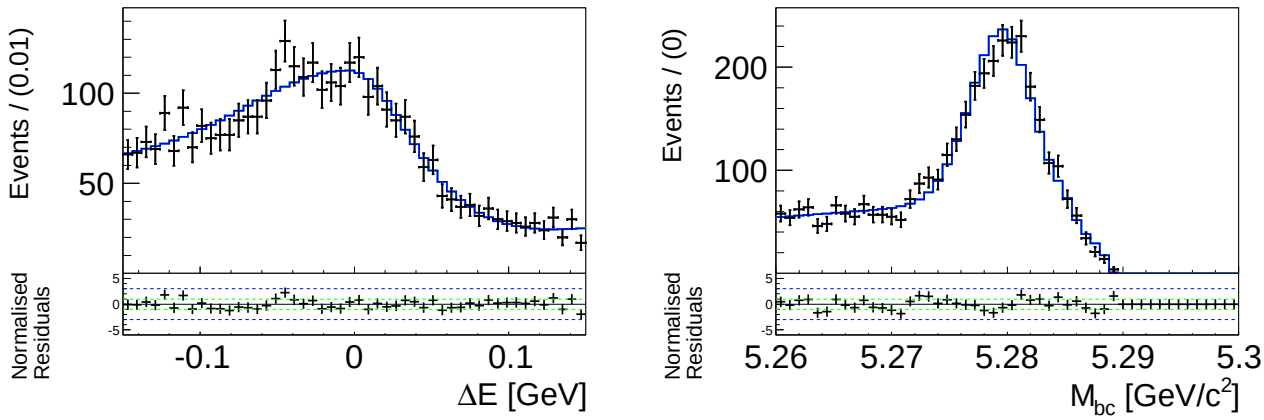

Figure C.86: Full projections onto ΔE and $M_{\rm bc}$ of $B^0 \to f_0\pi^0\pi^0$ decays. The black points show simulated MC events and the solid line shows the fit result. The residuals are given beneath each distribution.

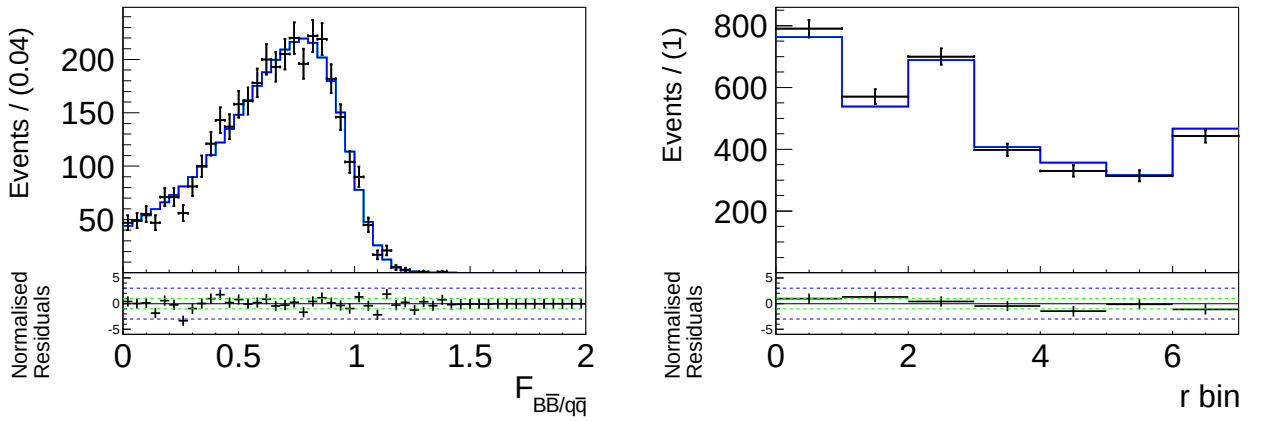

Figure C.87: Full projections onto $\mathcal{F}_{B\bar{B}/q\bar{q}}$ and the r-bin fractions of $B^0 \to f_0\pi^0\pi^0$ decays. The black points show simulated MC events and the solid line shows the fit result. The residuals are given beneath each distribution.

0	ΔE	M_{bc}	$m^1_{\pi^+\pi^-}$	$m^2_{\pi^+\pi^-}$	$\mathcal{F}_{B\bar{B}/q\bar{q}}$	$\cos\theta^1_{\rm H}$	$\cos\theta^2_{\rm H}$	Δt
ΔE	1	-0.05	-0.01	-0.03	0.02	-0.06	-0.04	-0.01
M_{bc}		1	0.04	0.03	0.07	0.04	0.06	-0.05
$m^1_{\pi^+\pi^-}$			1	0.01	-0.02	0.03	-0.09	-0.02
$m^2_{\pi^+\pi^-}$				1	0.02	-0.07	-0.02	-0.01
$\mathcal{F}_{B\bar{B}/q\bar{q}}$					1	-0.01	0.05	0.01
$\cos\theta^1_{\rm H}$						1	-0.55	0.01
$\cos\theta^2_{\rm H}$							1	-0.01
Δt								1

Table C.37: Correlation matrix for $B^0 \to f_0\pi^0\pi^0$ decays.

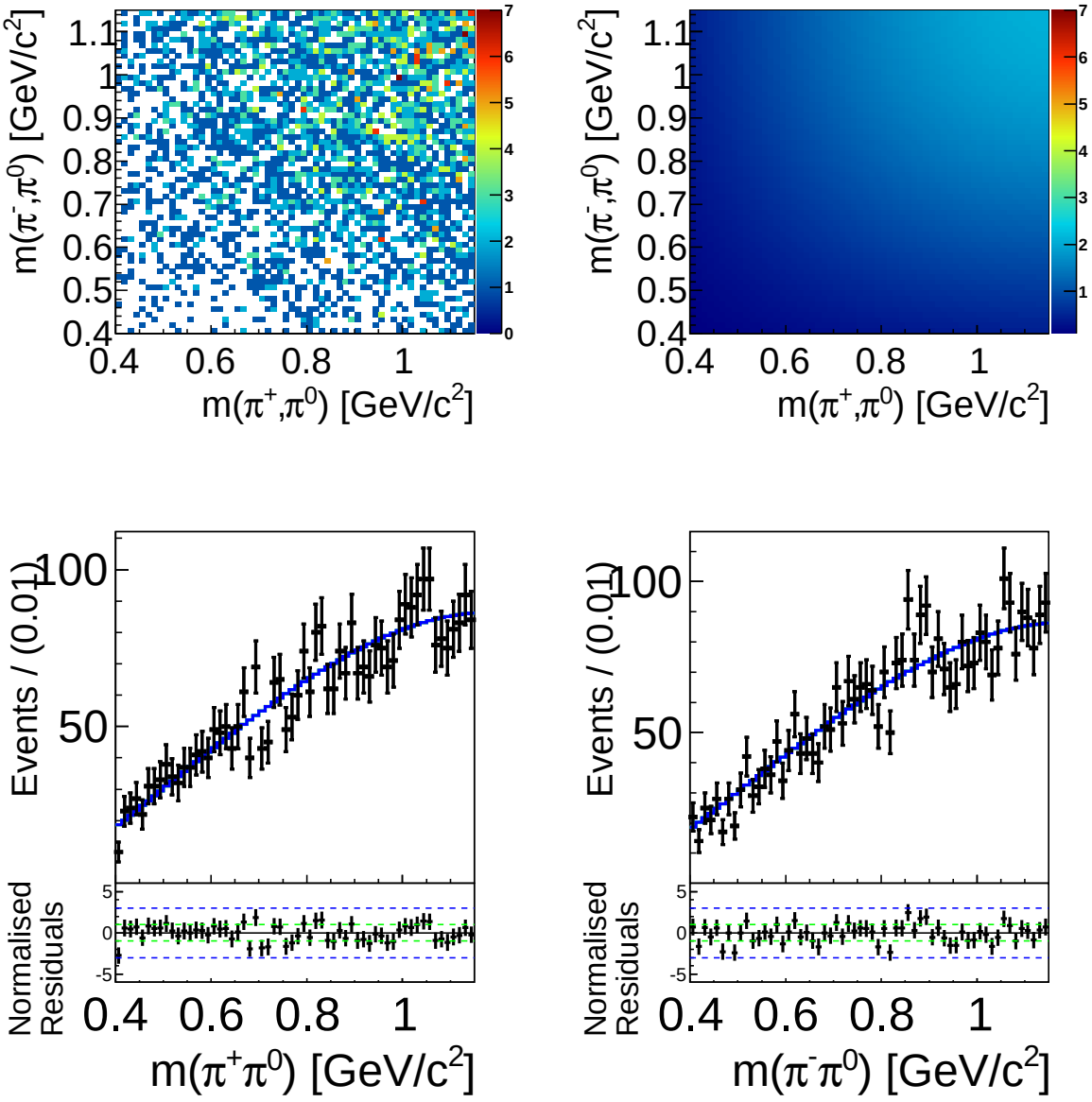

Figure C.88: Full projections onto $m_{\pi^+\pi^0} - m_{\pi^-\pi^0}$ of $B^0 \to f_0\pi^0\pi^0$ decays. The black points show simulated MC events and the solid line shows the fit result. The residuals are given beneath each distribution.

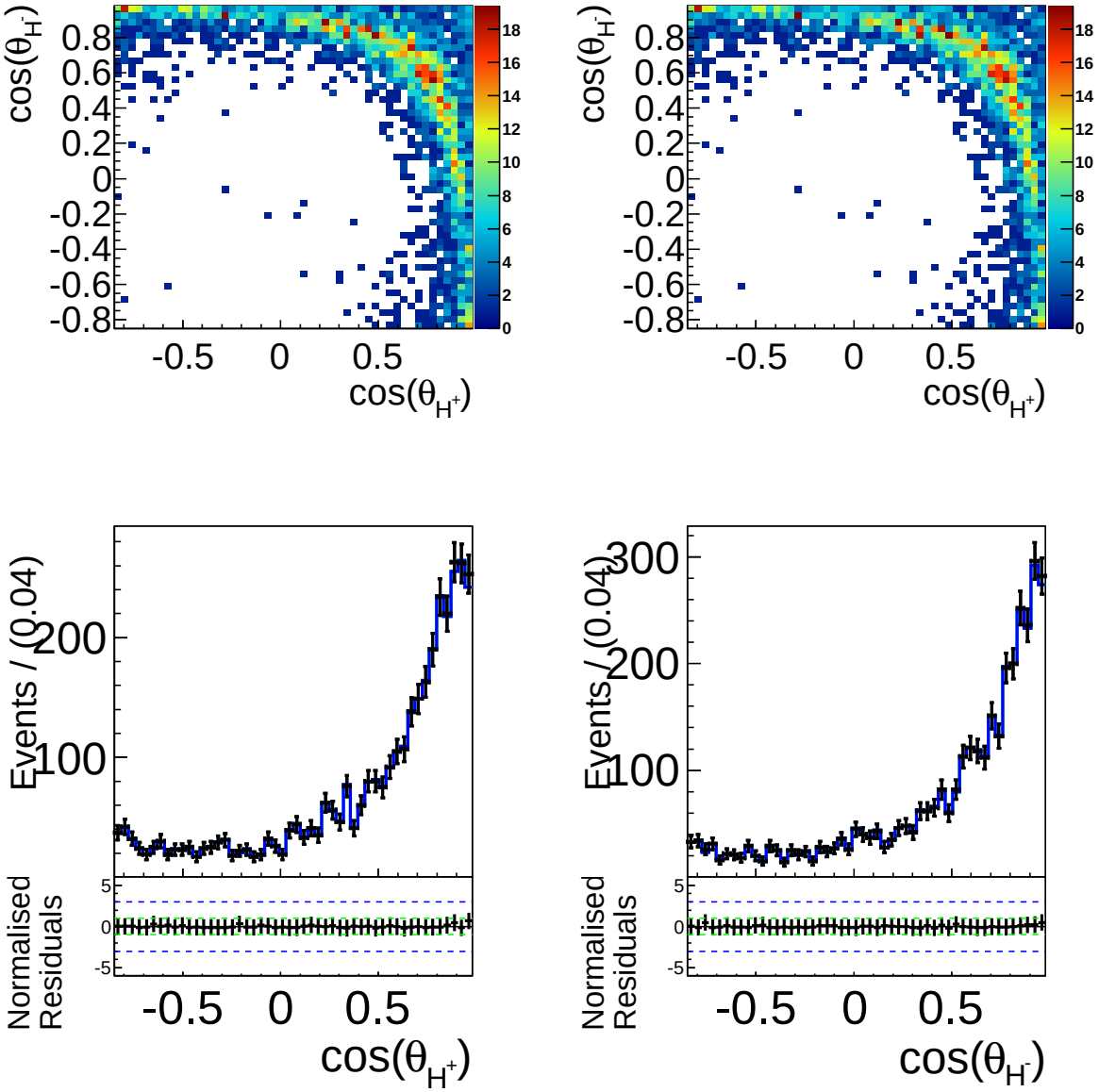

Figure C.89: Full projections onto $\cos\theta_{\rm H}^{+} - \cos\theta_{\rm H}^{-}$ of $B^0 \to f_0\pi^0\pi^0$ decays. The black points show simulated MC events and the solid line shows the fit result. The residuals are given beneath each distribution.

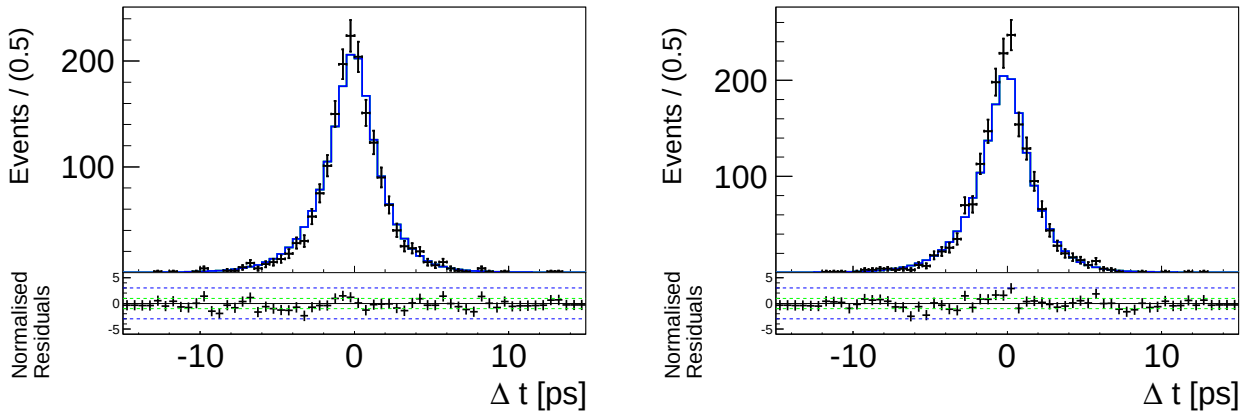

Figure C.90: Full projections onto Δt of $B^0 \to f_0\pi^0\pi^0$ decays for $q = +1$ (left) and $q = -1$. The black points show simulated MC events and the solid line shows the fit result. The residuals are given beneath each distribution.

C.2.5 Model For $B^0 \to \omega\pi^0$ Decays

Previous measurements of the mode $B^0 \to \omega\pi^0$ yield in an upper limit of 5×10^{-7} [45], which corresponds to an expected number of one event. Hence we fix this mode, and remove the event for the evaluation of an associated uncertainty. The model has a similar description of the $\mathcal{F}_{B\bar{B}/q\bar{q}}$ and $\Delta t, q$ distributions as the previous four-pion backgrounds, while the ΔE and $M_{\rm bc}$ distributions show a clear difference. Because only one $\pi^{\pm}\pi^0$ pair makes it into the mass region, all four pions are never correctly reconstruct to a B meson. Ergo, this mode is actually a non-peaking four-pion final state and the $\Delta E, M_{\rm bc}$ distributions are described by the PDFs for combinatorial background (see Eqs. (C.3) and (C.4)).
The two ρ-masses are depending on the helicity angles via

$$\mathcal{P}_{\omega\pi^0}(m_1, m_2|\cos\theta_{\rm H}^+, \cos\theta_{\rm H}^-) = (G(m_1) + c_1 C_1(m_1)) \times \sum_{i=1}^{3} c_i C_i(m_2), \tag{C.59}$$

where $m_1 = m_{\pi^+\pi^0}, m_2 = m_{\pi^-\pi^0}$ if $\cos\theta_{\rm H}^- > \cos\theta_{\rm H}^+$ and $m_1 = m_{\pi^-\pi^0}, m_2 = m_{\pi^+\pi^0}$ else. Two of the three pion daughters of the ω still result in a broad peak, shifted to the left of the ω mass.
The PDF for the helicity angles is the product of a sum of two Gaussians with a sum of Chebychev polynomials and is symmetrized as follows

$$\begin{aligned}\mathcal{P}_{\omega\pi^0}(\cos\theta_{\rm H}^+, \cos\theta_{\rm H}^-) = &\frac{1}{2}[(fG(\cos\theta_{\rm H}^+) + (1-f)G(\cos\theta_{\rm H}^+)) \times \sum_{i=1}^{3} c_i C_i(\cos\theta_{\rm H}^-)] \\ &+\frac{1}{2}[(fG(\cos\theta_{\rm H}^-) + (1-f)G(\cos\theta_{\rm H}^-)) \times \sum_{i=1}^{3} c_i C_i(\cos\theta_{\rm H}^+)].\end{aligned} \tag{C.60}$$

The projections onto each variable are shown in Figs. C.91 to C.95 and the correlation between the fit variables are listed in Table C.36. The total PDF for $B^0 \to \omega\pi^0$ events is in analogy to the previous described ones.

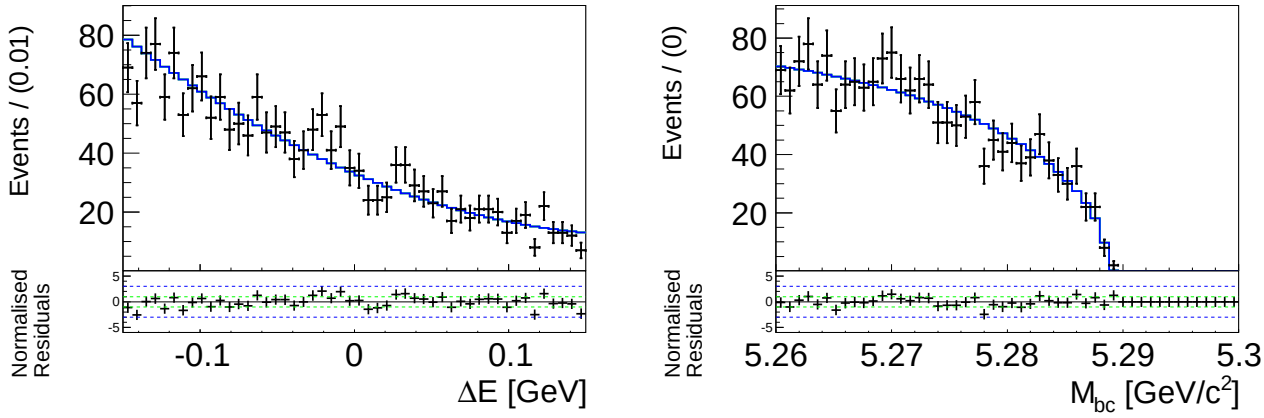

Figure C.91: Full projections onto ΔE and $M_{\rm bc}$ of $B^0 \to \omega\pi^0$ decays. The black points show simulated MC events and the solid line shows the fit result. The residuals are given beneath each distribution.

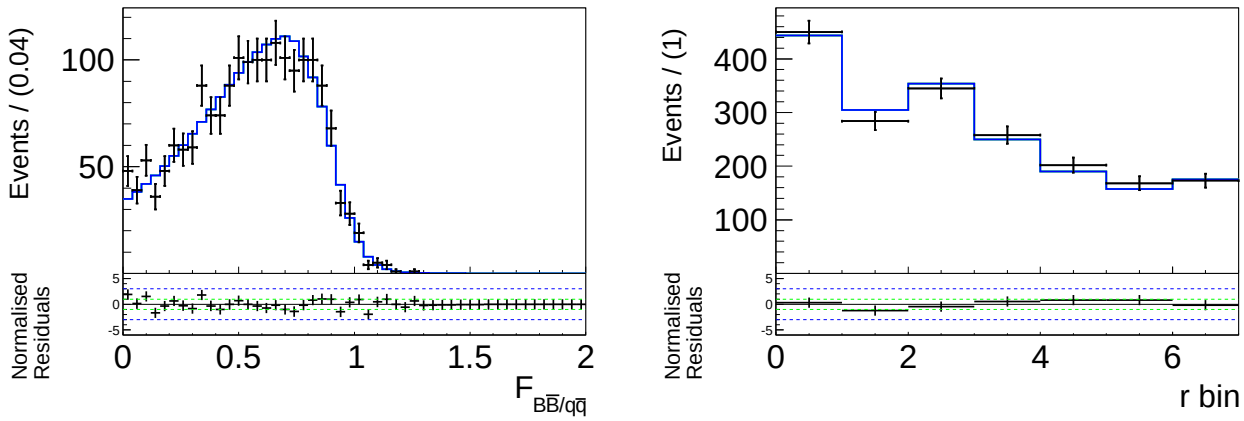

Figure C.92: Full projections onto $\mathcal{F}_{B\bar{B}/q\bar{q}}$ and the r-bin fractions of $B^0 \to \omega\pi^0$ decays. The black points show simulated MC events and the solid line shows the fit result. The residuals are given beneath each distribution.

0	ΔE	M_{bc}	$m^1_{\pi^+\pi^-}$	$m^2_{\pi^+\pi^-}$	$\mathcal{F}_{B\bar{B}/q\bar{q}}$	$\cos\theta^1_{\mathrm{H}}$	$\cos\theta^2_{\mathrm{H}}$	Δt
ΔE	1	-0.09	0.00	-0.01	-0.01	-0.03	-0.02	0.01
M_{bc}		1	0.01	-0.01	0.06	0.05	-0.01	-0.00
$m^1_{\pi^+\pi^-}$			1	-0.56	-0.04	0.59	-0.62	0.00
$m^2_{\pi^+\pi^-}$				1	-0.04	-0.63	0.59	-0.01
$\mathcal{F}_{B\bar{B}/q\bar{q}}$					1	-0.00	0.01	0.01
$\cos\theta^1_{\mathrm{H}}$						1	-0.67	0.01
$\cos\theta^2_{\mathrm{H}}$							1	0.01
Δt								1

Table C.38: Correlation matrix for $B^0 \to \omega\pi^0$ decays.

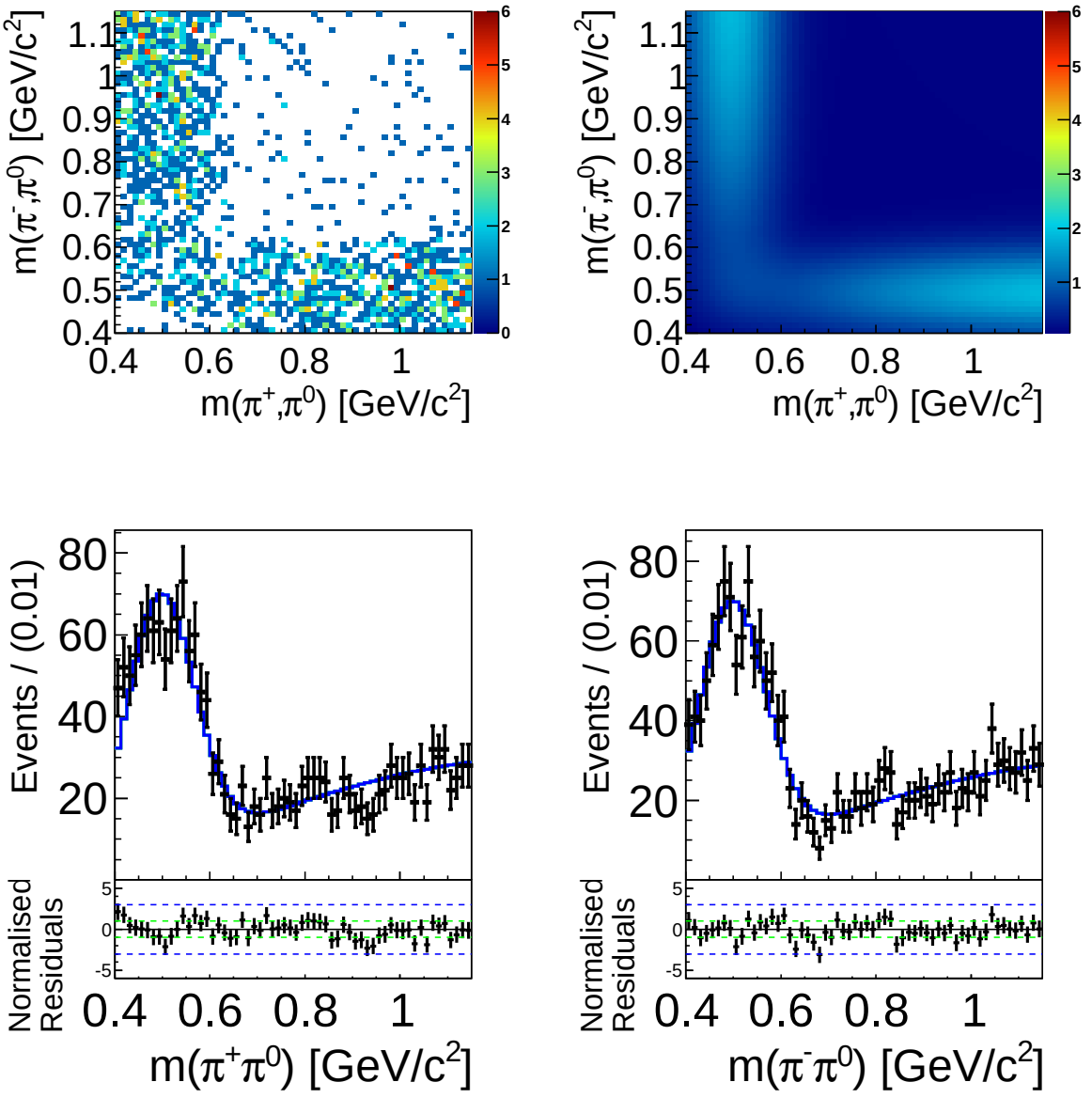

Figure C.93: Full projections onto $m_{\pi^+\pi^0} - m_{\pi^-\pi^0}$ of $B^0 \to \omega\pi^0$ decays. The black points show simulated MC events and the solid line shows the fit result. The residuals are given beneath each distribution.

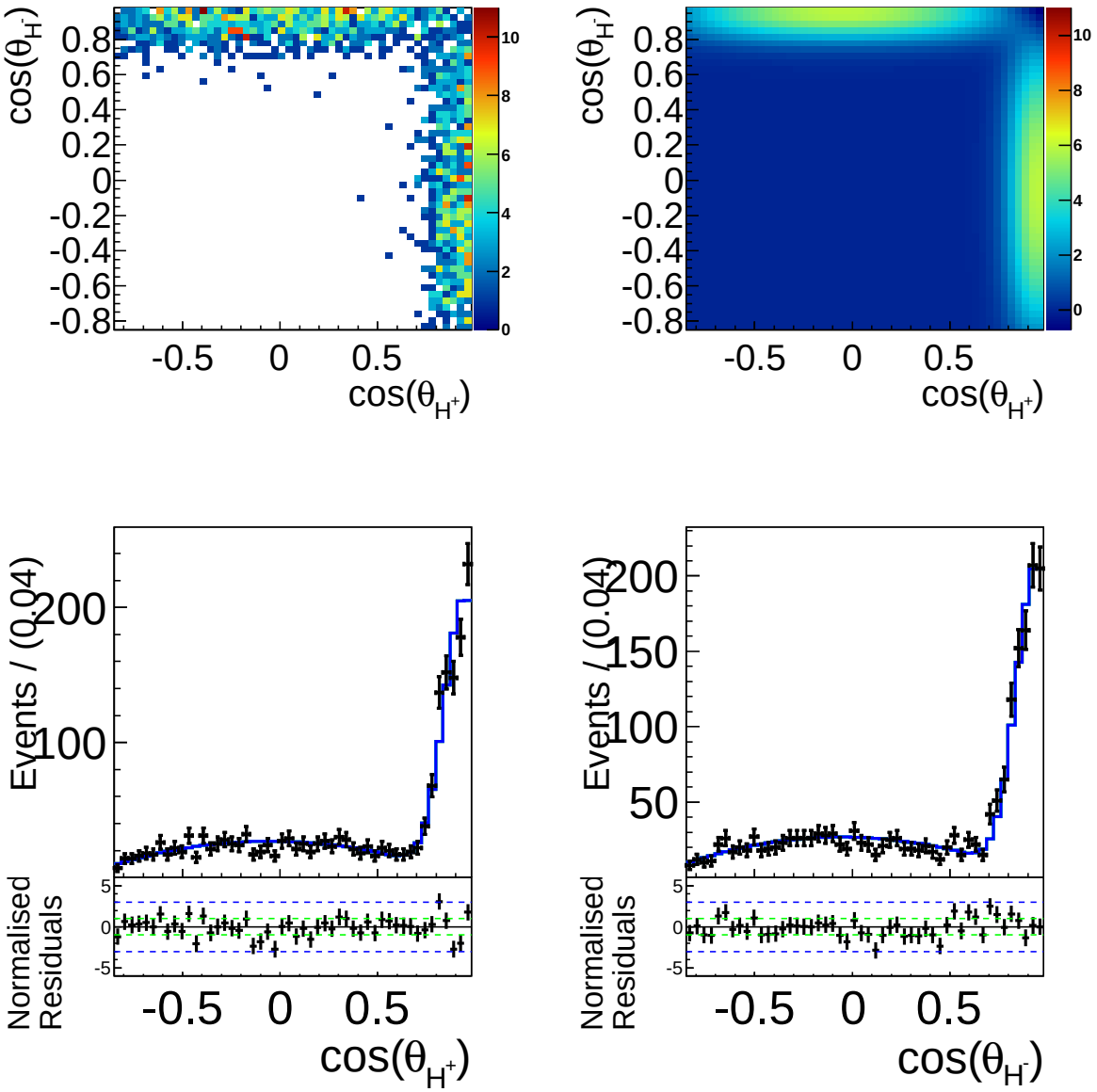

Figure C.94: Full projections onto $\cos\theta_{\rm H}^{+} - \cos\theta_{\rm H}^{-}$ of $B^0 \to \omega\pi^0$ decays. The black points show simulated MC events and the solid line shows the fit result. The residuals are given beneath each distribution.

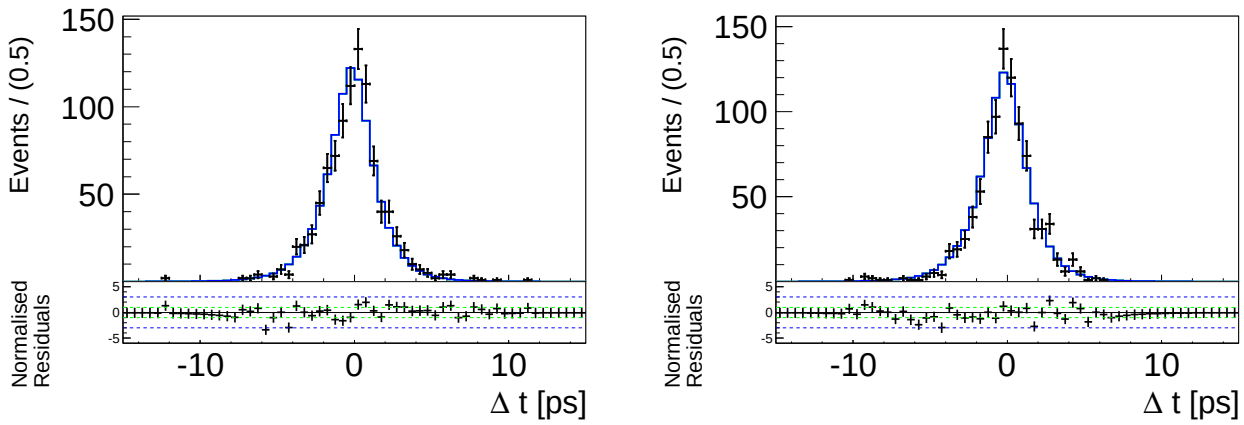

Figure C.95: Full projections onto Δt of $B^0 \to \omega\pi^0$ decays for $q = +1$ (left) and $q = -1$. The black points show simulated MC events and the solid line shows the fit result. The residuals are given beneath each distribution.

C.3 Off-Resonance Data

In the following, an alternative describtion of the continuum component is presented, obtained from studying off-resonance data taken 60 MeV below the $B\bar{B}$ threshold. However, we use the describtion from Section 4.4 as previously explained.
The ΔE distribution is described by the sum of Chebychev polynomials up to the second order,

$$\mathcal{P}_{q\bar{q}}(\Delta E) \equiv \sum_{i=1}^{2} c_i C_i(\Delta E), \tag{C.61}$$

and the $M_{\rm bc}$ distribution is described by an Argus function

$$\mathcal{P}_{q\bar{q}}(M_{\rm bc}) \equiv Ar(M_{\rm bc}). \tag{C.62}$$

The $\mathcal{F}_{B\bar{B}/q\bar{q}}$ distribution is described by a double-bifurcated Gaussian in each r-bin, k,

$$\mathcal{P}^k_{q\bar{q}}(\mathcal{F}_{B\bar{B}/q\bar{q}}) \equiv dbG^k(\mathcal{F}_{B\bar{B}/q\bar{q}}). \tag{C.63}$$

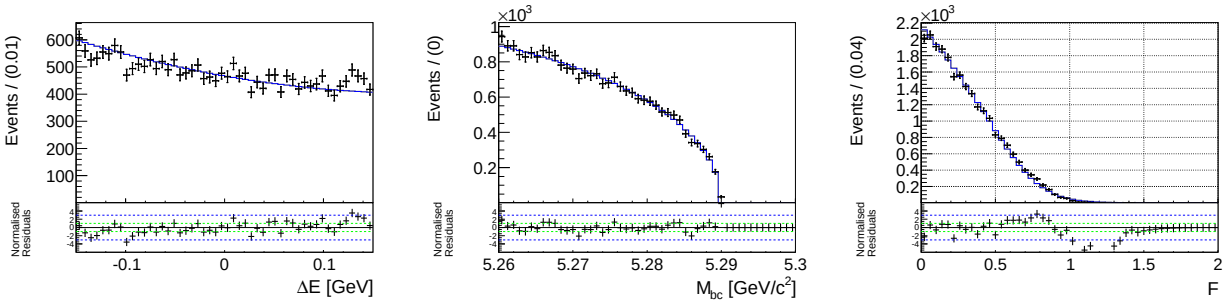

Figure C.96: Fit projections ont ΔE, $M_{\rm bc}$, and $\mathcal{F}_{B\bar{B}/q\bar{q}}$ of continuum data. The black points show simulated MC events and the solid line shows the fit result. The residuals are given beneath each distribution.

The PDF of each invariant dipion mass is taken to be the product of two Breit-Wigner functions and the sum of polynomials up to the fifth order,

$$\mathcal{P}_{q\bar{q}}(m_{\pi^\pm\pi^0}) \equiv BW(m_{\pi^\pm\pi^0}, m_1, \Gamma_1) \times BW(m_{\pi^\pm\pi^0}, m_2, \Gamma_2) \times \sum_{i=1}^{5} c_i^{\rm M} C_i(m_{\pi^\pm\pi^0}). \tag{C.64}$$

The sum of Chebychev polynomials up to the eighth order describes each $\cos\theta_{\rm H}$ distribution,

$$\mathcal{P}_{q\bar{q}}(\cos\theta_{\rm H}) \equiv \sum_{i=1}^{8} c_i^{\rm H} C_i(\cos\theta_{\rm H}). \tag{C.65}$$

The lifetime PDF is given by Eq. (4.69), projections onto Δt for each flavor q are shown in Fig. C.98.

The full PDF for continuum events is given by

$$\begin{aligned}\mathcal{PDF}_{q\bar{q}}(\Delta E, M_{\rm bc}, m_{\pi^+\pi^0}, m_{\pi^-\pi^0}, \cos\theta^+_{\rm H}, \cos\theta^-_{\rm H}, \mathcal{F}_{B\bar{B}/q\bar{q}}, \Delta t, q) \equiv \\ \mathcal{PDF}_{q\bar{q}}(\Delta E) \times \mathcal{PDF}_{q\bar{q}}(M_{\rm bc}) \times \mathcal{PDF}_{q\bar{q}}(m(\pi^+\pi^0)) \times \mathcal{PDF}_{q\bar{q}}(m(\pi^-\pi^0)) \\ \times \mathcal{PDF}_{q\bar{q}}(\cos\theta^+_{\rm H}) \times \mathcal{PDF}_{q\bar{q}}(\cos\theta^-_{\rm H}) \times \mathcal{PDF}_{q\bar{q}}(\mathcal{F}_{B\bar{B}/q\bar{q}}) \times \mathcal{PDF}_{q\bar{q}}(\Delta t, q).\end{aligned} \tag{C.66}$$

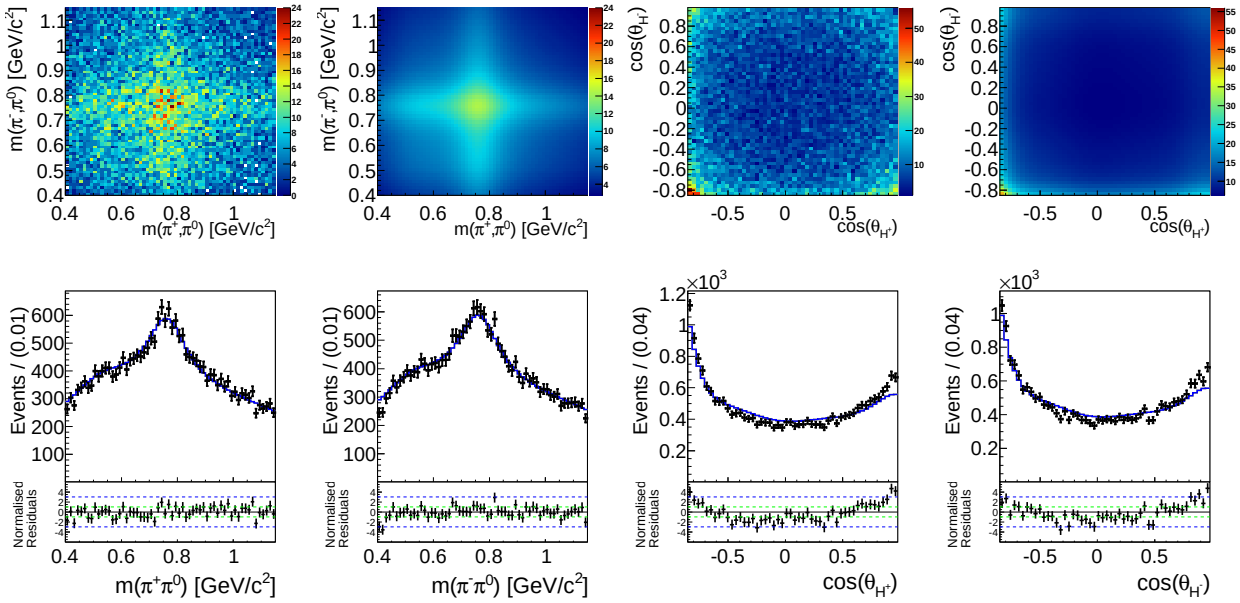

Figure C.97: Fit projections onto the dipion masses and helicity angles of continuum data. The helicity PDF is not finalized, because it is not used (see Section 4.4). The top row shows the 2D projection of the data (left) and the PDF (right) and the bottom row shows projection onto each axis, where the black points show simulated MC events and the solid line shows the fit result. The residuals are given beneath each distribution.

0	ΔE	M_{bc}	$m^1_{\pi^+\pi^-}$	$m^2_{\pi^+\pi^-}$	$\mathcal{F}_{B\bar{B}/q\bar{q}}$	$\cos\theta^1_{\rm H}$	$\cos\theta^2_{\rm H}$	Δt
ΔE	1	0.01	0.02	0.01	0.04	0.01	-0.00	0.01
M_{bc}		1	-0.00	0.01	-0.00	0.00	0.01	0.00
$m^1_{\pi^+\pi^-}$			1	-0.02	-0.03	0.06	0.01	-0.00
$m^2_{\pi^+\pi^-}$				1	0.02	-0.01	0.05	0.01
$\mathcal{F}_{B\bar{B}/q\bar{q}}$					1	-0.00	-0.00	0.01
$\cos\theta^1_{\rm H}$						1	-0.01	0.01
$\cos\theta^2_{\rm H}$							1	-0.01
Δt								1

Table C.39: Correlation matrix for SVD1 off-resonance data.

The full PDF for continuum events is given by

$$\begin{aligned}\mathcal{PDF}_{q\bar{q}}(\Delta E, M_{\rm bc}, m_{\pi^+\pi^0}, m_{\pi^-\pi^0}, \cos\theta^+_{\rm H}, \cos\theta^-_{\rm H}, \mathcal{F}_{B\bar{B}/q\bar{q}}, \Delta t, q) \equiv \\ \mathcal{PDF}_{q\bar{q}}(\Delta E)\mathcal{PDF}_{q\bar{q}}(M_{\rm bc}) \times \times \mathcal{PDF}_{q\bar{q}}(m_{\pi^+\pi^0}, m_{\pi^-\pi^0}) \\ \times \mathcal{PDF}_{q\bar{q}}(\cos\theta^+_{\rm H}, \cos\theta^-_{\rm H}) \times \ \mathcal{PDF}_{q\bar{q}}(\mathcal{F}_{B\bar{B}/q\bar{q}}) \times \mathcal{PDF}_{q\bar{q}}(\Delta t, q). \end{aligned} \tag{C.67}$$

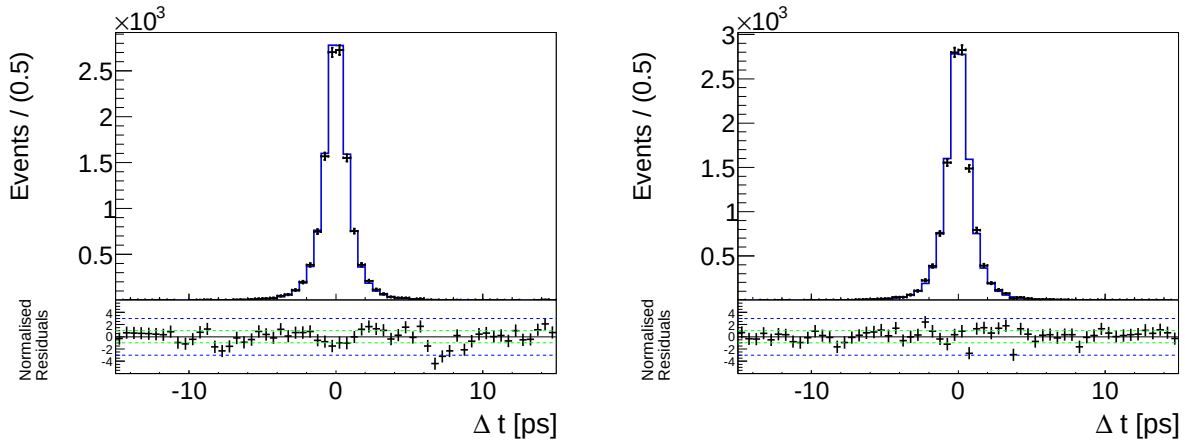

Figure C.98: Fit projections onto Δt of continuum data. Left shows events with $B_{\text{Tag}} = B^0$. The top row shows the 2D projection of the data (left) and the PDF (right) and the bottom row shows projection onto each axis, where the black points show simulated MC events and the solid line shows the fit result. The residuals are given beneath each distribution.

0	ΔE	M_{bc}	$m^1_{\pi^+\pi^-}$	$m^2_{\pi^+\pi^-}$	$\mathcal{F}_{B\bar{B}/q\bar{q}}$	$\cos\theta^1_{\text{H}}$	$\cos\theta^2_{\text{H}}$	Δt
ΔE	1	0.00	-0.00	0.01	0.02	-0.01	0.00	-0.00
M_{bc}		1	0.01	-0.00	-0.00	0.00	0.00	-0.00
$m^1_{\pi^+\pi^-}$			1	-0.02	0.01	0.06	-0.00	0.01
$m^2_{\pi^+\pi^-}$				1	0.02	-0.00	0.06	-0.00
$\mathcal{F}_{B\bar{B}/q\bar{q}}$					1	0.02	0.02	-0.00
$\cos\theta^1_{\text{H}}$						1	-0.01	0.01
$\cos\theta^2_{\text{H}}$							1	0.01
Δt								1

Table C.40: Correlation matrix for SVD2 off-resonance data.

C.4 Appendix Signal Model

Fig. C.99 shows the helicity angle dependent reconstruction efficiency in 29 bins of ΔE. Bins with similar shape are combined for the helicity PDF of the signal component, see Section 4.3.1. ΔE is varied in steps of 0.01 GeV.

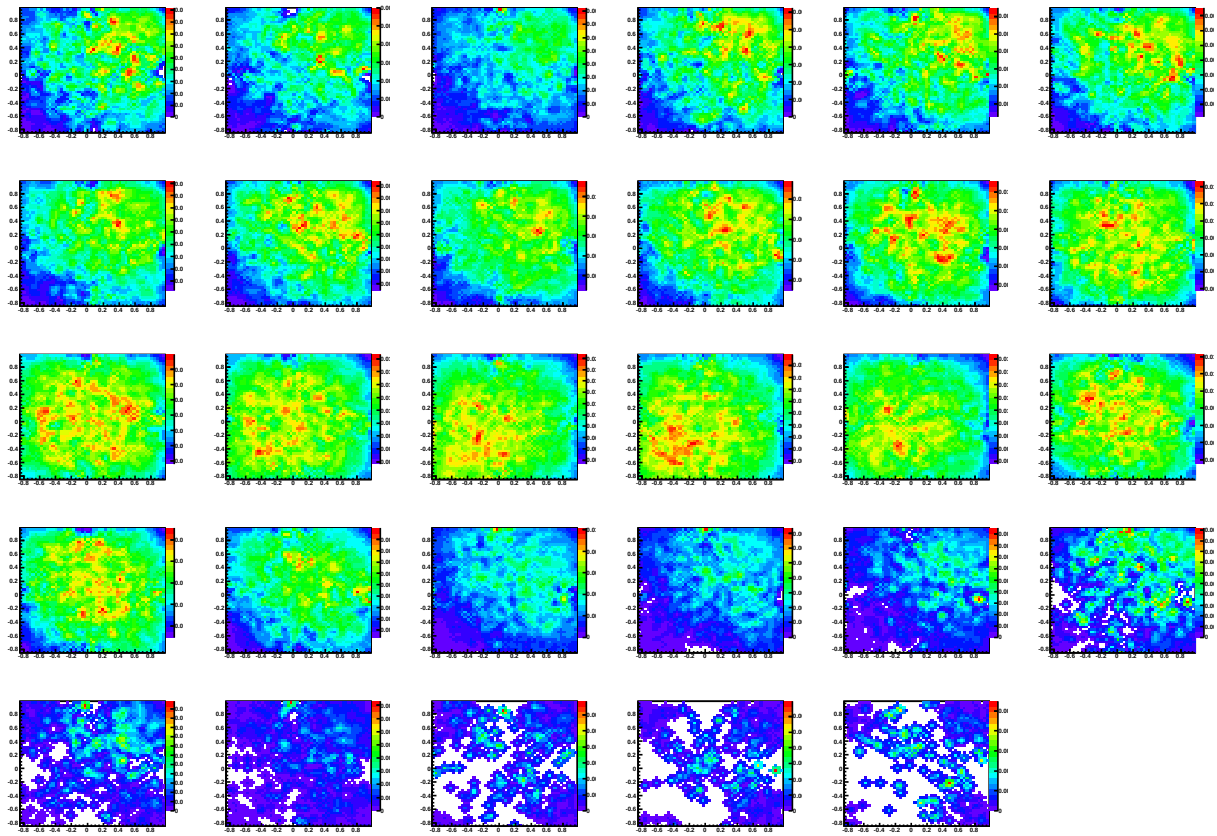

Figure C.99: $\cos\theta_{\mathrm{H}}$-dependent reconstruction efficiencies in 29 bins of ΔE obtained from fully reconstructed signal MC events used for choosing the five bins (Fig. 4.11) as explained in Section 4.3.

C.5 Appendix Continuum Model

To verify the continuum PDF, a visual comparison of the correlations of the fit distributions in on-resonance data and continuum MC simulation is presented. Fig. C.100 and Fig. C.101 show the distributions of dipion masses and helicity angles in slices of each other and Fig. C.102 shows the ΔE distributions in equidistant bins of $\mathcal{F}_{B\bar{B}/q\bar{q}}$.

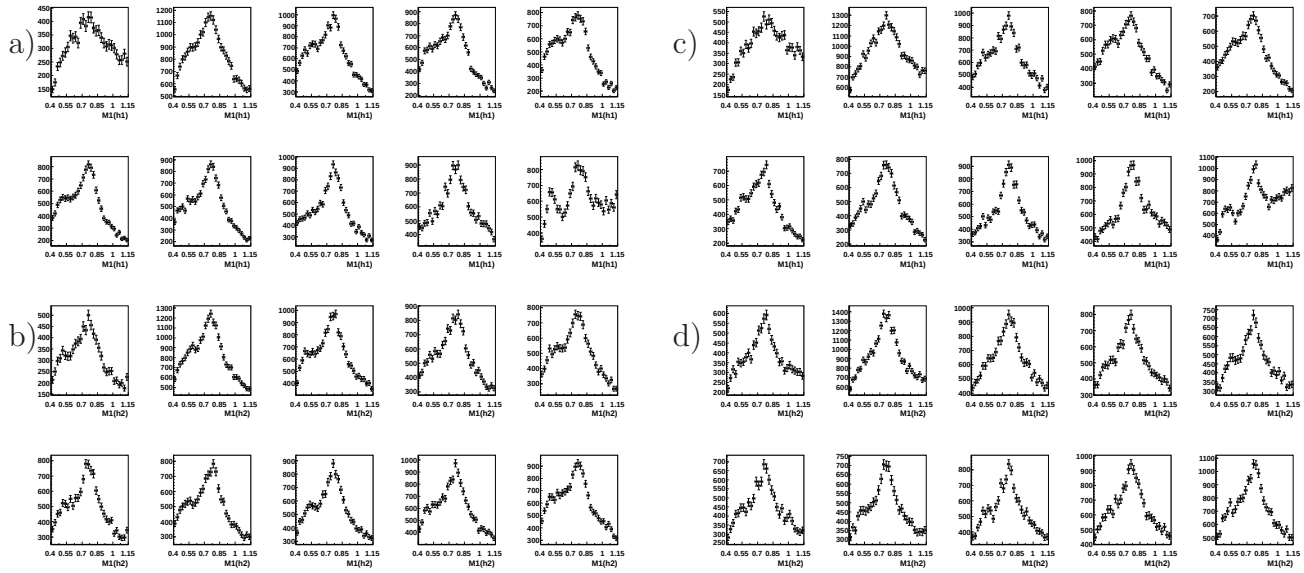

Figure C.100: $m_{\pi^+\pi^0}$ distributions of a,b) continuum MC simulation and c,d) on-resonance data in equidistant slices of $\cos\theta_{\mathrm{H}}^{+}$ (a,c) and $\cos\theta_{\mathrm{H}}^{-}$ (c,d). a) and c) show the good agreement of the correlation of $m_{\pi^+\pi^0}$ with $\cos\theta_{\mathrm{H}}^{+}$ in both data samples, while there is no significant correlation with $\cos\theta_{\mathrm{H}}^{-}$.

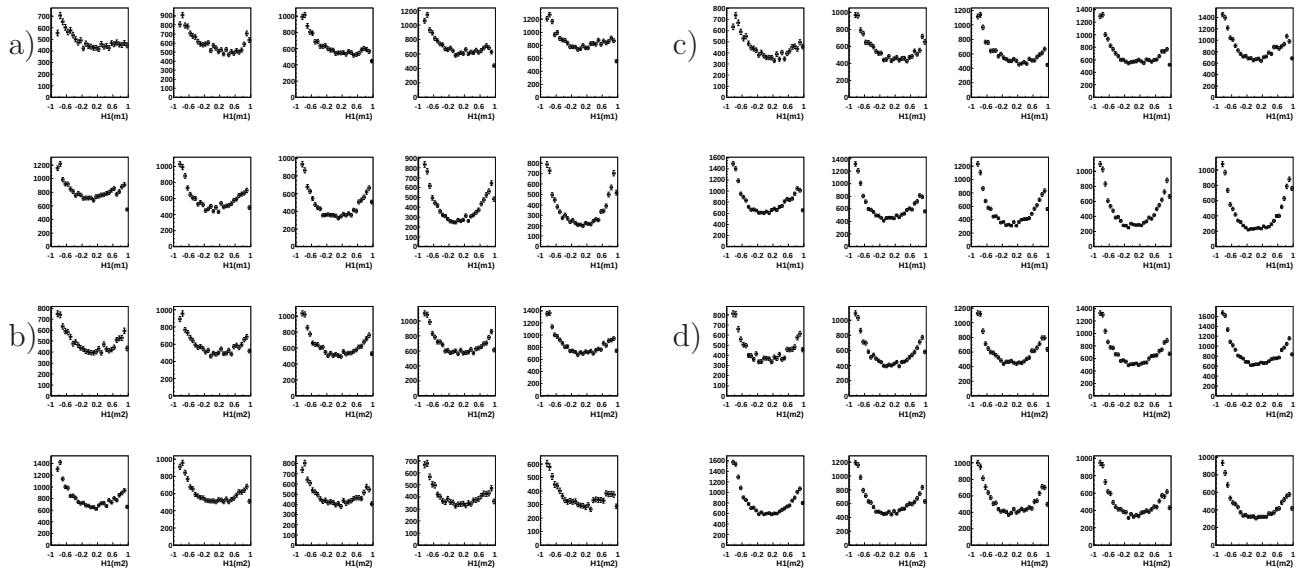

Figure C.101: $\cos\theta_{\mathrm{H}}^{+}$ distributions a,b) continuum MC simulation and c,d) on-resonance data in equidistant slices of $m_{\pi^+\pi^0}$ (a,c) and $m_{\pi^-\pi^0}$ (c,d). a) and c) show the good agreement of the correlation of $\cos\theta_{\mathrm{H}}^{+}$ with $m_{\pi^+\pi^0}$ in both data samples, while there is no significant correlation with $m_{\pi^-\pi^0}$.

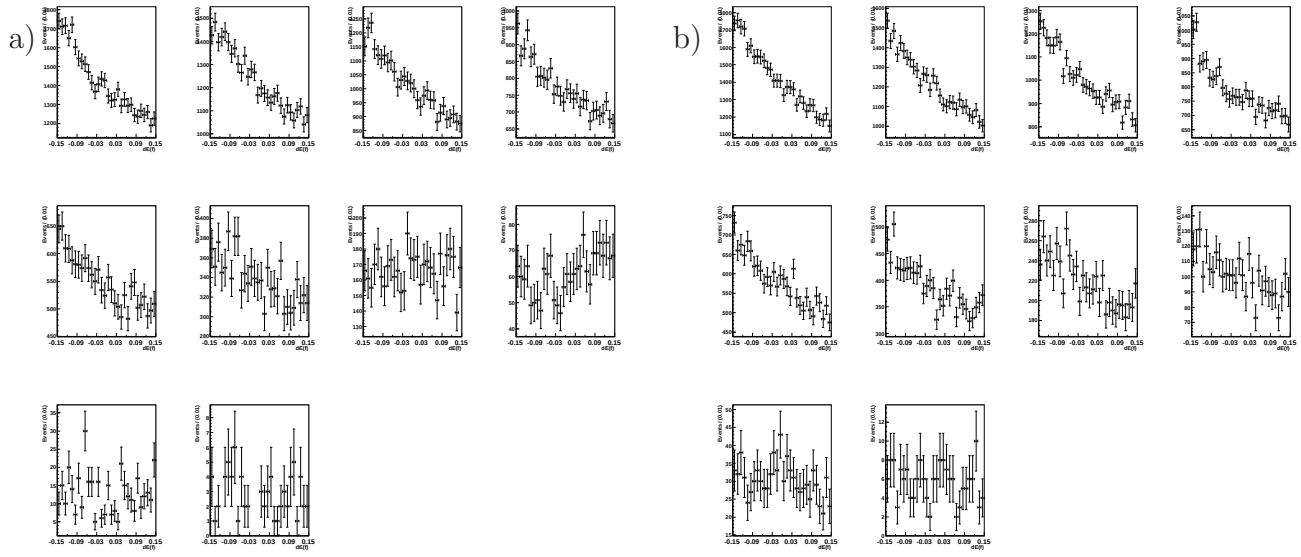

Figure C.102: ΔE distributions of a) continuum MC simulation and b) on-resonance data in equidistant slices of $\mathcal{F}_{B\bar{B}/q\bar{q}}$. The correlation in b) seems less strong, but the increasing $B\bar{B}$ contributions for larger values of $\mathcal{F}_{B\bar{B}/q\bar{q}}$ are polluting the distributions. The four-pion contribution is already visible through the peak arising in the bin before the last bin in b).

C.5.1 Correlations: Continuum MC Simulation

The following distributions of the dipion masses and helicity angles in bins of each other show the correlations among these fit variables in the continuum component. The distributions and PDFs were obtained from studying off-resonance events from MC simulation.

Component:0

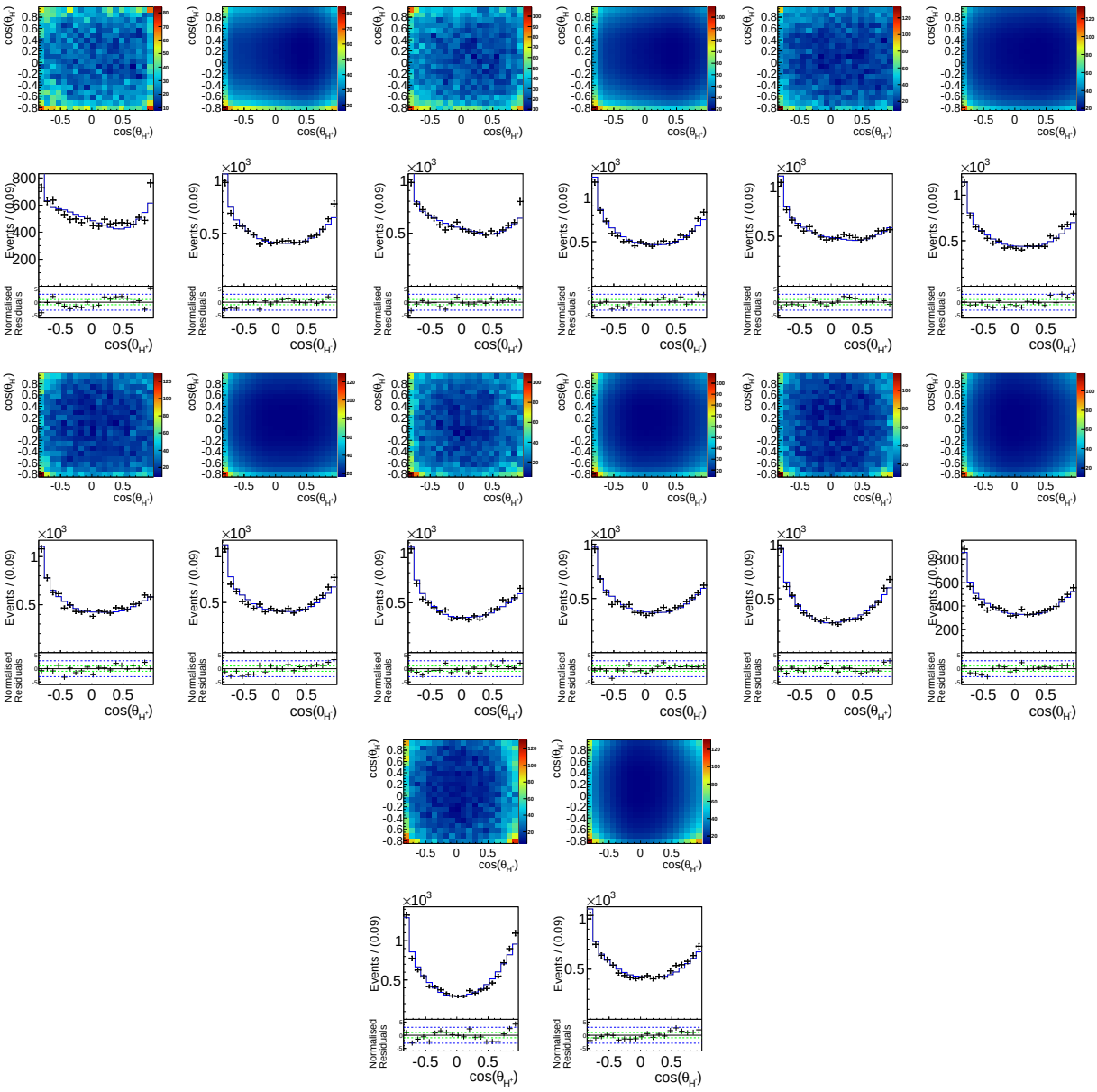

Figure C.103: Distributions of the helicity angles from continuum MC simulation for reconstruction type "0" in equi-distant bins of $m_{\pi^{\pm}\pi^{0}}$with the fit result on top.

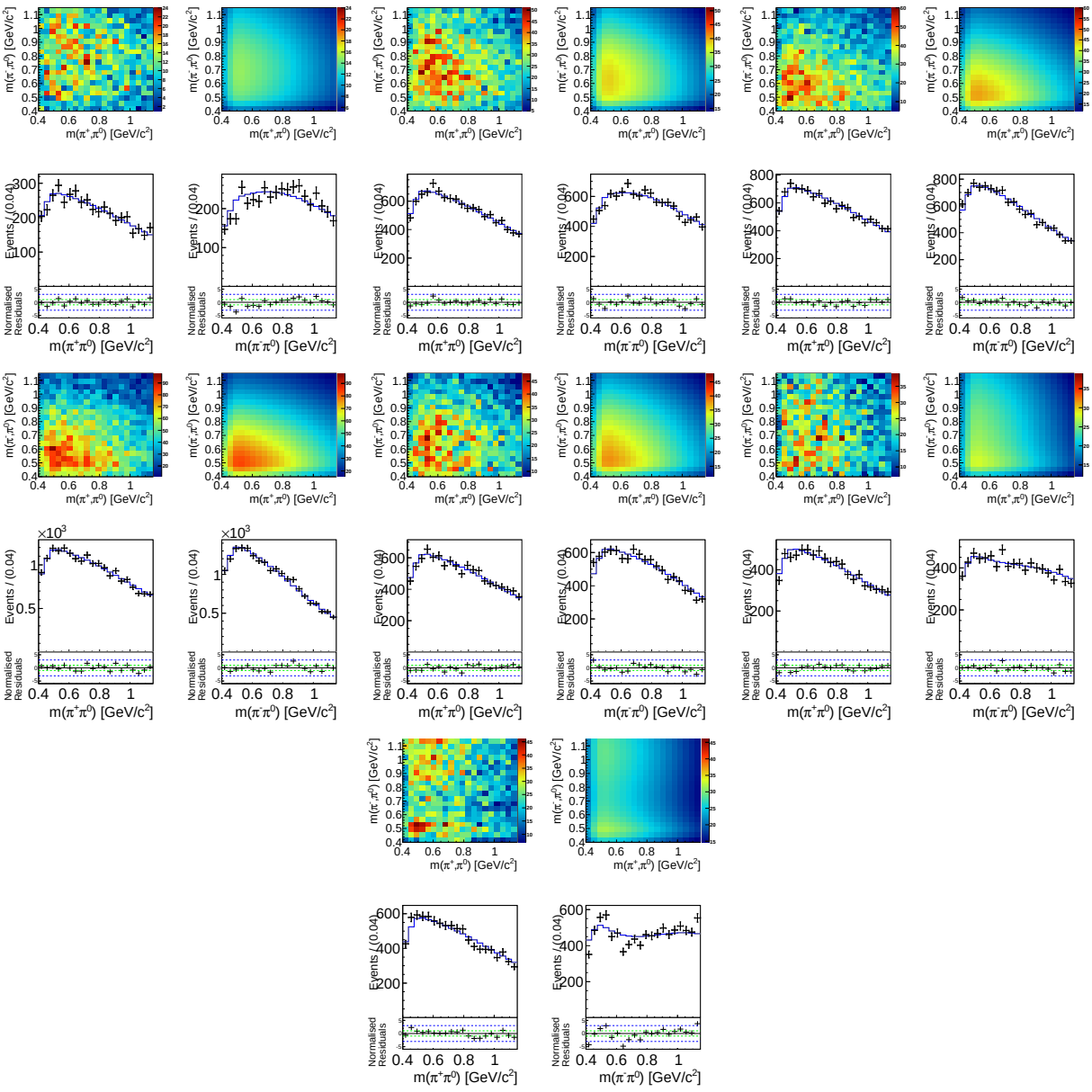

Figure C.104: Distributions of the dipion masses from continuum MC simulation for reconstruction type "0" in bins of $\cos\theta_{\mathrm{H}}^{-}$ with the fit result on top.

Component:±

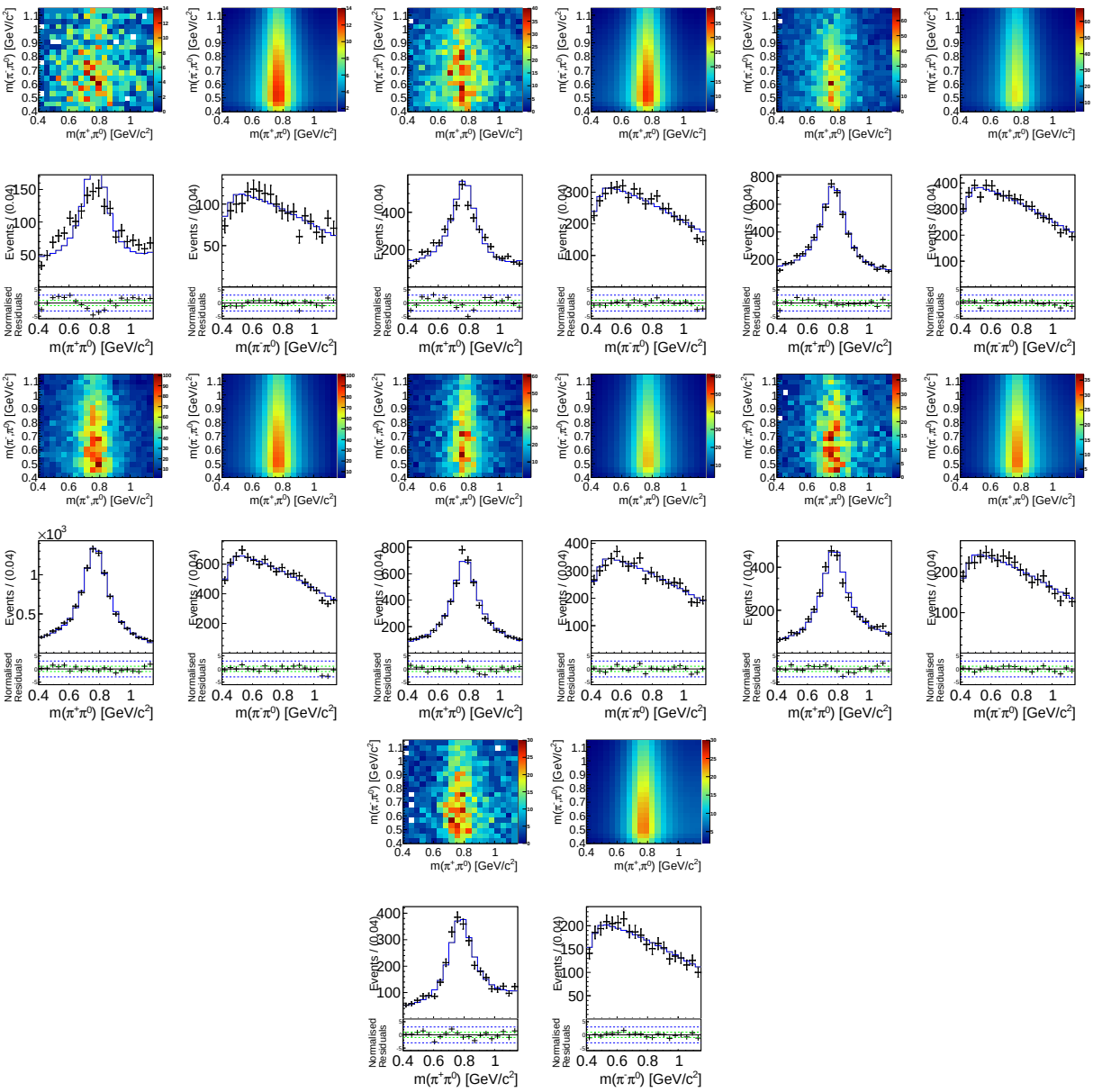

Figure C.105: Distributions of the dipion masses from continuum MC simulation for reconstruction type "+" in bins of $\cos\theta_{\mathrm{H}}^{+}$ with the fit result on top.

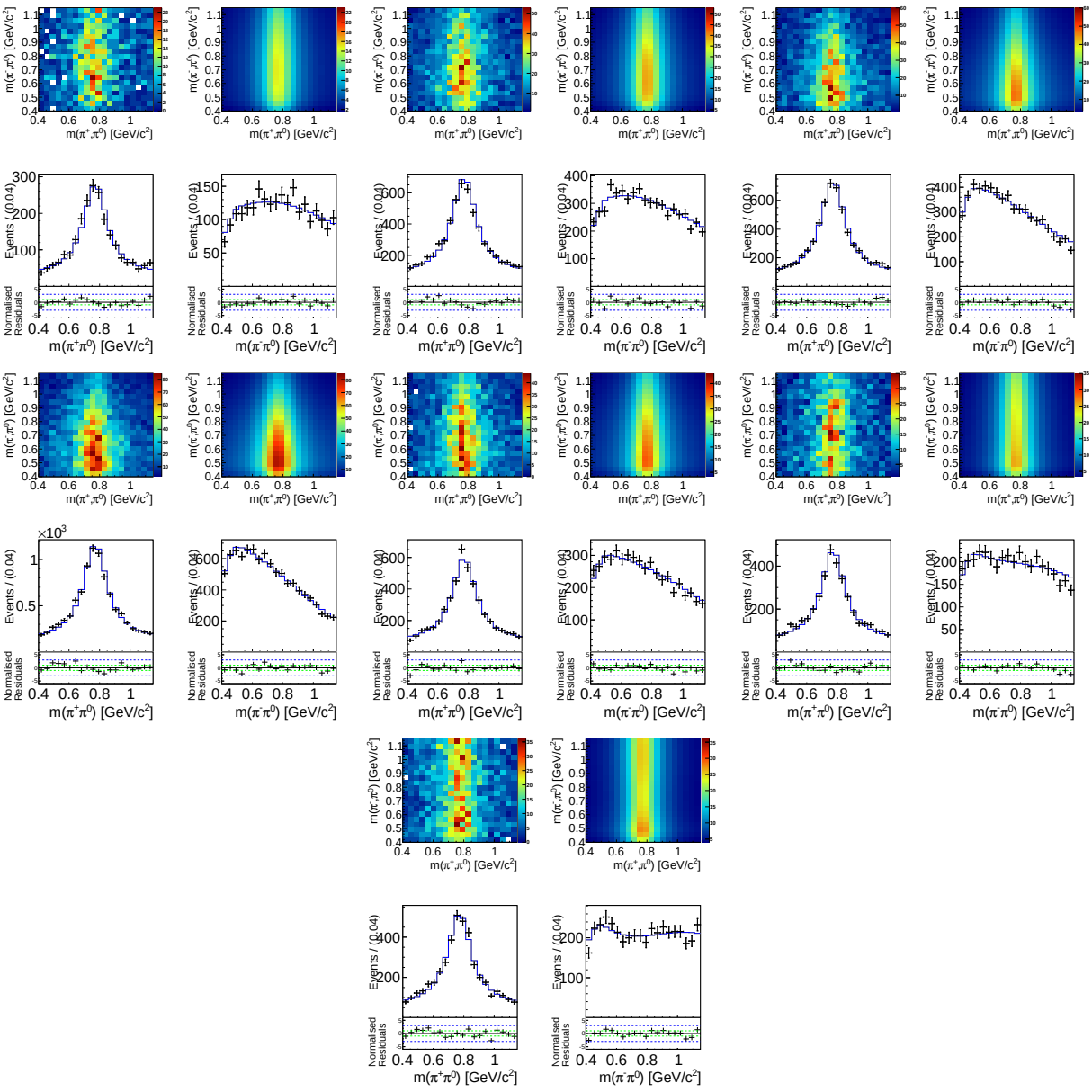

Figure C.106: Distributions of the dipion masses from continuum MC simulation for reconstruction type "+" in bins of $\cos\theta_{\mathrm{H}}^{-}$ with the fit result on top.

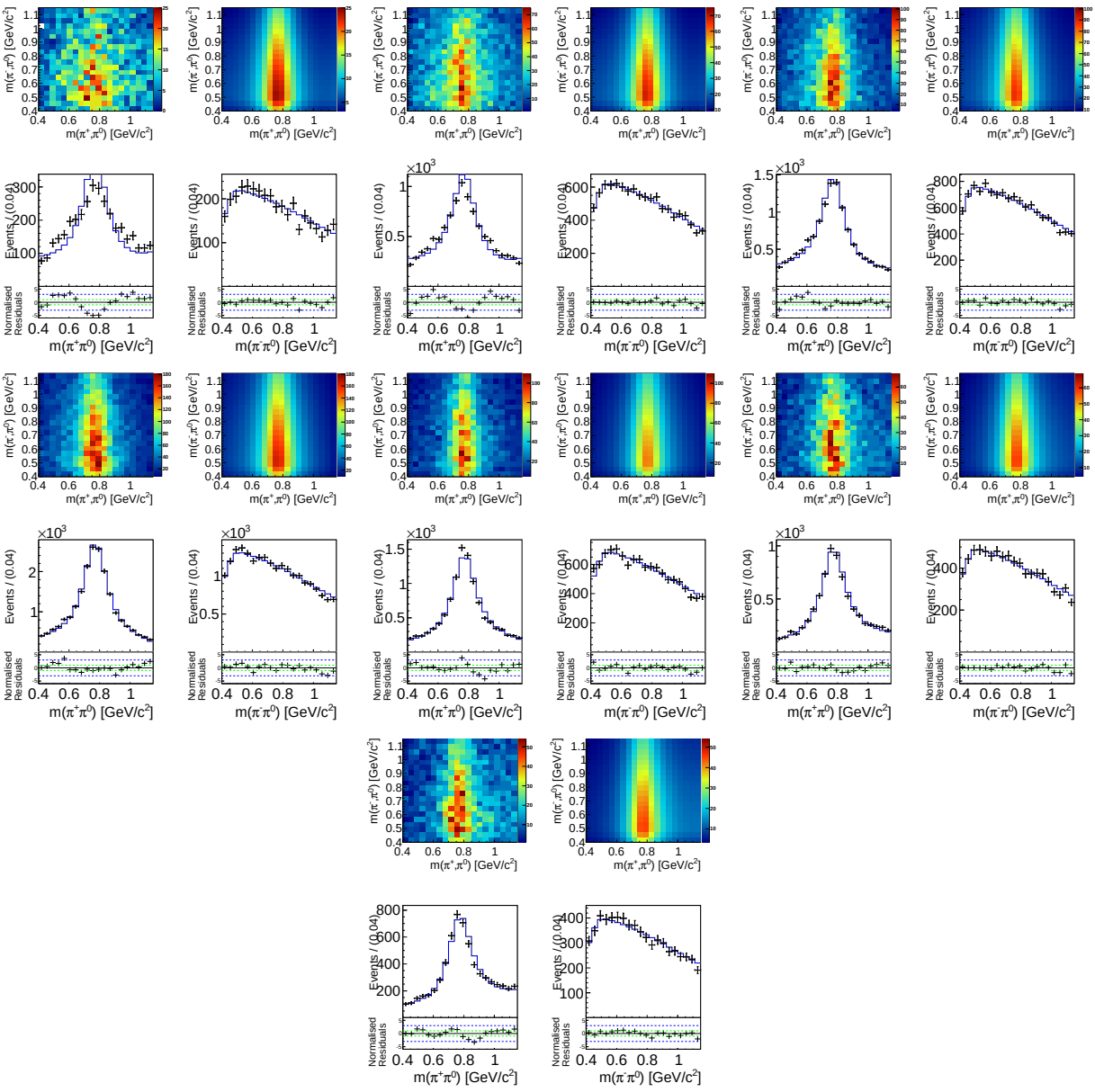

Figure C.107: Distributions of the dipion masses from continuum MC simulation for reconstruction types "+" and inverted "-" in bins of $\cos\theta_{\mathrm{H}}^{+}$ with the fit result on top.

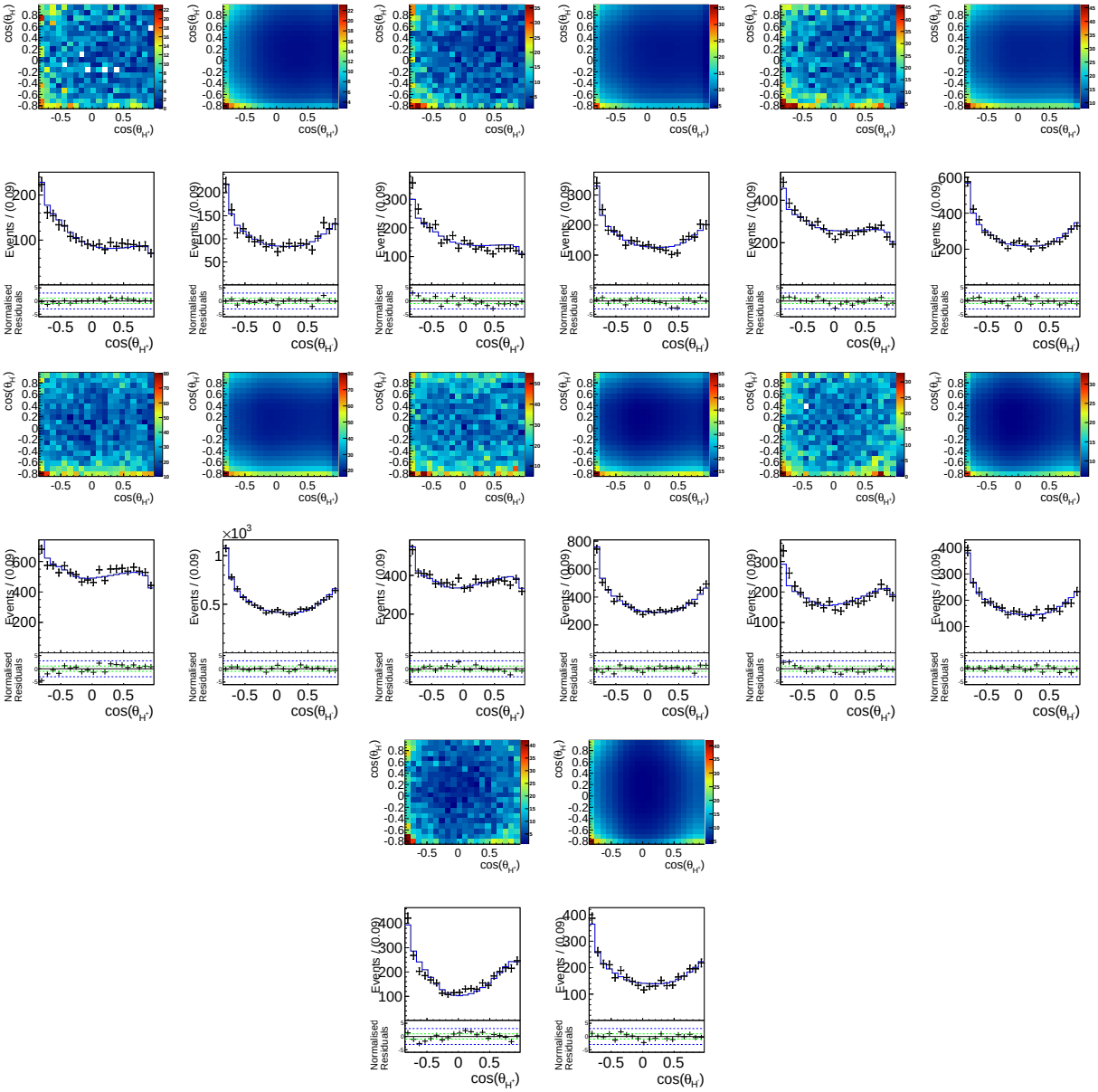

Figure C.108: Distributions of the helicity angles from continuum MC simulation for reconstruction type "+" in equi-distant bins of $m_{\pi^{\pm}\pi^0}$ with the fit result on top.

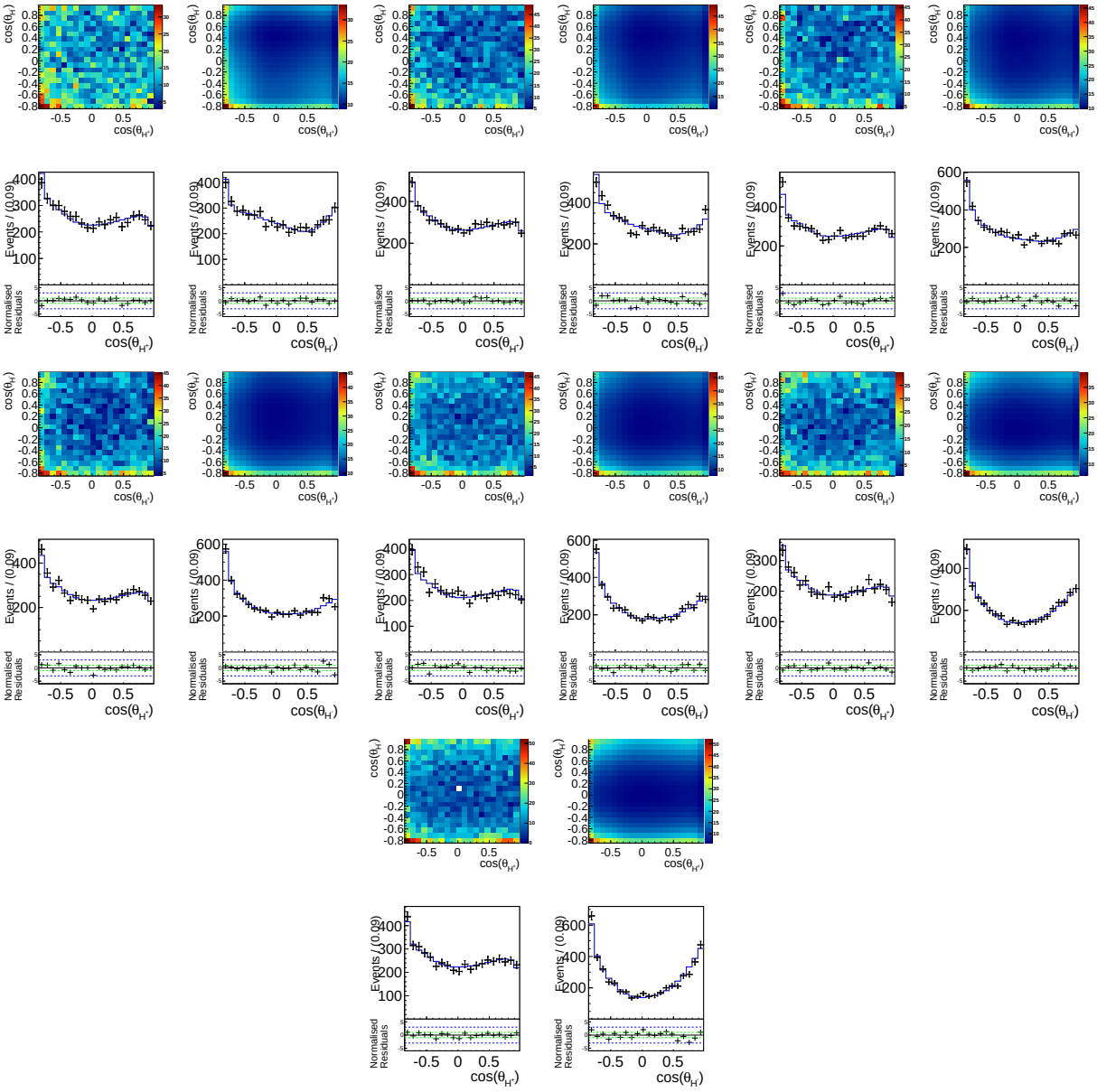

Figure C.109: Distributions of the helicity angles from continuum MC simulation for reconstruction type "+" in equi-distant bins of $m_{\pi^-\pi^0}$ with the fit result on top.

Component:2c

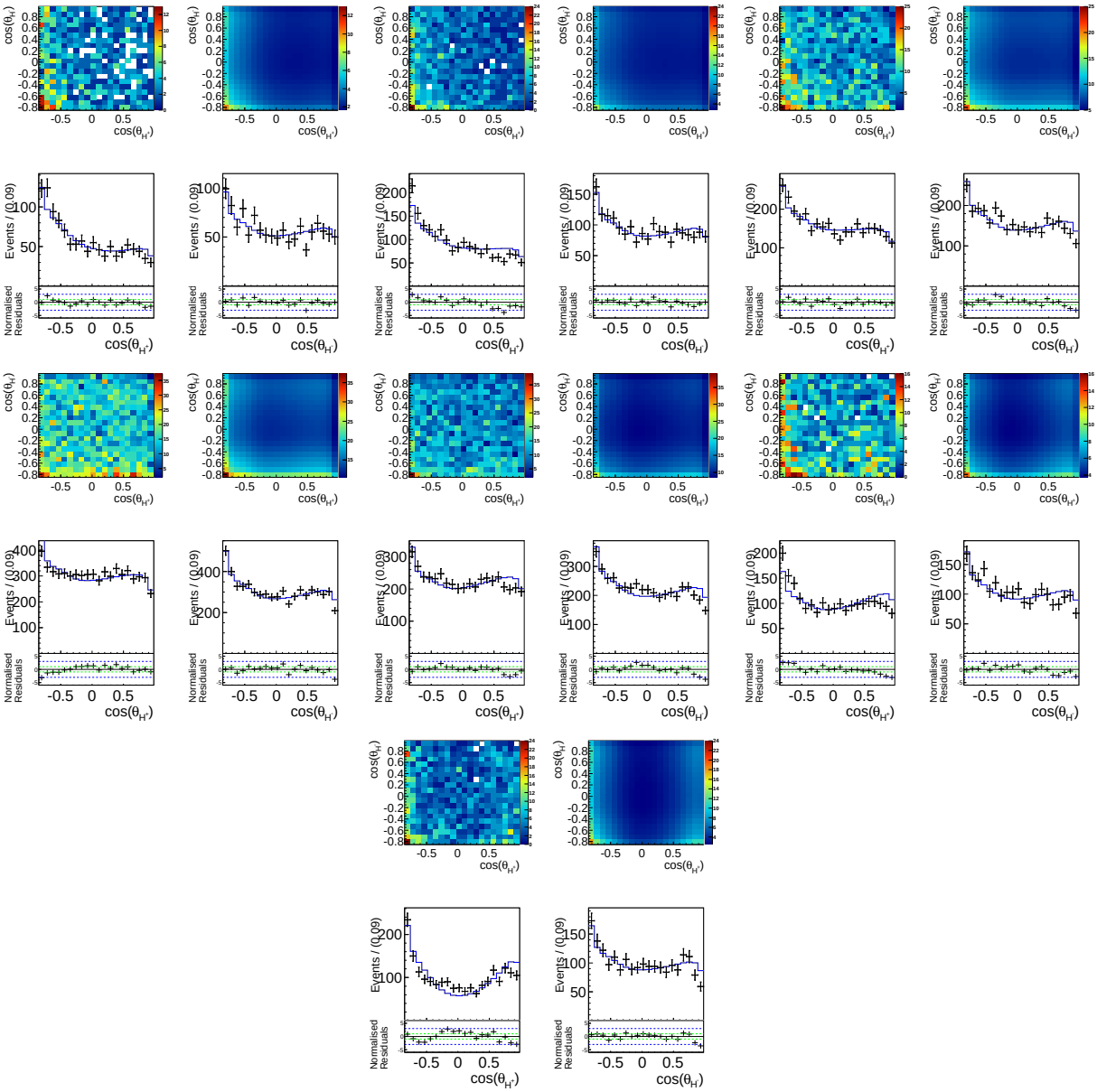

Figure C.110: Distributions of the helicity angles from continuum MC simulation for reconstruction type "2c" in equi-distant bins of $m_{\pi^+\pi^0}$ with the fit result on top.

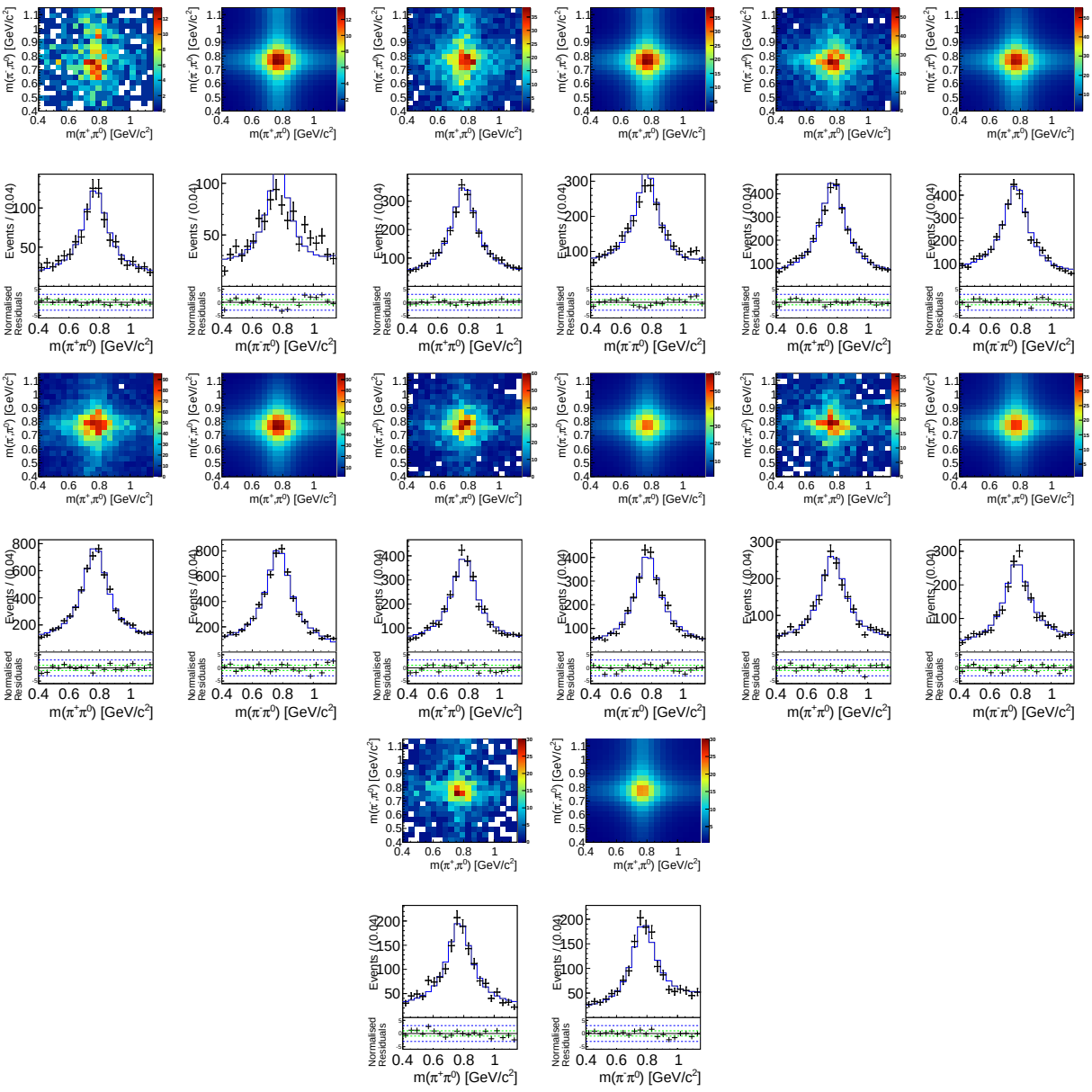

Figure C.111: Distributions of the dipion masses from continuum MC simulation for reconstruction type "2c" in bins of $\cos\theta_{\mathrm{H}}^{-}$ with the fit result on top.

Appendix D

Appendix Linearity Tests

This section shows the results of the toy MC ensemble tests used to validate the fitting procedure, see Section 4.7.

D.1 Branching Fraction

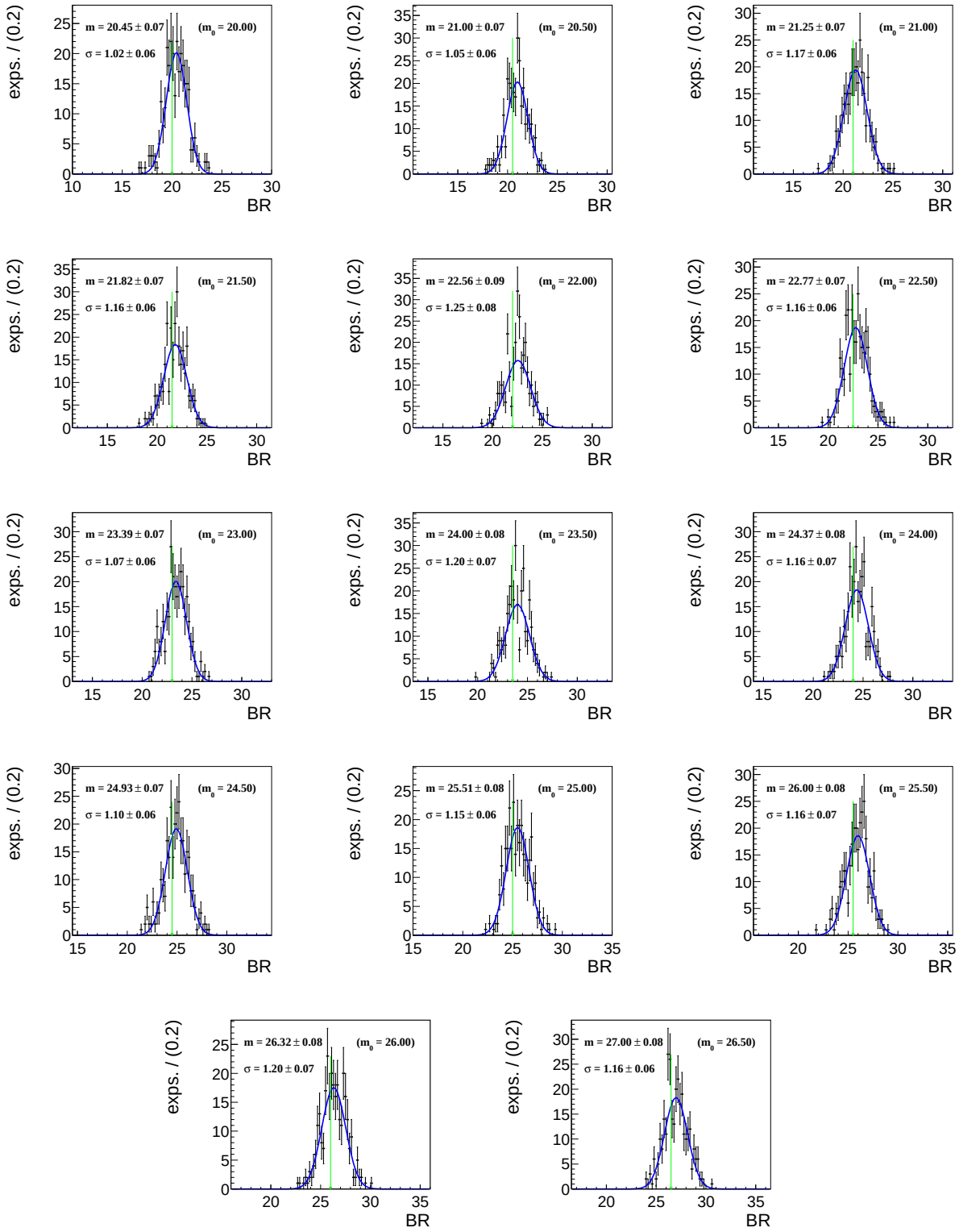

Figure D.1: Results of $\mathcal{B}(B^0 \to \rho^+\rho^-)$ from fits to pseudo experiments generated from fully simulated MC events. The generated value goes from $\mathcal{B}(B^0 \to \rho^+\rho^-) = 20 \times 10^{-6}$ (upper left) to 26.5×10^{-6} in steps of 0.5×10^{-6}. The generated values are indicated by the green arrows.

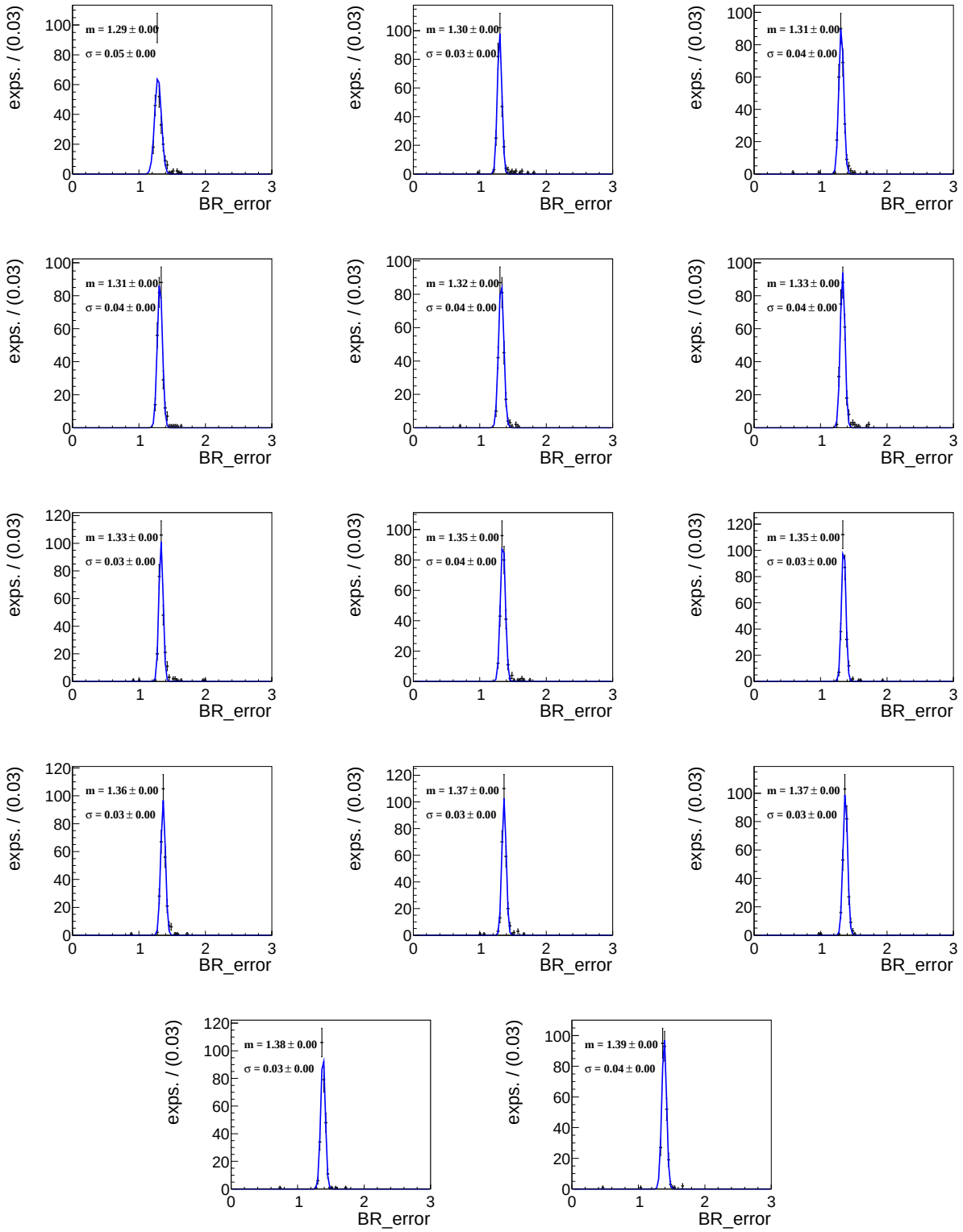

Figure D.2: Error distributions of $\mathcal{B}(B^0 \to \rho^+\rho^-)$ from the fits to pseudo experiments generated from fully simulated MC events. The generated value goes from $\mathcal{B}(B^0 \to \rho^+\rho^-) = 20 \times 10^{-6}$ (upper left) to 26.5×10^{-6} in steps of 0.5×10^{-6}.

D.2 Fraction of Longitudinal Polarization

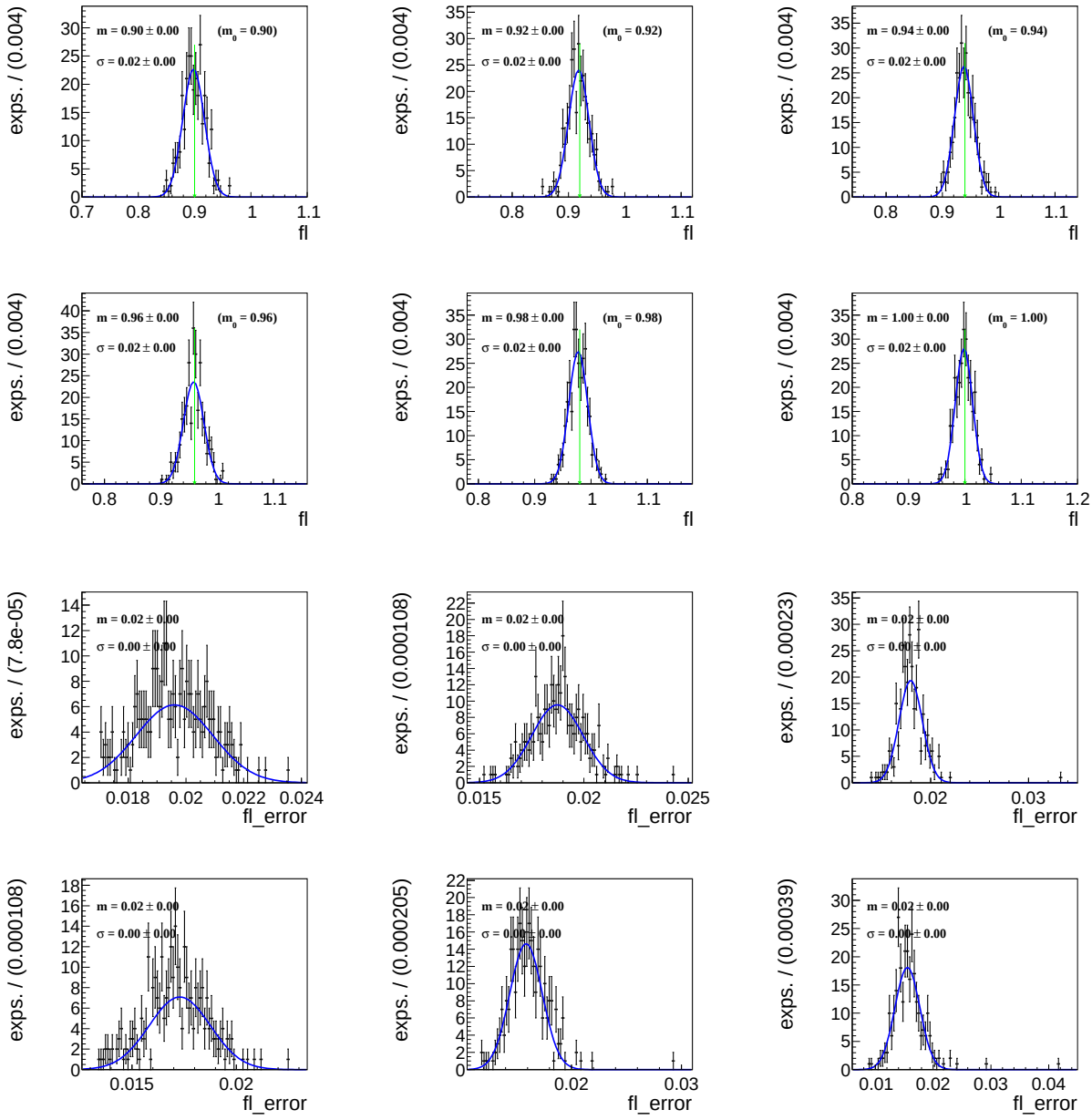

Figure D.3: Results of f_L from the fits to pseudo experiments generated from fully simulated MC events and their error distributions below. The generated value goes from $f_L = 0.90$ (upper left) to 1.00 in steps of 0.02. The generated values are indicated by the green arrows.

D.3 CPV Parameters

D.3.1 Acp

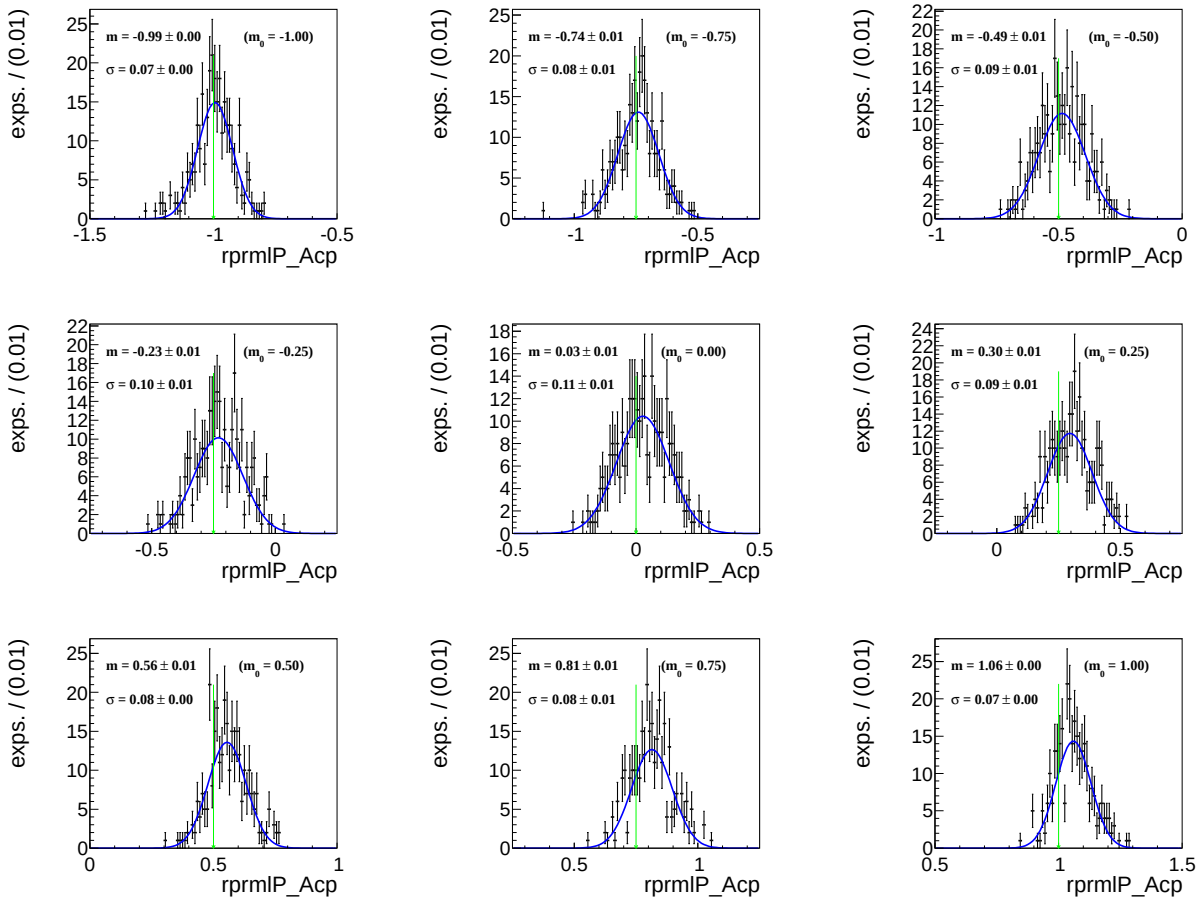

Figure D.4: Results of $\mathcal{A}_{CP}$ of $B^0 \to \rho^+\rho^-$ from the fits to pseudo experiments generated from fully simulated MC events. The generated value goes from $\mathcal{A}_{CP} = -1$ (upper left) to 1 in steps of 0.25. The generated values are indicated by the green arrows.

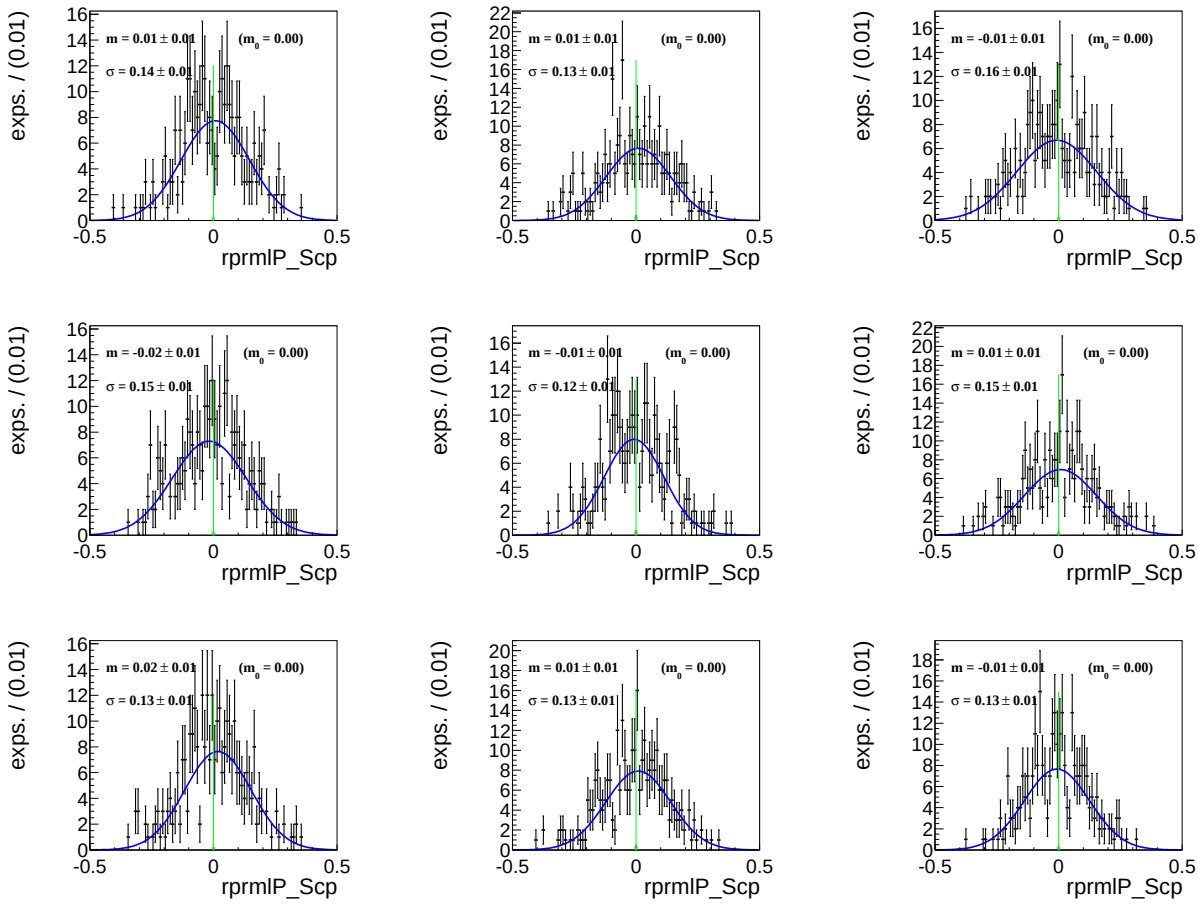

Figure D.5: Results of $\mathcal{S}_{CP}$ of $B^0 \to \rho^+\rho^-$ from the fits to pseudo experiments generated from fully simulated MC events. The generated value goes from $\mathcal{A}_{CP} = -1$ (upper left) to 1 in steps of 0.25. The generated values are indicated by the green arrows.

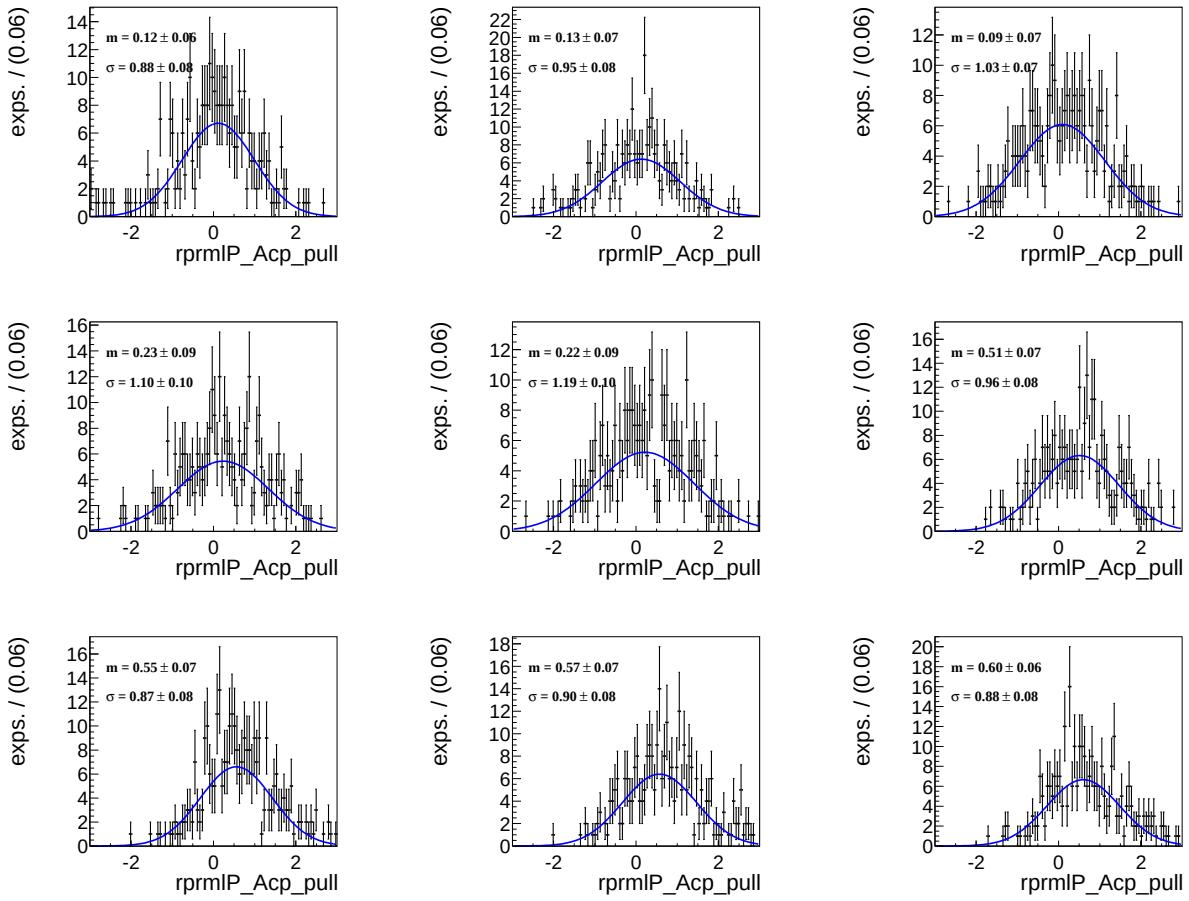

Figure D.6: Pull distributions for $\mathcal{A}_{CP}$ of $B^0 \to \rho^+\rho^-$ from the fits to pseudo experiments generated from fully simulated MC events. The generated value goes from $\mathcal{A}_{CP} = -1$ (upper left) to 1 in steps of 0.25. The generated values are indicated by the green arrows.

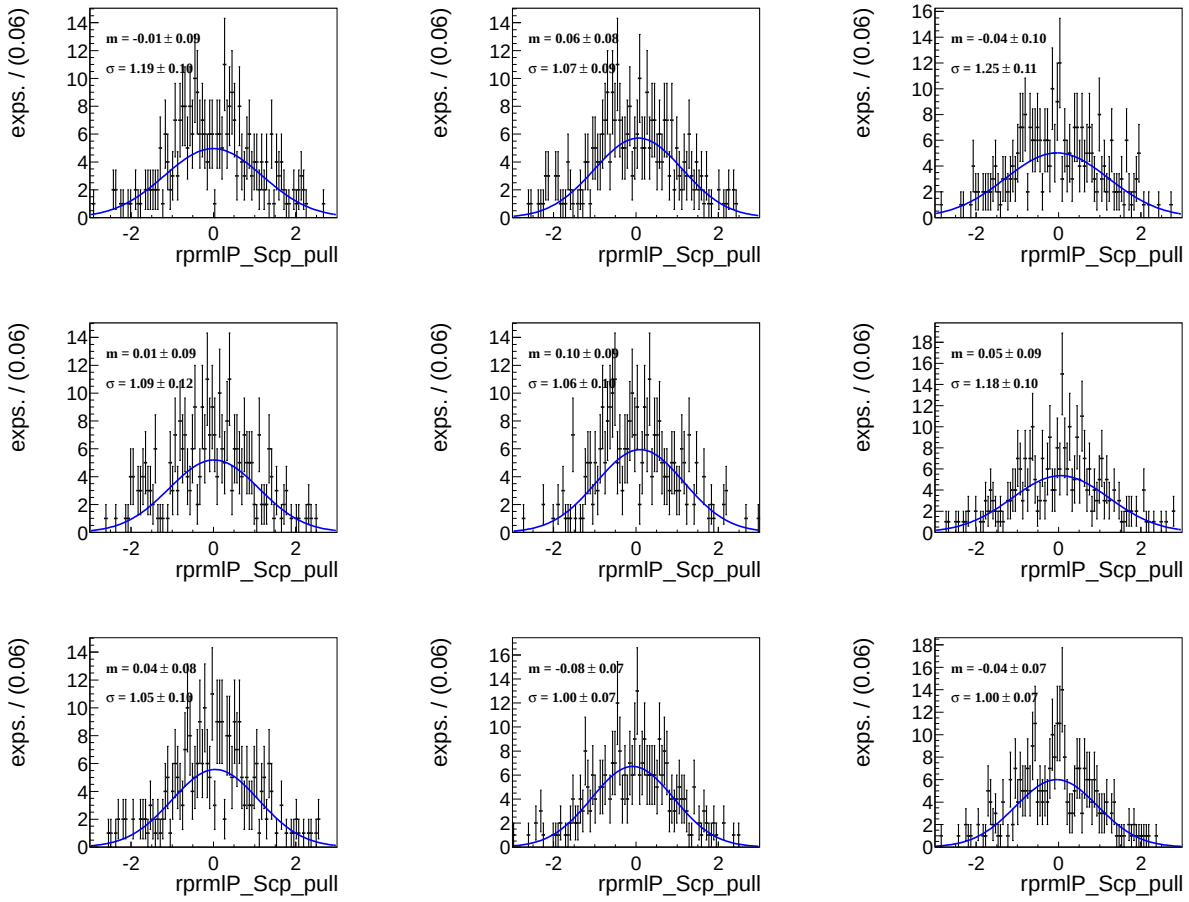

Figure D.7: Pull distributions for $\mathcal{S}_{CP}$ of $B^0 \to \rho^+\rho^-$ from the fits to pseudo experiments generated from fully simulated MC events. The generated value goes from $\mathcal{A}_{CP} = -1$ (upper left) to 1 in steps of 0.25. The generated values are indicated by the green arrows.

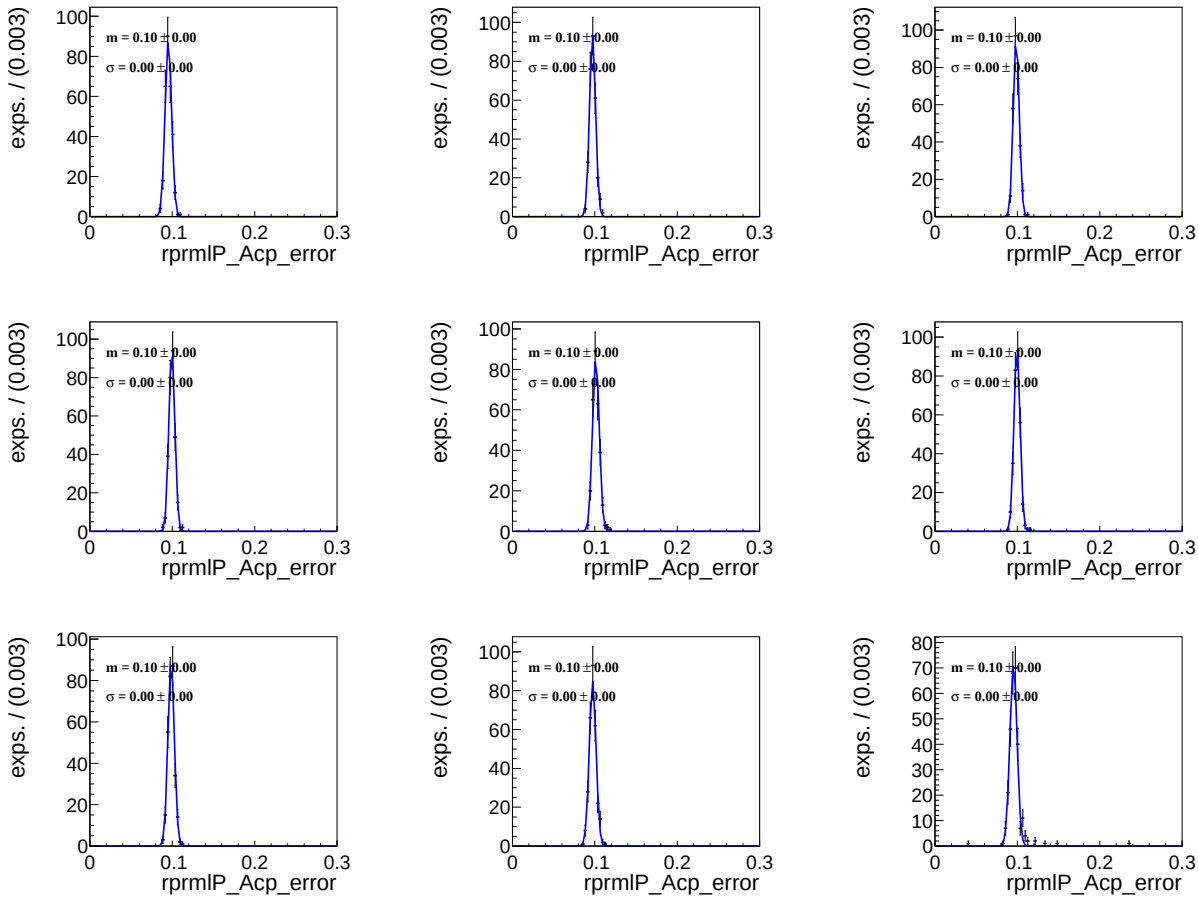

Figure D.8: Distribution of the errors of the fit results of $\mathcal{A}_{CP}$ for a variation of $\mathcal{S}_{CP}$ from fully simulated MC events. The generated value goes from $\mathcal{S}_{CP} = -1$ (upper left) to 1 in steps of 0.25.

D.3.2 Scp

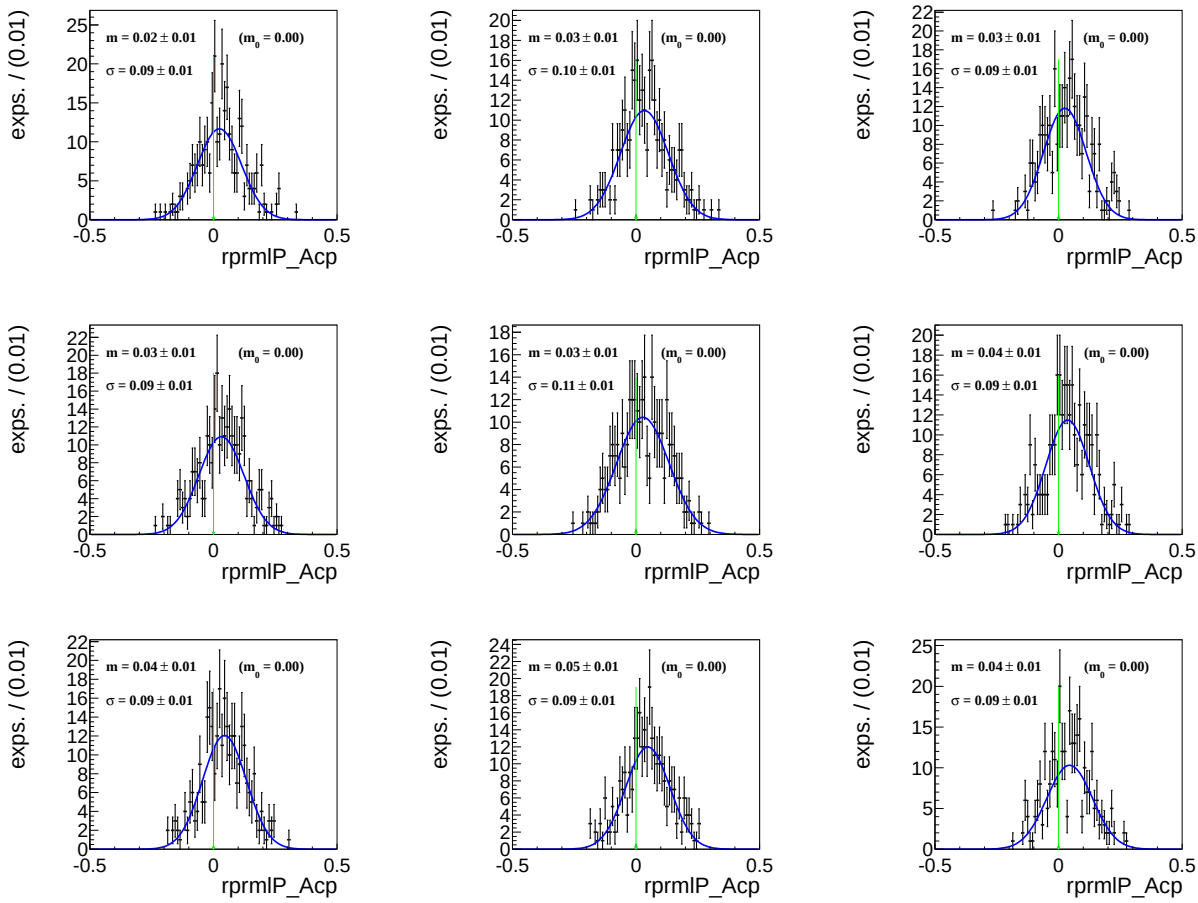

Figure D.9: Results of $\mathcal{A}_{CP}$ of $B^0 \to \rho^+\rho^-$ from the fits to pseudo experiments generated from fully simulated MC events. The generated value goes from $\mathcal{S}_{CP} = -1$ (upper left) to 1 in steps of 0.25. The generated values are indicated by the green arrows.

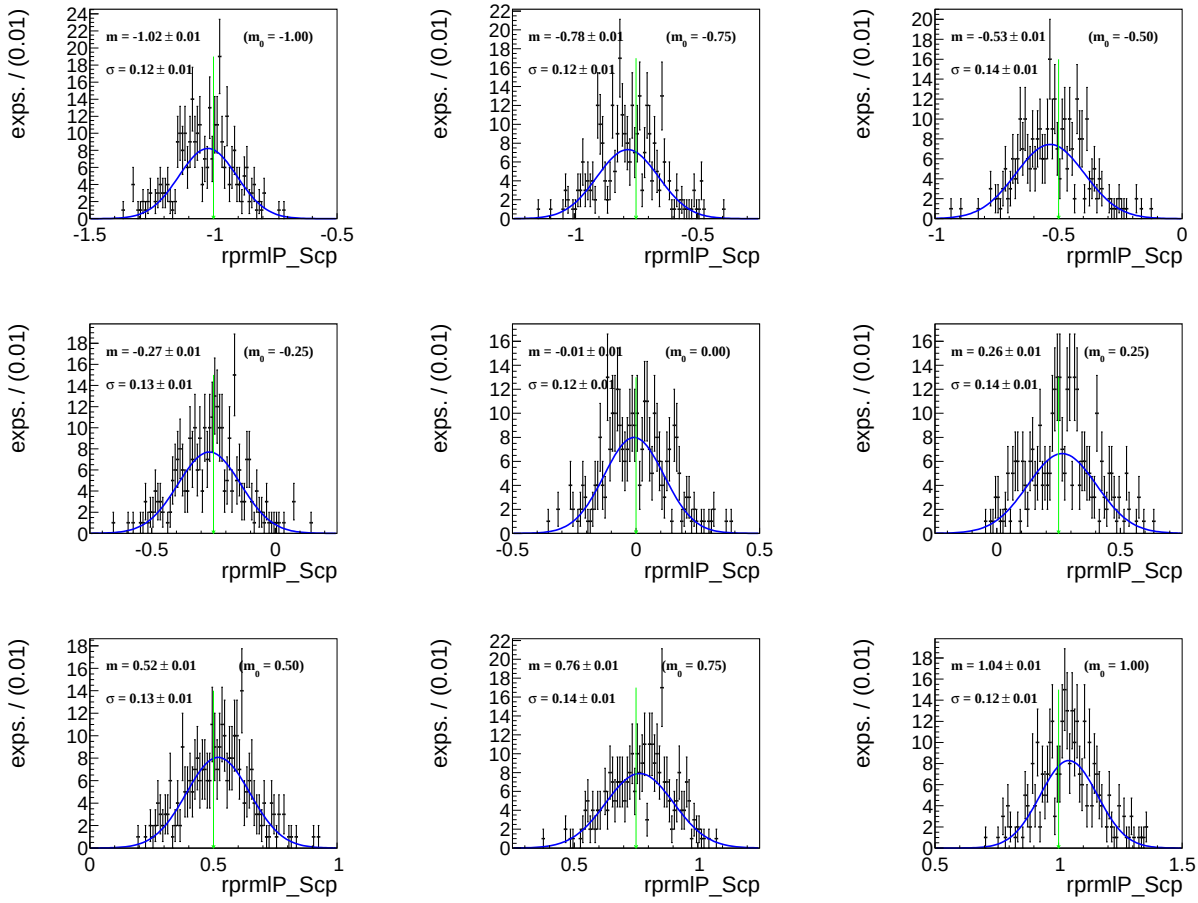

Figure D.10: Results of $\mathcal{S}_{CP}$ of $B^0 \to \rho^+\rho^-$ from the fits to pseudo experiments generated from fully simulated MC events. The generated value goes from $\mathcal{S}_{CP} = -1$ (upper left) to 1 in steps of 0.25. The generated values are indicated by the green arrows.

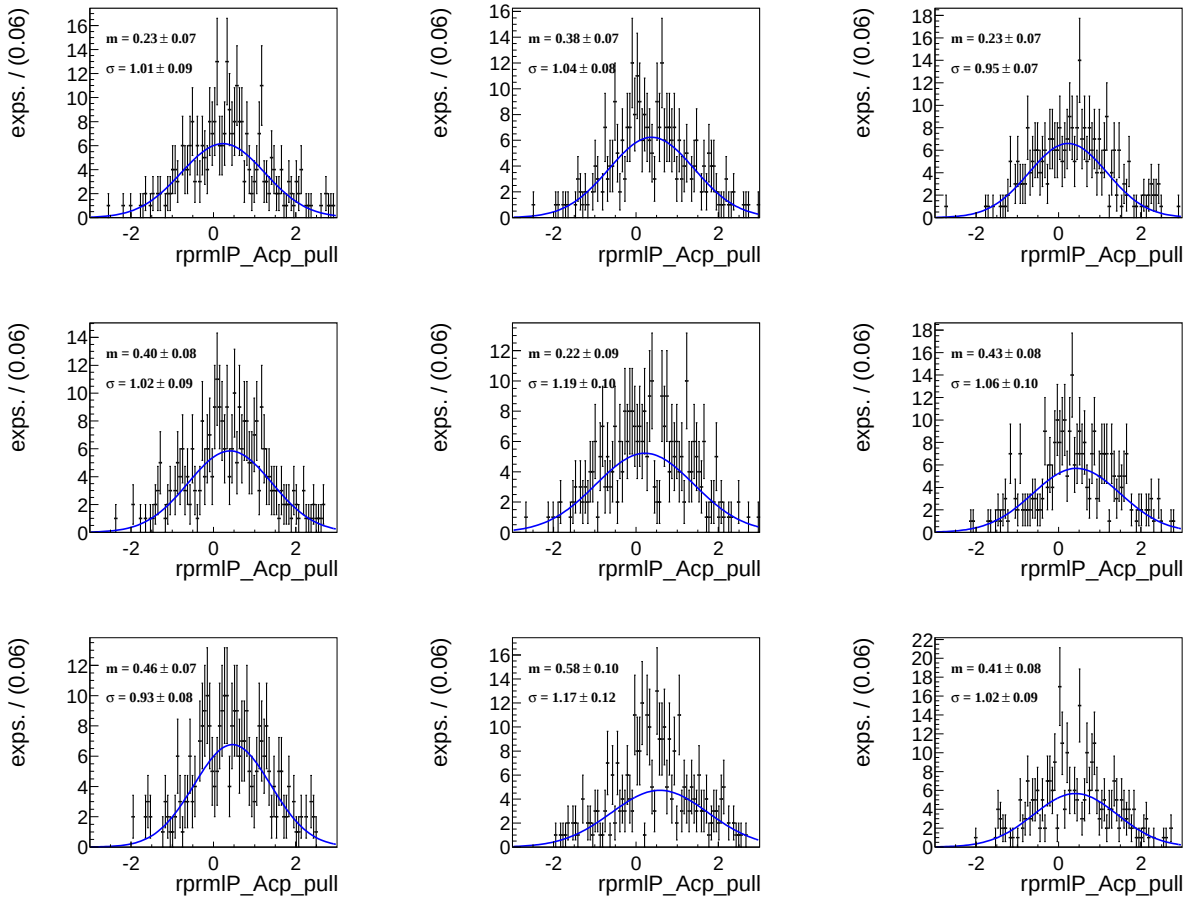

Figure D.11: Pull distributions for $\mathcal{A}_{CP}$ of $B^0 \to \rho^+\rho^-$ from the fits to pseudo experiments generated from fully simulated MC events. The generated value goes from $\mathcal{S}_{CP} = -1$ (upper left) to 1 in steps of 0.25. The generated values are indicated by the green arrows.

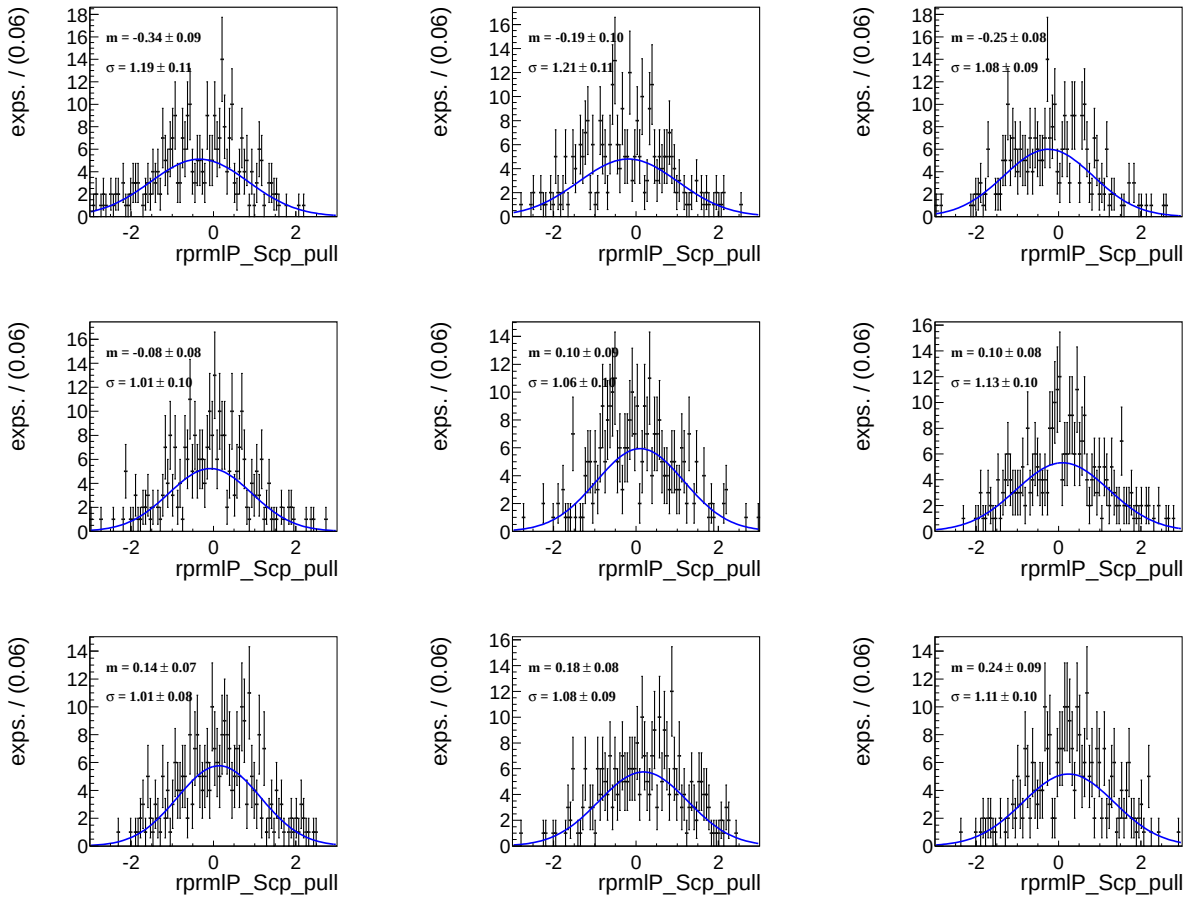

Figure D.12: Pull distributions for $\mathcal{S}_{CP}$ of $B^0 \to \rho^+\rho^-$ from the fits to pseudo experiments generated from fully simulated MC events. The generated value goes from $\mathcal{S}_{CP} = -1$ (upper left) to 1 in steps of 0.25. The generated values are indicated by the green arrows.

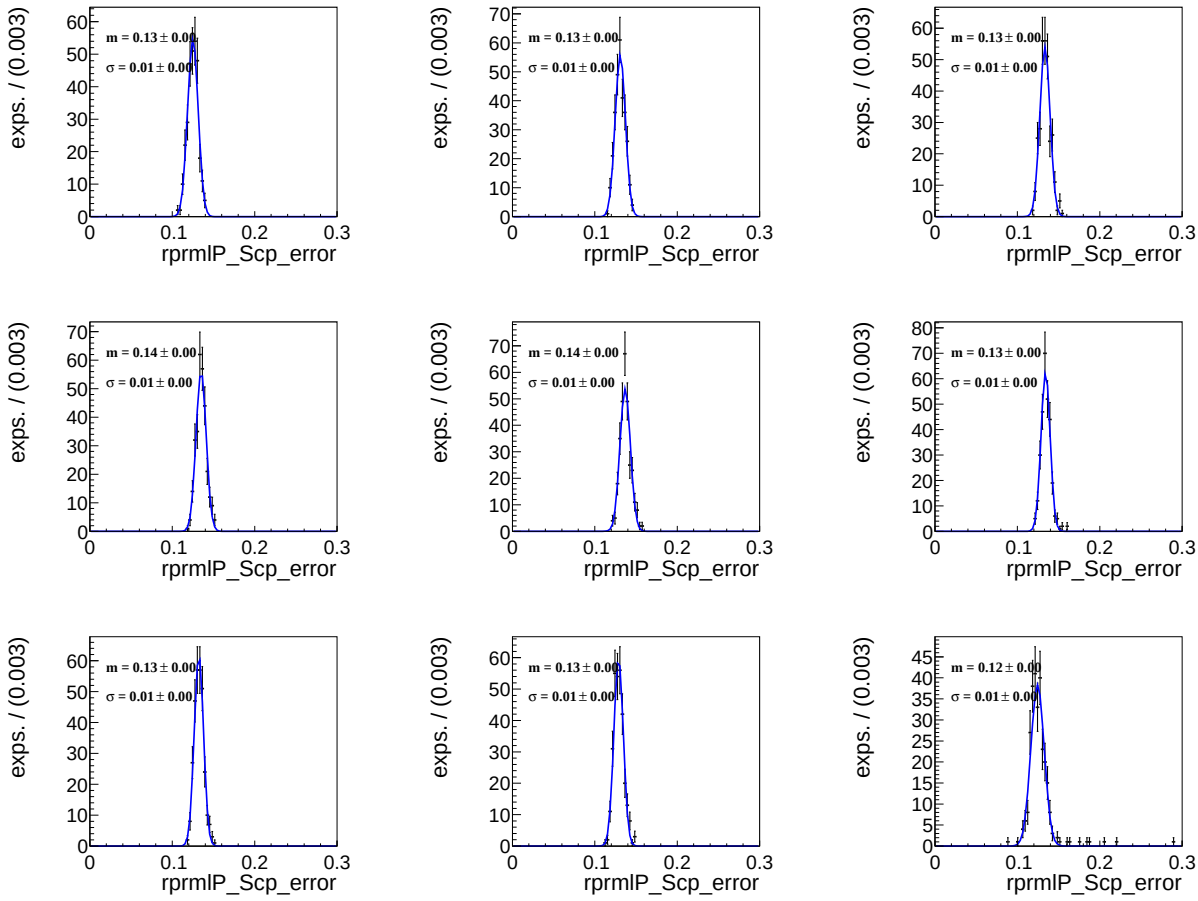

Figure D.13: Distribution of the errors of the fit results of $\mathcal{S}_{CP}$ for a variation of $\mathcal{A}_{CP}$ from fully simulated MC events. The generated value goes from $\mathcal{S}_{CP} = -1$ (upper left) to 1 in steps of 0.25.

Appendix E

Appendix Functions

E.1 Chebyshev Polynomials

The Chebyshev polynomials $C(x)$, are a set of polynomials, orthogonal in the range [-1,1], hence well suited for fitting as they provide more stability. Two kinds exist and we use the Chebyshev polynomials of the first kind. Up to the 9th order, they are given by,

$$\begin{aligned} C_0(x) &= 1, \\ C_1(x) &= x, \end{aligned} \tag{E.1}$$

and can be generated recursively,

$$C_{n+1}(x) = 2xC_n(x) - C_{n-1}(x). \tag{E.2}$$

E.2 Breit-Wigner

For a resonance decaying into two light spin-0 particles, D_1 and D_2, a relativistic Breit-Wigner(BW) is often used. In the case of $\rho^0 \to \pi^+\pi^-$, these two particles are identical in mass and magnitude of momentum, and the BW function takes the form

$$BW(m_{\pi^+\pi^-}) = \frac{1}{m_0^2 - m_{\pi^+\pi^-}^2 - im_0\Gamma(p_\pi)}, \tag{E.3}$$

where m_0 is the nominal mass of the ρ^0 resonance, $m_{\pi^+\pi^-}$is the invariant mass of the two pions and $\Gamma(p_\pi)$ is the "mass-dependent" width, in general given by

$$\Gamma(p) = \Gamma_0(\frac{p}{p_0})^{2L+1}(\frac{m_0}{m})B_L(p,p_0)^2, \tag{E.4}$$

with the nominal width Γ_0, and the Blatt-Weisskopf barrier factors $B_L(p,p_0)$. For the ρ^0, $L = 1$ and the corresponding barrier factor is

$$B_1(p, p_0) = \sqrt{\frac{1 + (p_0 d)^2}{1 + (pd)^2}}. \tag{E.5}$$

where $p(p_0)$ are the daughter 3-momenta coming from a resonance at rest with mass $m(m_0)$, and d is an impact parameter, $d \sim 1$ fm, which is roughly the meson diameter. The Blatt-Weisskopf factors desribes a decrease of the decay propability for smaller momenta if the spin of the resonance has to be conserved in the angular momentum of its daughters. The decrease is caused by a smaller phase space for lower momentum daughters, since the maximum angular momentum of slow particles with an impact parameter d, is limited by their momentum.

E.3 Gaussians

We often use a assymetric-width (bifurcated) Gaussian

$$G(x) \equiv . \frac{1}{\sigma\sqrt{2\pi}} e^{-0.5(x-\mu)^2/\sigma} \tag{E.6}$$

where $\sigma = \sigma_l$ for $x < \mu$ and $\sigma = \sigma_r$ else.

The sum of two bifurcated-width Gaussians is denoted as

$$\begin{aligned} dbG(x) \equiv & dbG(x, \mu_1, \sigma_{1l}, \sigma_{1r}, \mu_2, \sigma_{2l}, \sigma_{2r}, \mu_{\rm CF}, \sigma_{l,\rm CF}, \sigma_{r,\rm CF}, f, f_{\rm CF})) = \\ f_{\rm CF} f bG(x, \mu_1 + \mu_{\rm CF}, \sigma_{1l}\sigma_{l,\rm CF}, \sigma_{1r}\sigma_{r,\rm CF}) & + (1 - f_{\rm CF} f) bG(x, \mu_2 + \mu_{\rm CF}, \sigma_{2l}\sigma_{l,\rm CF}, \sigma_{2r}\sigma_{r,\rm CF}). \end{aligned} \tag{E.7}$$

where the factors $\mu_{\rm CF}, \sigma_{l,r\rm CF}$ and $f_{\rm CF}$ allow to correct a difference of the data to the MC and are determined by a control sample A. If no correction has to be applied $\mu_{\rm CF} = 0$ and $\sigma_{\rm CF} = f_{\rm CF} = 1$. We restrict $f > 0.5$ and refere to the first bG as "main" and to the second as "tail".

Similar, a tripple-bifurcated-width Gaussian is defined as

$$\begin{aligned} tbG(x) \equiv & tbG(x, \mu_1, \sigma_{1l}, \sigma_{1r}, \mu_2, \sigma_{2l}, \sigma_{2r}, f_2, \mu_3, \sigma_{3l}, \sigma_{3r}, f_3, \mu_{\rm CF}, \sigma_{l,\rm CF}, \sigma_{r,\rm CF}, f_{\rm CF}) = \\ (1 - f_{\rm CF} f_2 - f_3) bG(x, \mu_1 + \mu_{\rm CF}, \sigma_{1l}\sigma_{l,\rm CF}, \sigma_{1r}\sigma_{r,\rm CF}) & + (f_{\rm CF} f_2) bG(x, \mu_2 + \mu_{\rm CF}, \sigma_{2l}\sigma_{l,\rm CF}, \sigma_{2r}\sigma_{r,\rm CF}) + \\ & f_3 bG(x, \mu_3 + \mu_{\rm CF}, \sigma_{3l}\sigma_{l,\rm CF}, \sigma_{3r}\sigma_{r,\rm CF}). \end{aligned} \tag{E.8}$$

A set of n Gaussians with $1 \le k \le n$ is given by

$$dbG(x)^k \equiv dbG(x, \mu_1^k, \sigma_{1l}^k, \sigma_{1r}^k, \mu_2^k, \sigma_{2l}^k, \sigma_{2r}^k, \mu_{\rm CF}^k, \sigma_{l,\rm CF}^k, \sigma_{r,\rm CF}^k, f^k, f_{\rm CF}). \tag{E.9}$$

Tripple-bifurcated Gaussians in each r-bin are defined in a similar way.

Acknowledgements

I thank my supervisor, Christian Kiesling, for his motivation, his advice and for giving me the opportunity to work in his group.
I thank our postdocs, especially Jeremy Dalseno for showing me the fun of data analysis and also Luigi Li Gioi for proof reading this work.
I thank my second supervisor Thomas Kuhr for reading this manuscript.
Further I thank the Max-Planck Institut, in particular the Belle group (Hans-Günther, Martin, Veronika, Felix, Fernando and Manfred) as well as the colleagues from ILC (Frank Simon) and H1 (Vladimir Chekelian) and all others that I forgot or left already.
I also acknowledge the Belle collaboration, especially my chair referee Peter Krizan and the ICPV group.
Last but not least I like to thank my family, especially my mum, and of course Stanzerl for giving me great support.

Danke

List of Figures

List of Tables

Bibliography

[1] NASA/WMAP Science Team. http://wmap.gsfc.nasa.gov/media/. Updated: Friday, 12-10-2010.

[2] A.D. Sakharov. JETP Lett. **5**, 24 (1967).

[3] J. H. Christenson, J. W. Cronin, V. L. Fitch, and R. Turlay. "Evidence for the 2π Decay of the $K2$ Meson'. Phy. Rev. Lett. 13, 138-140 (1964).

[4] M. Kobayashi and T. Maskawa. Prog. Theor. Phys. **49**, 652 (1973).

[5] The Belle Collaboration P.Vanhoefer *et al.* Study of $B^0 \to \rho^0\rho^0$, implications for the CKM angle ϕ_2 and search for other B0 decay modes with a four-pion final state. Phys. Rev. D **89**, 072008 (2014).

[6] Wikipedia: The Free Encyclopedia. www.wikipedia.org. Wikimedia Foundation, Inc. 22 July 2004. Web. 10 Aug. (2004).

[7] Emmy Nother. "Invariant Variation Problems". Gott.Nachr.1918:235-257, (1918); Transp.Theory Statist.Phys.1:186-207 (1971).

[8] L.-F. Cheng, T.-P.; Li. "Gauge Theory of Elementary Particle Physics". Oxford University Press. ISBN 0-19-851961-3. (1983).

[9] A. Hey I. Aitchison. Gauge Theories In Particle Physics, Vol. 1. IOP Publishing Ltd (2003).

[10] S. Glashow. Partial-symmetries of weak interactions. Nuclear Physics **22** 4, (1961).

[11] S. Weinberg. A Model of Leptons. Phys. Rev. Lett. **19**, 1264 (1967).

[12] Wikipedia. Gamma matrices. http://en.wikipedia.org/wiki/Diracmatrix (2.8.2010).

[13] P. Higgs. Boken Symmetries and the Masses of Gauge Bosons. Phys. Rev. Lett. **13** 16, (1964).

[14] R. Brout F. Englert. Broken Symmetry and the Mass of Gauge Vector Mesons. Phys. Rev. Lett. **13** 16, (1964).

[15] Hagen Guralnik and Kibble. Global Conservation Laws and Massless Particles. Phys. Rev. Lett. **13** 16, (1964).

[16] F.J. Hasert *et al.* "Observation of neutrino-like interactions without muon or electron in the Gargamelle neutrino experiment". Phys. Lett. **46B**, 138 (1973).

[17] Bennett G. W. *et al.* "Final report of the E821 muon anomalous magnetic moment measurement at BNL'. Phy. Rev. D **73**, 072003 (2006).

[18] B. Malaescu C.Z. Yuan Z. Zhang M. Davier, A. Hoecker. "Reevaluation of the hadronic contribution to the muon magnetic anomaly using new $e^+e^- \rightarrow \pi^+\pi^-$ cross section data from BABAR'. Eur.Phys.J.C**66**:1-9 (2010).

[19] The ATLAS Collaboration. Observation of a new particle in the search for the Standard Model Higgs boson with the ATLAS detector at the LHC. Phys. Rev. Lett. B**716**, (2012).

[20] The CMS Collaboration. Observation of a new boson at a mass of 125 GeV with the CMS experiment at the LHC. Phys. Rev. Lett. B**716**, (2012).

[21] B. Pontecorvo. Mesonium and anti-mesonium. Soviet Physics JETP **6** 429 (1957).

[22] M. Nakagawa Z. Maki and S. Sakata. Remarks on the Unified Model of Elementary Particles. Prog. Theor. Phys. **28** (5): 870-880, (1962).

[23] B. T. Cleveland *et al.* Measurement of the Solar Electron Neutrino Flux with the Homestake Chlorine Detector. ApJ **496**: 505 (1998).

[24] The Super-Kamiokande Collaboration. http://www-sk.icrr.u-tokyo.ac.jp/sk/index-e.html.

[25] The ICECUBE Collaboration. http://icecube.wisc.edu/.

[26] Joel R. Primack. Dark Matter and Structure Formation in the Universe. Proceedings of the Jerusalem Winter School 1996, arXiv:astro-ph/9707285v2.

[27] F. Zwicky. Die Rotverschiebung von extragalaktischen Nebeln. Helvetica Physica Acta **6**: 110127 (1933).

[28] Sehgal M. S. Madhavacheril, N and T. R. Slatyer. Current dark matter annihilation constraints from CMB and low-redshift data. Phys. Rev. D **89**, 103508 (2014).

[29] Johan Richard Richard Massey, Thomas Kitching. The dark matter of gravitational lensing. Rep. Prog. Phys. **73**, 086901 (2010).

[30] The CRESST Collaboration. http://www.cresst.de/.

[31] The XENON Collaboration. http://xenon.astro.columbia.edu/.

[32] Y. Kawamura. Gauge hierarchy problem, supersymmetry and fermionic symmetry. arXiv:1311.2365 [hep-ph] (2013).

[33] L. Randall and R. Sundrum. Large Mass Hierarchy from a Small Extra Dimension. Phys. Rev. Lett. **83**, 3370 (1999).

[34] Steven Weinberg. The Quantum Theory of Fields Vol. 3. Cambridge University Press, ISBN 978-11-396-4419-8 (2000).

[35] C. A. Baker *et al.* Improved Experimental Limit on the Electric Dipole Moment of the Neutron. Phys. Rev. Lett. **97**, 131801 (2006).

[36] R. D. Peccei and Helen R. Quinn. CP Conservation in the Presence of Pseudoparticles. Phys. Rev. Lett. **38**, 1440 (1977).

[37] H. Zinkernagel S. E. Rugh. The Quantum Vacuum and the Cosmological Constant Problem. Studies in History and Philosophy of Modern Physics, **vol. 33**, 663-705 (2002).

[38] Michio Kaku. Introduction to Superstrings and M-Theory. Springer, 2. Eddition, ISBN 978-0-387-98589-3 (1999).

[39] C. Wu *et al.* "Experimental Test of Parity Conservation in Beta Decay". Phys. Rev. **105** (1957).

[40] M.Goldhaber *et al.* "Helicity of Neutrinos". Phys. Rev. **109**, Nr.3 (1975).

[41] H.Rollnik G. Grawert, G.Lders. "The TCP Theorem and its Applications'. Fortschr. d. Phys. **7**, 291 (1959).

[42] T. Higuchi *et al.* (The Belle Collaboration). Search for time-dependent CPT violation in hadronic and semileptonic B decays. Phys. Rev. D **85**, 071105 (2012).

[43] T. Inami and C.S. Lim. Prog. Theor. Phys. **65**, 297 (1981).

[44] F. Gilman and M. Wise. Phys. Rev. D **27**, 1128 (1983).

[45] K.A. Olive *et al.* (Particle Data Group). Chin. Phys. C **38**, 090001 (2014).

[46] N. Cabibbo. Phys. Rev. Lett. **8**, 214 (1964).

[47] L.Maiani S.L. Glashow, J.Illiopoulos. "Weak Interactions with Lepton-Hadron Symmetry'. Phys. Rev. D2. (1970).

[48] I.I. Bigi and A.I. Sanda. CP Violation. Cambridge Monographs on Particle Physics and Cosmology, 2nd edition (2009).

[49] L. Wolfenstein. Phys. Rev. Lett. **51**, 1945 (1983).

[50] J. Charles *et al.* CKMfitter Group. Eur. Phys. J. C **41**, 1-131 (2005).

[51] E.P.Wigner V.F.Weisskopf. *Z.Phys.* **63** 54 (1930); *Z.Phys.* **65** 18 (1930).

[52] E.A. Paschos. ELECTROWEAK THEORY. Cambridge University Press, (2007).

[53] B. Aubert *et al.* BABAR Collaboration. Phys. Rev. Lett. **87**, 091801 (2001).

[54] I. Adachi *et al.* Belle Collaboration. Phys. Rev. Lett. **108**, 171802 (2012).

[55] Guido Bell. "Higher order QCD corrections in exclusive charmless B decays'. PHD thesis, arXiv:07053133v2[hep-ph] (2008).

[56] M. Neubert. B Decays and the Heavy-Quark Expansion. Adv.Ser.Direct.High Energy Phys. **15**, 239, (1998).

[57] G.Buchalla. Heavy Quark Theory. CERN-TH/2002-018, arXiv:hep-ph/0202092 (2002).

[58] George Sterman John C. Collins, Davison E. Soper. Factorization of Hard Processes in QCD. Adv.Ser.Direct.High Energy Phys. **5**,1, (1988).

[59] M.Neubert C.T.Sachradja M.Beneke, G. Buchalla. QCD Factorisation for exclusive non-leptonic B-meson decays: General arguments and the case of heavy-light final states. arXiv:hep-ph/0006124v1 (2000).

[60] M.Neubert C.T.Sachradja M.Beneke, G. Buchalla. QCD Factorisation in B→piK,pipi Decays and Extraction of Wolfenstein Parameters. arXiv:hep-ph/0104110v1 (2001).

[61] M. Jamin A.J. Buras and P.H. Weisz. Nucl. Phys. B **347**, 491 (1990).

[62] J.S. Hagelin. Nucl. Phys. B **193**, 123 (1981).

[63] A.Soni M.Bander, D.Silverman. Phys.Rev.Lett.**43** 242 (1979).

[64] The Heavy Flavor Averaging Group Y. Amhis *et al.* Averages of b-hadron, c-hadron, and τ-lepton properties as of summer 2014. arXiv:1412.7515 [hep-ex] (2014).

[65] D.Yang M.Beneke, J.Rohrer. Branching fractions, polarisation and asymmetries of $B \to VV$ decays. Nucl.Phys.B **774**:64-101 (2007).

[66] I. Dunietz *et al.* Phys. Rev. D **43**, 2193 (1993).

[67] V.Pilipp G.Bell. "$B^- \to \pi^-\pi^0/\rho^-\rho^0$ to NNLO in QCD factorization'. Phys.Rev.D**80**, 054024, (2009).

[68] A.L. Kagan. Polarization in B→VV Decays. Phys. Lett. B **601**, 151-163, (2004).

[69] D.Yang M.Beneke, J.Rohrer. Enhanced electroweak penguin amplitude in B → VV decays. Phys.Rev.Lett. **96**:141801, (2006).

[70] C.Lu Y.Li. Branching Ratio and Polarization of $B \to \rho(\omega)\rho(\omega)$ Decays in Perturbative QCD Approach. Phys.Rev.D**73**: 014024, (2006).

[71] J.L.Rosner M.Gronau. Strong and weak phases from time-dependent measurements of $B \to \pi\pi$. Phy. Rev. D, **65** 093012, (2002).

[72] M. Beneke and S. Jaeger. Spectator scattering at NLO in non-leptonic B decays: Leading penguin amplitudes. arXiv:hep-ph/0610322v2, (2007).

[73] M. Beneke and M. Neubert. QCD factorization for B→PP and B→PV decays. Nucl. Phys. B **675**, 333 (2003).

[74] A. L. Kagan. Polarization in B→VV Decays. Phys. Lett. B **601**, 151 (2004).

[75] A.J.Schwartz A.Somov. Measurement of the branching fraction, polarization, and CP asymmetry for $B \to \rho^+\rho^-$ decays, and determination of the CKM phase phi2. Phys.Rev.Lett. **96**, 171801,(2006).

[76] A.J.Schwartz A.Somov. Improved measurement of CP-violating parameters in $B \to \rho^+\rho^-$. Phys. Rev. D **76**, 011104, (2007).

[77] J. Zhang *et al.* Observation of $B \to \rho^\pm\rho^0$. Phys.Rev.Lett. **91**, 221801, (2003).

[78] B. Aubert *et al.* BABAR Collaboration. Study of B→ $\rho^+\rho^-$ Decays and Constraints on the ckm Angle alpha. Phys.Rev.Lett.**96**, 171801 (2006).

[79] B. Aubert *et al.* BABAR Collaboration. Measurement of the Branching Fraction, Polarisation, and CP Asymmetries in $B \to \rho^0\rho^0$ Decay, and Implications for the CKM Angle α. Phys.Rev.Lett **98**, 111801 (2007).

[80] B. Aubert *et al.* BABAR Collaboration. Improved Measurement of $B \to \rho^\pm\rho^0$ and Determination of the Quark-Mixing Phase Angle alpha. Phys.Rev.Lett. **102** ,141802, (2009).

[81] National Laboratory for High Energy Physics. "KEKB B-factory Design Report". Phys. Rev. D **43**, 2193 (1993).

[82] The Belle Collaboration T. Abe *et al.* Compensation of the Crossing Angle with Crab Cavities at KEKB. Conf.Proc.C070625:27, arXiv:0706.3248, (2007).

[83] Belle Collaboration A. Abashian *et al.* Nucl. Instr. and Meth. A **479**, 117 (2002), also see detector section in J. Brodzicka *et al.*, Prog. Theor. Exp. Phys. **2012**, 04D001 (2012).

[84] V. Chabaud *et al.* Nucl. Instr. and Meth. A **368**, 314 (1996).

[85] G. Taylor. The Belle silicon vertex detector: present performance and upgrade plans . Nucl. Instr. and Meth. in Phys. Res. A **501**, 22-31 (2003).

[86] Y.Ohnishi. Track Parametrization. Belle Note #148.

[87] S.Nagayama. PANTHER - User's Manual; Rfefernce Manual; Primer. Belle Note #130, 131, 132.

[88] B. Casey. "HadronB". Belle Note #390.

[89] The Belle Collab. "The Number of B events in the Belle Hadronic Skims". http://belle.kek.jp/secured/nbb/nbb.html.

[90] J. Tanaka. "Kinematic Fitting". Belle Note #194.

[91] H. Tajima *et al.* Nucl. Instr. and Meth. A **533**, 370 (2004).

[92] H. Kakuno *et al.* Nucl. Instr. and Meth. A **533**, 516 (2004).

[93] T. Browder and S. Swain. "Beam Energy Calibration". Belle Note #567.

[94] M.Nakao. slides from BAS Oct 2009.

[95] R. A. Fisher. Annals of Human Genetics **7**, 179 (1936).

[96] G. C. Fox and S. Wolfram. Phys. Rev. Lett. **41**, 1581 (1978).

[97] D. J. Lange. *Nucl. Instrum. Methods Phys. Res. Sect.* **A462**, 152 (2001).

[98] R. Brune *et al.* "GEANT 3.21". CERN DD/EE/84-1 (1984).

[99] F.James. "MINUIT, Function Minimization and Error Analysis". CERN-D-506, CERN-D506 (1994).

[100] F.James. Minuit Tutorial on Function Minimazation, CERN 72-21 (1972).

[101] S. Nishida. "Study of Kaon and Pion Identification Using Inclusive D^* Sample". Belle Note #779.

[102] The Belle Collaboration S. Ryu *et al.* "Measurements of Branching Fractions of τ Lepton Decays with one or more K^0_S". Phys. Rev. D **89**, 072009 (2014).

[103] S. Ryu. "Study of π^0 efficiency using $\tau \to \pi^-\pi^0\nu$ events". Belle Note #1224.

[104] Samuel; Balakrishnan N Johnson, Norman L.; Kotz. Continuous univariate distributions. Vol. 1. Second edition. Wiley Series in Probability and Mathematical Statistics: Applied Probability and Statistics. John Wiley & Sons, Inc., New York, xxii+756 pp. ISBN: 0-471-58495-9, (1994).

[105] T. Higuchi. Vertexing,. Belle internal document, Belle Analysis School (2009).

[106] K. Miyabayashi. Measurement of time-dependent CP violation in $B^0 \to c\bar{c}K^0$ decays with 772M $B\bar{B}$. Belle Note #1149.

[107] O. Long *et al.* Phys. Rev. D **68**, 034010 (2003).

[108] K. Hara. Study of tag side interference effect in time-dependent CP violating asymmetry measurement. Belle Note # 872.

[109] G. Majumder. "Uncertainty of track finding efficiency with embedded tracks". Belle Note #641.

[110] P. Koppenburg. "A Measurement of the Track Finding Efficiency Using Partially Reconstructed D^* Decays". Belle Note #621.

[111] D.London M.Gronau. Isospin Analysis of CP Asymmetries in B Decays. Phy. Rev. Lett. **65** 27, (1990).

[112] The Belle Collaboration K.Abe *et al.* Observation of $b^0 \to \pi^0\pi^0$. Phys.Rev.Lett. **94**, 181803 (2005).

[113] The BABAR Collaboration J.P.Lees *et al.* Measurement of CP Asymmetries and Branching Fractions in Charmless Two-Body B-Meson Decays to Pions and Kaons. Phys.Rev. D**87** 5, 052009 (2013).

[114] The Belle Collaboration J.Dalseno *et al.* Measurement of the CP Violation Parameters in $b^0 \to \pi^+\pi^-$ Decays. .Phys. Rev. D **88**, 092003 (2013).

[115] The Belle Collaboration Y.Y.Duh *et al.* Measurements of Branching Fractions and Direct CP Asymmetries for B →Kpi, B→pipi and B → KK Decays. Phys.Rev. D**87** 031103 (2013).

[116] B. Aubert *et al.* BABAR Collaboration. Improved Measurements of the Branching Fractions for $b^0 \to \pi^+\pi^-$ and $b^0 \to k^\pm\pi^\mp$ and a Search for $b^0 \to k^+k^-$. Phys.Rev. D**75**, 012008 (2007).

[117] S. Jaeger M. Beneke, M.Gronau and M. Spranger. A precise determination of α using $B^0 \to \rho^+\rho^-$ and $B^+ \to k^*\rho^+$. Phys.Lett. B**638**: 68-73, (2006).

[118] The Belle Collaboration J. Zhang *et al.* Measurements of Branching Fraction and Polarization in $B^+ \to \rho^+ K^{*0}$ Decays. arXiv:hep-ex/0505039, (2005).

[119] C.Kraus M.Bartsch, G.Buchalla. $B \to V_L V_L$ Decays at Next-to-Leading Order in QCD. LMU-ASC 43/08, arXiv:hep-ph/08100249v1 (2008).

[120] The Belle Collaboration K.Trabelsi *et al.* Study of direct CP in charmed B decays and measurement of the CKM angle gamma at Belle. Proceedings of CKM 2012, the 7th International Workshop on the CKM Unitarity Triangle, arXiv:1301.2033 [hep-ex], (2012).

[121] A. J. Bevan *et al.* The Physics of the B Factories. Eur.Phys.J C**74**, 3026 (2014).

[122] CLEO Collaboration M.S. Alam *et al.* Exclusive hadronic B decays to charm and charmonium final states. Phys.Rev. D**50** 43-68 (1994).